1993

Stratigraphy And Geochemistry Of Neoproterozoic Iron Formation, South Australia

Kathryn Louise Neale

STRATIGRAPHY AND GEOCHEMISTRY OF NEOPROTEROZOIC IRON FORMATION, SOUTH AUSTRALIA

by
Kathryn Louise Neale
Department of Geology

Submitted in partial fulfilment
of the requirements for the degree of
Doctor of Philosophy

Faculty of Graduate Studies
The University of Western Ontario
London, Ontario
November, 1992

ISBN 0-315-81329-6

ABSTRACT

In the southern portion of the Adelaide geosyncline, the Neoproterozoic Yudnamutana Subgroup unconformably overlies older Neoproterozoic sedimentary rocks of the Adelaidean succession. The Braemar and Holowilena iron formations occur locally in the glacigenic Yudnamutana Subgroup at the transitional contact between the basal Pualco Tillite and overlying Benda Siltstone formations, or stratigraphic equivalents elsewhere.

Magnetite and/or hematite and absence of chert typify these iron formations which are associated with diamictite, subarkosic wacke, siltstone and minor carbonate. Diamictites are typically unstratified and have iron-poor (<20 wt.% Fe_2O_3) or iron-rich (>30 wt.% Fe_2O_3) matrices. The former commonly occur below the iron formation-bearing intervals whereas the latter are intercalated with them. Low Fe_2O_3 diamictites are typified by plutonic and/or extra-basinal clasts and are considered to represent glacimarine deposition from iceberg melt-out during waning glacial conditions. The high Fe_2O_3 diamictites locally exhibit evidence of ice grounding (glacial striae) and typically contain intraformational clasts incorporated by sediment gravity processes. Subarkosic Fe wackes and Fe siltstones generally contain 5 - 20% iron oxide minerals. Sharp-based, coarse-tail graded beds of subarkosic Fe wacke formed due to rapid deposition from high-concentration turbidity currents, whereas intervals of unstratified, ungraded and structureless subarkosic Fe wacke are considered to reflect deposition from density-modified grain flows.

Iron formation exhibits similar major, trace and rare earth element distributions to recent submarine hydrothermal deposits. The chemical composition of associated clastic rocks suggests that iron formation represents deposition of chemically precipitated iron oxides during periods of lessened clastic input. The iron-rich fluids probably emanated from extensional, fault-controlled conduits related to rifting during evolution of the Adelaide geosyncline.

ACKNOWLEDGMENTS

This project resulted from the common interest of Prof. Grant Young and the author in these Neoproterozoic iron formations. The study could not have taken place without the generous financial support of Grant Young for the travel to Australia, expenses involved in the field and analytical work and the preparation of this thesis. I wish to thank Grant for this support and opportunity, for discussions on the geology of the Adelaide geosyncline and accommodation in Adelaide. Access to his computing facilities, which contributed greatly to the form and appearance of this volume, was graciously granted and gratefully appreciated. His patience and the "free-hand" that he let me have during the course of this study are also to be acknowledged. Melissa Postian provided capable field assistance, friendship and good humour during several bath-less weeks, desert flash floods and midnight 'roo hunters. I owe her for her meticulous sampling of diamictite matrices; she owes me for killing the snake. *Mo* Young is thanked for her keen eye and timely recognition of glacial striae at Razorback Ridge. Her efforts to remove mouldy bread from our diet during field visits in the Flinders Ranges was especially appreciated.

There are many to thank for my stay in Adelaide and field work in South Australia. Dr. Vic Gostin and other faculty and administrators at the University of Adelaide provided office and lab facilities, affordable field transport and helpful geological and logistical discussions. Specific thanks are warranted to: Phil McDuie for assistance with sample preparation and AA analyses; John Stanley for the XRF analyses; Geoff Trevalyan and Wayne Mussared for being "thinnie" techs supreme; Rick Barrett for developing and printing several field photographs; Sherry Proferes for quickly sending several map legends upon request. Everyone at the Uni made me feel welcome, but in particular, the comraderie enjoyed with fellow Canadian, *Commander*

Bob Morrison, GI John(son of GI Joe) and other grad student cohorts for Friday night *pie floater* expeditions to downtown Adelaide was memorable. Wolfgang Preiss, Ron Coats and Bryan Forbes of the Geological Survey of South Australia contributed to my understanding of the geology of the Adelaide geosyncline, both through conversation and the published results of their own studies in the Flinders Ranges. I am grateful to the many station managers and residents who allowed us access to their properties. I especially thank Gary and Judy Shephard of Manunda station for their generous hospitality and kindness during our initial weeks in the field.

Technical assistance at U.W.O. was expertly provided by Charlie (Tsai-Way) Wu (XRF and REE analyses), Dave Kingston and Bob Barnett (microprobe lab), Peter Burns and Yuchi Cheng (XRD analyses), John Forth, Walt Harley and Gord Wood (thin section preparation), and Ian Craig, Keith Dewing, Barry Larson and Peter Stewart (photography). Launa Fuller is particularly thanked for the loan of her computer during a critical stage of thesis preparation. Bill Stone, Brigitte Gagné and Rob Rainbird provided valuable discussions on a myriad of topics during my time in London. Their friendship and that of other grad students at U.W.O. is appreciated. Malcolm Norris is thanked for promptly forwarding pertinent Australian literature upon request.

My spousal equivalent, Peter, who also is my best friend, provided moral, technical and geological support during this study and I have benefitted from his counsel and cooking (despite my present appearance). Merci!

TABLE OF CONTENTS

Chapter IV

MINERAL CHEMISTRY

Chapter V

RARE EARTH ELEMENT CHEMISTRY

Chapter VI

DISCUSSION & INTERPRETATION

Chapter VII

SUMMARY & CONCLUSIONS

Appendix A

Appendix B

Geochemical Methodology

Appendix C

Electron Microprobe Analyses

Appendix D

Electron Microprobe Analyses

Appendix E

Electron Microprobe Analyses

Appendix F

Electron Microprobe Analyses

LIST OF PHOTOGRAPHIC PLATES

LIST OF TABLES

LIST OF FIGURES

Chapter I

INTRODUCTION

General Statement

There is a global association of Neoproterozoic iron formation with sedimentary rocks of glacial origin (Young, 1976; Yeo, 1984, 1986; Maynard, 1991). Yeo (1984) focused on the most notable example of iron formation related to glacigenic deposits (i.e., Rapitan Group, northwestern Canada), and included geochemical analyses from, and discussion of, similar sequences from the western United States (Graff, 1985; Miller, 1985), South America (Hoppe *et al.*, 1987; Urban *et al.*, 1992), South West Africa (Breitkopf, 1988; Bühn *et al.*, 1992) and South Australia (Coats and Preiss, 1987). Extensive iron formation also occurs, together with intercalated mafic volcanic rocks, in the Sinian glacimarine sequences of south China (Jiafu *et al.*, 1987).

This thesis examines the Neoproterozoic iron formations in the Adelaide "geosyncline" of South Australia (Trendall, 1973). These are known as the 'Braemar' and 'Holowilena' iron formations (IFs) based on the areas from which they were originally described (Figure 1.1). These IFs occur at approximately the same stratigraphic level within the Yudnamutana Subgroup, and are considered to be equivalent units (e.g., Preiss, 1989). The present study focuses on stratigraphy, mineralogy and geochemistry in an attempt to determine the genesis of the Braemar and Holowilena IFs and associated clastic rocks.

Nomenclature

As established later in Chapter 1 (see p. 12), the Braemar and Holowilena IFs occur as facies variants of two formations; the Pualco "Tillite" and the Benda "Siltstone" so that neither iron formation is a formal stratigraphic unit. Coats and Preiss (1987) partially resolved this problem by introducing the informal name "Braemar ironstone

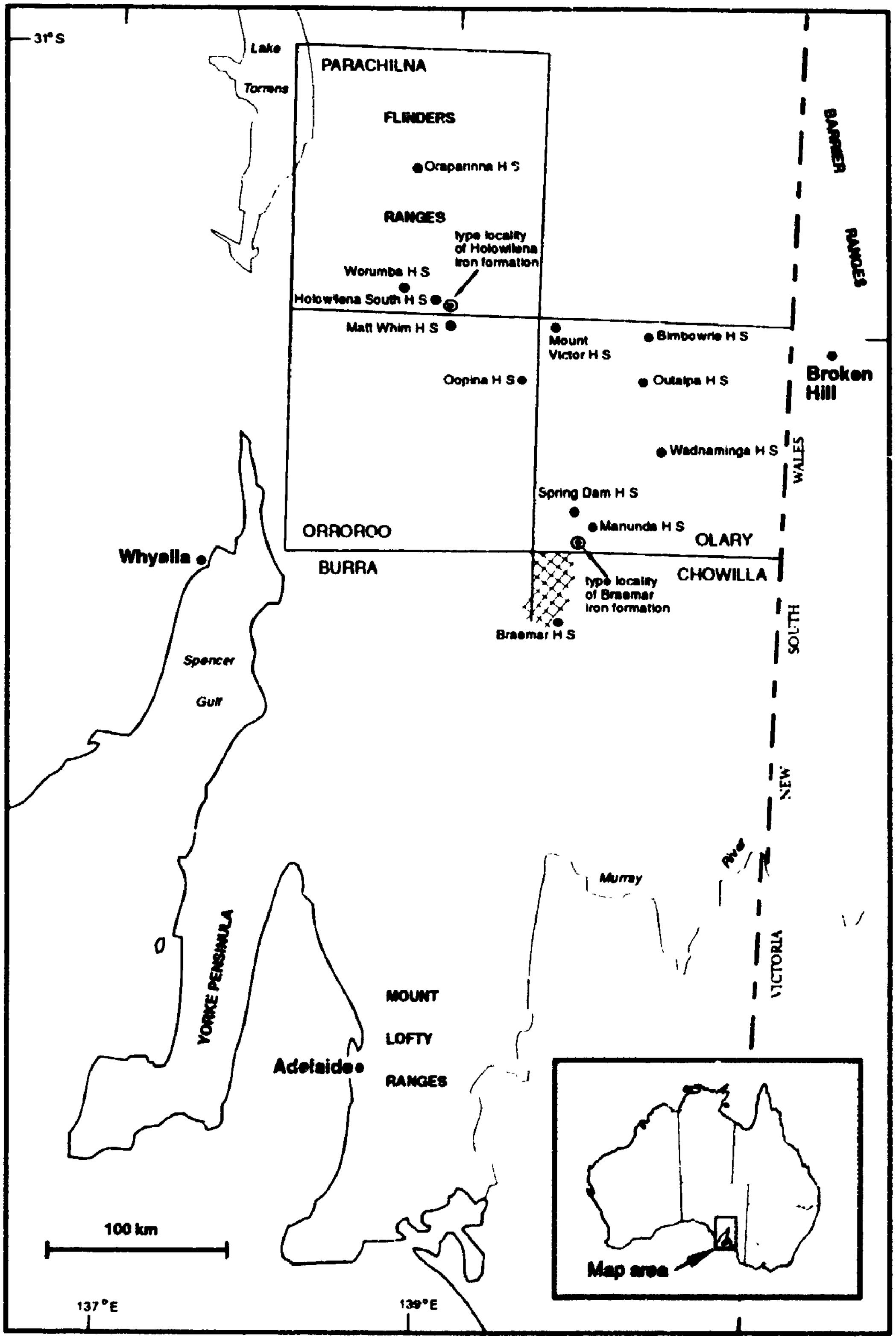

Figure 1.1 Map of a portion of South Australia showing outlines of the 1:250,000 scale map sheets within which the study was focused. Investigations on BURRA and CHOWILLA were restricted to the hatched area. The type localities of the Braemar and Holowilena iron formations are shown, as are the homestead (H.S.) locations of stations referred to in the text.

facies", but they retained the formal name "Holowilena Ironstone". In this study, the informal names "Braemar iron formation" and "Holowilena iron formation" are utilized.

Location

The field area occurs in the central and southern Flinders Ranges of South Australia (Figure 1.1). The Braemar and Holowilena IFs are mainly developed within the boundaries of 1:250,000 scale map sheets PARACHILNA, ORROROO and OLARY, but occurrences of Braemar IF on northeast BURRA and northwest CHOWILLA were also examined (Figure 1.1). All of the stratigraphic sections measured in this thesis were located on road-accessible tracts of land leased for sheep grazing (i.e., stations). Station homestead locations are denoted on Figure 1.1. Since these station names are referred to throughout the text, they are italicized for easy recognition (e.g., *Braemar*).

Components of the Adelaide geosyncline

Initial use of the term "Adelaide Geosyncline" was by W.R. Browne (Mawson and Sprigg, 1950, p. 70). Intrinsic to Sprigg's (1952) model of the geosyncline as a continental terrace (i.e., passive margin sequence) was the delineation of zones which he termed the "Gawler cratonic nucleus", "Stuart stable shelf" and "Torrens fault zone". The Stuart Shelf is a subhorizontal platform along the east-central periphery of the early Proterozoic Gawler nucleus (Gawler Craton). Detritus from the uplifted Gawler Craton (west) was thought to have been transported across the Stuart Shelf and down-faulted scarps of the Torrens fault zone (middle) to depositional sites within the geosyncline (east; Figure 1.2). Sprigg (1952) regarded the meridional "Torrens lineament" (western boundary of Torrens fault zone) as the western limit of the geosyncline, and Dickinson and Sprigg (1953, p. 432) suggested the MacDonald shear fault as the eastern limit. The MacDonald Fault defines one margin of the "Willyama Complex" (Mawson, 1912; Campana, 1958, p. 5). The Willyama Complex (Willyama Block) is a basement terrane

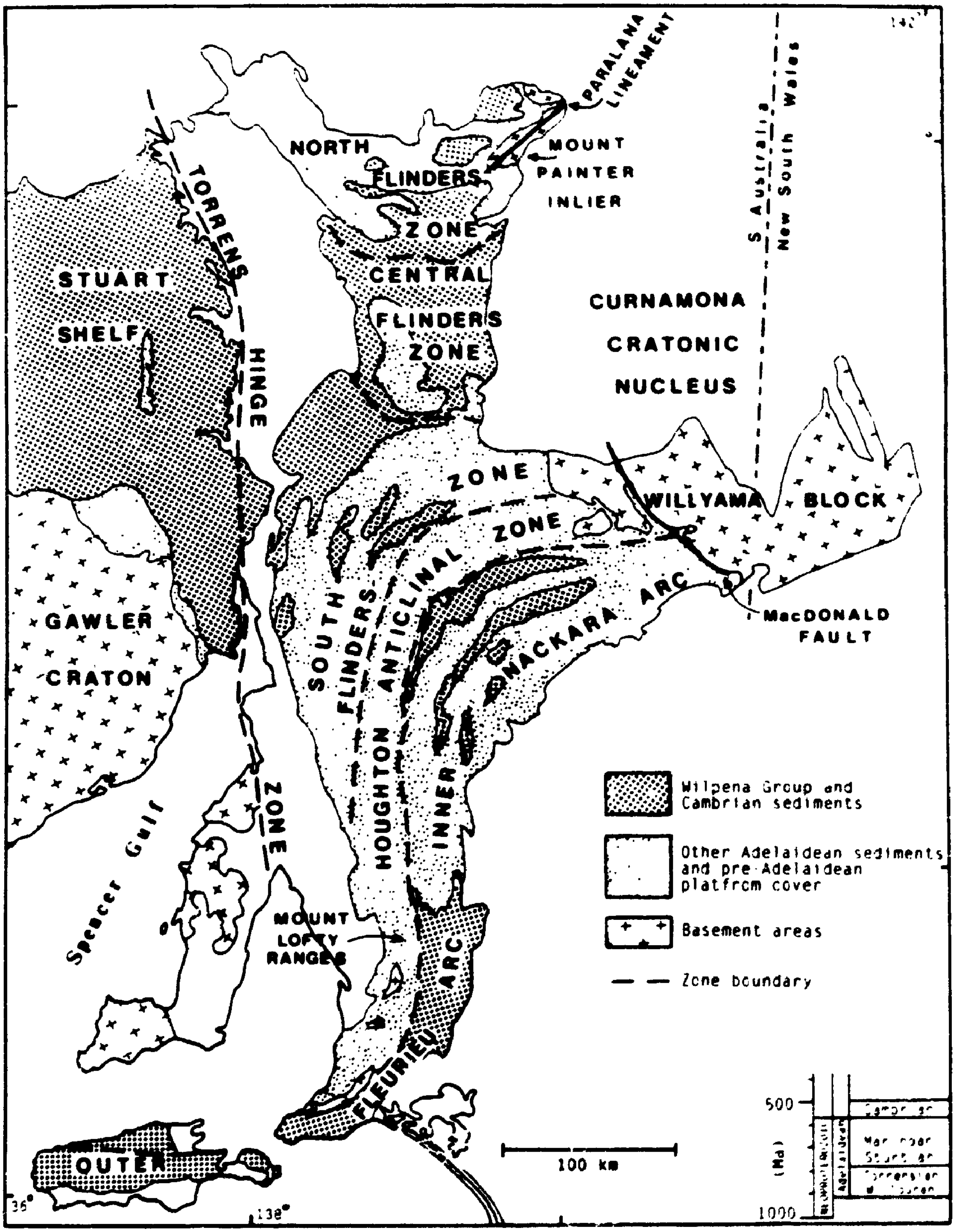

Figure 1.2 Tectonic components of the Adelaide geosyncline and peripheral regions, together with the general geology of the geosyncline, Torrens Hinge Zone and Stuart Shelf (after Rutland *et al.*, 1981 and Preiss, 1989). Neoproterozoic chronostratigraphic units utilized in South Australia are included (lower right).

comparable in age to the Gawler Craton, but it was not considered an important provenance area until midway through the evolution of the geosyncline (i.e., early Sturtian, Sprigg, 1952, p. 153; Preiss, 1987a, p. 265). The unexposed northward extension of the Willyama Block is the "Curnamona Cratonic Nucleus" (Thomson, 1970; Figure 1.2) the northwest margin of which is bounded by the "Paralana Lineament" (Dickinson and Sprigg, 1953, p. 431). This lineament is considered to have been an active fault zone in the early Willouran (Coats, 1962; Thomson, 1969a, p. 50), allowing clastic detritus from the then-emergent Curnamona Cratonic Nucleus to be transported into the northeast part of the geosyncline (Preiss and Forbes, 1987, p. 16; Preiss, 1987b, p. 318; Rutland *et al.*, 1981, p. 346).

The Neoproterozoic (Adelaidean) and Cambrian sedimentary rocks of the geosyncline were regionally folded during the Cambro-Ordovician Delamerian Orogeny. Tectonic terranes within the fold belt have been outlined by Rutland *et al.* (1981). The least deformed is the Central Flinders Zone (Figure 1.2) which is a region of broad, basin and dome folds, faulted along both eastern and western margins. The North and South Flinders zones are typified by arcuate, generally upright folds, whereas the Houghton Zone is a broad anticline which mimics underlying basement trends and provides a link between basement inliers of the Adelaide region (Mount Lofty Ranges) and those of the Olary area (Willyama Block) (Rutland *et al.*, p. 330). The Nackara and Fleurieu arcs comprise the Mount Lofty-Olary arc of Campana (1958) which is characterized by a strongly sigmoidal pattern of folding.

The Central Flinders Zone has been compared with domains to the west (Gawler Craton-Stuart Shelf) and east (Curnamona Cratonic Nucleus) in two respects: (1) stratigraphically comparable late Adelaidean and Cambrian sediments occur both on the Stuart Shelf and in the Central Flinders Zone (Daily, p. 14-15 in Thomson *et al.*, 1976) as well as in the subsurface near Lake Frome (Daily and Forbes, 1969, p. 23), and (2) within the geosyncline, the Central Flinders Zone is least affected by the

Delamerian deformation. This low degree of deformation is comparable to that of near-horizontal sequences of the Stuart Shelf and Lake Frome which are considered to have been protected by pressure shadows created by the Gawler Craton and Curnamona Cratonic Nucleus respectively. Both the Gawler Craton (Rutland *et al.*, 1981, p. 350; Preiss, 1987c, p. 35) and the Curnamona Nucleus (Preiss and Forbes, 1987, p. 16) were largely unaffected by Delamerian folding. The cover rocks of the Central Flinders Zone are probably also underlain by basement rocks comparable to those of the Gawler Craton and Curnamona Nucleus, so that the Central Flinders Zone may be considered "intracratonic" during geosynclinal evolution (Rutland *et al.*, 1981, p. 346).

Scheibner (1973), Rutland (1973), Preiss (1979) and von der Borch (1980) considered the Central Flinders Zone to be an aulacogen. These authors suggest that rifting took place between the Gawler Craton in the west and the Curnamona Nucleus/Willyama Block in the east. Von der Borch (1980) argued that the Central and Northern Flinders zones represent a failed rift whereas the Mount Lofty-Olary fold belt (combination of South Flinders, Houghton, Nackara and Fleurieu zones, Figure 1.2) represents a rifted passive continental margin. Rutland *et al.* (1981, p. 346), however, maintained that because the Central Flinders Zone links lithologically similar depositional sequences to the north and south, it can hardly be considered as an aulacogen. Preiss discussed the aulacogen analogy in greater detail (1987a, p. 256-257) and suggested the presence of an intracratonic "Central Flinders High" by early Torrensian time (1987b, p. 334).

Adelaidean deposition within the geosyncline and on the Stuart Shelf was divided into pre- and syn-rift Callana and Burra Groups, and post-rift Umberatana and Wilpena Groups by Preiss (1983a; Figure 1.3a). At the base of the Callana Group, fluvial clastics (Paralana Quartzite) and shallow marine carbonates (Wywyana Formation) sit adjacent to the syndepositional Paralana Fault in the Northern Flinders Zone (Thomson, 1969a, p. 50-53; Rutland *et al.*, 1981, p. 335; Figure 1.2). Initial rifting

Figure 1.3A Comparison of Neoproterozoic sedimentary rocks of the Adelaide geosyncline (1) with the Mesozoic-Cenozoic Atlantic continental margin of the United States (2). Note that the region delineated in (1) has been palinspastically expanded by 30% perpendicular to fold axes (from Preiss, 1983a).

Figure 1.3B Representative stratigraphic column for the Umberatana and Wilpena Group rocks of the North Flinders Zone (Figure 1.2). Glacial periods of Sturtian (G1a & G1b) and Marinoan (G2, G3?) age are denoted (after Young, 1992a).

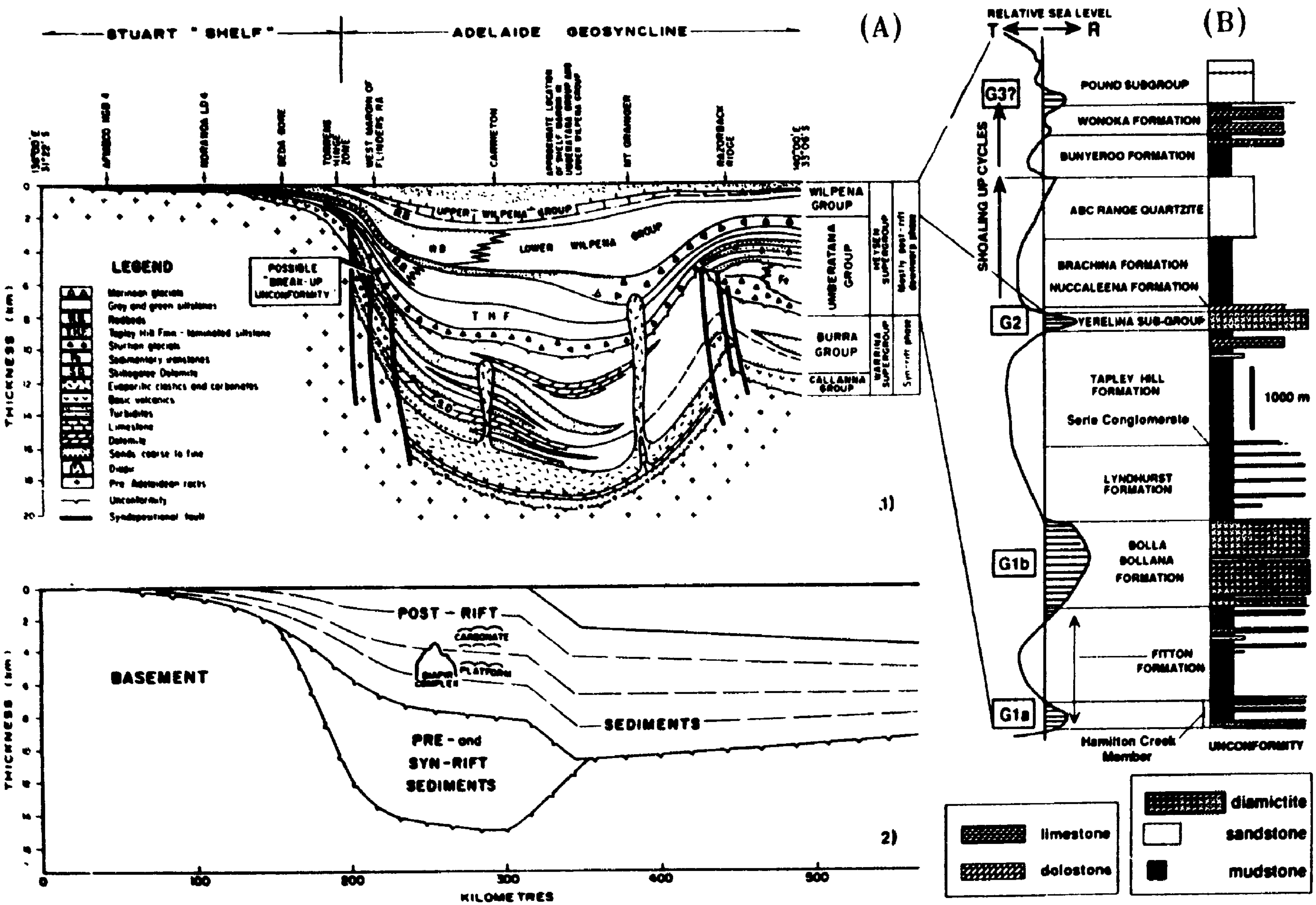
(A)
STUART "SHELF"
ADELAIDE GEOSYNCLINE
POSSIBLE "BREAK-UP" UNCONFORMITY
LEGEND
UPPER "WILPENA" GROUP
LOWER WILPENA GROUP
T H F
WILPENA GROUP
UMBERATANA GROUP
BURRA GROUP
CALLANNA GROUP
HEYSEN SUPERGROUP
WARRINA SUPERGROUP
THICKNESS (km)
1)
POST - RIFT
CARBONATE
PLATFORM
BASEMENT
PRE - and SYN-RIFT SEDIMENTS
SEDIMENTS
2)
KILOMETRES
(B)
RELATIVE SEA LEVEL
T R
SHOALING UP CYCLES
G3?
G2
G1b
G1a
POUND SUBGROUP
WONOKA FORMATION
BUNYEROO FORMATION
ABC RANGE QUARTZITE
BRACHINA FORMATION
NUCCALEENA FORMATION
YERELINA SUB-GROUP
TAPLEY HILL FORMATION
Serle Conglomerate
LYNDHURST FORMATION
BOLLA BOLLANA FORMATION
FITTON FORMATION
Hamilton Creek Member
UNCONFORMITY
1000 m
limestone
dolostone
diamictite
sandstone
mudstone

was marked by flood basalts preserved both on the Stuart Shelf and in the geosyncline, whereas the succeeding carbonate, clastic and evaporitic sequences are known only within the geosyncline (Rutland *et al.*, 1981, p. 344). Active faulting along the "Torrens Hinge Zone" (Thomson, 1969b, p. 25) provided detritus to the overlying Burra Group (Preiss, 1983a, p. 13; Parker, 1983, p. 24), which is particularly well preserved in the South Flinders Zone ("labile shelf" of Rutland *et al.*, 1981, p. 330) yet absent from the Stuart Shelf. The Burra Group consists of at least four transgressive (marine) and regressive (deltaic) cycles, all of which commence with marginal marine platform carbonates. A subsequent hiatus included block-faulting, erosion (Preiss, 1983a, p. 14) and a first phase of diapirism (Coats, 1965, p. 99), which all contributed to the unconformity betweeen the Burra and Umberatana Groups (Figure 1.3a). The basal Umberatana Group has been subdivided into two distinct glacial phases, both of Sturtian age (Mawson, 1949; Coats, 1973) but the presence of an unconformity between the two phases has been questioned (Murrell *et al.*, 1977; Circosta *et al.*, 1983; Young and Gostin, 1988, 1990, 1991). Although the lower Umberatana is restricted to the geosyncline proper, the post-glacial marine transgression and resultant deposits (Tapley Hill Formation) extended onto the Stuart Shelf (Figure 1.3a). A subsequent regression preceded deposition of the Marinoan age glacials (Yerelina Subgroup, Figure 1.3b) in the upper Umberatana Group. The Wilpena Group consists of three transgressive (shallow marine) and regressive (intertidal) cycles, the youngest of which contains soft-bodied metazoans of the Ediacara assemblage (Pound Subgroup; Figure 1.3b). Glacigenic rocks have recently been recognized in the upper Wilpena Group (Dibona, 1991), and may represent a third episode of glaciation (G3? of Figure 1.3b).

Framework of the Yudnamutana Subgroup

Introduction. The Yudnamutana Subgroup of the basal Umberatana Group (Figure 1.4), as first defined by Coats (in Thomson *et al.*, 1964), was restricted to the

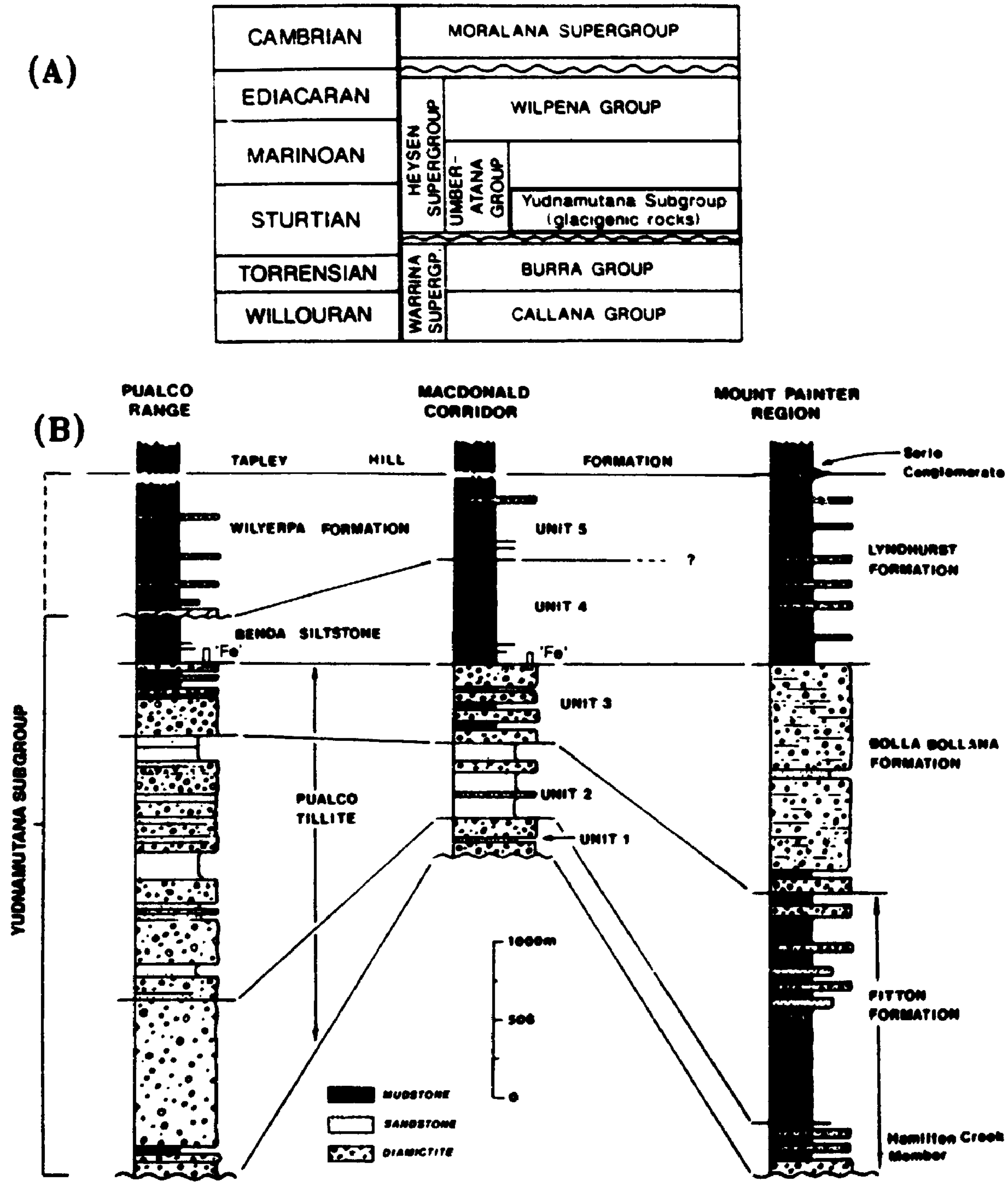

Figure 1.4 (A) Summary chart to show position of the Yudnamutana Subgroup relative to other Neoproterozoic and Cambrian units of the Adelaide geosyncline (after Preiss, 1989). (B) Generalized sections (by G.M. Young) for the Yudnamutana Subgroup from the Pualco Range (near Pualco West, Figure 1.5), the MacDonald Corridor (near MacDonald Fault, Figure 1.2) and the Mount Painter region (Young and Gostin, 1989a; Figure 1.2). Iron-bearing intervals occur in measured sections from OLARY (Figure 1.1), however, 'Fe' is in quotes because iron-rich (>15% Fe) diamictites were not observed at the exact locations of these sections, but do occur near the Pualco Tillite and Benda Siltstone contact in less well exposed sections elsewhere on OLARY.

Mount Painter area of the northern Flinders Ranges (Figure 1.2) and considered to represent the 'entire' Sturtian glacial sequence. Coats (1973) revised the Yudnamutana Subgroup to include only the 'first' of two major Sturtian glaciations, but the necessity of a division is debatable (Murrell *et al.*, 1977, Coats and Forbes, 1977; Young and Gostin, 1989a, 1989b, 1990). The area encompassed by the Subgroup was extended southward to include time-equivalent units recognized in the central Flinders and Olary regions (Dalgarno and Johnson, 1965; Whitten, 1966a). The proposed correlations between north and south were as follows:

Lyndhurst Formation ≈ Benda Siltstone (Forbes, 1970; Coats, 1981,p. 541)
Bolla Bollana Formation ≈ Pualco Tillite (Forbes and Cooper, 1976, p. 4)
Fitton Formation

However, Young (1992a; Figure 1.4b) recently suggested that:

Lyndhurst Formation ≈ Benda Siltstone and Wilyerpa Formation
Bolla Bollana Formation ≈ upper Pualco Tillite
Fitton Formation ≈ lower and middle Pualco Tillite

Obvious differences in the Yudnamutana Subgroup are a greater thickness at the type locality, 5,000 m at Mount Painter *versus* 3755 m in the OLARY region (Figure 1.1) to the south, and an absence of associated iron formations in the Yudnamutana Subgroup of the northern Flinders. The Yudnamutana Subgroup is tentatively considered to be older than 750 ± 50 Ma (Rb-Sr whole rock age from shale of the overlying Tapley Hill Formation, Webb *et al.*, 1983) and younger that 802 ± 10 Ma (U-Pb zircon age from dacite of the Callana Group, Fanning *et al.*, 1986).

Pualco Tillite. In its type section at Pualco West (southwest OLARY, Figure 1.5), the Pualco Tillite shows a low angle discordance to Belair Subgroup siltstones of the underlying Burra Group (Forbes and Cooper, 1976). The Torrensian-Sturtian boundary was placed at the base of the Belair "group" by Mawson and Sprigg (1950, p. 71) because they considered a unit of arkose-shale couplets (above the Mitcham Quartzite of the Belair 'group') to resemble glacial varves. Coats (1967) observed mudcracks and ripple marks in the same unit. These features are typical of the Burra and Callana Groups throughout the Adelaide Geosyncline, but are generally absent from units of the Yudnamutana Subgroup. Hence, Coats (1967) suggested that the Belair 'group' (renamed Belair Subgroup by Binks, 1968) be considered part of the shallow water environment, typical of the Burra Group.

At Pualco West, where the Pualco Tillite attains a thickness of 3,300 m, the dominant unit is a generally unstratified diamictite comprised of granule- to pebble-size clasts set in a sand- to silt-size matrix (Forbes and Cooper, 1976; Figure 1.4b). Recognized clast types include quartz, quartzite, siltstone, carbonate, pegmatite and granitoids. The common matrix components are quartz, calcite and dolomite. Units interfingering with the diamictite include parallel- and ripple cross-laminated quartzite, laminated siltstone and carbonate. Interpretations proposed for the Pualco Tillite are "deposition from a grounded ice sheet under shallow marine conditions" (Forbes and Cooper, 1976, p. 4) or glacimarine deposition from a floating ice sheet (Coats, 1981; Coats and Preiss, 1987).

Benda Siltstone. The Pualco Tillite is conformably overlain by the Benda Siltstone, the type locality of which is located 6.5 km southwest of *Wadnaminga* (central OLARY, Figure 1.1) in the Benda Range (Forbes, 1970). The Benda Siltstone here consists of a 260 m-thick sequence dominated by grey-green laminated calcareous siltstones. Quartzite and dolomite are locally interstratified. The Benda Siltstone is characterized by a lack of lonestones; an observation which has lent support to interpretations of this formation as having been deposited during a marine interglacial period (Coats, 1981) or in a basinal marine setting with limited glacial influence (Preiss *et al* in Rutland *et al.*, 1981; Coats and Preiss, 1987).

With respect to facies variants of the Pualco Tillite and Benda Siltstone, Dalgarno and Johnson (1965) proposed that the Holowilena Ironstone[1] was laterally

---

[1] The formal names of "Braemar Iron Formation" and "Holowilena Ironstone" are used in this introductory chapter when quoting the work of previous geologists. The informal names of "Braemar iron formation" and "Holowilena iron formation" suggested earlier are used elsewhere.

equivalent to "massive boulder tillites" (Pualco Tillite Equivalent of Circosta, 1978). Forbes (1970) and Forbes and Cooper (1976, p. 2) suggested that the Braemar Iron Formation[1] "represents local deposition of iron oxide in the upper Pualco Tillite and lower Benda Siltstone"; an observation which implies hematite-magnetite precipitation during an interglacial period (Coats, 1981, p. 541) or during waning glacial (Pualco) and interglacial (Benda) stages (Whitten, 1966a; Circosta, 1978; Preiss *et al.* in Rutland *et al.*, 1981; Coats and Preiss, 1987).

Previous Work on the Braemar and Holowilena iron formations

According to excerpts from Mawson's August 1930 personal notes (as interpreted by Whitten, 1966a, p. 88; Whitten, 1970, p. 5), he named the Braemar Iron Formation[1] as such because of its common development on Braemar Station (northwest CHOWILLA). Mawson (1930) studied Razorback Ridge and Pualco Range (now both part of Spring Dam Station, southwest OLARY, Figure 1.1) as well as the Levi Range and Ironback Range (now both part of Braemar Station, Figure 1.5). For the Pualco Range traverse, Whitten (1966a, 1970) cited Mawson's documentation of quartzite-bearing schistose tillites conformably overlain by "fluvial and glacio-fluvial beds with iron sands" (August 28, 1930). Neoproterozoic iron formation comparable to IF exposures on *Braemar*, have been described throughout OLARY (Jack, 1922; Thomas, 1950; Miles, 1951; Campana and King, 1958; Pitt, 1971).

Razorback Ridge was chosen as the type locality for the Braemar Iron Formation[1] by Mirams (1962; Table 1.1a) because it is there that the unit is "best developed" (Mirams, 1962, p. 7; Whitten, 1966a, p. 89). The type section occurs on Tiverton Station (now part of *Spring Dam*, Figure 1.1) so that the name 'Braemar' is now inappropriate but was retained by Mirams (1962, p. 22) because of its established usage. The present study also showed that the exposure and development of the iron formation at Razorback Ridge surpass those to the south on Braemar Station (e.g.,

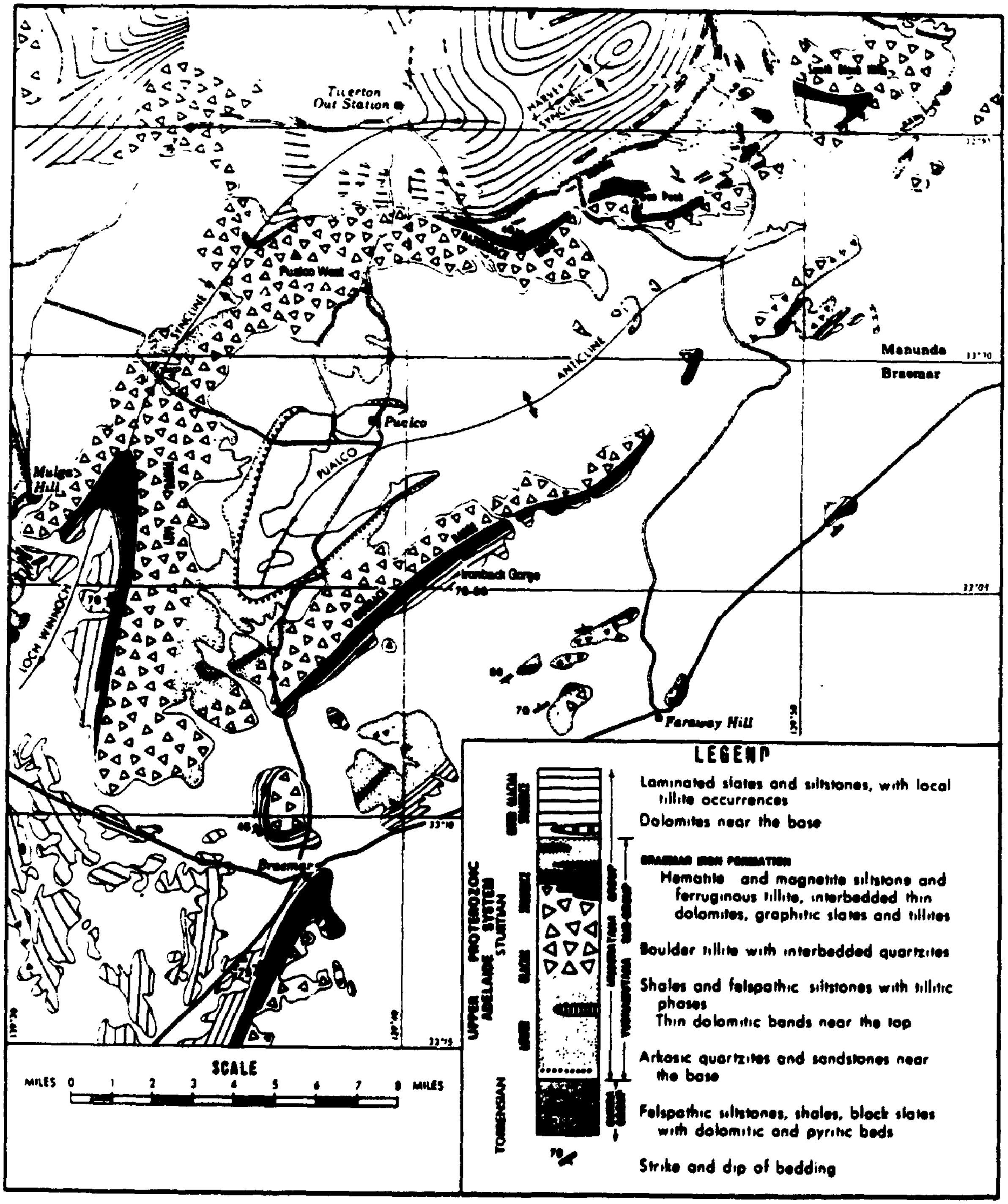

Figure 1.5 General geology of the area surrounding the Braemar station homestead (from Whitten, 1970). See text for discussion.

Table 1.1 (A) Formal definition of Braemar Iron Formation[1] in the type locality at Razorback Ridge (from Mirams, 1962). (B) Petrographic summary (from Whitten, 1970) of bedded and tillitic iron formation from Razorback Ridge (Figure 1.5).

Figure 1.6 (A) Stratigraphic column of the Braemar Iron Formation[1] (from Whitten, 1970). (B) Schematic representation (after Cann *et al.*, 1981) of a faulted contact between diapiric breccia and Holowilena Ironstone[1] on *Oraparinna* (Figure 1.1).

(A) Formal Definition of Type Locality

Name	Braemar Iron Formation
Locality of Section	Vanunda One Mile geological sheet. Lat. 32 deg. 57 min. 30S Long. 139 deg. 42 min. 42E (17 miles on bearing 016 deg. from Braemar Homestead).
Direction of Section	South to north across Razorback Ridge. South of Teatree well.
Lithology	Banded hematite-siltstone or shale and interbedded glacio-marine shales with occasional lenses of tillite with a ferruginous matrix.
Thickness	Lenticular, 2500 feet maximum development at Razorback Ridge.
Age	Upper Proterozoic (Adelaide System, Sturtian Series.)

(B) BRAEMAR IRON FORMATION

COMPONENT	BEDDED ORE	TILLITIC ORE
Iron Oxide (percent)	40 - 50	30 - 35
Clastics (percent)	60 - 50	70 - 65
Analysis of Iron Oxides		
Magnetite Euhedra		
Volume (percent)	45 - 50	40 - 55
Grain Size (microns)	12 - 80	15 - 90
Martite (percent)	0 - 5	0 - 5
Fine Hematite		
Volume (percent)	55 - 50	60 - 45
Grain Size (microns)	2 - 15	2 - 15
Iron Oxides recalculated to Original Ore (Average components)		
Magnetite Euhedra		
Volume (percent)	20 - 22½	13 - 18
Fine Hematite		
Volume (percent)	25 - 22½	19½ - 14½
Hematite / Magnetite Ratio	1.0 - 1.25	.78 - 1.5

(A)

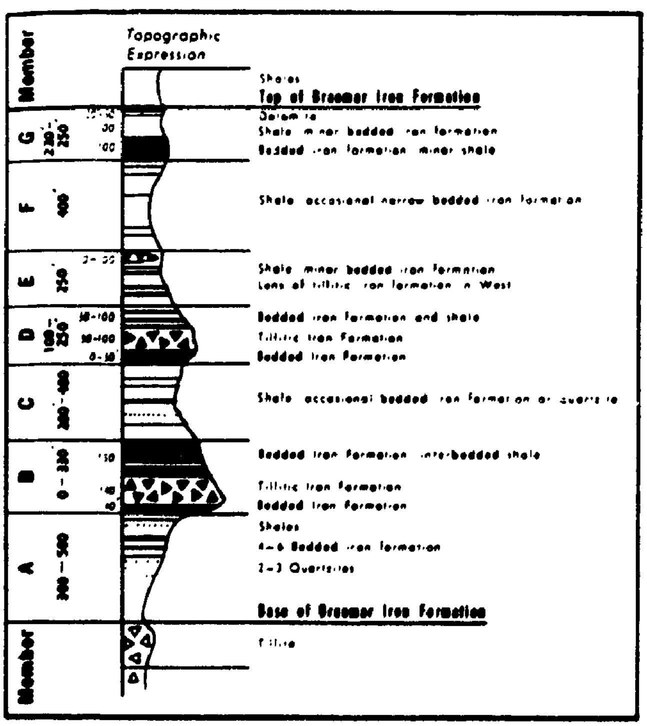

(B)

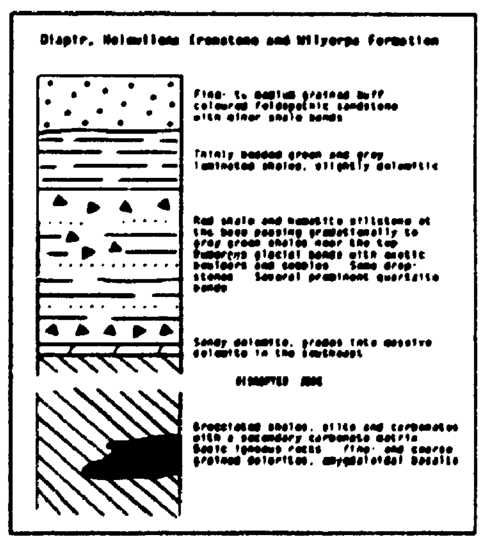

southward from Windmill Bore in the Levi Range, Ironback Gorge, and the area south-southwest of the homestead, Figure 1.5).

Four localities of Braemar Iron Formation[1] examined by Whitten (1966a) include: (1) Razorback Ridge, (2) Ironback Range, (3) Levi Range, and (4) the Braemar Homestead area (Figure 1.5). Within the district delineated by these localities, Whitten (1966a, p. 90) described "the Braemar Iron Formation as a ferruginous tillitic formation (having bedded and carbonate variants) which forms the top of the main glacial development." (1) At Razorback Ridge, the iron formation conformably overlies "tillite" (Pualco Formation of Forbes and Cooper, 1976) and dips northerly at about 30° (Whitten, 1966a, p. 92). He observed (p. 94) that the unstratified tillitic and bedded ironstone, together with the intervening shale, quartzite and dolomite are lenticular. He therefore assigned ranges rather than absolute numbers for the thicknesses of "members" A - G (Figure 1.6a; Whitten, 1966a, 1970). (2) In the Ironback Creek section, Whitten (1966a, p. 94) described 6400' of quartzite-bearing boulder tillites overlain by sandstone beds which form the "ironback" of the associated range. These rocks are overlain by the Braemar Iron Formation[1] which is about 1800' thick in the Ironback Range. Whitten found that 550' of the 1800' total is well exposed in Ironback Gorge and consists of bedded iron formation (15%), tillitic iron formation (20%) and graphitic shale (65%). (3) For the Levi Range, Whitten (1966a, p. 95) inferred that the underlying sequence was similar to that at Razorback and Ironback, but that the iron formation proper was essentially an impure dolomite. Tillitic horizons are rare. (4) In the area south-southwest of the Braemar Homestead, Whitten (1966a, p. 96) observed an "overlapping relationship of the Braemar with the underlying boulder tillite". The ferruginous portion of this boulder tillite together with the more abundant stratified iron formation, varies in thickness from 1000' (south) to 2500' (north).

Whitten's (1966a, p. 100) detailed macroscopic description of the tillitic iron formation revealed that:

i) stratification is generally absent except for some concentrations of clasts, defining 3" thick layers;

ii) clasts range from 0.5" to 4' but are most abundant in the 1 - 6" range;

iii) common clast types are limestone, quartzite, arkose and minor granite;

iv) rare striated clasts are present.

Microscopic examination of the matrix revealed a mineral assemblage comparable to the bedded iron formation, including magnetite (± martite), hematite, quartz, Al-rich chlorite, dolomite, sericite, tourmaline, apatite and feldspar (± limonite- or goethite-after-hematite). Two microscopic differences between the tillitic and bedded iron formations are:

i) a greater percentage of clastic grains in the tillitic IF;

ii) greater variability of the hematite:magnetite ratio in the tillitic IF (Table 1.1b; Whitten, 1966a, 1970).

Other microscopic observations of the bedded iron formation included:

i) a transitional contact from a dominantly chemical magnetite (euhedral) layer to subrounded magnetite grains with minor clastic material to isolated rounded magnetite and abundant clastic debris;

ii) ripple marks and microfaults.

Whitten (1966a, p. 106; 1970, p. 23) observed that rounded magnetite grains were rare and he considered the magnetite euhedra to have formed from colloids in close proximity to the site of deposition. Whitten (1966a, p. 143; 1970, p. 28) interpreted:

> "...the Braemar Iron Formation as having formed by the chemical precipitation of iron oxides in a cold sea into which glaciers were delivering rock flour, transported by meltwater, and erratics dropped from melting icebergs."

It would appear that he was undecided as to what percentage of the magnetite had been reworked, because Whitten (1970, p. 28) stated that:

> "Near the source area, where tillitic ore may be expected to be deposited, turbulent meltwater reworked the finer-grained material and obliterated bedding.

> The finer particles - **magnetite euhedra, hematite** and fine clastics were picked up and transported further away and were redeposited in shallow seas under conditions more closely resembling normal sedimentation."

Whitten (1970, p. 28) summarized this by saying that:

> "...bedded ore horizons were deposited within a few miles of the tillitic horizons from which the hematite and magnetite had been winnowed."

Whitten also suggested that the tillite-poor, hematite-dominated Holowilena Ironstone[1] (on PARACHILNA and ORROROO, Figure 1.1) was the distal equivalent of the Braemar. He considered that coarse and fine clastics, magnetite and hematite would have been deposited in proximal (tillitic) and intermediate (bedded) environments. Very fine hematite and very fine clastic fractions (i.e., the Holowilena Ironstone[1]) were deposited at distance from the source (Whitten, 1966b, p. 11; Whitten, 1970, p. 29).

The term "Holowilena Ironstone" was first proposed by Thomson *et al.* (1964) because the rock unit is well developed on what was then Holowilena Station (subsequently referred to as *Mattawarrangala* and now known as Holowilena South Station, Figure 1.1). The unit was described as "...hematite siltstone with lenses of dolomite and greywacke with glacial erratics" (p. 17).

Dalgarno and Johnson (1965) outlined four areas on PARACHILNA where the Holowilena Ironstone[1] is exposed and selected a type section at the third locality, the northern flank of the Yednalue Anticline on *Holowilena South* (Figure 1.1). At the type locality Dalgarno and Johnson (1965) compared the sequence of massive boulder tillites through laterally equivalent Holowilena Ironstone[1] overlain by Wilyerpa Quartzite with that described by Campana and King (1958) at *Mount Victor* (northwest OLARY, Figure 1.1). The lower tillite horizon has been interpreted as glacimarine (Dalgarno and Johnson, 1965) and/or subaqueous (Campana and King, 1958) whereas the upper quartzite was considered to be fluvio-glacial, hence "...the Holowilena Ironstone illustrates a transition between a probable glacio-marine environment and a transgressive morainic phase at the margin of a half graben." (Dalgarno and Johnson, 1965, p. 3). The interpretation put forth for these two northerly areas (Figure 1.1) contrasts with that suggested for the type locale of the Braemar Iron Formation[1], namely, that the "...described sequence is essentially glaciomarine both below and above the iron formation." (Whitten, 1966a, p. 107; Whitten, 1970, p. 24).

On the ORROROO 1:250,000 map sheet, exposures of hematite and magnetite siltstone correlated with the Holowilena Ironstone[1] (Binks, 1971, p. 32) are restricted to:

i) an area approximately 5 km south-southwest of *Matt Whim* on the eastern limb of the Yednalue Anticline;

ii) north of *Oopina* where an east-west-trending band lies within the nose and northern limb of the Waukaringa Anticline (Figure 1.1).

At the second locality, W. B. Robinson in Binks (1968, 1971) recorded a sequence of:

Appila Tillite
Holowilena Ironstone[1] - generally a facies variant of Yudnamutana Subgroup
Appila Tillite - *revised to Pualco Tillite (Y.S.) by Preiss (1983b)*
Kadlunga Slate - laminated green-grey siltstone of the Belair Subgroup

The renaming of the lower unit of Appila Tillite to Pualco Tillite (Preiss, 1983b) was probably prompted by Forbes and Cooper (1976, p. 2) who stated that:

> "The Pualco Tillite was previously referred to as Appila Tillite but is now considered, as the result of work by R.P. Coats, to be older than the Appila."

Binks (1971, p. 33) equates the upper unit of true Appila Tillite with the Wilyerpa Formation of Dalgarno and Johnson (1965, 1966) on PARACHILNA because both are underlain by correlative units of Holowilena Ironstone[1].

In the vicinity of the type section of the Holowilena Ironstone[1] (PARACHILNA, Figure 1.1), Circosta (1978) studied the stratigraphy of the upper Burra Group and lower to middle Umberatana Group (Figure 1.4a). His work included measurement of five stratigraphic sections between Back Creek (west) and Holowilena Creek (east, Figure A.4). The main findings of his thesis were summarized by Circosta *et al.* (1983). These authors observed that the Sturtian glacigenic rocks unconformably overlie dolomite, siltstones and quartzites of the Burra Group. The glacigenic rocks thicken from approximately 30 m (west) to 1600 m (east) over a lateral distance of 12 km. Paleocurrent data suggested that sediment was derived mainly from the west. Circosta (1978) indicated that the Pualco Tillite was glacigenic and that the conformably overlying Holowilena Ironstone[1] was lacustrine. An episode of basinward faulting is considered to have preceded glacimarine deposition of the Wilyerpa Formation. However, the presence of a sandstone dyke (90 m long) sourced in the Pualco Tillite and passing upwards into the Wilyerpa Formation, suggests that the pre-Wilyerpa faulting occurred over a short enough time span to permit the Pualco sediments to remain unlithified. Link and Gostin (1981, p. 367) also supported the idea of a lacustrine origin for the Holowilena Ironstone[1] in the type locality (above), whereas Coats (1981, p. 541) and Coats and Preiss (1987, p. 137 & 140) extended this interpretation to include 'all' exposures of 'both' the Braemar and Holowilena Ironstones[1].

The Holowilena Ironstone[1] lies in close proximity to breccia bodies of Callana Group lithologies at two regions (PARACHILNA, localities 1 and 2 of Dalgarno and Johnson, 1965). These are the Oraparinna Diapir (Cann, 1985) and the Worumba Diapir (Preiss, 1983c, 1985). At *Oraparinna* (Figure 1.1), the breccia/hematitic siltstone contacts examined by Cann *et al.* (1981), Cann (1985) and Coats and Preiss (1987) occur between Bakker Creek and Lizard Ridge along a strike line which commences at, and runs southeast from, the ruins of the Oraparinna Asbestos Mine through to Panta Well (Figure A.2). Near the Bakker Creek/'Dropstone Creek' junction, N.M. Lemon (in Cann, 1985) described a faulted contact where rocks of the Holowilena Ironstone[1] and Wilyerpa Formation have been up-thrusted along the periphery of the breccia (Figure 1.6b). Up-section of the fault-bounded sandy dolomite, Cann (1985, site 18) detailed a tillite which contains granite, gneiss and pegmatite clasts (up to 1 m in size) set in an iron oxide-bearing sand- to silt-size matrix. This tillite and associated laminated hematitic siltstone-shale couplets and quartzite bands, here comprises the Holowilena Ironstone[1]. Cann (1985) regarded the tillite as a melt-out deposit below an ice shelf and interpreted the hematitic rhythmites as glacilacustrine varves.

Early Paleozoic Deformation

Regional deformation of the Adelaide Geosyncline was associated with granitoid intrusions in the southern region (495 - 504 Ma, Preiss, 1987d, p. 252) coincident with cessation of Late Cambrian sedimentation. The intrusive event and folding which affected the entire geosyncline was named "Delamerian Orogeny" by Thomson (1969c, p. 98), though previous workers had recognized the occurrence of early Paleozoic tectonism (e.g., Dickinson and Sprigg, 1953, p. 448; Glaessner and Parkin, 1958). Subsequent studies of the regional structure include those of Thomson *et al.* (1976), Rutland *et al.* (1981), Parker (1983), Preiss (1987a), Clarke and Powell (1989), and Jenkins (1989).

This study focuses on areas where the Braemar and Holowilena iron formations are exposed; namely OLARY, ORROROO, PARACHILNA (Figure 1.1) and the northern perimeter of BURRA and CHOWILLA (hatched on Figure 1.1). Berry *et al.* (1978) recognized five deformational stages within the Willyama Block (basement) of OLARY. The younger two events affected rocks of the Adelaidean System. These authors considered northwest-trending folds, commonly located between basement inliers (Figure 1.7, locality 1) as first stage Delamerian folds (F_4) and the more widespread east-northeast-trending folds as second stage (F_5). Campana and King (1958, p. 40) previously recorded these fold patterns but with a reverse order of folding. They interpreted northwest-trending sedimentary rocks between basement inliers at locality 2 (Figure 1.7) to be "sleeves" infolded with the basement during compression. Sprigg (1954) regarded this distribution of sedimentary rocks as the result of early basement faulting (e.g., MacDonald Fault). Sprigg's interpretation of the MacDonald Fault as a syndepositional fault scarp was reiterated by Preiss (1987b, p. 360; Figure 1.8).

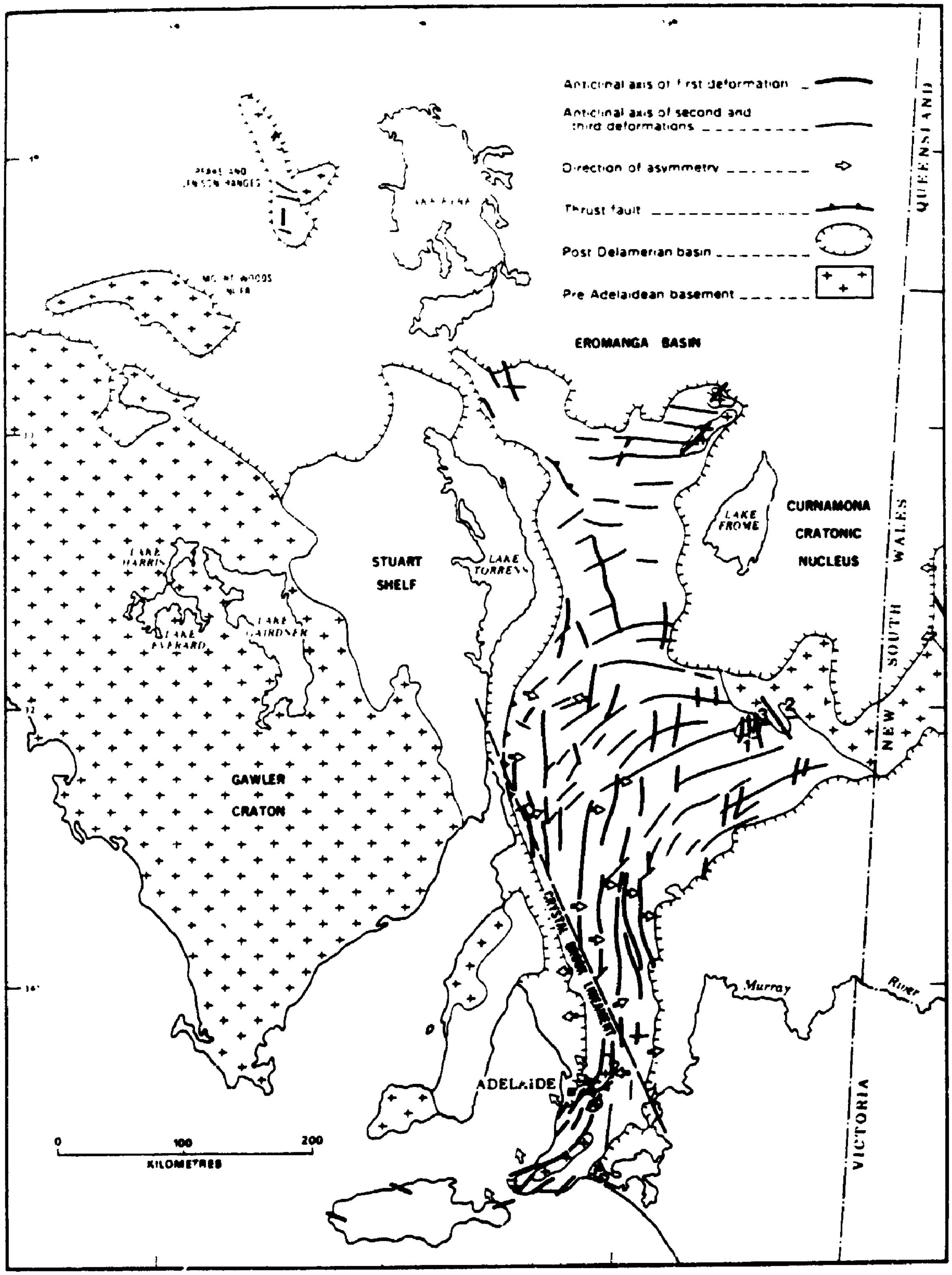

Figure 1.7 Distribution of anticlinal axes produced by Delamerian folding and the outline of the Crystal Brook Lineament (modified from Preiss, 1989). Localities 1, 2 and 3 are referred to in the text.

Figure 1.8 Suggested paleogeography (from Preiss, 1987b) of the Adelaide geosyncline during deposition of the Pualco Tillite. In the OLARY region (Figure 1.1), the Curnamona Cratonic Nucleus was considered to be the main site of ice accumulation. The adjoining MacDonald Fault was regarded as an active fault scarp which facilitated transfer of glacially-entrained debris to depocentres in the southern basin. Numbers 1, 2 and 3 refer to the zones of iron formation deposition examined in the present study and outlined on Figure 2.1.

S-3 PUALCO TIME

OLDER STURTIAN GLACIAL MAXIMUM

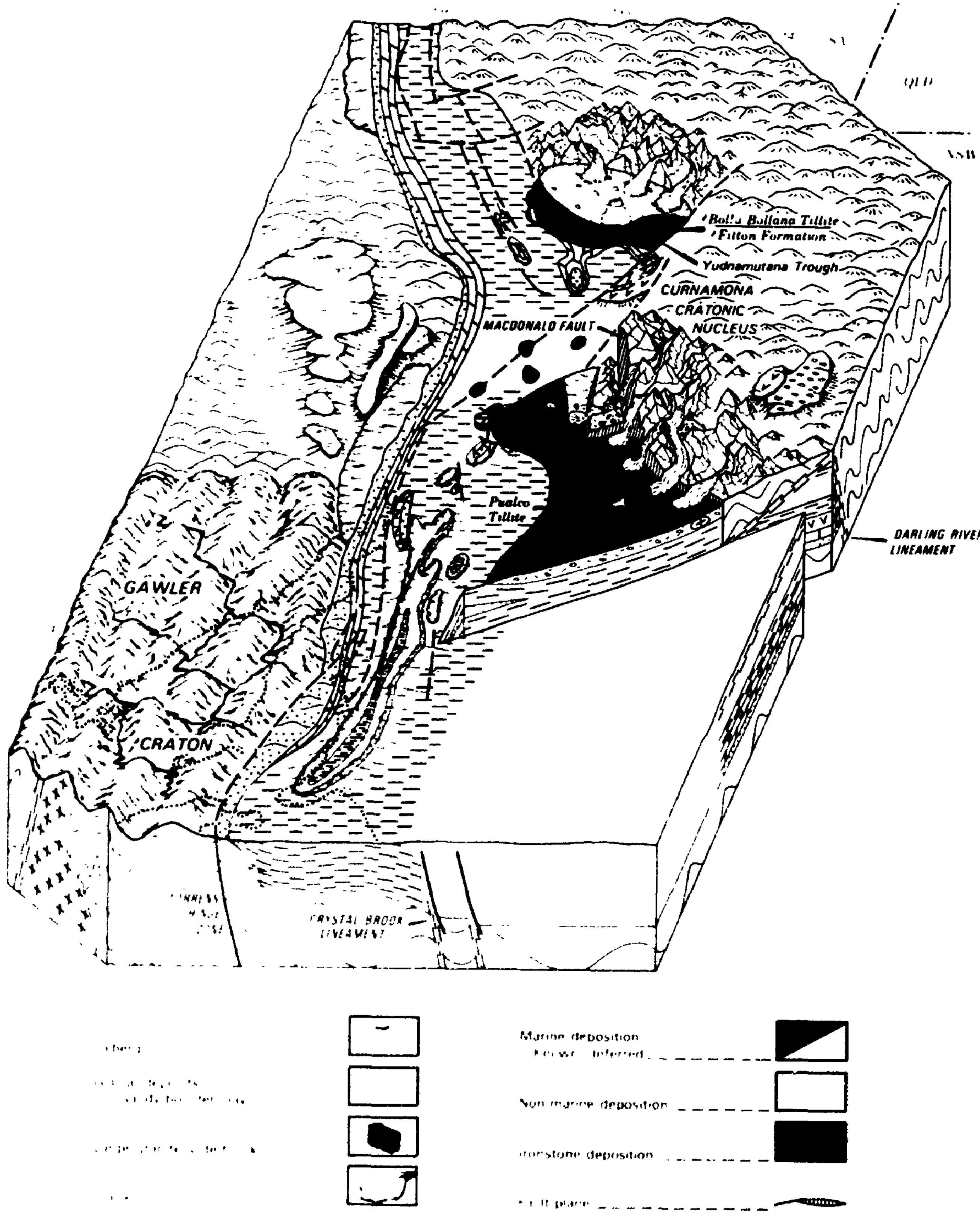

86 750 SADME

The sedimentary succession at locality 3 (Figure 1.7), stratigraphically similar to that of #2, is interpreted to have been emplaced by post-folding overthrusting of basement and Adelaidean sequences from the east (i.e., locality 2; Dickinson and Sprigg, 1953, p. 431-432; Campana, 1958, p. 6; Thomson, 1969b, p. 33-34).

Comparable to the findings of Campana and King (1958) on OLARY and Forbes (1972, p. 17) on PARACHILNA, Richert (1976) recognized two Delamerian fold patterns in the Mount Painter Inlier of the Northern Flinders Zone (Figure 1.2). He then extrapolated his results southward to PARACHILNA where he interpreted north- to north-northwest-trending folds as first phase and east- to east-northeast-trending as second (Figure 1.7). Richert (1976) noted that diapiric breccia bodies are commonly located at the intersection foci of the two fold types and suggested that the main control on diapir disposition was an early Paleozoic structural one. This conclusion is also implicit in the model of White (1983, p. 5). However, investigations throughout PARACHILNA have shown that diapiric breccias were forming in the pre- to early Sturtian (Coats, 1965, p. 99; Preiss, 1985, p. 61; Preiss, 1987a, p. 278) and continued throughout the Sturtian, Marinoan and Early Cambrian (Figure 1.4a; Dalgarno and Johnson, 1968; Dalgarno, 1983a, p. 35, 1983b, p. 71; Haslett, 1983, p. 55; Lemon, 1985, figure 9). Coats (1965) maintained that anticlinal structures such as the Blinman Dome are the result of Delamerian fold interference and not ascending diapirs, because even though 50 percent of South Australia's breccias reside in the cores of domes or anticlines, the remaining 50 percent intrude the limbs of anticlines, keels of synclines, or along faults (ibid., p. 99). In addition, Mount (1975, cited by Preiss, 1987a, p. 278) noted that the Arkaba Diapir locally truncates fold axes in the host rock. One of the more plausible suggestions to explain the diapir/anticlinal dome association is that the presence of a "pre-existing diapir may have provided a weakness exploited by Delamerian folding" (Preiss, 1987a, p. 278).

With respect to fold outlines on ORROROO, Preiss (1985, p. 60) extended the interpretations of Richert (1976) southward and those of Berry *et al.* (1978) westward in order to identify first and second phase Delamerian folds on ORROROO (Figure 1.7). Binks (1971, p. 56) previously described both north-south-trending and northeast- to east-trending fold patterns on ORROROO, but had considered them as varieties of a single phase.

In the Central Flinders Zone of PARACHILNA, Forbes (1972) noted that the broad, first phase north-northwest-trending folds are transected by northeast-trending faults. As to whether compression for this phase of folding was dominantly east-northeast (Rutland *et al.*, 1981, p. 354) or westerly (Preiss, 1987a, p. 277) is debatable, as is the direction of tension deemed responsible for faulting. Also, some low-angle thrust faults are observed in the vicinity of diapirs (Cann *et al.*, 1983, p. 38; Cann, 1985, p. 6).

To the south on ORROROO and OLARY, sinistral strike-slip movements along a basement structure (i.e., Crystal Brook Lineament, Figure 1.7), coupled with compression from the southeast are considered responsible for the first phase Delamerian folds of the Mount Lofty-Olary fold belt. Subsequent compression in a northwest-southeast direction (Rutland *et al.*, 1981, p. 351) or solely from the south-southeast (Preiss, 1987a, p. 278) is the suggested mode of formation for the second phase folds.

Chapter II

LITHOLOGIC DESCRIPTIONS

MACRO- & MICROSCOPIC

Introduction

The sites selected for detailed study occupy a triangular-shaped zone of 13,600 km^2 contained within 1:250,000 scale map sheets PARACHILNA, ORROROO and OLARY (Figure 1.1). Field work included measurement of stratigraphic sections using a Jacob's staff, and sampling of representative layers for geochemical and thin section analyses. As all of the measured intervals occur on sheep grazing stations, the locations of station homesteads are shown on Figure 2.1. The station names are commonly used herein to denote the **general** locality of a given section, whereas the **exact** locations are outlined in the appendix (Figures A.2 - A.9) together with the detailed stratigraphic descriptions (Tables A.1 - A.12).

Individual lithologies encountered during mapping were grouped into three main facies: diamictite, iron formation & subarkosic Fe wacke, and two minor facies: Fe siltstone & carbonate. These facies, defined on the basis of compositional and/or textural attributes, occur near the contact of the Pualco "Tillite" and the Benda "Siltstone" (Figure 1.4b). The contact is transitional and so the formal names were abandoned. The three major facies are regional in extent as they are laterally and vertically recurrent, whereas the two minor facies have a more localized development, in that they may recur within a given vertical section they are not laterally extensive.

Since this study focuses on the iron oxide content of the lithologies, the three main facies have been subdivided into three zones (Figure 2.1) defined mainly on the type(s) of iron oxide which occur in diamictite macro-matrices, iron formation and subarkosic Fe wacke. At least three measured sections from each zone are discussed in this chapter. The stratigraphic positions of samples taken for petrographic and

Figure 2.1 Map showing outline of study area within the Flinders Ranges of South Australia. Zones 1, 2 and 3 are defined mainly on the type(s) of iron oxide which occurs in the three major facies:

a) diamictite;

b) iron formation (IF);

c) subarkosic Fe wacke.

The informal name Holowilena iron formation is equated here with IF from zone 1, whereas Braemar iron formation is equated with IF from zones 2 and 3. The homestead (H.S.) locations of stations referred to in the text are shown.

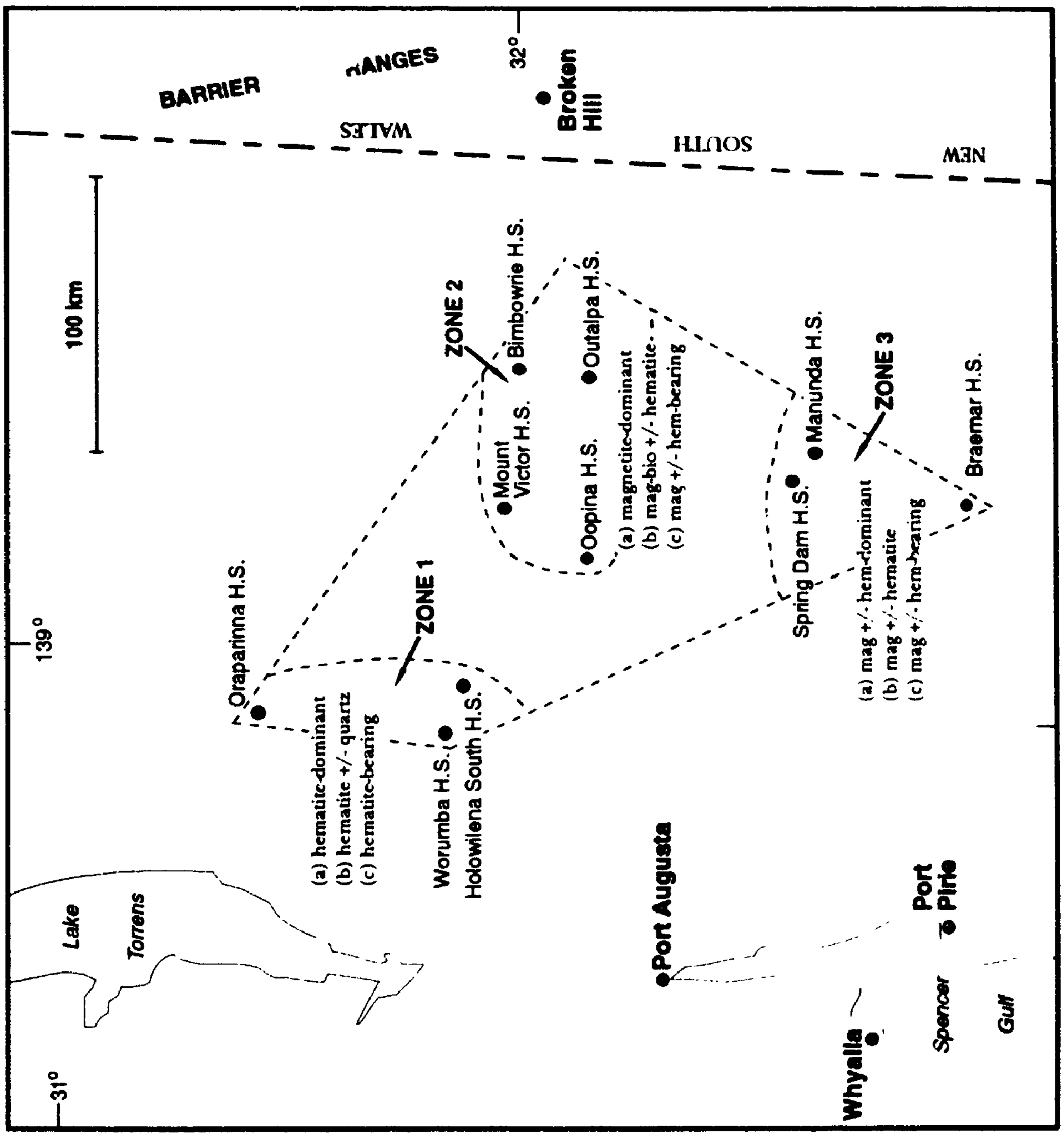
BARRIER RANGES
32°
Broken Hill
WALES
SOUTH
NEW
100 km
ZONE 2
Bimbowrie H.S.
Outalpa H.S.
Mount Victor H.S.
Oopina H.S.
(a) magnetite-dominant
(b) mag-bio +/- hematite
(c) mag +/- hem-bearing
Manunda H.S.
ZONE 3
Braemar H.S.
Spring Dam H.S.
(a) mag +/- hem-dominant
(b) mag +/- hematite
(c) mag +/- hem-bearing
139°
Oraparinna H.S.
ZONE 1
(a) hematite-dominant
(b) hematite +/- quartz
(c) hematite-bearing
Worumba H.S.
Holowilena South H.S.
Lake Torrens
Port Augusta
Port Pirie
Whyalla
Spencer Gulf
31°

geochemical analyses are given in Tables A.1 - A.13. Petrographic details from zones 1 - 3 are grouped according to facies (Tables 2.1 - 2.4), and for host sections (e.g., #13) are listed in ascending stratigraphic order (lowermost = a). Although most of the stratigraphic sections are designated by only one number (e.g., #13), there are two sections (i.e., #20/14, #9/2) that were measured as two intervals which were subsequently linked to form a continuous section. Hence samples 20c - $20q_2$ occur stratigraphically below samples $14a_2$ - $14o_1$, and samples $9a_1$ - $9L_2$ occur below samples $2m_1$ - 2A and 2p - $2y_1$. The #2 interval is an exception to the a = lowermost sample practice.

The area is structurally complex. There are first or second phase Delamerian folds (Figure 1.7), and localized shear zones in which enhanced penetrative deformation subparallel to bedding suggests either a late-stage origin, or late-stage overprinting of a previously defined trace. These zones are denoted in Tables A.1 - A.12 as are the early, brittle faults of synsedimentary origin. The effect of metamorphism on the three zones appears to be greatest in zone 2 (biotite dominant), moderate in zone 3 (biotite + chlorite) and lowest in zone 1 (chlorite + phlogopite).

In the summary tables for the diamictite (2.1) and iron formation (2.2) facies, the components have been divided into macro-framework, micro-framework and micro-matrix (Figure 2.2). Macro-framework, observable with the naked eye, is considered to be of primary detrital origin, whereas at least some of the micro-framework (e.g., biotite & ferroan dolomite) and micro-matrix (e.g., sericite) have formed by metamorphism of precursor minerals so that they are actually orthoframework and orthomatrix (Dickinson, 1970). However, for purposes of simplicity the latter two divisions have not been included. The abundant iron oxide minerals, magnetite and hematite, do not fit well into divisions intended for detrital rocks. The placement of these minerals in the micro-framework and/or micro-matrix is based on their present grain size, which unlike their strictly detrital counterparts, may have significantly increased during diagenesis and metamorphism. Micro-framework and micro-matrix

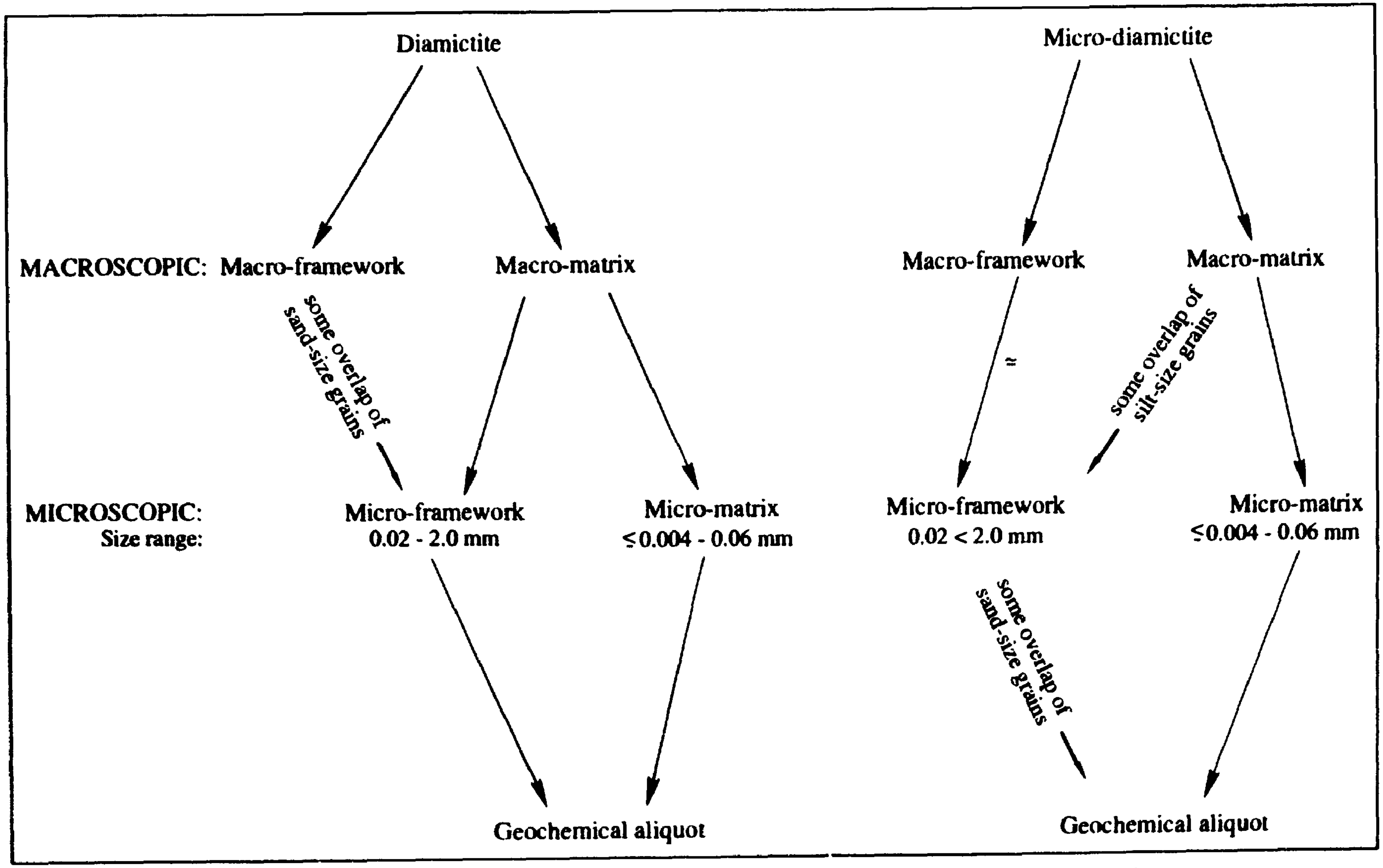

Figure 2.2 Components of diamictite and micro-diamictite used in descriptive Table 2.1.

together form macro-matrix, which is what was sampled for geochemistry (e.g., % Fe_2O_3 of Tables 2.1 & 2.2), except for some of the micro-diamictites in which macro-framework (< 2 mm) ≈ micro-framework. In these instances, pockets of clast-free matrix were sampled, the maximum grain size of which is quoted adjacent to the Fe_2O_3 content.

Classification of the metasedimentary rocks is based on Pettijohn *et al.* (1972, figure 5-3), but as with any sandstone classification, it does not account for metamorphic mineral grains that grew *in situ*, and therefore cannot be strictly applied (Figure 2.3). Also, the scheme has been modified to accommodate hematite and magnetite. If iron oxide minerals constitute < 1% of a rock (or diamictite macro-matrix) it is referred to as non Fe, 1 - 5% is Fe-poor, 5 - 21.5% is Fe-moderate and > 21.5% is Fe-rich. For example, a subarkosic Fe wacke (Fe-moderate) has 5 - 25% feldspar, at least 15% matrix-size material and 5 - 21.5% hematite and/or magnetite. The upper limit of 21.5% Fe as oxides was chosen because it translates roughly to 15% Fe which is the minimum requirement for an iron formation (James, 1954; Trendall, 1983). Hence, lithologies or diamictite macro-matrices designated as 'Fe-rich' are also iron formations. Grain sizes have been documented using the Wentworth scale and bed thickness terminology follows that of Ingram (1954).

Rocks of the thesis area are metamorphosed to at least lower greenschist facies. Therefore, the prefix 'meta' should be understood to apply to all of the described rocks.

Diamictite Facies

Introduction. This regional facies occurs within all three of the studied zones (Figure 2.1), where macro-matrices are:

1) **hematite**-dominant,

2) **magnetite**-dominant,

or 3) **magnetite** ± **hematite**-dominant.

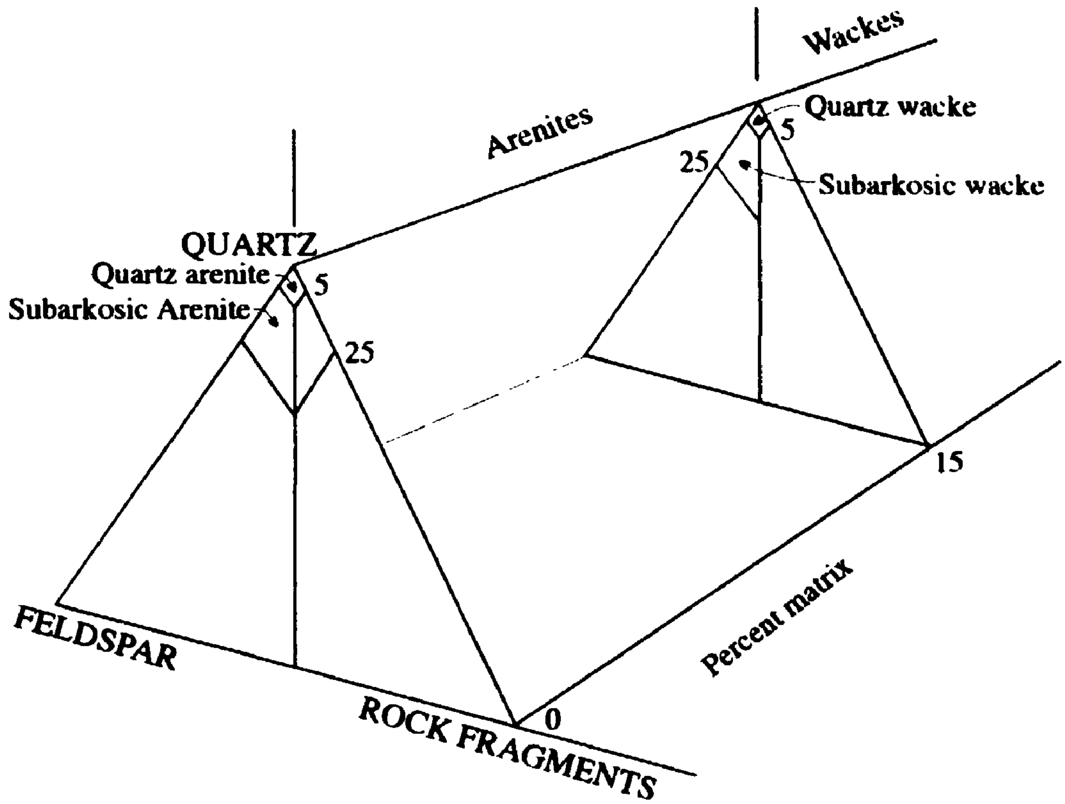

Iron oxide minerals as a percentage of entire sample	Classification
< 1	Non Fe
1 - 5	Fe-poor
5 - 21.5	Fe-moderate
> 21.5	Fe-rich

Figure 2.3 Diagram for classification of sandstones (upper; modified from Pettijohn et al., 1972) and descriptive terms for iron oxide content in lithologies examined in this study (lower).

The diamictites are closely associated with iron formation; defined by Kimberley (1978) as a mappable stratigraphic unit consisting mainly of iron-rich chemical sedimentary rock which contains more than 15% Fe ($\approx$21.5% Fe_2O_3). The diamictites occur either at the base of iron formation-bearing sections or as units within it. Where developed at the base, diamictites are generally unstratified and tens of metres thick, but those within IF range from 0.5 - 41 m thick. The diamictite macro-matrices are locally sufficiently iron-rich that they too are IFs (Table 2.1). The maximum size of macro-matrix (normally equals upper limit of micro-framework, see p. 31) from individual sample sites is also documented in Table 2.1.

(1) **Hematite**-dominant matrix

At the two northerly localities, *Oraparinna* and *Worumba* (Table 2.1), diamictite is most prevalent at the base of the iron formation-bearing section (Tables A.1 & A.2, Figure 2.4). However, diamictite at *Holowilena South* occurs both at the base of and throughout the IF (Tables A.3 & A.4, Figure 2.5).

At 'Dropstone Creek' (section #12, Table A.1) on *Oraparinna*, the described interval parallels that of Cann (1985, site 18; see p. 21). The base of section 12 (i.e., diamictite) overlies the fault-bounded sandy dolomite of Figure 1.6b. The diamictite exposure is thin (3.3 m) and consists mainly of sand- and granule-size clasts (greater than 0.8 mm) set in a reddish-brown matrix dominated by quartz-hematite lutite (sample $12a_1$, Table 2.1). Macro-framework is typically too fine for positive identification but there are a few angular, pebble-size clasts of grey subarkosic wacke. Micro-framework is abundant but the rock is micro-matrix-supported. The most prevalent micro-framework component is subangular to subrounded solitary or monocrystalline quartz (0.02 - 0.8 mm), which is weakly undulose and riddled with tiny inclusions (not resolvable at 50x). Second in abundance are subangular potassium feldspar grains (0.02 - 0.5 mm) in which poorly preserved, relict albite twins are common, suggesting that at least some of the potassium feldspar has formed by metasomatic replacement of

Table 2.1 Summary of macro- and microscopic features of diamictite facies samples from study localities in zones 1, 2 and 3 (Figure 2.1). *Oraparinna*, *Worumba* and *Holowilena South* occur in zone 1; *Oopina*, *Mount Victor*, *Outalpa* and *Bimbowrie* occur in zone 2; *Spring Dam* and *Manunda* are localities in zone 3. Multiple samples from one measured section (e.g., #13) are listed in ascending stratigraphic order. s = sand; g = granule; p = pebble; c = cobble; b = boulder; FD = ferroan dolomite; qtz = quartz; PF or plagio = plagioclase feldspar; T-DQ = tonalite-derived quartz; phlogo = phlogopite; WM = white mica; I.F. = iron formation; sub. = subarkosic. See Figures A.1 - A.9 for locations of measured sections from which these samples were collected.

Locality	Graparinna (Graparinna Creek)	Worumba	Worumba	Worumba	Worumba	Worumba	Worumba
Sample #	$12a_1$	$13a_1$	$13b_1$	$13c_1$	$13h_1$	$13i_1$	6
Macro framework							
Size and percent of weathered surface covered	s-g-w 10%	s-g-c 7%	s-g-p 2%	s-g-p 2%	sand 35%	sand 10 - 25%	sand 10 - 15%
Components							
1)	subarkosic wacke	subarkosic arenite	subarkosic arenite	subarkosic arenite			
2)		chlorite-plagio-schist		chlorite-plagio-schist			
3)		rusty polycrystalline quartz		white carbonate			
Micro framework							
Size	0.02 - 0.8 mm	0.02 - 0.4 mm →	→	→	0.02 - 0.4 mm	0.02 - 3.56 mm	0.02 - 0.5 mm
Components							
1)	monocrystalline quartz	monocrystalline quartz →	→	→	monocrystalline quartz →	→	→
2)	K-feldspar	K-feldspar →	→	→	K-feldspar →	→	→
3)	hematite-FD-intraclast	chlorite-after-phlogopite →	→	→	ferroan dolomite →	→	→
4)		ferroan dolomite →	→	→	chlorite-after-phlogopite	olive green phlogopite →	→
Total Fe_2O_3	5.08%	13.26%	10.25%	10.40%	12.21%	9.63%	12.65%
Micro-matrix							
Size	≤ 0.004 - 0.02 mm	≤ 0.004 - 0.02 mm →	→	→	≤ 0.004 - 0.02 mm	≤ 0.004 - 0.08 mm	≤ 0.004 - 0.05 mm
Components							
1)	hematite lutite	hematite platy →	→	→	hematite platy →	→	→
2)	quartz	hematite lutite →	→	→	hematite lutite	ferroan dolomite	hematite lutite
3)	sericite	FD + quartz →	→	→	ferroan dolomite	hematite lutite	ferroan dolomite
4)	ferroan dolomite	sericite →	→	→	quartz	quartz	quartz

Locality	Holowilena South	Holowilena South	Holowilena South	Holowilena South	Holowilena South	Holowilena South	Holowilena South	Holowilena South
Sample #	20c	$20f_2$	$20h_1$	$20h_3$	$14d_1$	14e	14h	$14h_7$
Macro-framework								
Size and percent of weathered surface covered	g-g 20%	sand-silt-g	sand-g 10%	sand	silt-sand	sand-g 15%	sand 25%	sand-granule
Components								
1)	ferroan dolomite		FD - quartz intraclast					
2)	tonalite							
3)	vein quartz							
Micro-framework								
Size	0.02 - 0.3 mm	0.02 - 0.10 mm	0.02 - 1.0 mm		0.02 - 1.4 mm	0.02 - 2.0 mm		0.02 - 2.8 mm
Components								
1)	monocrystalline quartz →	→	→		monocrystalline quartz →	→		monocrystalline quartz
2)	K-feldspar →	→	→		K-feldspar →	→		K-feldspar
3)	yellowish-brown phlogo	olive green phlogo	FD - quartz intraclast		FD ± quartz intraclast	FD - quartz intraclast		FD - quartz intraclast
4)	hematite serrate →	→	hematite intraclast		olive green phlogopite	hematite intraclast		hematite-quartz intraclast
Total Fe_2O_3		10.83%		0.60% (< 0.5 mm)	33.04% (< 0.5 mm)		33.1% (< 0.1 mm)	32.40% (< 0.1 mm)
Micro-matrix								
Size	≤ 0.004 - 0.02 mm →	→	→		≤ 0.004 - 0.32 mm →	→		≤ 0.004 - 0.02 mm
Components								
1)	quartz →	→	→		hematite lutite →	→		hematite lutite
2)	ferroan dolomite →	→	hematite lutite		quartz →	→		quartz
3)	hematite lutite →	→	ferroan dolomite		hematite platy →	→		ferroan dolomite
4)	hematite platy →	→	hematite platy					

Table 2.1 cont'd

Locality	Helowilena South (Back Creek)	Helowilena South (Back Creek)	Helowilena South (Back Creek)	Oopina	Oopina	Mount Victor (Razorback hill)
Sample #	21b	$21h_1$	$21j_1$	19c	$19h_1$	$19a_1$
Macro framework						
Size and percent of weathered surface covered	s-g-p 20%	g-p-s-c 5%	p-g-s-c-b 15%	g-p 4%	p g 6%	p g c 10 - 15%
Components						
1)	ferroan dolomite →	→	→	quartz arenite	tonalite	tonalite
2)	light green siltstone →	→	hematite-quartz (I.F.)	carbonate-rich sandstone	vein quartz	smokey quartz
3)		hematite-quartz (I.F.?)			purplish-grey quartzite	ferroan dolomite
Micro-framework						
Size	0.02 - 1.2 mm	0.02 - 0.7 mm	0.02 - 0.4 mm		0.06 - 0.9 mm	0.06 - 0.5 mm
Components						
1)	monocrystalline quartz →	→	→		monocrystalline quartz →	→
2)	K-feldspar →	→	→		plagioclase feldspar →	→
3)	quartz - FD ± WM siltstone	hematite-quartz (I.F.) clast →	→		ferroan dolomite →	→
4)	hematite intraclast	ferroan dolomite →	→		olive green biotite	yellowish-brown biotite
Total Fe_2O_3		11.90%	12.23%		3.00%	2.04%
Micro-matrix						
Size	≤ 0.004 - 0.02 mm	≤ 0.004 - 0.02 mm →	→		< 0.06 mm	< 0.06 mm
Components						
1)	hematite lutite	hematite lutite →	→		quartz	quartz
2)	quartz	ferroan dolomite →	→		ferroan dolomite	ferroan dolomite
3)	hematite platy	quartz →	→		sericite	yellowish-brown biotite
4)		hematite platy →	→			sericite

Locality	Mount Victor (Razorback hill)	Mount Victor (Razorback hill)	Outalpa	Bimbowrie (Bimbowrie Hill)	Bimbowrie (Bimbowrie Hill)	Bimbowrie (Bimbowrie Hill)
Sample #	$18b_1$	$18c_1$	$17a_1$	$15d_2$	$15f_1$	$15g_1$
Macro-framework						
Size and percent of weathered surface covered	p-g-c 10%	p-g-c 10%	p-g-s-c-b 40%	p-c-b-g-s 10%	p-c-b-g-s	
Components						
1)	ferroan dolomite →	→	tonalite	tonalite →	→	tonalite
2)	quartz arenite →	→	vein quartz	diorite schist →	→	vein quartz
3)	tonalite T-08 →	→	ferroan dolomite	vein quartz →	→	
Micro framework						
Size	0.06 - 0.5 mm →	→	0.06 - 0.5 mm		0.06 - 0.4 mm	
Components						
1)	monocrystalline quartz →	→	monocrystalline quartz		monocrystalline quartz	
2)	plagioclase feldspar	ferroan dolomite	K-feldspar		magnetite	
3)	ferroan dolomite	plagioclase feldspar	olive green biotite		plagioclase feldspar	
4)	olive green biotite →	→	ferroan dolomite		garnet ± olive green biotite	
Total Fe_2O_3	4.44%	8.41%	8.62%	4.24%	11.53%	41.19%
Micro-matrix						
Size	< 0.06 mm	< 0.06 mm	< 0.06 mm		< 0.06 mm	
Components						
1)	quartz	quartz	quartz		quartz	
2)	ferroan dolomite	ferroan dolomite	olive green biotite		olive green biotite	
3)	olive green biotite	olive green biotite ± sericite	ferroan dolomite		ferroan dolomite	
4)	sericite	magnetite			sericite	

Table 2.1 cont'd

Locality	Spring Dam (Pualco West)	Spring Dam Pualco West	Spring Dam (Pualco West)	Spring Dam (Pualco West)	Spring Dam (Pualco West)	Spring Dam (Pualco West)	Spring Dam (Razorback Ridge)	Spring Dam (Razorback Ridge)	Spring Dam (Razorback Ridge)
Sample #	10g	10j₂	10m₁	10N₃	10P₁	10u	9a₁	9e₁	9p
Macro-framework									
Size and % of w.s. covered	g-p-s-c 10%	g-p	g-p-s	g-p	g-p-s	sand-silt	p-g-c	p-g-s	g p s b
Components									
1)	quartz arenite	greyish quartz	subarkosic wacke →	→			subarkosic wacke	smokey quartz	ferroan dolomite
2)	ferroan dolomite						vein quartz	subarkosic arenite	FD qtz-PF intraclast
3)							ferroan dolomite →	→	
Micro-framework									
Size	0.02 - 1.1 mm		0.02 - 0.7 mm	0.02 - 1.2 mm	0.02 - 0.7 mm	0.02 - 0.8 mm	0.02 - 0.84 mm	0.02 - 0.5 mm	0.02 - 1.4 mm
Components									
1)	monocrystalline quartz		monocrystalline quartz →	→	→	→	monocrystalline quartz →	→	→
2)	plagioclase feldspar		magnetite	olive green biotite	magnetite	plagioclase feldspar	plagioclase feldspar	magnetite →	→
3)	biotite-replacing PF		plagioclase feldspar	pale green chlorite →	→	manganese oxide	olive green biotite	plagioclase feldspar	pale green chlorite
4)	ferroan dolomite		ferroan dolomite	ferroan dolomite	plagioclase feldspar	magnetite	ferroan dolomite →	→	→
5)	pale green chlorite		pale green chlorite	plagioclase feldspar		qtz - WM intraclast	pale green chlorite	olive green biotite	
Total Fe_2O_3	3.21%	7.37%	18.11%	Fe-poor	Fe-moderate	Fe-rich	Fe-poor	14.55%	35.09%
Micro-matrix									
Size	< 0.02 mm		< 0.02 mm	< 0.02 mm	< 0.02 mm	< 0.02 mm	< 0.02 mm	< 0.02 mm	< 0.02 mm
Components									
1)	sericite		sericite	quartz →	→	→	sericite →	→	hematite platy
2)	ferroan dolomite		quartz	sericite →	→	hematite platy	ferroan dolomite →	→	quartz
3)	quartz		plagioclase feldspar		magnetite/hematite(?)	sericite	quartz →	→	sericite
4)	olive green biotite		ferroan dolomite				olive green biotite	magnetite/hematite(?)	

Locality	Spring Dam (Razorback Ridge)	Spring Dam (Razorback Ridge)	Spring Dam (Razorback Ridge)	Spring Dam (Razorback Ridge)	Manunda (Iron Peak)	Manunda (Iron Peak)	Manunda (Iron Peak)	Manunda (Iron Peak)	Manunda (Iron Peak)
Sample #	2L	2J₁	2V	2w₁	7A	7S	7T	7V₁	7aa₁
Macro framework									
Size and % of w.s. covered	g-p-s-b →	→	g-s-p-c →	→	p-g-c	g p-c-b →	→	very coarse sand-g	g-p-s
Components									
1)				ferroan dolomite	subarkosic arenite	subarkosic wacke →	→		sub. Fe arenite rip-up
2)				greyish siltstone					ferroan dolomite
3)									tonalite
Micro-framework									
Size		0.02 - 0.72 mm		0.02 - 1.1 mm			0.02 - 0.7 mm		0.02 - 0.7 mm
Components									
1)		monocrystalline quartz		monocrystalline quartz			monocrystalline quartz		monocrystalline quartz
2)		magnetite		magnetite			olive green biotite		magnetite
3)		pale green chlorite		pale green chlorite			plagioclase feldspar		plagioclase feldspar
4)		ferroan dolomite		plagioclase feldspar			magnetite		pale green chlorite
5)		hematite intraclast		ferroan dolomite			ferroan dolomite		ferroan dolomite
Total Fe_2O_3	35.83%	30.01%	35.18%	31.69%	7.05%	15.89%	Fe-moderate	45.25%	31.01%
Micro-matrix									
Size		< 0.02 mm		< 0.02 mm			< 0.02 mm		< 0.02 mm
Components									
1)		hematite platy		hematite platy			quartz		hematite
2)		quartz		quartz			sericite		quartz
3)		sericite		sericite			ferroan dolomite		sericite

Figure 2.4 Measured sections of zone 1 iron formation-bearing intervals at *Oraparinna* and *Worumba*. *Oraparinna* section #12 in 'Dropstone Creek' is approximately 64 km north of section #13 at *Worumba* (Figures A.1 - A.3).

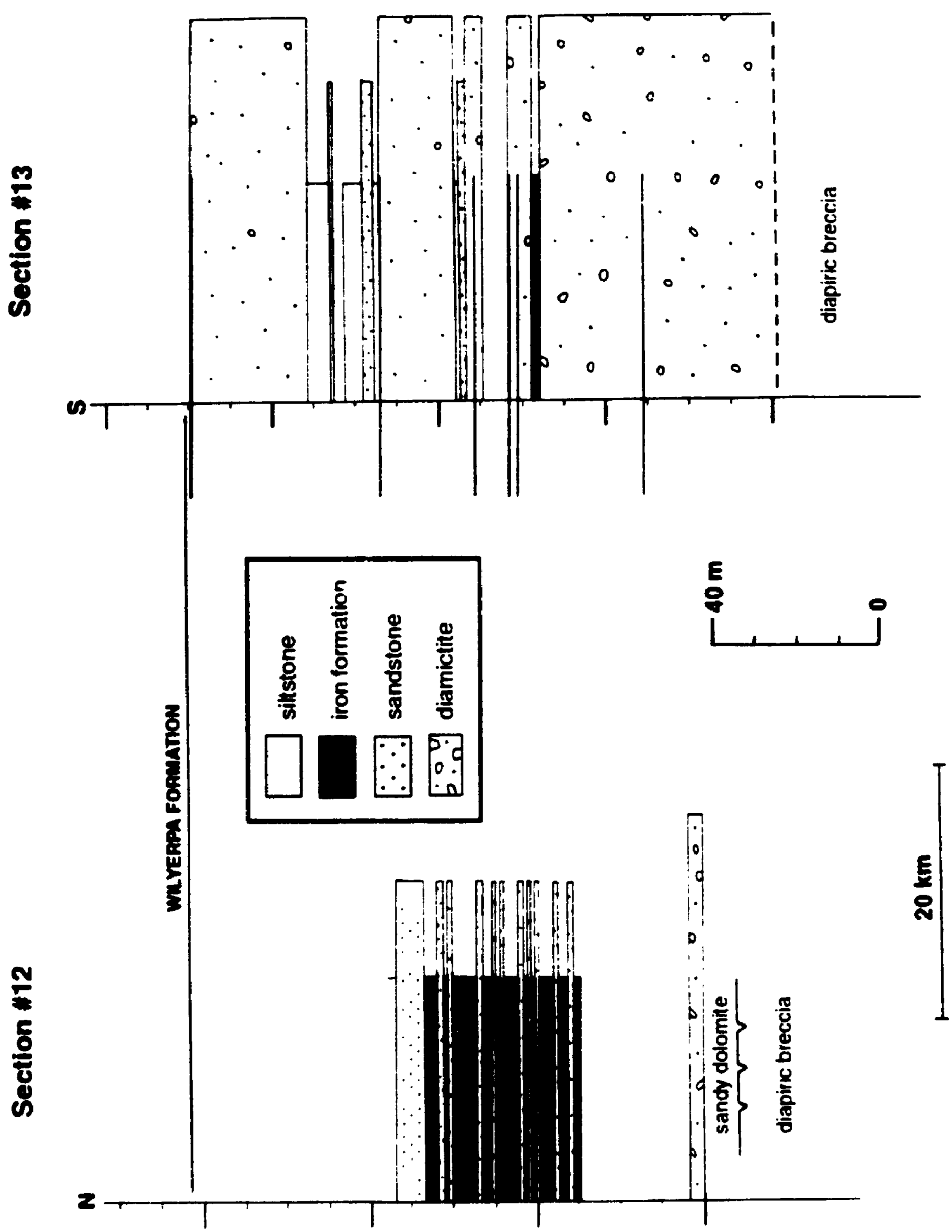
Section #13
Section #12
S
N
WILYERPA FORMATION
siltstone
iron formation
sandstone
diamictite
40 m
0
20 km
diapiric breccia
sandy dolomite
diapiric breccia

plagioclase. Intraformational hematite-ferroan dolomite lutite clasts (0.02 - 0.2 mm) rank third.

As at *Oraparinna*, iron formation at *Worumba* occurs in close proximity to diapiric breccia (Preiss, 1985). The contact, however, between the Worumba Diapir and the 55.5 m thick diamictite, basal to the IF at section #13 was not exposed (Table A.2). Sand- and granule-size clasts are common in this dark grey diamictite. Pebbles are restricted to framework-supported lenses (0.5 m thick) and define the only apparent stratification. One of the more widespread clast types is pink-tinged greyish-white subarkosic arenite, but others include: chlorite-plagioclase schist, rusty polycrystalline quartz and white carbonate (Table 2.1). Granitoid and fine-grained intermediate igneous clasts are minor. The most abundant micro-framework components are solitary quartz (0.02 - 0.4 mm, subangular to subrounded) and potassium feldspar (0.02 - 0.08 mm, typically subangular and untwinned). Chlorite-after-phlogopite (0.06 - 0.2 mm, subangular rectangle-shaped) occupies third place and ferroan dolomite clasts rank fourth. The micro-matrix hematite at *Worumba* (#13) is slightly more crystalline than at section #12. Together with the reddish-brown minute flakes, the grain boundaries of which are not discernible at 50x and are referred to as hematite lutite, there are distinct tiny plates ("platy habit", Heinrich, 1965, p. 74). These opaque plates generally range from 0.01 - 0.02 mm but many are finer.

The second type of 'diamictite' exposed at section #13 (e.g., $13h_1$, $13l_1$, $13m_1$, Table 2.1) is also a lithic subarkosic Fe wacke (Fe-moderate). It forms unstratified intervals which range from 1.4 - 27.9 m thick (Table A.2). The dark green or brownish-green weathered surface is typically 10 - 35% covered by 0.5 - 1.0 mm size fragments, the majority of which appear to be of translucent grey quartz. This lithic wacke is classified as a micro-diamictite because it is macroscopically similar to, but finer grained than, the down-section diamictites at *Worumba*.

Samples $13h_1$, $13l_1$ and $13m_1$ are also microscopically similar to diamictites from section #13 (Table 2.1). The four main micro-framework components are monocrystalline quartz, potassium feldspar, ferroan dolomite and locally chloritized olive green phlogopite. Platy hematite is evident in the micro-matrix, but the total iron of the three wacke macro-matrices (Fe_2O_3 averages 11.5%) is slightly less than that of the three diamictite macro-matrices sampled (Fe_2O_3 averages 15.3%).

At *Holowilena South*, the first of two detailed stratigraphic sections (#20/14, Table A.3, Figure 2.5) is equated with and occurs approximately 635 m northeast of the "Holowilena Ironstone" type section (Dalgarno and Johnson, 1965; Figure 1.1). The second detailed interval (#21) at Back Creek (Table A.4, Figures 2.5 & A.4) is dominated by transitional (Fe/non Fe) rocks of the overlying Wilyerpa Formation (Thomson *et al.*, 1964; Dalgarno and Johnson, 1966).

As at *Worumba* (#13), the diamictite of sections #20/14 and #21 has two forms:

i) diamictite - macro-framework is typically larger than 2 mm but there is a minor amount of fragments of coarse to very coarse sand-size. Macro-matrix (= micro-framework + micro-matrix) is a mixture of fine sand-, silt- and mud-size grains.

ii) micro-diamictite - macro-framework ≈ micro-framework as it is less than 2 mm. It consists of medium-, coarse- and very coarse sand-size particles supported by a macro-matrix of mud- and silt-size (= lutite) grains (Figure 2.2).

Both diamictite (7.88 m maximum) and micro-diamictite (18.44 m maximum) horizons are thickest at the base of the iron formation-bearing section (#20/14, Table A.3, Figure 2.5). Diamictite is most apparent within the lower half of section #20/14, whereas micro-diamictite is equally distributed throughout.

Stratification, which in the diamictite (#20/14 & #21) is only locally developed, occurs as a clast-free lens of subarkosic arenite (23 m long x 1.7 m thick) within the lowermost exposure of #20/14, and up-section, as successive layers defined by diminishing clast size. Pebble- and granule-size clasts typify the diamictite (i.e., 20c,

Figure 2.5 Measured sections of zone 1 iron formation-bearing intervals at *Holowilena South*. Section #21 occurs in Back Creek and is approximately 2,000 m southwest of section #20/14 (Figures A.1 & A.4).

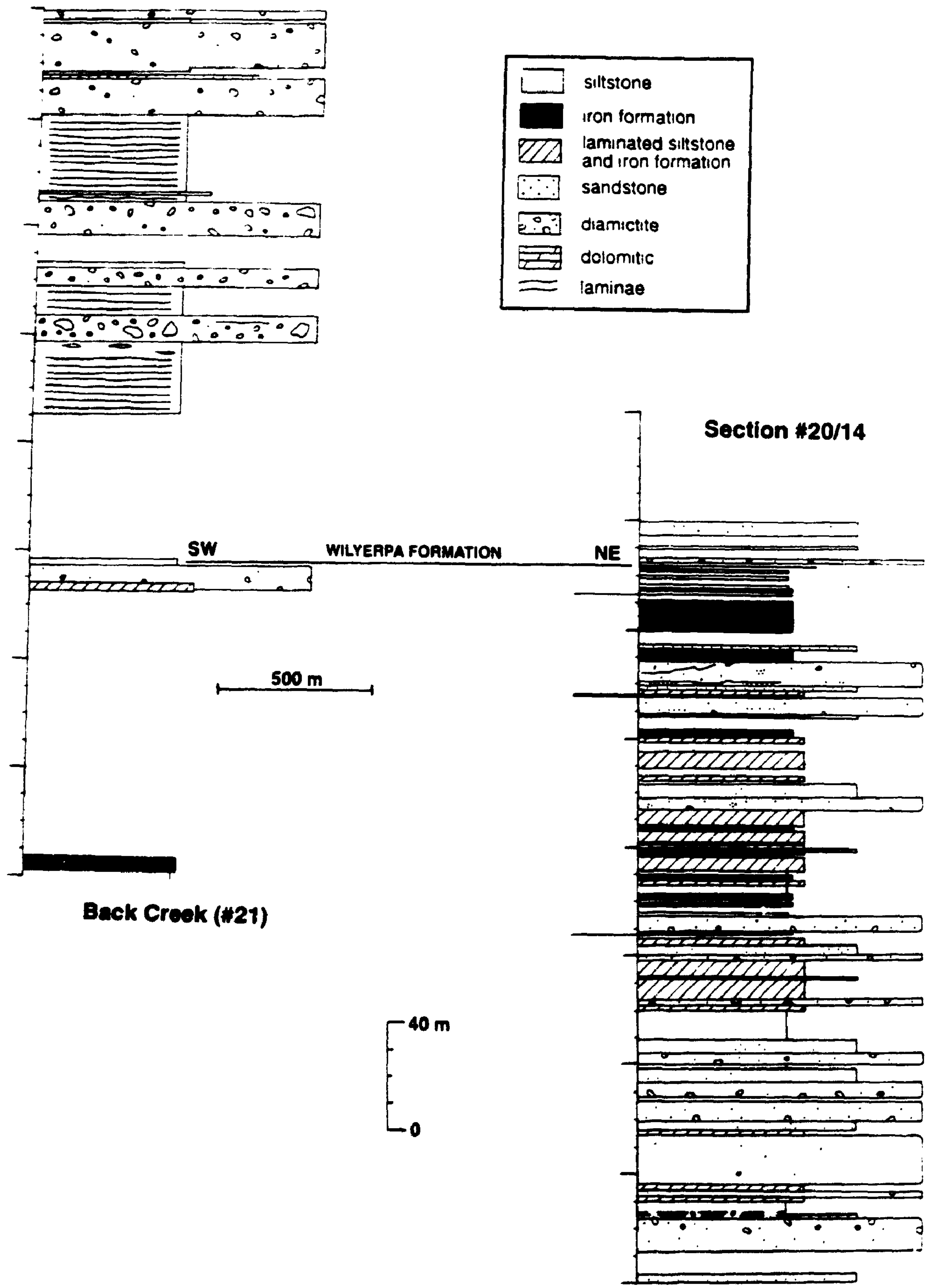
siltstone
iron formation
laminated siltstone and iron formation
sandstone
diamictite
dolomitic
laminae
Section #20/14
SW
WILYERPA FORMATION
NE
500 m
Back Creek (#21)
40 m
0

$20M_1$, 14e, $14M_2$, 21b, $21h_1$, $21j_1$, Table 2.1) and include: recessive-weathered ferroan dolomite, fine- to medium-grained tonalite, translucent vein quartz, fine-grained subarkosic green wacke (20c, base of #20/14), ferroan dolomite-quartz siltstone ($20M_1$, middle of #20/14; Plate 2.1a) which is considered intraformational because of its similarity to the dominant layer type in $20L_1$ (see Table 2.3), or ferroan dolomite, light green siltstone, hematite-quartz lutite (21b, $21h_1$, $21j_1$, throughout section #21). The latter two are regarded as intraformational.

With respect to macro-matrix composition, monocrystalline quartz (0.02 - 1 mm) and potassium feldspar (0.02 - 0.4 mm) are the two most prevalent micro/framework components of both the diamictites (listed above) and micro-diamictites (i.e., $20f_2$, $20m_3$, $14d_1$, 14k, Table 2.1). As in the basal diamictite at *Worumba* (#13), locally chloritized phlogopite (0.02 - 0.06 mm) is the third most abundant micro/framework component in samples 20c and $20f_2$ which occur within the lower 35 m of section #20/14. In contrast, stratigraphically higher samples have intraformational ferroan dolomite-quartz siltstone (0.08 - 2 mm) ranked third and hematite$\pm$quartz rip-ups (0.08 - 2 mm) fourth. The micro-matrix components at *Holowilena South* (#20/14 & #21) are similar to those at *Worumba* (#13), namely, quartz, ferroan dolomite, hematite lutite and platy hematite; the relative abundances vary.

Thin section examination of micro-diamictite (e.g., $20f_2$, $14d_1$) reveals stratification in the form of thin subarkosic Fe wacke (Fe-poor) laminae (Plate 2.1b) which locally form colinear balls (cf. Pettijohn *et al.*, 1972, p. 371), or crude strata defined by subtle variations in the density of clastic detritus within the hematite lutite host ($14d_1$).

(2) **Magnetite**-dominant matrix

Southeast of *Holowilena South* there is a second type of iron formation-diamictite association. Diamictites with subarkosic wacke macro-matrices dominated

Plate 2.1 Diamictite facies.

(a) Diamictite. Dominant clast type is intraformational ferroan dolomite-quartz siltstone (light grey). Hematite-quartz lutite intraclasts are also evident (black). Diameter of coin is 18 mm (sample 20h, Table A.3, *Holowilena South*).

(b) Abrupt termination of subarkosic Fe wacke (Fe-poor) lamina (left) due to synsedimentary fault. Matrix of this micro-diamictite is quartz-hematite-ferroan dolomite lutite. Plane light; bar = 0.5 mm (sample $20f_2$, Table A.3, *Holowilena South*).

(c) Unstratified diamictite typified by clasts of recessively-weathered ferroan dolomite, and light grey arenite and tonalite clasts. Subarkosic Fe wacke (Fe-poor) matrix. Length of magnet is 12.2 cm (vicinity of sample $18b_1$, Table A.6, *Mount Victor*).

(d) Unstratified diamictite. Greyish-white clasts are tonalitic, whereas the generally smaller black clasts are mudstone (section #17, Table A.7, *Outalpa*).

(e) Glacial striae on upper surface of diamictite bedding plane. Matrix dominated by hematite-magnetite-quartz lutite (211.37 m mark of section #9/2, Table A.11, *Spring Dam*).

(f) Diamictite. Light grey, rectangular clast is an intraformational rip-up of silt-size subarkosic Fe arenite (Fe-poor). Recessively-weathered clasts are ferroan dolomite. Matrix dominated by hematite-magnetite-quartz lutite (vicinity of sample $7aa_1$, Table A.12, *Manunda*).

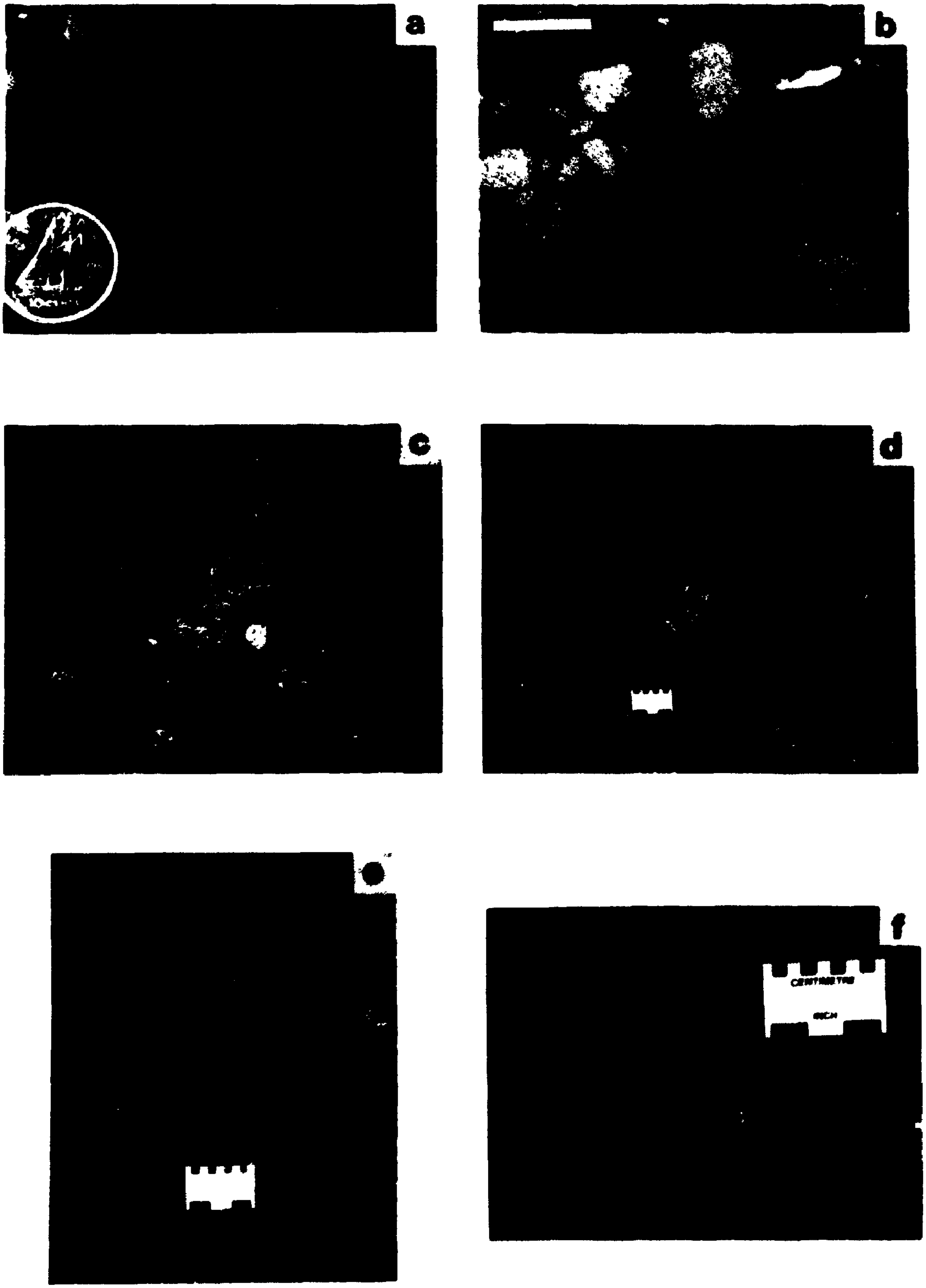
a
b
c
d
f

by one or more of biotite, ferroan dolomite or **magnetite** are exposed at *Oopina*, *Mount Victor*, *Outalpa* and *Bimbowrie* (Table 2.1). With the exception of *Oopina*, (Figure 2.6, Table A.5), diamictite at these localities is best preserved/developed at the **base** of the iron formation intervals (Figures 2.6 & 2.7, Tables A.6 - A.9).

The thin (2 m) basal exposure of granule-pebble diamictite at *Oopina* (sample 19c, Table 2.1) unconformably overlies laminated siltstone (Kadlunga Slate, **Pl**) of the Belair Subgroup according to Binks (1971, p. 28) and Preiss (1983b; see p. 20). At the site of section #19, a 0.5 m wide shear zone (094°/64°) occurs at the siltstone (**Pl**) and diamictite contact.

The basal greenish-grey diamictite includes clasts of light greyish-white quartz arenite, carbonate-bearing sandstone and aphanic carbonate supported by a subarkosic wacke matrix. In contrast, the light brown-weathering pebble-granule diamictite (28 m thick) which overlies the iron formation ($19h_1$, Table 2.1) is dominated by clasts of fine- to medium-grained tonalite, translucent vein quartz and purplish-grey quartzite with subordinate recessive-weathering carbonate clasts. The macro-matrix composition of $19h_1$ is however similar to 19c, in that iron oxide minerals are virtually absent (Fe_2O_3 = 3.00%). As at *Oraparinna* (#12), *Worumba* (#13) and *Holowilena South* (#20/14, #21), the micro-framework of $19h_1$ is dominated by monocrystalline quartz (0.06 - 0.9 mm), but in contrast to these three localities, plagioclase feldspar (0.06 - 0.4 mm) is the second most abundant component. Ferroan dolomite and olive green biotite (both 0.06 - 0.3 mm) rank third and fourth, respectively.

As at *Oopina*, the diamictite basal to the iron formation at *Mount Victor* (section #18, Table A.6) is considered to unconformably overlie **Pbs** (Minburra Quartzite) of the Belair Subgroup (Preiss, 1983b) or **Pb** of the Burra Group (Forbes, 1989). The quartzite was only seen as large blocks of scree on the lee side of the asymmetrical ridge (i.e., Razorback hill).

In contrast to *Oopina* (#19), where the exposure of basal diamictite is thin (2

Figure 2.6 Measured sections of zone 2 iron formation-bearing intervals at *Oopina* and *Mount Victor*. Section #18 crosses Razorback hill at *Mount Victor* and is approximately 25 km northeast of section #19 at *Oopina* (Figures A.1, A.5 & A.6).

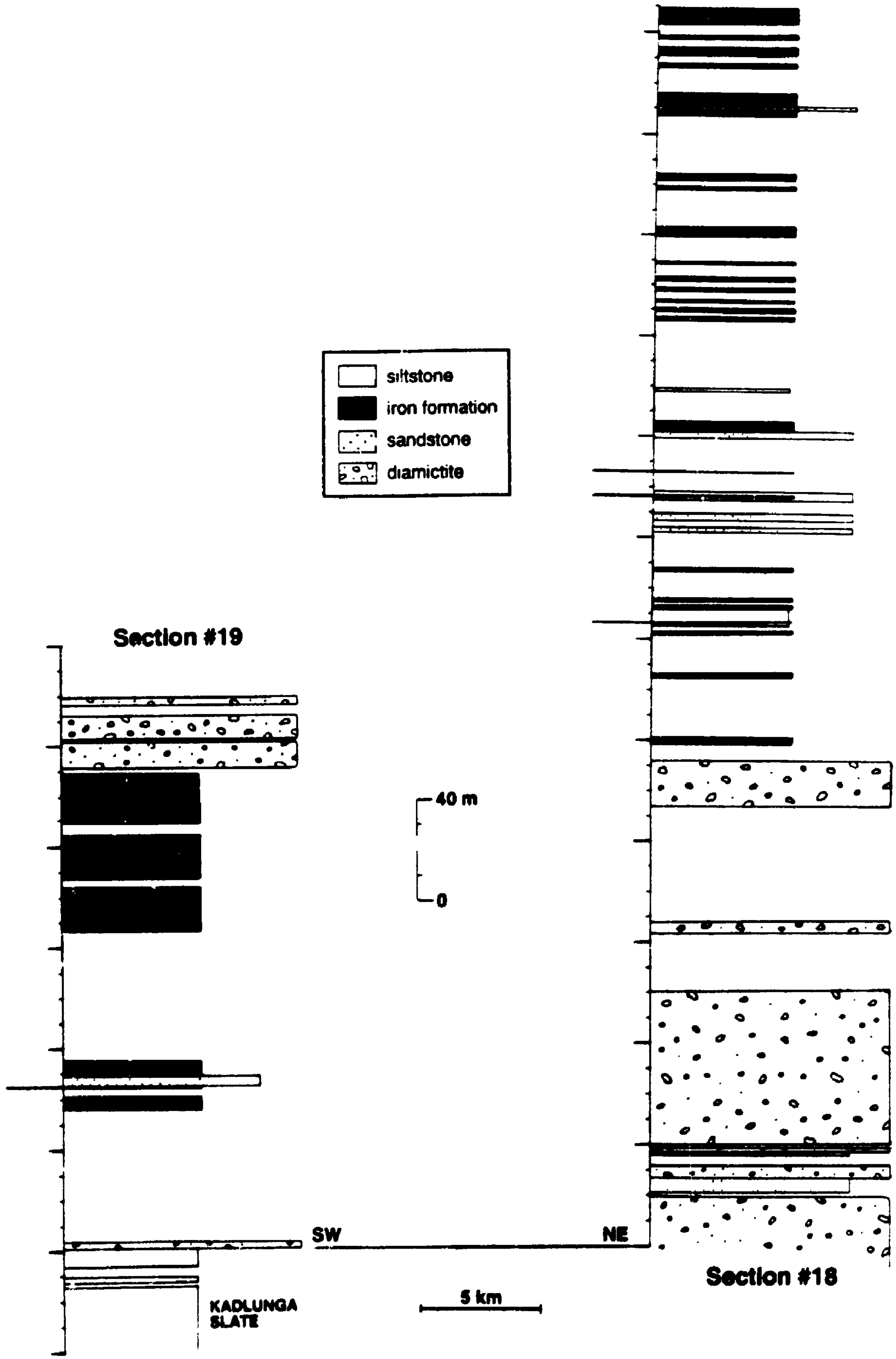

siltstone
iron formation
sandstone
diamictite
Section #19
40 m
0
SW
NE
KADLUNGA SLATE
5 km
Section #18

m, Figure 2.6), the equivalent horizon at section #18 is at least 100 m thick (Figure 2.6). Dominant clast types within the lower 75 m ($18a_1$, Table 2.1) are similar to those described for sample $19h_1$, but are more comparable to those of sample 19c in the upper 25 m ($18b_1$, Table 2.1, Plate 2.1c). Stratification, present in the lower 40 m of the diamictite (#18), appears as three massive lenses of subarkosic wacke (similar to lower portion of section #20/14, p. 43).

As in the five previously described diamictite-bearing sections (nos. 12, 13, 20/14, 21 and 19), solitary (monocrystalline) quartz is the most abundant micro-framework component (#18, Table 2.1). Albite-twinned plagioclase feldspar is dominant over ferroan dolomite in both samples $18a_1$ and $18b_1$, however, the order is reversed in sample $18c_1$. This change may be linked to the predominance of recessive-weathering ferroan dolomite in the macro-framework of samples $18b_1$ and $18c_1$. The fourth ranking micro-framework component is yellowish-brown ($18a_1$) or olive green ($18b_1$ & $18c_1$) biotite. Magnetite, absent from $18a_1$ (Fe_2O_3 = 2.04%), is present in $18b_1$ (Fe_2O_3 = 4.44%) and ranks fifth in $18c_1$ (Fe_2O_3 = 6.41%). This increased magnetite content, rather than the relatively consistent ferroan dolomite and biotite contents, is most likely responsible for the accompanying up-section increase of iron.

Seemingly equatable to $18c_1$ is sample $17a_1$ from *Outalpa* (section #17, Tables 2.1 & A.7) because like $18c_1$, it represents diamictite which most closely underlies iron formation (Figure 2.7) and has a comparable Fe_2O_3 content (i.e., 6.62%). However, iron oxides are minor in $17a_1$. Biotite is the principal iron-bearing phase and locally contains zircon inclusions (both $18c_1$ & $17a_1$), a feature common in igneous biotites.

Diamictite at *Outalpa* (#17) is poorly sorted (sand- through boulder-size). Tonalite clasts are both the most prevalent and the largest. Clasts of vein quartz and recessive-weathered reddish-brown ferroan dolomite(?) rank second and third respectively. Collectively, these dominant clast types are similar to those observed at the site of samples $19h_1$ (*Oopina*) and $18a_1$ (*Mount Victor*), whereas ancillary types at

Figure 2.7 Measured sections of zone 2 iron formation-bearing intervals at *Outalpa*. Section #17 is 2.35 km southeast of section #16, which occurs near the I.D. Hut (Figures A.1 & A.7).

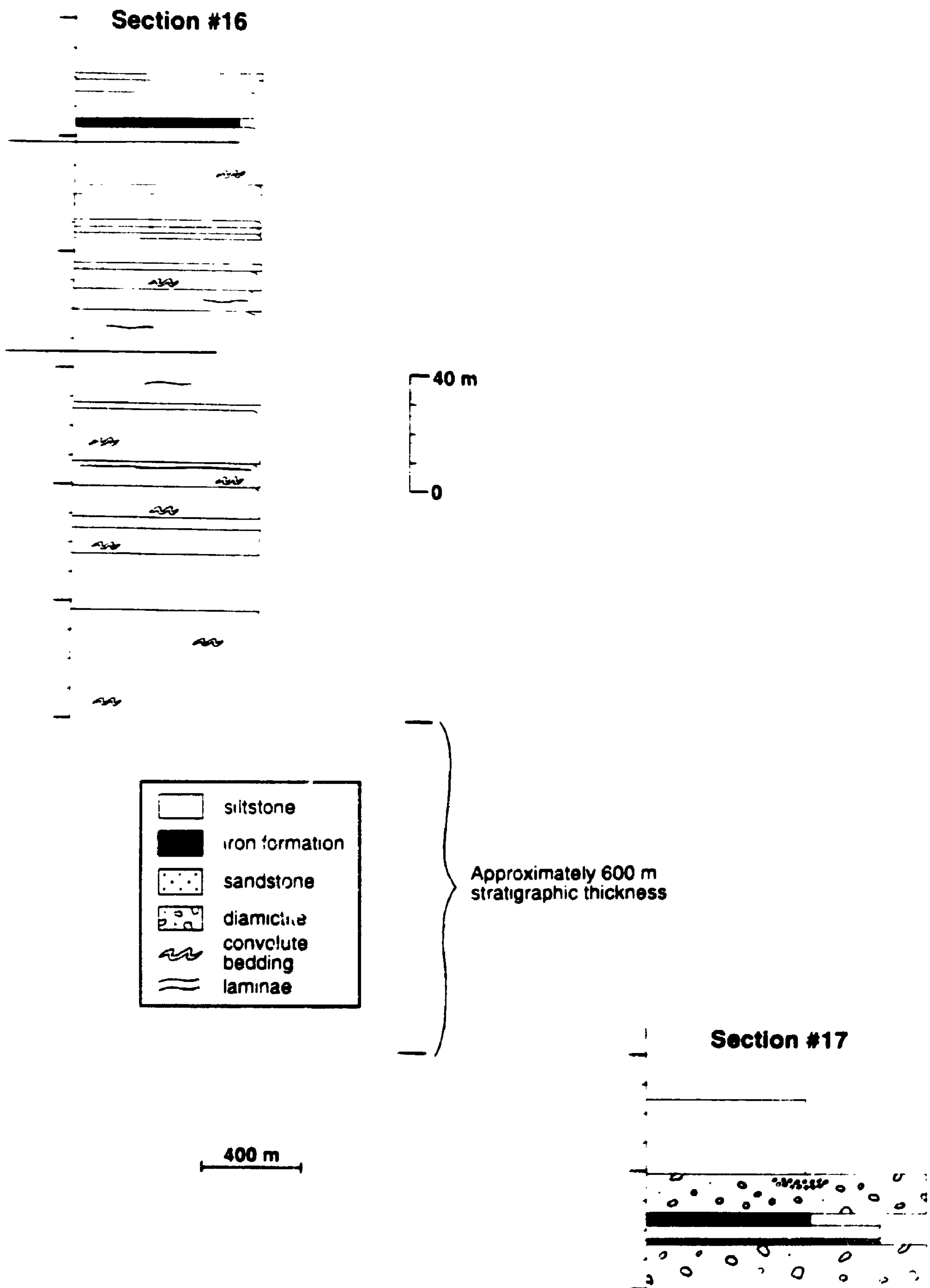
Section #16
40 m
0
siltstone
iron formation
sandstone
diamictite
convolute
bedding
laminae
Approximately 600 m
stratigraphic thickness
Section #17
400 m

$17a_1$, namely, lenticular black mudstone (Plate 2.1d) and fine-grained subarkosic arenite (comparable to lithology at base of section #15, Table A.9) are not correlative. Micro-framework in $17a_1$ (Table 2.1) consists mainly of quartz (0.06 - 0.5 mm, monocrystalline), potassium feldspar (0.06 - 0.1 mm, untwinned), biotite (0.1 - 0.3 mm, olive green) and ferroan dolomite. This is similar to that found in $19h_1$ and $18a_1$.

The relationship of the blackish-green diamictite at *Bimbowrie* (section #15, Tables 2.1 & A.9) to the underlying light grey subarkosic arenite is uncertain, because the arenite is classified as Belair Subgroup (**Pl**) by Preiss (1983b) and as Yudnamutana Subgroup (**Pyp**) by Forbes (1989). The former interpretation implies that an angular unconformity exists between the arenite and the diamictite, whereas the latter suggests a conformable transition. Sporadic lonestones and clast-rich lenses in the subarkosic arenite argue for a glacial affinity (conformable). The presence of a strongly flattened/foliated siltstone (0.6 m wide; as at *Oopina*) at the contact of the typically massive subarkosic arenite and diamictite suggests a possible stratigraphic break.

Diamictite at *Bimbowrie* (#15) is unsorted (sand- through boulder-size), has tonalite and vein quartz as main clast types, and contains sporadic clasts of subarkosic arenite; features which all mimic those of $17a_1$ (*Outalpa*). Comparable to section #18 (*Mount Victor*), is the up-section increase in iron content at *Bimbowrie*, which is due to increasing magnetite contents in $15d_2$ (Fe_2O_3 = 4.24%) through $15f_1$ (Fe_2O_3 = 11.53%) to $15g_1$ (Fe_2O_3 = 41.19%).

(3) **Magnetite** ± **hematite**-dominant matrix

South of *Oopina* is the third type of iron formation-associated diamictite, which is similar to type #2 in that one or more of biotite, ferroan dolomite or **magnetite** occur in the macro-matrix, but where Fe_2O_3 content is sufficiently high (e.g., 31 - 38%, Table 2.1) **hematite** is also present. The three diamictite-bearing sections described in detail (Figure 2.8, Tables A.10 - A.12) are from west to east, #10 (Pualco West), #9/2 (Razorback Ridge) and #7 (Iron Peak), the former two of which occur on *Spring Dam*

Figure 2.8 Measured sections of zone 3 iron formation-bearing intervals at *Spring Dam* and *Manunda*. *Spring Dam* section nos. 10 and 9/2 are from Pualco West and Razorback Ridge, respectively. *Manunda* section #7 occurs at Iron Peak. See Figures A.1 & A.9.

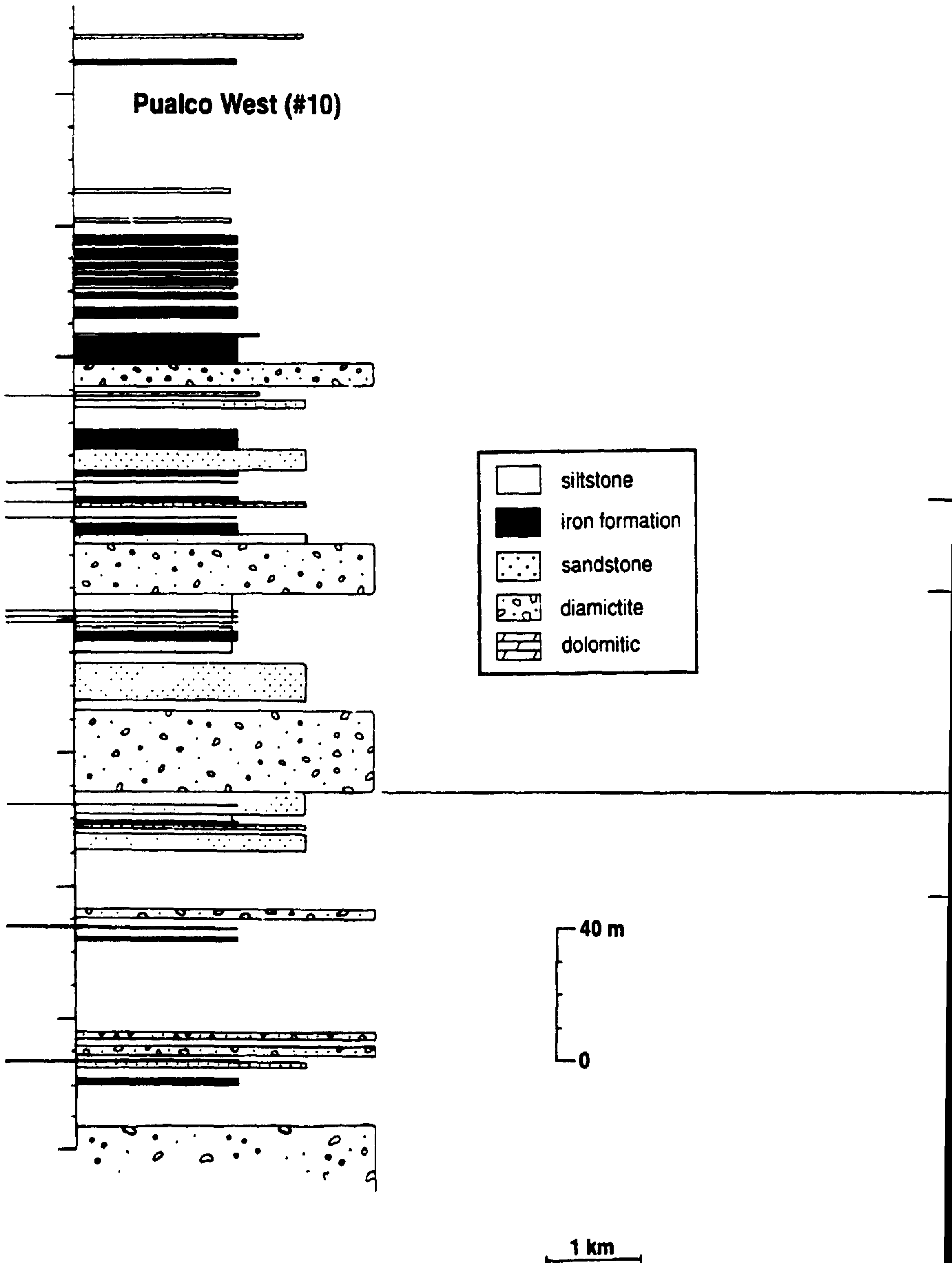
Pualco West (#10)
siltstone
iron formation
sandstone
diamictite
dolomitic
40 m
0
1 km

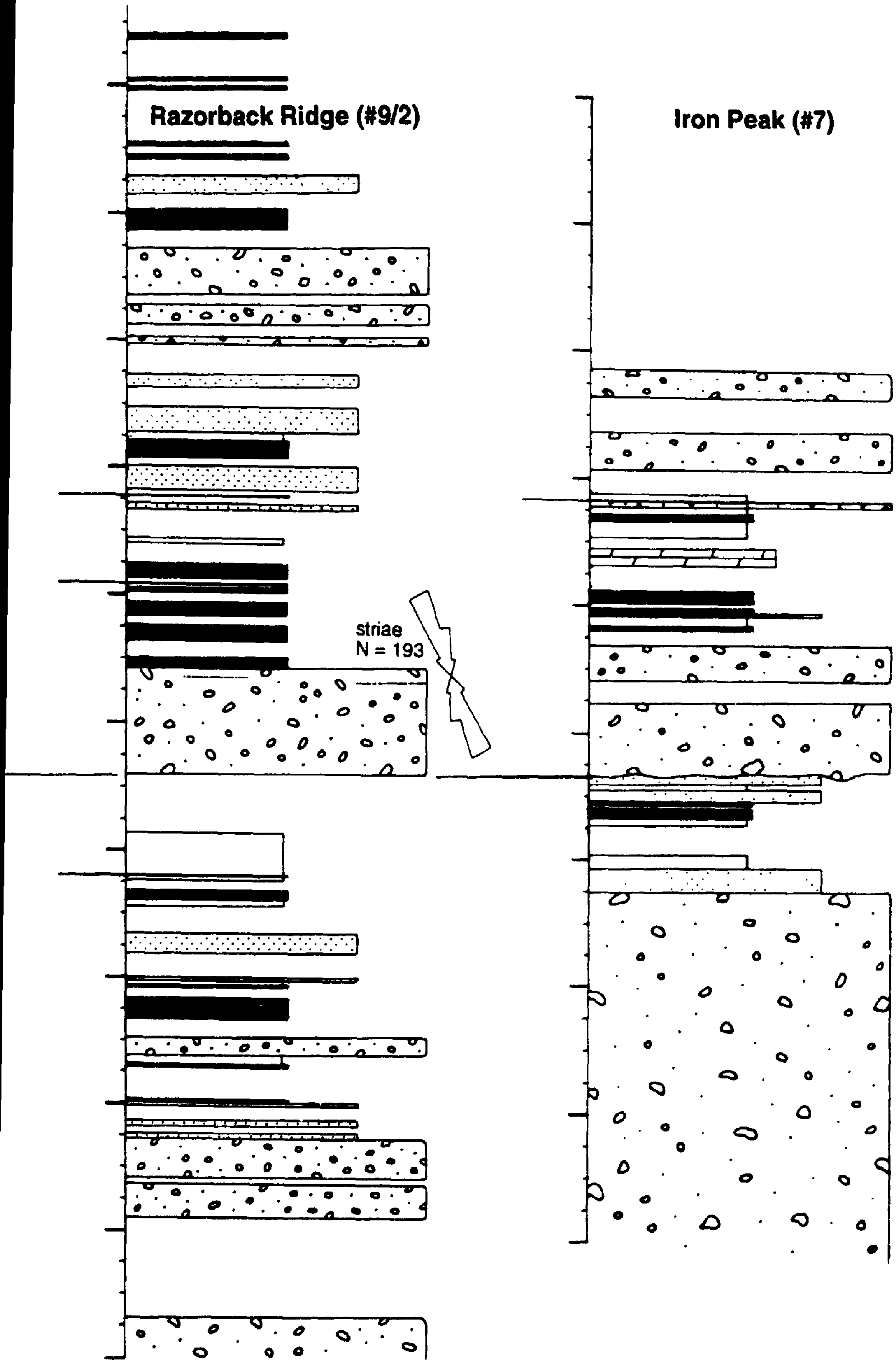
Razorback Ridge (#9/2)
Iron Peak (#7)
striae
N = 193

station and the third on *Manunda*.

Diamictite basal to the iron formation (section nos. 10, 9/2 & 7) has exposed thicknesses of 7 - 110 m (eastward thickening), whereas diamictite intercalated with IF ranges from 0.5 - 40.9 m thick. These units are typically unstratified, except at the midpoint of section #9/2 where the upper surfaces of four successive bedding planes (0.2 - 3 m apart) are striated (Plate 2.1e, Figure 2.9) and imbricated clasts are visible directly below the diamictite/iron formation contact (Adit through Razorback Ridge, Table A.13).

Pebble- and granule-size clasts are widespread, and dominantly of sedimentary origin (Table 2.1). Prevalent types include light grey or beige coloured subarkosic arenite ($10g_1$, $9e_1$, 7a), green-tinged subarkosic wacke ($10m_1$, $10M_3$, $9a_1$, 7S, 7T) and reddish-brown ferroan dolomite ($10g_1$, $9a_1$, $9e_1$, $2m_1$, $2w_1$, $7aa_1$). The most obvious intraformational clasts are rectangular rip-ups ($2m_1$, $7aa_1$, Plate 2.1f) of ferroan dolomite-quartz-plagioclase Fe siltstone (Fe-poor) which are comparable to the subordinate layer type in $9l_2$ (see Table 2.2). Granitoid (e.g., tonalite) clasts are minor, and restricted to the uppermost diamictite at Razorback Ridge ($2w_1$, Table A.11) and Iron Peak ($7aa_1$).

As in the macro-matrices of the two previously discussed diamictite types, monocrystalline quartz (0.02 - 1.4 mm) is the dominant micro-framework component at sections 10, 9/2 and 7 (Table 2.1). In the Fe-poor diamictite matrices (<5% Fe oxide, $10g_1$, $10M_3$, $9a_1$), plagioclase feldspar or olive green biotite ranks second in abundance, whereas in the Fe-moderate (5 - 21.5% Fe oxide) and Fe-rich (>21.5% Fe oxide) matrices, magnetite is most commonly ranked second ($10m_1$, $10R_1$, $9e_1$ and $2m_1$, $2j_1$, $2w_1$, $7aa_1$). In fact, the occurrence together of olive green biotite and pale green chlorite is restricted to Fe-poor and Fe-moderate matrices ($10g_1$, $10M_3$, $9a_1$, $9e_1$, 7T), whereas only pale green chlorite occurs in the Fe-rich matrices (10u, $2m_1$, $2j_1$, $2w_1$, $7aa_1$) and two of the Fe-moderate matrices ($10m_1$, $10R_1$). Monocrystalline ferroan dolomite (0.02 - 1.0 mm) is widespread as a fourth or fifth ranked micro-framework component; it is

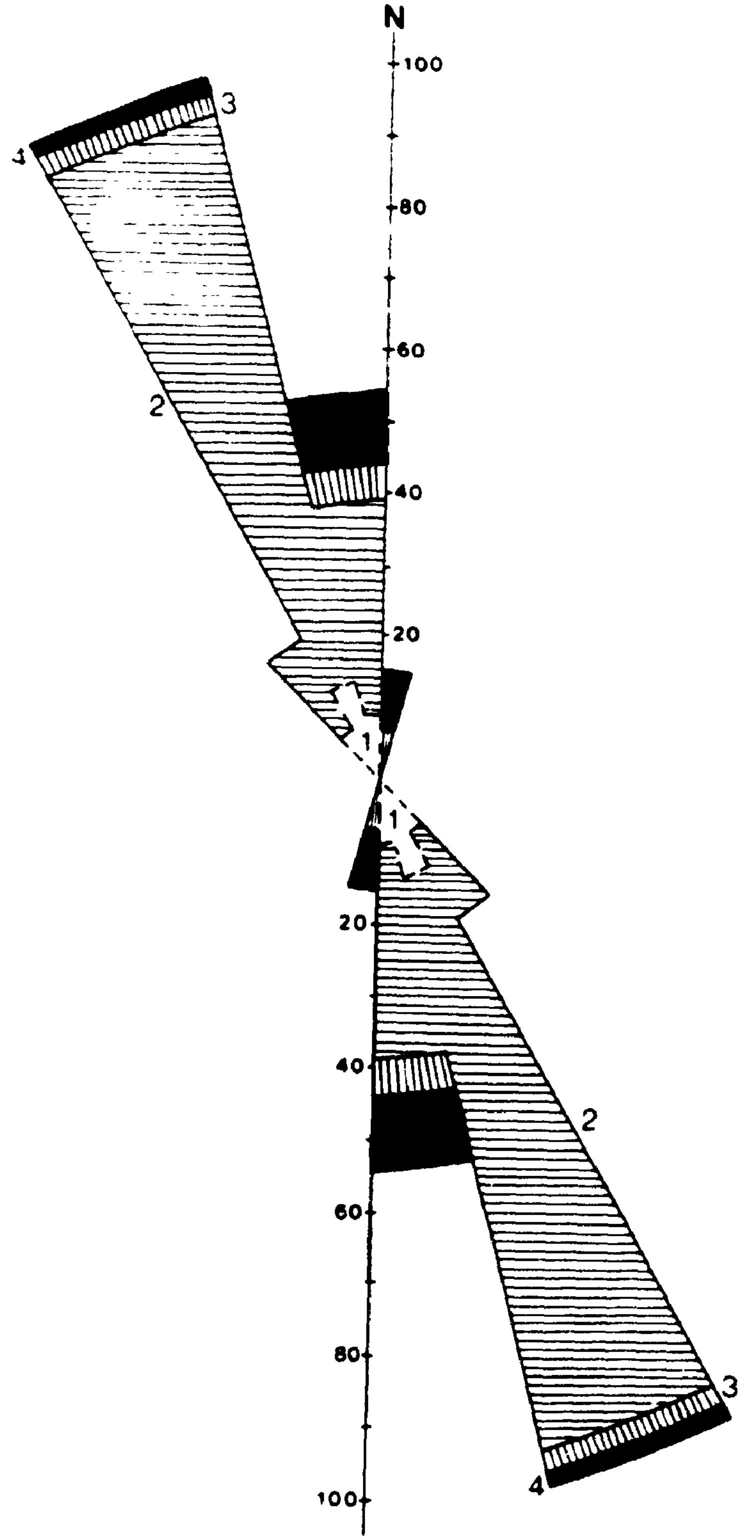

Figure 2.9 Orientation of glacial striae exposed on four successive diamictite facies bedding planes at Razorback Ridge (211.17 - 215.57 m). Data are plotted from the oldest bedding surface (1) to the youngest (4). Total number of measurements = 193.

marginally (1 - 2%) more abundant in the Fe-poor and Fe-moderate matrices than in the Fe-rich matrices.

The absence of biotite in the Fe-rich diamictites coincides with the appearance of platy hematite in the micro-matrix (<0.02 mm). White mica shreds (e.g., sericite) are also less abundant in the Fe-rich matrices than in the Fe-poor and Fe-moderate ones. This positive relationship between biotite and sericite might suggest that in the matrix of the Fe-rich diamictites, there was insufficient sericite and hence potassium to permit the formation of biotite.

Iron Formation Facies

Introduction. Iron formation occurs as a regionally developed facies in all three zones (Figure 2.1). The zones are defined by mineralogical divisions similar to those specified for the diamictites (p. 33). The divisions of the iron formation facies are:

1) **hematite** ± quartz;

2) **magnetite-biotite** ± hematite;

3) **magnetite** ± **hematite**.

Some of the iron formation samples have basally concentrated grains of fine sand-size quartz which are designated as macro-framework (e.g., $12g_2$, $12k_1$, Table 2.2). During geochemical sampling, an attempt was made to avoid incorporation of these millimetre thick layers in the aliquot, hence like the diamictite facies the micro-framework and micro-matrix (equals macro-matrix) form the bulk of any sample taken for geochemical analysis (e.g., percent Fe_2O_3 of Table 2.2). Clastic-dominated laminae (e.g., $10d_1$, $9L_2$) were also excluded from geochemical samples.

(1) **Hematite** ± quartz

The iron formation facies in measured sections at *Oraparinna* (#12), *Worumba* (#13) and *Holowilena South* (#20/14, #21) has a common micro-matrix component,

Table 2.2 Summary of macro- and microscopic features of iron formation facies samples from study localities in zones 1, 2 and 3 (Figure 2.1). ***Oraparinna***, ***Worumba*** and ***Holowilena South*** occur in zone 1; ***Oopina***, ***Mount Victor*** and ***Outalpa*** occur in zone 2; ***Spring Dam*** and ***Manunda*** are localities in zone 3. Multiple samples from one measured section (e.g., #12) are listed in ascending stratigraphic order. FD = ferroan dolomite; qtz = quartz; hem = hematite; sub. = subarkosic. See Figures A.1 - A.9 for locations of measured sections from which these samples were collected.

Locality	Oraparinna (Dropstone Creek)	Oraparinna (Dropstone Creek)	Oraparinna (Dropstone Creek)	Oraparinna (Dropstone Creek)	Oraparinna (Dropstone Creek)	Oraparinna (Dropstone Creek)	Oraparinna (Dropstone Creek)	Oraparinna (Dropstone Creek)
Sample #	12b$_1$	12g$_2$	12h	12j$_1$	12k$_1$	12n$_1$	12o	12p
Macro-framework								
Size	fine sand	fine sand		fine sand	fine sand			
Component	quartz	quartz		quartz	quartz			
Micro-framework								
Size	0.02 - 0.14 mm				0.02 - 0.14 mm	0.02 - 0.08 mm		
Components								
1)	monocrystalline quartz				monocrystalline quartz	monocrystalline quartz		
2)	k-feldspar				k-feldspar	k-feldspar		
3)	sub. Fe wacke intraclast				hem-qtz lutite intraclast	plagioclase feldspar		
4)					sub. Fe wacke intraclast	hem-qtz lutite intraclast		
Total Fe_2O_3 =	27.10%	24.18%	25.19%	25.08%	27.14%	30.01%	22.84%	
Micro-matrix								
Size	≤ 0.004 - 0.02 mm				≤ 0.004 - 0.02 mm	≤ 0.004 - 0.02 mm		≤ 0.004 - 0.02 mm
Components								
1)	hematite lutite				hematite lutite	hematite lutite		hematite lutite
2)	quartz				quartz	quartz		quartz
3)	k-feldspar				k-feldspar	hematite orthomatrix, white		hematite orthomatrix, rust
4)					plagioclase feldspar			sericite

Locality	Oraparinna (Dropstone Creek)	Oraparinna (Dropstone Creek)	Worumba	Worumba	Holowilena S.	Holowilena South	Holowilena South	Holowilena South (Back Creek)	Holowilena S (Back Creek)
Sample #	12q	12s	13d$_1$	13d$_2$	14a$_2$	14n$_1$	14o$_1$	21a$_1$	21d
Macro-framework									
Size									
Component									
Micro-framework									
Size			0.02 - 0.3 mm	0.02 - 0.14 mm		0.02 - 0.14 mm →	→	0.004 - 0.08 mm	
Components									
1)			phlogopite	chlorite-after-phlogopite	jasper	monocrystalline quartz →	→	magnetite	
2)					hem platy	sub. Fe wacke intraclast →	→	monocrystalline quartz	
3)						k-feldspar →	→	hematite platy	
4)						apatite-chlorite lens →	→	k-feldspar	
5)						plagioclase feldspar →	→	pale green chlorite	
Total Fe_2O_3 =	18.50%	22.57%	20.40%	27.93%	37.07%	53.36%	32.27%	47.20%	31.05%
Micro-matrix									
Size			≤ 0.004 - 0.02 mm →	→		≤ 0.004 - 0.02 mm →	→		
Components									
1)			hematite platy →	→		hematite lutite →	→		
2)			hematite lutite →	→		quartz →	→		
3)			k-feldspar →	→					
4)			quartz →	→					
5)			ferroan dolomite →	→					

Table 2.2 cont'd

Locality	Oopina	Oopina	Mount Victor (Razorback hill)	Mount Victor (Razorback hill)	Mount Victor (Razorback hill)	Mount Victor (Razorback hill)	Outalpa	Outalpa (I D hut)	Outalpa (I D hut)
Sample #	$19E_2$	$19C_1$	$18E_1$	18h	$18J_1$	18k	17d	$16d_1$	16i
Micro components									
Size	0.004 - 0.1 mm	0.004 - 0.08 mm	0.004 - 0.068 mm		0.004 - 0.08 mm			0.004 - 0.16 mm	0.008 - 0.1 mm
1)	quartz	quartz	quartz		quartz			quartz	quartz
2)	magnetite	magnetite	magnetite		magnetite			magnetite	green biotite
3)	hematite platy	hematite platy	chlorite-after-biotite ┐ =		chlorite-after-biotite			olive green biotite	magnetite
4)	chlorite-after-biotite	chlorite-after-biotite	ferroan dolomite ┘		ferroan dolomite			ferroan dolomite	sericite
5)	sericite	pale green chlorite	hematite platy		hematite platy			apatite	
6)	pale green chlorite	sericite	plagioclase feldspar		plagioclase feldspar				
7)	K-feldspar	FD ± apatite	sericite		sericite				
Total Fe_2O_3		43.06%	34.18%	54.29%	38.54%	55.85%	20.00%	41.67%	

Locality	Spring Dam (Pualco West)	Spring Dam (Pualco West)	Spring Dam (Pualco West)	Spring Dam (Pualco West)	Spring Dam (Pualco West)	Spring Dam (Pualco West)	Spring Dam (Pualco West)	Spring Dam (Razorback Ridge)	Spring Dam (Razorback Ridge)
Sample #	$10d_1$	$10h_1$	$10h_3$	$10S_1$	$10S_3$	$10T_1$	$5A_L$	$9c_2$	$9F_1$
Quartz-dominated layer									
Size	≤ 0.004 - 0.2 mm					0.004 - 0.08 mm	0.004 - 0.08 mm		≤ 0.008 - 0.08 mm
Components									
1)	monocrystalline quartz					quartz	quartz		quartz
2)	calcite					magnetite	hematite platy		magnetite
3)	plagioclase feldspar					hematite platy	magnetite		hematite(?) platy
4)	apatite					pale green chlorite	pale green chlorite		pale green chlorite
5)	olive green biotite								ferroan dolomite
6)	magnetite								olive green biotite
Total Fe_2O_3 (= both layers)	52.51%	45.40%	55.55%	37.37%			56.05%	39.18%	
Magnetite-dominated layer									
Size	0.016 - 0.3 mm	≤ 0.008 - 0.068 mm			0.004 - 0.104 mm	0.004 - 0.08 mm	0.004 - 0.08 mm		≤ 0.008 - 0.06 mm
Components									
1)	magnetite →	→			magnetite →	→	quartz		magnetite
2)	quartz →	→			quartz →	→	magnetite		quartz
3)	pale green chlorite →	→			hematite platy →	→	→		hematite platy
4)	calcite/ferroan dolomite →	→			pale green chlorite →	→	→		pale green chlorite
5)	plagioclase feldspar →	→			biotite-after-chlorite(?)				olive green biotite
6)	sericite (< 1%)	sericite							FD (trace, < 1%)

Table 2.2 cont'd

Locality	Spring Dam (Razorback Ridge)	Spring Dam (Razorback Ridge)	Spring Dam (Razorback Ridge)	Spring Dam (Razorback Ridge)	Spring Dam (Razorback Ridge)	Spring Dam (Razorback Ridge)	Spring Dam (Razorback Ridge)	[illegible]
Sample #	$9F_1$	$9F_2$	$9I_1$	PD93 - 90'	$2H_2$	2G	2F	$9A_4$
Quartz-enriched layer								
Size			≤ 0.004 - 0.08 mm					0.006 - [illegible] mm
Components								
1)			ferroan dolomite					hematite platy
2)			quartz					quartz
3)			plagioclase feldspar					magnetite
4)			magnetite					chlorite after biotite
5)			apatite (trace, < 1%)					
6)			hematite platy (trace)					
7)			tourmaline (trace)					
Total Fe_2O_3	41.50%	55.16%	67.23%	48.20%	59.93%	58.35%	64.73%	65.19%
Magnetite-dominated layer								
Size			≤ 0.004 - 0.14 mm					< 0.004 - 0.088 mm
Components								
1)			magnetite					magnetite
2)			hematite platy					quartz
3)			quartz					hematite platy
4)								pale green chlorite
5)								
6)								

Locality	Spring Dam (Razorback Ridge)	Spring Dam (Razorback Ridge)	Spring Dam (Razorback Ridge)	Manunda (Iron Peak)	Manunda (Iron Peak)	Manunda (Iron Peak)	Manunda (Iron Peak)	Manunda (Iron Peak)
Sample #	2A	$2C_2$	$2x_2$	7I	7J	1A	7V	$7I_2$
Quartz-dominated layer								
Size					0.004 - 0.12 mm			0.008 - 0.06 mm
Components								
1)					quartz			quartz
2)					magnetite			magnetite
3)					pale green chlorite			k-feldspar
4)					yellowish-brown biotite			
5)								
6)								
Total Fe_2O_3	51.13%	59.03%	48.99%	55.71%		63.45%	61.04%	54.44%
Magnetite-dominated layer								
Size					0.004 - 0.068 mm			0.038 - 0.048 mm
Components								
1)					magnetite			magnetite
2)					pale green chlorite			quartz
3)					quartz			biotite
4)								k-feldspar
5)								hematite(?)
6)								

namely, **hematite** lutite (Table 2.2) consisting of both silt- and mud-size particles. A widespread, though not ubiquitous micro-matrix constituent is quartz, and although quartz may occur as outsized sand grains within hematite lutite, it is not everywhere present as silt- and clay-size grains, hence the IF is here termed hematite ± quartz lutite.

At *Oraparinna* (#12), iron formation (Fe_2O_3 = 21.5%, Table 2.2) is the most profuse of three preserved facies (Figure 2.4), and the variations observed in IF are documented in Table A.1. The most recurrent type of IF is represented by sample $12b_1$. These are laminated to very thin-bedded (e.g., 3 - 13 mm) couplets of hematite-quartz lutite and hematite lutite. The lower division of these couplets weathers a blood red colour and has fine sand-size quartz which is either randomly distributed over 15% of the fresh surface (e.g., $12b_1$, $12J_1$) or basally concentrated in millimetre thick layers (e.g., $12g_2$, $12k_1$). Sand-free upper divisions of the couplets weather dark purple and the red:purple ratio can vary from 5:1 - 1:1 - 1:2.

The micro-framework of $12b_1$ is comparable to that of the underlying sand-granule-pebble diamictite ($12a_1$, Table 2.1, see p. 35) except that $12b_1$ is clearly micro-matrix-supported. It also has subangular to angular, weakly undulose and vacuole-bearing monocrystalline quartz (0.02 - 0.06 mm) as its most prevalent micro-framework component and subangular potassium feldspars (0.02 - 0.04 mm) rank second in abundance. Clasts (0.1 - 0.3 mm) consisting of quartz and potassium feldspar set in hematite lutite are interpreted as intraformational subarkosic Fe wacke which is the third facies type developed at section #12.

In $12k_1$, where quartz is basally concentrated (see above), the micro-components are similar to those of $12b_1$ (see Table 2.2). The types of strata noted in $12k_1$, from base to top of this 3 cm thick interval are:

i) micro-framework-supported subarkosic Fe arenite which pinches and swells in thickness from 0.4 - 0.9 mm;

ii) randomly distributed micro-framework-size quartz and feldspar supported by hematite lutite forms a 0.4 mm thick layer which has diffuse lower and upper boundaries;

iii) a 1.4 mm thick layer made up of sublayers: one grain thick colinear trains in which framework grains are touching. These trains are not continuous (2 - 3 mm maximum) across the thin section width;

iv) 1 - 2 grain thick isolated layers in which colinear framework grains are either touching or slightly scattered, and unlike sublayers of (iii) continue across the section width;

v) similar to (ii) but 2 mm thick.

The material intervening between these five layers is opaque hematite lutite in which randomly distributed framework- and matrix-size quartz and feldspar have a poikilitic appearance.

The second most obvious type of iron formation exposed at section #12 is equivalent to that from which sample $12n_t$ (Table 2.2) was taken, namely, couplets of hematite-quartz (red) lutite (1.0 - 1.4 cm typical, 4.5 cm maximum) capped by hematite (purple) lutite (1 - 3 mm). Sample $12n_t$ is similar to the hematite lutite portion of $12k_t$ in that scattered, angular to subangular framework- and matrix-size quartz and feldspar grains are microscopically poikilitic relative to the opaque matrix which hosts them. The matrix hematite occurs in two forms: (i) hematite lutite, the grain boundaries of which are not resolvable at 50x and appears light rust-coloured in plane polarized reflected light and (ii) hematite orthomatrix, which consists of anhedral, irregular-shaped grains (0.004 - 0.06 mm) that are off-white in plane polarized reflected light. The latter hematite type tends to conform to the shape of any silicate detritus against which it may abut.

Also present in $12n_t$ is an apatite-rich lens (1 x 11 mm), probably equivalent to the "distinct bodies of carbonate apatite" described by Circosta (1978, p. 8) in the iron formation at *Holowilena South*. He considered them to be either concretions or secondary replacements of another mineral.

Located within the hematite ± quartz lutite in the upper half of section #12 are two granule-dominated horizons (40.94 m & 59.09 m, Table A.1) which are only 2 - 3 grains thick. The tops are planar but the lower contacts are irregular, due in part to the presence of a few outsized pebbles (1.2 - 3 cm) which project downward into the lutite host. Laterally traceable for 2 m, the layers are possible macroscopic equivalents of layer types (ii) and (iv) in sample $12k_1$ (see p. 66). Also within the upper half of the section are two lonestones: one of which is a boulder of subarkosic wacke (44.95 m mark) and the other a small, subrounded cobble (53.83 m mark). In both instances, foliation planes of the hematite ± quartz lutite envelope the clast, but it is unclear whether the foliation-parallel laminae are actually pierced by the lonestone (i.e., dropstone origin).

Iron formation occurs as thin blackish-grey horizons throughout section #13 at *Worumba* (Figure 2.4, Table A.2). Two IF samples $13d_1$ and $13e_2$ contain sporadic thin arkosic Fe wacke laminae, the boundaries of which are more clearly defined than the sand-size quartz mentioned on p. 65. These laminae were avoided in the aliquot for geochemical analysis (e.g., % Fe_2O_3 of Table 2.2), hence the micro-components listed for $13d_1$ and $13e_2$ (Table 2.2) pertain only to the Fe-rich layers.

The subordinate laminae are ferroan dolomite-phlogopite arkosic Fe wacke which are iron oxide-poor ($\approx$5%) and in $13d_1$, they are internally stratified (Plate 2.2a). For example, the arkosic Fe wacke forms a basal ungraded division (0.6 mm thick), above which there is a change defined by:

i) marked K-feldspar decrease (framework- and matrix-size);

ii) increase of framework phlogopite;

iii) abrupt increase of matrix hematite.

This second division is a hematite-potassium feldspar-quartz-phlogopite lutite (1.0 mm

Plate 2.2 Iron formation facies.

(a) Clastic lamina in iron formation. The light grey, basal division is ferroan dolomite-phlogopite arkosic Fe wacke (Fe-poor), whereas the darker, upper division is hematite-potassium feldspar-quartz-phlogopite lutite. Plane light; bar = 0.5 mm (sample $13d_1$, Table A.2, *Worumba*).

(b) Alternating laminae of jasper (dark grey) and hematite (light grey) in sample of iron formation. Diameter of coin is 18 mm (sample $14a_4$, Table A.3, *Holowilena South*).

(c) Framework-supported basal division of subarkosic Fe wacke (Fe-poor) is abruptly overlain by a hematite-rich lutite division, within which quartz and feldspar grains have a dispersed appearance. Plane light; bar = 0.2 mm (sample $14a_2$, Table A.3, *Holowilena South*).

(d) Thinly laminated iron formation (vicinity of sample $16d_1$, Table A.8, *Outalpa*).

(e) Subarkosic Fe arenite (Fe-poor) layers (light grey) in iron formation (dark grey). Starved ripple of Fe arenite evident (centre right). (section #7, Table A.12, *Manunda*).

(f) Gradational contact between magnetite-hematite-quartz lutite (iron formation, base) and ferroan dolomite-quartz-plagioclase [subarkosic Fe arenite (Fe-poor), top]. Plane light; bar = 0.05 mm (sample $9l_2$, Table A.11, *Spring Dam*).

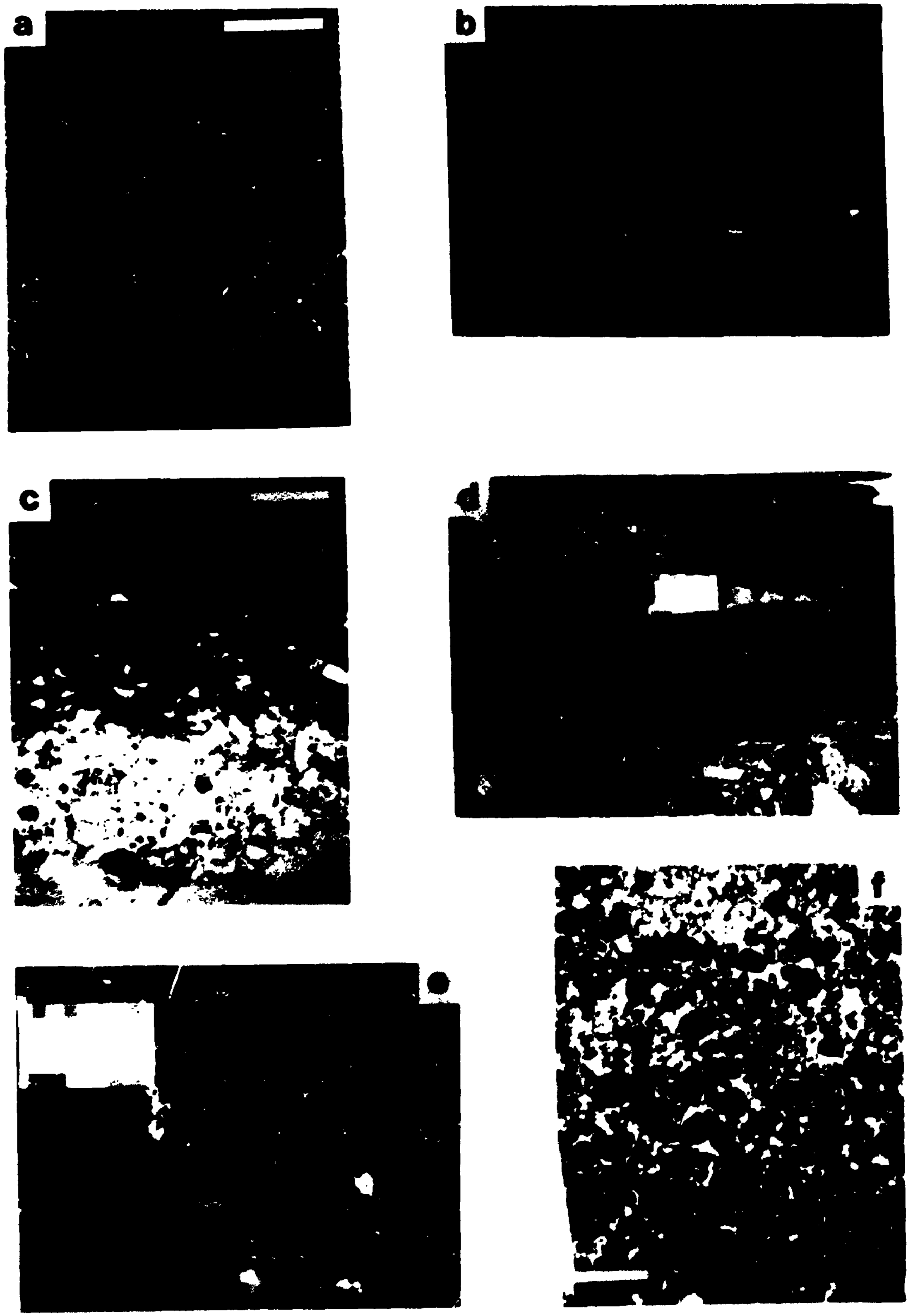
a
b
c
d
e
f

thick) throughout which phlogopite decreases in size and abundance. A possible transition occurs at the halfway point where there is:

iv) a subtle decrease in matrix potassium feldspar content; and

v) further increase of matrix hematite.

The majority of laminae in $13d_1$ and $13e_2$ are of comparable thickness and composition to the second division, with variations in matrix-size hematite and, to a lesser degree, potassium feldspar serving as layer discriminants. However, the aforementioned "grading" of phlogopite is atypical; it more typically occurs as outsized grains (0.02 - 0.3 mm) set in the hematite-dominated lutite.

The micro-matrix hematite in $13d_1$ and $13e_2$ has two habits, just as it does in the diamictites at *Worumba* (see p. 42). Platy hematite locally occurs along cleavage planes of the outsized phlogopite grains, especially where phlogopite has been partially retrogressed to chlorite (see Chapter 4, Plate 4.2c). This suggests that at least some of the matrix-type hematite has a late-stage origin.

At *Holowilena South*, iron formation is most apparent as laminated intervals ($\leq$11.8 m thick) within the upper half of section #20/14 (Figure 2.5, Table A.3) and as the lowermost exposure (7.1 m thick) of section #21 (Figure 2.5, Table A.4). It also occurs throughout #20/14 as the upper layer of a couplet with subarkosic Fe siltstone (Fe-poor), but because the Fe siltstone is commonly the dominant phase, and is here considered the fine grained equivalent of a subarkosic Fe wacke, this second type of IF will be described with the wackes (see p. 89).

The foremost type of iron formation at *Holowilena South* (#20/14, 0.4 - 11.8 m thick) is equivalent to the subordinate type at *Oraparinna* (#12, p. 66), namely, laminated couplets of hematite-quartz (red) and hematite (purple) lutite ($14n_1$, $14o_1$, Table 2.2). As at section #12 (e.g., $12n_1$), the IF contains bedding-parallel lenses of apatite and chlorite (see Plate 4.?a). The secondary type of IF (#20/14, 0.02 - 0.92 m thick) occurs as thin laminae of jasper (brick red, dominant) alternating with platy hematite (steel grey, Plate 2.2b). Locally developed within the jasper-hematite are subarkosic Fe wacke laminae, which in $14a_2$ (Plate 2.2c) show features similar to those described in $13d_1$ from *Worumba* (p. 67, Plate 2.2a). The two thickest jasper-hematite intervals, which occur at the 166 m mark of section #20/14, are laterally traceable for 980 m & 1185 m along strike to the southwest and northeast respectively, though they are commonly offset by syndepositional faults.

(2) **Magnetite-biotite** ± hematite

Exposures of iron formation at *Oopina* (#19), *Mount Victor* (#18) and *Outalpa* (#16) contain **magnetite**, whereas hematite may or may not be present. The prevailing iron-bearing silicate is either chloritized biotite or **biotite** (Table 2.2). As at *Oraparinna* (#12), IF at *Oopina* (Figure 2.6) overlies a thin horizon of diamictite, then persists as the dominant facies of the section. In contrast to the macroscopic clastic contaminants in the IF at sections 12 (i.e., sand-size quartz), 13 and 20/14 (i.e., felsic laminae), the equivalent facies at *Oopina* (#19) is devoid of clastic-dominated layers except for a 17 m thick interval at the 2/3 mark in section. The dark steel grey-weathering IF here contains weakly magnetic light grey Fe siltstone layers (Fe-moderate, 8 - 10 mm thick) which are both flat-based and flat-topped (Table A.5).

Micro-components of laminated iron formation samples $19E_2$ and $19G_1$ (Table 2.2) are dominated by quartz, magnetite, hematite and chlorite-after-biotite. Magnetite occurs as rhombs (0.008 - 0.048 mm), hematite as small plates (0.004 - 0.008 mm) and chlorite-after-biotite as isolated, golden yellow fibrous patches (0.04 - 0.3 mm). It is conceivable that these dissociated patches are equivalent to the outsized phlogopites seen at *Worumba* (#13, see p. 70). Although hematite at *Worumba* is present as both anhedral silt/mud particles and subhedral plates, it occurs solely as plates at *Oopina*, which suggests enhanced crystallization of matrix hematite.

Iron formation dominates the upper 300 m of the stratigraphic section at *Mount Victor* (#18, Figure 2.6). As at *Oopina* (#19), the majority of IF at section #18 is devoid of compositionally-distinct macroscopic laminae (Table A.6). The lowermost exposures of IF contain thin sporadic laminae of either felsic siltstone (similar to *Worumba*, see p. 67 re sampling) or ferroan dolomite (i.e., $18E_1$, Table 2.2).

Closer examination of $18E_1$, however, reveals that ferroan dolomite is not restricted to the thin reddish-brown laminae (0.5 - 2 mm thick) of the greyish-black weathering host. As evident from Table 2.2, ferroan dolomite rivals chlorite-after-biotite as the third most abundant component of the iron formation *sensu stricto* (L.O.I. = 3.40%). The mineralogy and mineral hierarchy of the reddish-brown laminae (not present in the geochemical aliquot) mimic those of the host, except that ferroan dolomite (3rd) > hematite > chlorite-after-biotite (5th). Hence ferroan dolomite serves as the main discriminant between successive layer types.

Up-section of the 365 m mark in section #18, iron formation, with few exceptions, displays macroscopic qualities similar to those of sample $18j_1$ (370 m, Table A.6). Stratification is neither apparent on the dark greyish-black weathered surface nor the greyish-green fresh surface. Sample 18k (Fe_2O_3 = 55.85%) is visually comparable to $18j_1$ (Fe_2O_3 = 36.54%, Table 2.2), but the higher iron content together with a blackish-grey fresh surface for 18k (449 m mark) and all IF horizons up-section of it, suggests a higher iron oxide content.

Thin horizons of IF constitute only a minor facies in both measured sections at *Outalpa* (Figure 2.7). It is inter-stratified with diamictite and quartz wacke in the lowermost section (#17, Table A.7), whereas higher in the stratigraphy, it occurs sporadically within a section dominated by subarkosic Fe wacke (#16, Table A.8).

At *Oopina* and *Mount Victor*, macroscopic clastic-dominated layers were rarely developed. They are not apparent in the iron formation at *Outalpa* in contrast with the hematite ± quartz iron formation of *Oraparinna*, *Worumba*, and *Holowilena South*. This difference is reflected in higher iron contents of the magnetite-biotite ± hematite facies (20.80 - 55.85%, Table 2.2) relative to the hematite ± quartz facies (18.50 -

30.81%, Table 2.2).

The IF at *Outalpa* has two forms: thinly laminated (e.g., $16d_1$, Plate 2.2d) or unstratified (e.g., 17d, 16i). The main components of both kinds are quartz, biotite and magnetite; it is only the relative abundances of these minerals which varies (Table 2.2). For example, $16d_1$ is dominated by quartz and subhedral to euhedral rhombs of magnetite (0.008 - 0.056 mm). Third in abundance is olive green biotite (0.02 - 0.16 mm). The quartz has weakly sutured grain boundaries. The diffuse laminations (0.5 - 1.2 mm thick) cited on the weathered surface are defined mainly by subtle changes in magnetite content. Notably absent from the IF at *Outalpa* is hematite. It appears that the void created by hematite's nonoccurrence has been filled not by magnetite, but by biotite; at least some of which is considered to be detrital (see p. 52).

(3) **Magnetite ± hematite**

Comparable to type #2 iron formation (p. 71), **magnetite**, with or without **hematite**, occurs in IF at Pualco West (#10), Razorback Ridge (#9/2) and Iron Peak (#7). In contrast to type #2, neither chloritized biotite nor biotite is common in the Fe-rich lutite (i.e., iron formation) layers (Table 2.2). Biotite may occur in the macroscopic, clastic-dominated laminae (e.g., 0.006 - 2.5 cm thick in $10d_1$, $10k_1$, $9l_2$, 1A, 7V; Plate 2.2e) within the IF, but as at *Oopina*, *Mount Victor* and *Outalpa*, such interlayers are only locally developed.

Iron formation which occurs throughout sections 10, 9/2 and 7 is typically black-weathering and thinly laminated (Figure 2.8, Tables A.10 - A.13). Magnetite-dominant laminae prevail (Table 2.2); the two main components of which are subhedral to euhedral rhombs of locally hematized magnetite (0.008 - 0.14 mm; see Plates 4.1c & 4.2d) and weakly undulose quartz (0.008 - 0.3 mm), which has planar boundaries. The presence or absence of hematite appears to be linked to the amount of chlorite in the magnetite-dominant laminae. For example, where chlorite is the third most abundant component then hematite does **not** occur ($10d_1$, $10k_1$, 7J, Table 2.2), whereas if chlorite is ranked fourth, hematite appears as the third most abundant component ($10S_3$, $10T_1$, $5A_{t.}$, $9F_1$, $9I_2$, $8A_{t}$). This hematite and chlorite relationship is similar to that observed in sample $21a_1$ (Table 2.2), which was the only magnetite-dominated horizon found at *Holowilena South*.

The macroscopic, clastic-dominated laminae which locally occur within the iron formation are white-weathering subarkosic Fe arenites (Fe-poor). A ubiquitous component of these layers is carbonate, either as calcite ($10d_1$, Table 2.2) or ferroan dolomite ($9I_2$; 1A, 7V at 192 & 202.5 m, Table A.12; $8q_1$, $8E_1$, 8C, $8B_2$ within Adit, Table A.13). Apatite is also present. Gradational contacts between the magnetite ± hematite IF and the arenite layers locally occur (Plate 2.2f), as does ripple cross-lamination defined by the iron oxide grains (e.g., $10d_1$, interval hosting $9I_2$, 8C), and soft-sediment deformation of these laminae (Plate 2.3a). The Fe arenite also forms colinear starved ripples (e.g., 1A, 7V, 8C; Plate 2.2e; Figure 2.10a) or infills flutes which have scoured the upper surfaces of magnetite-dominant lutite laminae (228 & 231 m, Table A.12; Plate 2.3b; Figure 2.10b).

Subarkosic Fe Wacke Facies

Introduction. This third facies type is regionally developed (Figure 2.1) and, like the diamictite and iron formation facies, is divisible into three mineralogically distinct zones, namely:

1) **hematite**-bearing;
2) **magnetite**-bearing; and
3) **magnetite** ± **hematite**-bearing.

Subarkosic Fe wacke (1 - 21.5% Fe oxide minerals), which can be either bedded or unstratified, is more commonly intercalated with iron formation than diamictite. Minor amounts of subarkosic Fe arenite (1 - 5% Fe oxide minerals) and subarkosic arenite (non Fe, <1% Fe oxides) occur within the Fe wacke facies. Unlike the diamictite facies and

Plate 2.3 Iron formation and Subarkosic Fe wacke facies.

(a) Negative image of thin section 8C-1 (IF); iron oxides are white and the silicate and carbonate minerals appear black. Lower half of photo is a carbonate-rich subarkosic Fe arenite (Fe-poor) layer in which sporadic iron oxide laminae have been folded by soft-sediment deformation. Iron oxide grains also form cross-laminated horizons. Field of view is 21 mm wide (sample 8C, Table A.13, Adit on *Spring Dam*).

(b) Flutes on upper surface of iron formation bedding plane. Length of magnet is 12.2 cm (vicinity of sample $7X_1$, Table A.12, *Manunda*).

(c) Starved ripples of subarkosic Fe arenite (Fe-poor) in hematite-quartz lutite (iron formation) (vicinity of sample $12d_2$, Table A.1, *Oraparinna*).

(d) Negative image of thin section $12f_3$ (wacke) so that the silicate minerals appear black and the iron oxides are white. Alternating laminae of Fe-rich and Fe-moderate subarkosic Fe wacke comprise parallel laminated T_b division. This is overlain by a cross-laminated subarkosic Fe arenite (Fe-poor) division (T_c). Contact between T_c and overlying layer (arrow) is enlarged in Plate 2.3e. Field of view is 33 mm wide (sample $12f_3$, Table A.1, *Oraparinna*).

(e) Uppermost hematitic cross-lamina of T_c division (previous photo) with microscopic flame structures, and E_1 division of alternating silt (white) and lutite (black) laminae. Plane light; bar = 0.1 mm (sample $12f_3$, Table A.1, *Oraparinna*).

(f) Framework-supported subarkosic Fe wacke (Fe-moderate), overlain by a hematite-rich lutite division, within which quartz and feldspar grains have a dispersed appearance. Plane light; bar = 0.5 mm (sample 12p, Table A.1, *Oraparinna*).

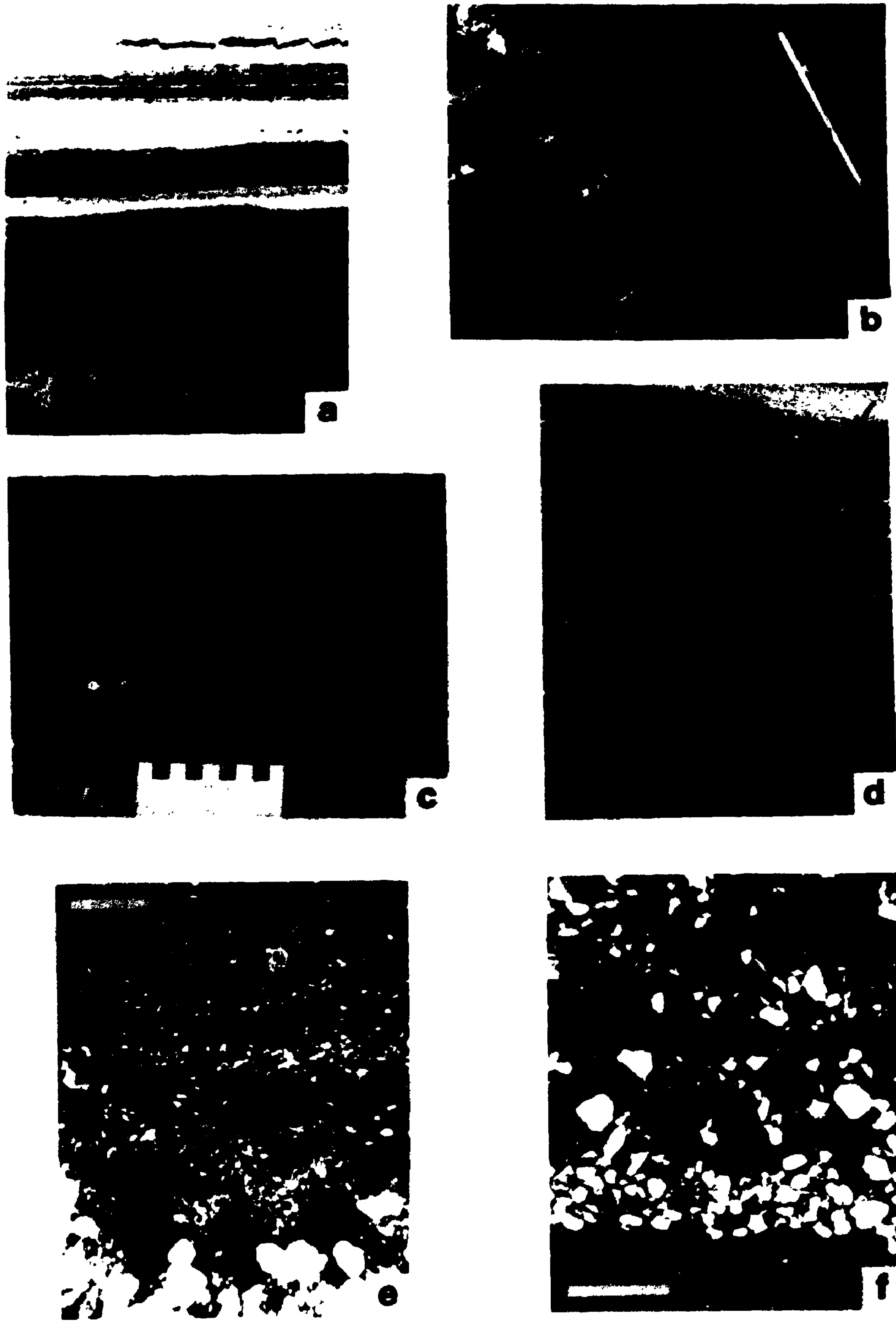

Figure ? 10A Orientation of paleocurrent data derived mainly from cross-laminated starved ripples within iron formation facies at Razorback Ridge and Iron Peak. Data from Pualco West were collected from ripple cross-laminations in subarkosic Fe wacke and subarkosic arenite facies (G.M. Young data). Unshaded, enclosed pattern = Pualco West; horizontal lines = Razorback Ridge; shaded = Iron Peak. Total number of measurements = 35.

Figure 2.10B Orientation of paleocurrent data derived from flute molds perserved on the upper surfaces of bedding planes within Fe siltstone and iron formation facies at Iron Peak (227.71 - 228.71 and 230.96 - 231.76 m). Total number of measurements = 273.

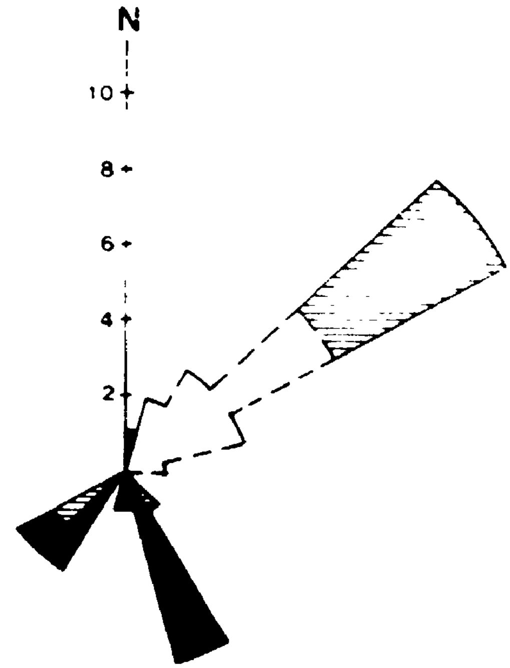
N
10
8
6
4
2

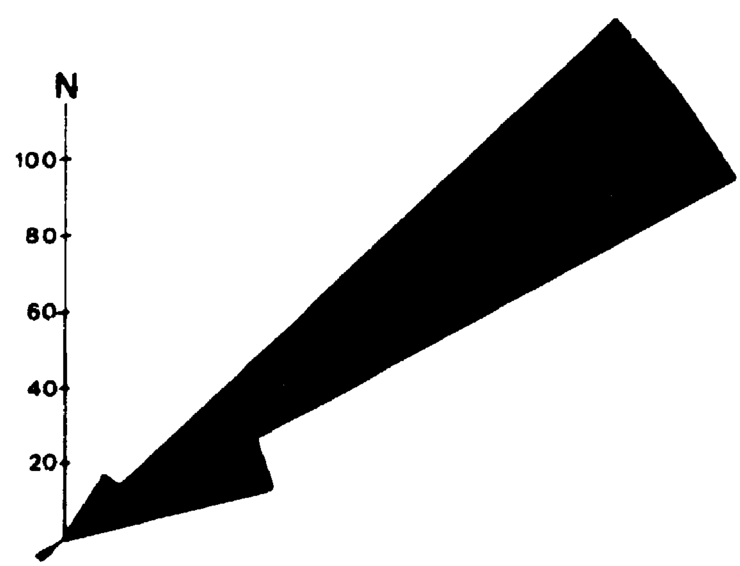
N
100
80
60
40
20

some of the IF samples (Tables 2.1 & 2.2), macroscopic components of the Fe wackes are not common enough to incorporate in Table 2.3. Therefore, the prefix micro- has been removed from the terms 'framework' and 'matrix', which are the components of samples taken for geochemical analyses (e.g., percent Fe_2O_3 of Table 2.3).

(1) **Hematite**-bearing

At the three hematite-bearing localities studied, subarkosic Fe wacke is most intimately associated with iron formation at *Oraparinna* (#12) and *Holowilena South* (#20/14), whereas it is commonly interstratified with Fe siltstone at *Worumba* (#13; Tables A.1 - A.3, Figures 2.4 & 2.5).

There are ten thinning- and fining-upward cycles delineated at *Oraparinna* (#12), six of which are based by subarkosic Fe wacke layers and capped by laminated couplets of hematite-quartz (red) and hematite (purple) lutite (Table A.1). A **transition** from subarkosic Fe wacke to hematite-quartz lutite is most evident in the basal beds of cycles 1 and 2 (samples $12d_1$, $12d_2$ and $12f_1$, $12f_3$ respectively, Table 2.3). For example, the flat-based bottom bed (50 cm thick) of cycle 1 consists of four zones:

i) lone cobble (quartz arenite) in basal layer of yellowish-white, medium-grained, Fe-poor (1 - 5% Fe oxide) subarkosic Fe wacke, which pinches and swells from 3 - 9 cm. Layer-scale grading of sand-size grains was not observed;
ii) red-tinged, fine- to very fine sand-size Fe-moderate subarkosic Fe wacke (21 cm thick, Fe_2O_3 = 8.57%) within which there are a few discontinuous yellowish-white wisps (e.g., 7 x 0.1 cm) of Fe-poor subarkosic wacke;
iii) homogeneously red-coloured very fine sand- to silt-size Fe-moderate subarkosic Fe wacke (10 cm thick, Fe_2O_3 = 12.10%) which is structureless;
iv) thinly laminated yellowish-white Fe-poor subarkosic Fe arenite and red hematite-quartz lutite (11 cm thick) within which the Fe-poor arenite locally forms starved ripples (Plate of 2.3c; cf. Facies D2.2 of Pickering *et al.*, 1986, 1989).

The lower three zones form a 40 cm-thick layer in which there is an overall fining-

Table 2.3 Summary of microscopic features of subarkosic Fe wacke facies samples from study localities in zones 1, 2 and 3 (Figure 2.1). Samples that are associated with, but are not actual subarkosic Fe wacke, include subarkosic Fe arenite (e.g., Fe-poor layers of $12D_3$, $12f_1$, $12r_1$, 13k, $20q_2$, $14B_1$, 14f, $18l_1$, $9B_2$, $2u_3$, 7o) or subarkosic arenite (e.g., non Fe layers of $13F_1$, 10J, $2y_1$). *Oraparinna*, *Worumba* and *Holowilena South* occur in zone 1; *Mount Victor* and *Outalpa* occur in zone 2; *Spring Dam* and *Manunda* are localities in zone 3. Multiple samples from one measured section (e.g., #12) are listed in ascending stratigraphic order. FD = ferroan dolomite; qtz = quartz; plag. = plagioclase; hem = hematite; hem-aft-mag = hematite-after-magnetite; phlogo = phlogopite; chl = chlorite; bio = biotite; WM = white mica; sub. = subarkosic. See Figures A.1 - A.9 for locations of measured sections from which these samples were collected.

Location / Sample #	Oraparinna (Dropstone Creek) (19)	Oraparinna (Dropstone Creek) (24)	Oraparinna (Dropstone Creek) (20) (lower 1.1 cm)	Oraparinna (Dropstone Creek) (20) (upper 5.2 cm)	Oraparinna (Dropstone Creek) (21) (lower 4.4 cm, then	Oraparinna (Dropstone Creek) (21) next 4.2 cm)	Oraparinna (Dropstone Creek) (23)	Oraparinna (Dropstone Creek) ( )	Oraparinna (Dropstone Creek) ( )
DOMINANT layer	Fe moderate	Fe-moderate	Fe-poor	Fe-moderate	Fe-poor	Fe-rich	Fe-moderate	Fe moderate	Fe-poor
Framework									
Size			0.1 - 0.3 mm	0.1 - 0.5 mm	0.04 - 0.6 mm	0.04 - 0.24 mm		0.04 - 0.34 mm	0.1 - 0.5 mm
Components									
1)			monocrystalline quartz →	→	monocrystalline quartz →	→		monocrystalline quartz	monocrystalline quartz
2)			K-feldspar →	→	K-feldspar →	→		K feldspar	K feldspar
3)			plagioclase feldspar →	→	plagioclase feldspar →	→		plagioclase feldspar	plagioclase feldspar
4)			white mica flake	hem-qtz lutite rip-up	hem-qtz lutite rip-up	WM flake (trace)		hem-qtz lutite rip up	hem qtz lutite rip up
5)			glauconite (trace, < 1%)	white mica flake	magnetite (trace, < 1%)	chlorite (trace)			calcite ferroan dolomite
Total Fe_2O_3	8.57%	12.10%				13.65%	9.63%		2.09%
Cement					apatite →	→			
Matrix									
Size			≤ 0.004 - 0.24 mm →	→	≤ 0.004 - 0.06 mm →	→		< 0.004 - 0.012 mm	< 0.004 - 0.06 mm
Components									
1)			hematite mud →	→	hematite orthomatrix, rust →	→		hematite orthomatrix, rust	calcite/ferroan dolomite
2)			hematite orthomatrix, rust →	→	hematite orthomatrix, white	hematite lutite		hematite lutite	hematite lutite
3)			hematite orthomatrix, white →	→	hematite lutite				hematite orthomatrix, rust
4)			ferroan dolomite →	→	FD = sericite				
SUBORDINATE layer			Hematite-quartz lutite		Fe-moderate	Fe-moderate		Hematite-quartz lutite	
Framework									
Size			0.1 - 0.3 mm		0.04 - 0.4 mm	0.04 - 0.2 mm			
Components									
1)			monocrystalline quartz		monocrystalline quartz →	→			
2)			K-feldspar		K-feldspar →	→			
3)			plagioclase feldspar		plagioclase feldspar →	→			
4)					hem-qtz lutite rip-up				
Cement					apatite →	→			
Matrix									
Size			≤ 0.004 - 0.02 mm		≤ 0.004 - 0.06 mm →	→		< 0.004 - 0.02 mm	
Components									
1)			hematite mud		hematite orthomatrix, rust →	→		hematite lutite	
2)			quartz silt		hematite lutite →	→		quartz silt	
3)			ferroan dolomite		hematite orthomatrix, white			hematite orthomatrix, rust	
4)			sericite		sericite (trace)			sericite	
					magnetite (trace)			hematite orthomatrix, white	

Table 2.3 cont'd

Locality	Worumba	Worumba	Worumba	Worumba	Holowilena South	Holowilena South	Holowilena South	Holowilena South	Holowilena South
Sample #	$13F_1$	13g	$13i_2$	13h	$20g_1$	$20i_3$	$20i_1$	$20g_5$	[illegible]
Sand dominated layer	Non Fe			Fe-poor	Fe poor	Fe poor	Fe poor	Fe poor	Fe poor
Framework									
Size	0.02 - 0.3 mm			0.02 - 0.2 mm	0.04 - 0.24 mm		0.02 - 0.2 mm		0.04 - 0.8 mm
Components									
1)	monocrystalline quartz			monocrystalline quartz	monocrystalline quartz		monocrystalline quartz		monocrystalline quartz
2)	K-feldspar			K-feldspar	K-feldspar		K-feldspar		K feldspar
3)	ferroan dolomite			ferroan dolomite	ferroan dolomite		ferroan dolomite		FD quartz intraclast
4)	olive green phlogo			chlorite-after-phlogo	hematite serrate &		chlorite-after-phlogo		hem qtz intraclast =
					hematite intraclast				plagioclase feldspar
Total Fe_2O_3		5.71%	13.62%		5.08%	5.34%		4.34%	
Matrix									
Size	0.004 - 0.02 mm			≤ 0.004 - 0.020	< 0.04 mm		< 0.02 mm		0.04 mm
Components									
1)	ferroan dolomite			ferroan dolomite	quartz		FD orthomatrix(?)		ferroan dolomite
2)	hematite platy			hematite platy	ferroan dolomite		chlorite-after-phlogo		olive green phlogo
3)	apatite			hematite lutite	chlorite-after-phlogo				hematite lutite
4)				quartz	hematite lutite				hematite platy (trace)
Silt dominated layer	Fe-moderate			Fe-moderate			Fe-poor		Fe poor
Size	≤ 0.004 - 0.024 mm			≤ 0.004 - 0.14 mm			≤ 0.004 - 0.032 mm		< 0.004 - 0.12 mm
Components									
1)	quartz			quartz			ferroan dolomite		quartz
2)	K-feldspar			K-feldspar			quartz		olive green phlogo
3)	hematite platy			ferroan dolomite			chlorite-after-phlogo		K feldspar
4)	ferroan dolomite			hematite platy			hematite platy		FD orthomatrix(?)
5)	olive green phlogo			chlorite-after-phlogo			tourmaline (trace, < 1%)		hematite intraclast
6)	sericite			hematite lutite					hematite lutite

Locality	Holowilena South		Holowilena South	Holowilena South		Mount Victor (Razorback hill)	Mount Victor (Razorback hill)	Outalpa (I.B. Hut)	Outalpa (I.B. Hut)	Outalpa (I.B. Hut)
Sample #	14f		$14g_1$	$14i_2$		$18g_1$	$18i_1$	$16A_1$	$16C_4$	$16e_3$
Sand dominated layer	Fe-poor	Fe-moderate	Fe-moderate	Fe-poor	Fe-poor	Fe-poor	Fe-poor	Fe poor	Fe poor	Fe poor
Framework										
Size	0.04 - 0.44 mm	0.04 - 0.5 mm	0.04 - 0.8 mm	0.04 - 1 mm	0.04 - 0.4 mm	0.04 - 0.3 mm	0.04 - 0.16 mm			
Components										
1)	monocrystalline quartz	sub Fe wacke intraclast	monocrystalline quartz	monocrystalline quartz →	→	→	→			
2)	K-feldspar	monocrystalline quartz	sub Fe wacke intraclast	hem-qtz intraclast	K-feldspar	ferroan dolomite →	→			
3	sub Fe wacke intraclast	K feldspar	K feldspar	sub Fe wacke intraclast	plagioclase feldspar	plag + K feldspar	plag feldspar			
4)	olive green phlogopite →	→	olive green phlogo	K-feldspar	hem-qtz intraclast	Ti hematite	K-feldspar			
5			plagioclase feldspar	FD - quartz intraclast →	→	chl after-bio	Ti hem + magnetite			
Total Fe_2O_3			11.52%			4.73%	4.81%	3.[illegible]%	5.[illegible]4%	[illegible]
Matrix										
Size	0.34 mm	0.04 mm	0.04 mm	< 0.04 mm	0.04 mm	0.04 mm	0.04 mm			
Components										
1	FD orthomatrix(?)	hematite lutite	hematite lutite	ferroan dolomite →	→	quartz	ferroan dolomite			
2)	hematite lutite	quartz	quartz	quartz →	→	hematite platy(?)	sericite			
3	quartz	K feldspar	ferroan dolomite			sericite + FD				
4						apatite (trace)				

Table 2.3 cont'd

Locality	Spring Dam (Pualco West)	Spring Dam (Pualco West)	Spring Dam (Razorback R.)	Spring Dam (Razorback R.)	Spring Dam (Razorback Ridge)	Spring Dam (Razorback Ridge)	Spring Dam (Razorback Ridge)	Spring Dam (Razorback Ridge)	Manunda (Iron Peak)	Manunda (Iron Peak)
Sample #	10h	$10J_1$	$9B_1$	9H	2b	$2T_1$	$2v_3$	$2v_1$	3	1w
Coarser layer	Fe-moderate	Non Fe	Fe-poor	Fe poor	Fe-moderate	Fe-moderate	Fe-poor	Non Fe	Fe poor	Fe moderate
Framework										
Size		0.06 - 0.8 mm			0.02 - 0.08 mm	0.02 - 0.07 mm	0.02 - 0.08 mm	0.06 - 0.14 mm	0.02 - 0.14 mm	0.02 - 0.44 mm
Components										
1)		monocrystalline quartz			quartz	→	→	monocrystalline quartz	quartz	monocrystalline quartz
2)		plagioclase feldspar			plagioclase feldspar	→	→	→	limonite	magnetite
3)		ferroan dolomite			magnetite	→	olive green biotite	hem-aft-mag (trace)	plagioclase feldspar	→
4)		chl-bio-replacing plag			pale green chlorite	pale green biotite	magnetite	tourmaline (trace)	magnetite	golden yellow biotite
5)					pale green biotite	WM flake (trace)	pale green chlorite		WM flake (trace)	tourmaline (trace)
Total Fe_2O_3	7.89%	0.65%	3.19%	7.70%			7.61%	1.08%		15.94%
Matrix										
Size		0.06 mm			< 0.02 mm	< 0.02 mm	< 0.02 mm	< 0.06 mm	0.02 mm	0.02 mm
Components										
1)		chlorite network			sericite	→	→	quartz	sericite	quartz
2)		sericite			plagioclase feldspar	ferroan dolomite		sericite	quartz	sericite
3)					hematite platy(?)	plagioclase feldspar		FD (trace)	apatite (trace)	magnetite
4)						hematite platy(?)				apatite (trace)
Silt dominated layer						Fe-moderate	Fe-moderate			
Size						≤ 0.008 - 0.08 mm	≤ 0.008 - 0.06 mm			
Components										
1)						quartz	quartz			
2)						magnetite	magnetite			
3)						sericite	sericite			
4)						hematite platy(?)	hematite platy(?)			

upward of framework quartz and feldspar grains (coarse-tail grading) combined with an upward increase in matrix hematite (compositional grading). These trends also occur in thin sections $12f_1$ and $12f_3$ taken through the 11.5 cm-thick subarkosic Fe wacke bed at the base of cycle 2 and which reveal what are here considered Bouma T_{bc} and Piper (1978) E_{1-3} divisions.

Sample $12f_1$, approximately 5 cm thick, consists of alternating laminae of dominant Fe-poor (1.0 - 4.3 mm thick) and subordinate Fe-moderate (0.5 - 6.5 mm thick) subarkosic Fe arenite & wacke respectively (T_b division, Table 2.3). These parallel laminae are most evident in the lower 1.86 cm of the slide. They are, in the remaining 3 cm, macroscopically apparent, but microscopically the boundaries between layer types are too diffuse for meaningful thickness measurements. In the succeeding 4.2 cm ($12f_3$, Plate 2.3d) layer composition has shifted to Fe-rich (greater than 21.5% Fe oxide, dominant, 0.9 - 19.2 mm) and Fe-moderate (5 - 21.5% Fe oxide, subordinate, 0.7 - 1.2 mm) subarkosic Fe wacke (T_b division continued, Table 2.3). Within the uppermost 11 mm of the Fe-moderate T_b division, there is a starved ripple (8.2 x 0.6 mm) of Fe-poor subarkosic Fe arenite, which represents a transition into, the overlying cross-laminated zone (T_c, Plate 2.3d).

The uppermost 21.5 mm of $12f_3$, details of which are not given in Table 2.3, has at its base 13.6 mm of Fe-poor subarkosic Fe arenite with cross-laminae (0.8 mm thick, inclined 19° to horizontal) defined by matrix-size hematite (T_c). The highest cross-lamina either flames into (Plate 2.3e) or is draped by quartz-enriched hematite-quartz lutite (7.8 mm thick). The basal 1.8 mm of lutite is parallel laminated (0.1 mm thick); alternating quartz-dominant and Fe-dominant (E_1 division of Piper, 1978). The remaining 6 mm are structureless ($E_{2\&3}$) except that framework grains (i.e., quartz) continue to fine-upward (i.e., 0.06 mm max. at base of E_1 to 0.02 mm at top of E_3).

Stratigraphically up-section, the subarkosic Fe wacke at the base of cycle 9 is different from the thick (e.g., 50 cm) wacke beds described from cycles 1 and 2. It forms three closely spaced, laterally continuous subarkosic Fe wacke layers (1.6 - 2.0 cm thick) separated by hematite-quartz lutite (Table A.1). A thin section, 12p, across these layer contacts reveals that at least one of the subarkosic Fe wacke (Fe-moderate) layers is moderately sharp-based and has divisions (Plate 2.3f) which are texturally comparable to those observed in iron formation from *Worumba* ($13d_1$, Plate 2.2a) and *Holowilena South* ($14a_2$, Plate 2.2c).

The thickest subarkosic interval is of Fe arenite (7 m thick, $12r_1$), which sits close to, but not at, the top of the iron formation at *Oraparinna* (#12, Figure 2.4). It is typically unstratified. Hematite lutite (Fe-poor), which is interstitial to the framework-supported quartz and feldspar, decreases up-section.

Monocrystalline quartz, potassium feldspar and plagioclase feldspar are the dominant minerals in subarkosic Fe wackes (Table 2.3) throughout section #12. The grain size and abundances of these three framework minerals varies, but their relative order (i.e., 1st - 3rd) remains constant. In samples $12D_3$, $12f_1$, 12p and $12r_1$, the fourth most prevalent framework component is hematite-quartz lutite (typically 0.2 - 0.6 mm in $12f_1$) which occurs as a lenticular rip-up clast from the IF facies. The largest observed clast of this type measures 3.2 x 1 mm. These intraformational clasts are comparable to those in the diamictite ($12a_1$, p. 42) and iron formation ($12n_1$, Table 2.2) at *Oraparinna* (#12).

Also common to most of the subarkosic Fe wackes at section #12, are three forms of matrix hematite (Table 2.3):

i) hematite mud or lutite (both silt- and mud-size) which is reddish-brown in plane polarized transmitted light (see p. 42) and is light rust-coloured in plane polarized reflected light (see p. 66);

ii) hematite orthomatrix, black in transmitted light but comparable to mud or lutite in reflected light, forms anhedral, irregular grains which in $12D_3$ range in size from 0.06 - 0.24 mm (Plate 2.4a);

Plate 2.4 Subarkosic Fe wacke facies.

(a) Petrographic comparison of hematite lutite (centre of photo) and hematite orthomatrix (black, upper right). Plane light; bar = 0.2 mm (sample $12D_3$, Table A.1, *Oraparinna*).

(b) Close-set and ungraded nature of basal grains in subarkosic Fe wacke bed. Many of these grains are intraformational since they resemble the colour and texture of the underlying hematite-quartz lutite layer. Diameter of coin is 18 mm (sample $12i_1$, Table A.1, *Oraparinna*).

(c) Lithic subarkosic Fe wacke (Fe-moderate) in which the basal grains are close-set and ungraded. Lenticular hematite-quartz rip-ups occur in the middle portion of the bed. Diameter of coin is 18 mm (sample 14j, Table A.3, *Holowilena South*).

(d) Coarse-tail grading developed in bed of subarkosic Fe wacke. Length of black bar at base of bed is 10 cm (vicinity of sample 14f, Table A.3, *Holowilena South*).

(e) Alternating laminae of subarkosic Fe siltstone (Fe-poor) and hematite-quartz lutite (Fe-rich). Note synsedimentary loading and faulting. Diameter of coin is 18 mm (sample 20p, Table A.3, *Holowilena South*).

(f) Gradual upward increase in hematite content (black) from subarkosic Fe siltstone (Fe-poor) to hematite-quartz lutite (Fe-rich). Plane light; bar = 0.2 mm (sample $14B_1$, Table A.3, *Holowilena South*).

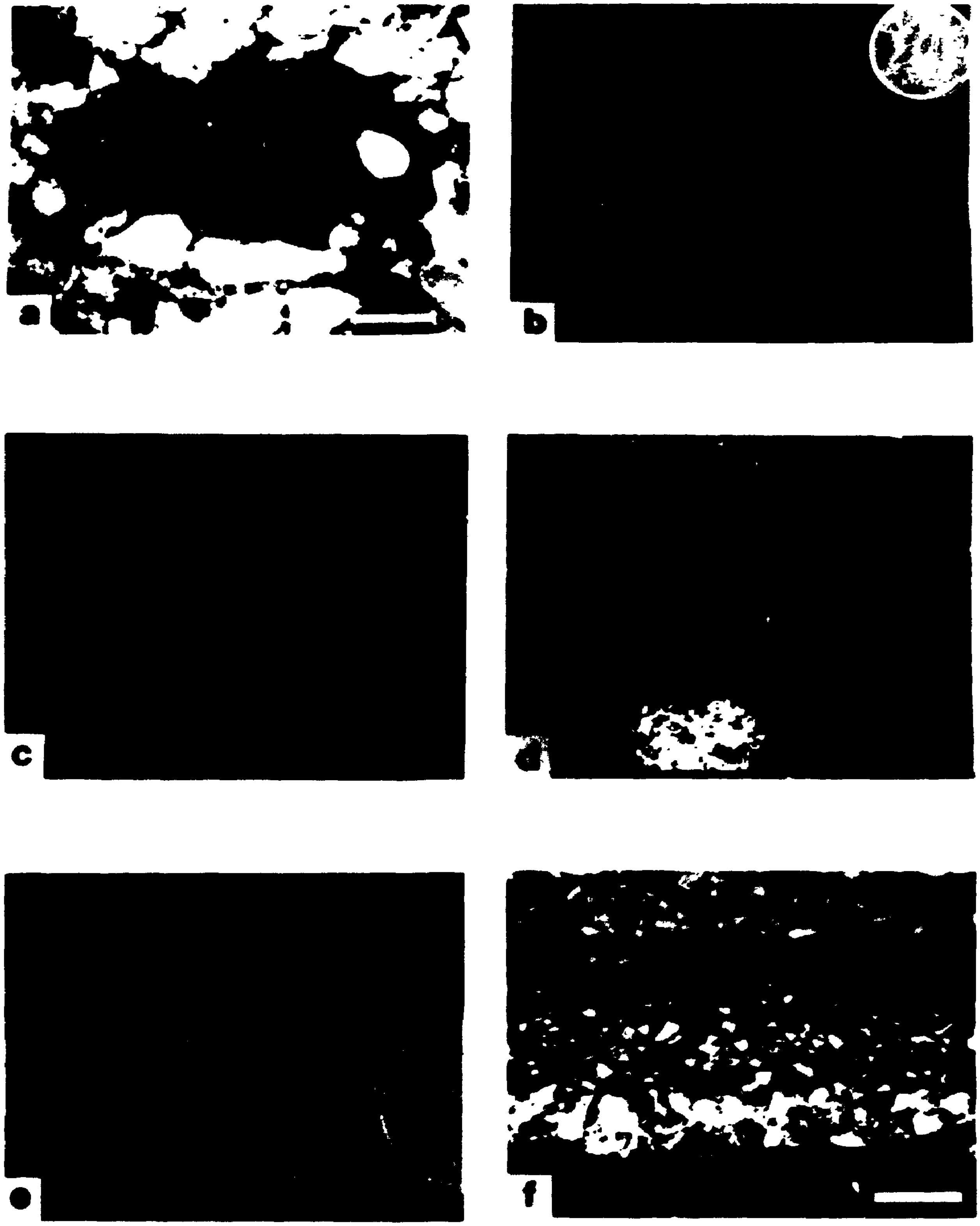
a
b
c
d
e
f

iii) hematite orthomatrix, black in plane polarized transmitted light and white in plane polarized reflected light, can form either irregular grains like type ii (see p. 66) or subhedral plates. They can range from 0.02 - 0.2 mm in $12D_3$.

As mentioned on p. 79, subarkosic Fe wacke at *Worumba* (#13) is commonly interstratified with Fe siltstone (Table A.2). The Fe siltstones are compositionally similar to the subarkosic Fe wackes. The Fe wackes and Fe siltstones are therefore described together as the subarkosic Fe wacke facies. Samples taken at *Worumba* which represent this association include $13F_1$, 13g, $13i_2$ and 13k (Table 2.3).

Samples $13F_1$ and 13k occur within intervals (0.3 and 5 m thick respectively) of olive green-weathering Fe siltstone which have planar, flat-based and yellowish-white weathering sub/arkosic Fe wacke/ arenite layers (1 - 10 mm) throughout. When viewed in thin section, these layers tend to be both sharp-based and sharp-topped. The sharpness of the subarkosic Fe arenite//Fe siltstone layer contacts in $13F_1$ and 13k is intensified by their coincidence with an abrupt change in grain size (sand to silt-mud) and an abrupt change in iron content [oxide-poor (1 - 5%) to oxide-moderate (5 - 21.5%)]. The silicate and carbonate components, namely, quartz, potassium feldspar, ferroan dolomite and phlogopite in decreasing order of abundance, persist in both the sand- and silt-size laminae; an observation which precludes a winter (dirty)/summer(clean) varve-type origin. Features which are possibly related to dewatering and observed in both $13F_1$ and 13k include: micro-scale synsedimentary faults, soft-sediment folds and flame structures.

As at *Oraparinna* (#12, p. 79), subarkosic Fe wacke at *Holowilena South* is interstratified with iron formation in section #20/14, whereas neither IF nor wacke is common in the stratigraphically higher section #21 (Figure 2.5, Tables A.3 - A.4). As at *Worumba* (see above), the majority of Fe siltstone in section #20/14 is subarkosic and hence described here with the Fe wackes (n.b., Fe siltstone samples 20d, $20k_2$, $21i_3$ of Table 2.4 are not subarkosic).

Intervals of unstratified subarkosic Fe wacke (Fe-poor) range from 0.57 - 5.1 m thick (e.g., $20g_1$, $20i_2$, $20q_{2\text{ - Fe arenite}}$, Table 2.3), whereas stratified beds of either Fe wacke or Fe arenite are commonly 3 - 56 cm thick (e.g., $14g_1$, $14l_2$) and locally < 2 cm thick (e.g., $20L_1$, $14B_1$). These beds are similar to those described at *Oraparinna* (#12, p. 79) in that zone (i) is host to coarser clasts (1 - 4 mm) which are either close-set and not graded (e.g., beds based at: 30.06 m, 56.01 m, 56.16 m, 106.32 m, 123.95 m, 162.12 m; 171.0 m = $14B_1$; Plate 2.4b; 208.58 m, Plate 2.4c), or dispersed and graded (e.g., beds based at: 56.45 m, 107.73 m, 111.63 m, 119.8 m, 123.48 m; 183.08 m, Plate 2.4d; 218.94 m = $14l_2$). Zone (ii) may contain a few dispersed clasts (2 - 64 mm) then be structureless (e.g., beds based at: 30.06 m, 162.12 m, 208.58 m), or simply be structureless (e.g., beds based at: 56.45 m, 56.01 m, 56.16 m, 106.32 m, 107.73 m, 111.63 m, 119.8 m, 123.48 m, 123.95 m, 171.0 m = $14B_1$, 183.08 m, 218.94 m = $14l_2$). In zone (iii) there are some diffuse parallel laminae (e.g., beds based at: 56.01 m, 119.8 m, 162.12 m, 183.08 m, 218.94 m = $14l_2$). As at *Oraparinna* (#12, p. 84), the sand-size (< 1 mm) framework grains throughout zones i - iii may fine-upward (coarse-tail grading, e.g., beds based at: 30.06 m, 162.12 m, 183.08 m, 218.94 m = $14l_2$). There are also several sharp-based beds which apparently lack a coarser basal zone (i); they are simply structureless then parallel laminated (zones ii & iii, e.g., beds based at: 109.68 m, 112.1 m, 119.71 m, 120.8 m, 181.37 m = $14g_1$ & 14f, 208.04 m).

The subarkosic Fe wacke (Fe-poor or Fe-moderate) and Fe arenite (Fe-poor) beds are commonly overlain by laminated to very thin-bedded couplets of subarkosic Fe siltstone (Fe-poor) and hematite-quartz lutite (Fe-rich, iron formation, Plate 2.4e). An example is $14B_1$ (171.0 m, Table A.3; Table 2.3), where siltstone/lutite contacts display either a gradational (Plate 2.4f) or abrupt (cf. Plate 2.2c) increase in hematite. Gradational hematite increases are elsewhere reflected by hematite-defined ripple cross-laminae in the Fe siltstone layers (Plate 2.5a, Figure 2.11). Load, flame and slump

Plate 2.5 Subarkosic Fe wacke facies.

(a) Hematite-defined ripple cross-laminae in subarkosic Fe siltstone layer. Length of bar = 1.0 cm (section #20/14, Table A.3, *Holowilena South*).

(b) Loaded flute casts preserved on the base of a very thin subarkosic Fe wacke bed. Diameter of coin is 18 mm (section #20/14, Table A.3, *Holowilena South*).

(c) Convolute lamination developed in the arenaceous base (non Fe) of a subarkosic Fe wacke (Fe-poor) bed. An upward increase in magnetism and iron oxide content throughout the bed culminates in the layering displayed in Plate 2.5d. Length of magnet is 12.2 cm (vicinity of sample $16b_1$, Table A.8, *Outalpa*).

(d) Alternating laminae of resistant Fe-moderate and recessive Fe-poor quartz-biotite-magnetite Fe siltstone (section #16, Table A.8, *Outalpa*).

(e) Tri-layered bed (behind magnet) in which the basal zone (i) is ripple cross-laminated and arenaceous (non Fe), the middle portion (ii) is structureless subarkosic Fe wacke, and the upper zone (iii) is parallel laminated subarkosic Fe wacke and siltstone. Length of magnet is 12.2 cm (140 m mark of section #7, Table A.12, *Manunda*).

(f) Syndepositional folding and faulting of a subarkosic Fe arenite (non Fe) layer. Length of magnet is 12.2 cm (146 m mark of section #7, Table A.12, *Manunda*).

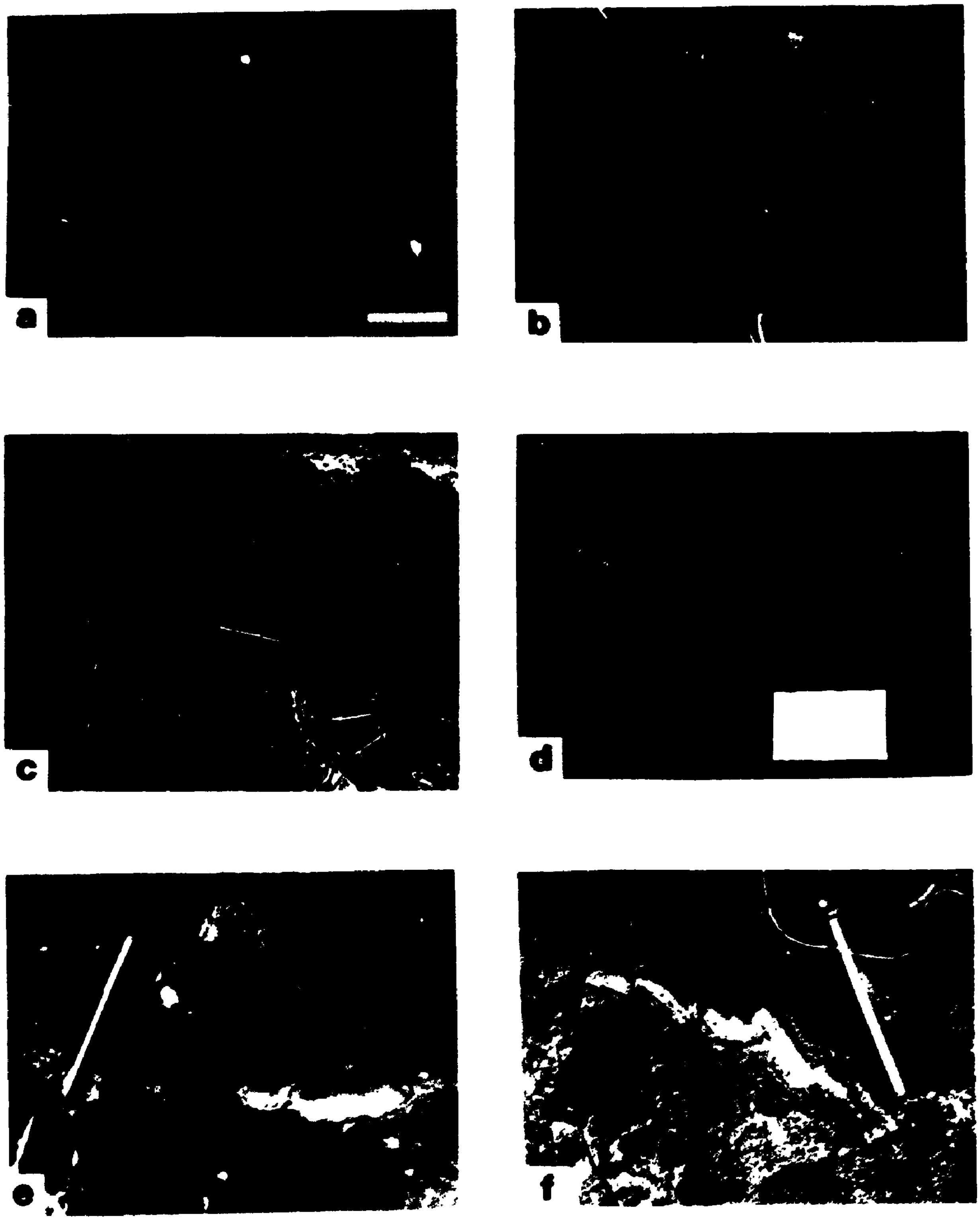

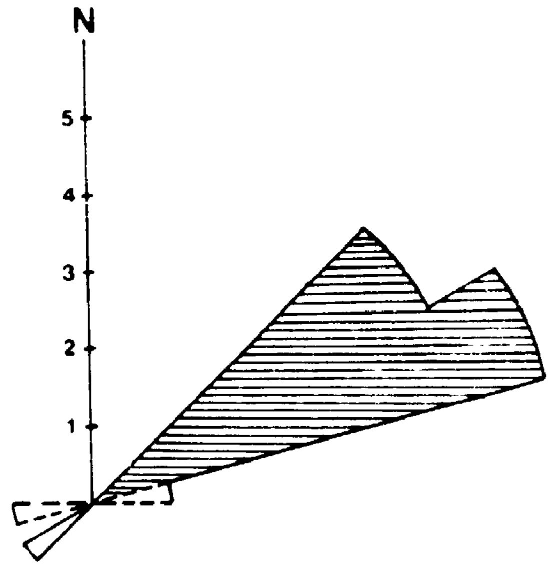

Figure 2.11 Orientation of paleocurrent data for ripple cross-laminations in subarkosic Fe siltstone layers (section #20/14) and for cross-laminated starved ripples in siltstones at Back Creek (section #21, 190.18 - 196.89 m). Both sections occur at the *Holowilena South* study location. Unshaded, enclosed pattern = Back Creek; horizontal lines = section # 20/14. Number of measurements = 14.

structures are commonly developed in these couplets (Plates 2.4e & 2.5b), as are small-scale synsedimentary faults.

As in the stratigraphically low-level micro/diamictites of section #20/14 (p. 46), intraformational framework components are not widespread in the associated wacke beds (e.g., $20L_1$ at 117.45 m, Tables 2.3 & A.3). The stratigraphically higher samples, however, have one or all of intraformational ferroan dolomite-quartz siltstone (0.1 - 1 mm, comparable to dominant layer type in $20L_1$), subarkosic Fe wacke (Fe-moderate, 0.1 - 0.8 mm) and hematite-quartz lutite (IF, 0.1 - 0.6 mm) present in the top five framework components (i.e., $14B_1$, 14f, $14g_1$, $14l_2$, Table 2.3). These locally derived grain types have a higher minimum and maximum size (0.1 - 1 mm), relative to the monocrystalline quartz and potassium feldspar (0.04 - 0.5 mm) by which they are commonly embayed. The subarkosic Fe wacke grains have in 14f, a ribboned, semi-continuous appearance which is attributed to burial-induced flattening.

(2) **Magnetite**-bearing

Subarkosic Fe wacke at *Mount Victor* (#18) occurs as 0.7 - 2.8 m thick beds within an interval dominated by iron formation. The situation is reversed at *Outalpa* (#16), where the entire section is of subarkosic Fe wacke except for a few IF horizons (Tables A.6 & A.8, Figures 2.6 & 2.7)

Of the two subarkosic beds sampled at section #18, one is a Fe wacke ($18g_1$) and the other a Fe arenite ($18l_1$, Table 2.3). Macroscopically, they are both light to medium brown-weathering with diffuse black laminae. In $18g_1$, these thin laminae (<0.5 mm thick) are spaced from 4 - 5 mm apart and are locally contorted due to soft-sediment folding. In $18l_1$, there are sporadically developed discontinuous (2 cm strike length) black cross-laminae which are defined by heavy minerals (i.e., Ti hematite, magnetite, rutile, zircon, tourmaline).

The subarkosic Fe wacke and iron formation association at sections 18 and 16 (see above) is also evident in thin section. In both the Fe wacke and IF at *Mount Victor*

(#18), the non-oxide iron is present mainly as chlorite-after-biotite and ferroan dolomite, whereas the iron oxide minerals are magnetite and Ti hematite (Tables 2.2 & 2.3). At *Outalpa* (#16), the Fe wacke and iron formation share one type of iron silicate, biotite, and one type of iron oxide, magnetite.

As mentioned on p. 72, subarkosic Fe wacke is the dominant facies developed in the stratigraphically higher of the two sections measured at *Outalpa* (#16, Figure 2.7, Table A.8). Fe wacke is not apparent in the basal section (#17, Table A.7); only non iron-oxide bearing quartz wacke occurs here.

The initial 106 m of section #16 has medium- to thick-beds of what is predominantly weakly magnetic subarkosic Fe wacke (e.g., $16A_1$, $16b_4$, Table 2.3; Plate 2.5c). Internal stratification in these beds is restricted to the lower 13 - 36 mm which is non magnetic and more quartzo-feldspathic (i.e., subarkosic arenite without the 'Fe' prefix). These quartzo-feldspathic layers locally exhibit parallel or cross-lamination, basal loading and tight soft-sediment folding (e.g., h = 3 cm, λ = 6 cm); the latter two of which tend to obscure what may originally have been a sharp-based bed. The undulose nature of these beds contrasts with the flat-based subarkosic Fe wacke beds described at *Oraparinna* (#12, p. 79) and *Holowilena South* (#20/14, p. 89). However, section #16 is comparable to section #12 by virtue of:

i) an absence of normally graded dispersed grains in the lower few centimetres of the beds;

ii) an overall fining-upward of framework grains (coarse-tail); and

iii) an upward increase in magnetism and iron oxide content from < 1% Fe_2O_3 in the basal subarkosic arenite to an averaged Fe_2O_3 of 4.5% in the unstratified mid section ($16A_1$, $16b_4$, Table 2.3), to 14.6% Fe_2O_3 in the locally developed upper zones of parallel laminae (e.g., $16b_1$, Table 2.4).

This third layer-type, first observed at the 81.6 m mark, consists of rhythmic alternations of resistant Fe-moderate and recessive Fe-poor Fe siltstone (Plate 2.5d).

These layers are in thin section, $16b_1$, considered to be an iron oxide-depleted/clastic-enriched version of the laminated iron formation at *Outalpa* (p. 73).

An interruption in the sequence of triple-zoned wacke beds (i.e., subarkosic non Fe arenite base, subarkosic Fe-poor wacke middle, Fe-moderate siltstone top), occurs from 108 - 147 m and from 168 - 183 m. Within these two intervals, the weakly magnetic and previously unstratified middle zone of the subarkosic Fe wacke beds has diffuse felsic (subarkosic non Fe) laminae throughout. Where weathered, these laminae are wavy, slumped and loaded, and locally the subarkosic non Fe arenite can, in lieu of laminae, form colinear starved ripples (< 1 cm thick). Associated with these sand-starved horizons are resistant nodules which are layer parallel.

The nodules, which have a carbonate core and a quartzose rim, also occur in the triple-zoned wacke beds up-section of the 147 m mark. The wacke beds here are locally thin- to medium-bedded (3 - 20 cm thick) whereas equivalent beds down-section are consistently medium- to thick-bedded (16 - 40 cm; Plate 2.5c). This change may represent a transitional stage of a thinning-upward cycle, but the exposure ends before such a suggestion can be confirmed or refuted.

Microscopic examination of the transition from the middle to upper zone of a thin-bedded wacke (16g, Table 2.4) reveals Fe-poor subarkosic Fe wacke/siltstone (dominant) with thin laminae of Fe-moderate non subarkosic Fe siltstone (subordinate). As in samples $16b_1$ and $16d_1$ (Tables 2.4 & 2.2), the layer contacts, if flat, are defined though not sharp (as in $16b_1$) whereas if undulose, are diffuse (as in $16d_1$). These laminae vary in thickness from 1 - 5 mm over a short strike length (e.g., 5 cm). Monocrystalline quartz and rhombic magnetite are the framework components which serve to demarcate successive layers.

(3) **Magnetite ± hematite**-bearing

As at sections 12, 13, 20/14, 18 and 16, both subarkosic Fe wacke and Fe arenite occur at Pualco West (#10), Razorback Ridge (#9/2) and Iron Peak (#7). As at

Holowilena South (#20/14), bedded or unstratified subarkosic horizons occur throughout these three sections (Figure 2.8, Tables A.10 - A.12). In contrast to section #20/14, the Fe siltstone is not subarkosic and hence is discussed separately (see p. 100).

Layers of stratified wacke (Fe-poor & Fe-moderate) are 0.8 - 8 cm thick (e.g., 10h, 9H, $2T_1$, Table 2.3) and of arenite (non Fe & Fe-poor) are 0.06 - 86 cm thick (e.g., $10J_1$, $2u_3$), whereas unstratified intervals of wacke (non Fe, Fe-poor & Fe-moderate) are commonly 0.74 - 2.2 m thick (e.g., 2p, 7R) and of arenite (non Fe & Fe-poor) are normally 0.6 - 2.95 m thick (e.g., $9B_2$, $2y_1$, 7o). The most widespread type of stratified subarkosic Fe arenite and Fe wacke is similar to beds at *Outalpa* (#16, p. 94), which are either bi-layered (e.g., 98.15 m, Table A.10; 276.35 m, Table A.11) or tri-layered (e.g., 139.7 m, Table A.12, Plate 2.5e). As at section #16, the weakly undulose base is subarkosic ±Fe arenite (0.06 - 4 cm thick, subordinate), the structureless middle is subarkosic Fe wacke (0.8 - 8 cm thick, dominant) and where present, the parallel laminated top is subarkosic Fe wacke/siltstone (2 - 7.4 cm thick). In some bi-layered beds, Fe siltstone (0.04 - 10 cm thick) replaces Fe wacke (e.g., $2u_3$, Table A.11). The bases of some arenite layers are loaded and display flame structures and are internally ripple cross-laminated (Plate 2.5e). Notable syndepositional faulting and folding of these layers occurs below the second diamictite horizon at Iron Peak (146.45 m, Table A.12, Plate 2.5f).

Fe Siltstones

Mineralogically varied Fe siltstone (Fe-poor & Fe-moderate) is regionally a minor facies (Tables A.3 - A.8, A.10 - A.13). In the three southerly sections, however, it forms a vertically recurrent unit (Tables A.10 - A.12, Table 2.4). There are two varieties of Fe siltstone at sections 10, 9/2 and 7. The most common type is laminated (e.g., 10L, $9j_1$, $9L_1$, $9L_2$, 7K, 7L, 7u, $7X_1$, Table 2.4) and the second is typically non laminated and ferroan dolomite-bearing (e.g., $9d_{2a}$, $9K_2$, 8M, $2T_2$, L.O.I. = 7.5 -

Table 2.4 Summary of microscopic features of Fe siltstone facies samples from study localities in zones 1, 2 and 3 (Figure 2.1). *Holowilena South* occurs in zone 1; *Mount Victor* and *Outalpa* occur in zone 2; *Spring Dam* and *Manunda* are localities in zone 3. Multiple samples from one measured section (e.g., #20) are listed in ascending stratigraphic order. phlogo = phlogopite; plag. = plagioclase. See Figures A.1, A.4, A.6, A.7 & A.9 for locations of measured sections from which these samples were collected.

Locality:	Holowilena South	Holowilena South	Holowilena South (Back Creek)	Mount Victor (Razorback hill)	Mount Victor (Razorback hill)	Outalpa (I.D. hut)	Outalpa (I.D. hut)
Sample #:	20d	$20k_2$	$21i_3$	$18f_1$	$18i_2$	$18b_1$	18g
Layer-type:	Fe-poor	Fe-moderate	Fe-poor	Fe-moderate	Fe-moderate	Fe-poor	Fe-poor
Size:	≤ 0.02 mm			0.008 - 0.1 mm		≤ 0.01 - 0.24 mm	0.01 - 0.1 mm
Components:							
1)	ferroan dolomite			quartz		quartz	→
2)	quartz			brownish-yellow biotite		olive green biotite	→
3)	chlorite-after-phlogo			magnetite		magnetite	ferroan dolomite
4)				pale green chlorite		sericite	magnetite
5)				tourmaline (trace)			
Total Fe_2O_3:		15.83%	5.14%	13.40%	17.03%	14.64%	
Layer-type:						Fe-moderate	Fe-moderate
Size:						≤ 0.01 - 0.18 mm	0.01 - 0.1 mm
Components:							
1)						quartz	quartz
2)						biotite = magnetite	olive green biotite
3)						sericite	magnetite
4)							ferroan dolomite

Table 2.4 cont'd

Locality	Spring Dam (Pua co West)	Spring Dam (Razorback Ridge)	Spring Dam (Razorback Ridge)	Spring Dam (Razorback Ridge)	Spring Dam (Razorback Ridge)	Spring Dam (Razorback Ridge)	Spring Dam Adit thru Razorback R	Spring Dam Adit thru Razorback R
Sample #	10L	$9d_{1a}$	$9J_1$	$9K_1$	$9L_1$	$9L_2$	9M	9A
Fe-moderate layer								
Size	≤ 0.008 - 0.04 mm		≤ 0.004 - 0.08 mm	< 0.004 - 0.06 mm	≤ 0.004 - 0.08 mm			< 0.004 - [illegible] mm
Components 1)	quartz		quartz	ferroan dolomite	quartz			quartz
2)	sericite		ferroan dolomite	quartz	pale green chlorite			hematite platy
3)	magnetite		sericite	magnetite	magnetite			magnetite
4)	ferroan dolomite		magnetite	pale green chlorite	ferroan dolomite			ferroan dolomite
5)	pale green chlorite		olive green biotite	plagioclase feldspar	sericite			apatite
6)	olive green chlorite			olive green biotite				pale green chlorite
Total Fe_2O_3		10.79%	12.12%	16.93%		22.26%	8.34%	24.38%
Fe-moderate layer								
Size	≤ 0.008 - 0.04 mm		≤ 0.004 - 0.08 mm		≤ 0.004 - 0.04 mm			
Components 1)	quartz		quartz		quartz			
2)	pale green chlorite		sericite		magnetite			
3)	magnetite		magnetite		sericite			
4)	ferroan dolomite				pale green chlorite			
5)	sericite				olive green biotite			

Locality	Spring Dam (Razorback Ridge)	Manunda (Iron Peak)	Manunda (Iron Peak)	Manunda (Iron Peak)	Manunda (Iron Peak)	Manunda (Iron Peak)	Manunda (Iron Peak)	Manunda (Iron Peak)
Sample #	$2T_2$	7B	7F	6d	7K	7L	7u	$7L_1$
Layer-type		Fe-poor	Fe-poor			Fe-moderate		Fe-moderate
Size		0.016 - 0.08 mm	0.004 - 0.08 mm			0.008 - 0.1 mm		0.008 - 0.06 mm
Components 1)		quartz →	(quartz)			quartz		quartz
2)		chamosite network	pale yellow chlorite			olive green biotite		magnetite
3)		yellowish-blue biotite →	(yellowish-blue biotite)			magnetite		plagioclase feldspar
4)		magnetite →	(magnetite)			ferroan dolomite		ferroan dolomite
5)			apatite (trace)			pale green chlorite		olive [illegible] biotite
6)						plag. (trace)		hematite platy(?)
Total Fe_2O_3	8.50%			9.70%	13.51%		27.07%	
Layer-type			Fe-moderate			Fe-poor		Fe-rich
Size			0.008 - 0.06 mm			0.008 - 0.04 mm		0.008 - 0.06 mm
Components 1)			quartz			quartz		magnetite
2)			chamosite network			chamosite network		quartz
3)			magnetite			olive green biotite		olive green biotite
4)			pale green biotite			plagioclase feldspar		ferroan dolomite
5)			apatite (trace)			magnetite		hematite platy(?)
6)						ferroan dolomite		

20.5%). The laminated Fe siltstone locally has transitional layer contacts typical of a couplet (e.g., 10L, $9j_1$, Table 2.4). In 10L, a pale green-weathering quartz-sericite-magnetite layer forms the couplet base, then near the top there is a gradual increase in chlorite content marking the transition into a dark green-weathering quartz-chlorite-magnetite layer which is the couplet top. In $9j_1$, it is sericite which increases at the expense of ferroan dolomite during the transition from the basal, medium grey-weathering quartz-ferroan dolomite-sericite-magnetite layer to the upper, white-weathering quartz-sericite-magnetite layer. Normal grading of framework grains is more apparent in the thicker, Fe siltstone beds. For example, sample $8H_3$ (within Adit, Table A.13) contains a 23 mm-thick bed in which the size of its main component, quartz, decreases from base to top, and becomes subordinate to sericite in the uppermost 8.5 mm of the bed. At the mouth of the Adit, sample $8A_L$ (Table 2.4) was taken from a 12.5 cm-thick bed in which coarse-tail grading is most evident. The matrix content is higher (but not finer) at the top of thin section $8A_L$ than it is at the base. It is still composed of ferroan dolomite and apatite, and does not display the size change which accompanied the aforementioned quartz to sericite transition.

Carbonates

As with the Fe siltstones, carbonate layers are rarely developed/exposed except at the three most southerly sections (#10, #9/2, #7). They occur in the iron formation, either as reddish-brown, ferroan dolomite-enriched (sparite) layers (3 - 20 cm thick; e.g., $5A_U$, 4A, $8E_2$, Table 3.6) or orange-brown, laminated dolomitic micrite (0.6 - 1.2 m thick; e.g., $10q_{1}$, $7W_1$ of Tables A.10 & A.12 and $10q_2$, $7W_2$ of Table 3.6. Both types of carbonate weather recessively. The ferroan dolomite-enriched (sparite) layers are locally cross-laminated (244.6 m, Table A.11) and the dolomitic micrite may contain siliciclastic laminae similar to those observed in iron formation from *Worumba* (Plate 2.2a).

Chapter III

MAJOR & TRACE ELEMENT GEOCHEMISTRY

Preface. Major and trace element analyses of samples representative of the facies outlined in Chapter 2 serve as (1) an extension of the petrography (Tables 2.1 - 2.4), and (2) as genetic indicators. The former application of the data (1) is examined in this chapter, whereas the latter (2) is utilized in Chapter 6.

Sampling and Analytical Methods

Samples were collected for chemical analysis from each of the five facies types described in Chapter 2. Individual geochemical aliquots are considered to be representative and homogeneous by virtue of: collecting only the matrices of the diamictite facies (p. 33; Figure 2.2); excluding macroscopic, clastic-dominated laminae of the iron formation facies (p. 60); avoiding laminated portions of the subarkosic Fe wacke facies and excluding sand-dominated laminae of the Fe siltstone facies. Methods of preparing samples for analysis are described in Appendix B. The samples were split into two groups; the first of which includes all samples from zone 3 (Figure 2.1) which were analyzed by x-ray fluorescence spectrometry at the University of Adelaide for: Si, Al, total Fe reported as Fe_2O_3, Mn, Mg, Ca, K, Ti, P, Rb, Sr, Ba, Y, Zr, Nb, V, Cr, Ni, Cu, Zn and Pb. Na was determined by atomic absorption spectrophotometry. The second group of samples is from zones 1 and 2 (Figure 2.1), for which the x-ray fluorescence spectrometer at the University of Western Ontario was used to analyze all elements, including Na. A summary of the relative precision and accuracy of the analyses is presented in Appendix B.

It is important to note that for both the major and trace element data (Tables 3.1 - 3.6 and 3.8 - 3.11), the subarkosic Fe wacke facies described in Chapter 2 has been broken down into (1) subarkosic Fe wacke (1 - 21.5% iron oxide minerals) and (2) subarkosic Fe-poor (1 - 5% Fe oxide minerals) and non Fe (< 1% Fe oxide minerals) arenite (Figure 2.3). These two groups are treated together in Chapter 2 because of their macroscopic similarities and close association, but are here divided because of chemical differences. Many of the geochemical samples listed in Tables 3.1 - 3.6 and 3.8 - 3.11 have corresponding thin section samples which are documented in Tables 2.1 - 2.4 and Table A.13. For example, sample $12a_2$ (Table 3.1) corresponds to thin section sample $12a_1$ (Table 2.1); both samples are 12a but the presence of a subscript indicates that two samples were collected from the same site to constitute a thin section-geochemistry set. Correspondingly, samples such as 14k, 2L, 2V, 7A, 7S and 8j (Table 3.1) do not have a thin section equivalent.

Major Element Results

The major elements and loss on ignition (L.O.I.) are presented with the corresponding Pearson's correlation coefficients in Tables 3.1 - 3.6. Pearson's product-moment coefficient, r, was chosen over the Spearman rank correlation coefficient once it was established that the data had a normal rather than a ranked distribution (Till, 1974, chapters 5 & 7). Correlation coefficients generated from a closed-number system (e.g., oxides which sum to ≈ 100%) exhibit a tendency for negative correlations to be enhanced (Davis, 1973, p. 82; Till, 1974, p. 91), hence as a precautionary measure, only those coefficients which are graphically plotted are discussed.

As evident from Chapter 2, iron oxide minerals are not restricted to the iron formation; they commonly occur in the associated diamictite, subarkosic wacke, siltstone (Tables 2.1 - 2.4) and carbonate facies. These rocks are compared with 'normal' sedimentary rocks on Figure 3.1. With the exception of jasper-bearing sample $14a_3$, the samples have a more limited SiO_2/Al_2O_3 range than normal sedimentary rocks. The five samples designated as carbonates plot close to, but not within, the normal carbonate field.

Table 3.1 Chemical analyses of diamictite matrices (Figure 2.2) from measured sections 12, 13, 20/14, 21, 19, 18, 17, 15, 10, 9/2, 7 and 8 (Figure A.1), which are located within zones 1, 2 and 3 (Figure 2.1). Correlation coefficients for the 38 samples are also listed. Sample numbers followed by $\bar{x}$ represent mean values for analyses of two aliquots.

Sample	SiO2	Al2O3	Fe2O3	MnO	MgO	CaO	Na2O	K2O	TiO2	P2O5	L.O.I.	Total	ZONE
12a2	68.49	5.75	5.68	0.06	3.46	4.85	0.59	2.40	0.47	0.15	7.70	99.60	
13a2	45.35	7.89	13.26	0.07	8.92	7.39	0.00	3.73	0.48	0.34	12.30	99.73	
13b2	41.05	8.38	16.25	0.08	10.05	7.37	0.00	3.41	0.47	0.40	12.20	99.66	
13c2	44.54	9.41	16.40	0.08	9.72	4.87	0.00	3.95	0.53	0.40	9.40	99.30	
13h2	45.55	7.54	12.21	0.07	9.41	6.94	0.00	4.37	0.46	0.54	12.40	99.49	
13l2	49.65	7.70	9.63	0.06	10.28	4.94	0.00	4.07	0.49	0.26	12.70	99.78	
13m2	45.37	8.35	12.65	0.04	9.73	6.53	0.00	3.78	0.51	0.31	12.10	99.37	1
20f1	52.85	10.67	10.83	0.14	7.41	4.37	0.57	2.58	0.88	0.16	9.20	99.66	
20m3	61.76	7.65	6.60	0.09	4.38	5.46	1.77	2.60	0.49	0.10	9.00	99.90	
14d2	37.63	4.50	33.84	0.07	5.59	6.11	0.32	0.91	0.38	0.32	9.80	99.47	
14k	44.13	3.84	33.10	0.06	4.82	4.79	0.01	0.69	0.30	0.49	7.50	99.73	
14M1	38.60	4.29	32.40	0.05	5.67	6.66	0.14	0.94	0.31	0.39	10.40	99.85	
21h2	51.46	9.51	11.96	0.09	7.14	5.51	0.45	2.20	0.67	0.27	10.69	99.95	
21j2	52.03	7.77	12.23	0.11	6.42	6.44	0.23	2.14	0.58	0.25	11.70	99.90	
19h2	74.82	7.61	3.00	0.06	2.25	3.18	2.27	1.88	0.60	0.08	3.90	99.65	
18a2	75.80	6.70	2.04	0.05	2.33	3.48	0.07	2.99	0.47	0.03	5.50	99.46	
18b2	63.51	9.21	4.44	0.16	4.81	4.76	0.85	2.81	0.69	0.08	8.00	99.32	
18c2	62.71	9.09	6.41	0.11	4.34	4.68	1.06	2.73	0.68	0.09	7.90	99.80	2
17a2	62.99	10.54	6.62	0.13	5.41	4.26	1.17	3.10	0.73	0.13	5.10	100.18	
15d2	73.02	9.67	4.24	0.49	2.50	1.98	1.70	2.53	0.36	0.13	3.20	99.82	
15f2	57.39	12.55	11.53	1.51	2.30	3.00	2.62	2.99	0.60	0.24	4.60	99.33	
15g2	38.85	5.63	41.19	0.30	2.65	3.37	1.53	1.31	0.36	0.44	3.60	99.23	
10g2 x̄	72.83	7.08	3.21	0.19	3.11	3.77	1.46	1.73	0.51	0.09	6.00	99.98	
10i2 x̄	65.57	9.44	7.37	0.18	3.75	3.71	1.09	2.41	0.76	0.15	5.40	99.83	
10m2 x̄	54.79	9.19	18.11	0.19	4.23	3.39	0.73	2.43	0.73	0.29	5.90	99.98	
9e2 x̄	55.13	9.68	14.55	0.23	4.63	4.17	1.08	2.59	0.78	0.25	7.00	100.09	
2m2	42.33	7.05	35.09	0.11	2.76	3.99	0.77	1.85	0.48	0.49	5.20	100.12	
2L x̄	42.94	6.98	35.83	0.09	2.07	3.97	0.67	1.84	0.53	0.44	4.40	99.76	
2j2 x̄	41.93	6.95	38.01	0.09	2.12	3.49	0.73	1.81	0.53	0.47	4.00	100.13	
2V x̄	44.33	7.69	35.16	0.09	2.81	2.85	0.41	2.17	0.59	0.43	3.40	99.93	3
2w2 x̄	47.31	6.76	31.69	0.09	2.86	3.11	1.06	1.68	0.51	0.41	4.40	99.88	
7A	60.38	10.66	7.05	0.22	4.83	4.29	1.40	2.68	0.81	0.16	7.60	100.08	
7S x̄	54.75	9.21	15.89	0.21	4.45	4.07	1.33	2.21	0.71	0.23	6.70	99.76	
7Y1	44.76	3.72	45.25	0.09	0.37	1.79	1.97	0.04	0.21	0.82	1.10	100.12	
7aa2 x̄	44.51	7.62	31.01	0.11	3.05	3.89	1.19	2.03	0.54	0.36	5.70	100.01	
8j	45.03	7.01	33.90	0.10	2.98	3.05	0.84	1.80	0.51	0.40	4.60	100.22	
8k2 x̄	41.83	6.73	37.47	0.10	2.77	3.42	0.74	1.75	0.52	0.43	4.40	100.16	
8l2 x̄	41.53	6.51	37.65	0.10	2.77	3.53	0.76	1.57	0.48	0.43	4.40	99.73	
Average	52.30	7.80	19.31	0.16	4.71	4.41	0.83	2.33	0.55	0.30	7.08		
Std Dev	11.08	1.94	13.35	0.24	2.60	1.39	0.67	0.94	0.15	0.16	3.09		

SiO2	1.00												
Al2O3	0.40	1.00											
Fe2O3	-0.81	-0.61	1.00										
MnO	0.19	0.50	-0.15	1.00									
MgO	-0.23	0.23	-0.35	-0.24	1.00								
CaO	-0.27	-0.05	-0.24	-0.31	0.81	1.00							
Na2O	0.43	0.26	-0.08	0.57	-0.65	-0.64	1.00						
K2O	0.22	0.63	-0.65	0.09	0.69	0.42	-0.30	1.00					
TiO2	0.36	0.79	-0.48	0.12	0.12	-0.04	0.13	0.38	1.00				
P2O5	-0.82	-0.53	0.84	-0.15	-0.05	-0.04	-0.20	-0.36	-0.55	1.00			
L.O.I.	-0.17	0.10	-0.39	-0.25	0.91	0.93	-0.65	0.56	0.07	-0.15	1.00		
	SiO2	Al2O3	Fe2O3	MnO	MgO	CaO	Na2O	K2O	TiO2	P2O5	L.O.I.		ZONE

Table 3.2 Chemical analyses of iron formation from measured sections 11, 12, 13, 20/14, 21, 19, 18, 17, 16, 10, 9/2, 7 and 8 (Figure A.1), which are located within zones 1, 2 and 3 (Figure 2.1). Samples $5A_L$ and 1A are laterally removed from, but considered part of sections 10 and 7, respectively (Figure A.9). Samples RD#1 - 116' and RD#3 - 96' are from drill holes through Razorback Ridge (Whitten, 1970), which are subparallel to section #9/2. Correlation coefficients for the 56 samples are also listed. Sample numbers followed by $\overline{x}$ represent mean values for analyses of two or more aliquots.

Sample	SiO2	Al2O3	Fe2O3	MnO	MgO	CaO	Na2O	K2O	TiO2	P2O5	L.O.I.	Total	ZONE
11E3	61.53	4.05	26.67	0.02	0.77	1.65	0.00	1.60	0.21	0.62	2.60	99.72	
11f2	34.03	5.57	45.57	0.04	1.29	4.63	0.00	2.12	0.33	1.14	5.01	99.73	
11g1 x̄	34.02	4.95	51.02	0.05	0.89	2.47	0.00	1.91	0.32	0.81	3.10	99.54	
11i2	39.78	5.92	42.94	0.04	1.04	2.81	0.00	2.31	0.39	0.76	3.80	99.79	
12b2	50.74	7.87	27.10	0.03	0.88	3.91	0.21	3.10	0.38	1.49	3.99	99.70	
12g2	53.27	7.61	24.18	0.02	1.03	4.13	0.17	3.02	0.42	1.83	3.90	99.58	
12h	49.50	8.32	25.19	0.03	0.79	5.46	0.20	3.23	0.46	3.24	3.09	99.51	
12J1	52.71	8.52	26.08	0.02	0.94	2.90	0.04	3.54	0.46	1.28	3.10	99.59	
12k2	43.89	6.07	27.14	0.02	1.45	9.46	0.05	2.16	0.36	6.04	2.91	99.55	
12n2	48.45	7.27	30.81	0.02	1.08	3.82	0.14	2.73	0.40	2.54	2.31	99.57	1
12o	54.27	9.59	22.84	0.02	0.91	2.88	0.08	3.80	0.54	2.06	2.81	99.80	
12q	55.89	11.63	18.50	0.02	1.47	1.94	0.00	4.64	0.56	1.03	4.00	99.68	
12s	47.03	8.77	22.57	0.03	3.13	5.68	0.07	3.32	0.57	1.40	8.00	100.57	
13d2	39.28	8.64	20.40	0.08	10.32	4.59	0.00	3.98	0.41	0.59	11.41	99.70	
13e1	34.02	7.36	27.93	0.06	10.65	3.89	0.00	3.45	0.40	0.70	11.20	99.66	
14a3 x̄	61.35	0.00	37.07	0.01	0.20	0.43	0.00	0.03	0.03	0.34	0.30	99.76	
14n2	36.62	2.79	53.36	0.02	0.73	2.44	0.00	0.53	0.23	1.71	2.10	100.53	
14o2	42.76	4.11	32.27	0.02	0.43	9.45	0.94	1.29	0.28	6.61	1.20	99.36	
21a2	39.66	8.19	41.20	0.02	4.81	0.45	0.00	1.64	0.51	0.33	3.30	100.11	
21d	37.87	5.31	31.05	0.06	6.10	6.58	0.00	0.85	0.38	0.95	10.50	99.65	
19G2	43.83	5.48	43.06	0.05	1.76	0.88	1.36	1.19	0.45	0.56	1.10	99.72	
18E2	48.02	4.60	34.86	0.15	1.75	3.08	2.30	0.39	0.40	0.41	3.40	99.36	
18h	34.57	4.64	54.29	0.03	1.73	1.11	0.00	1.20	0.47	0.29	1.40	99.73	
18j2	46.24	6.00	36.54	0.06	2.53	2.21	0.00	1.65	0.59	0.34	3.70	99.86	2
18k	34.43	3.89	55.85	0.02	1.13	1.20	0.57	0.45	0.33	0.82	1.40	100.09	
17d	48.00	10.88	20.80	0.24	7.02	4.58	0.45	2.87	0.84	0.27	3.80	99.75	
16d2	40.39	6.70	41.67	0.06	3.36	2.47	0.21	2.29	0.52	0.56	0.90	99.13	
10d2	31.61	4.85	52.51	0.26	2.91	2.81	1.32	0.16	0.33	0.31	2.25	99.32	
10k2	32.95	5.99	49.46	0.15	3.90	2.08	1.37	0.26	0.41	0.34	2.42	99.33	
10N3	27.99	6.71	55.55	0.10	3.31	1.16	1.33	1.07	0.49	0.31	1.56	99.58	
10S1	25.56	3.66	37.37	0.19	5.75	9.83	1.88	0.15	0.24	0.30	14.63	99.56	
5AL x̄	28.64	3.01	56.05	0.11	2.33	3.17	1.19	0.10	0.32	0.27	4.43	99.62	
9c2	37.82	5.45	39.18	0.35	3.26	4.76	2.23	0.45	0.49	0.48	5.65	100.12	
9F2 x̄	34.24	6.74	41.50	0.19	3.12	4.65	1.99	0.97	0.47	1.05	4.95	99.87	
9F3 x̄	34.21	4.02	55.16	0.08	1.00	1.22	1.61	0.42	0.4[illegible]	0.30	0.98	99.41	
9I3	27.07	2.09	67.23	0.11	0.35	0.76	1.12	0.03	0.37	0.14	0.09	99.36	
RD#3-96'	33.90	5.64	48.20	0.10	2.76	2.78	1.48	0.84	0.44	0.38	3.33	99.85	
RD#1-116'	47.49	8.47	28.65	0.11	3.20	2.90	0.25	2.86	0.80	0.32	5.18	100.23	
2h2	29.15	4.47	59.93	0.06	2.43	0.25	0.30	0.65	0.45	0.23	1.66	99.58	
2G	29.87	4.69	58.35	0.07	2.52	0.96	0.71	0.72	0.38	0.29	1.33	99.89	
2F	26.49	3.46	64.73	0.06	1.16	0.70	0.92	0.31	0.33	0.56	1.08	99.80	
8Au x̄	27.05	3.43	65.19	0.13	1.75	0.25	0.86	0.19	0.38	0.11	0.35	99.69	3
2A	37.89	4.37	51.13	0.09	0.91	1.23	1.42	0.58	0.39	0.37	1.28	99.66	
2S2	28.50	4.50	59.08	0.16	2.61	1.33	1.28	0.22	0.38	0.18	1.58	99.82	
[illegible]	35.4[illegible]	6.33	48.99	0.06	4.59	0.46	0.04	0.98	0.68	0.33	2.11	100.00	

17d 48.00 10.88 20.80 0.24 7.02 4.58 0.45 2.87 0.84 0.27 3.80 99.75

10d2	31.61	4.85	52.51	0.26	2.91	2.81	1.32	0.16	0.33	0.31	2.25	99.32	
10k2	32.95	5.99	49.46	0.15	3.90	2.08	1.37	0.26	0.41	0.34	2.42	99.33	
10N3	27.99	6.71	55.55	0.10	3.31	1.16	1.33	1.07	0.49	0.31	1.56	99.58	
10S1	25.56	3.66	37.37	0.19	5.75	9.83	1.88	0.15	0.24	0.30	14.63	99.56	
5AL x̄	28.64	3.01	56.05	0.11	2.33	3.17	1.19	0.10	0.32	0.27	4.43	99.62	
9c2	37.82	5.45	39.18	0.35	3.26	4.76	2.23	0.45	0.49	0.48	5.65	100.12	
9F2 x̄	34.24	6.74	41.50	0.19	3.12	4.65	1.99	0.97	0.47	1.05	4.95	99.87	
9F3 x̄	34.21	4.02	55.16	0.08	1.00	1.22	1.61	0.42	0.41	0.30	0.98	99.41	
9I3	27.07	2.09	67.23	0.11	0.35	0.76	1.12	0.03	0.37	0.14	0.09	99.36	
RD#3-96'	33.90	5.64	48.20	0.10	2.76	2.78	1.48	0.84	0.44	0.38	3.33	99.85	
RD#1-116'	47.49	8.47	28.65	0.11	3.20	2.90	0.25	2.86	0.80	0.32	5.18	100.23	
2h2	29.15	4.47	59.93	0.06	2.43	0.25	0.30	0.65	0.45	0.23	1.66	99.58	
2G	29.87	4.69	58.35	0.07	2.52	0.96	0.71	0.72	0.38	0.29	1.33	99.89	
2F	26.49	3.46	64.73	0.06	1.16	0.70	0.92	0.31	0.33	0.56	1.08	99.80	
8Au x̄	27.05	3.43	65.19	0.13	1.75	0.25	0.86	0.19	0.38	0.11	0.35	99.69	3
2A	37.89	4.37	51.13	0.09	0.91	1.23	1.42	0.58	0.39	0.37	1.28	99.66	
2S2	28.50	4.50	59.08	0.16	2.61	1.33	1.28	0.22	0.38	0.18	1.58	99.82	
2x2	35.43	6.33	48.99	0.06	4.59	0.46	0.04	0.98	0.68	0.33	2.11	100.00	
7i	28.76	6.53	55.71	0.13	3.26	1.96	0.00	0.90	0.38	0.32	1.90	99.85	
1A	23.83	3.73	63.45	0.11	1.69	2.28	1.61	0.50	0.27	0.11	1.76	99.34	
7V	27.28	3.55	61.04	0.13	1.01	2.37	1.72	0.18	0.32	0.14	2.32	100.06	
7Z1	35.18	5.18	54.44	0.09	0.14	0.64	2.48	0.24	0.36	0.33	0.64	99.72	
8r2	44.61	10.82	21.30	0.18	4.66	5.02	0.08	3.89	0.63	0.48	8.58	100.25	
8q2	23.45	3.54	66.82	0.09	1.89	1.10	0.85	0.38	0.36	0.25	0.60	99.33	
8o	36.50	6.31	46.20	0.08	1.93	2.19	1.06	1.63	0.44	0.38	3.16	99.88	
8i	26.73	3.89	64.06	0.06	1.69	0.28	0.32	0.59	0.51	0.19	1.44	99.76	
8G3	29.80	4.76	58.61	0.07	2.25	1.02	0.72	0.68	0.34	0.30	0.91	99.46	
8G1	38.25	7.86	39.18	0.12	3.63	2.96	0.80	1.92	0.47	0.40	4.61	100.20	
8E1	32.46	3.73	54.90	0.10	1.95	2.11	1.15	0.36	0.37	0.35	2.05	99.53	
Average	38.12	5.76	43.66	0.09	2.50	2.83	0.69	1.46	0.42	0.86	3.34		
Std Dev	9.56	2.28	14.42	0.07	2.14	2.23	0.72	1.26	0.13	1.22	2.96		

SiO2	1.00										
Al2O3	0.47	1.00									
Fe2O3	-0.83	-0.72	1.00								
MnO	-0.35	0.00	0.15	1.00							
MgO	-0.14	0.39	-0.31	0.32	1.00						
CaO	0.21	0.27	-0.59	0.12	0.26	1.00					
Na2O	-0.43	-0.36	0.41	0.61	-0.13	-0.04	1.00				
K2O	0.63	0.86	-0.81	-0.32	0.27	0.33	-0.61	1.00			
TiO2	0.18	0.73	-0.34	0.20	0.34	-0.01	-0.18	0.49	1.00		
P2O5	0.35	0.15	-0.42	-0.37	-0.22	0.66	-0.23	0.32	-0.12	1.00	
L.O.I.	0.09	0.38	-0.56	0.20	0.71	0.64	-0.13	0.41	0.14	-0.01	1.00
	SiO2	Al2O3	Fe2O3	MnO	MgO	CaO	Na2O	K2O	TiO2	P2O5	L.O.I.

Table 3.3 Chemical analyses of subarkosic Fe wackes (1 - 21.5% iron oxide minerals) from measured sections 12, 13, 20/14, 18, 16, 10, 9/2 and 7 (Figure A.1), which are located within zones 1, 2 and 3 (Figure 2.1). Correlation coefficients for the 17 samples are also listed. Sample 17c, as a quartz wacke (Table A.7) was excluded from the coefficient calculation.

	SiO2	Al2O3	Fe2O3	MnO	MgO	CaO	Na2O	K2O	TiO2	P2O5	L.O.I.	Total	ZONE
12d1	69.84	4.75	8.57	0.13	2.97	2.69	0.72	1.87	0.30	0.88	6.80	99.52	
12d2	45.07	7.69	12.10	0.14	3.86	11.63	0.88	2.72	0.52	3.17	11.99	99.77	
12f2	65.79	5.82	13.85	0.07	0.92	4.71	0.80	2.15	0.35	2.38	3.00	99.84	
12J2	69.30	4.22	9.83	0.14	0.62	6.20	0.18	1.81	0.26	2.44	4.70	99.70	
13g	46.62	5.80	5.71	0.09	9.58	8.50	0.00	4.91	0.41	0.14	17.98	99.74	1
13i2	39.29	7.83	13.62	0.07	14.84	4.22	0.00	3.43	0.43	0.47	15.32	99.52	
20g2	63.56	7.89	5.06	0.11	4.24	4.91	1.76	2.69	0.53	0.10	8.50	99.35	
20i2	54.33	7.32	5.34	0.09	7.31	8.07	1.18	2.34	0.33	0.05	13.41	99.77	
14g2	60.78	6.37	11.52	0.05	4.57	4.70	1.40	1.81	0.40	0.16	7.98	99.74	
18g2	73.51	5.93	4.73	0.08	2.79	3.62	1.50	0.95	0.55	0.19	5.80	99.65	
16A1	72.12	6.95	3.17	0.08	1.26	6.83	1.69	0.95	0.38	0.08	6.21	99.72	
16b4	69.73	8.05	5.74	0.07	2.14	5.54	1.00	1.83	0.57	0.19	4.89	99.75	2
16e3	68.14	7.24	3.00	0.10	1.50	8.43	1.47	1.21	0.40	0.06	8.00	99.55	
16h2	67.20	7.25	3.76	0.10	1.26	8.96	1.83	1.23	0.36	0.09	7.39	99.43	
10h	58.13	10.36	7.69	0.52	5.46	4.73	1.30	2.64	0.75	0.16	8.32	100.06	
9H	68.33	11.96	7.70	0.05	3.55	0.40	1.71	2.33	0.84	0.24	2.80	99.91	3
7R	66.43	8.38	15.94	0.20	1.01	1.19	1.18	2.47	0.65	0.31	2.49	100.25	
Average	62.25	7.28	8.08	0.12	3.99	5.61	1.09	2.20	0.47	0.65	7.98		
Std Dev	9.89	1.83	3.95	0.11	3.59	2.82	0.58	0.95	0.16	0.96	4.28		

SiO2	1.00												
Al2O3	-0.11	1.00											
Fe2O3	-0.35	-0.01	1.00										
MnO	-0.09	0.33	0.09	1.00									
MgO	-0.84	0.14	0.15	-0.01	1.00								
CaO	-0.38	-0.29	-0.34	-0.06	0.05	1.00							
Na2O	0.56	0.44	-0.46	0.03	-0.51	-0.11	1.00						
K2O	-0.78	0.13	0.32	0.13	0.71	0.07	-0.62	1.00					
TiO2	0.03	0.87	0.08	0.40	0.01	-0.46	0.37	0.15	1.00				
P2O5	-0.18	-0.34	0.52	-0.01	-0.22	0.28	-0.43	0.06	-0.26	1.00			
L.O.I.	-0.85	-0.12	-0.12	-0.03	0.82	0.55	-0.47	0.66	-0.27	-0.10	1.00		
	SiO2	Al2O3	Fe2O3	MnO	MgO	CaO	Na2O	K2O	TiO2	P2O5	L.O.I.		
17c	82.75	3.11	2.37	0.15	0.88	4.34	0.16	0.56	0.16	0.05	4.50	99.03	2

Table 3.4 Chemical analyses of subarkosic Fe (1 - 5% iron oxide minerals) and non Fe (<1% iron oxide minerals) arenites from measured sections 12, 20/14, 18, 10, 9/2 and 7 (Figure A.1), which are located within zones 1, 2 and 3 (Figure 2.1). Sample 6A is laterally removed from, but considered part of section #7 (Figure A.9). Correlation coefficients for the 8 samples are also listed.

	SiO2	Al2O3	Fe2O3	MnO	MgO	CaO	Na2O	K2O	TiO2	P2O5	L.O.I.	Total	ZONE
12r2	73.77	2.44	2.89	0.10	3.33	5.39	0.00	1.45	0.14	0.07	9.71	99.29	1
20q2	60.57	2.09	4.34	0.12	7.02	8.81	0.05	0.99	0.08	0.03	15.60	99.70	
18l2	61.02	4.47	4.81	0.15	4.63	8.78	1.36	0.69	0.38	0.22	12.91	99.42	2
10J2	85.24	1.54	0.65	0.18	0.67	5.33	0.66	0.21	0.06	0.01	4.95	99.50	
9B2	64.67	8.54	3.19	0.27	2.32	7.33	3.88	0.98	0.53	0.12	8.25	100.08	
2x1	74.16	6.92	7.61	0.06	2.86	1.67	0.78	1.88	0.47	0.14	3.31	99.86	3
2y2	93.63	2.27	1.08	0.07	0.21	0.21	1.19	0.11	0.11	0.04	0.38	99.30	
6A	62.06	8.67	3.33	0.30	2.50	8.04	4.57	0.41	0.50	0.12	9.64	100.14	
Average	71.89	4.62	3.49	0.16	2.94	5.70	1.56	0.84	0.28	0.09	8.09		
Std Dev	11.48	2.81	2.06	0.08	2.03	3.04	1.61	0.57	0.19	0.07	4.70		

SiO2	1.00										
Al2O3	-0.50	1.00									
Fe2O3	-0.54	0.46	1.00								
MnO	-0.48	0.62	-0.23	1.00							
MgO	-0.78	-0.05	0.55	-0.09	1.00						
CaO	-0.85	0.19	0.07	0.62	0.65	1.00					
Na2O	-0.35	0.84	-0.06	0.86	-0.26	0.29	1.00				
K2O	-0.33	0.25	0.79	-0.36	0.43	-0.07	-0.28	1.00			
TiO2	-0.53	0.97	0.56	0.52	-0.00	0.19	0.75	0.31	1.00		
P2O5	-0.56	0.61	0.63	0.18	0.24	0.28	0.37	0.30	0.77	1.00	
L.O.I.	-0.86	0.00	0.25	0.29	0.88	0.91	-0.01	0.16	0.03	0.24	1.00
	SiO2	Al2O3	Fe2O3	MnO	MgO	CaO	Na2O	K2O	TiO2	P2O5	L.O.I.

Table 3.5 Chemical analyses of Fe siltstones (1 - 21.5% iron oxide minerals) from measured sections 20/14, 21, 18, 16, 9/2, 8 and 7 (Figure A.1), which are located within zones 1, 2 and 3 (Figure 2.1). Sample 6d is laterally removed from, but considered part of section #7 (Figure A.9). Correlation coefficients for the 16 samples are also listed. Sample 21f$_2$ is considered to be a non Fe siltstone and excluded from average and coefficient calculations. Sample numbers followed by $\bar{x}$ represent mean values for analyses of two (sample 8A$_L$) or four (sample 7u) aliquots.

Sample	SiO2	Al2O3	Fe2O3	MnO	MgO	CaO	Na2O	K2O	TiO2	P2O5	L.O.I	Total	ZONE
20b	51.72	10.92	7.22	0.13	9.02	5.30	1.03	2.41	0.93	0.14	10.91	99.73	
20k2	36.98	6.21	15.83	0.07	12.09	9.55	0.00	0.99	0.60	0.14	17.32	99.78	1
21i2	29.80	6.35	5.14	0.22	11.11	16.92	1.44	1.64	0.41	0.05	26.60	99.68	
18f2	62.63	11.98	13.40	0.02	3.17	0.55	0.00	3.31	0.86	0.40	3.20	99.52	
18i2	55.85	9.67	17.03	0.04	3.40	3.17	0.00	3.15	0.68	0.34	6.39	99.72	2
16b2	57.68	12.77	14.64	0.06	3.52	2.45	1.46	3.52	1.04	0.41	1.89	99.44	
9d2a	59.13	8.95	10.79	0.28	3.78	4.74	1.36	2.58	0.66	0.23	7.53	100.03	
9j2	54.44	10.82	12.12	0.62	3.82	4.72	0.98	3.56	0.82	0.16	7.94	100.00	
9K3	31.76	5.02	16.93	0.69	8.68	13.54	0.97	0.84	0.41	0.21	20.50	99.55	
9L2	53.71	8.94	22.26	0.14	3.39	2.63	0.53	2.62	0.85	0.25	4.56	99.88	
8M	55.66	5.95	8.34	0.18	1.85	12.35	2.54	0.64	0.40	0.30	11.78	99.99	3
8AL $\bar{x}$	49.25	6.55	24.30	0.29	2.43	6.42	1.71	1.26	0.39	2.78	4.62	100.00	
2T2	52.82	7.88	8.50	0.66	4.17	8.79	2.35	1.66	0.55	0.11	11.90	99.39	
6d	64.21	11.01	9.70	0.09	4.00	2.05	0.06	3.05	0.76	0.21	5.06	100.20	
7K	55.90	10.95	16.51	0.18	4.32	3.12	0.79	1.72	0.80	0.26	5.52	100.07	
7u $\bar{x}$	48.43	8.48	27.07	0.11	3.63	3.05	1.82	1.97	0.71	0.28	4.51	100.06	
Average	51.25	8.90	14.36	0.24	5.15	6.21	1.07	2.18	0.68	0.39	9.39		
Std Dev	9.80	2.31	6.07	0.22	3.07	4.57	0.79	0.95	0.20	0.62	6.66		

	SiO2	Al2O3	Fe2O3	MnO	MgO	CaO	Na2O	K2O	TiO2	P2O5	L.O.I.
SiO2	1.00										
Al2O3	0.74	1.00									
Fe2O3	-0.03	-0.09	1.00								
MnO	-0.32	-0.38	-0.14	1.00							
MgO	-0.79	-0.37	-0.30	0.06	1.00						
CaO	-0.81	-0.82	-0.38	0.43	0.58	1.00					
Na2O	-0.11	-0.37	-0.11	0.40	-0.24	0.42	1.00				
K2O	0.63	0.87	-0.06	-0.26	-0.36	-0.74	-0.43	1.00			
TiO2	0.58	0.92	0.04	-0.40	-0.20	-0.79	-0.41	0.79	1.00		
P2O5	0.04	-0.19	0.48	-0.01	-0.33	-0.08	0.18	-0.19	-0.31	1.00	
L.O.I.	-0.86	-0.70	-0.45	0.37	0.81	0.93	0.13	-0.59	-0.63	-0.29	1.00

Sample	SiO2	Al2O3	Fe2O3	MnO	MgO	CaO	Na2O	K2O	TiO2	P2O5	L.O.I.	Total
21f2	49.26	10.73	5.94	0.06	9.33	6.59	0.49	2.52	0.76	0.10	13.71	99.49

Table 3.6 Chemical analyses of carbonates from measured sections 20/14, 10, 9/2, 8 and 7 (Figure A.1), which are located within zones 1 and 3 (Figure 2.1). Samples 5Au and 4A are laterally removed from, but considered part of sections 10 and 9/2 respectively (Figure A.9). Correlation coefficients for the 6 samples are also listed. $\bar{x}$ = mean value of two aliquots.

	SiO2	Al2O3	Fe2O3	MnO	MgO	CaO	Na2O	K2O	TiO2	P2O5	L.O.I.	Total	ZONE
20j	34.27	5.50	7.94	0.10	12.78	14.28	0.00	1.25	0.43	0.04	23.30	99.89	1
10q2	22.05	3.47	10.91	1.09	13.83	17.85	1.28	0.35	0.28	0.09	28.98	100.18	
5Au $\bar{x}$	29.69	4.60	10.29	0.46	9.47	17.09	2.43	0.19	0.23	0.67	24.77	99.89	
4A	35.46	6.15	11.16	0.48	7.96	15.15	0.83	1.84	0.36	0.43	20.28	100.10	3
8E2	37.00	6.21	12.26	0.53	7.34	13.31	2.22	0.95	0.23	0.83	19.05	99.93	
7W1	34.18	4.91	9.53	0.83	10.62	14.30	0.56	1.44	0.40	0.12	22.80	99.69	
Average	32.11	5.14	10.35	0.58	10.33	15.33	1.22	1.00	0.32	0.36	23.20		
Std Dev	5.02	0.95	1.36	0.31	2.37	1.62	0.87	0.58	0.08	0.30	3.21		

	SiO2	Al2O3	Fe2O3	MnO	MgO	CaO	Na2O	K2O	TiO2	P2O5	L.O.I.
SiO2	1.00										
Al2O3	0.94	1.00									
Fe2O3	-0.01	0.17	1.00								
MnO	-0.63	-0.66	0.42	1.00							
MgO	-0.70	-0.75	-0.61	0.27	1.00						
CaO	-0.91	-0.83	0.05	0.48	0.47	1.00					
Na2O	-0.15	-0.07	0.71	0.18	-0.49	0.27	1.00				
K2O	0.71	0.69	-0.15	-0.30	-0.32	-0.68	-0.65	1.00			
TiO2	0.30	0.18	-0.75	-0.28	0.36	-0.37	-0.97	0.72	1.00		
P2O5	0.36	0.46	0.71	-0.20	-0.84	-0.17	0.85	-0.21	-0.77	1.00	
L.O.I.	-0.96	-0.97	-0.27	0.52	0.84	0.85	-0.04	-0.66	-0.09	-0.54	1.00

Figure 3.1 Log [(CaO + Na_2O)/K_2O] vs. log (SiO_2/Al_2O_3) plot of Holowilena & Braemar iron formation and associated iron oxide-bearing clastic rocks. Fields of igneous rocks (shaded pattern), mudstones (dashed pattern), sandstones (stippled pattern) and carbonates (bricked pattern) from Garrels and MacKenzie (1971) are shown.

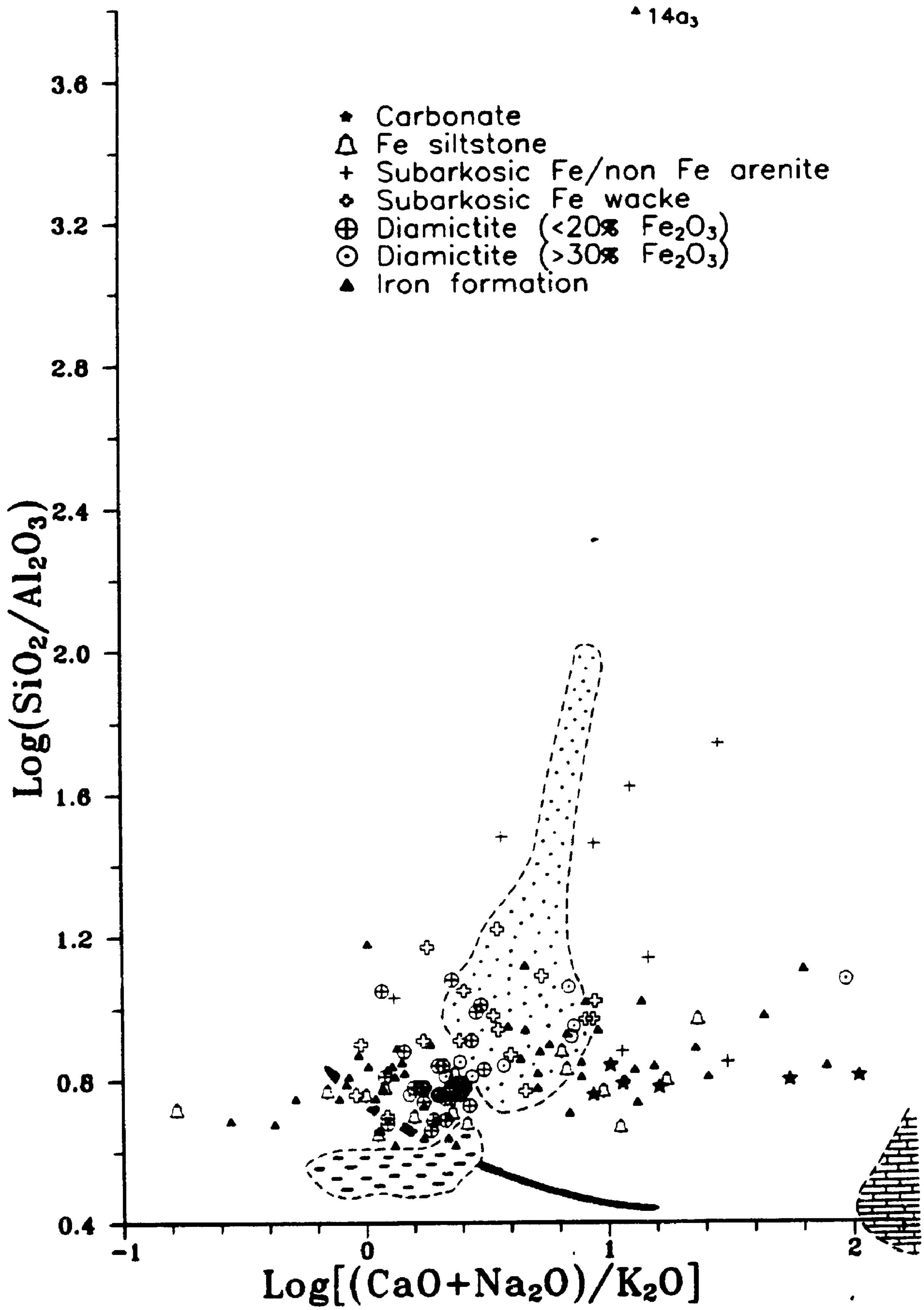
14a3
Carbonate
Fe siltstone
Subarkosic Fe/non Fe arenite
Subarkosic Fe wacke
Diamictite (<20% Fe2O3)
Diamictite (>30% Fe2O3)
Iron formation
3.6
3.2
2.8
2.4
2.0
1.6
1.2
0.8
0.4
Log(SiO2/Al2O3)
-1
0
1
2
Log[(CaO+Na2O)/K2O]

Discussion of Correlation Coefficients

The correlation coefficients (Tables 3.1 - 3.6) were calculated on L.O.I.-intact results in order to document any correspondence between L.O.I. and the ten major elements. Where presented graphically, however, the major elements have been recalculated to 100 percent on a volatile-free basis. Hence graphically represented correlations are similar but not identical to the coefficients of Tables 3.1 - 3.6. Discussion here emphasizes correlation coefficients (c.c.) between −0.60 and −1.00 and 0.60 and 1.00.

Of the five facies types described in Chapter 2, the diamictite and iron formation facies were the most extensively sampled (Tables 3.1 & 3.2). The major oxides are dominated by SiO_2 and Fe_2O_3, which in samples of diamictite macro-matrix (Figure 2.2) and IF have an inverse relationship (Figure 3.2). The negative slope of this plot is attributed to dilution of chemically precipitated iron oxides by detrital silicates (Tables 2.1 & 2.2). This dilution has led to the development of two populations of diamictites, which are distinguished by Fe_2O_3 contents of < 20% (low) and > 30% (high) respectively (Figure 3.2). As evident from Figures 3.3 - 3.5, the low Fe_2O_3 diamictites can be grouped together with the subarkosic Fe wackes/arenites and the carbonates. Only in Figure 3.4 do the low Fe_2O_3 diamictites follow the negative slope of the iron formation. In contrast, the high Fe_2O_3 diamictites consistently show patterns similar to those of IF samples. For example, the negative correlation between Fe_2O_3 and all three of Al_2O_3, K_2O and TiO_2 for the high Fe_2O_3 diamictites and IF (Figures 3.3 - 3.5), suggests that an increase in iron oxide content should result in decreased abundances of aluminum silicate phases (e.g., feldspar, clay). Admittedly, the Fe_2O_3 vs. TiO_2 plot (Figure 3.5) is only slightly negative for both rock types; a correlation which is probably weakened by the occurrence of Ti-bearing hematite in several samples (see Chapter 4).

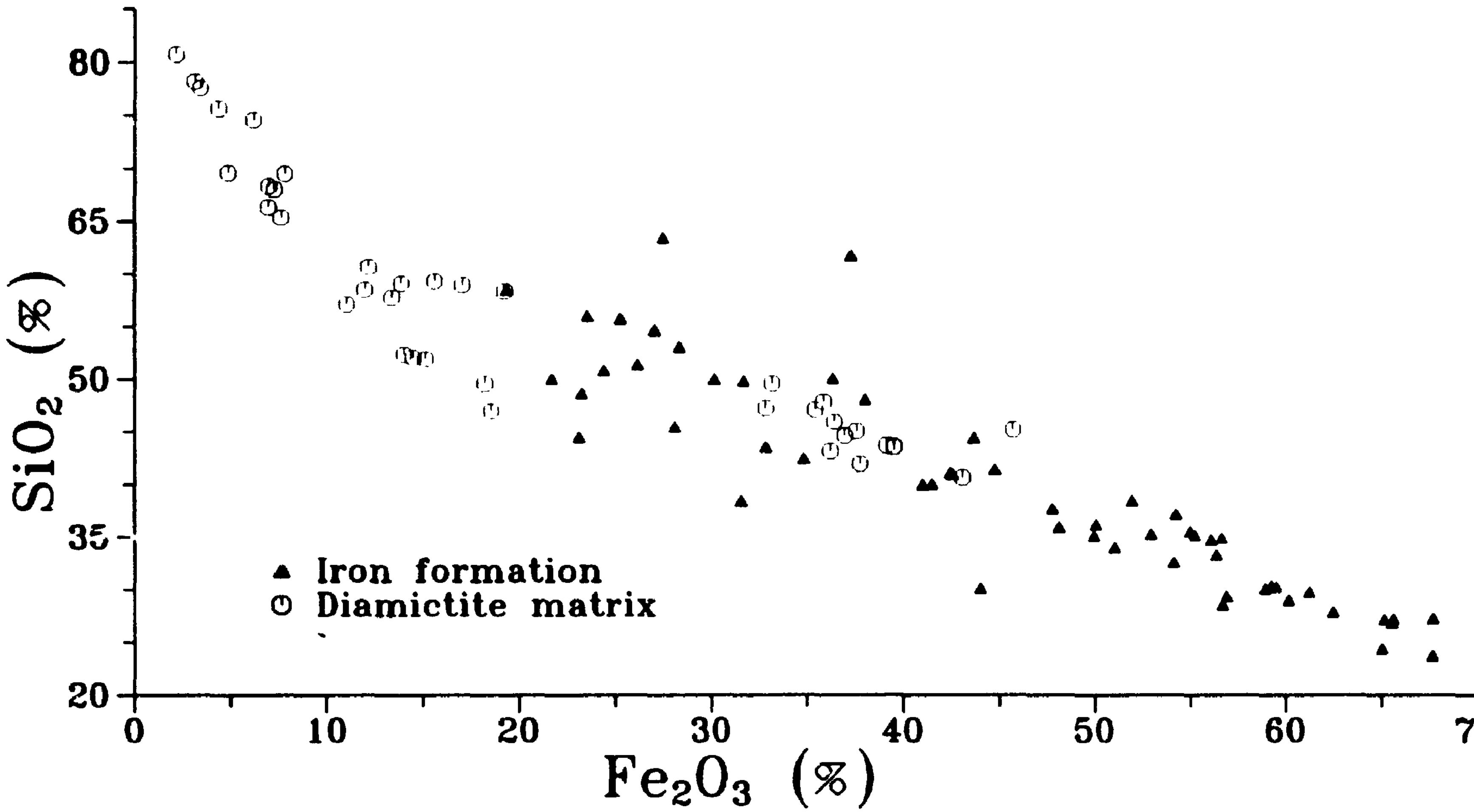

Figure 3.2 Fe_2O_3 vs. SiO_2 plot of iron formation and diamictite matrices.

Figure 3.3 Fe_2O_3 vs. Al_2O_3 plot of Holowilena & Braemar iron formation and associated iron oxide-bearing clastic rocks. Zones 1, 2 and 3 (Figure 2.1) are identified for iron formation and diamictite samples.

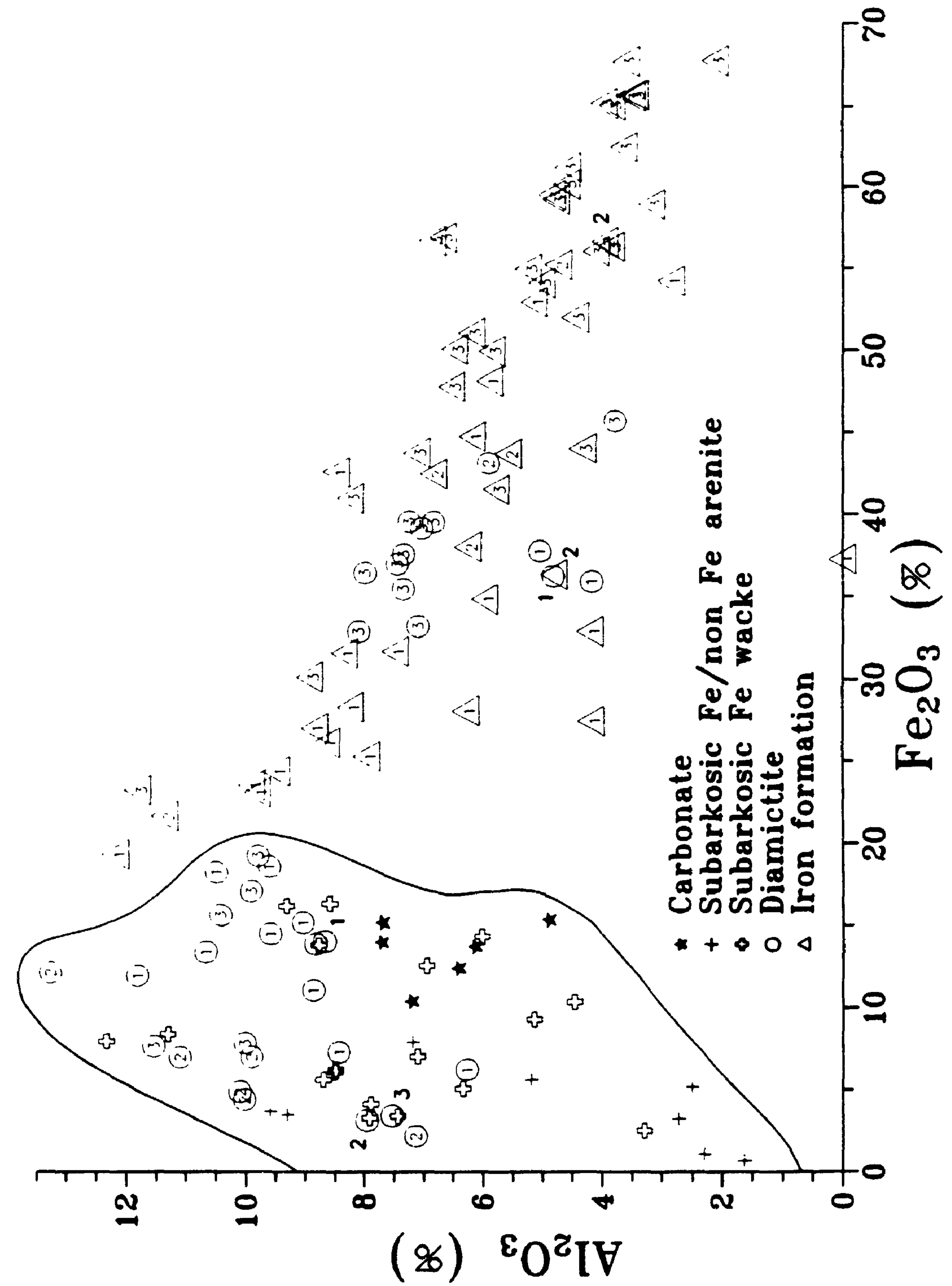
Al2O3 (%)
Fe2O3 (%)
Carbonate
Subarkosic Fe/non Fe arenite
Subarkosic Fe wacke
Diamictite
Iron formation

Figure 3.4 Fe_2O_3 vs. K_2O plot of Holowilena & Braemar iron formation and associated iron oxide-bearing clastic rocks. Zones 1, 2 and 3 (Figure 2.1) are identified for iron formation and diamictite samples. Samples $14d_2$, 14k and $14M_1$ are the Holowilena samples mentioned on page 121. On the inset diagram (right), diamictite samples are grouped according to the potassium silicate minerals observed in thin section (Table 2.1).

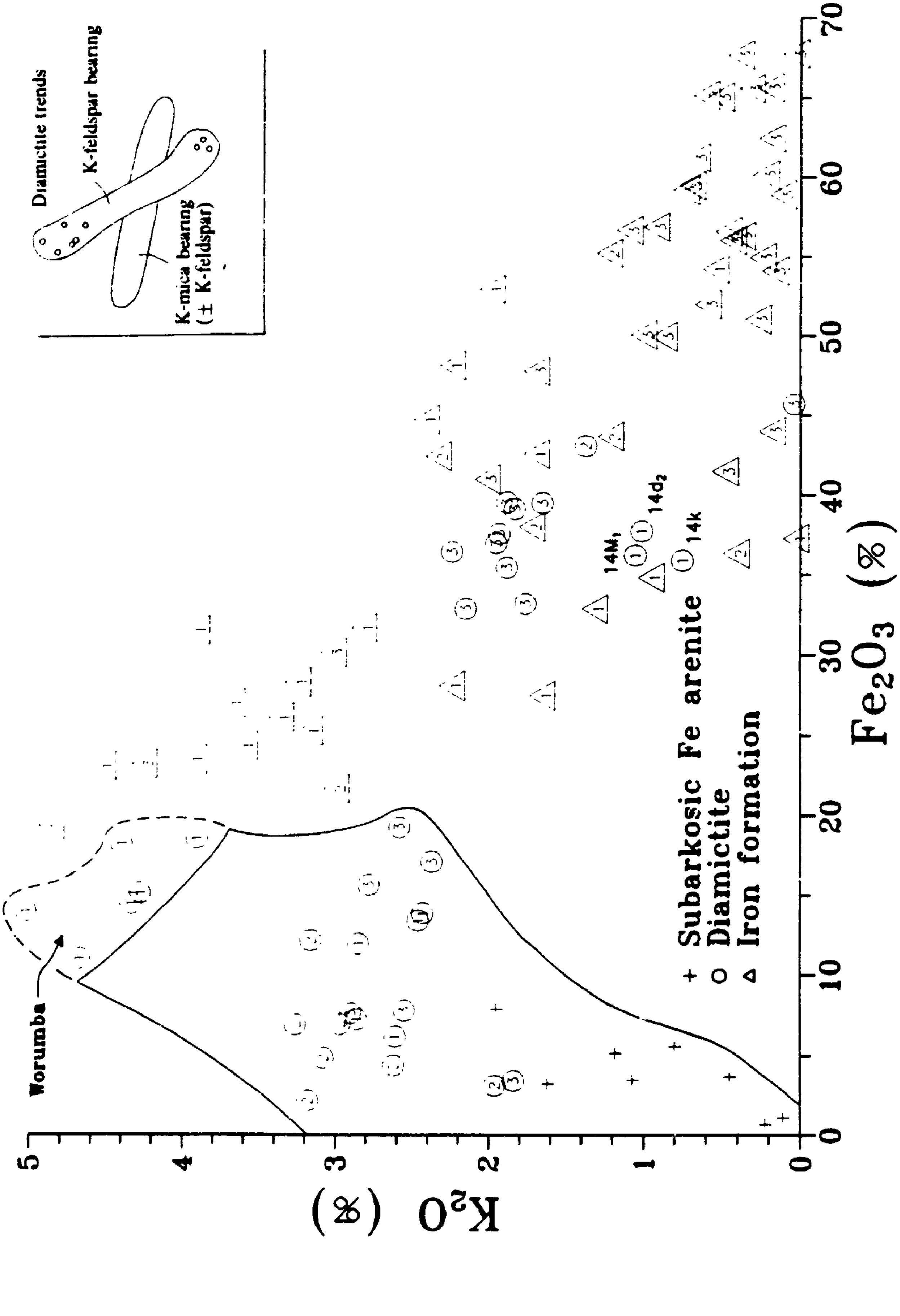
K₂O (%)
Fe₂O₃ (%)
Worumba
+ Subarkosic Fe arenite
o Diamictite
△ Iron formation
14M₁
14d₂
14k
Diamictite trends
K-feldspar bearing
K-mica bearing
(± K-feldspar)
0
1
2
3
4
5
10
20
30
40
50
60
70

Figure 3.5 Fe_2O_3 vs. TiO_2 plot of Holowilena & Braemar iron formation and associated iron oxide-bearing clastic rocks. Zones 1, 2 and 3 (Figure 2.1) are identified for iron formation and diamictite samples.

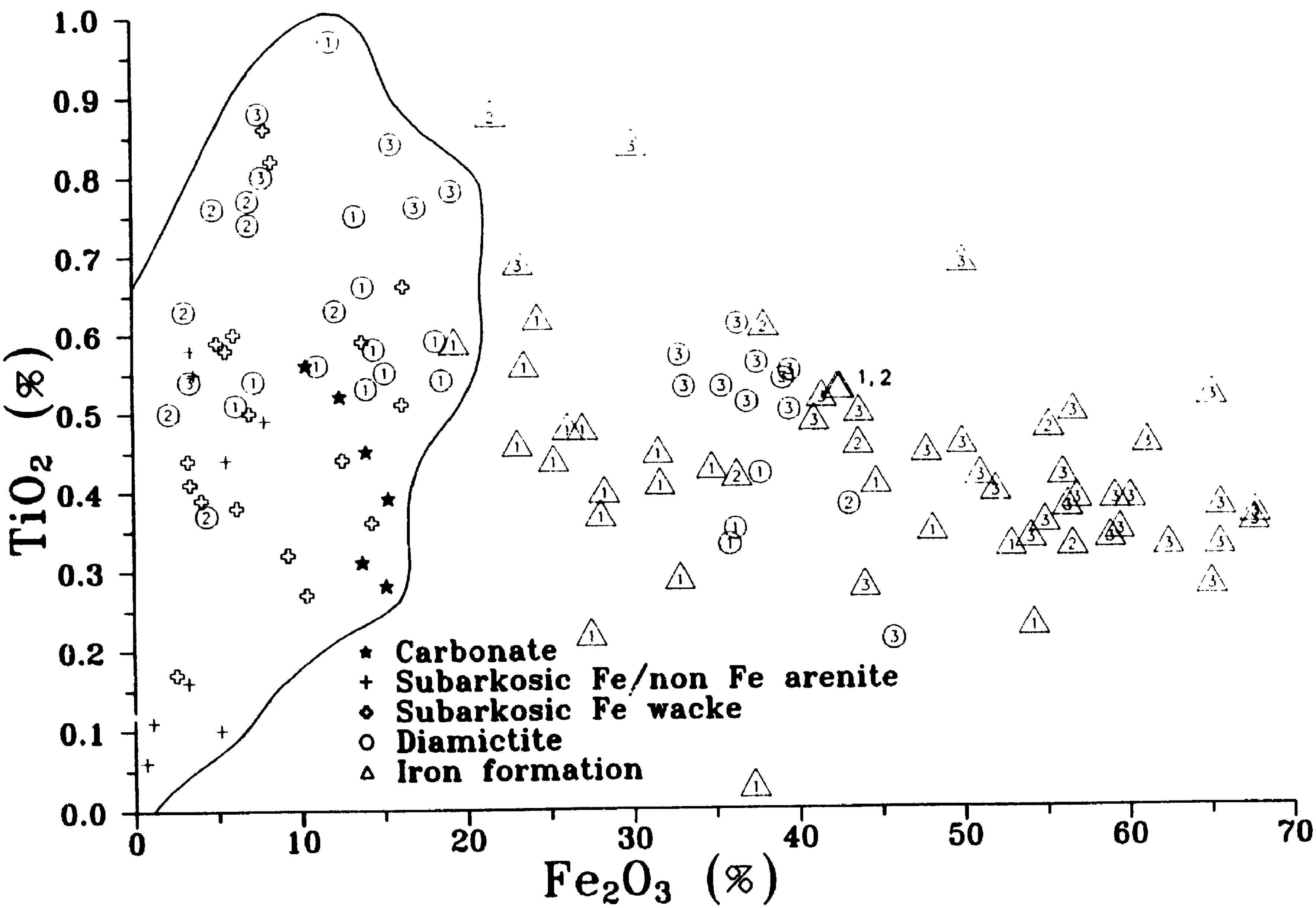
1.0
0.9
0.8
0.7
0.6
0.5
0.4
0.3
0.2
0.1
0.0
TiO2 (%)
0
10
20
30
40
50
60
70
Fe2O3 (%)
Carbonate
Subarkosic Fe/non Fe arenite
Subarkosic Fe wacke
Diamictite
Iron formation
1, 2

With regard to chemical changes between zones (Figure 2.1, Table 3.7), IF from zone 1 typically has the lowest percent Fe_2O_3, whereas that from zone 3 has the highest (Figures 3.3 - 3.5). Iron-rich diamictites are most common within zone 3 and least common within zone 2. Iron formation samples from zone 1 tend to cluster near the high end of the Al_2O_3, K_2O, but not the TiO_2 scales, which probably reflects the presence of K-feldspar in these samples (Table 2.2). In addition, diamictites from *Worumba* (zone 1) have the highest percent K_2O (Figure 3.4) and have K-feldspar as their second most abundant micro-framework component (Table 2.1). Also within zone 1 are K-feldspar-bearing diamictites at *Holowilena South* which have the lowest percent K_2O; they are considered the iron-rich equivalent of the *Worumba* diamictites (Figure 3.4).

A positive correlation occurs between Al_2O_3 and K_2O for samples from the iron formation, diamictite and Fe siltstone facies (Figure 3.6). Increasing amounts of potassium-bearing aluminum silicate minerals define this trend. These minerals, identified in thin sections of the IF and diamictite (Tables 2.1 & 2.2), are used here to group the samples (Figures 3.7 & 3.8). The potassium silicate phases present in the IF and diamictite include: K-feldspar, white mica (e.g., sericite), phlogopite and biotite. The mineral used to identify a group is generally the most dominant potassium silicate phase in samples within the group, but where an identifying mineral is not dominant, it is at least present. The mineral groups defined for both the iron formation and diamictite reflect two main trends (Figures 3.7 & 3.8), which are that: (1) K-feldspar and (2) K-mica (phlogopite, biotite, sericite) decrease with increasing amounts of iron oxide. These trends were observed earlier in the diamictite plot of Fe_2O_3 vs. K_2O (Figure 3.4); they are also evident on a graph of SiO_2 vs. K_2O (Figure 3.9).

The positive correlation between SiO_2 and K_2O for iron formation and diamictite (Figures 3.9 & 3.10a) is predictable since these two oxides show negative correlations with Fe_2O_3 (Figures 3.2 & 3.4). A positive sloping SiO_2-K_2O line reflects

Table 3.7 Highest and lowest major element cation content of diamictite and iron formation by zone. Empty box indicates that there is no clear and consistent difference between zones.

		Diamictite	Iron Formation
Fe_2O_3	Highest	zone 3 (all localities; iron oxides)	zone 3 (all localities; iron oxides)
	Lowest		zone 1 ('Dropstone Creek', *Worumba*)
K_2O	Highest	zone 1 (*Worumba*; K-feldspar)	zone 1 ('Dropstone Creek', *Worumba*)
	Lowest	zone 1 (section #20/14)	zone 3
Na_2O	Highest		zone 3 (all localities)
	Lowest		zone 1 (all localities)
MgO	Highest	zone 1 (all localities; ferroan dolomite)	zone 1 (*Worumba*)
	Lowest		
CaO	Highest	zone 1 (all localities; ferroan dolomite)	
	Lowest		
P_2O_5	Highest		zone 1 (all localities)
	Lowest		zone 3

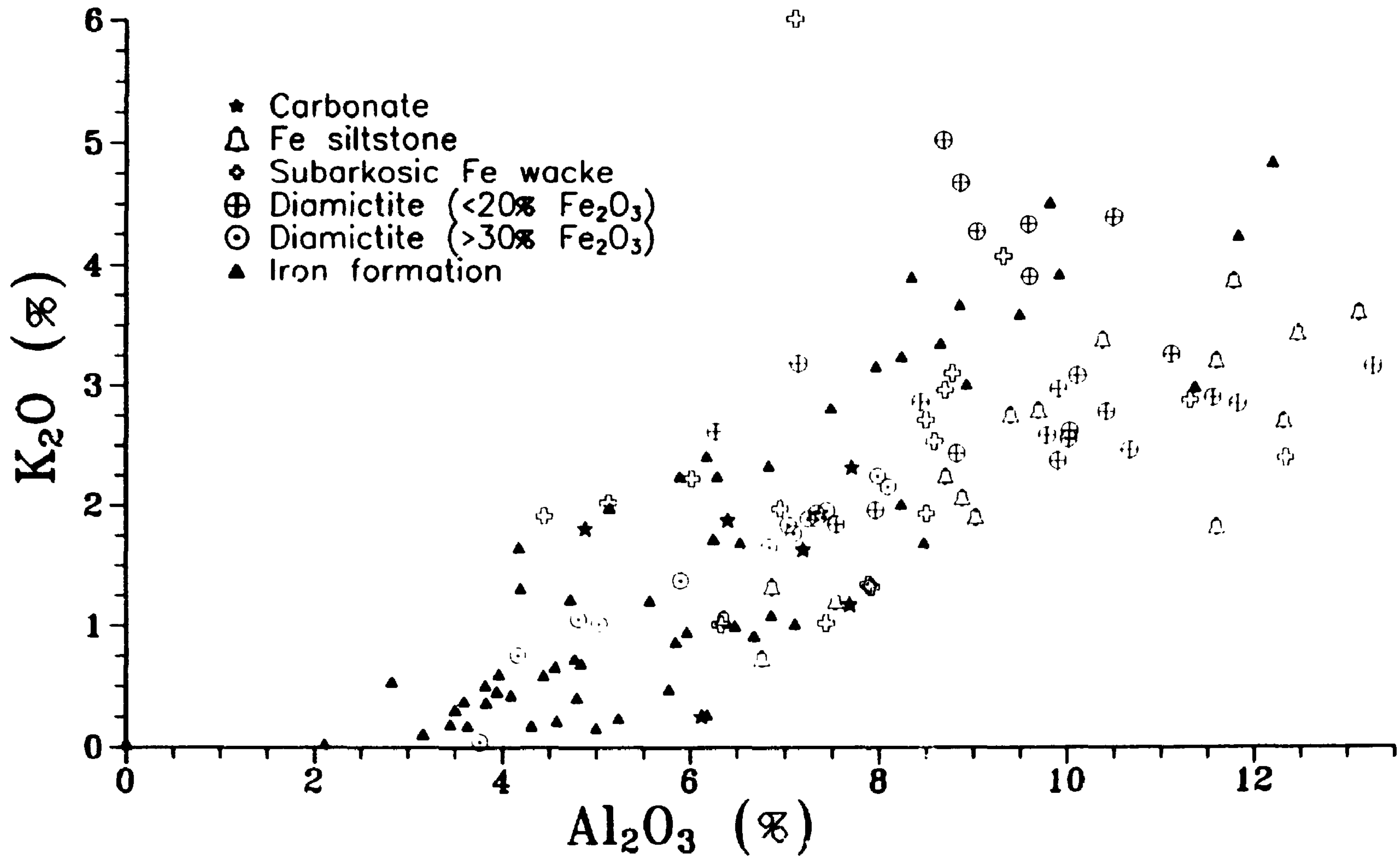

Figure 3.6 Al_2O_3 vs. K_2O plot of Holowilena & Braemar iron formation and associated iron oxide-bearing clastic rocks.

Figure 3.7 Al_2O_3 vs. K_2O plot of Holowilena & Braemar iron formation from zones 1, 2 and 3 (Figure 2.1). Samples are grouped according to the potassium silicate minerals observed in thin section (Tables 2.2 & A.13).

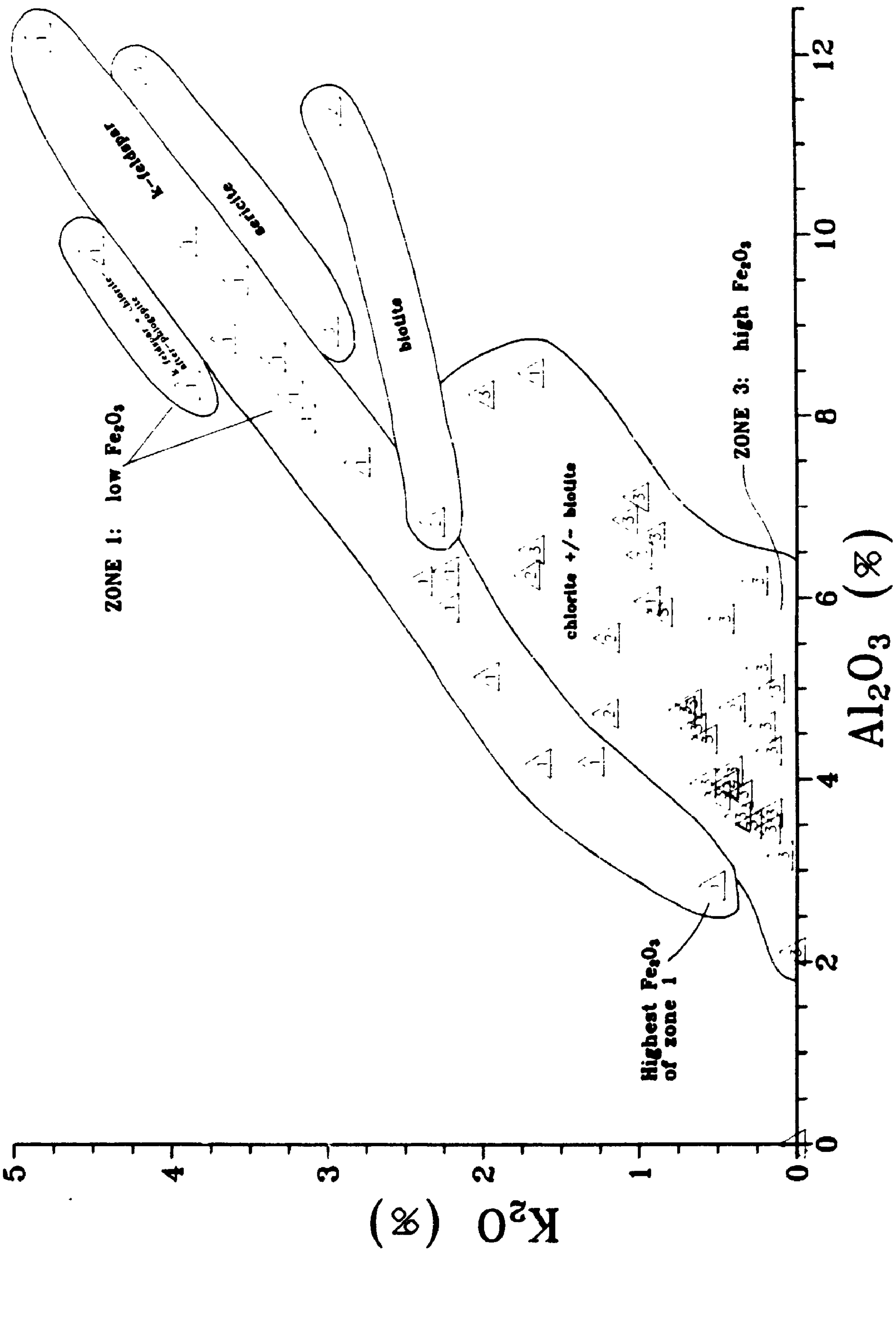
ZONE 1: low Fe_2O_3
ZONE 3: high Fe_2O_3
K-feldspar
sericite
biotite
chlorite +/- biotite
Highest Fe_2O_3 of zone 1
K_2O (%)
Al_2O_3 (%)
0
1
2
3
4
5
0
2
4
6
8
10
12

Figure 3.8 Al_2O_3 vs. K_2O plot of diamictite matrices from zones 1, 2 and 3 (Figure 2.1). Samples are grouped according to the potassium silicate minerals observed in thin section (Table 2 1).

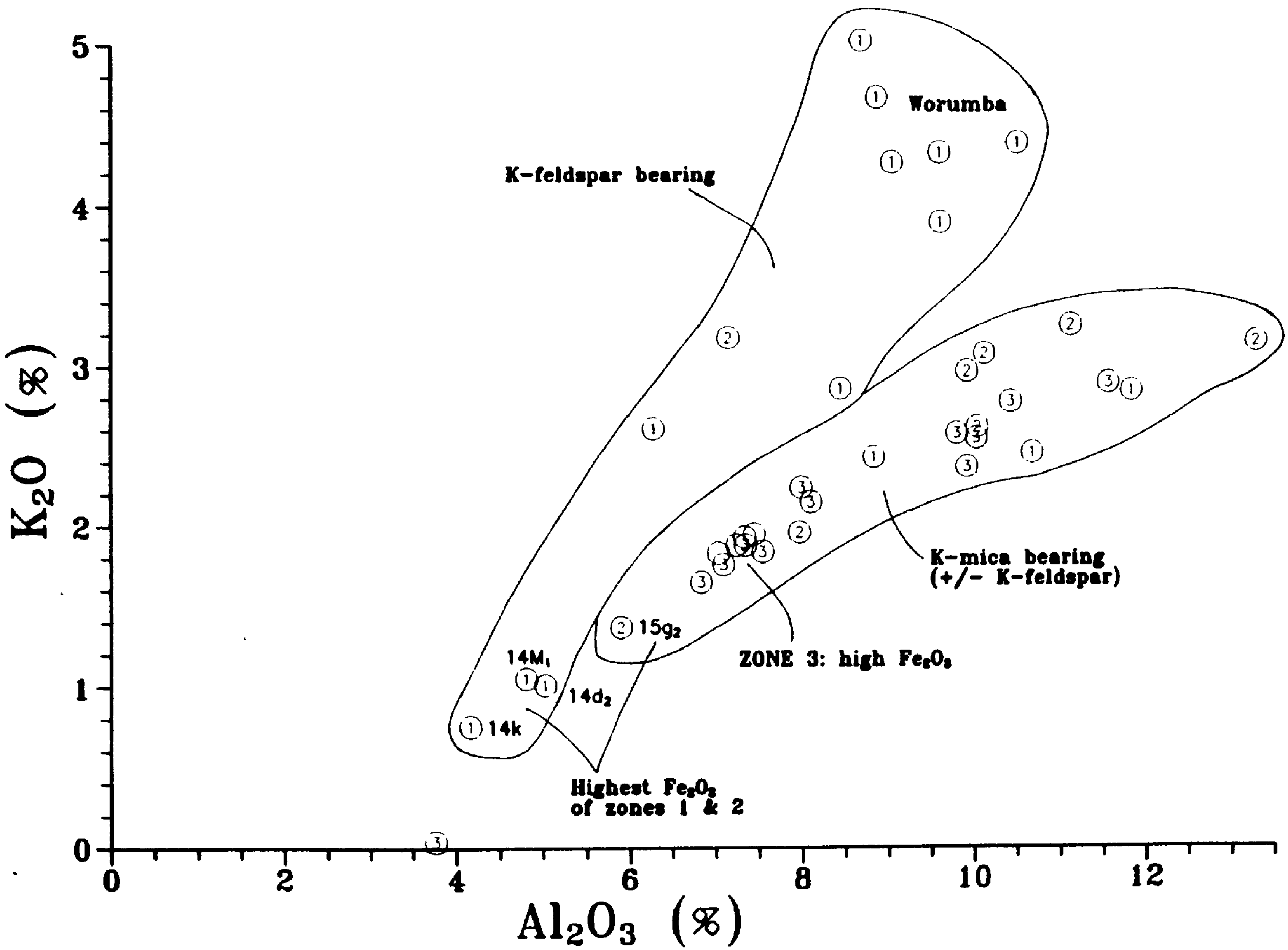
Worumba
K-feldspar bearing
K-mica bearing
(+/- K-feldspar)
ZONE 3: high Fe2O3
Highest Fe2O3
of zones 1 & 2
15g2
14M1
14d2
14k
K2O (%)
Al2O3 (%)
0
1
2
3
4
5
0
2
4
6
8
10
12

Figure 3.9 SiO_2 vs. K_2O plot of diamictite matrices from zones 1, 2 and 3 (Figure 2.1). Samples are grouped according to the potassium silicate minerals observed in thin section (Table 2.1).

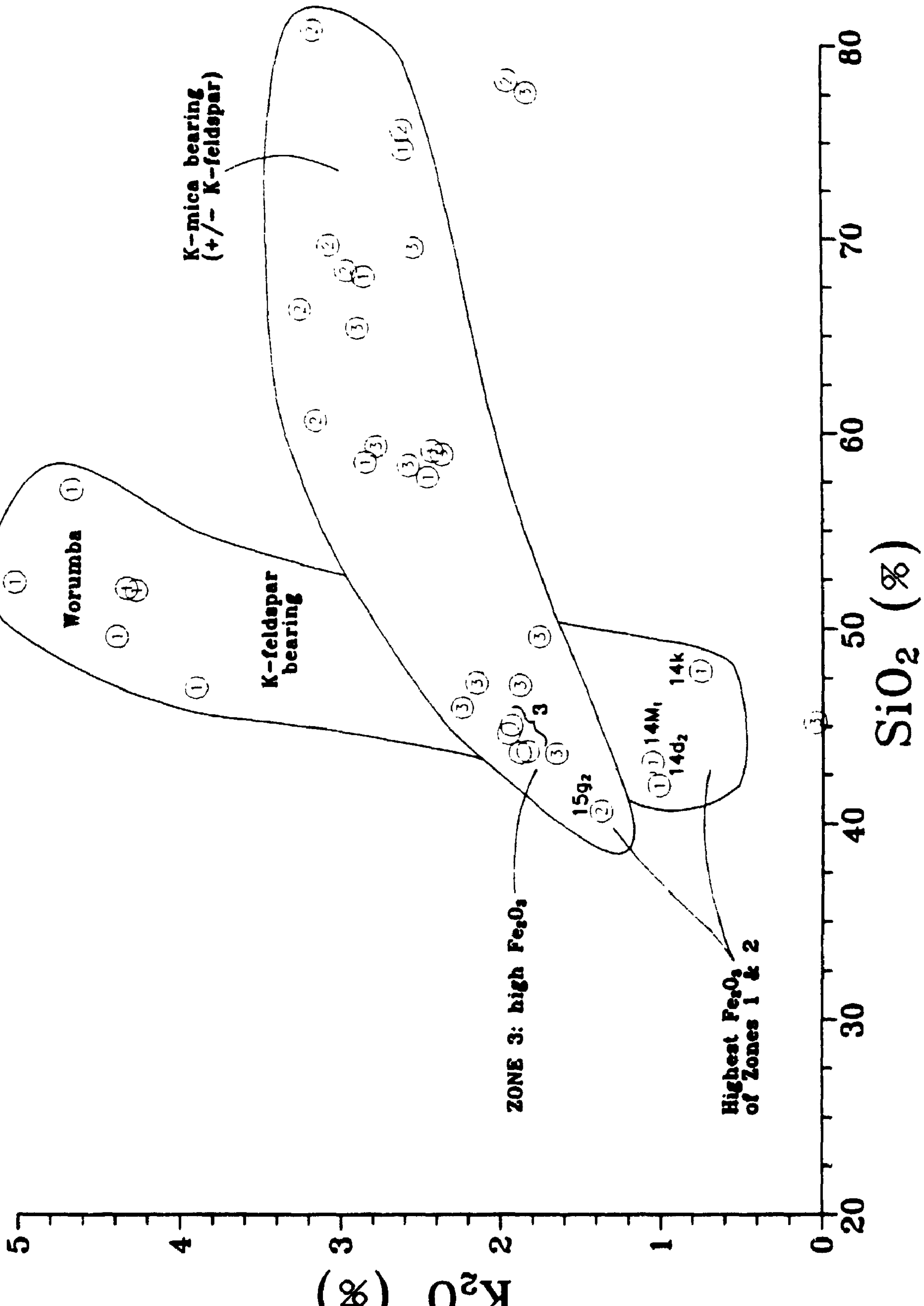
K-mica bearing
(+/- K-feldspar)
Worumba
K-feldspar bearing
ZONE 3: high Fe_2O_3
Highest Fe_2O_3 of Zones 1 & 2
14k
$14M_1$
$14d_2$
$15g_2$
SiO_2 (%)
K_2O (%)
20
30
40
50
60
70
80
0
1
2
3
4
5

Figure 3.10A SiO_2 vs. K_2O plot of Holowilena & Braemar iron formation and associated iron oxide-bearing clastic rocks.

Figure 3.10B SiO_2 vs. Al_2O_3 plot of iron formation (triangle), diamictite matrices (circle), subarkosic Fe wacke (open cross), subarkosic Fe/non Fe arenite (solid cross) and carbonate (star).

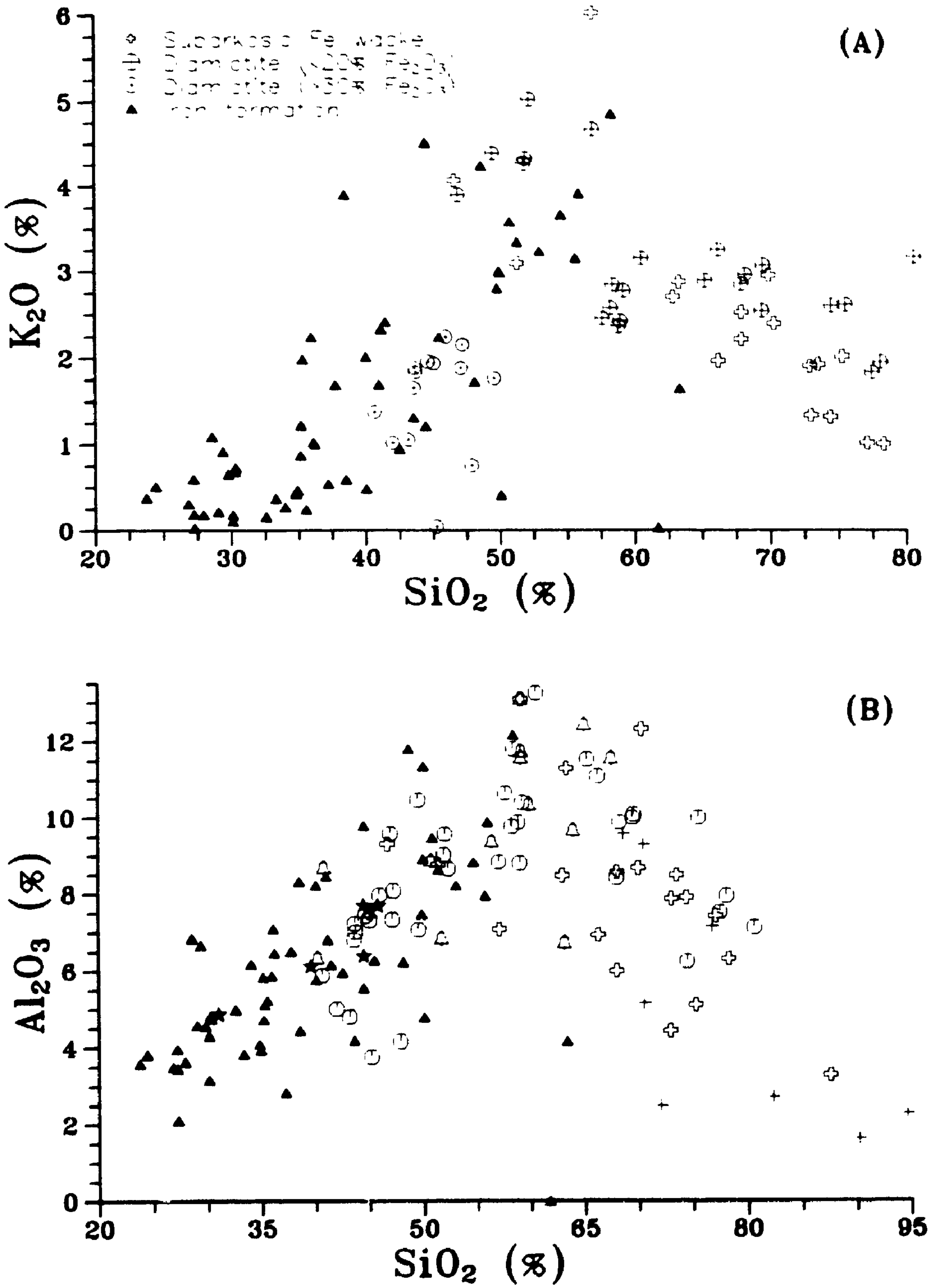
(A)
K_2O (%)
SiO_2 (%)
0
1
2
3
4
5
6
20
30
40
50
60
70
80
(B)
Al_2O_3 (%)
SiO_2 (%)
0
2
4
6
8
10
12
20
35
50
65
80
95

increasing amounts of potassium silicate (cf. Figures 3.7 & 3.8), whereas the negative sloping plot of the subarkosic Fe wacke samples suggests that an increase in quartz coincides with a decrease in potassium silicates (Figure 3.10a). These same samples show only a weakly negative correlation between SiO_2 and Al_2O_3 (Figure 3.10b).

Positive correlations occur between Al_2O_3 and TiO_2 for all rock types except carbonate, which reflects a general increase in clay content (Figure 3.11). As evident from Figures 3.12 and 3.13, the steepest slope is defined by biotite-bearing samples whereas shallower sloping lines transect chloritized phlogopite- and chlorite-bearing samples. The groups outlined on these two figures approximate those defined on Figures 3.7 and 3.8, the main difference being that the group positions are reversed in a "northwest-southeast" direction. This reversal confirms that the most potassic samples are not the most titaniferous. Positive Al_2O_3-K_2O, SiO_2-K_2O, SiO_2-Al_2O_3 and Al_2O_3-TiO_2 correlations need not imply that potassium resides primarily in the clay minerals; it is only in the Fe siltstone and high Fe_2O_3 (>30%) diamictite samples that a well developed covariance occurs between K_2O and TiO_2 to indicate such a relationship (Figure 3.14).

A negative sloping K_2O vs. Na_2O plot is defined by samples of iron formation, carbonate and to a lesser degree, high Fe_2O_3 (>30%) diamictite (Figure 3.15a). This graph reflects a decrease in Na-feldspar as K-bearing silicates increase (e.g., K-feldspar, clay). Noted on this plot are the most Fe_2O_3-rich diamictite macro-matrix and IF samples from each of the three zones. Of the six samples, the two from zone 3 have the lowest percent K_2O, and the two from zone 1 have the lowest percent Na_2O. These differences parallel the zonal contrasts established for the IF facies (Table 3.7). In fact, IF samples from zone 3, which are generally the most Fe_2O_3-rich (p. 121), tend to have the highest percent Na_2O (Figure 3.15b). The Fe_2O_3 and Na_2O contents of zone 2 iron formation lie between the two main sample populations of zones 1 and 3.

The most positive covariance between MgO and CaO occurs for samples from

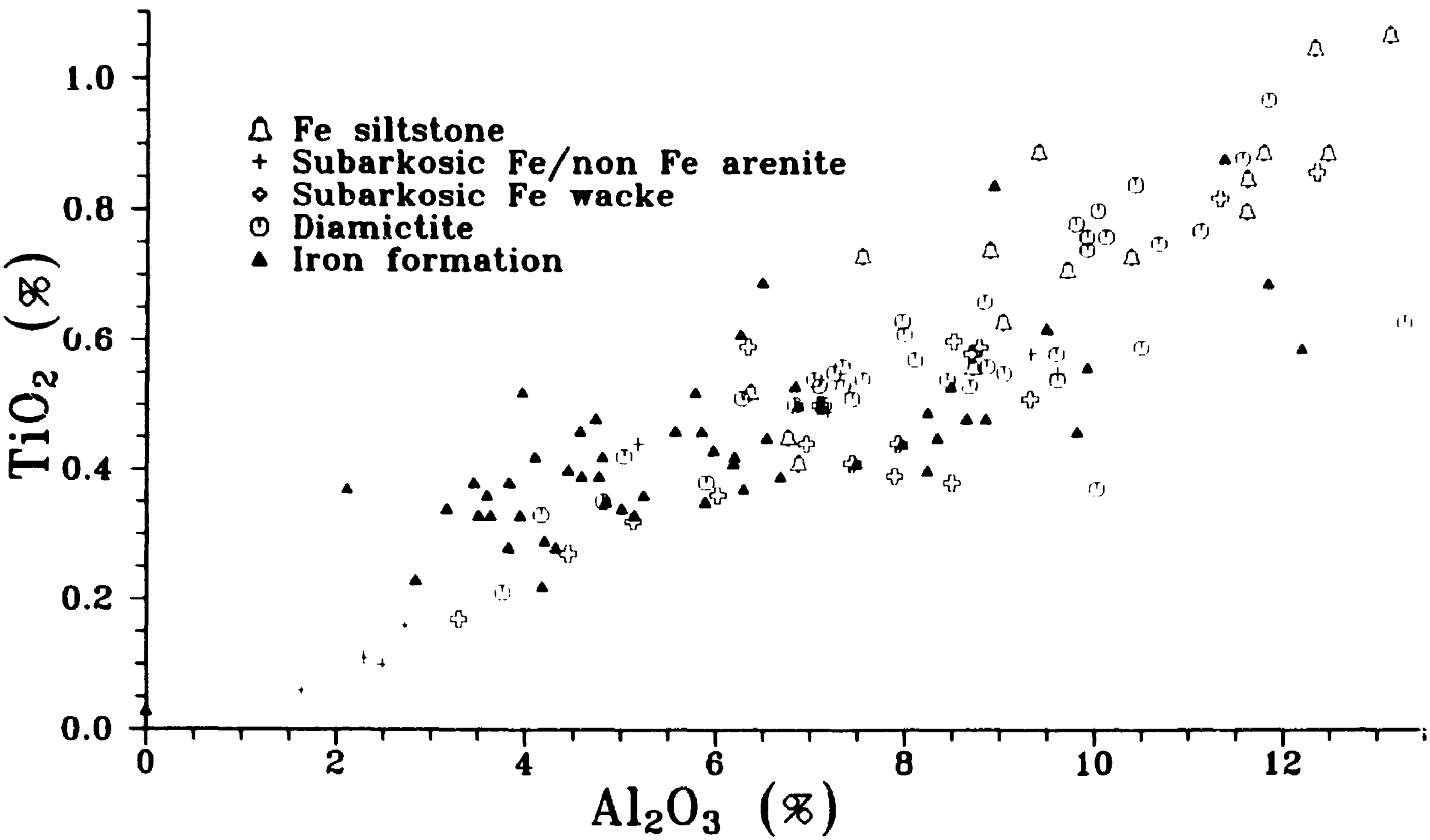

Figure 3.11 Al_2O_3 vs. TiO_2 plot of Holowilena & Braemar iron formation and iron oxide-bearing clastic rocks.

Figure 3.12 Al_2O_3 vs. TiO_2 plot of Holowilena & Braemar iron formation from zones 1, 2 and 3 (Figure 2.1). Samples are grouped according to the potassium silicate minerals observed in thin section (Table 2.2).

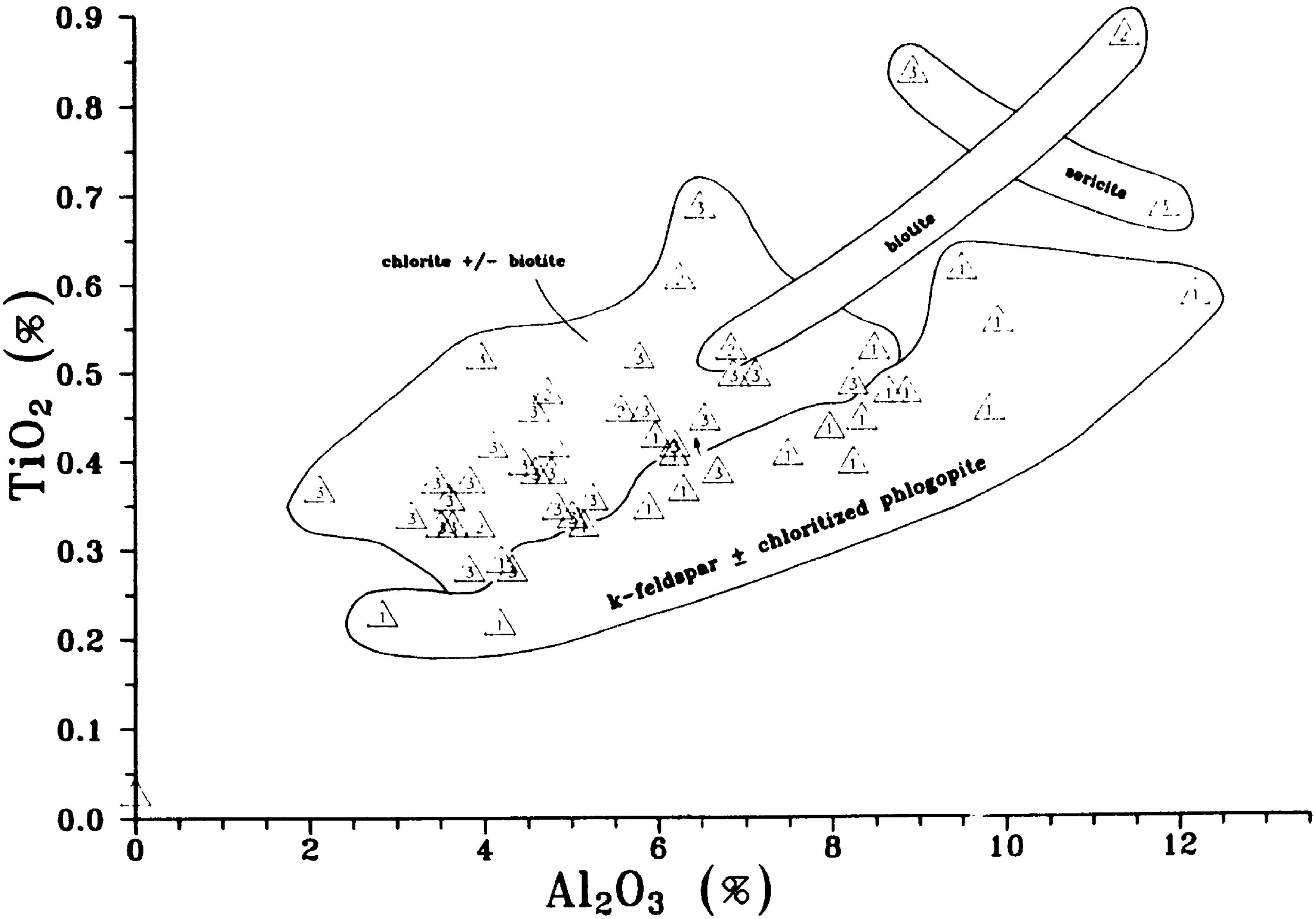
chlorite +/- biotite
biotite
sericite
k-feldspar ± chloritized phlogopite
TiO2 (%)
Al2O3 (%)
0.0
0.1
0.2
0.3
0.4
0.5
0.6
0.7
0.8
0.9
0
2
4
6
8
10
12

Figure 3.13 Al_2O_3 vs. TiO_2 plot of diamictite matrices from zones 1, 2 and 3 (Figure 2.1). Samples are grouped according to the potassium silicate minerals observed in thin section (Table 2.1).

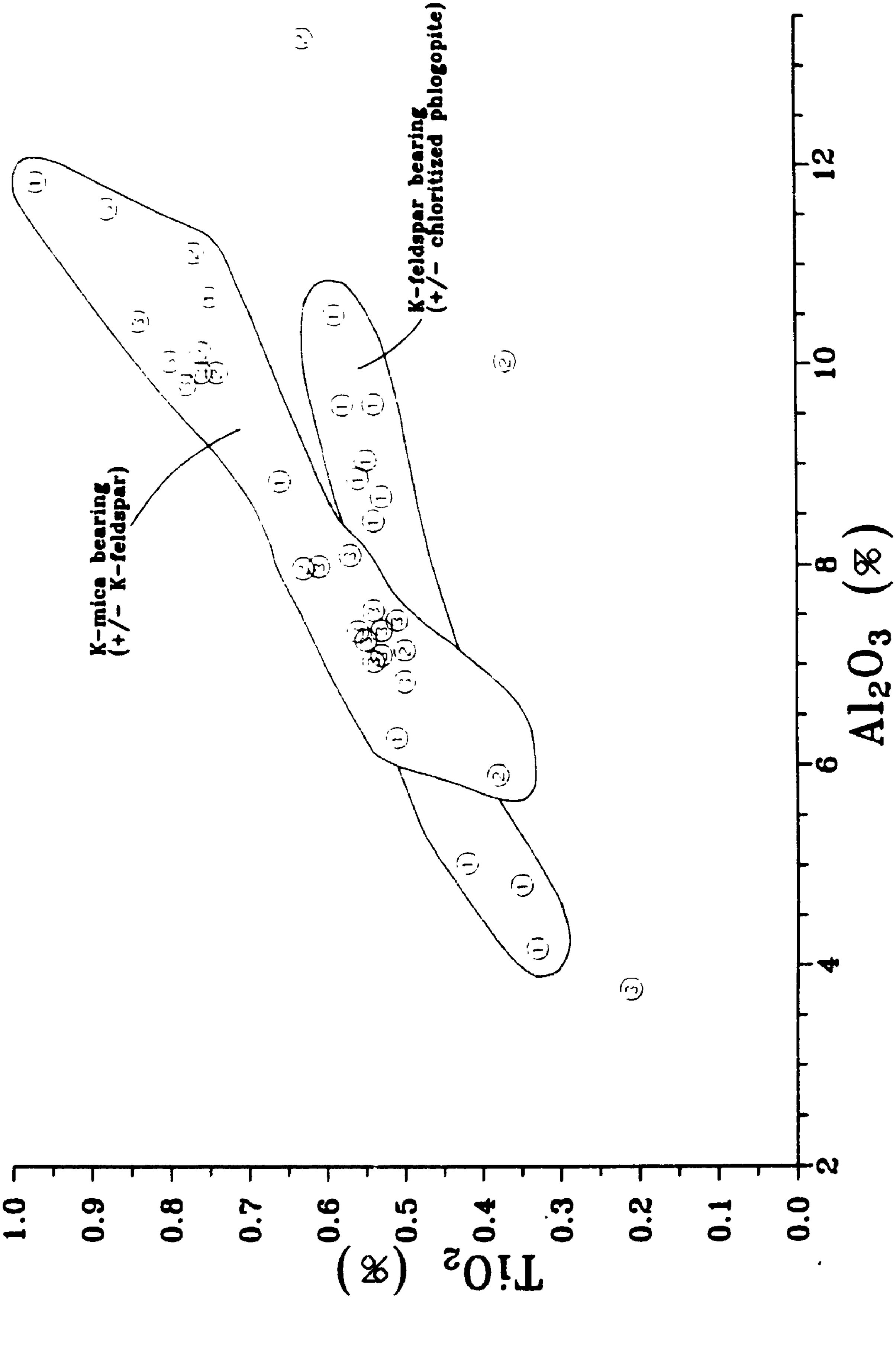
K-mica bearing
(+/- K-feldspar)
K-feldspar bearing
(+/- chloritized phlogopite)
Al_2O_3 (%)
TiO_2 (%)
2
4
6
8
10
12
0.0
0.1
0.2
0.3
0.4
0.5
0.6
0.7
0.8
0.9
1.0

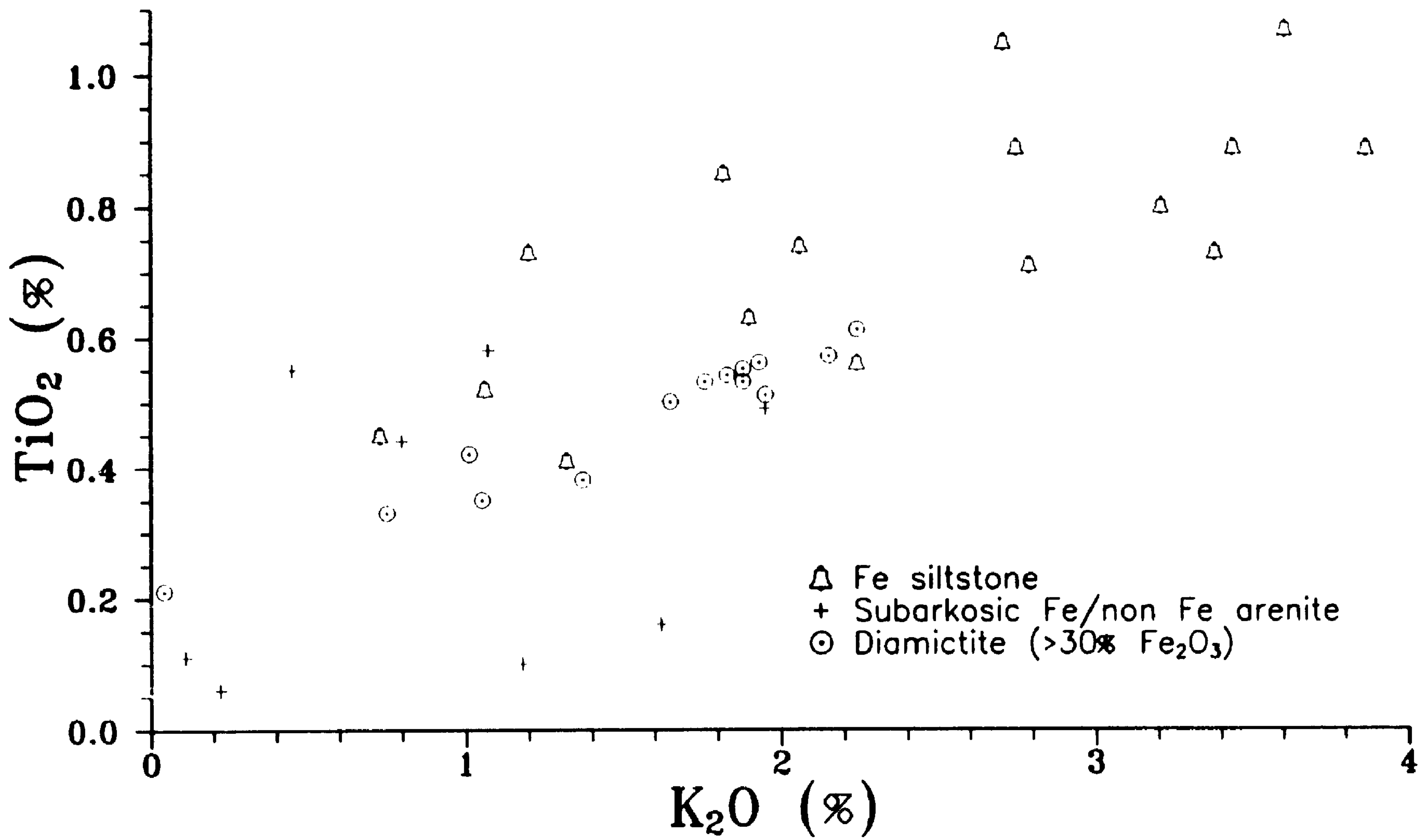

Figure 3.14 K_2O vs. TiO_2 plot of high Fe_2O_3 diamictite matrices, subarkosic Fe or non Fe arenite, and Fe siltstone.

Figure 3.15A K_2O vs. Na_2O plot of iron formation, high Fe_2O_3 diamictite matrices and carbonate. The six numerically denoted samples are the most Fe_2O_3-rich iron formation and diamictite from zones 1, 2 and 3 (Figure 2.1).

Figure 3.15B Fe_2O_3 vs. Na_2O plot of Holowilena and Braemar iron formation. Numbers 1, 2 and 3 refer to the zones (Figure 2.1) from which the samples were taken.

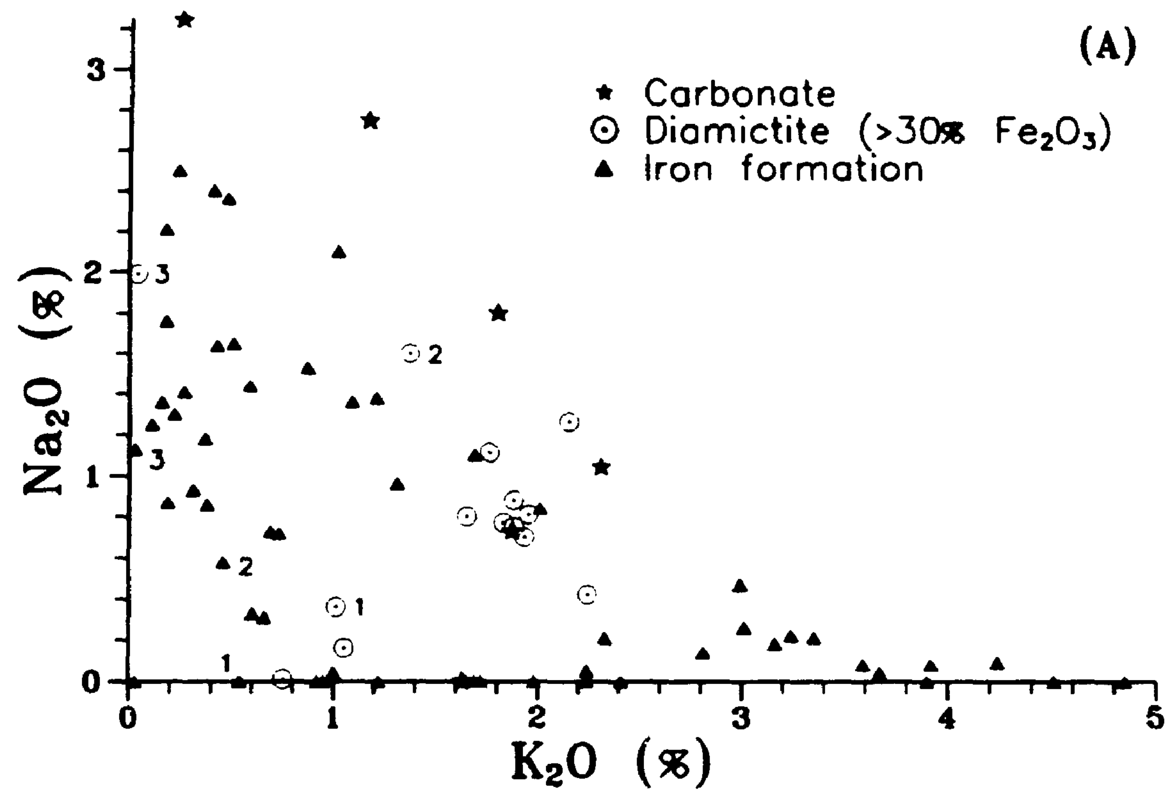
(A)
Carbonate
Diamictite (>30% Fe_2O_3)
Iron formation
Na_2O (%)
K_2O (%)
0
1
2
3
4
5

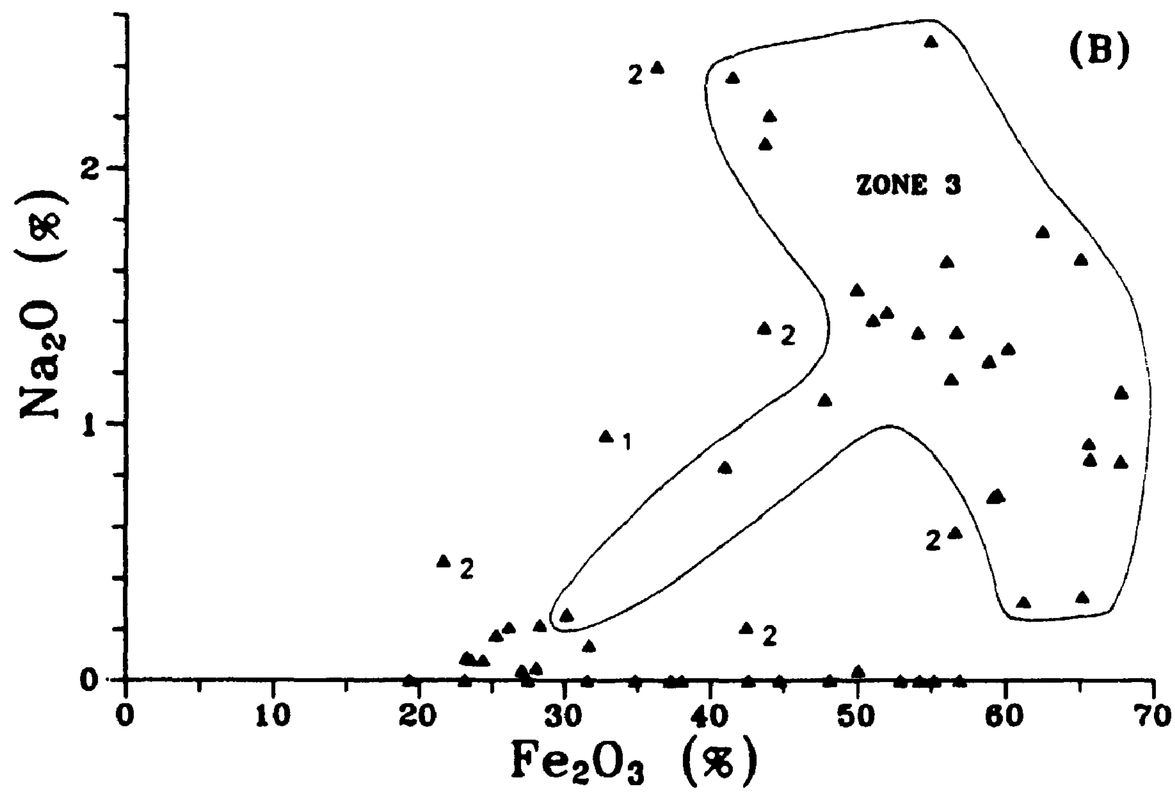
(B)
ZONE 3
Na_2O (%)
Fe_2O_3 (%)
0
10
20
30
40
50
60
70

the diamictite facies (Figure 3.16). This graph is a reflection of increasing dolomite content, most of which is considered to be ferroan since probe analyses of carbonate minerals in several samples were of this composition (see Chapter 4). Ferroan dolomite is a component common to all four of the mineral groups outlined on Figure 3.16 (Table 2.1). The occurrence and type of Mg-bearing silicate distinguishes any one group from the rest. Diamictite matrices from *Worumba* and *Holowilena South* (both zone 1) have the highest percent MgO and CaO (Table 3.7), which is primarily attributed to ferroan dolomite being the third or fourth most abundant micro-framework component (Table 2.1). This carbonate is considered to be detrital.

Calcium oxide (CaO) shows a positive correlation with P_2O_5 for iron formation samples, which is an indication of increasing apatite content (Figure 3.17). The positive slope of this graph is, however, defined mainly by P_2O_5-enriched samples from sections 12 and 20/14 of zone 1 (Figure A.1). In general, IF from this zone has the highest percent P_2O_5 (Table 3.7), which is manifested as bedding-parallel lenses of apatite and chlorite (p. 66 & 70; see Plate 4.2a). As evident from Figure 3.18, the samples from 'Dropstone Creek' and *Holowilena South* (sections 12 & 20/14) which host the apatite-chlorite lenses commonly plot near the lower limit of percent Fe_2O_3 for IF. Thin section examination of samples from zone 3 reveals that macroscopic, clastic-dominated laminae encased by iron formation have microscopically apparent, chemically precipitated apatite crystals (e.g., $10d_1$, $9I_2$, Table 2.2; $8A_L$, 7F, Table 2.4; $8q_1$, Table A.13), whereas clastic layers removed from IF do not. Also shown on Figure 3.18 are subarkosic Fe wacke samples in which $P_2O_5 \approx 1\%$ or greater. In at least one of these four samples (i.e., $12f_2$), apatite occurs as interframework cement ($12f_2 = 12f_3$ of Table 2.3; see Plate 4.2b).

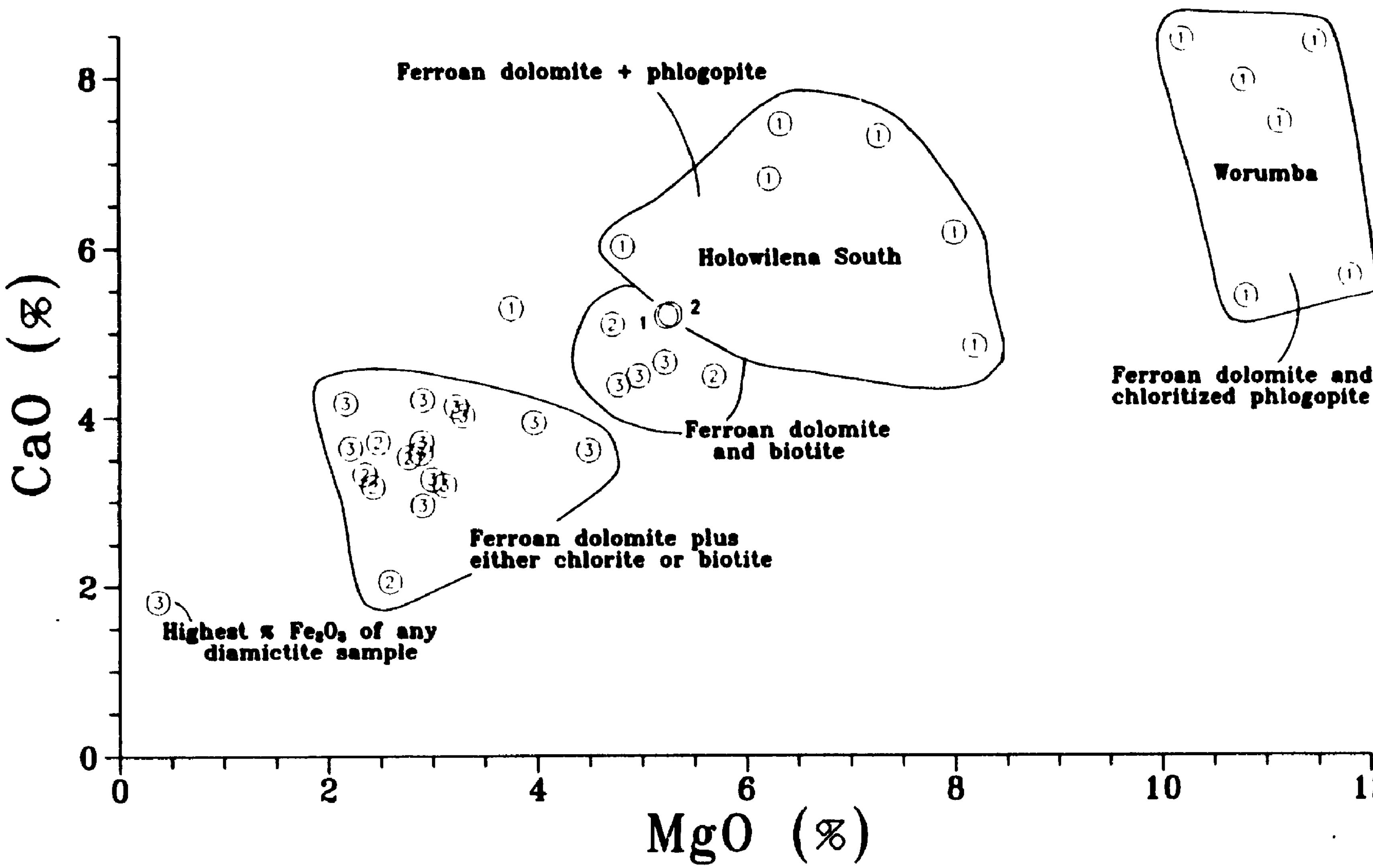

Figure 3.16 MgO vs. CaO plot of diamictite matrices from zones 1, 2 and 3 (Figure 2.1). Samples are grouped according to the Mg-bearing minerals observed in thin section (Tables 2.1 & A.13).

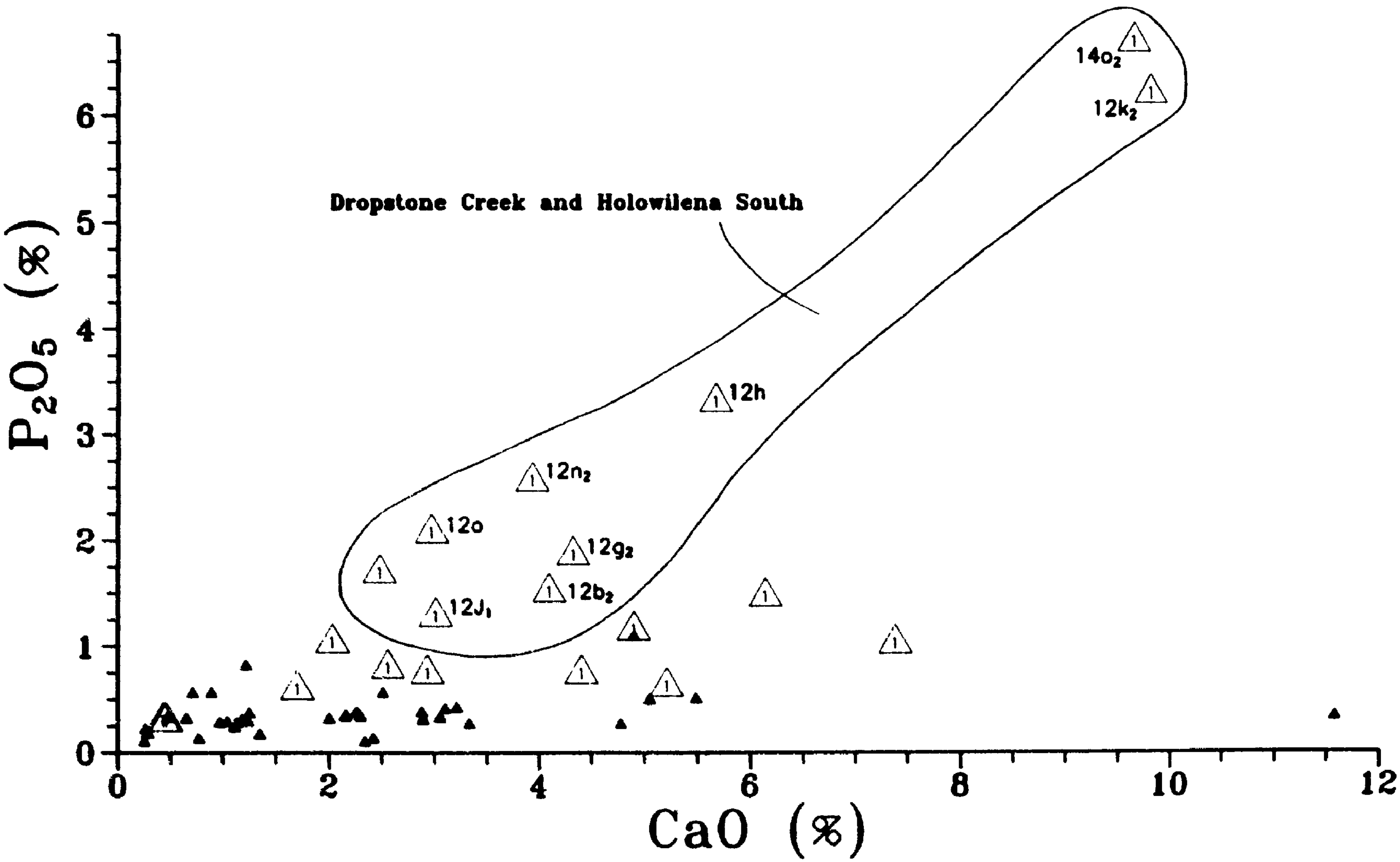

Figure 3.17 CaO vs. P_2O_5 plot of iron formation from zones 1 (open), 2 and 3 (filled).

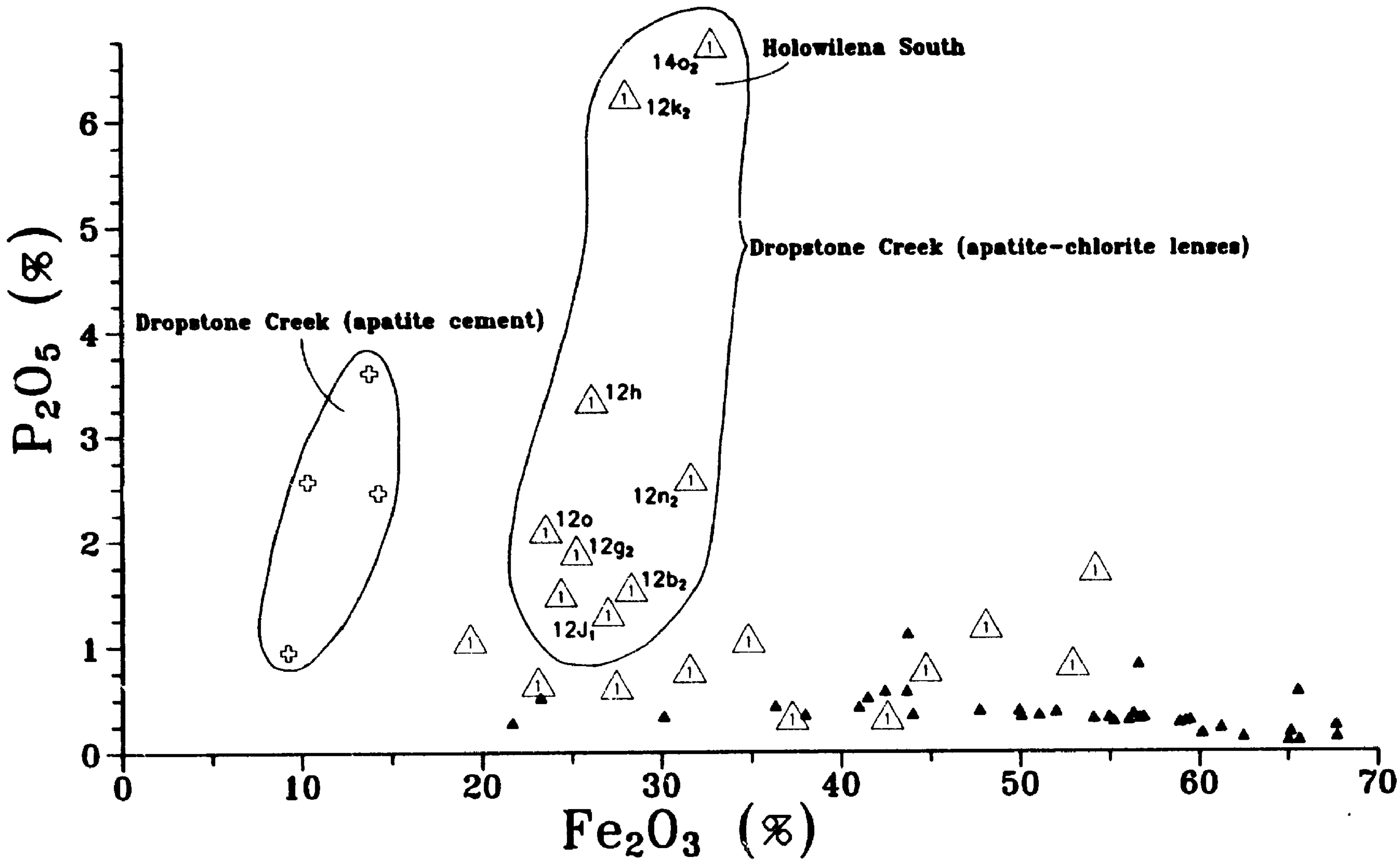

Figure 3.18 Fe_2O_3 vs. P_2O_5 plot of iron formation from zone 1 (open triangle), zones 2 and 3 (filled triangle), together with subarkosic Fe wackes (cross) from 'Dropstone Creek', *Oraparinna* (Figures 2.1 & A.2).

Line Diagrams

As evident from Figures 3.2 - 3.5, the detritally-hosted elements which, in both iron formation and diamictite, have well developed negative correlations with iron are silica and potassium. Potassium, present in fewer mineral phases and much smaller amounts than silica, is examined here with iron and sodium for individual samples of diamictite and IF (Figures 3.19 & 3.20). An antithetic relationship between Fe_2O_3 and K_2O is developed, albeit crudely, throughout zones 1 - 3 for the two facies types. The most iron-rich samples from each of the three zones have been linked to show that Fe_2O_3 tends to peak when K_2O is at a zonal low. This relationship probably reflects less dilution of chemically precipitated iron oxides during a lull in the supply of K-bearing detritus. An example of potassium and iron coincidence is shown by the K_2O-rich diamictites at *Worumba* (#13, Figure 3.19; Table 3.7). K_2O occurs to the exclusion of Na_2O which may be partly attributed to the presence of more K-feldspar than plagioclase within zone 1 (see p. 35). Linking of the most iron-rich samples (Figures 3.19 & 3.20) shows that Na_2O and K_2O have opposing slopes throughout zones 1 - 3. In contrast, Na_2O and Fe_2O_3 have similar slopes, and for the iron formation at least, samples with the highest overall Na_2O and Fe_2O_3 contents occur in zone 3 (Figure 3.20; Table 3.7). A possible explanation for the higher sodium/lower potassium is that feldspar albitization by seawater was most active in zone 3.

Lower potassium contents also typify most of the subarkosic Fe-poor (1 - 5% Fe oxide) and non Fe (<1% Fe oxide) arenite samples (Figure 3.21) of zone 3. Coeval subarkosic Fe wackes, however, are not as potassium-poor, which is probably a reflection of their higher mica contents (Table 2.3). Within zone 1, the subarkosic Fe arenites and wackes are not as sodium-poor as their diamictite and iron formation counterparts (Figures 3.19 & 3.20), but they gravitate toward the lower end of the Na_2O axis (Figure 3.21).

Analyses of diamictite matrix (Table 3.1) or iron formation (Table 3.2) from

Figure 3.19 Line diagrams of percent Fe_2O_3, K_2O and Na_2O for diamictite matrices from zones 1, 2 and 3 (Figure 2.1). Low (<20%; open circle) and high (>30%; filled circle) Fe_2O_3 diamictites are presented in ascending stratigraphic order for each individual measured section (i.e., nos. 12, 13, 20/14, 21, 19, 18, 17, 15, 10, 9/2 & 7, Figure A.1). Samples designated as #8 are from the adit 'through' Razorback Ridge (Figure A.9, Table A.13) which subparallels section #9/2 'across' Razorback Ridge (Figure A.9, Table A.11). The adit samples have been projected onto section # 9/2 so as to establish the relative order of ascension between #9/2 and #8 samples.

The most Fe_2O_3-rich samples from each of the three zones have been linked together for the different oxides. The very generalized LESS and MORE weathered source divisions are based on mineral groups established in Figures 3.4, 3.8, 3.9 and 3.13.

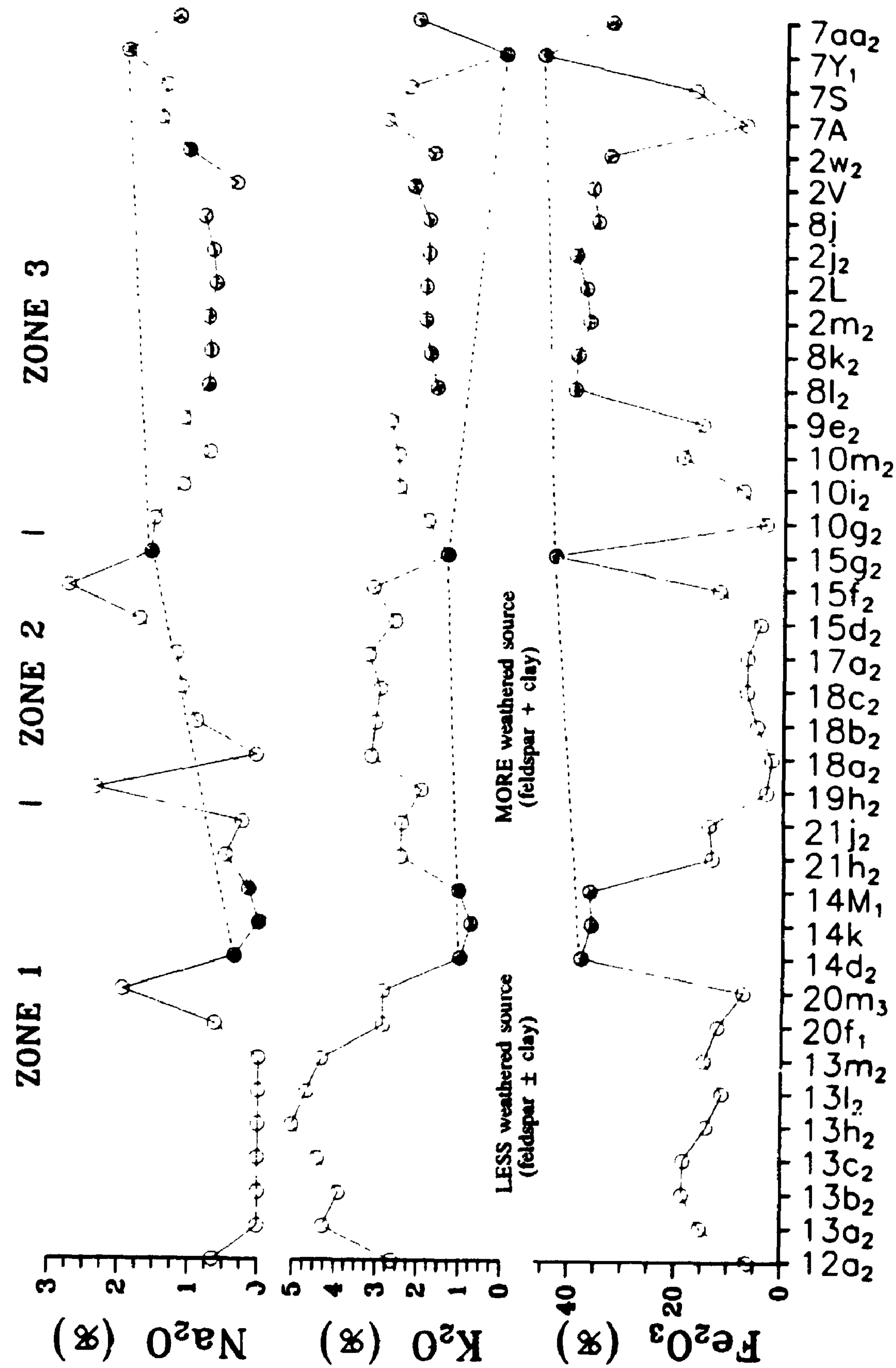
ZONE 1
ZONE 2
ZONE 3
MORE weathered source
(feldspar + clay)
LESS weathered source
(feldspar ± clay)
Na2O (%)
K2O (%)
Fe2O3 (%)
7aa2
7Y1
7S
7A
2w2
2V
8j
2j2
2L
2m2
8k2
8l2
9e2
10m2
10i2
10g2
15g2
15f2
15d2
17a2
18c2
18b2
18a2
19h2
21j2
21h2
14M1
14k
14d2
20m3
20f1
13m2
13l2
13h2
13c2
13b2
13a2
12a2

Figure 3.20 Line diagrams of percent Fe_2O_3, K_2O and Na_2O for Holowilena and Braemar iron formation from zones 1, 2 and 3 (Figure 2.1). Samples are presented in ascending order from left to right for an individual measured section (i.e., nos. 11, 12, 13, 20/14, 21, 19, 18, 17, 16, 10, 9/2 & 7, Figure A.1). Samples designated as #8 are from the adit 'through' Razorback Ridge (Figure A.9, Table A.13) whereas RD#1 and RD#3 are from drill holes through this same ridge (Whitten, 1970). Both the adit and drill holes subparallel section #9/2 'across' Razorback Ridge (Figure A.9, Table A.11), so that the adit and drill core were projected onto section #9/2 so as to establish the relative stratigraphic order amongst #9/2, #8 and drill core samples.

The most Fe_2O_3-rich samples (filled triangles) from each of the three zones have been linked together for the different oxides. The mineral divisions are based on mineral groups established in Figures 3.7 and 3.12.

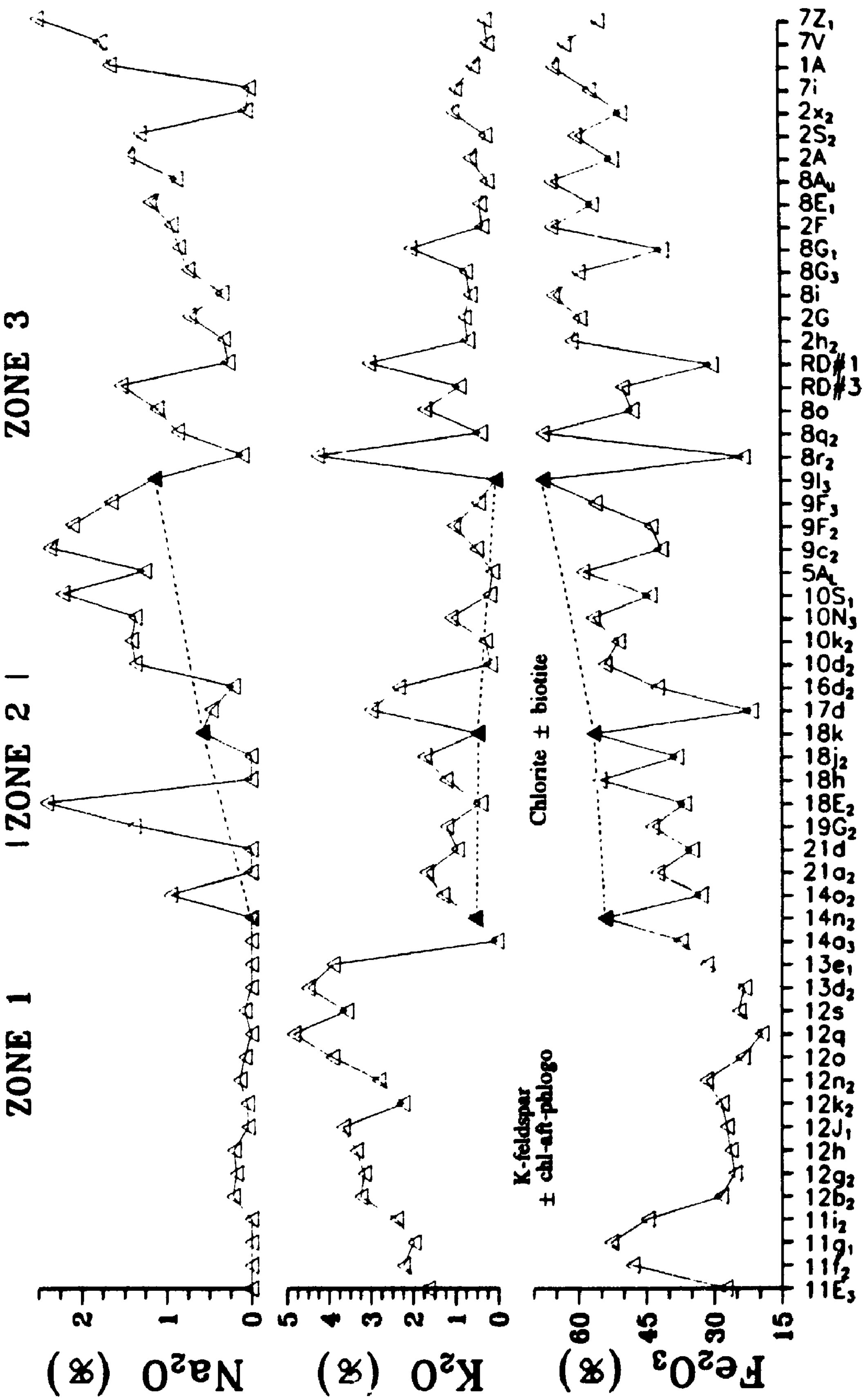
ZONE 1
ZONE 2
ZONE 3
Na_2O (%)
K_2O (%)
Fe_2O_3 (%)
K-feldspar
± chl-aft-phlogo
Chlorite ± biotite
7Z₁ 7V 1A 7i 2x₂ 2S₂ 2A 8A 8E₁ 2F 8G₁ 8G₃ 8i 2G 2h₂ RD#1 RD#3 8o 8q₂ 8r₂ 9l₃ 9F₃ 9F₂ 9c₂ 5A 10S₁ 10N₃ 10k₂ 10d₂ 16d₂ 17d 18k 18j₂ 18h 18E₂ 19G₂ 21d 21a₂ 14o₂ 14n₂ 14a₃ 13e₁ 13d₂ 12s 12q 12o 12n₂ 12k₂ 12J₁ 12h 12g₂ 12b₂ 11i₂ 11g₁ 11f₂ 11E₃

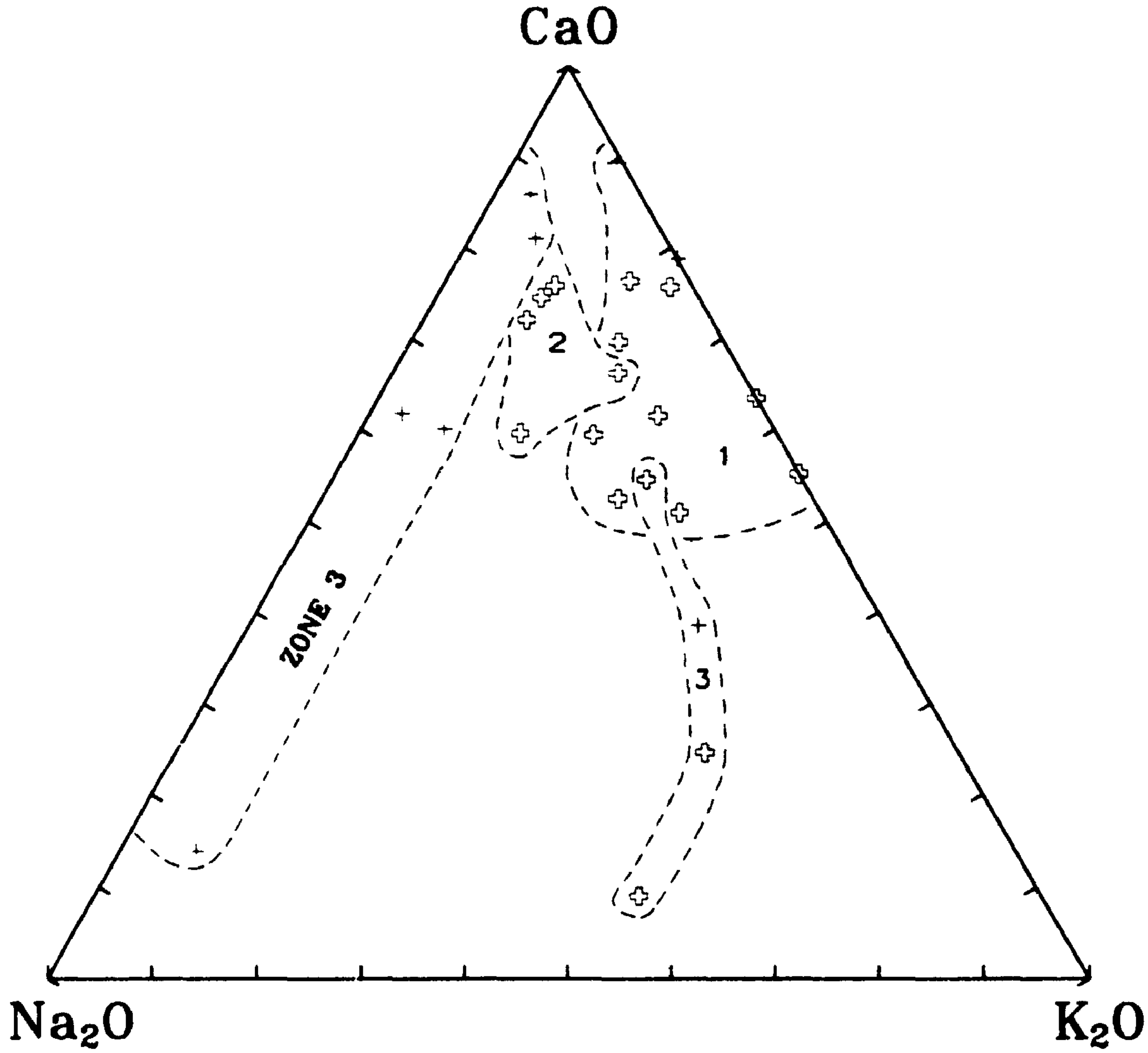

Figure 3.21 CaO - Na_2O - K_2O ternary plot showing compositional fields of zone 1, 2 and 3 subarkosic Fe wackes (open cross) and subarkosic Fe and non Fe arenites (solid cross). Plot after Condie (1967).

individual stratigraphic sections have been averaged and presented in elemental percent on Figures 3.22 and 3.23. For the two facies types, these diagrams provide a multi-element comparison of both measured sections and zones (Figure 2.1). Previously established and documented generalizations (Table 3.7) which are upheld by Figures 3.22 and 3.23 include:

i) diamictite and iron formation from zone 3 tend to be the most iron-rich; IF from zone 1 generally has the lowest iron at sections 12 and 13 (though zone 2 IF sample from section #17 is also low);

ii) diamictites from zone 1 have the highest calcium and magnesium contents; IF at section #13 (zone 1) has the highest percent Mg;

iii) diamictite at section #13 (zone 1) has the greatest potassium content; IF at sections 12 and 13 (zone 1) has the highest potassium content whereas IF from zone 3 tends to have the lowest;

iv) iron formation from zone 3 generally has the most sodium, and IF from zone 1 the least; and

v) iron formation from zone 1 has the highest phosphorous content and IF from zone 3 has the lowest.

A multi-element comparison of samples collected within the adit through Razorback Ridge (Figure A.9) is given in Figure 3.24. The mouth of the adit coincides with the 248.32 m mark of section #9/2 (Table A.11, Figure 2.8). The adit is approximately horizontal, covers a stratigraphic thickness of 55.27 m and like 171.72 - 248.32 m of section #9/2, has a general stratigraphy of iron formation at the base (e.g., $8r_2$, $8q_2$, 8o), overlain by diamictite with > 30% Fe_2O_3 in the matrix, then a return to iron formation in the upper two fifths (Table A.13). As was shown in Figure 3.2, there is an antithetic relationship between iron and silica for most rock types sampled in the adit. The isolation of sample, $8E_2$, precludes whether or not the carbonate facies follows a negative Fe:Si trend. Sample $8E_2$ has the highest calcium, magnesium and manganese

Figure 3.22 Line diagrams of percent Fe, Si, Al, Ca, Mg, Mn, K, Na, Ti and P for averaged diamictite analyses from measured sections within zones 1, 2 and 3 (Figures 2.1 & A.1). Unaveraged analyses are plotted for sections 12, 19 and 17 since only one sample of diamictite matrix was collected from each of these stratigraphic sections (Table 3.1). Oxide analyses were recalculated to 100% on an LOI-free basis prior to conversion to elemental percent.

Section locations are as follows:

Section #	Station Name	Local Feature	Figure
12	Oraparinna	'Dropstone Creek'	A.2
13	Worumba		A.3
20/14	Holowilena South		A.4
21	Holowilena South	Back Creek	A.4
19	Oopina		A.5
18	Mount Victor	Razorback hill	A.6
17	Outalpa		A.7
15	Bimbowrie	Bimbowrie Hill	A.8
10	Spring Dam	Pualco West	A.9
9/2	Spring Dam	Razorback Ridge	A.9
8 or ADIT	Spring Dam	Razorback Ridge	A.9
7	Manunda	Iron Peak	A.9

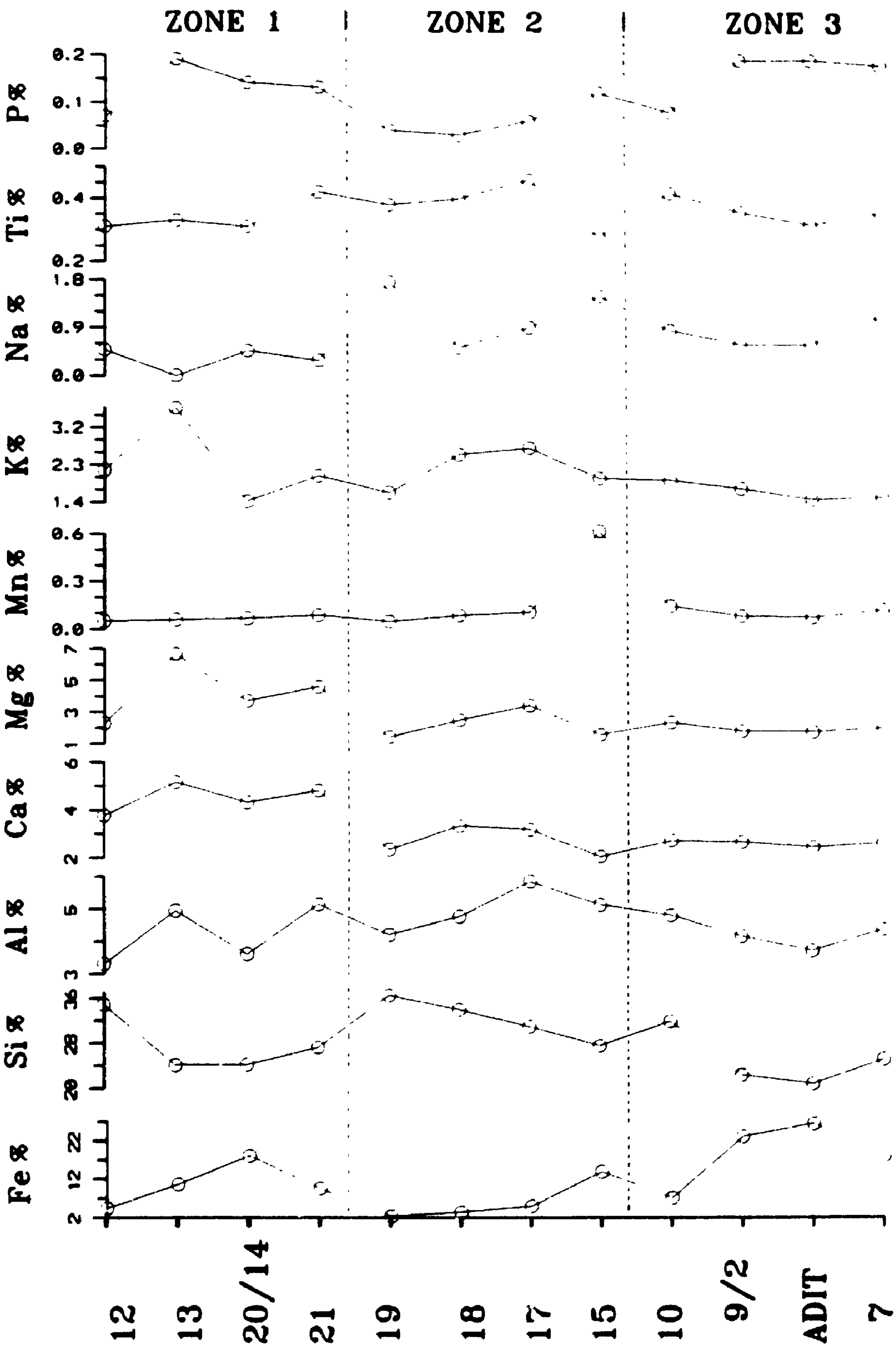
ZONE 1
ZONE 2
ZONE 3
P%
Ti%
Na%
K%
Mn%
Mg%
Ca%
Al%
Si%
Fe%
12
13
20/14
21
19
18
17
15
10
9/2
ADIT
7

Figure 3.23 Line diagrams of percent Fe, Si, Al, Ca, Mg, Mn, K, Na, Ti and P for averaged iron formation analyses from measured sections within zones 1, 2 and 3 (Figures 2.1 & A.1). Unaveraged analyses are plotted for sections 19, 17 and 16 since only one sample of iron formation was collected from each of these stratigraphic sections (Table 3.2). Oxide analyses were recalculated to 100% on an LOI-free basis prior to conversion to elemental percent.

Section locations are as follows:

Section #	Station Name	Local Feature	Figure
11	Oraparinna	Panta Well	A.2
12	Oraparinna	'Dropstone Creek'	A.2
13	Worumba		A.3
20/14	Holowilena South		A.4
21	Holowilena South	Back Creek	A.4
19	Oopina		A.5
18	Mount Victor	Razorback hill	A.6
17	Outalpa		A.7
16	Outalpa	I.D. hut	A.7
10	Spring Dam	Pualco West	A.9
9/2	Spring Dam	Razorback Ridge	A.9
8 or ADIT	Spring Dam	Razorback Ridge	A.9
7	Manunda	Iron Peak	A.9

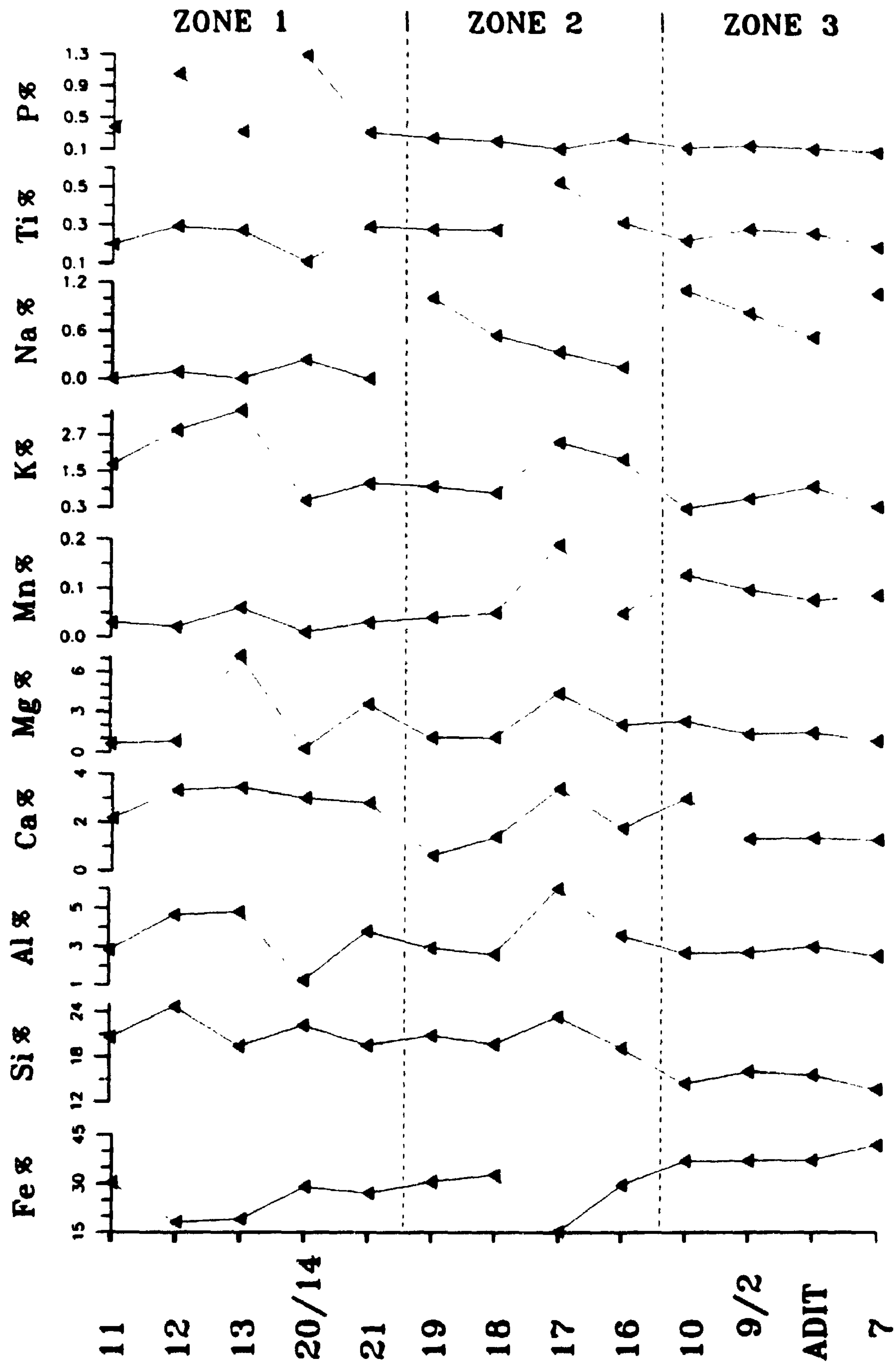
ZONE 1
ZONE 2
ZONE 3
P%
Ti%
Na%
K%
Mn%
Mg%
Ca%
Al%
Si%
Fe%
11
12
13
20/14
21
19
18
17
16
10
9/2
ADIT
7

Figure 3.24 Line diagrams of percent Fe, Si, Al, Ca, Mg, Mn, K, Na, P and Ti for samples collected within the adit through Razorback Ridge (Figure A.9, Table A.13). The samples are listed in stratigraphic order from $8r_2$ near the base of adit through $8A_U$ at the top. Metric depth relative to the mouth of the adit _is_ stratigraphic and was measured from the base of the sample. Oxide analyses were recalculated to 100% on an LOI-free basis prior to conversion to elemental percent.

★ Carbonate

△ Fe siltstone

⊙ Diamictite matrix

▲ Iron formation

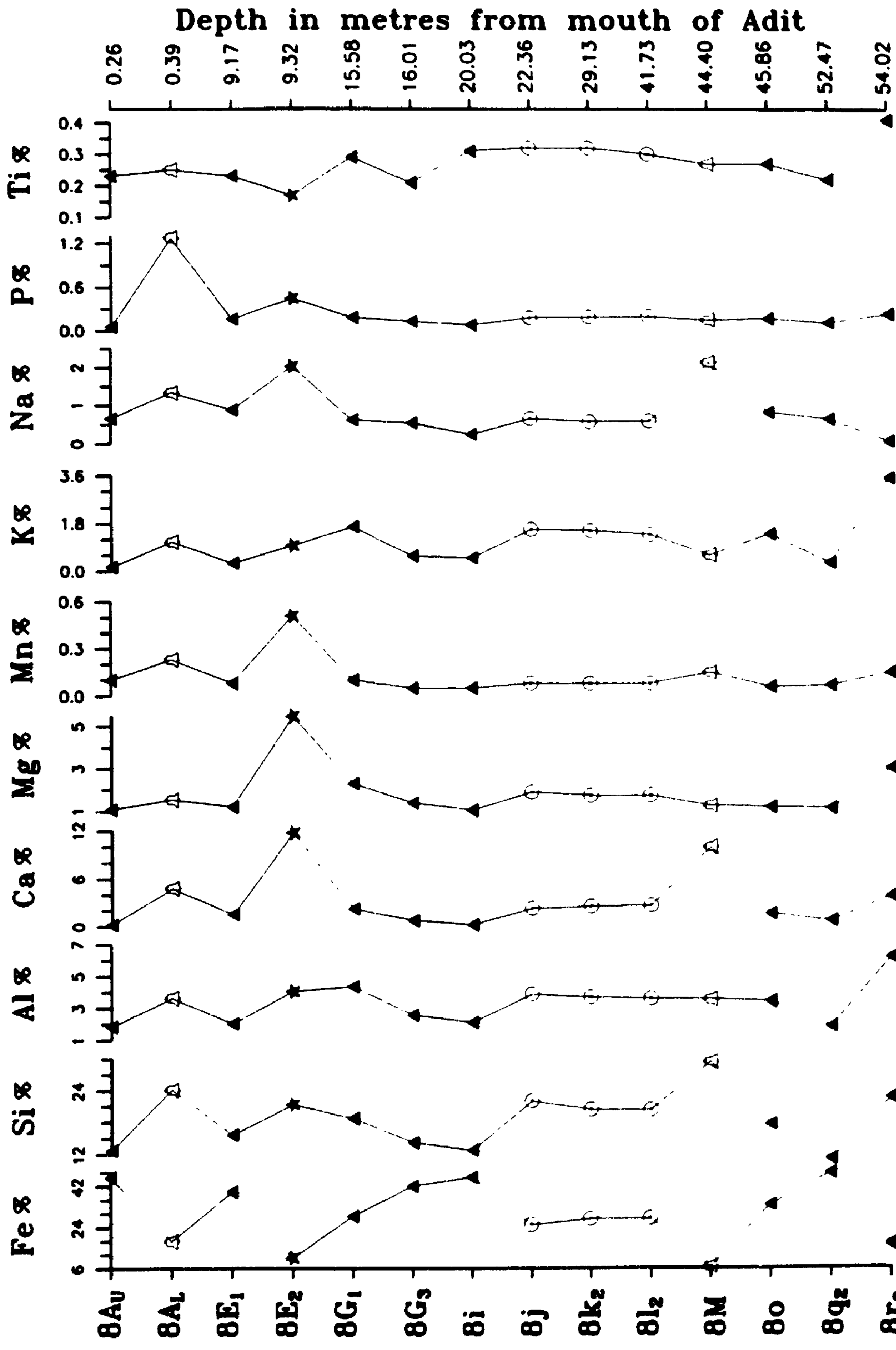
Depth in metres from mouth of Adit
0.26
0.39
9.17
9.32
15.58
16.01
20.03
22.36
29.13
41.73
44.40
45.86
52.47
54.02
Ti %
P %
Na %
K %
Mn %
Mg %
Ca %
Al %
Si %
Fe %
8AU
8AL
8E1
8E2
8G1
8G3
8i
8j
8k2
8l2
8M
8o
8q2
8r2

contents, all of which are common in probe analyses of carbonate minerals (see Chapter 4). Iron formation sample $8r_2$ has the highest aluminum, potassium and titanium contents, which are attributed to abundant sericite (Figures 3.7 & 3.12). Fe siltstone sample $8A_L$ has the highest percent phosphorous, which is a reflection of apatite (Table 2.4; see Plate 4.1f).

Summary of Major Elements

With the exception of a few thin horizons similar to jasper-bearing sample $14a_s$ (Figure 3.1), there is little evidence of chemically precipitated SiO_2 in either the Holowilena or Braemar IFs. SiO_2 occurs mainly as detrital quartz mixed in with the chemically precipitated iron oxides (cf. Whitten, 1965, p. 310). For iron formation and diamictite matrices, this juxtaposition of detritally and chemically derived components evinces an inverse relationship between Fe_2O_3 and SiO_2 (Figure 3.2). The iron oxides are considered to have been diluted by silicate minerals; a suggestion which is supported by negative correlations between Fe_2O_3-Al_2O_3, Fe_2O_3-K_2O and Fe_2O_3-TiO_2 for iron formation and diamictite matrices (with >30% Fe_2O_3; Figures 3.3 - 3.5). Silicate dilution during IF deposition is on average lowest in zone 3 (Figure 3.23), and highest at sections 12, 13 (zone 1) and 17 (zone 2). The zone 1 and 2 localities probably reflect proximity to detrital sources. The development of low (<20%) and high (>30%) Fe_2O_3 diamictites is attributed to differences in depositional mode (see Chapter 6), but iron oxide minerals are a significant factor in both diamictite groups, and in the associated subarkosic Fe wackes, Fe siltstones and carbonates (Tables 2.1, 2.3 & 2.4, Figure 3.3). The presence of hematite and/or magnetite in these dominantly clastic facies suggests that iron precipitation was ongoing during deposition of detrital material.

Potassium-bearing minerals observed in diamictite matrices (both low and high Fe_2O_3) are utilized to reveal a general separation between matrices of zone 1 and those of zones 2 & 3 (Figures 3.4, 3.8 & 3.9). K-feldspar typifies the matrices of zone 1 diamictites, whereas K-mica is common to matrices of zones 2 and 3. This mineralogical distinction is attributed to source material differences (Figure 3.19). Zone 1 matrices also contain high amounts of MgO and CaO relative to those of zones 2 and 3 (Figures 3.16 & 3.22), which is due to the presence of clastic ferroan dolomite (Table 2.1) probably derived from carbonates of the underlying Burra Group (Figure 1.3a).

The generally higher phosphorous content of zone 1 IF, relative to that of zones 2 and 3 (Figures 3.17, 3.18 & 3.23) is ascribed to the occurrence of bedding-parallel apatite-chlorite lenses (see Plate 4.2a). These lenses may represent diagenetic addition of apatite, which was enriched due to the extreme insolubility of apatite in alkaline solution.

Trace Element Results

The trace element data for all samples collected from zone 3 (Figure 2.1) are presented in Tables 3.8 - 3.11. In an effort to minimize the detritally-hosted trace elements, analyses were restricted to samples from zone 3, because as previously established, zone 3 iron formation and diamictite tend to have the highest percent Fe_2O_3 (Table 3.7) and as evident from Figures 3.2 - 3.5, Fe_2O_3 increases at the expense of detritally-hosted elements. Pearson's correlation coefficients were calculated for the three largest sample populations (Tables 3.8, 3.9 & 3.11).

Discussion of Trace Elements

As with the major elements, an attempt is made to relate the trace element data to the mineral phases o' erved in thin section (Tables 2.1 - 2.4). Trace elements, however, are commonly not represented in the formula of an individual mineral, so that their distribution is not as clearly defined.

On a Rb vs. Ni diagram of the samples collected within zone 3, there is a general separation between iron formation and the other rock types (Figure 3.25). This

Table 3.8 Trace element analyses of diamictite matrices (Figure 2.2) from measured sections 10, 9/2, 7 and 8 (Figure A.9), which are located within zone 3 (Figure 2.1). Correlation coefficients for the 16 samples are also listed. Sample numbers followed by $\bar{x}$ indicate mean values of two aliquots.

Sample	Rb	Sr	Ba	Y	Zr	Nb	V	Cr	Ni	Cu	Zn	Pb
10g2 $\bar{x}$	75.5	94.5	299.5	18.4	174.5	7.2	62.0	44.5	16.0	16.5	30.0	8.5
10l2 $\bar{x}$	110.0	84.5	479.5	22.5	189.5	10.1	87.0	69.0	19.0	16.5	49.0	9.0
10m2 $\bar{x}$	107.5	85.5	408.0	28.0	167.5	10.7	97.0	63.0	22.5	39.0	67.0	3.0
9e2	120.0	101.0	349.0	27.0	170.0	10.2	96.0	63.0	25.0	16.0	60.0	16.0
2m2	83.0	105.0	386.0	27.0	[illegible]	8.4	84.0	43.0	12.0	11.0	43.0	5.0
2L $\bar{x}$	82.5	63.0	410.0	26.5	113.5	8.0	88.5	42.5	19.5	11.0	45.5	4.0
2j2 $\bar{x}$	81.0	56.5	420.5	28.5	113.0	7.8	91.0	44.5	18.5	9.0	47.5	3.5
2V $\bar{x}$	94.5	54.5	398.[illegible]	29.5	135.0	9.0	97.5	49.5	23.5	13.0	70.0	3.5
2w2 $\bar{x}$	75.0	95.5	278.0	26.5	110.0	7.7	80.5	41.5	17.5	11.5	43.0	8.0
7A	100.0	153.0	589.0	26.0	188.0	10.9	103.0	72.0	23.0	12.0	55.0	4.0
7S $\bar{x}$	92.5	177.5	436.5	27.5	168.5	9.0	91.5	60.5	23.5	24.0	66.0	6.5
7Y1	1.2	116.0	81.0	29.0	79.0	4.2	50.0	14.0	15.0	6.0	12.0	5.0
7aa2 $\bar{x}$	88.0	135.5	426.0	25.0	118.0	7.5	85.0	42.5	14.0	11.0	45.0	6.0
8j	82.0	96.0	345.0	24.0	118.0	6.9	84.0	41.0	19.0	8.0	42.0	3.0
8k2 $\bar{x}$	78.0	105.0	344.0	29.0	106.5	8.2	86.5	38.0	16.5	11.5	46.0	5.0
8l2	72.0	87.0	321.0	28.0	104.0	7.0	82.0	39.0	23.0	9.0	50.0	4.0
Average	83.9	100.6	373.2	26.4	135.8	8.3	85.3	48.0	19.2	14.1	48.2	5.9
Std Dev	25.2	32.0	104.6	2.8	33.6	1.6	12.8	14.1	3.8	7.6	13.9	3.2

	Rb	Sr	Ba	Y	Zr	Nb	V	Cr	Ni	Cu	Zn	Pb
Rb	1.00											
Sr	-0.04	1.00										
Ba	0.79	0.16	1.00									
Y	-0.18	-0.07	-0.12	1.00								
Zr	0.72	0.26	0.63	-0.48	1.00							
Nb	0.90	0.09	0.81	-0.02	0.79	1.00						
V	0.84	-0.01	0.83	0.29	0.45	0.85	1.00					
Cr	0.89	0.19	0.83	-0.21	0.90	0.95	0.76	1.00				
Ni	0.51	-0.00	0.36	0.25	0.49	0.56	0.61	0.60	1.00			
Cu	0.50	0.12	0.28	-0.03	0.60	0.60	0.36	0.58	0.40	1.00		
Zn	0.82	0.00	0.68	0.30	0.51	0.80	0.90	0.75	0.73	0.57	1.00	
Pb	0.31	0.14	-0.10	-0.31	0.40	0.24	-0.04	0.29	0.15	0.07	0.02	1.00
	Rb	Sr	Ba	Y	Zr	Nb	V	Cr	Ni	Cu	Zn	Pb

Table 3.9 Trace element analyses of iron formation from measured sections 10, 9/2, 7 and 8 (Figure A.9), which are located within zone 3 (Figure 2.1). Samples $5A_L$ and 1A are laterally removed from, but considered part of sections 10 and 7, respectively. Correlation coefficients for the 27 samples are also listed. Sample numbers followed by $\bar{x}$ indicate mean values of two aliquots.

Sample	Rb	Sr	Ba	Y	Zr	Nb	V	Cr	Ni	Cu	Zn	Pb
10d2	8.6	95.0	51.0	27.0	74.0	7.1	116.0	28.0	18.0	5.0	79.0	2.0
10k2	12.0	59.0	36.0	32.0	69.0	6.6	89.0	29.0	21.0	4.0	125.0	3.0
10N3	51.0	40.0	151.0	24.0	88.0	6.0	95.0	22.0	23.0	2.0	95.0	4.0
10S1	5.8	299.0	23.0	22.0	45.0	4.1	49.0	13.0	8.0	8.0	23.0	18.0
5AL $\bar{x}$	4.1	81.5	23.0	25.5	50.0	6.9	82.0	21.5	11.5	18.5	31.5	10.0
9c2	23.0	125.0	50.0	29.0	98.0	7.0	74.0	35.0	17.0	8.0	26.0	3.0
9F2	43.0	132.0	114.0	36.0	75.0	8.7	75.0	24.0	21.0	8.0	40.0	9.0
9F3	21.0	40.0	37.0	21.0	91.0	5.4	81.0	22.0	17.0	6.0	21.0	3.0
9I3	1.4	24.0	4.0	12.0	34.0	5.9	103.0	12.0	8.0	3.0	12.0	2.0
2h2	28.0	36.0	105.0	23.0	86.0	7.0	93.0	22.0	30.0	3.0	88.0	3.0
2G	33.0	41.0	124.0	21.0	69.0	6.2	92.0	20.0	17.0	4.0	69.0	0.0
2F	12.9	44.0	50.0	25.0	49.0	4.4	92.0	20.0	13.0	5.0	50.0	3.0
8Au	12.6	14.8	27.0	18.7	51.0	8.3	94.0	16.0	14.0	1.0	50.0	0.0
2A	26.0	42.0	184.0	23.0	99.0	5.6	83.0	35.0	20.0	6.0	19.0	0.0
2S2	7.9	44.0	37.0	32.0	57.0	5.0	89.0	17.0	16.0	3.0	84.0	0.0
2x2	43.0	24.0	160.0	33.0	76.0	7.5	113.0	47.0	30.0	41.0	133.0	5.0
7i	51.0	73.0	71.0	39.0	69.0	7.8	121.0	20.0	21.0	7.0	78.0	2.0
1A	27.0	112.0	39.0	21.0	60.0	5.2	87.0	15.0	12.0	2.0	36.0	5.0
7V	10.8	110.0	29.0	26.0	40.0	7.7	83.0	29.0	12.0	5.0	58.0	0.0
7Z1	11.2	74.0	65.0	28.0	81.0	7.3	74.0	23.0	9.0	9.0	9.0	2.0
8r2	175.0	142.0	1221.0	29.0	141.0	11.3	104.0	70.0	21.0	9.0	43.0	2.0
8q2	17.0	37.0	119.0	12.2	48.0	6.9	92.0	12.0	13.0	2.0	55.0	2.0
8o	72.0	81.0	389.0	27.0	102.0	5.8	77.0	30.0	14.0	3.0	28.0	1.0
8i	24.0	20.0	95.0	13.2	66.0	7.7	104.0	15.0	14.0	2.0	71.0	4.0
8G3	31.0	38.0	123.0	26.0	68.0	6.2	88.0	26.0	24.0	5.0	67.0	4.0
8G1	89.0	97.0	359.0	37.0	118.0	7.3	91.0	45.0	20.0	4.0	58.0	8.0
8E1	17.0	70.0	59.0	28.0	61.0	6.4	86.0	19.0	11.0	4.0	38.0	3.0
Average	31.8	73.9	138.7	25.6	72.8	6.7	89.9	25.5	16.9	6.6	55.1	3.6
Std Dev	34.8	56.6	230.9	6.8	24.3	1.4	14.5	12.4	5.8	7.6	31.5	3.8

	Rb	Sr	Ba	Y	Zr	Nb	V	Cr	Ni	Cu	Zn	Pb
Rb	1.00											
Sr	0.17	1.00										
Ba	0.95	0.18	1.00									
Y	0.35	0.24	0.19	1.00								
Zr	0.80	0.07	0.74	0.40	1.00							
Nb	0.61	-0.02	0.60	0.26	0.43	1.00						
V	0.24	-0.57	0.18	0.07	0.07	0.40	1.00					
Cr	0.79	0.14	0.80	0.49	0.79	0.59	0.21	1.00				
Ni	0.39	-0.28	0.26	0.44	0.50	0.31	0.42	0.49	1.00			
Cu	0.08	0.02	0.07	0.33	0.07	0.18	0.16	0.42	0.34	1.00		
Zn	0.05	-0.33	-0.04	0.31	-0.01	0.14	0.55	0.15	0.68	0.29	1.00	
Pb	-0.04	0.70	-0.09	0.12	-0.11	-0.18	-0.48	-0.0	-0.12	0.26	-0.14	1.00
	Rb	Sr	Ba	Y	Zr	Nb	V	Cr	Ni	Cu	Zn	Pb

Table 3.10 Trace element analyses of subarkosic Fe wackes and subarkosic Fe & non Fe arenites from measured sections 10, 9/2 and 7 (Figure A.9), which are located within zone 3 (Figure 2.1). Sample 6A is laterally removed from, but considered part of section #7.

Subarkosic Fe WACKES (1 - 21.5% iron oxide minerals)

Sample	Rb	Sr	Ba	Y	Zr	Nb	V	Cr	Ni	Cu	Zn	Pb
10h	119.0	130.0	465.0	23.0	182.0	9.3	83.0	59.0	35.0	18.0	64.0	8.0
9H	110.0	42.0	349.0	27.0	216.0	10.8	90.0	69.0	22.0	21.0	52.0	5.0
7R	124.0	87.0	467.0	22.0	192.0	9.3	85.0	55.0	19.0	11.0	34.0	5.0
Average	117.7	86.3	427.0	24.0	196.7	9.8	86.0	61.0	25.3	16.7	50.0	6.0
Std Dev	5.8	35.9	55.2	2.2	14.3	0.7	2.9	5.9	6.9	4.2	12.3	1.4

Subarkosic Fe ARENITES (1 - 5% iron oxide minerals) and subarkosic arenites (<1% iron oxide minerals)

Sample	Rb	Sr	Ba	Y	Zr	Nb	V	Cr	Ni	Cu	Zn	Pb
10J2	6.1	140.0	40.0	5.2	43.0	0.7	6.0	6.0	2.0	4.0	3.0	9.0
9B2	36.0	131.0	147.0	20.0	237.0	6.8	37.0	34.0	9.0	10.0	11.0	4.0
2u1	91.0	47.0	290.0	21.0	129.0	5.9	65.0	41.0	20.0	55.0	51.0	6.0
2y2	2.9	16.0	58.0	5.2	83.0	0.9	7.0	10.0	5.0	8.0	3.0	10.0
6A	11.9	155.0	102.0	20.0	186.0	6.2	35.0	26.0	10.0	13.0	126.0	45.0
Average	29.6	97.8	127.4	14.3	135.6	4.1	30.0	23.4	9.2	18.0	38.8	14.8
Std Dev	32.8	55.5	89.4	7.4	69.6	2.7	21.9	13.5	6.1	18.7	47.1	15.2

Table 3.11 Trace element analyses of Fe siltstones and carbonates from measured sections 10, 9/2, 7 and 8 (Figure A.9), which are located within zone 3 (Figure 2.1). Samples 6d, 5Au and 4A are laterally removed from, but considered part of sections 7, 10 and 9/2, respectively. Correlation coefficients for the 10 siltstone samples are also listed. Sample numbers followed by $\overline{x}$ indicate mean values of two aliquots.

Fe SILTSTONES (1-21.5% iron oxide minerals)

	Rb	Sr	Ba	Y	Zr	Nb	V	Cr	Ni	Cu	Zn	Pb
9d2a	122.0	96.0	328.0	21.0	158.0	9.2	74.0	47.0	20.0	13.0	34.0	5.0
9j2	168.0	123.0	605.0	22.0	221.0	12.2	101.0	73.0	26.0	5.0	30.0	10.0
9K3	38.0	238.0	148.0	18.0	67.0	6.4	55.0	36.0	17.0	4.0	44.0	5.0
9L2	122.0	58.0	401.0	39.0	126.0	11.2	110.0	79.0	28.0	33.0	50.0	3.0
8M	29.0	248.0	189.0	23.0	140.0	4.9	24.0	30.0	8.0	7.0	7.0	2.0
8AL $\overline{x}$	59.3	224.5	242.5	43.5	121.5	8.2	59.8	38.7	3.0	8.5	18.3	3.8
2T2	70.0	293.0	273.0	17.0	125.0	6.6	67.0	40.0	14.0	7.0	12.0	2.0
6d	135.0	51.0	582.0	26.0	194.0	11.6	78.0	54.0	17.0	6.0	34.0	2.0
7K	74.0	129.0	262.0	27.0	145.0	10.9	95.0	78.0	19.0	9.0	65.0	0.0
7u	103.0	131.0	292.0	28.0	127.0	8.0	103.0	56.0	29.0	45.0	77.0	4.0
Average	92.0	164.2	332.3	26.5	142.5	8.9	76.7	53.2	18.1	13.8	37.1	3.7
Std Dev	42.8	80.4	146.3	8.2	40.0	2.4	25.2	17.1	8.0	13.1	21.3	2.6

	Rb	Sr	Ba	Y	Zr	Nb	V	Cr	Ni	Cu	Zn	Pb
Rb	1.00											
Sr	-0.77	1.00										
Ba	0.92	-0.71	1.00									
Y	0.05	-0.28	0.05	1.00								
Zr	0.77	-0.56	0.87	-0.07	1.00							
Nb	0.85	-0.86	0.82	0.29	0.67	1.00						
V	0.75	-0.64	0.56	0.26	0.33	0.79	1.00					
Cr	0.66	-0.71	0.56	0.28	0.44	0.86	0.89	1.00				
Ni	0.67	-0.56	0.46	-0.12	0.24	0.54	0.83	0.72	1.00			
Cu	0.22	-0.24	-0.02	0.39	-0.18	0.09	0.57	0.35	0.62	1.00		
Zn	0.25	-0.42	0.03	0.14	-0.13	0.38	0.71	0.60	0.72	0.66	1.00	
Pb	0.52	-0.10	0.42	-0.16	0.35	0.24	0.22	0.10	0.34	-0.06	-0.08	1.00

CARBONATES

	Rb	Sr	Ba	Y	Zr	Nb	V	Cr	Ni	Cu	Zn	Pb
10q2	21.0	185.0	27.0	11.0	51.0	3.2	28.0	23.0	9.0	4.0	44.0	17.0
5Au	7.8	514.5	28.0	27.5	49.5	5.6	18.5	26.5	4.0	4.5	15.5	19.5
4A	84.0	676.0	373.0	12.8	105.0	4.5	59.0	33.0	10.0	7.0	22.0	6.0
8E2	44.0	374.0	184.0	17.0	62.0	2.8	32.0	33.0	7.0	9.0	18.0	8.0
7W1	69.0	263.0	236.0	15.0	91.0	3.9	51.0	33.0	10.0	4.0	37.0	6.0
Average	45.2	402.5	169.6	16.7	71.7	4.0	37.7	29.7	8.0	5.7	27.3	11.3
Std Dev	28.5	176.0	131.4	5.8	22.3	1.0	15.0	4.2	2.3	2.0	11.2	5.8

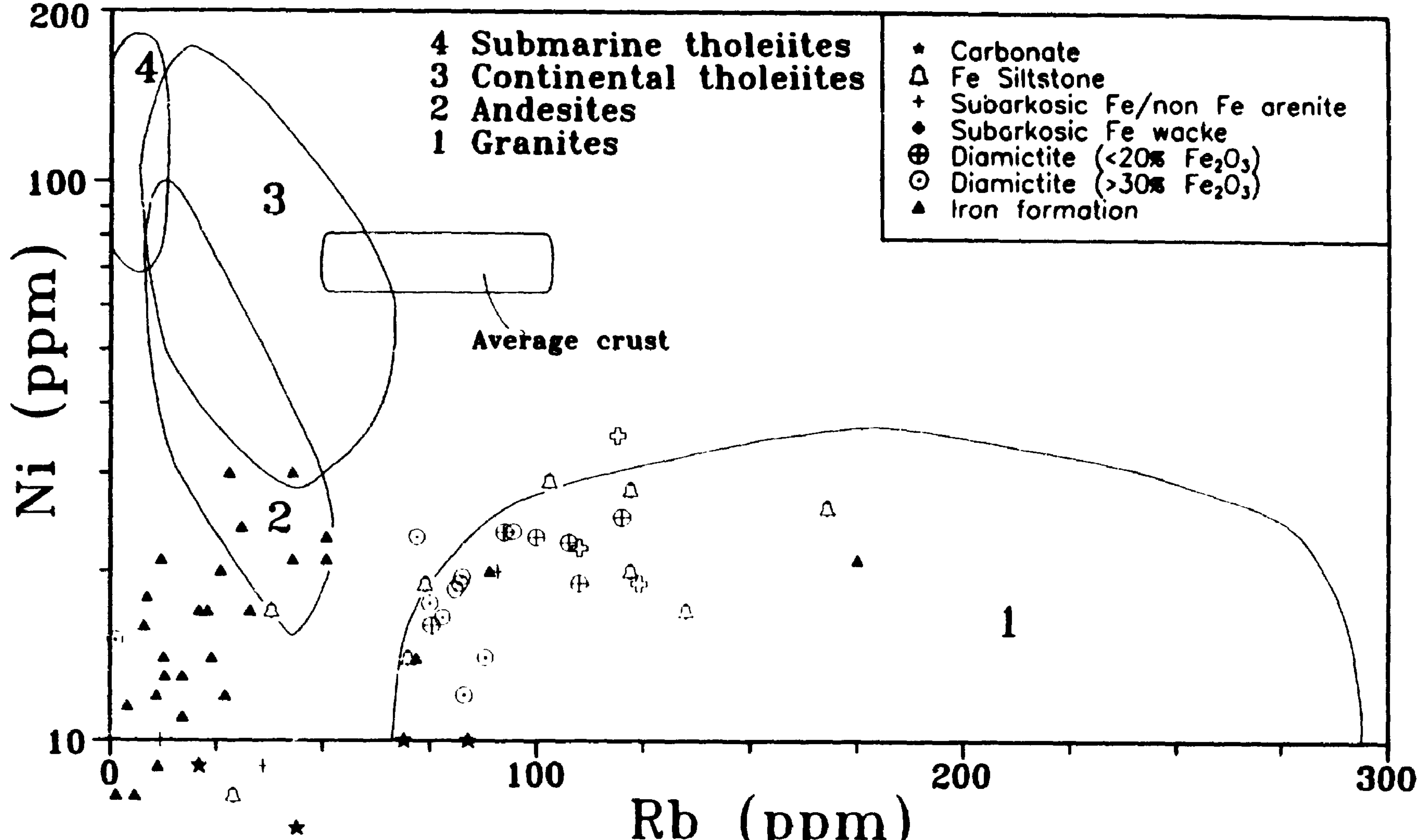

Figure 3.-- Rb vs. Ni plot of Braemar iron formation and associated iron oxide-bearing clastic rocks from zone 3 (Figure 2.1) su[illegible]p[illegible]ed on the diagram after Condie *et al.* (1970).

separation is defined mainly by higher Rb contents in the diamictite matrices, subarkosic Fe wackes and Fe siltstones; all of which have higher clastic contents than the associated iron formation. The clastic components which are here most likely to host Rb are feldspars (e.g., plagioclase) and sheet silicates (e.g., mica & chlorite, Tables 2.1 - 2.4; Wedepohl, 1978, p. 37-K-2). The majority of the diamictite matrices, subarkosic Fe wackes and Fe siltstones plot within the granite range (Figure 3.25), whereas iron formation samples plot within or close to the andesite field. However, both the granite-associated and andesite-associated samples have similar Ni contents, suggesting that iron formation (Table 2.2) simply has smaller amounts of the Rb-bearing minerals (Tables 2.1, 2.3 & 2.4).

The high and low Fe_2O_3 diamictite matrices cluster together on Figure 3 25, whereas a more clearly defined separation occurs on plots of Ba vs. Rb and Ba vs. Nb (Figure 3.26a & b). The reason for generally lower Rb and Nb contents in the high Fe_2O_3 diamictites is that plagioclase (Rb) and clay-type minerals (Nb) are not as abundant. The wider range in Ba content of the low Fe_2O_3 diamictites may reflect the presence of variable amounts of biotite in these samples (p. 58). Low Fe_2O_3 sample $10g_2$ plots with the high Fe_2O_3 diamictites. Since it is the most quartz-rich diamictite from zone 3 (SiO_2 = 72.83%), Rb-Ba-Nb-bearing aluminum silicates may have been diminished. These elements are also depleted in the most iron-rich diamictite, $7Y_1$ (Fe_2O_3 = 45.25%), which clusters with the iron formation samples (Figure 3.26a & b).

Sample $7Y_1$ also falls with the iron formation on a plot of Zr vs. Cr (Figure 3.27a). Sample $10g_2$ has a Cr content comparable to the high Fe_2O_3 diamictites but the Zr content causes it to be grouped with the low Fe_2O_3 diamictites. The higher Zr content of the low Fe_2O_3 diamictites may be attributed to the occurrence of biotite, which is not apparent in thin sections of high Fe_2O_3 diamictites (p. 58; Table 2.1).

As evident from Figure 3.27b, there is a positive correlation between V and Cr for all rock types except iron formation. The positive sloping portion of the graph

Figure 3.26A Ba vs. Rb plot of Braemar iron formation and associated iron oxide-bearing clastic rocks from zone 3 (Figure 2.1). Labelled samples $10g_2$ and $7Y_1$ are referred to in the text.

Figure 3.26B Ba vs Nb plot of Braemar iron formation and associated iron oxide-bearing clastic rocks from zone 3 (Figure 2.1).

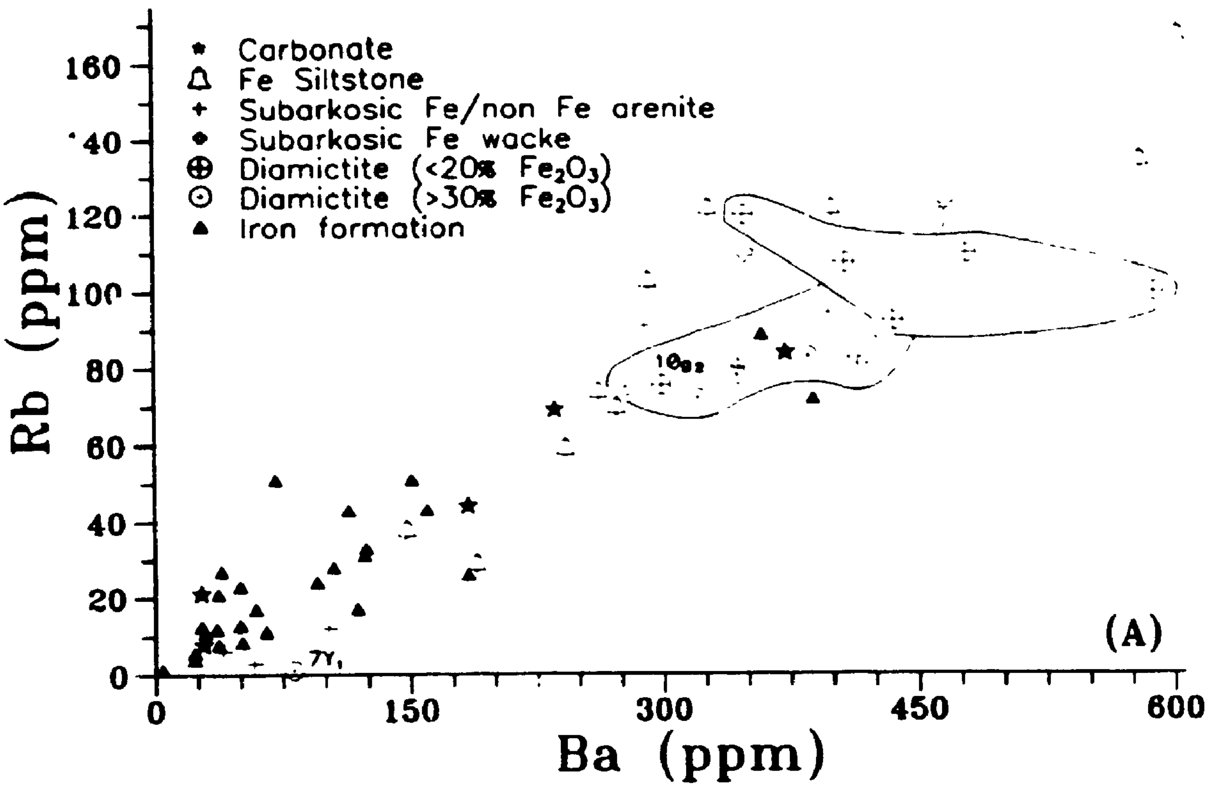
Carbonate
Fe Siltstone
Subarkosic Fe/non Fe arenite
Subarkosic Fe wacke
Diamictite (<20% Fe2O3)
Diamictite (>30% Fe2O3)
Iron formation
Rb (ppm)
Ba (ppm)
10a2
7Y1
(A)

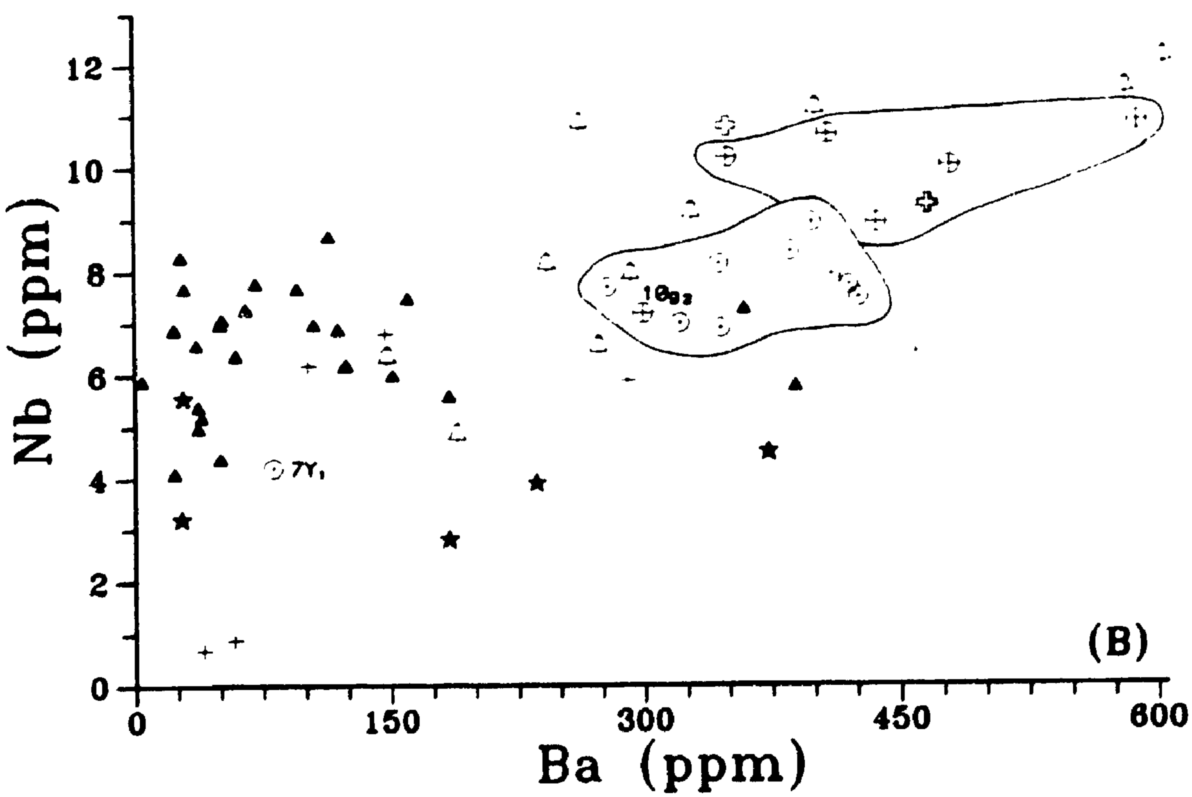
Nb (ppm)
Ba (ppm)
10a2
7Y1
(B)

Figure 3.27A Zr vs. Cr plot of Braemar iron formation and associated iron oxide-bearing clastic rocks from zone 3 (Figure 2.1). The two types of diamictite matrices are differentiated by the occurrence of biotite (Zr-bearing) in the low Fe_2O_3 diamictites (Table 2.1). Labelled samples $10g_2$ and $7Y_1$ are referred to in the text.

Figure 3.27B V vs. Cr plot of Braemar iron formation and associated iron oxide-bearing clastic rocks from zone 3 (Figure 2.1). Grouping of samples is based on the dominant V-Cr-bearing silicate(s) observed in thin section (Tables 2.1, 2.2 & A.13).

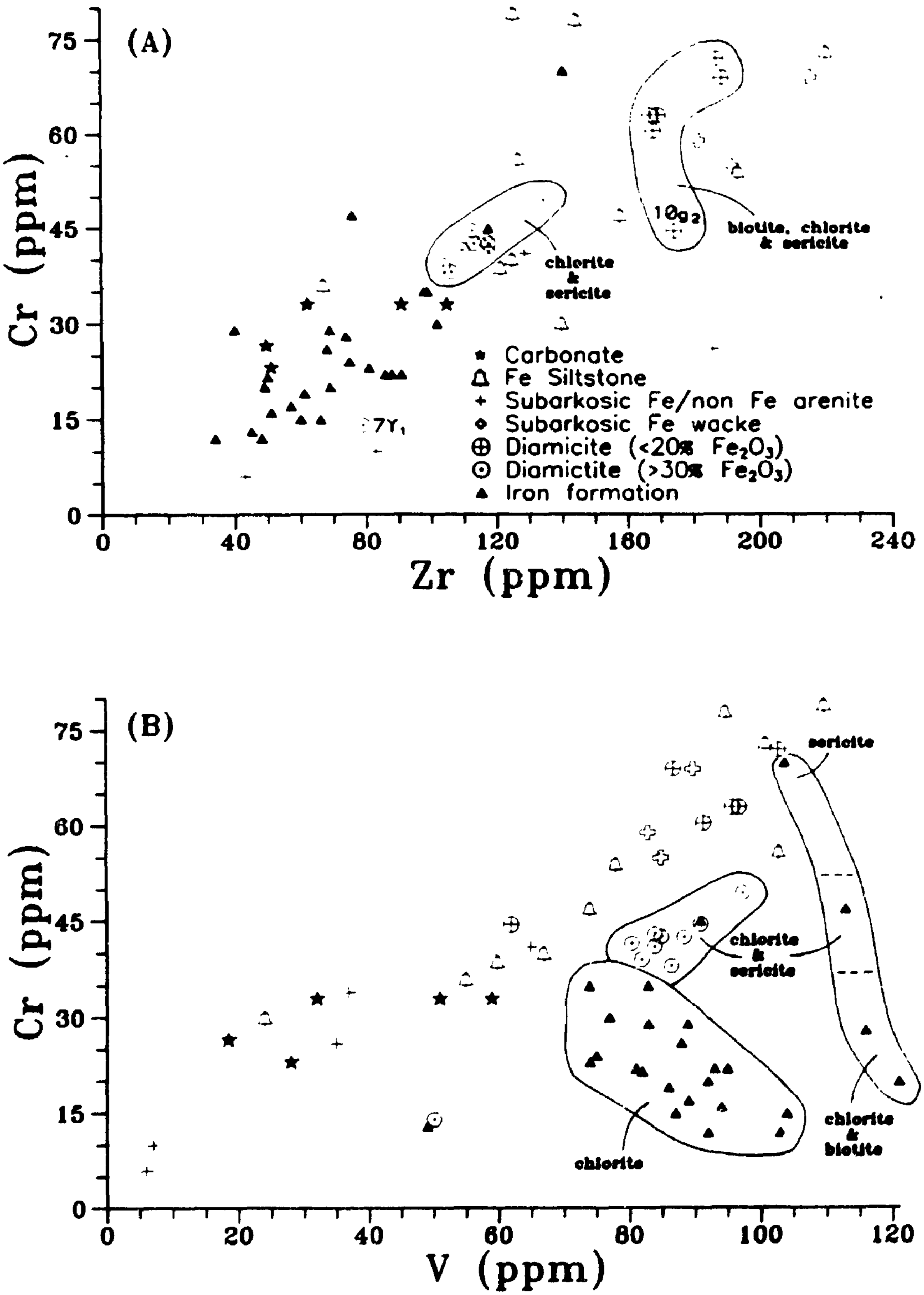
(A)
Cr (ppm)
Zr (ppm)
0
15
30
45
60
75
0
40
80
120
160
200
240
chlorite & sericite
biotite, chlorite & sericite
10g2
7Y1
Carbonate
Fe Siltstone
Subarkosic Fe/non Fe arenite
Subarkosic Fe wacke
Diamicite (<20% Fe2O3)
Diamictite (>30% Fe2O3)
Iron formation
(B)
Cr (ppm)
V (ppm)
0
20
40
60
80
100
120
sericite
chlorite & sericite
chlorite
chlorite & biotite

reflects increasing clay content, whereas the weakly negative sloping iron formation probably represents V-bearing iron oxides increasing at the expense of V-Cr-bearing silicates. Where observed in thin section, such silicates were used to group the iron formation and high Fe_2O_3 diamictite samples (Figure 3.27b).

A weak, positive covariance between Ni and Zn is evident for samples of iron formation and diamictite (Figure 3.28a). For iron formation, this correlation probably reflects increased amounts of Ni-Zn-bearing iron oxide (e.g., magnetite, hematite) and Zn-bearing chlorite (Wedepohl, 1978, p. 30-K-1). For diamictite, the positive correlation may only represent increasing clay content (e.g., chlorite, sericite) since the low Fe_2O_3 (<20%) diamictites tend to have higher Ni-Zn contents than the high Fe_2O_3 (>30%) diamictites.

A plot of Sr vs. Pb (Figure 3.28b) reveals that the nine samples with the greatest percent L.O.I. (>11.8%) have higher than normal Sr contents and that three of these same samples have the highest Pb content. However, a direct linear covariance between Sr and Pb is not apparent. Sr in the nine samples with high L.O.I. is hosted primarily by ferroan dolomite or calcite and these carbonate minerals are locally Pb-bearing.

<u>Summary of Trace Elements</u>

The clastic-rich facies of diamictite, subarkosic Fe wacke, subarkosic Fe/non Fe arenite and Fe siltstone generally have higher abundances of Rb, Ba, Zr and Cr than the chemically-dominated iron formation facies (Figures 3.25, 3.26a & 3.27a). This is attributed to greater amounts of detrital material in the clastic facies. Included in the detrital fraction of all zone 3 facies are chlorite, sericite and biotite (Figure 3.27a & b), which probably originated by metamorphism of clay-like precursors. The exclusion of biotite from the high Fe_2O_3 diamictite matrices (p. 58, Figure 3.27a) may be attributed to flocculation of clays in an environment more seaward than the depositional zone envisaged for the low Fe_2O_3 diamictites (see Figure 7.1).

Figure 3.28A Zn vs. Ni plot of Braemar iron formation and associated iron oxide-bearing clastic rocks from zone 3 (Figure 2.1).

Figure 3.28B Sr vs. Pb plot of Braemar iron formation and associated iron oxide-bearing clastic rocks from zone 3 (Figure 2.1). Samples with the highest LOI (loss on ignition) are enclosed by a solid line. Sample $10S_1$ has an LOI of 14.63%.

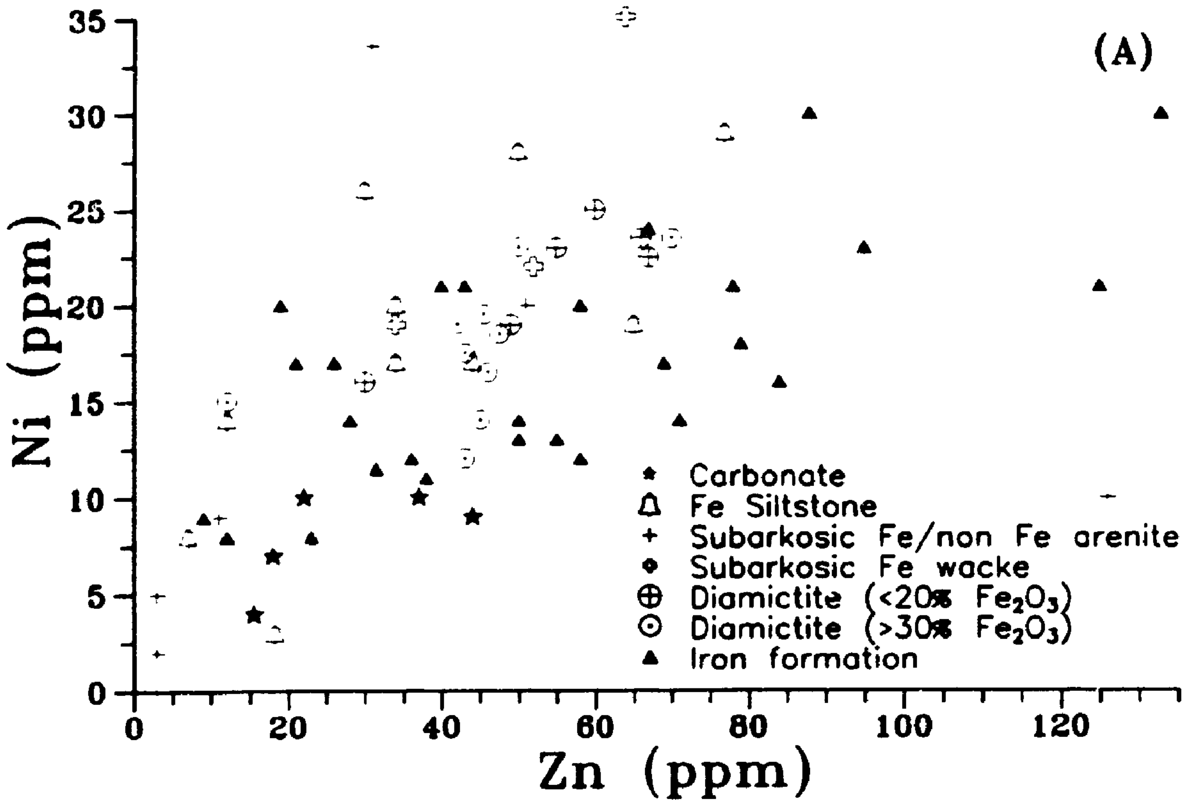
(A)
Ni (ppm)
Zn (ppm)
35
30
25
20
15
10
5
0
0
20
40
60
80
100
120
Carbonate
Fe Siltstone
Subarkosic Fe/non Fe arenite
Subarkosic Fe wacke
Diamictite (<20% Fe2O3)
Diamictite (>30% Fe2O3)
Iron formation

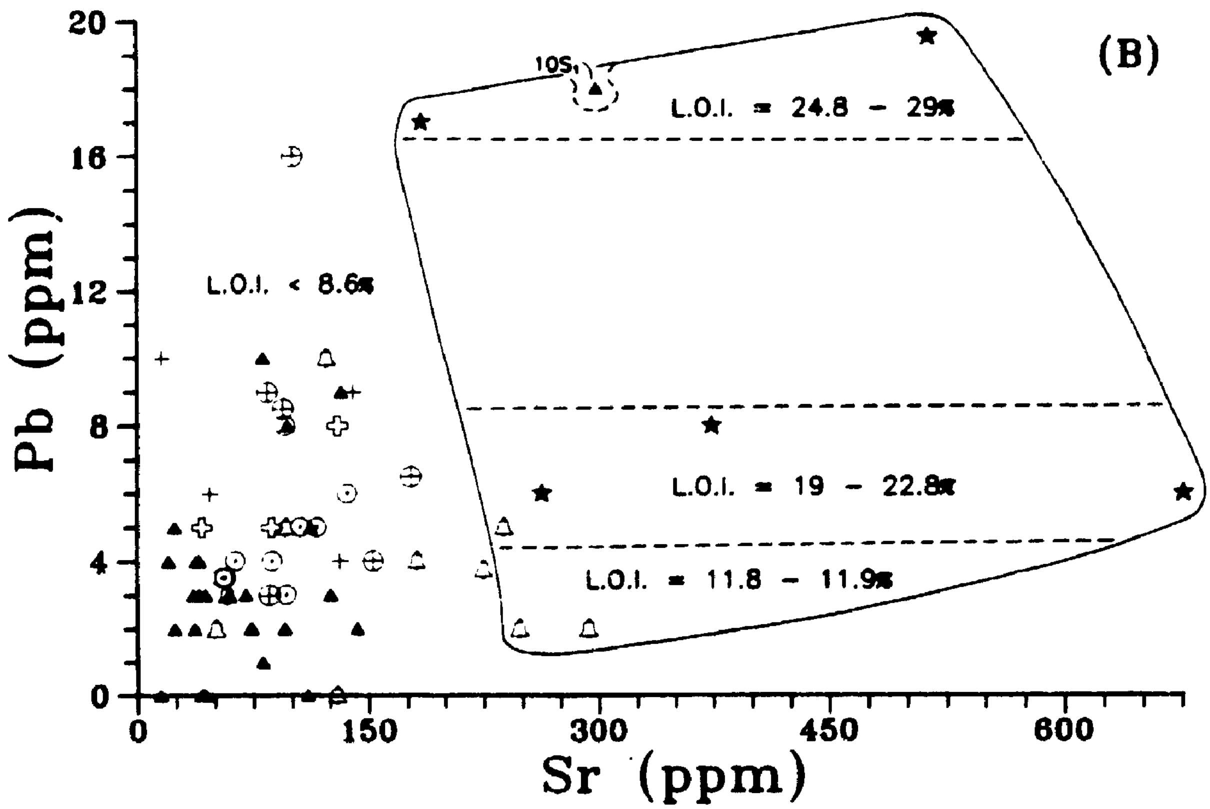
(B)
Pb (ppm)
Sr (ppm)
20
16
12
8
4
0
0
150
300
450
600
10S1
L.O.I. = 24.8 - 29%
L.O.I. < 8.6%
L.O.I. = 19 - 22.8%
L.O.I. = 11.8 - 11.9%

174

Chapter IV

MINERAL CHEMISTRY

Introduction

Acquisition of mineral composition data by electron microprobe was initiated for the purpose of examining mineral relationships within the lutite fraction (silt- & clay-size) of iron formation and high Fe_2O_3 (>30%) diamictite samples. In these samples, study focused primarily on the abundant iron oxide minerals, but was expanded to include apatite because of its common appearance in iron formation (p. 66 & 70, Figure 3.18), clastic laminae intimately encased by IF (p. 74), and high Fe_2O_3 diamictite matrices. Apatite is rarely evident in the associated, more clastic rocks (cf. Yeo, 1984, p. 229). In contrast, iron-bearing silicate and carbonate minerals occur in all five facies described in Chapter 2, and hence these minerals were analyzed to see how their compositions varied amongst the different rock types. Also, previous studies of ferromagnesian silicates (e.g., mica) have revealed compositional changes controlled by the oxidation state of the host rock (Klein, 1966; Hounslow and Moore, 1967; Annersten, 1968). This possibility was examined since the three zones outlined in Figure 2.1 are defined mainly on the types of iron oxide minerals that occur in each (i.e., hematite, magnetite, combination of the two).

Analytical Method

Mineral compositions were determined with a four spectrometer JEOL 8600 x-ray microprobe at the University of Western Ontario. The analyzed components comprise four mineral groups: oxides, phosphates, phyllosilicates and carbonates. Individual elements were calibrated using natural and synthetic mineral and rock samples. The analyses were conducted at 15 kv, with a beam current and width of 9 - 11 nanoamps and 5 - 10 μm respectively. Elemental abundances were calculated using

ZAF corrections on a Tracor Northern computer.

As a means of determining precision and accuracy, mineral standards appropriate to each mineral group listed above were analyzed. Relative precision, calculated from replicate analyses of the standards, ranges from a maximum ±26.04% (Fluorine of Apatite 104021) to a minimum ±0.77% (MgO of Dolomite). Accuracy, which is the relative error (from reference values) converted to percent, is a maximum -41.91 and +3.19 (SiO_2 of Apatite 104021; Al_2O_3 of Kaersutite) and a minimum -0.39 and +0.25 (FeO of Chromite #5; SiO_2 of Kaersutite).

Microprobe Results

The weight percent oxide abundances generated from microprobe analyses are tabulated in Appendices C - F. The rock type and sample number from which individual analyses were acquired are also listed.

Although a few rutile analyses are included in Appendix C, the majority of analyses are of iron oxide minerals; hematite and magnetite. The analyses have been recalculated on a magnetite-ulvöspinel basis and an ilmenite-hematite basis using the computer program ILMAG (Carmichael, 1967). Analyses for which the totals have been highlighted/bolded in Appendix C are generally those plotted in Figure 4.1, whereas ambiguous totals are not highlighted. Apatite commonly occurs with hematite and magnetite, so that these minerals are discussed together (see below) but the apatite analyses are tabulated separately (Appendix D). All analyzed grains are fluor-apatite, which is defined as apatite with fluorine predominant over chlorine and hydroxyl (Bates and Jackson, 1980). Microprobe analyses of apatite total between 98 and 102% (Appendix D), however, replicate analyses of the apatite standard generally revealed P_2O_5 to be slightly low.

The microprobe analyses of phyllosilicate minerals phlogopite, biotite and chlorite are tabulated in Appendix E. For both chlorite and the micas, the proportioning of elements into atomic structural formula units was calculated with the computer program SUPREC (written by J.C. Rucklidge, University of Toronto, 1969) from the weight percent oxide abundances. The mica and chlorite calculations are based on twenty-two and twenty-eight oxygens respectively. With regard to the carbonate minerals, the weight percent oxide microprobe analyses and corresponding atomic formula units (calculated with SUPREC) are presented in Appendix F.

Iron Oxides and Apatite

Four different habits of primary hematite commonly observed in thin section include:

i) hematite lutite (p. 42; restricted to zone 1, Figure 2.1);

ii) hematite platy (p. 42; zones 1 & 3; Plate 4.1a);

iii) hematite subhed (zones 1, 2 & 3; Plate 4.1a); and

iv) hematite serrate (zones 1 & 3; Plate 4.1b).

Only the latter three types were suitable for analysis with the microprobe; the hematite lutite grains were too fine.

The platy, subhedral and serrate-edged hematite have TiO_2 contents which generally range from 0.77 - 2.77% with up to 4.43% detected locally (Figure 4.1). Similar ranges of TiO_2 occur in hematite within one sample and between samples of varied composition (e.g., diamictites & iron formation). This suggests that titanium variations in hematite are unrelated to bulk rock compositions. Although Floran and Papike (1978) reported trace (<0.10%) amounts of TiO_2 in iron formation-hosted hematite, Annersten (1968) described hematite in IF which contained 1.5 - 6.8% TiO_2. Annersten (1968, p. 390) suggested that because Ti-bearing hematite occurred with Ti-poor biotite and Ca-amphibole, titanium and iron are partitioned from silicates to the oxide phase when subjected to increasing oxygen pressure during metamorphism. However, hematite from zones 1 and 3 shows comparable ranges in titanium content

Plate 4.1

(a) Backscatter SEM image of subhedral to euhedral magnetite rhombs, subhedral hematite (slightly greyer and smaller than magnetite) and platy hematite (upper left). Analyzed subhedral hematite has 0.99% (1) and 0.86% (3) TiO_2, whereas adjoining magnetite (2) has TiO_2 below detection limit (b.d.l.). I. F. sample $8q_l$ from adit through Razorback Ridge, *Spring Dam* (zone 3, Figures A.1 & A.9).

(b) Interpenetrating boundaries of a magnetite (right) - hematite serrate (left) grain pair. Analyzed spots 1 and 4 have b.d.l. and 1.60% TiO_2 respectively. Fe siltstone sample $8A_L$ from mouth of adit through Razorback Ridge.

(c) Titanium-free euhedral magnetite (centre) and three adjoining subhedral hematite grains which have 1.51% (2), 1.50% (17) and 1.26% (16) TiO_2. The magnetite rhomb is criss-crossed by thin bands of posttectonic hematite (darker grey, Ti-free). Iron formation sample $8A_U$ from the mouth of adit through Razorback Ridge.

(d) Interpenetrating boundaries of an apatite (medium grey) - magnetite (white) grain pair. Blade-like sericite evident in matrix. Iron formation sample $8r_l$ from adit through Razorback Ridge.

(e) Serrate hematite (centre) - apatite (A) grain pair. Hematite serrate in lower left forms an overgrowth on detrital grain of ilmenite-titanhematite. Average TiO_2 content of the overgrowth is 0.77% (0.31 1σ). Diamictite matrix sample $13c_l$ from the stratigraphic section #13 on *Worumba* (zone 1, Figures A.1 & A.3).

(f) Overgrowth of hematite serrate (with medium grey apatite inclusions) on detrital grain of titanomagnetite-rutile (centre). Subhedral apatite crystals (two) rim the left and right sides of the overgrowth. Fe siltstone sample $8A_L$ from the mouth of the adit through Razorback Ridge, *Spring Dam* (zone 3, Figures A.1 & A.9).

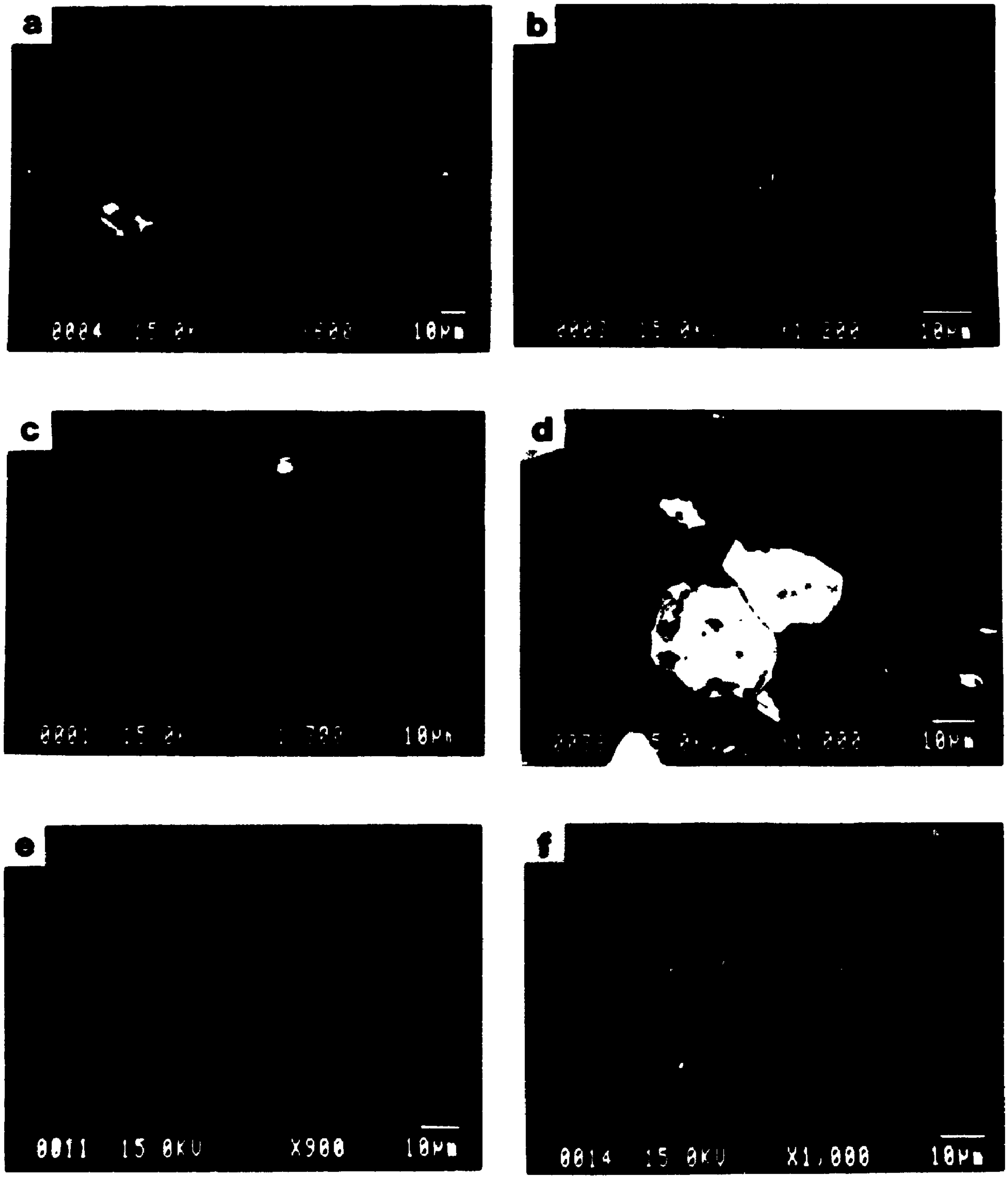
a
0004
10μm
b
10μm
c
10μm
d
10μm
e
0011 15.0KV X900 10μm
f
0014 15.0KV X1,000 10μm

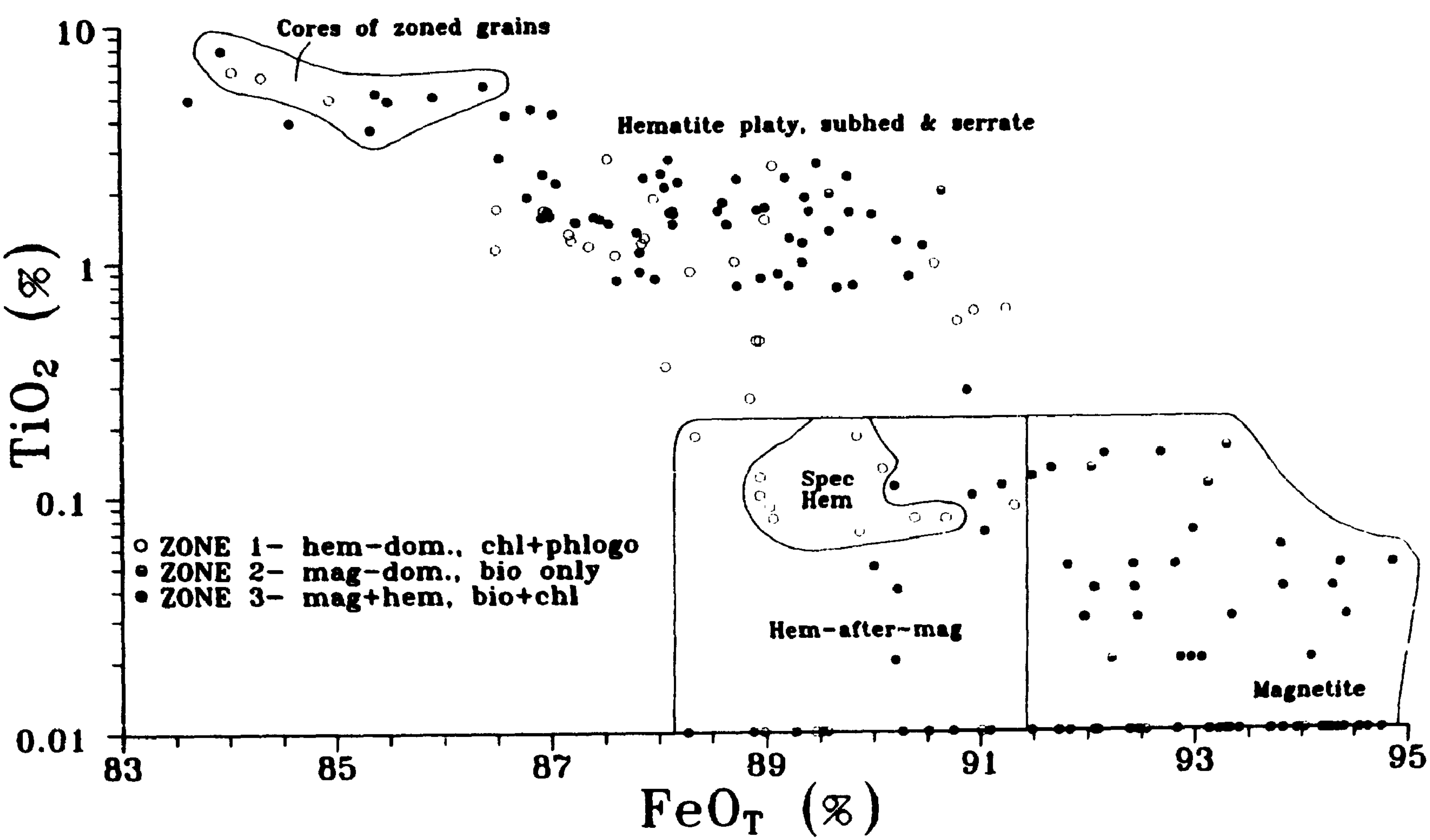

Figure 4.1 FeO_T vs. TiO_2 plot of iron oxide analyses from samples of diamictite ($13c_1$, $21j_1$, $15f_1$, RD#3-11'), iron formation ($13e_2$, $21a_1$, $19E_2$, $16d_1$, $10d_1$, $10T_1$, $8q_1$, $8E_1$, $8A_U$), Fe siltstone ($8A_L$) and carbonate ($10q_1$) collected within zones 1 - 3 (Figure A.1).

with zone 3 hematites slightly more titaniferous (Figure 4.1). Mica from the hematite-dominated zone 1 is Ti-poor compared with micas from magnetite-bearing rocks in zones 2 and 3 (see Figure 4.3). This relationship appears to indicate that increased Ti substitution in hematite reflects increased metamorphism as demonstrated by Frey (1969; referred to by Kramm, 1973, p. 189). However, variations in TiO_2 in hematite within a single zone 1 sample ($13c_1$ with 0.26 - 2.76%) overlap almost the entire range in TiO_2 shown by zone 3 hematites. Such variable TiO_2 in zone 1 hematite likely reflects the presence of coexisting rutile in these rocks following the suggestion of Kramm (1973), that the higher the oxidation ratio, the lower the titanium content of hematite. Nonetheless, both the wide range and slightly higher titanium content of hematite in rutile-free zone 3, where magnetite is common and biotite predominates over chlorite (which contrasts with lower metamorphic grade zone 1), indicate that no single factor adequately explains the observed variations in titanium in hematite.

Within iron-rich (>21.5% iron oxide) samples of zone 1 (base of section #21) and zone 3, subhedral or serrate-edged hematite commonly forms grain pairs with magnetite (Plate 4.1b & c). The mutually interpenetrating grain boundaries suggest that these pairs represent coexisting phases which crystallized during diagenesis and low-grade metamorphism. A similar interpretation is proposed for magnetite-apatite (Plate 4.1d) and hematite-apatite pairs (Plate 4.1e).

Local evidence of authigenic (early diagenetic?) iron and phosphorous addition takes the form of serrate-edged hematite or hematite-apatite overgrowths on detrital grains of ilmenite-titanhematite (Plate 4.1e), twinned titanhematite, or titanomagnetite-rutile (Plate 4.1f; cf. Ixer *et al.*, 1979). The detrital grains which range in size from 16 - 44 μm, probably resulted from the oxidation of high temperature magmatic iron-titanium oxides (Haggerty, 1991). The core grain present in Plate 4.1e shows evidence of the triangular Widmanstätten texture, which typically occurs parallel to the octahedral planes of cubic minerals such as magnetite (Ineson, 1989, p. 66). The hematite overgrowth on ilmenite-titanhematite in Plate 4.1e was traversed with the microprobe outward. The five analyses from this traverse average 0.77% TiO_2 (0.31 1σ) which is considerably lower that the three analyses of the core (i.e., 34.15%, 15.17% & 6.51% TiO_2). The disparity between the TiO_2 contents of core and overgrowth argues against simple titanium encroachment from the core into the overgrowth. Also evident in Plate 4.1e is an **unzoned** hematite serrate in which TiO_2 has an even distribution (< 1% throughout) which suggests that a detrital core grain is not present. The homogeneous distribution of TiO_2 together with the mutually interpenetrating boundary with the adjacent apatite grain implies that this hematite serrate is primary and like the magnetite-apatite grain pair of Plate 4.1d has simply crystallized during diagenesis.

As previously mentioned (p. 66 & 70), bedding-parallel lenses of apatite and chlorite (Plate 4.2a) occur within iron formation samples at sections 12 and 20/14 (zone 1, Figures 2.1 & A.1). These are considered to reflect diagenetic dissolution and reprecipitation of matrix material since they are compositionally similar to the surrounding lutite matrix. Some addition of apatite is likely since these samples are generally enriched in P_2O_5 relative to iron formation elsewhere (Figures 3.17, 3.18 & 3.23). Apatite cement has been observed in subarkosic Fe arenite (Fe-poor, Plate 4.2b) layers within what are dominantly subarkosic Fe wacke samples (Figure 3.18).

There is very localized evidence of hematite formation during retrograde metamorphism (Plate 4.2c). Rectangular plates of hematite, which occur parallel to phlogopite cleavage planes, are accompanied by partial chloritization of phlogopite. The TiO_2 content of this form of hematite is relatively low (e.g., 0.36%), which is typical of secondary iron oxides associated with partially chloritized mafic minerals (Buddington *et al.*, 1955). The titanium was probably released from phlogopite during chloritization, whereas the iron required to form hematite was either added to, or remobilized from within, the iron formation host.

Magnetite occurs at the base of section #21 at Back Creek (zone 1) and

Plate 4.2

(a) Bedding-parallel lens of apatite (homogenous grey) and prismatic chlorite (darker grey). Iron formation sample $12n_1$ from the stratigraphic section #12 in 'Dropstone Creek', *Oraparinna* (zone 1, Figures A.1 & A.2).

(b) Photomicrograph of finely crystalline apatite cement. Subarkosic Fe arenite (Fe-poor) layer within subarkosic Fe wacke sample $12f_3$ from section #12 in 'Dropstone Creek', *Oraparinna*. Plane light; bar = 0.1 mm.

(c) Relict grain of phlogopite (centre, light grey) showing almost complete replacement by chlorite (dark grey) and hematite (white). Hematite parallels cleavage planes in phlogopite. Subhedral apatite crystals (A) occur to the right of and 'above' the replaced grain. Iron formation sample $13e_2$ from the stratigraphic section #13 on *Worumba* (zone 1, Figures A.1 & A.3).

(d) Central magnetite rhomb has been partially oxidized to hematite (darker grey right half). Both halves are Ti-free, whereas adjoining platy hematite has 0.79% TiO_2. Iron formation sample $8q_1$ from the adit through Razorback Ridge, *Spring Dam* (zone 3, Figures A.1 & A.9).

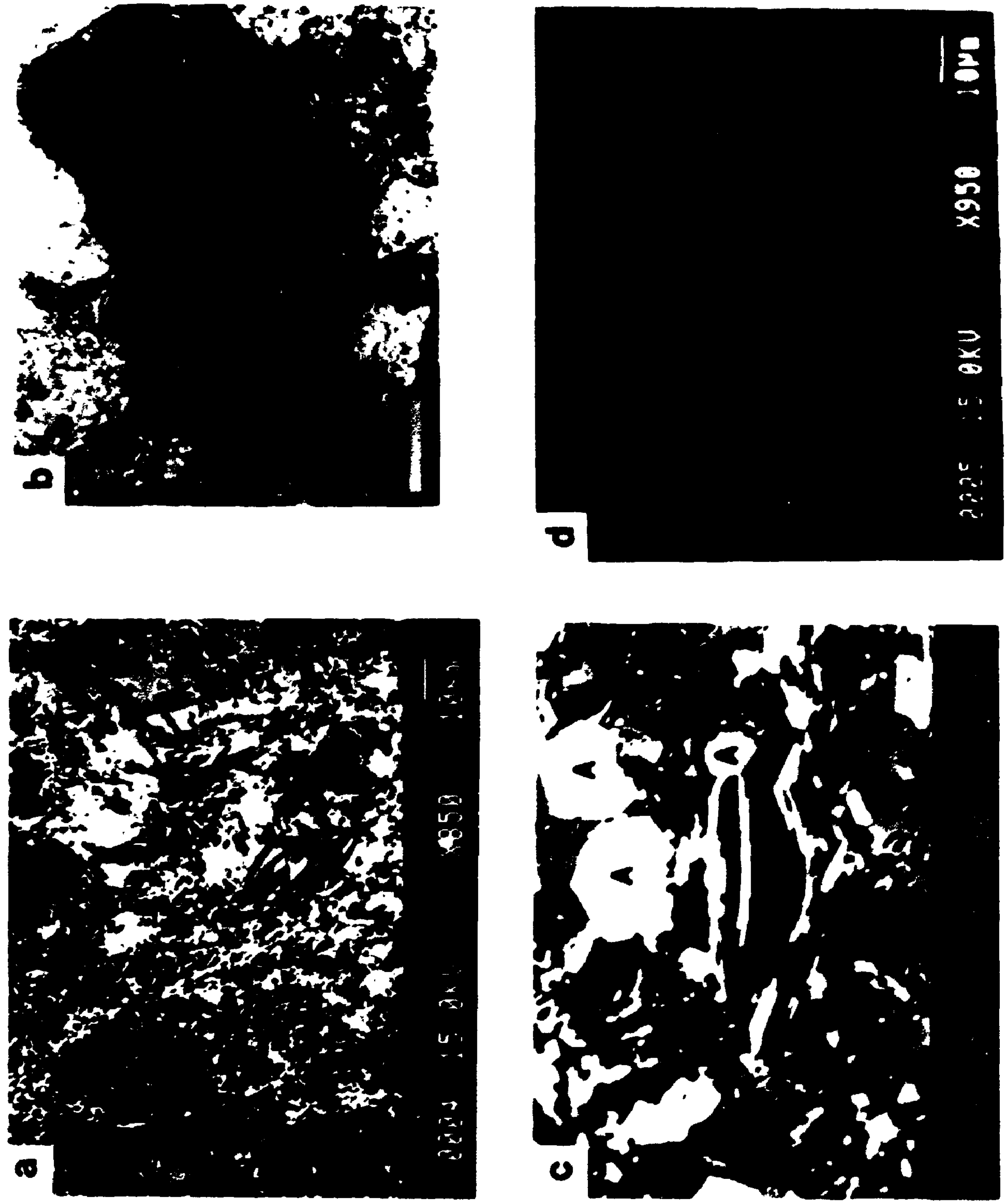
a
b
c
d
X950
10μm

throughout zones 2 and 3 (Figure 2.1). It is typically subhedral to euhedral (Plate 4.1a-d) and contains 0.00 - 0.16% TiO_2 (Figure 4.1). A low TiO_2 content is to be expected since the majority of magnetite rhombs analyzed occur together with platy, subhedral or serrated hematite (p. 175); the presence of which indicates that oxygen pressure was high enough to prevent appreciable amounts of titanium from being incorporated into magnetite (Annersten and Ekström, 1971; Lindsley, 1962).

Hematite-after-magnetite (Plates 4.1c & 4.2d) and specular hematite are considered to be posttectonic. Both have low TiO_2 (0.00 - 0.18%) comparable to magnetite, and lower than the other habits of hematite (Figure 4.1). Oxidation of magnetite to hematite occurs either as thin bands (0.8 - 3 μm) of hematite cross-cutting magnetite (Plate 4.1c) or as a hematized portion of a magnetite rhomb (Plate 4.2d). Specular hematite, which is only locally developed, is considered to be a cavity- or druse-fill.

Apatite, which can be a trace or minor (sections 12 & 20/14) component of iron-rich rocks within zones 1 - 3 (e.g., see % Fe and P of Figures 3.22 & 3.23), was analyzed from various layer types within the adit through Razorback Ridge on *Spring Dam* (zone 3, Figure 2.1; Appendix D). These adit layers were iron formation proper or clastic layers encased by IF (i.e., diamictite, Fe arenite and Fe siltstone); apatite is not apparent in clastic rocks more removed from IF. In contrast to the bedding-parallel apatite-rich lenses described on p. 180 (Plate 4.2a), fluor-apatite from the adit is subhedral (Plate 4.1d & f) and uniformally disseminated. This type of distribution is similar to that described by Breitkopf (1988) in the upper Proterozoic Chuos iron formation of Namibia. Breitkopf considered this apatite to have an exhalative origin, based in part on its distribution, which differs from that of iron formation-hosted apatite, confined to distinct bands and interpreted as phosphorite seams (Laajoki and Gehör, 1986). In addition, Breitkopf (1988, p. 127) cited Plimer (1983), who "considered iron formations containing phosphatic fluor-apatite to be exhalative rocks, normally associated with mafic or bimodal volcanism." A similar uniform distribution of apatite is also widespread throughout iron-enriched rocks of zones 1 - 3 (Plates 4.1e & 4.2c), whereas lensoid apatite (Plate 4.2a) is more locally developed (sections 12 & 20/14, Figure A.1).

<u>Magnesium-Iron Micas and Chlorite</u>

Phyllosilicate minerals chlorite, phlogopite and biotite are here considered together because chlorite commonly occurs in association with one of the two mica types. Biotite and phlogopite are trioctahedral phyllosilicates in which individual layers consist of two tetrahedral sheets and one octahedral sheet sandwiched between them. The negatively charged layers, bound together by large positively charged interlayer cations, have the generalized structural formula:

$$X_2Y_6Z_8O_{20}(OH,F)_2$$

where X = interlayer site, Y = octahedral site and Z = tetrahedral site (Bailey, 1984). The elements assigned to these sites are:

$$(K,Na,Ca,Ba)_2(Mg,Fe,Mn,Cr,Ti,Al)_6(Si,Al)_8O_{20}(OH,F,Cl)_2$$

The chlorite structure is similar to that of biotite-phlogopite, except that an octahedral sheet occurs in lieu of interlayer cations (Bailey, 1988).

Magnesium-Iron Micas. The analyzed grains, which occur mainly in iron formation and diamictite samples from zones 1 - 3, are generally divisible into phlogopite (zone 1) and biotite fields (zones 2 & 3; Figure 4.2). Biotite is distinguished from phlogopite in having Fe/(Fe + Mn + Mg) > 0.33 and Mg:Fe < 2:1 (Deer *et al.*, 1962). The occurrence of the more magnesium-rich phase, phlogopite (Mg:Fe > 2:1) is related to a higher oxidation state (as implied by the oxide minerals present) of the analyzed samples. For example, the phlogopite-bearing samples contain hematite-rutile or magnetite-hematite, whereas the biotite-bearing samples contain either magnetite or no oxide minerals (Figure 4.3). The relatively high oxygen fugacity implied by hematite-rutile or magnetite-hematite would result in the production of Fe^{3+} from Fe^{2+}

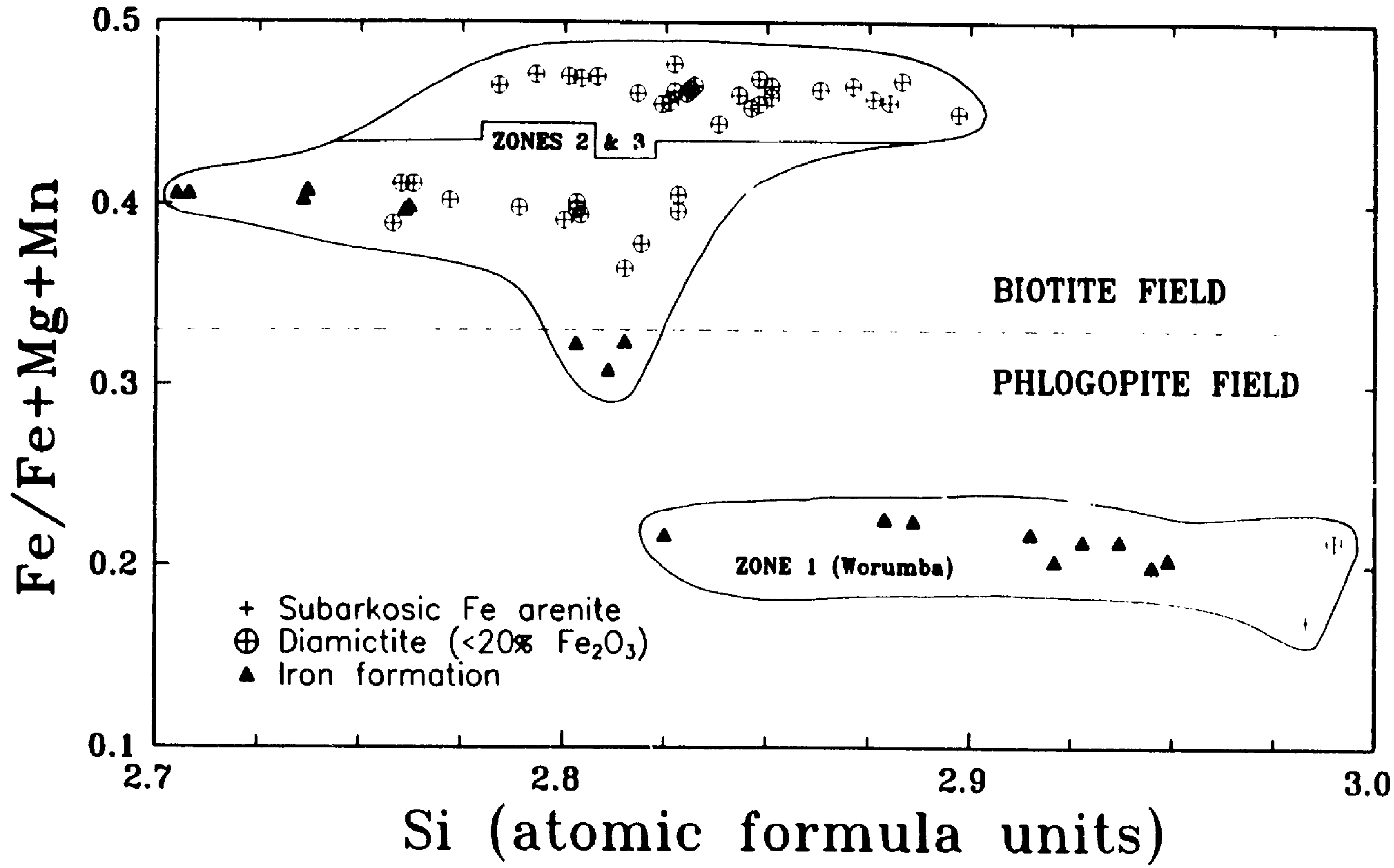

Figure 4.2 Chemistry of magnesium - iron micas from samples of diamictite ($13c_1$, $18a_1$, $17a_1$, $15f_1$, 7T), iron formation ($13e_2$, $18E_1$, $16d_1$) and a subarkosic Fe arenite (Fe-poor) layer (13k) collected within zones 1 - 3 (Figure A.1). Compositional fields after Deer *et al.* (1962).

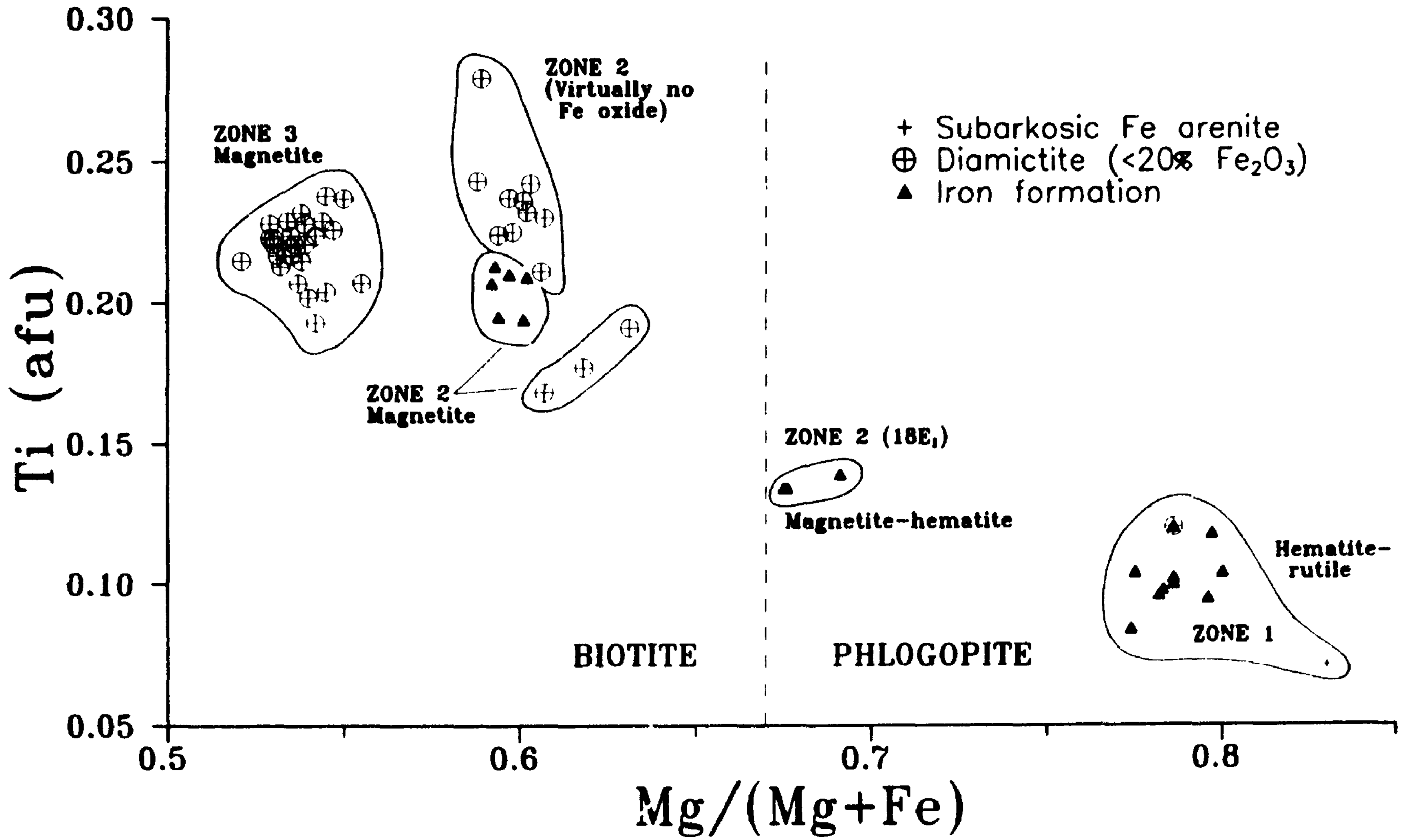

Figure 4.3 The ratio of magnesium to iron plus magnesium in biotite-phlogopite plotted against atomic formula units (afu) of Ti. Analyses from the .ame or similar sample(s) are encircled and the type of oxide mineral(s) present in the host rock is indicated.

and thus deplete the amount of Fe^{2+} available to form silicates (Guidotti, 1984). Magnesium would likely substitute for Fe^{2+} and hence promote the formation of phlogopite rather than biotite. A positive correlation between the Mg/(Mg + Fe) ratio in ferromagnesian silicates and the oxidation state of the assemblage has also been observed by Klein (1966), Hounslow and Moore (1967) and Annersten (1968). It should, however, be noted that the biotite-bearing diamictite samples from zone 2 deviate from this trend since they have variable magnetite contents (Fe_2O_3 = 2.04 - 11.53%) yet show Mg/(Mg + Fe) ratios comparable to iron formation from zone 2 (Fe_2O_3 = 41.67%; Figure 4.3). This deviation may reflect the presence of some detrital igneous biotites observed in thin sections of zone 2 diamictites (see p. 52); a suggestion which is supported by the generally higher totals for these biotites (94.46 - 98.22%) relative to the metamorphic bioites (92.38 - 96.43%; Deer *et al.*, 1962).

Chlorite. The majority of analyzed chlorites plot within the clinochlore field (Figure 4.4), and unlike the biotite-phlogopite grains there is no clear segregation between clinochlore grains from different zones. Most of the clinochlore from zone 1 samples (i.e., 13c$_1$, 13e$_1$, 13k of Appendix E) formed by retrogression of phlogopite (Plate 4.2c). The only analyzed sample which contained chamosite was a Fe siltstone from *Manunda* (7B, zone 3), however its interlocking, networked appearance was observed in at least three samples from section #7 (Table 2.4). This chamosite is considered to be authigenic on textural grounds.

Carbonates

Carbonate minerals were analyzed from only six samples, four of which were from within zone 3 (Figure 2.1). The majority of analyzed grains are of ferroan dolomite which is defined as having up to 20% of the Mg position filled by Fe^{2+} or Mn (Deer *et al.*, 1966, p. 494). Carbonate minerals that are richer than this in ferrous iron and manganese are termed ankerite (Figure 4.5). The dolomite and ankerite analyses

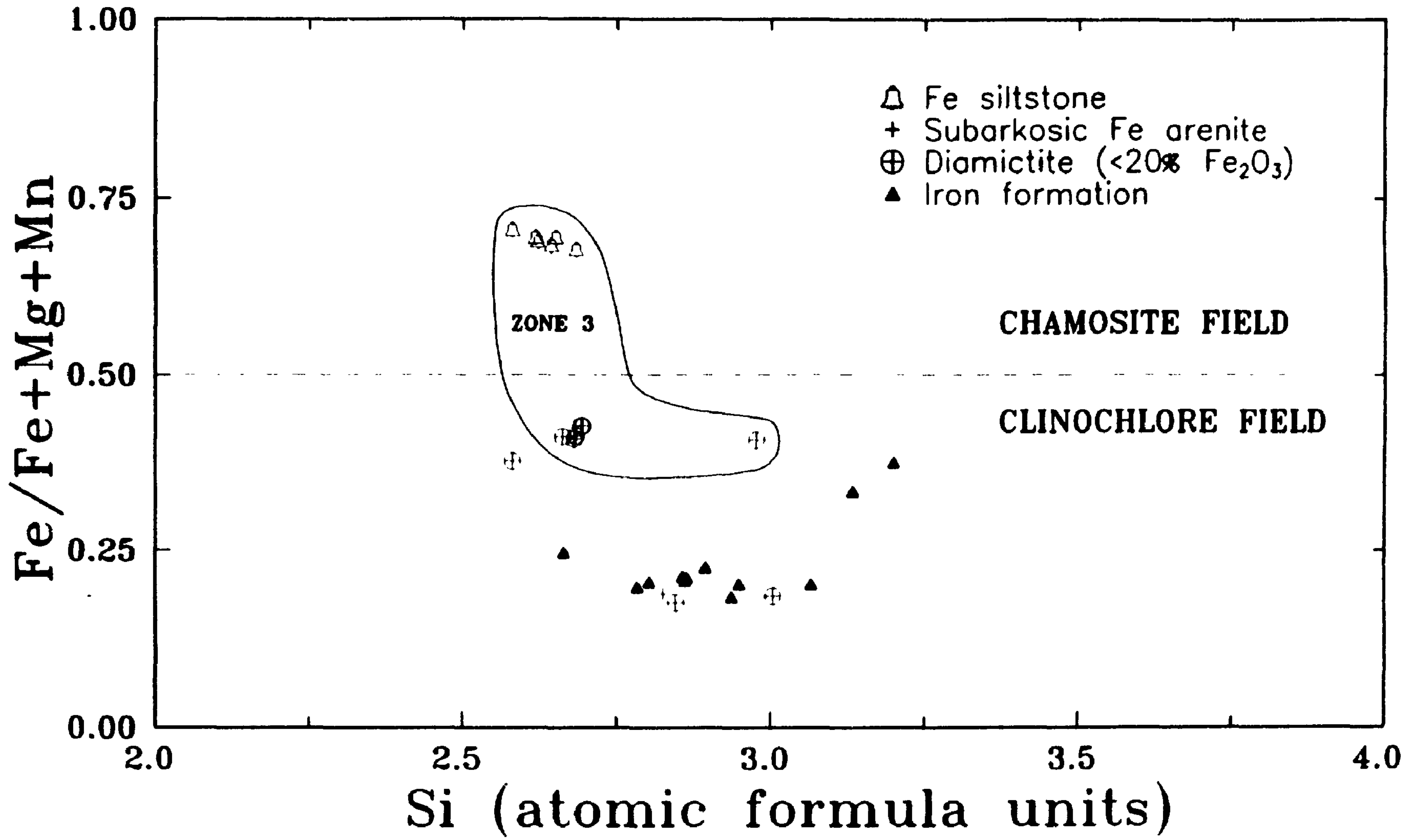

Figure 4.4 Chemistry of chlorites from samples of diamictite ($13c_1$, 7T), iron formation ($13e_2$, $19E_2$), subarkosic Fe arenite (Fe-poor, 13k) and Fe siltstone (7B) collected within zones 1 - 3 (Figure A.1). Boundary between chamosite and clinochlore fields from McLeod and Stanton (1984).

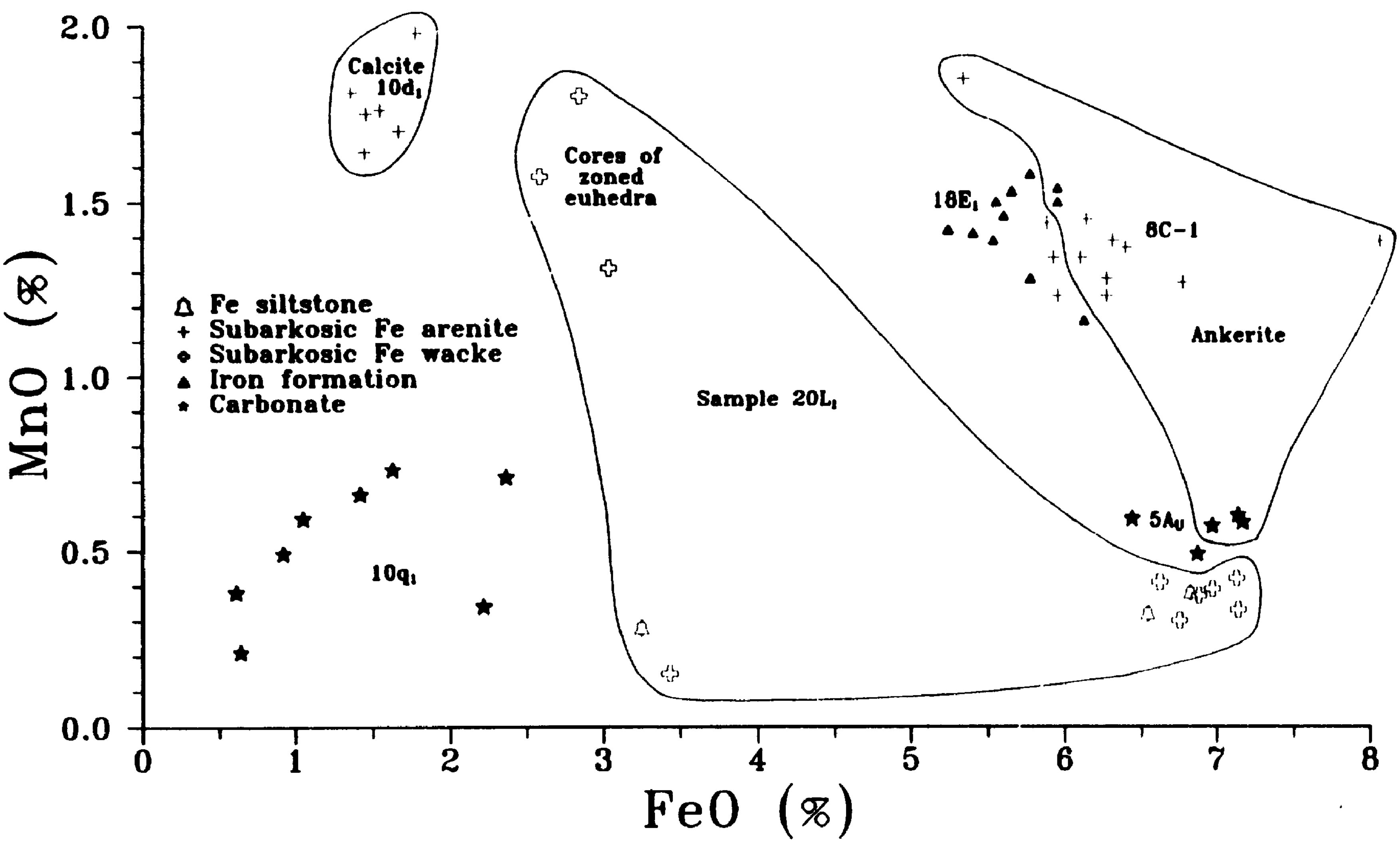

Figure 4.5 FeO vs. MnO plot of carbonate analyses from samples $20L_1$ (zone 1), $18E_1$ (zone 2), and $10d_1$, $10q_1$, $5A_U$ and 8C-1 (zone 3, Figure A.1).

show relatively small fluctuations in CaO (27.62 - 29.98%) and MgO (15.06 - 20.94%) contents, hence these elements are not presented graphically. The samples which contain ankerite ($18E_t$, $5A_U$ & 8C-1) are the most intimately associated with iron formation. These three samples have varied compositions (i.e., iron formation, Fe arenite & carbonate; Figure 4.5), so that the occurrence of ankerite is more likely source-related than bulk rock controlled. In contrast to the homogeneous carbonate minerals probed in the five samples from zones 2 and 3, laminated subarkosic Fe wacke and Fe siltstone sample $20L_1$ (zone 1) contains zoned ferroan dolomite euhedra. These zoned grains have a dark inner zone in which FeO = 2.59 - 3.04%, MnO = 1.31 - 1.80% and a lighter rim with FeO = 6.62 - 6.88% and MnO = 0.30 - 0.41%. Unzoned grains within $20L_1$ have variable FeO content (3.25 - 3.43% or 6.54 - 7.14%) and a relatively homogeneous MnO content (0.15 - 0.42%).

Summary

Hematite-magnetite pairs with mutually interpenetrating grain boundaries occur in iron-rich rocks of zones 1 ($21a_1$) and 3 (Plate 4.1b & c). Hematite-apatite (zones 1 & 3, Plate 4.1e) and magnetite-apatite (zone 3, Plate 4.1d) grain pairs are also observed. These mineral pairs are considered to represent chemically precipitated precursor phases which have crystallized during diagenesis and low-grade metamorphism. The compositions of these initial phases are discussed in Chapter 7. Magnetite is weakly titaniferous (<0.2%) whereas platy, subhedral and serrate hematite show much greater variations in TiO_2 (0.77 - 4.43%). This variability of Ti hematite cannot be ascribed solely to different bulk rock (oxide assemblages) compositions, metamorphic grade or oxygen pressure during metamorphism.

There is localized evidence of early diagenetic(?) iron and phosphorous addition. Serrate-edged hematite (Plate 4.1e) or hematite-apatite (Plate 4.1f) overgrowths on detrital grains of iron-titanium oxide suggest that the core grains functioned as points onto which Fe-P-(Ti)-bearing fluids nucleated. Disparities between the TiO_2 contents of core (averages 18.61% in Plate 4.1e) and overgrowth (averages 0.77% in Plate 4.1e) argue against simple titanium encroachment from the core into the overgrowth.

Posttectonic hematite-after-magnetite (Plates 4.1c & 4.2d) and specular hematite are distinguished from primary forms of hematite (platy, subhed & serrate) by their lower titanium contents (Figure 4.1). Hematite-after-magnetite has TiO_2 abundances comparable to those of the magnetite it pseudomorphs.

Phlogopite occurs almost exclusively in hematite-rutile-bearing zone 1, whereas biotite predominates in magnetite-bearing samples from zones 2 and 3 (Figure 4.3). The occurrence of phlogopite in zone 1 is attributed to the higher oxidation state reflected by the predominant hematite and the presence of rutile. Zone 2 magnetite + hematite-bearing iron formation sample $18E_1$, contains micas which plot near the phlogopite-biotite boundary.

Chapter V

RARE EARTH ELEMENT CHEMISTRY

Introduction

In studies of clastic sedimentary rocks, relative abundances of rare earth elements (REEs) can be used to deduce their source (Piper, 1974; McLennan *et al.*, 1979; Taylor and McLennan, 1985). The main exceptions to this coherency include: (1) enrichment of light REEs in clay-size sediments due to extreme chemical weathering at the source rather than to source composition (e.g., Nesbitt *et al.*, 1990), and (2) the REEs which may deviate from the predominantly trivalent oxidation state of the group, namely, Ce (3^+, 4^+) and Eu (2^+, 3^+). For example, modern seawater, a plausible source of REEs to sediments, has variably negative Ce anomalies relative to the North American Shale Composite (NASC; Figure 5.1a). These anomalies are attributed primarily to the oxidation of Ce^{3+} and preferential incorporation of Ce^{4+} into Mn nodules; many of which have large positive Ce anomalies (Piper, 1974). Elderfield (1988) ascribed the 'variability' of seawater cerium anomalies to increasing removal of cerium (via oxidation) in the direction of deep-water flow. The transformable valence state of Eu is reflected in Figure 5.1b, in that Eu^{2+} is the most stable form of Eu in hydrothermal solutions until relatively high dilutions by seawater. Once Eu is oxidized to the trivalent state, it will function in a manner similar to other rare earth elements in the marine environment (e.g., Byrne *et al.*, 1988).

The current study focuses on the REE properties of chemically precipitated iron formation. As in clastic sedimentary rocks, iron formation REEs have been used (to a lesser degree) to elicit information about the medium within or from which they formed (i.e., seawater, hydrothermal fluid, mixture of the two; Fryer 1977a; Graf, 1978; Crocket and Bowins, 1985; Barrett *et al.*, 1988a; Dymek and Klein, 1988; Derry and Jacobsen, 1990).

Figure 5.1

(A) Comparison of rare earth element abundance patterns, normalized to average shale ($x10^{6}$), of the dissolved pool for river waters (from Figure 5.1c), Atlantic Ocean surface waters, and Atlantic and Pacific deep waters. From Elderfield *et al.* (1990).

(B) REE abundance patterns for typical North Atlantic seawater and East Pacific Rise hydrothermal fluid, both normalized to NASC. The REE patterns for three mixtures of these 'end-members' are also shown. From Dymek and Klein (1988).

(C) REE abundance patterns of river water filtrates normalized to average shale ($x10^{6}$). Numbers 1, 2 and 3 refer to the three types of river material analyzed, which include: particulate (1), colloidal (2) and dissolved (3). From Elderfield *et al.* (1990).

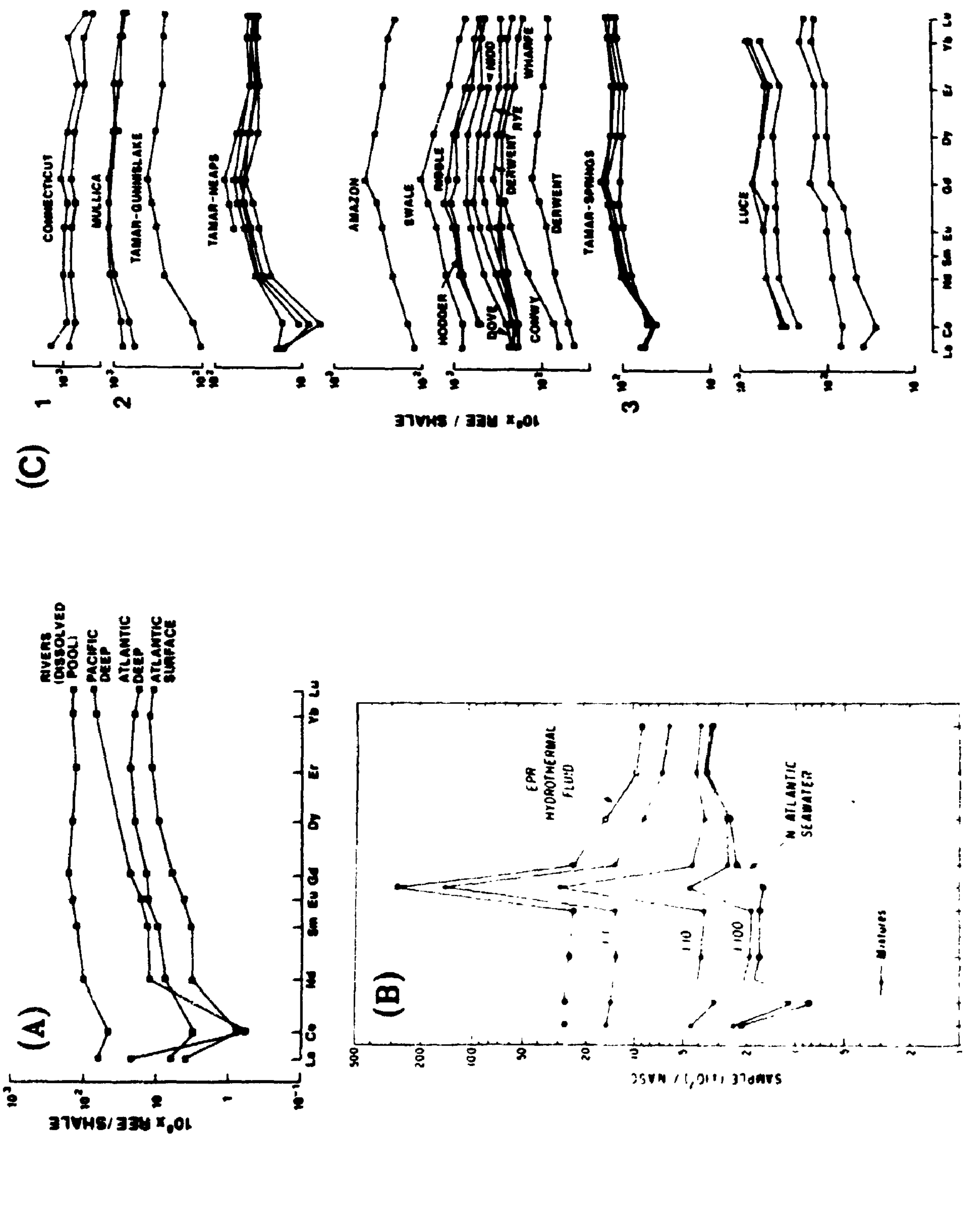
(A)
10^n x REE/SHALE
RIVERS (DISSOLVED POOL)
PACIFIC DEEP
ATLANTIC DEEP
ATLANTIC SURFACE
La Ce Nd Sm Eu Gd Dy Er Yb Lu
(B)
EPR HYDROTHERMAL FLUID
N ATLANTIC SEAWATER
1:10
1:100
Mixtures
SAMPLE (1:10) / NASC
(C)
10^n x REE / SHALE
CONNECTICUT
MULLICA
TAMAR-GUNNISLAKE
TAMAR-HEAPS
AMAZON
SWALE
RIBBLE
HODDER
DOVE
DERWENT
NIDD
NYE
WHARFE
CONWY
TAMAR-SPRINGS
LUCE

Analytical Method

Rare earth element abundances were procured by instrumental neutron activation analysis at the University of Western Ontario. The procedure followed that outlined by Jolly *et al.* (1992) and the analyzed elements included: La, Ce, Nd, Sm, Eu, Gd, Yb, Lu, Th and U. Individual aliquots, consisting of 250 - 300 g of powder, were irradiated for three hours in the reactor at McMaster University, Hamilton. Counting of gamma ray spectra occurred in two stages: La, Ce, Nd, Sm and U were counted one week after irradiation for 1,000 seconds; the remaining REE elements were counted four weeks after irradiation over a counting time of 100,000 seconds.

International standards MRG-1 and BHVO-1 (Govindaraju, 1989) were analyzed together with the other specimens to check the accuracy of the method. Accuracy, which is the relative error (from literature values) converted to percent, is a maximum -13.98 and +41.67 (Th of MRG-1; Lu of MRG-1) and a minimum -1.04 and +0.32 (Tb of BHVO-1; Sm of BHVO-1).

Rare Earth Element Abundances and Patterns

Six samples from zones 1 and 3 (Figure 2.1) were selected for REE analysis; the results of which are, together with a brief sample description, presented in Table 5.1. The four iron formation (IF) samples have Fe_2O_3 contents which range from 27.14 - 67.23% (Table 3.2). Two aliquots were analyzed from Fe siltstone sample $8A_L$, one of which was of the whole rock and the other a magnetite separate of approximately 77% Fe. Whole rock samples $12k_2$, $14o_2$ and $8A_L$ were analyzed together in the first of three lots. These samples were selected for their potential to host REEs based on their high apatite content (2.78 - 6.61% P_2O_5), and to alleviate concerns that a sample consisting solely of iron oxides may have REE abundances below detection limits, since oxides such as magnetite tend to contain only low to moderate REE concentrations (Graf, 1978).

Table 5.1 Rare earth element data and sample descriptions for Yudnamutana iron formation, carbonate (8P), Fe siltstone ($8A_L$) and magnetite separate ($8A_{L\,mag}$), together with those of Rapitan IF. Abundances in ppm. $(La/Yb)_N$, $(La/Nd)_N$, Ce^* and Eu^* are calculated relative to REE abundances in NASC (N) of Haskin *et al.* (1968).

Sample	La	Ce	Nd	Sm	Eu	Gd	Tb	Yb	Lu	(La/Yb)N	(La/Nd)N	Ce*	Eu*
12k2	22.12	62.20	47.64	13.54	3.17	12.89	1.77	3.18	0.44	0.67	0.48	0.90	1.07
14a3	4.22	9.11	4.94	1.23	0.35	1.38	0.29	1.91	0.30	0.21	0.88	0.91	1.17
14o2	17.21	38.35	24.20	6.60	1.89	7.50	1.30	3.45	0.50	0.48	0.73	0.87	1.17
913	8.00	17.12	7.50	1.53	0.38	1.45	0.30	1.51	0.27	0.51	1.10	0.97	1.12
8P	9.2	18.7	8.31	1.71	0.43	1.79	0.34	2.27	0.40	0.39	1.14	0.93	1.08
8AL	18.57	42.59	25.60	6.66	1.79	7.50	1.29	3.21	0.49	0.56	0.75	0.90	1.11
8ALmag	2.31	5.26	2.74	0.62	0.17	0.76	0.15	0.70	0.12	0.32	0.87	0.95	1.08
Rapitan iron formation (XRF, Fryer, 1977a)													
#5	0.949	1.14	0.716	0.171	0.045	0.24		0.86		0.11	1.37	0.58	0.95
#6	3.96	7.64	4.91	1.20	0.29	1.37					0.83	0.79	0.99

12k2 - hematite-quartz lutite iron formation, Dropstone Creek on Oraparinna
14a3 - jasper-hematite iron formation, section #20/14 on Holowilena South
14o2 - hematite-quartz lutite iron formation, section #20/14 on Holowilena South
913 - magnetite-hematite iron formation, south side of Razorback Ridge, Spring Dam
8P - carbonate-iron oxide layer within adit through Razorback Ridge, Spring Dam
8AL - Fe siltstone bed near mouth of adit, Razorback Ridge, Spring Dam
8ALmag - magnetite separate from previous Fe siltstone bed

#5 - banded hematite-chert iron formation, Snake River, Canada
#6 - pisolitic-cherty iron formation, Snake River, Canada

The REE analyses have been normalized relative to the North American Shale Composite (NASC) of Haskin *et al.* (1968), then plotted on Figure 5.2. The samples show light REE depleted patterns relative to NASC (N) with $(La/Nd)_N > 1$ for samples $9I_3$ and 8P, and $(La/Nd)_N = 0.48 - 0.88$ for the remaining. All analyses have $(La/Yb)_N$ ratios which lie between 0.21 and 0.67. The samples have negative Ce anomalies ($Ce^* < 1$) in which Ce^* is calculated as $Ce^* = 3Ce_N/(2La_N + Nd_N)$ (Goldstein and Jacobsen, 1988) and positive Eu anomalies ($Eu^* > 1.05$) wherein $Eu^* = Eu_N/(Sm_N + Gd_N)/2)$ (Derry and Jacobsen, 1990). Consideration of alternate methods of calculating Ce^* and analytical uncertainties may render the validity of the small negative Ce anomalies questionable. The consistency of a slightly negative Ce anomaly for samples of varied composition (cf. Ce* of Table 5.1) suggests that this anomaly is real.

<u>Discussion of Rare Earth Elements</u>

The aforementioned apatite-bearing samples $12k_2$, $14o_2$ and $8A_L$ are intermediate REE enriched relative to NASC (Figure 5.2). This convexity of the intermediate rare earth elements and the weakly negative Ce anomaly, are similar to the 'colloidal pool' patterns of modern river waters documented by Elderfield *et al.* (1990) and included herein as part of Figure 5.1c. Of the three pools presented in Figure 5.1c, particulate, colloidal and dissolved, only the colloidal pool shows convexity centred on the intermediate rare earth elements. Since iron typically has a colloidal form in the rivers studied by Elderfield *et al.* (1990, p. 977), it is appropriate to compare the whole rock pattern of $8A_L$ with that of the magnetite separate (77% Fe). The whole rock pattern is convex whereas that of the magnetite separate is not, which implies that the iron in sample $8A_L$ is not derived from river water iron colloids. Also, the negative cerium anomaly of the whole rock pattern (0.90) approximates that of the magnetite separate (0.95), which suggests that it is the iron oxides that are controlling the Ce anomaly rather than, for example, apatite [REE abundance relationships for apatite are:

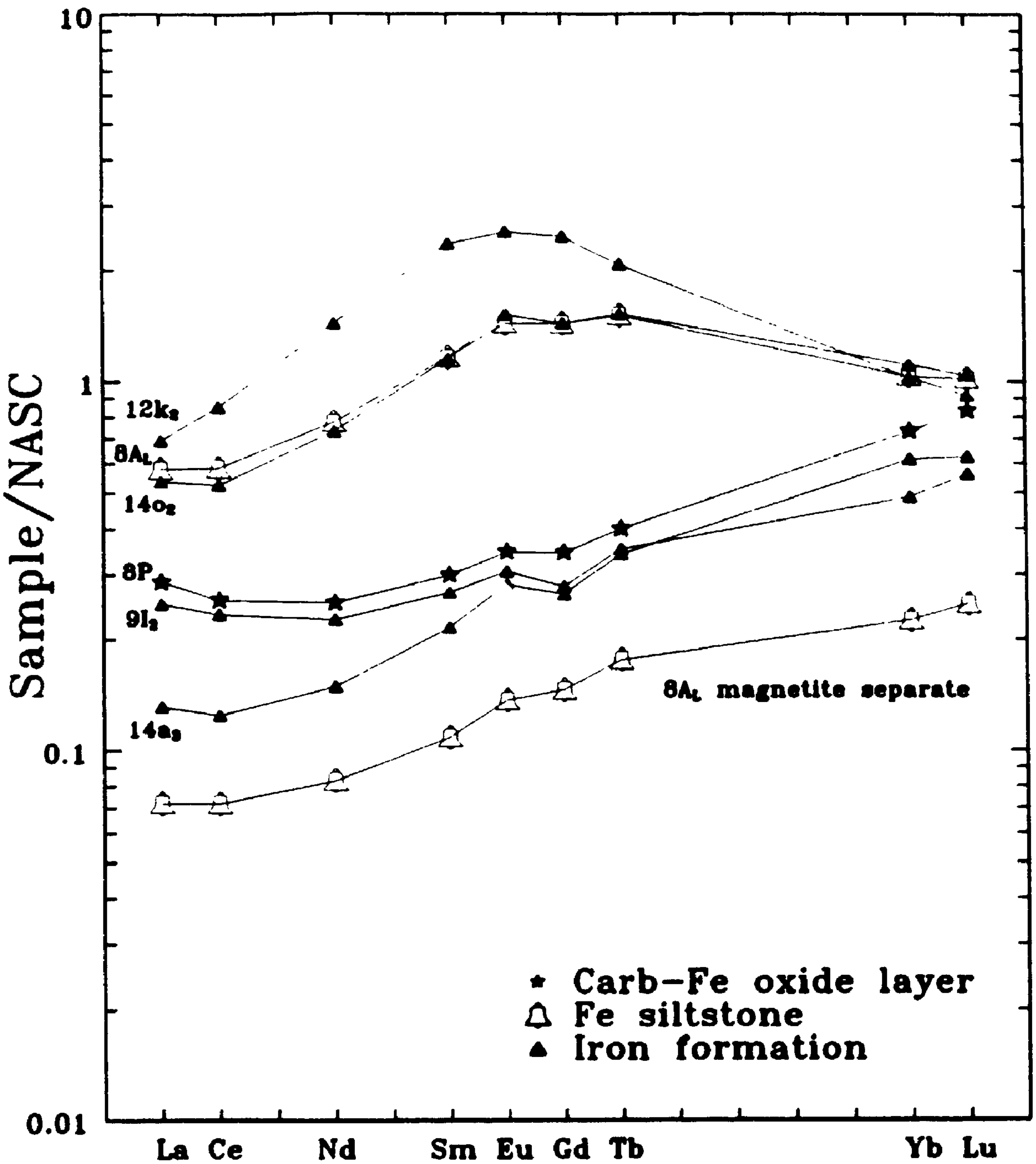

Figure 5.2 REE patterns of Holowilena IF (12k$_2$, 14a$_3$, 14o$_2$), Braemar IF (9l$_3$), and samples 8P and 8A$_L$, which were collected from beds interstratified with Braemar IF (Figure A.1).

Ce > Nd > Gd > Sm > La > Eu > Yb > Lu (Milodowski and Zalasiewicz, 1991, p. 112)]. For all three samples of $12k_2$, $14o_2$ and $8A_L$ there is no direct relationship between Ce and apatite content since P_2O_5 of $14o_2 > 12k_2 > 8A_L$, whereas Ce of $12k_2 > 8A_L > 14o_2$. The intermediate REE convexity of these three whole rock patterns is attributed to the presence of additional apatite in these samples relative to the others (cf. Plate 4.2a; Milodowski and Zalasiewicz, 1991).

In Figure 5.3, shale-normalized patterns of iron formation samples $14a_3$, $9I_3$ and magnetite separate $8A_L$ are compared with two other Neoproterozoic iron formations, a few recent shallow marine to lacustrine ferromanganese concretions and one Upper Triassic rift margin mudstone (Fe_2O_3 = 29.2%, MnO = 0.2%). Based primarily on the heavy REE enrichment, $14a_3$, $9I_3$ and $8A_{Lmag}$ are considered to be more comparable to the Urucum and Rapitan iron formations (Figure 5.3a) than to the hydrogenic ferromanganese samples (Figure 5.3b). All patterns in Figure 5.3a show $(La/Yb)_N < 1$, negative Ce anomalies and non to slightly positive Eu anomalies, whereas those of Figure 5.3b reveal $(La/Yb)_N > 1$ and variably positive and negative Ce/Eu anomalies.

The REE analyses of the two Rapitan iron formation samples (nos. 5 & 6, Fryer, 1977a) are included in Table 5.1. The pattern created from the analysis of #5 (Fryer, 1977b) has been compared to modern seawater (Figure 5.1a) by Derry and Jacobsen (1990) in which $(La/Yb)_N = 0.43$, $(La/Nd)_N > 1$ and the Ce anomaly is negative (average seawater of Goldstein and Jacobsen, 1988; NASC of Haskin *et al.*, 1968). A similar seawater comparison was made for the Urucum iron formation pattern, but it contains a slight positive Eu anomaly atypical of seawater (Derry and Jacobsen, 1990). The patterns generated in this study which most closely parallel modern seawater are those of $14a_3$, $9I_3$, 8P and $8A_{Lmag}$ in which $(La\backslash Yb)_N = 0.21 - 0.51$, $(La/Nd)_N = 0.87 - 1.14$ and $Ce^* < 1$ (Table 5.1). As in the Urucum iron formation, these four patterns have slight positive Eu anomalies ($Eu^* = 1.08 - 1.17$).

Figure 5.3A REE patterns of Neoproterozoic samples from the Yudnamutana Subgroup (Braemar & Holowilena IF, magnetite separate), and the Rapitan (Canada; Fryer, 1977a) and Urucum (Bolivia; Derry and Jacobsen, 1990) iron formations.

Figure 5.3B REE patterns of averaged shallow marine concretions (Gulf of Bothnia; Ingri and Pontér, 1987), a lacustrine concretion (Ontario; Calvert and Price, 1977), and an Upper Triassic rift margin mudstone (Turkey; Robertson and Boyle, 1983).

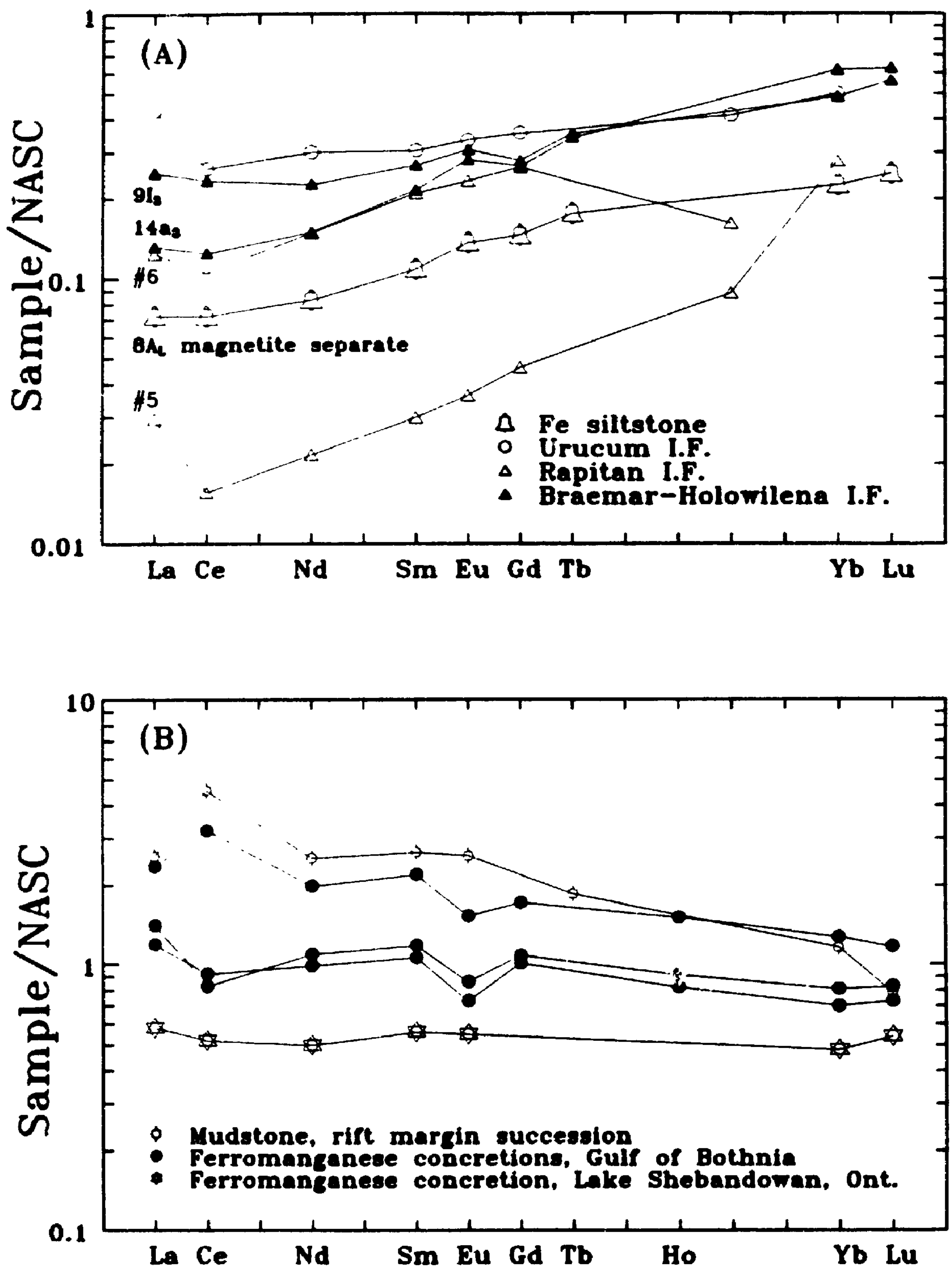
(A)
Sample/NASC
1
0.1
0.01
9Is
14a3
#6
8A1 magnetite separate
#5
Fe siltstone
Urucum I.F.
Rapitan I.F.
Braemar-Holowilena I.F.
La Ce Nd Sm Eu Gd Tb Yb Lu
(B)
Sample/NASC
10
1
0.1
Mudstone, rift margin succession
Ferromanganese concretions, Gulf of Bothnia
Ferromanganese concretion, Lake Shebandowan, Ont.
La Ce Nd Sm Eu Gd Tb Ho Yb Lu

Although such positive Eu anomalies deviate from the pattern for modern seawater, they are common in hydrothermal fluids (Figure 5.1b), hence these anomalies have been interpreted as evidence of hydrothermal input to the seawater from which iron formation of Archean, early and late Proterozoic age was deposited (Barrett *et al.*, 1988a; Dymek and Klein, 1988; Klein and Beukes, 1989; Derry and Jacobsen, 1990). For the late Proterozoic Yudnamutana samples, iron and phosphorous, which commonly occur together as iron oxide and apatite (see Chapter 4), are considered to be the main elements derived from a hydrothermal source. Much of the Ca (trace Mn) in sample 8P may also have a hydrothermal origin since this white-weathering, predominantly carbonate layer taken from within the adit has REE abundances and a pattern comparable to iron formation sample $9I_3$ (Fe_2O_3 = 67.23%) collected at the same locality (Table 5.1, Figure 5.4). These patterns, together with those of $14a_3$ and $8A_{Lmag}$ are in Figure 5.4 compared with recent trace element-poor hydrothermal deposits, which are most compositionally similar to sample $14a_3$. They include two hydrothermal crusts (Toth, 1980): Mn 1775 (Fe = 25.4%, Mn = 4.4%) from the Dellwood Seamount in the northeast Pacific and Mn 1777 (Fe = 38.1%, Mn = 1.5%) from the Mid-Atlantic Ridge, as well as two nontronite samples: N4 (Fe = 11.8%, Mn = 0.34%, Corliss *et al.*, 1978) and 506-6-2:24-25 (Fe_2O_3 = 28.85%, MnO = 0.04%, Barrett *et al.*, 1988b) from the Galapagos hydrothermal mounds. Nontronite is an iron-rich, aluminum-poor smectite.

Nontronite samples from the hydrothermal mounds located about 20 - 30 km south of the Galapagos Rift, have been compared to Archean (Dymek and Klein, 1988) and early Proterozoic (Klein and Beukes, 1989) iron formations. Despite the mineralogical differences between the recent and ancient deposits, these authors documented major, trace and rare earth element similarities between nontronite and typical banded iron formations. Hence shale-normalized REE patterns of two nontronite samples are here compared with the patterns of $14a_3$, $9I_3$, 8P and $8A_{Lmag}$ (Figure 5.4a).

Figure 5.4A REE patterns of samples from the Neoproterozoic Yudnamutana Subgroup and recent nontronites from the Galapagos mounds (N4, Corliss *et al.*, 1978; 506, Barrett *et al.*, 1988b).

Figure 5.4B REE patterns of samples from the Neoproterozoic Yudnamutana Subgroup and recent iron-rich hydrothermal crusts (Toth, 1980).

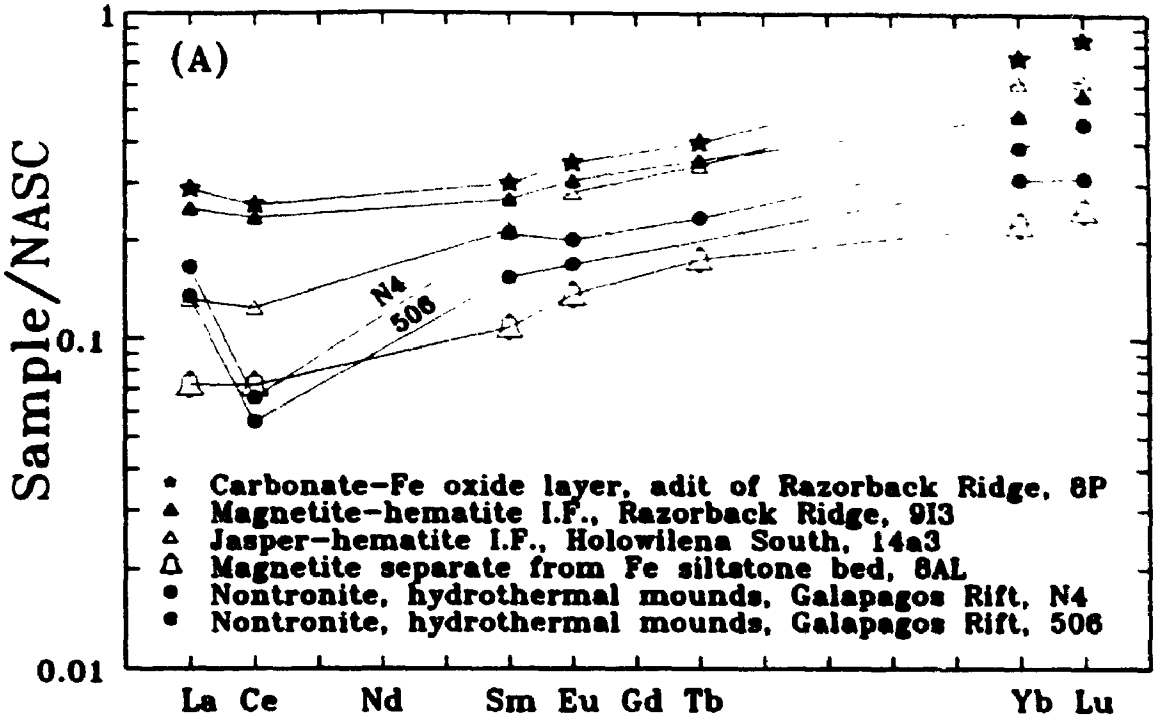
(A)
Sample/NASC
1
0.1
0.01
La Ce Nd Sm Eu Gd Tb Yb Lu
N4
506
Carbonate-Fe oxide layer, adit of Razorback Ridge, 8P
Magnetite-hematite I.F., Razorback Ridge, 9I3
Jasper-hematite I.F., Holowilena South, 14a3
Magnetite separate from Fe siltstone bed, 8AL
Nontronite, hydrothermal mounds, Galapagos Rift, N4
Nontronite, hydrothermal mounds, Galapagos Rift, 506

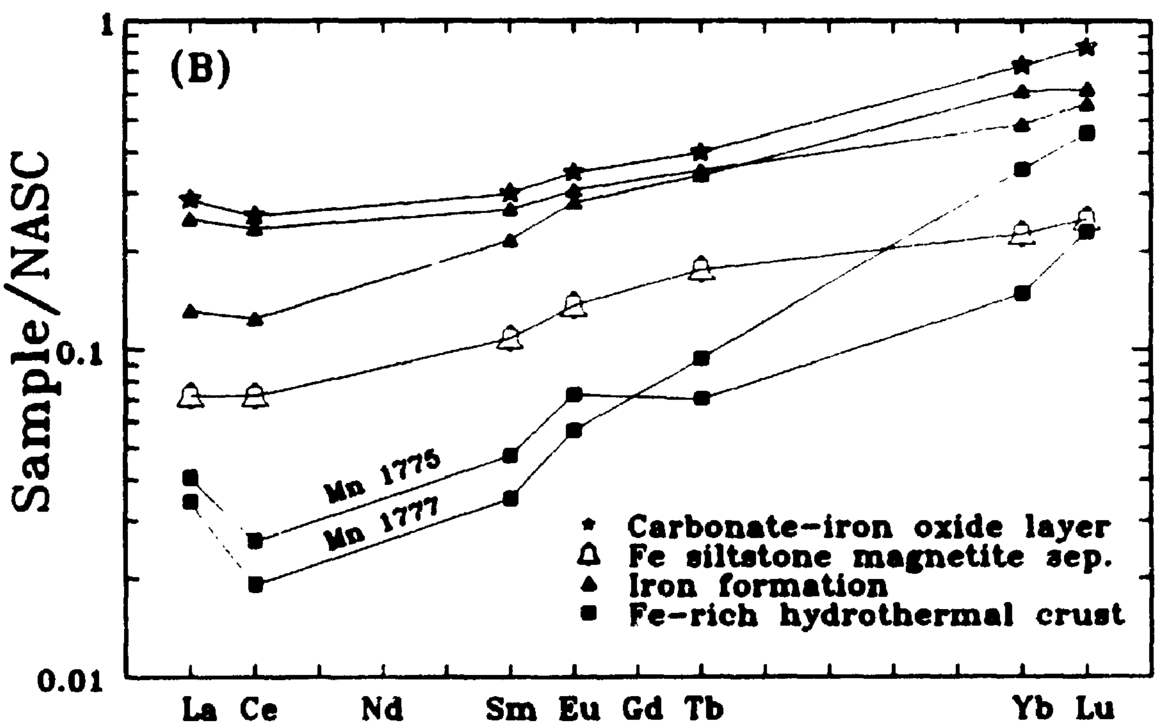
(B)
Sample/NASC
1
0.1
0.01
La Ce Nd Sm Eu Gd Tb Yb Lu
Mn 1775
Mn 1777
Carbonate-iron oxide layer
Fe siltstone magnetite sep.
Iron formation
Fe-rich hydrothermal crust

The nontronites with a $(La/Yb)_N$ ratio of 0.43 have comparable REE abundances and patterns to those of the Yudnamutana samples. The negative Ce anomaly is somewhat larger but this may be a function of the age difference (see below). The Ce anomaly of the relatively proximal hydrothermal nontronites is not as strongly negative as that of modern deep sea metalliferous sediments distal from the hydrothermal plume or ridge axis (Ruhlin and Owen, 1986; Barrett and Jarvis, 1988). However, the latter are considered more comparable to Archean, early and late Proterozoic banded iron formations studied by Derry and Jacobsen (1990) which have variable Ce anomalies (Ce^* averages 0.96). Derry and Jacobsen (1990, p. 2971) speculated that "the small negative Ce anomaly in late Proterozoic banded iron formations indicates the beginning of a global oxidative removal process for Ce (and possibly Mn) which was considerably less efficient than in the modern oceans." A parallel suggestion for the less negative Ce anomalies of nontronite relative to metalliferous sediments is that "nontronite may reflect precipitation from pore waters that were less oxidized than normal seawater thus allowing some Ce^{3+} to remain in solution" (Barrett *et al.*, 1988b, p. 851).

Although the depositional setting of the Neoproterozoic Yudnamutana IF is considered to differ from that of Galapagos nontronite, they are both characterized by an absence of hydrothermal alteration in the rocks which underlie or form the basement to these chemical sediments. For the Galapagos mounds, this has been utilized to support an interpretation of nontronite precipitation from low temperature ($\leq 25^\circ C$) hydrothermal fluids (Honnorez *et al.*, 1981). Iron oxide formation from equally cool hydrothermal solutions is envisaged for the Yudnamutana samples.

The shale-normalized patterns of iron-rich hydrothermal crusts are also deemed comparable to samples $14a_3$, $9I_3$, 8P and $8A_{Long}$ (Figure 5.4b). The crusts occur on the northernmost slope of the Dellwood Seamount, northeast Pacific (Mn 1775, Piper *et al.*, 1975) and around fissures on the Mid-Atlantic Ridge in the vicinity of the French-American Mid-Ocean Undersea Study (FAMOUS; Mn 1777, Toth, 1980). Unlike the aforementioned suggestion for the less negative Ce anomalies in nontronite, those of the iron-rich hydrothermal crusts have been attributed to mixing of rare earth elements from hydrogenous and hydrothermal sources (Fleet, 1983). This suggests that Ce^{4+} or CeO_2, which might normally accumulate in a strictly hydrogenous nodule, has been incorporated into the dominantly hydrothermal iron-rich crust. Such an interpretation cannot be entirely discounted for the small negative Ce anomalies observed in the Neoproterozoic patterns. In mixed hydrogenous and hydrothermal deposits, however, "the relative proportion of 'hydrothermal' REEs has to be high for the deposit to be depleted in Ce" (Fleet, 1983, p. 546).

Summary

The REE patterns for samples of iron formation ($14a_3$, $9I_3$), carbonate (8P) and magnetite separate ($8A_{Lmag}$) with $(La/Yb)_N = 0.21 - 0.51$, $(La/Nd)_N = 0.87 - 1.14$ and $Ce^* < 1$, show features similar to patterns of both modern seawater (Figure 5.1a & b) and recent hydrothermal deposits (Figure 5.4). The listed samples exhibit slight positive Eu anomalies ($Eu^* = 1.08 - 1.17$), which are atypical of seawater, but similar to hydrothermal, patterns. The anomalies are considered to result from the input of Eu-enriched hydrothermal fluids into seawater (Figure 5.1b). These fluids are considered to be the main source of Fe, P ($14a_3$, $9I_3$, $8A_L$, Plate 4.1b & f) and Ca (8P) to the samples.

The Neoproterozoic Urucum and Rapitan iron formations also have REE patterns comparable to those of seawater, hydrothermal deposits and samples $14a_3$, $9I_3$, 8P and $8A_{Lmag}$ (Figure 5.3a). Both the Urucum and Rapitan IFs are attributed to a hydrothermal source (Derry and Jacobsen, 1990; Yeo, 1981), but the Rapitan patterns do not exhibit an Eu anomaly. This suggests that, relative to Urucum and Yudnamutana samples, the Rapitan source fluids may have been more strongly diluted by seawater prior to IF deposition.

Ferromanganese concretions from shallow marine and lacustrine settings have REE patterns which contrast with those of samples $14a_3$, $9I_3$, 8P and $8A_{Lmag}$ (cf. Figure 5.3a & b). The hydrogenic concretion patterns differ due to: (1) an enrichment of light relative to heavy REEs $(La/Yb)_N > 1$, and (2) a non or negative Eu anomaly. The light REE enrichment is attributed mainly to the fractionation of Ce (i.e., Ce^{3+} to Ce^{4+}) and its preferential incorporation in hydrogenous deposits. In contrast, the Yudnamutana samples reflect the heavy REE enriched pattern of seawater (Elderfield and Greaves, 1982) and exhibit slight positive Eu anomalies indicative of hydrothermal input (Figure 5.1b). These observations support the conclusions of Fleet (1983), who stated that the REE contents of hydrothermal deposits appear to be incorporated in deposits from seawater without significant fractionation of the REEs from each other.

Chapter VI

DISCUSSION & INTERPRETATION

Introduction

Previously established interpretations which are intrinsic to this discussion include: (1) the major role of rifting in the evolution of the Adelaide geosyncline (Figure 1.8), (2) a chemically precipitated origin for the iron oxides (Chapter 4), and (3) REE patterns of iron formation resemble those of recent hydrothermal deposits (Chapter 5). The IF patterns show disparities with those of hydrogenic concretions, and hence the first of this three part chapter is a more extensive examination of the chemical attributes utilized to discriminate hydrogenous from hydrothermal deposits. The former are the result of precipitation from normal seawater, whereas the latter involve mixing of submarine exhaled fluids with seawater prior to precipitation. An in-depth comparison of shallow-weathering (subaerial or subaqueous) and deep-weathering (e.g., hydrothermal) sources of iron in IFs is provided by Kimberley (1989). The second part of this chapter complements the REE comparisons made amongst various Neoproterozoic IFs (e.g., Figure 5.3a), since it includes major and trace element data. The third and final portion of Chapter 6 is an interpretation of the five facies types described in Chapter 2.

Origin of the Iron

As discussed in Chapter 5, samples of iron formation (Braemar & Holowilena) have rare earth element abundances and patterns comparable to those of recent nontronite and iron-rich hydrothermal crusts (Figure 5.4). These deposits also show major element similarities with iron formation, which is manifested here as a clustering of nontronite, crusts and iron formation near the iron apex of an Fe-Mn-Al ternary plot (Figure 6.1). This diagram is based on the premise that in classical hydrothermal deposits, iron and

Figure 6.1 Al - Fe - Mn ternary plot for Holowilena & Braemar IF and associated high Fe_2O_3 diamictite matrices. Samples from the Red Sea goethite-amorphous (25) and iron montmorillonite (17) facies of Bischoff (1969) are also plotted. Inset diagram (right) shows compositional fields of various oceanic metalliferous-oxide sediments from Robertson and Boyle (1983). Shaded portion of small diagram at left depicts the field represented by the main plot.

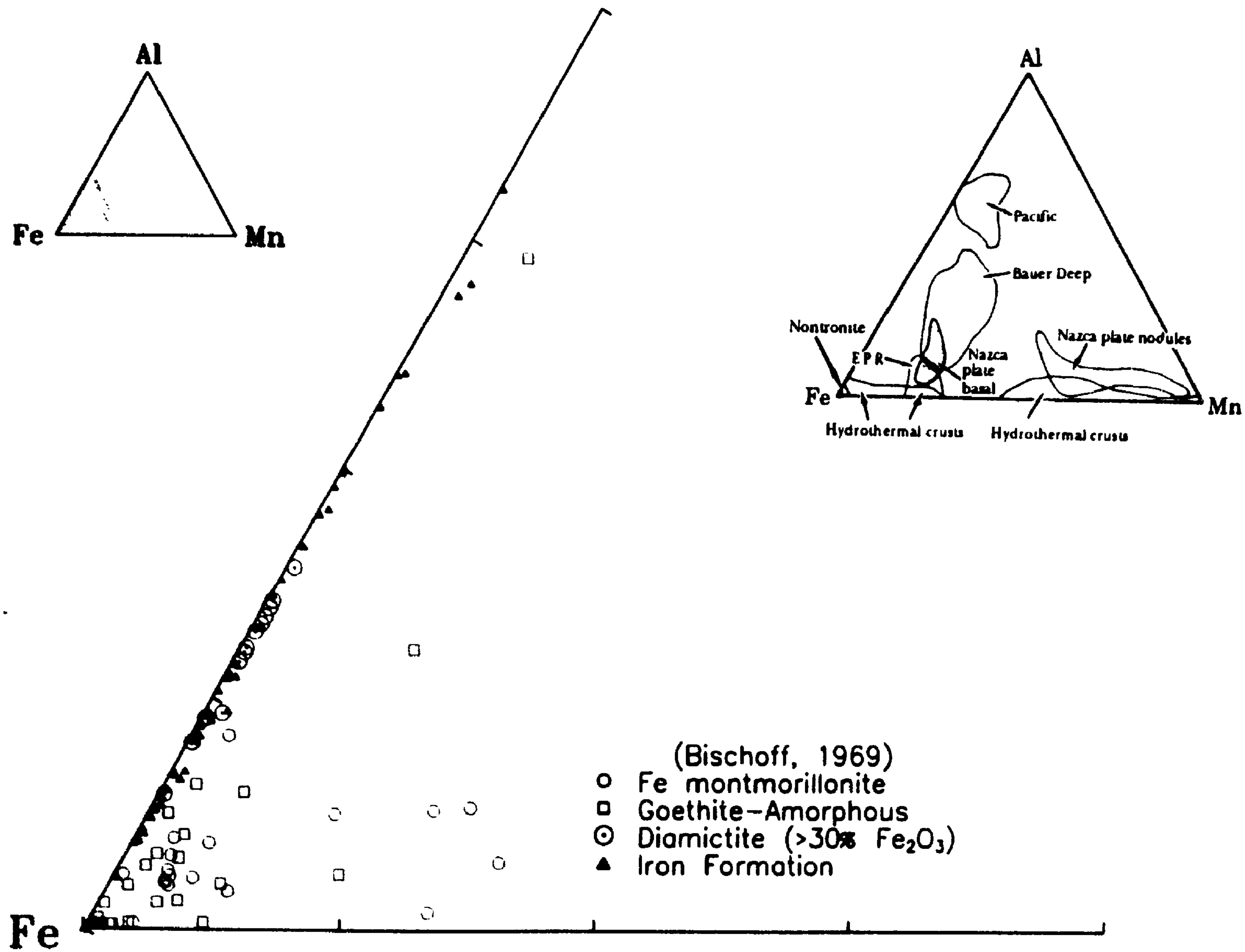
Al
Fe
Mn
Al
Pacific
Bauer Deep
Nontronite
EPR
Nazca plate basal
Nazca plate nodules
Fe
Mn
Hydrothermal crusts
Hydrothermal crusts
(Bischoff, 1969)
Fe montmorillonite
Goethite–Amorphous
Diamictite (>30% Fe2O3)
Iron Formation
Fe

manganese are well separated during precipitation, thus forming an iron- and a manganese-rich phase (e.g., Lalou, 1983). This fractionation is attributed to the more limited solubility of iron relative to manganese (Krauskopf, 1957), which results in iron precipitating first (close to the source) while manganese remains in solution. A possible reason for the range of Fe/Mn ratios present in the "hydrothermal crust" fields of Robertson and Boyle (1983; Figure 6.1) is that this ratio is extreme in early precipitates of Fe and Mn, then becomes variable in later deposits due to minor incorporation of hydrogenous Fe and Mn. Aluminum forms the third apex of Figure 6.1 since pure hydrothermal sediments contain very little Al (cf. Boström and Peterson, 1969).

The aluminum content of most iron formation samples is not as low as nontronite nor hydrothermal crusts, but is similar to that of the hydrothermal goethite-amorphous and Fe montmorillonite facies of the Red Sea (Bischoff, 1969; Figure 6.1). It is attributed to input of detrital Al; a factor which is also evident in the diamictite matrices (>30% Fe_2O_3). The Fe/Mn ratios of the modern Red Sea deposits are slightly lower than those of iron formation and diamictite, and slightly higher than those of the recent East Pacific Rise (EPR) metalliferous sediment field (Figure 6.1). Relative to the EPR sediments, the higher Fe/Mn ratio of the Red Sea facies can be attributed to deposition in a restricted brine pool, wherein conditions were sufficiently reducing that most Mn remained in solution (as Mn^{2+}) and was carried outside of the pool (cf. Bonatti *et al.*, 1972b, figures 4 & 5).

In Figure 6.2, the U and Th contents of the Red Sea (RSHBD) and EPR (EPRD) deposits are compared with those of the Neoproterozoic Yudnamutana and Rapitan samples analyzed for REEs (Table 5.1), and other marine sediments. Hydrogenous (MN) and pelagic sediments (OPS) accumulate at a slow enough rate to incorporate Th from seawater, whereas hydrothermal precipitates scavenge U from hydrothermal fluids (Bonatti, 1975). As a result, there are distinctly different U/Th ratios in hydrothermal, hydrogenous and pelagic sediments (Figure 6.2). The

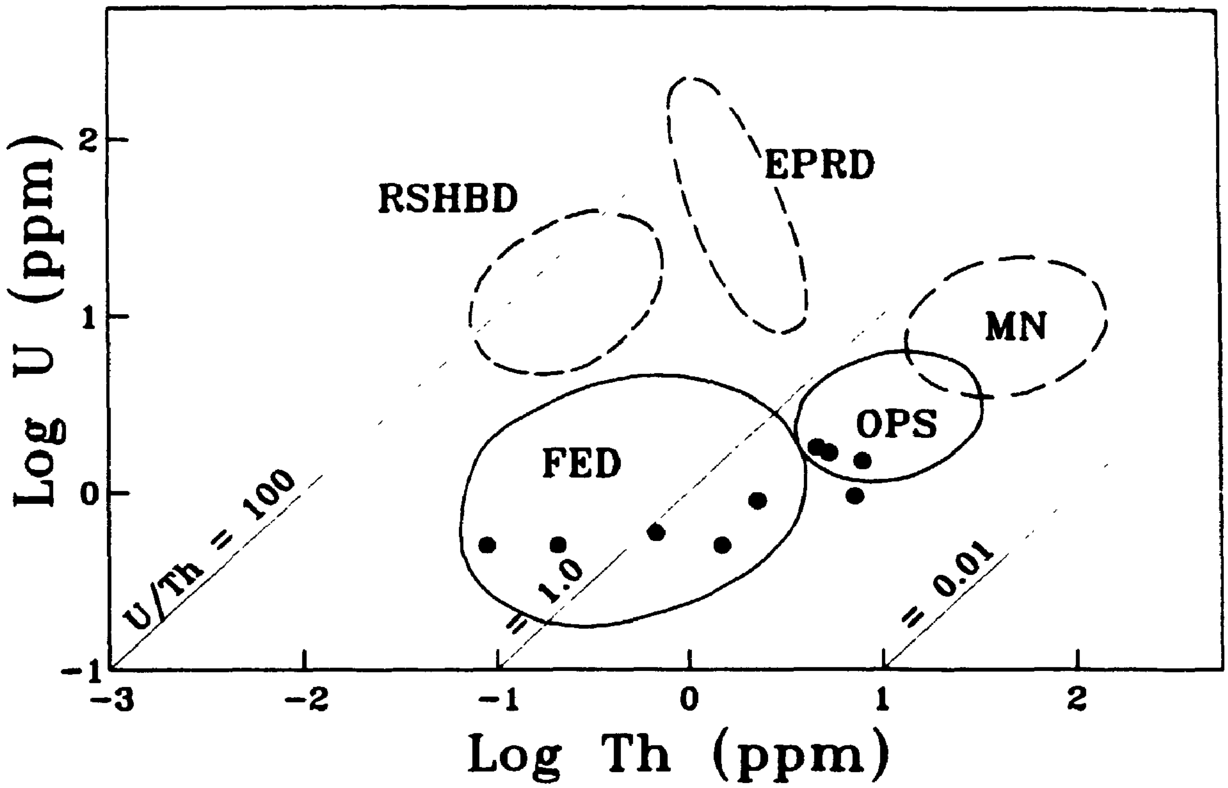

Figure 6.2 Relations between Th and U in the Yudnamutana and Rapitan samples analyzed for REEs (Table 5.1) superposed on diagram after Boström (1983). RSHBD = Red Sea hot brine deposits; EPRD = East Pacific Rise deposits; FED = Fossil exhalative deposits; OPS = ordinary pelagic sediments; MN = manganese nodules.

Neoproterozoic samples have U/Th ratios of 0.13 - 5.56, and plot within the fields of fossil exhalative deposits (FED) and ordinary pelagic sediments (OPS) as outlined by Boström (1983). The fossil exhalative field was defined by samples from the Pleistocene En Kafala deposit (Fe-Mn-Ba) of the Afar Rift, Ethiopia (Bonatti *et al.*, 1972a) and the Precambrian Långban deposit (Fe-Mn) of southern Sweden (Boström *et al.*, 1979). The occurrence of the Neoproterozoic samples within and near both the FED and OPS fields is attributed to deposition from hydrothermal fluids which have been strongly diluted by normal seawater (cf. Figure 5.1b).

At least some of the Yudnamutana samples plotted on Figure 6.2 are amongst the purest chemical sediments collected in this study (i.e., $14a_3$, $9I_3$, 8P and $8A_{Lmag}$, Table 3.2), hence seawater rather than detrital dilution is the suggested reason for sample positioning on the U-Th plot. However, as shown in Figures 3.2 - 3.5, chemically precipitated iron oxides are in many iron formation and diamictite samples diluted by detritally-hosted elements (e.g., Si, Al, K & Ti). As a means of testing for the presence of a hydrothermal component in these genetically mixed rocks, the Fe/Ti and Al/(Al+Fe+Mn) diagram established for this purpose by Boström (1973) was utilized to plot all iron formation and high Fe_2O_3 diamictite samples (Figure 6.3). Pure hydrothermal metalliferous sediments have high Fe/Ti ratios and, as mentioned earlier (p. 211), contain minimal Al. Contamination by either pelagic or terrigenous sediments causes dilution of the hydrothermal elements (Fe, Mn) and enriches detrital ones (Al, Fe, Ti). As a result, the Fe/Ti ratio decreases and the proportion of Al increases relative to Fe and Mn. This trend is represented by the solid curve in Figure 6.3, which is a mixing line of East Pacific Rise metalliferous sediment with terrigenous and pelagic sediment.

With the exception of the jasper-hematite iron formation sample $14a_3$, all of the iron formation and diamictite samples plot slightly below and subparallel to the mixing line (Figure 6.3). The occurrence of $14a_3$ between the EPR metalliferous and Galapagos

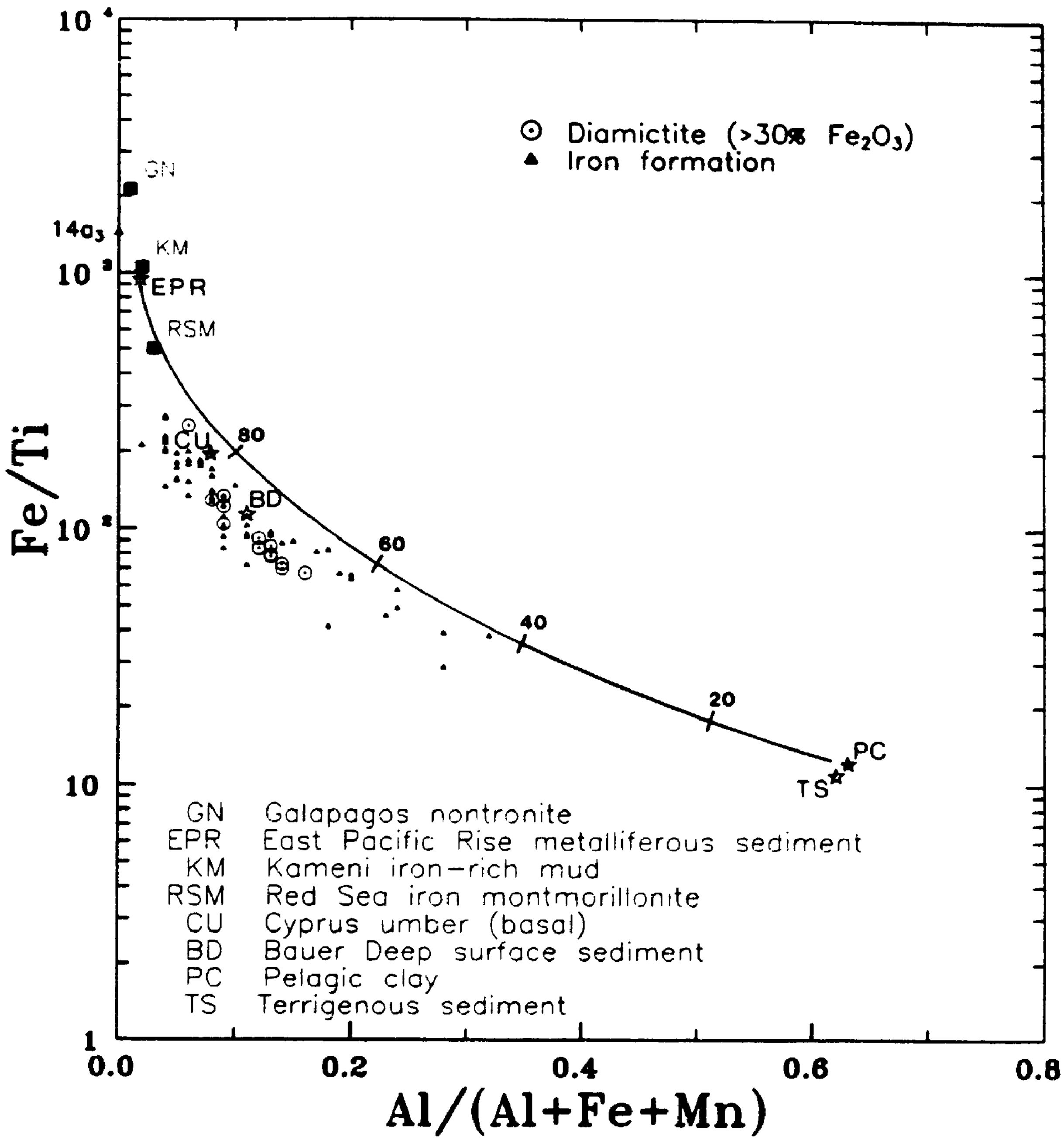

Figure 6.3 Composition of Holowilena and Braemar IF and associated high Fe_2O_3 diamictite matrices in terms of Al/(Al + Fe + Mn) vs. Fe/Ti. C· /e represents mixing of East Pacific Rise metalliferous sediment with terrigenous sediment. Diagram modified from Barrett (1981). Added data points include: GN = avg. 5 samples (Barrett *et al.*, 1988b); KM = avg. 25 samples (Boström and Widenfalk, 1984); RSM = avg. 17 samples (Bischoff, 1969).

nontronitic sediments suggests that it is the least detritally contaminated sample and most like a hydrothermal sediment. The other samples plot in the vicinity of basal Cyprus umbers (Tethyan iron-rich mudstones) and Bauer Deep surface sediments (ferromanganoan), both of which contain hydrothermal iron (Robertson and Hudson, 1973; Sayles and Bischoff, 1973). Based on the mixing line of Figure 6.3, these samples contain between 50 and 85 percent hydrothermal material. However, since the mixing curve was established from modern deposits, these numbers are regarded only as approximations.

The iron formation and high Fe_2O_3 diamictite samples may reflect mixing of hydrothermal and detrital material in Figure 6.4, since they occupy the area intervening between the hydrothermal and pelagic fields. This Zr/Cr and Y/P_2O_5 diagram was created by Marchig *et al.* (1982) for distinguishing amongst hydrothermal, deep-sea (pelagic) and hydrogenous metalliferous (diagenetic) sediments. Marchig *et al.* (1982) explained this separation by noting that phosphorous and yttrium, both derived from biogenous apatite, show a positive correlation in pelagic and diagenetic metalliferous sediments. They become enriched during diagenesis due to the insolubility of apatite in alkaline solutions. However, in hydrothermal sediments, there is little or no correlation between P and Y, since P is extracted via leaching and coprecipitated with iron without inclusion of Y. Hence P may be enriched in hydrothermal sediments. Marchig *et al.* (1982) observed a significant positive correlation between Zr and Cr in pelagic and diagenetic metalliferous sediments since both elements occur in detrital material. In hydrothermal sediments, Cr, but not Zr, is enriched in hydrothermal precipitates. Therefore, an increase in Cr does not coincide with an increase in Zr and Zr/Cr ratios are more restricted.

As shown in Figure 3.27a, there is a weak positive correlation between Zr and Cr for samples of iron formation and high Fe_2O_3 diamictite. This is attributed to contamination of the hydrothermal precipitates by clastic detritus, and as a result, these

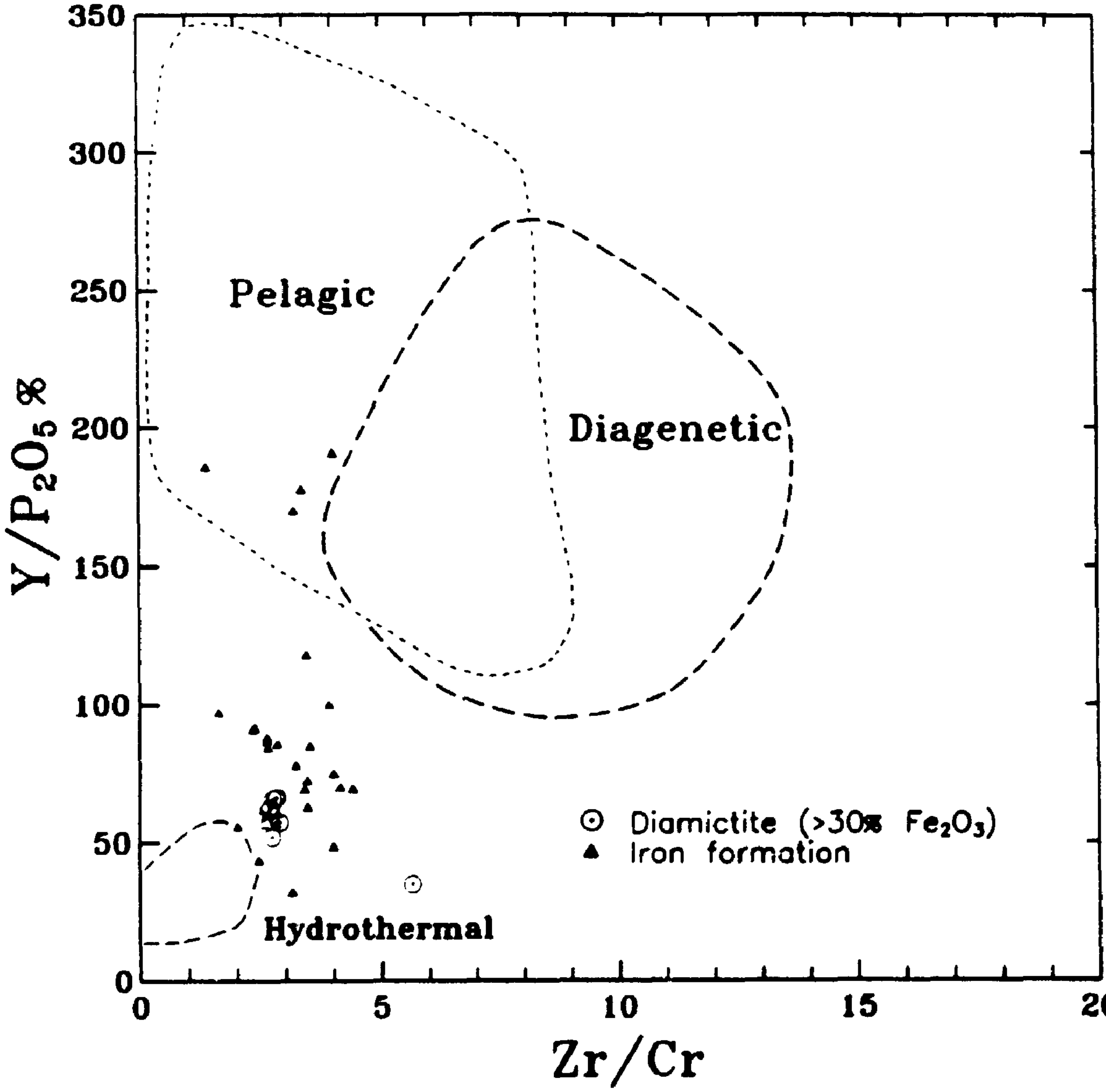

Figure 6.4 Zr/Cr vs. Y/P_2O_5 plot of Braemar IF and associated high Fe_2O_3 diamictite matrices (zone 3, Figure 2.1). Pelagic, diagenetic metalliferous, and hydrothermal metalliferous compositional fields are based on data of Marchig *et al.* (1982). Field outlines after Wonder *et al.* (1988).

samples have Zr/Cr ratios which are slightly higher than those of the hydrothermal field (Figure 6.4). With respect to the Y/P_2O_5 ratio, the majority of samples plot closest to the hydrothermal field, which together with the occurrence of magnetite-apatite grain pairs and apatite inclusions in hematite (e.g., Plate 4.1d & f), suggests that the phosphorous is hydrothermally derived and coprecipitated with iron oxide as apatite.

Summary. The Neoproterozoic iron formation samples show geochemical similarities to modern hydrothermal deposits, but no single type of recent sediment is completely comparable. For example, nontronite and iron-rich crusts reveal REE abundances and patterns like those of iron formation (Figure 5.4), however, nontronite and iron-rich crusts have virtually no detrital aluminum and hence plot closer to the iron apex of Figure 6.1. The goethite-amorphous and iron montmorillonite facies of the Red Sea show localized mixing with the detrital facies (Bischoff, 1969) which is similar to iron formation, but the goethite-amorphous and iron montmorillonite facies have a broader range of manganese content (Figure 6.1), higher amounts of uranium (Figure 6.2) and shale-normalized REE patterns with strong positive Eu anomalies (e.g., Fleet, 1983, figure 15). Iron-rich hydrothermal muds from the Kameni Islands at Santorini, Greece probably have Mn (<0.1%) and trace element contents (Boström and Widenfalk, 1984) most comparable to the iron formation samples (Tables 3.2 & 3.9), however, detrital elements such as Ti and Al are relatively low in these shallow marine volcanic muds (Figure 6.3). Unlike the Red Sea, in which brine pool conditions were sufficiently reducing to allow most of the Mn to remain in solution and be carried away (Bonatti *et al.*, 1972b), the hydrothermal solutions at Kameni never contained much Mn (Boström and Widenfalk, 1984). The solutions which formed the iron formation may also have been originally Mn-poor since Mn averages 0.07% in the iron formation proper (Table 3.2) and is only a minor component of ankerite-bearing laminae within the iron formation (Figure 4.5). Iron and phosphorous (Plate 4.1d & f, Figure 6.4) are the most evident precipitates from hydrothermal fluids that have been diluted by normal seawater (cf. Figures 5.1b & 5.3a; Figure 6.2).

Geochemical comparison of Yudnamutana IF with other Neoproterozoic IFs

Introduction. As emphasized by Yeo (1984, 1986) and Maynard (1991), there is a global association of Neoproterozoic iron formation with sedimentary rocks of glacial origin. This glacial association provides a basis for comparing the geochemistry of the Holowilena and Braemar iron formations (Yudnamutana IF) with that of two other Neoproterozoic iron formation-bearing intervals. The other Neoproterozoic IFs for which detailed geochemical studies exist occur within two geographically distant stratigraphic sequences, namely:

i) the sedimentary (glacigenic) and volcanic (amphibolite) sequence of the Chuos Formation, Namibia, South West Africa (Henry *et al.*, 1986; Breitkopf, 1988; Bühn *et al.*, 1992); and

ii) the glacial-marine sedimentary sequence of the Rapitan Group (Sayunei and Shezal iron formations), which straddles the Yukon-Northwest Territories boundary, Canada (Yeo, 1981, 1984, 1986).

Chuos Formation. The Chuos Formation consists primarily of diamictite, quartzite, amphibolite and iron formation. Breitkopf (1988) described two main categories of Chuos IF: diamictite- and amphibolite-associated, which he further divided into diamictite-associated, amphibolite-associated type 1 and amphibolite-associated type 2 (Figure 6.5). The iron formation horizons within diamictite (magnetite-quartz) and amphibolite (type 1, magnetite-quartz or hematite-quartz) are pure chemical sedimentary rocks, whereas the amphibolite-affiliated type 2 IF is a mixture of chemical precipitates and volcanic detritus (magnetite-quartz-silicate$\pm$carbonate). Breitkopf (1988) considered all three forms of Chuos iron formation to have a hydrothermal exhalative origin.

The Ti/Fe vs. V/Fe diagram of Figure 6.5 was used by Loberg and Horndahl (1983) to differentiate amongst apatite iron ore (V > 100 ppm) and titaniferous iron ore

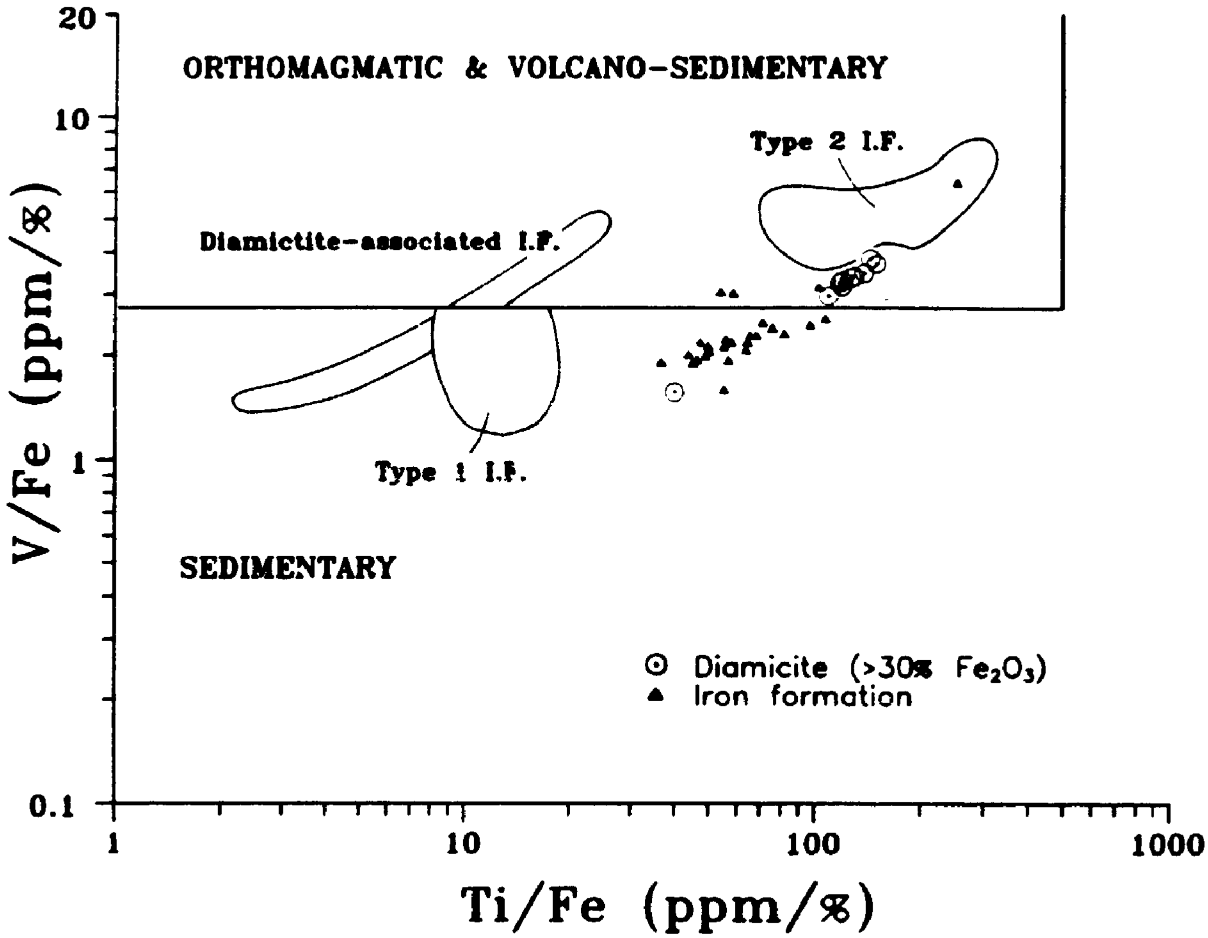

Figure 6.5 Ti/Fe vs. V/Fe plot of Braemar IF and associated high Fe_2O_3 diamictite matrices (zone 3, Figure 2.1) together with compositional fields of Chuos iron formation (diamictite-associated IF, type 1 IF and type 2 IF). Diagram after Lohberg and Horndahl (1983) and Breitkopf (1988).

(Ti > 10,000 ppm) of orthomagmatic origin, and banded iron formation of sedimentary origin (V/Fe < ≈2.75). Breitkopf (1988, figure 13) included a volcano-sedimentary field with that of the apatite iron ores and designated it as the "orthomagmatic & volcano-sedimentary" field (Figure 6.5). The Braemar IF and high Fe_2O_3 diamictite samples occupy a position intermediate between the strictly chemical iron formations of the Chuos Formation (diamictite-associated and amphibolite-associated type 1) and those of a mixed chemical-volcanogenic origin (amphibolite-associated type 2). The Braemar IF has V/Fe ratios similar to those of the diamictite-associated and type 1 IFs, however, it has higher Ti/Fe ratios which suggest that the Braemar IF is not as pure as the diamictite-associated and type 1 IFs. More comparable to type 2 IF are the high Fe_2O_3 diamictite matrices, which generally have similar Ti/Fe, but lower V/Fe, ratios. Both the diamictite matrices and type 2 IF contain clastic detritus, however, there is no apparent evidence to suggest that the detritus within the diamictite matrices has a volcanogenic origin (Table 2.1).

Recalculated and averaged major element analyses for the Neoproterozoic IFs and high Fe_2O_3 diamictite matrices are listed in Table 6.1 and plotted (IFs only) on Figure 6.6. Of the seven different IFs, the amphibolite-associated type 2 IF has the highest Al, Mg, Ca, Na and Ti content, which reflects the added volcanic material (Breitkopf, 1988). Type 2 IF has percentages of Fe, Si, Al, Mg and Ca very similar to those of Holowilena IF. All three of Al, Mg and Ca are in Holowilena IF and high Fe_2O_3 diamictite matrices hosted primarily by clastic detritus or the metamorphosed equivalent (zone 1 samples of Figures 3.7, 3.8 & 3.16). The amphibolite-associated type 1 IF has the highest Fe and lowest Si with Fe/Si = 3.72, whereas the second highest Fe/Si ratio (2.34) is that of the Braemar IF. The former ratio reflects high amounts of chemically precipitated iron oxides relative to chemically precipitated quartz (Breitkopf, 1988), whereas the latter ratio represents high amounts of chemically precipitated iron oxides relative to detrital silicates (IF of zones 2 & 3 in Figures 3.2 -

Table 6.1 Recalculated and averaged oxide analyses of Neoproterozoic iron formations from the Yudnamutana Subgroup (Table 3.2), Rapitan Group (Yeo, 1986), and Chuos Formation (Breitkopf, 1988). High Fe_2O_3 (>30%) diamictite matrices from the Yudnamutana Subgroup (Table 3.1) are included. Elemental percentages were derived from the recalculated and averaged oxide analyses. Yudnamutana Subgroup samples 12q, 13d$_2$, 17d and 8r$_2$ were removed from the Holowilena and Braemar IF averages, since their Fe_2O_3 contents are slightly less than the 21.5% required for an IF.

	Yudnamutana IF		Rapitan IF		Chuos iron formation			Yudnamutana 'IF'	
	Holowilena	Braemar	Sayunei	Shezal	Chuos Dia IF	Chuos type 1	Chuos type 2	Holo Fe diamictite	Braemar Fe diamictite
SiO2	47.61	34.10	53.31	42.55	57.08	26.51	46.12	44.32	45.10
Fe2O3	34.50	53.42	36.09	49.84	38.74	65.94	35.37	36.62	38.13
Al2O3	6.55	5.10	5.27	2.15	1.26	1.72	7.11	4.66	6.90
MgO	2.23	2.43	2.37	0.90	0.08	0.42	2.37	5.93	2.59
MnO	0.03	0.11	0.10	0.17	0.12	0.09	0.18	0.07	0.12
CaO	4.26	2.14	1.04	3.59	1.78	2.92	4.64	6.48	3.47
Na2O	0.11	1.11	0.46	0.00	0.11	0.55	2.61	0.17	1.01
K2O	2.37	0.77	0.69	0.03	0.43	0.11	0.15	0.94	1.70
TiO2	0.39	0.43	0.47	0.24	0.04	0.08	0.64	0.37	0.50
P2O5	1.95	0.36	0.21	0.54	0.37	1.66	0.81	0.44	0.48
Si	22.26	15.94	24.92	19.89	26.68	12.39	21.56	20.72	21.09
Fe	24.13	37.36	25.24	34.86	27.09	46.12	24.74	25.61	26.67
Al	3.47	2.70	2.79	1.14	0.67	0.91	3.77	2.47	3.65
Mg	1.34	1.47	1.43	0.54	0.05	0.25	1.43	3.58	1.56
Mn	0.02	0.09	0.08	0.13	0.09	0.07	0.14	0.05	0.09
Ca	3.05	1.53	0.75	2.57	1.27	2.09	3.32	4.63	2.48
Na	0.08	0.82	0.34	0.00	0.08	0.41	1.94	0.13	0.75
K	1.97	0.64	0.57	0.02	0.35	0.09	0.13	0.78	1.41
Ti	0.23	0.26	0.28	0.14	0.02	0.05	0.38	0.22	0.30
P	0.85	0.16	0.09	0.23	0.16	0.72	0.35	0.19	0.21
Fe/Si	1.08	2.34	1.01	1.75	1.02	3.72	1.15	1.24	1.26
# of samples	(18)	(34)	(6)	(7)	(4)	(3)	(7)	(3)	(11)

Figure 6.6 Plot of recalculated and averaged elemental percentages (Table 6.1) for Neoproterozoic iron formations from the Yudnamutana Subgroup (Holowilena & Bramar IF), Rapitan Group (Sayunei & Shezal IF), and Chuos Formation.

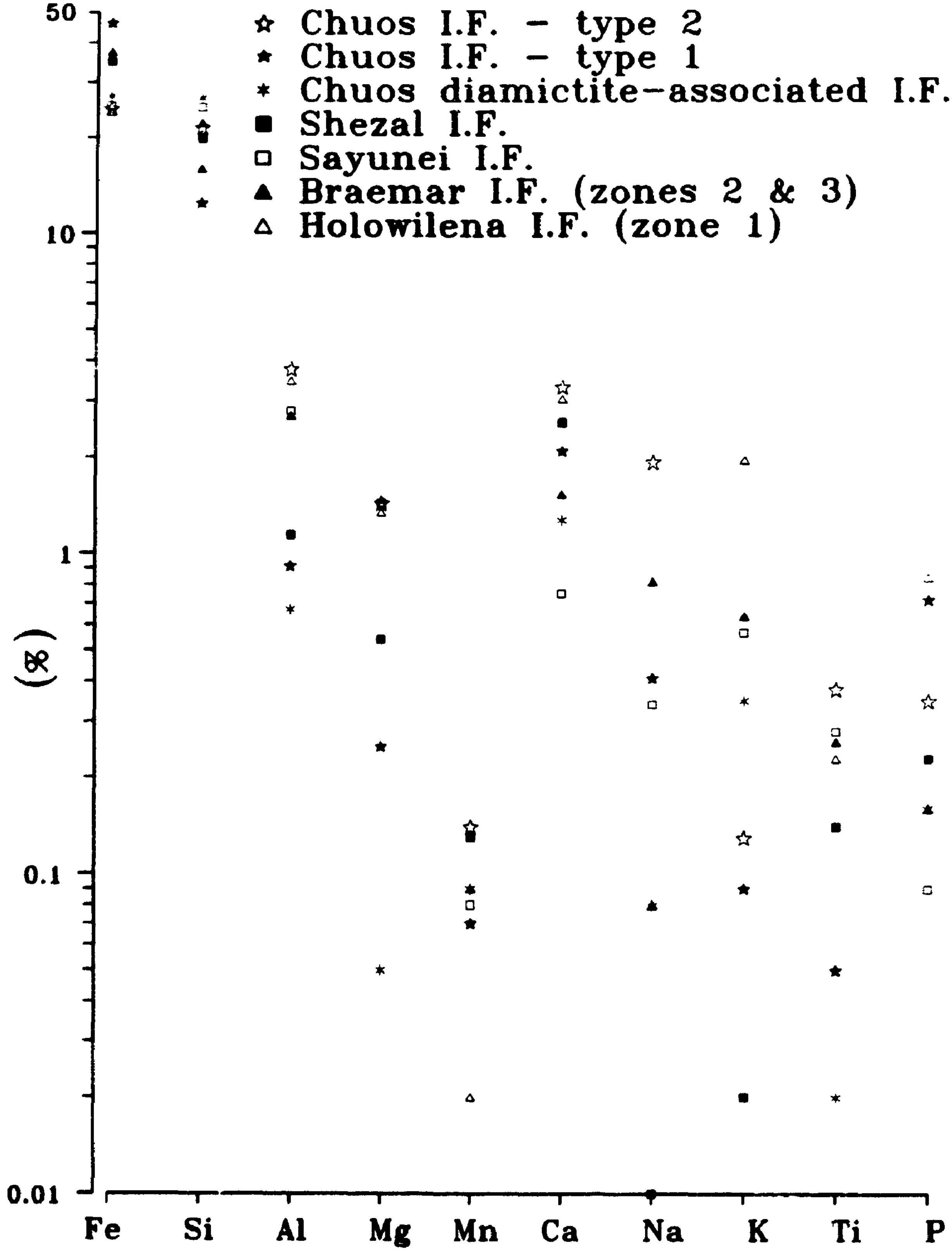
50
10
1
0.1
0.01
(%)
Chuos I.F. - type 2
Chuos I.F. - type 1
Chuos diamictite-associated I.F.
Shezal I.F.
Sayunei I.F.
Braemar I.F. (zones 2 & 3)
Holowilena I.F. (zone 1)
Fe
Si
Al
Mg
Mn
Ca
Na
K
Ti
P

3.5). Type 1 IF has a phosphorous content most comparable to that of the Holowilena IF, which has the highest P of all averaged sample types (Table 6.1). Phosphorous occurs as apatite in both these iron formations and as previously mentioned (p. 183), is considered to have a hydrothermal exhalative origin in all three forms of Chuos IF (Breitkopf, 1988). The disseminated apatite within the Holowilena IF may also have a hydrothermal origin, however, the bedding-parallel apatite-rich lenses (Plate 4.2a) reflect at least some diagenetic addition of apatite. This additional apatite may represent a seawater source of phosphorous, which was enriched during diagenesis due to the extreme insolubility of apatite in alkaline solution.

Rapitan Group. Within the Rapitan Group of northwestern Canada, the two successive formations which host iron formation are the Sayunei (upper) and Shezal (lower) Formations (Yeo, 1981, 1984, 1986). The Sayunei Formation consists of "resistant maroon rhythmites with minor conglomerate, sandstone and mixtite", whereas the overlying Shezal Formation comprises "relatively recessive, maroon or greenish-grey, pebble-siltstone mixtites" (Yeo, 1986, p. 144). Laminated hematite and jasper is the common form of iron formation in both the upper part of the Sayunei Formation, and the lower part of the Shezal Formation. Hematite femicrite iron formation, in which silt-size clastic detritus is locally present, also occurs in the upper part of the Sayunei Formation. The hematite mixtites are rarely sufficiently iron-rich to be deemed iron formation. As in the Chuos IF, iron formation of the Rapitan Group is considered to have a hydrothermal origin (Yeo, 1981).

Recalculated and averaged major element analyses for the Sayunei and Shezal IFs (Yeo, 1984, 1986) are included in Table 6.1 and Figure 6.6. The Sayunei IF has Fe and Si contents (Fe/Si = 1.01) very comparable to those of Holowilena IF (Fe/Si = 1.08), whereas the Shezal IF has Fe and Si contents (Fe/Si = 1.75) more resemblant of Braemar IF (Fe/Si = 2.34). For the Rapitan IFs, the Fe/Si ratios mainly reflect the proportions of chemical precipitates (hematite:jasper), but for the Yudnamutana IFs, these ratios are a measure of chemically precipitated iron oxides relative to detrital silicates (Figures 3.2 - 3.5). With respect to Al and K contents, which are considered partial measures of clastic material, the amount of Al in Shezal IF < Braemar IF ≈ Sayunei IF < Holowilena IF and the amount of K in Shezal IF < Sayunei IF ≈ Braemar IF < Holowilena IF. The Rapitan IFs have lower Ca contents than those of the Yudnamutana, which reflects local development of diagenetic carbonate in Rapitan IF (Yeo, 1986), as opposed to the more widespread occurrence of clastic carbonate grains in the Yudnamutana IF. Both the Rapitan IFs and the Holowilena IF have lower Na contents than the Braemar IF. As suggested on p. 145, the higher amounts of Na in Braemar IF of zone 3 at least (Figure 3.15b), may be due to albitization by seawater.

The above-mentioned comparisons of averaged Fe, Si and Al contents for the Holowilena, Braemar, Sayunei and Shezal iron formations are also evident on a Si-Fe-Al ternary plot of individual samples (Figure 6.7a). The Braemar and Shezal IFs generally plot closer to the Fe, rather than the Si, apex, whereas the Holowilena and Sayunei IFs cluster midway between the Si and Fe apices. The Holowilena IF typically has the highest Al content, the Braemar and Sayunei IFs have moderate amounts of Al, and the Shezal IF generally has the lowest Al content. All four types of IF, along with the high Fe_2O_3 diamictites, plot within or close to the iron formation compositional field of James (1969; Figure 6.7). Comparison of Figure 6.7a & b also reveals that the Braemar and Shezal IFs show similarities with two of the three averaged analyses of Red Sea hydrothermal deposits. These include the bottom sediment of James (1969) and the iron montmorillonite facies of Bischoff (1969). One sample of Shezal IF resembles the averaged analysis of the Red Sea goethite-amorphous facies. On Figure 6.8, most of the Holowilena and Sayunei IF samples plot within the field of Galapagos nontronite. These geochemical similarities between Neoproterozoic iron formations and modern hydrothermal deposits lend support to a hydrothermal interpretation for the Rapitan IF (Yeo, 1981) and the Yudnamutana IF (Yeo, 1984, 1986; p. 217 of this thesis).

Figure 6.7A Al - Si - Fe ternary plot for Neoproterozoic iron formations from the Yudnamutana Subgroup (Holowilena & Braemar IF) and Rapitan Group (Sayunei & Shezal IF). Inset diagram shows compositional fields of ironstone and iron formation together with averaged (4 analyses) Red Sea sediment (from James, 1969).

Figure 6.7B Al - Si - Fe ternary plot for Holowilena and Braemar IF and associated high Fe_2O_3 diamictite matrices, compared with averaged analyses of the Red Sea goethite-amorphous (27) and iron montmorillonite (17) facies of Bischoff (1969).

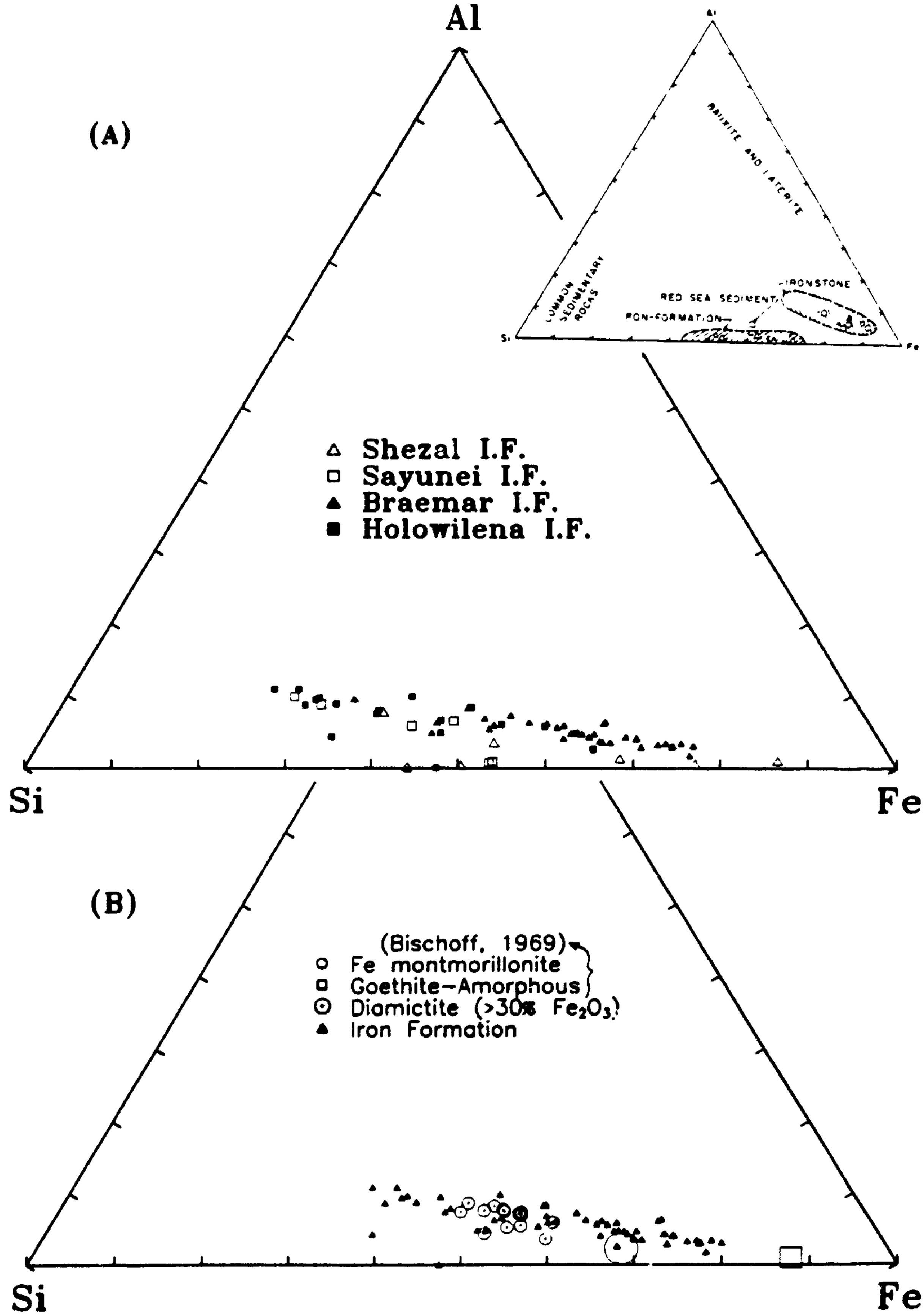
Al
(A)
Si
Fe
BAUXITE AND LATERITE
COMMON SEDIMENTARY ROCKS
IRONSTONE
RED SEA SEDIMENT
Shezal I.F.
Sayunei I.F.
Braemar I.F.
Holowilena I.F.
Si
Fe
(B)
(Bischoff, 1969)
Fe montmorillonite
Goethite–Amorphous
Diamictite (>30% Fe_2O_3)
Iron Formation
Si
Fe

Figure 6.8 Si - Fe - Mnx10 ternary plot for Neoproterozoic iron formations from the Yudnamutana Subgroup (Holowilena & Braemar IF) and Rapitan Group (Sayunei & Shezal IF). Inset diagram (right) shows compositional field of nontronite from the Galapagos mounds (from Corliss *et al.*, 1978). Shaded portion of small diagram at left depicts the field represented by the main plot.

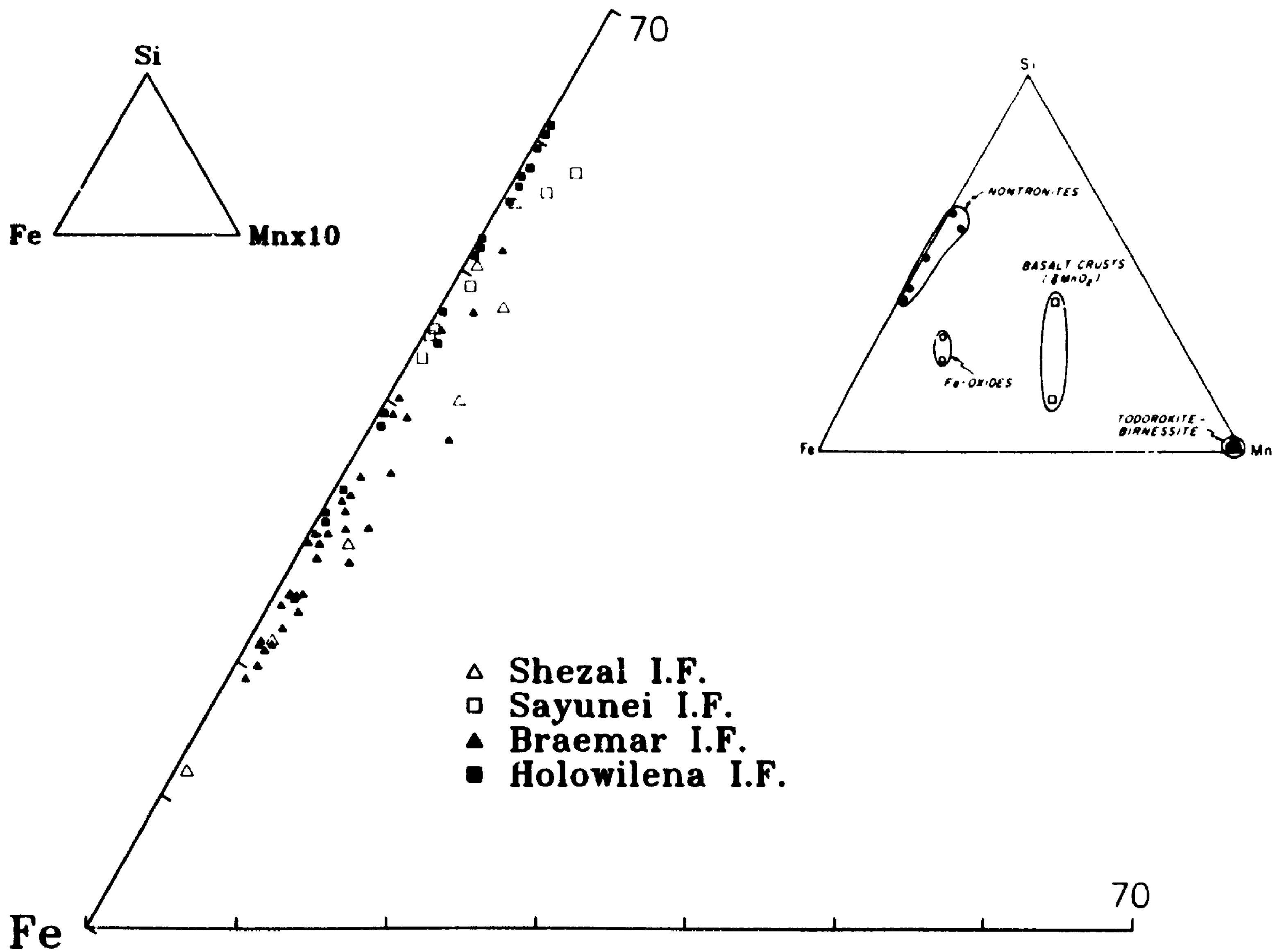
Si
Fe
Mnx10
70
70
Fe
Shezal I.F.
Sayunei I.F.
Braemar I.F.
Holowilena I.F.
Si
Fe
Mn
NONTRONITES
BASALT CRUSTS
Fe-OXIDES
TODOROKITE-BIRNESSITE

Summary. The most apparent difference between the Yudnamutana IF and both the Chuos and Rapitan IFs is the absence of chemically precipitated quartz or jasper. The Chuos and Rapitan IFs contain layers of pure quartz and jasper respectively, whereas with the exception of sample $14a_3$, the Yudnamutana IF does not. In the Yudnamutana IF, SiO_2 occurs mainly as detrital quartz mixed with the iron oxides (Table 2.2). Despite this difference, the Holowilena IF has Fe and Si contents comparable to those of the Sayunei IF, diamictite-associated Chuos IF and amphibolite-associated type 2 Chuos IF (Table 6.1). The diamictite-associated Chuos IF , however, has much lower Al and Ti contents than those of the Holowilena IF. Type 2 Chuos IF has Al, Mg and Ca percentages similar to those of Holowilena IF (Table 6.1). The detritus hosting these elements has a volcanogenic origin (actinolite, hornblende) in type 2 Chuos IF and a clastic origin (K-feldspar, carbonate) in Holowilena IF. These distinctly different types of detritus, together with the contrasting settings of type 2 Chuos IF (horizons within mafic metavolcanic rock/amphibolite) and Holowilena IF (strata within a purely sedimentary sequence) preclude additional comparisons of the two iron formations. Although the Sayunei IF has slightly less clastic detritus (lower Al, K) than the Holowilena IF, it has a similar Fe/Si ratio and is hosted entirely by sedimentary rocks. A geochemical equivalent to the Braemar IF is not present in the other regions since it has Fe and Si contents which lie between those of the Shezal IF and the amphibolite-associated type 1 Chuos IF, and the Al, K and Ti contents are most comparable to Sayunei IF (Table 6.1).

Both the volcanic association and the geochemistry support a hydrothermal interpretation for the Chuos IF (Breitkopf, 1988), whereas for the sediment-hosted Rapitan and Yudnamutana IFs, geochemistry provides the best means of determining their origin (e.g., Figures 6.2, 6.7 & 6.8).

Facies Interpretation

Introduction

As established in Chapter 1 (p. 12), the Braemar and Holowilena iron formations are considered to be facies variants of the Pualco Tillite and the Benda Siltstone (Figure 1.4b). Because of this, the stratigraphic sections measured in this study (e.g., Figures 2.4 - 2.8) focused on the contact between the Pualco Tillite (waning glacial stage) and the Benda Siltstone (interglacial stage). This 'contact' is, however, transitional since "tillite" and "siltstone" are intercalated throughout the interval of iron deposition, and hence the formal names were abandoned in Chapter 2 and the observed lithologies grouped into three major facies: diamictite, iron formation and subarkosic Fe wacke, and two minor facies: Fe siltstone and carbonate.

Diamictite

Introduction. The matrices of diamictites associated with iron formation are either low in Fe_2O_3 (<20%) or high in Fe_2O_3 (>30%; Figure 3.2). The former commonly occur at the base of iron formation-bearing intervals, whereas the latter, if present, are intercalated with the iron formation (Figures 2.4 - 2.8). Stratification is only locally developed. In the low Fe_2O_3 diamictites, it takes the form of lenses of either framework-supported pebbles (section #13) or clast-free subarkosic sandstone (nos. 20/14, 18, 17). In the high Fe_2O_3 diamictites, stratification is defined by microscopic variations in the density of clastic detritus (#20/14) or by clast-rich lenses in which imbrication is locally developed (#8). The latter occur within poorly defined beds whose upper surfaces are striated (Plate 2.1e, Figure 2.9).

Zone 3. The juxtaposition of striated high Fe_2O_3 diamictite overlain by lonestone-free iron formation (Figure 2.8) is enigmatic. As evident from Figure 6.9b, diamictite deposition from a partially floating ice shelf allows for localized grounding

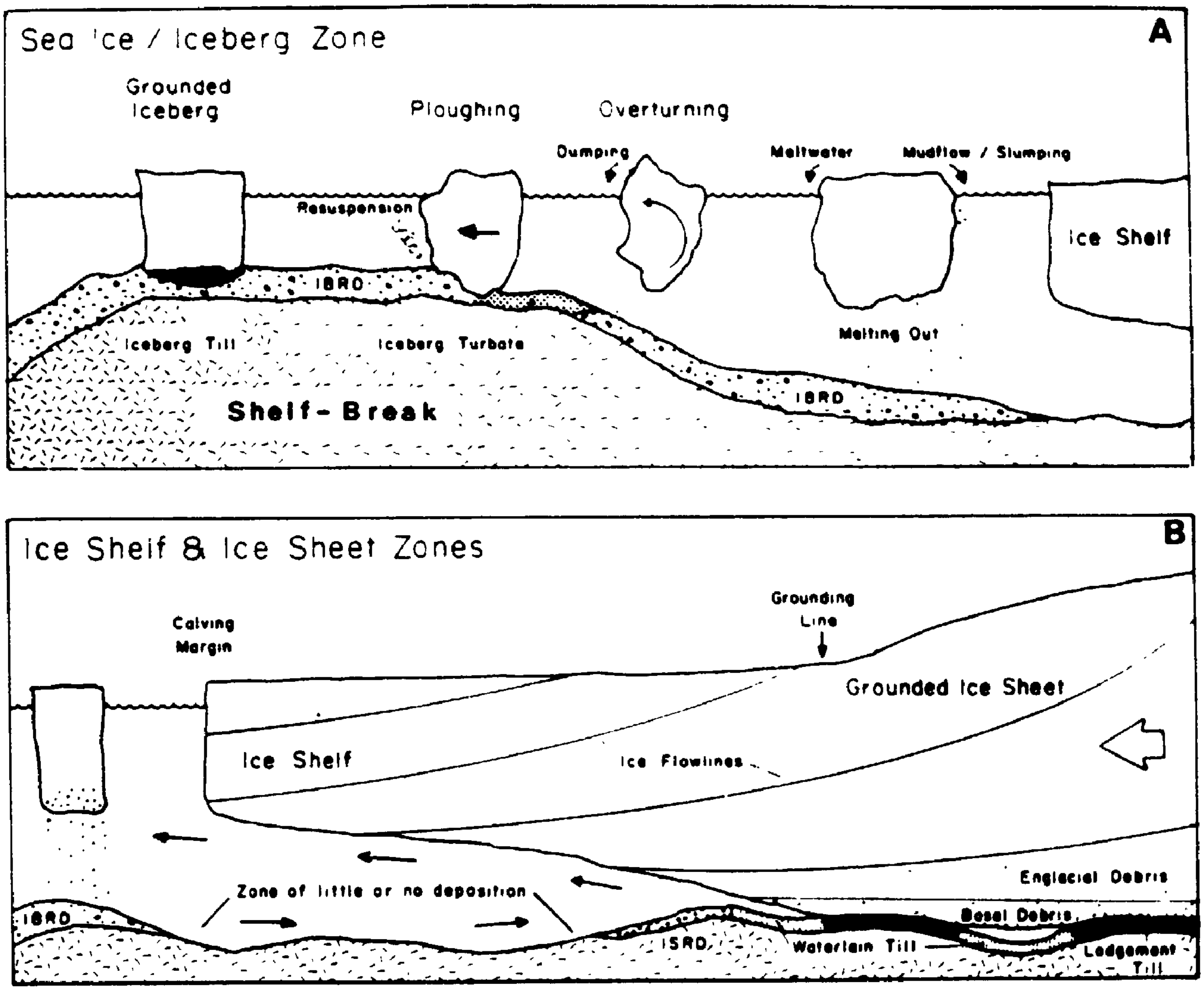

Figure 6.9 Model for glacimarine sedimentation (after Kellogg and Kellogg, 1988). (A) Icebergs calved from large, polar ice shelves do not carry subglacial, englacial or superglacial debris, hence the debris-laden icebergs shown are derived from outlet or tidewater glaciers that discharge directly into the sea. IBRD = iceberg rafted debris. (B) Minimal deposition occurs between the grounding zone and calving margin of large polar ice shelves. The iceberg carrying debris (left) is derived from an outlet or tidewater glacier. ISRD = ice shelf rafted debris.

of ice and formation of striae, but subglacial deposition beneath such an ice shelf is commonly considered to be minimal and would not account for the thick sequences (up to 120 m) of non striated, low Fe_2O_3 diamictites which underlie the iron formation-bearing intervals. A modified version of the sea ice/iceberg zone model of Kellogg and Kellogg (1988; Figure 6.9a) is preferred. The unstratified low Fe_2O_3 diamictites represent melt-out deposition from recently calved, debris-laden icebergs. In open-marine conditions, icebergs are rapidly swept away from the ice-proximal zone (Boulton and Deynoux, 1981). Deposition of the Yudnamutana Subgroup probably occurred in an actively rifting, partially restricted small marine basin (e.g., Figure 1.8) where iceberg "jams" would have been common. Faulted blocks of the underlying substrate (Burra Group?, p. 9) may also have impeded iceberg removal. At least one such block is envisaged in lieu of the Antarctic continental shelf-break in the model of Kellogg and Kellogg (1988; Figure 6.9a). An uplifted, rifted block would permit ploughing of icebergs to coincide with deposition of diffusely stratified, high Fe_2O_3 diamictite from melt-out and sediment gravity flow processes. Evidence of modern iceberg grounding has been documented at depths of over 500 m (Lien, 1981; Barnes, 1987). The decreased clastic content of icebergs in ice-distal settings permitted accumulation of relatively pure chemical precipitates of iron oxides. The iron was derived from hydrothermal fluids which came up along the faulted margins of rifted blocks seaward of the high Fe_2O_3 diamictite depositional area. These fluids are interpreted to have mixed with marine and melt waters during deposition. Based on the presence of NNW-SSE-trending glacial striae (Figure 2.9) and NE-directed paleocurrent data (Figure 2.10), it is possible that icebergs moving in a NNW-SSE direction grounded near the crest of a NE-dipping rifted block(s).

Zones 1 - 3. As emphasized in Table 6.2, the diamictites throughout zones 1 - 3 (Figure 2.1) can be distinguished by depositional process and iron content. Clasts and matrix of low Fe_2O_3 diamictites typically have a plutonic and/or extra-basinal origin,

Table 6.2 Summary of diamictite characteristics from stratigraphic sections (e.g., #12) and samples (e.g., 20c) within zones 1 - 3 (Figure A.1). Unshaded headers = low Fe_2O_3; shaded = high Fe_2O_3.

ZONE 1	Oraparinna	Worumba	Holowilena South		
Section	# 12	# 13	20c	20M$_1$	# 21
Clasts	subarkosic wacke	subarkosic arenite chlorite-plag schist	ferroan dolomite (FD) tonalite vein quartz	FD-quartz intraclast	ferroan dolomite light green siltstone hem-quartz lutite
Dominant source(s)	Extra-basinal		Plutonic and Supracrustal	→	Intraformational and Supracrustal
Matrix	monocrystalline quartz (MQ) K-feldspar hematite-FD intraclast	MQ K-feldspar chlorite after phlogopite ferroan dolomite	MQ K-feldspar phlogopite	MQ K-feldspar FD-qtz intraclast hematite intraclast	MQ K-feldspar I.F. intraclast ferroan dolomite
Dominant sources(s)	Plutonic and Intraformational	Plutonic and Extra-basinal	Plutonic	→	Plutonic and Intraformational

ZONE 2	Oopina		Mount Victor		Oulalpa	Bimbowrie
Section	19c	19h$_1$	18a$_1$	18c$_1$	# 17	# 15
Clasts	quartz arenite, carbonate-rich sandstone	tonalite vein quartz quartzite	tonalite smokey quartz ferroan dolomite	ferroan dolomite quartz arenite tonalite	tonalite vein quartz ferroan dolomite	tonalite diorite schist vein quartz
Dominant Source(s)	Extra-basinal	Plutonic and Extra-basinal		Extra-basinal and plutonic	Plutonic and Extra-basinal	Plutonic
Matrix		MQ plagioclase ferroan dolomite biotite	MQ plagioclase ferroan dolomite biotite	MQ ferroan dolomite plagioclase biotite	MQ K-feldspar biotite ferroan dolomite	MQ magnetite plagioclase biotite
Dominant Source(s)		Plutonic and Extra-basinal				Plutonic

ZONE 3	Spring Dam	Spring Dam			Manunda	
Section	# 10	9a$_1$	2m$_1$	2w$_1$	7a	7aa$_1$
Clasts	arenite & wacke ferroan dolomite	subarkosic wacke vein quartz ferroan dolomite	ferroan dolomite FD-quartz-plagioclase intraclast	ferroan dolomite siltstone tonalite (minor)	subarkosic arenite	Fe arenite rip-up ferroan dolomite tonalite
Dominant source(s)	Extra-basinal	Extra-basinal and Plutonics	Extra-basinal and Intraformational	Extra-basinal and Plutonic	Extra-basinal	Intraformational Extra-basinal and Plutonic
Matrix	MQ plagioclase bio-after-plagioclase ferroan dolomite	MQ plagioclase biotite ferroan dolomite	MQ magnetite chlorite ferroan dolomite	MQ magnetite chlorite plagioclase		MQ magnetite plagioclase chlorite
Dominant source(s)	Plutonic and Extra-basinal			Plutonic		Plutonic

	Holowilena South	
	20M$_1$	# 21
(FD)	FD-quartz intraclast	ferroan dolomite light green siltstone hem-quartz lutite
tal	→	Intraformational and Supracrustal
	MQ K-feldspar FD-qtz intraclast hematite intraclast	MQ K-feldspar I.F. intraclast ferroan dolomite
	→	Plutonic and Intraformational

	Mount Victor		Outalpa	Bimbowrie
	18a$_1$	18c$_1$	# 17	# 15
	tonalite smokey quartz ferroan dolomite	ferroan dolomite quartz arenite tonalite	tonalite vein quartz ferroan dolomite	tonalite diorite schist vein quartz
Plutonic and Extra-basinal		Extra-basinal and plutonic	Plutonic and Extra-basinal	Plutonic
te	MQ plagioclase ferroan dolomite biotite	MQ ferroan dolomite plagioclase biotite	MQ K-feldspar biotite ferroan dolomite	MQ magnetite plagioclase biotite
	Plutonic and Extra-basinal			Plutonic

	Manunda	
2w$_1$	7a	7aa$_1$
n dolomite iltstone ite (minor)	subarkosic arenite	Fe arenite rip-up ferroan dolomite tonalite
ra-basinal Plutonic	Extra-basinal	Intraformational Extra-basinal and Plutonic
MQ agnetite hlorite gioclase		MQ magnetite plagioclase chlorite
'lutonic		Plutonic

and the low Fe_2O_3 diamictites are considered to have been deposited primarily by iceberg melt-out. The high Fe_2O_3 diamictites likely formed from sediment gravity flows (zone 1) or a combination of melt-out and sediment gravity flows (zone 3), because the clasts and matrices of high Fe_2O_3 diamictites commonly include an additional intraformational component, which is attributed to the operation of erosive sediment gravity flows. The source of iron in the high Fe_2O_3 diamictites is discussed in Chapter 7.

With respect to the source of extra-basinal material (Table 6.2), the subarkosic wacke, arenite, ferroan dolomite and light green siltstone clasts of zone 1 diamictites probably reflect derivation from the platformal deposits of the underlying Burra Group (Figure 1.3a). An equivalent source is proposed for the ferroan dolomite in zone 1 matrices; it is particularly abundant in diamictite samples from *Worumba* (Figure 3.16; cf. Fairchild and Spiro, 1990). Clasts of plutonic material are rare in zone 1 diamictites (i.e., tonalite of 20c), whereas K-feldspar is a common matrix component possibly derived from plutonic complexes of the Curnamona Cratonic Nucleus (Figure 1.8). It should, however, be noted that at least some of the potassium feldspar has formed by metasomatic replacement of plagioclase (see p. 35). Metamorphically generated phlogopite is not as abundant in zone 1 as its counterpart, biotite, is in zone 2. In the event that both were produced by metamorphism of clay-like precursors (e.g., sericite + chlorite), it is suggested that zone 1 diamictite matrices were derived from a less weathered source than those of zone 2 (Figure 3.19).

Within zone 2 (Table 6.2), plutonic clasts (e.g., tonalite, diorite schist, vein & smokey quartz) are more prevalent than sedimentary clasts (e.g., sandstone, ferroan dolomite). This reflects the close proximity of the Curnamona Cratonic Nucleus (CCN) to the depositional site of zone 2 diamictites (Figure 1.8). With regard to zone 2 matrices, plagioclase feldspar and the components which combined during prograde metamorphism to form biotite (see above) are also considered derivatives of the CCN. Detrital igneous biotites are locally present in zone 2 diamictite matrices (see p. 52 &

187).

Within zone 3, the clasts are similar to those of zone 1 diamictites (e.g., arenite, wacke, ferroan dolomite), whereas the matrices are more like those of zone 2 (e.g., biotite, plagioclase, Figures 3.4, 3.8, 3.9 & 3.16). Only in the uppermost parts of measured sections 9/2 and 7 is there evidence of tonalite clasts like those common in zone 2 (Table 6.2). The prevalence of sedimentary clasts in diamictites of zones 1 and 3, together with the NNW-SSE-trending glacial striae in zone 3 (Figure 2.9), suggests that there was an additional source of ice on the north-northwest side of the rifted basin diagrammed in Figure 1.8. This ice provided debris entrained from the Burra Group sedimentary sequence to diamictites of zones 1 and 3.

Iron formation

Variations in mineralogy provided the basis for definition of the three zones (Figure 2.1). Zone 1 iron formation is dominated by **hematite** ± quartz, zone 2 IF by **magnetite-biotite** ± hematite and zone 3 IF by **magnetite** ± **hematite**. In general terms, the dominant form of iron oxide distinguishes Holowilena IF (hematite) from Braemar IF (magnetite). The most apparent difference in character between these two IFs is that clastic detritus is more intimately associated with Holowilena IF than it is with Braemar IF.

Zone 1. The relationship between clastic material and IF is attributed to the proximity of zone 1 to the ice source proposed above. Ice proximity may also explain why lonestones/possible dropstones were only observed in zone 1 IF (section #12), and deposition during a period of ice retreat would provide an abundant supply of fine material derived from proglacial meltwaters. Since mixing of iron oxides and clastics within a single layer is common to zone 1 IF, it is probable that iron-rich fluids amalgamated with sediment gravity flows carrying clastic detritus. For example, the laminated to very thin-bedded couplets of hematite-quartz lutite (red) and hematite lutite (purple) are interpreted as deposition from low-concentration turbidity currents which have been modified by tractional flow. Evidence of grain traction includes the basally concentrated millimetre-thick fine sand-size quartz layers within couplets of $12k_1$, which represents the most recurrent type of IF at section #12. The higher hematite content in the upper purple layer of the couplets probably reflects greater influence of primary chemical precipitation as the supply of clastic material waned. Bedding-parallel apatite-chlorite lenses (Plate 4.2a) located within these couplets at *Oraparinna* and *Holowilena South* represent at least some diagenetic addition of phosphorous (see p. 180 & 224). The laminated to very thin-bedded couplets of subarkosic Fe siltstone (Fe-poor) and hematite-quartz lutite (Fe-rich) developed at *Holowilena South* are also interpreted as deposits from low-concentration turbidity currents (Stow and Bowen, 1980). Load, flame and slump structures are commonly developed (Plate 2.4e) and microscopic hematite intraclasts are present. The most obvious evidence of redeposited iron oxide are the hematite-defined ripple cross-laminae in the siltstone layers (Plate 2.5a). Incorporation of this hematite is attributed to reworking of Fe-rich chemical precipitates by turbidity currents. The siltstone/lutite contacts can be either transitional (Plate 2.4f) or abrupt (Plate 2.2c), which suggests that the hematite in the lutite layers may be either redeposited (gradational) or primary precipitate (abrupt). The latter is interpreted as having formed from interturbidite chemical precipitation (cf. Barrett and Fralick, 1984). Deposition of clastic-poor, laminated jasper-hematite units (e.g., 14a, of Figure 6.3) is considered to have coincided with a complete clastic hiatus.

Zones 2 and 3. In contrast to zone 1, macroscopic clastic-dominated layers are rarely developed within iron formation of zones 2 (**magnetite-biotite** ± hematite) and 3 (**magnetite ± hematite**). In zone 3 IF, carbonate-bearing subarkosic Fe arenite (Fe-poor) layers commonly have sharp bounding surfaces (Plate 2.2e), are of near-uniform grain size throughout, and lack any IF intraclasts. They are locally observed infilling flutes (Plate 2.3b) and are regarded as subaquatically accumulated fines (winnowed from glacial debris) which have been rapidly deposited by low-concentration turbidity currents. They are equated with the thick irregular silt laminae of Facies D2.2 and occurrences described by Pickering *et al.* (1986, 1989).

The thinly laminated character of IF (Plate 2.2d) is defined by alternating iron-rich and slightly less iron-rich (due to clastic contamination) laminae. The latter reflect influxes of fine clastic material during a period otherwise dominated by chemical precipitation. Microscopic comparison of hematite-free laminated IF from zones 2 ($16d_1$, Table 2.2) and 3 (7J) reveals that in zone 2, biotite occurs in both types of laminae whereas it is restricted to the more clastic laminae in zone 3. Aluminum concentrations within individual layers generally remain constant during prograde metamorphism (Carmichael, 1969), and hence the present distribution of biotite is considered to reflect that of its precursor(s). The clastically derived, clay-like(?) precursor(s) was (were) more prevalent during deposition of the zone 2 IF, since unlike the zone 3 IF, biotite persists in even the most iron-rich laminae. An abundance of Fe^{2+}-bearing silicate (biotite precursor(s)) intimately associated with iron oxide may explain the absence of hematite within much of zone 2, since it could serve as a reducing agent and force the transformation of hematite to magnetite during prograde metamorphism (Mel'nik, 1982). This argument is also applicable to the hematite-free IF of zone 3 (7J) except the precursor minerals would be those of chlorite rather than biotite. Throughout zone 3, the presence or absence of hematite appears to be linked to the amount of chlorite in the iron-rich laminae (see p. 73). There are some samples (e.g., $9I_2$) in which chlorite is virtually absent and magnetite-hematite-quartz is the observed assemblage. Klein (1973) has shown, by examples of banded iron formation from the southern part of the Labrador Trough, the Lake Superior district, the Hamersley Group of Western Australia, and the iron ranges in the state of Minas Gerais (Brazil), that the quartz-magnetite, quartz-hematite, and quartz-hematite-magnetite associations are preserved when metamorphism of higher rank is imposed. On this basis, oxygen is considered to be an inert (buffered) component. Studies by Frost (1979) and Stanton (1976, 1989) support this conclusion. Klein (1983, p. 442) acknowledged examples of non supergene hematite↔magnetite pseudomorphing described by several authors and suggested "that some movement of oxygen has taken place in some instances, but that in most metamorphic assemblages only enough movement took place to allow for the replacement of only a small amount of the original iron oxide." In the current study, the only evidence of pseudomorphing is posttectonic (Plates 4.1c & 4.2d). The magnetite-hematite-quartz assemblages within zone 3 IF are, therefore, considered to mainly reflect the compositions of the primary minerals. Zone 1 sample $21a_1$, which is the only magnetite-bearing IF from the Holowilena IF, is also considered primary since there is minimal Fe^{2+}-bearing silicate (chlorite) in its magnetite-quartz-hematite assemblage. The geographic proximity of $21a_1$ (section #21) to IF samples in which chlorite coexists with hematite in the absence of magnetite (section #20/14, Figure 2.5), also argues against invoking regional metamorphism to account for the magnetite in sample $21a_1$.

Subarkosic Fe wacke

Introduction. As stated in Chapter 2, the subarkosic Fe wackes and arenites which occur intercalated with iron formation are both bedded and unstratified. Variable amounts of iron oxide minerals occur within these dominantly clastic rocks (Figure 2.3). Iron oxide composition and distribution are similar to those established for the iron formation facies in that sandstones of zone 1 are **hematite**-bearing, those of zone 2 are **magnetite**-bearing, and in zone 3 they are **magnetite** ± **hematite**-bearing.

Bedded wackes. Subarkosic Fe wacke beds are commonly sharp-based, coarse-tail graded and have tops which are transitional into the overlying lutite or siltstone layer. These features typify deposition from high-concentration turbidity currents in a glacimarine environment (Wright *et al.*, 1983). Coarse-tail grading of framework quartz and feldspar grains is locally accompanied by an upward increase in matrix hematite (compositional grading, section #12). This matrix hematite is, together with the hematite-quartz lutite IF rip-up clasts (Table 2.3), attributed to erosion of Fe-rich chemical precipitates by turbidity currents. Locally developed clasts at the base of subarkosic Fe wacke beds are either close-set and ungraded (Plate 2.4b & c) or dispersed and graded (Plate 2.4d). This type of clast distribution is similar to that described by Hein (1979) and Hein and Walker (1982) in 'structureless pebbly sandstone and sandstone' of the Cambro-Ordovician Cap Enragé Formation. These clasts are interpreted as deposits from concentrated clast dispersions developed at the base of turbidity currents (Hein, 1979, 1982). The combination of dispersed textures and coarse-tail grading indicates that good lateral segregation of grain sizes did not occur within the current prior to deposition. The lack of grain segregation suggests that at least the lower and middle portions (zones i & ii of p. 79 & 89) of subarkosic Fe wacke beds represent conditions of very rapid sedimentation. Upper bed portions (zone iii) locally show diffuse parallel laminae which may reflect the influence of tractional flow during upper bed deposition.

At some localities within zones 2 and 3 (Figure 2.1), the basal parts of subarkosic Fe wacke beds are generally devoid of clasts and typified instead by locally convoluted and/or cross-laminated subarkosic arenite layers ($\leq$4 cm thick, Plate 2.5c & e). The association of ripple cross-laminae and convolute laminae is similar to that described in "CCC-turbidites" (Walker, 1985). He interprets the convolute lamination as evidence of low strength sediments which were susceptible to deformation by shear from the turbidity current. The cross-laminae may represent basal traction deposition from sandy high-concentration turbidity currents (Lowe, 1982).

Subarkosic Fe wacke laminae which are intimately associated with iron formation (Plates 2.2a, 2.2c & 2.3f) reveal microscopic features similar to the macroscopic attributes of the Cambro-Ordovician 'graded-dispersed fine conglomerate and pebbly sandstone' facies (Hein, 1979, p. 46) and the "S" turbidite divisions of Lowe (1982). According to Lowe (1982), there are three main stages of deposition from a coarse-grained sandy high-density turbidity current. These are: a traction sedimentation stage (S_1), a traction-carpet stage (S_2), and a suspension sedimentation stage (S_3). The subarkosic Fe wacke beds have an ungraded, framework-supported basal division (S_1) which is superceded by a fairly abrupt increase in hematite lutite and accompanying change to matrix-support (S_3). Above the hematite increase, the framework grains are dispersed within a quartz-hematite lutite matrix and locally exhibit coarse-tail grading. The framework-supported division is interpreted as traction deposition (S_1), whereas the overlying dispersed framework grains represent S_1 grains that did not settle and were entrained by turbulent suspension during depositon of quartz-hematite lutite (S_3). The absence of a traction-carpet stage (S_2) is attributed to the very fine grain size, since the intergranular dispersive pressure required to form a traction carpet layer is negligible between such fine grains (Lowe, 1982). The localized development of coarse-tail grading within the S_3 division may reflect instances where the sediment settled from an only partially turbulent suspension (Middleton, 1967).

Partial Bouma sequences (T_{abc} and T_{bc}) are sporadically developed (Plate 2.3d). In lieu of T_{de} divisions, they can be overlain by quartz-hematite lutite (Plate 2.3e) in which the fine-grained turbidite divisions (E_{1-3}) of Piper (1978) are evident. For example, the lutite in sample 12f$_3$ has a graded and parallel laminated lower division (E_1), a non laminated but graded middle division (E_2), and an ungraded and structureless hematite-enriched upper division (E_3). This intimate grading of clastic and chemical material supports a primary or locally reworked origin for the hematite since if the hematite is metasomatic, it has entirely replaced the original phase and has done so on a remarkably fine scale. Quartz-hematite lutite beds with an irregular order of internal structures may be attributed to deposition during storms (Pickering *et al.*, 1989).

Unstratified 'wackes'. The unstratified sandstone beds (typically 0.6 - 3 m thick), composed of either subarkosic Fe wacke or arenite, have sharp bounding surfaces and are ungraded and generally structureless. These features are similar to those of the 'massive sandstone without dish structure' facies B2 described by Walker and Mutti (1973) and the 'thick/medium-bedded disorganized sands' facies B1.1 of Pickering *et al.* (1986, 1989). Facies B1.1 is attributed to rapid mass deposition from a high-concentration turbidity current with intergranular friction in a concentrated grain dispersion proposed as the sediment support mechanism (Pickering *et al.*, 1989, p. 53). However, grading may be "poorly developed" in facies B1.1, but is absent in the unstratified 'wackes' and hence non-turbulent transport is suggested. The unstratified 'wackes' are interpreted as density-modified grain flows of cohesionless silt-sand suspensions (Lowe, 1976). These modified grain flows probably represent a stage transitional between cohesive debris flows and high-concentration turbidity flows. Development of sediment gravity flows in a glacimarine environment may account for the locally arenaceous nature of the subarkosic Fe 'wackes', for in the Weddell Sea, slumped glacial sediment consisting of 25 - 47% lithic fragments is transformed to well-sorted turbidites of arkosic sand (<3% lithics) over distances of < 10 km on the upper continental slope and shelf (Wright and Anderson, 1982).

Fe siltstone and Carbonate

Fe siltstone and carbonate are both minor facies intercalated with iron formation. They mostly occur in zone 3 (Figure 2.1).

Fe siltstones. Laminated Fe siltstones (e.g., 10L, $9j_1$) display couplets in which the lower layer is mineralogically transitional into the upper layer, but typical Bouma divisions T_{cde} or Piper (1978) E_{1-3} divisions were not observed. The lack of these features may be partly attributed to metamorphic recrystallization obscuring the original grain sizes of the sericite and chlorite precursors. A second explanation for the laminated Fe siltstones stems from their mineralogical and chemical similarities to the associated subarkosic Fe wackes and arenites (Tables 2.2 & 2.4, Figures 3.10 & 3.11). The Fe siltstones may represent more or less in situ reworking of sand-silt turbidites by bottom currents (Stow and Lovell, 1979; Lovell and Stow, 1981). Such reworking has produced bottom-current-modified silts which are considered to be common on continental slopes and rises (Pickering *et al.*, 1986).

The thicker Fe siltstone beds in which coarse-tail grading is developed (e.g., $8H_3$, $8A_L$) are regarded as finer grained equivalents of stratified subarkosic Fe wacke beds (see p. 240). The coarse-tail grading is attributed to rapid deposition from low-concentration turbidity currents. Sample $8A_L$ is unique since it contains approximately 1% bicoloured, subhedral tourmaline. The prismatic, nonclastic appearance of this tourmaline was observed in three dimensions during separation of magnetite for REE analysis (Table 5.1). The occurrence of subhedral tourmaline in a rock containing primary iron oxide and apatite precipitates (Plate 4.1b & f) implies that the boron, now present in tourmaline, formed as part of the same hydrothermal system that produced the iron oxides and apatite (Slack, 1982).

Carbonates. As evident from Figure 3.1, the five carbonate samples plot close to, but not within, the normal carbonate field. This is attributed to the presence of significant amounts of siliciclastic material. The primarily dolomitic carbonate is also considered to have a detrital origin. Comparable to the ferroan dolomite in zone 1 diamictites (see p. 236), it is probably derived from platformal deposits of the underlying Burra Group (Figure 1.3a). A similar detrital origin has been proposed for much of the dolomite in time-equivalent glacigenic deposits of the North Flinders Basin (Young and Gostin, 1990, 1991).

There is, however, localized evidence of nonclastic carbonate. For example, carbonate-bearing layers intimately associated with iron formation contain ankerite (i.e., $18E_1$, $5A_U$ & 8C-1 of Figure 4.5), whereas samples more distant from IF do not. Also, carbonate sample 8P has REE abundances and a pattern comparable to associated IF sample $9I_3$ (Table 5.1, Figure 5.2), and hence it is suggested that the Fe, Ca, (trace Mn) of sample 8P, like the iron of $9I_3$, was derived predominantly from a hydrothermal source.

Chapter VII

SUMMARY & CONCLUSIONS

Depositional Setting

The variable thicknesses of the iron formations and their relationships with the four associated facies (Figures 2.4 - 2.8) are partly attributed to differences in paleogeographic setting (cf. Anderson *et al.*, 1983). Rift-induced faulting of the substrate is considered to be responsible for the irregular bottom topography (Figure 1.3a). The effect of an irregular surface on facies distribution is considered to be most evident at the type locality of the Braemar IF (zone 3, Table 1.1a), where the iron formation is the most Fe_2O_3-rich (Table 3.7) and is most intimately associated with structures of a glacial origin (Plate 2.1e, Figure 2.8). As discussed in Chapter 6, the juxtaposition of glacially striated high Fe_2O_3 diamictite overlain by lonestone-free IF is attributed to local iceberg grounding on an up-faulted block as opposed to a more stable continental shelf-break (Figure 6.9a). After grounding of north-northwesterly derived(?) icebergs (see p. 237, Figure 2.9), the rafted debris is considered to have been deposited on a NE-dipping paleoslope (Figure 2.10). The 60° difference between the direction of ice movement and clastic transport may be due to the existence of a topographic high. A redirection of clastic material would permit the precipitation of relatively pure IFs in zone 3, since seawater:hydrothermal fluid mixing (Figure 5.1b) could take place without much contamination by clastic debris (Figure 7.1).

The abrupt contact between striated diamictite and lonestone-free IF (Figure 2.8) is comparable to the massive diamictite/lonestone-free mudrock contact described by Visser (1991) from the Late Paleozoic Dwyka Formation, southern Africa. Visser (1991) interpreted the abruptness as evidence of rapid disintegration of a marine ice sheet. The grounding icebergs which provided debris to the high Fe_2O_3 diamictite are also considered to have calved during a period of rapid, but oscillatory, ice retreat; a

Figure 7.1 Proposed setting of the Braemar IF and associated iron oxide-bearing clastic rocks from zone 3 (Figure 2.1). Debris-laden icebergs are considered to have rafted from a north-northwesterly ice source, whereas clastic deposition occurred on a northeast-dipping paleoslope. Icebergs which locally grounded atop rifted blocks of the underlying substrate, provided clastic detritus to the high Fe_2O_3 diamictites. Hydrothermal fluids carrying Fe and P emanated from the faulted margins of rifted blocks. The absence of alteration in rocks which underlie the striated, high Fe_2O_3 diamictite indicates that hydrothermal fluids were transported from discharge sites to depositional areas. For example, deep circulation of cold, oxygenated glacial meltwaters is considered to have displaced warmer, buoyant and relatively reduced hydrothermal fluids (cf. Yeo, 1981). Mixing of hydrothermal fluids and meltwaters (i.e., "normal" seawater) may have formed an upwelling countercurrent which carried Fe-rich fluids to platformal and slope environments, where Fe and P precipitated in intimate association with diamictites.

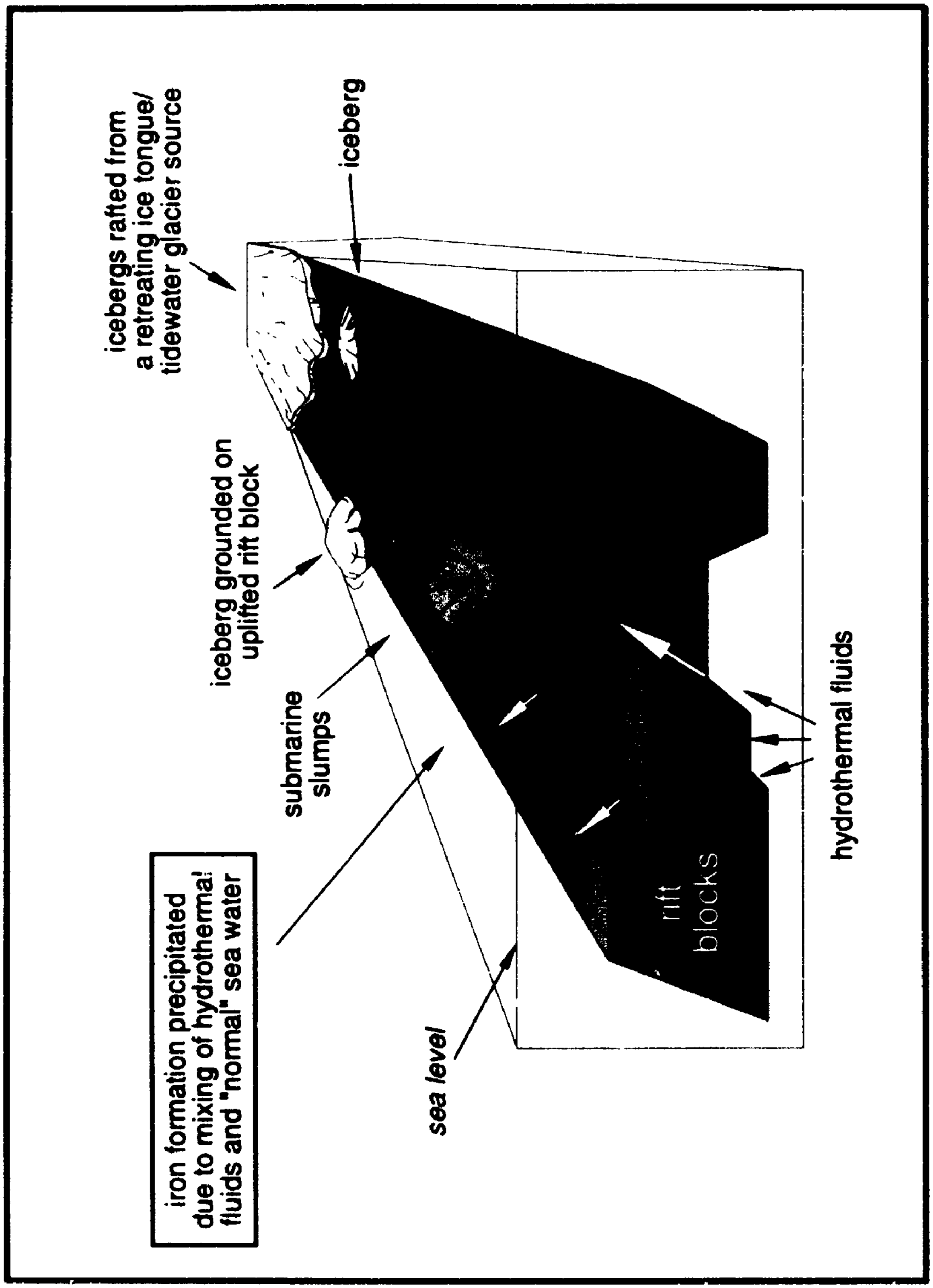
icebergs rafted from
a retreating ice tongue/
tidewater glacier source
iceberg
iceberg grounded on
uplifted rift block
submarine
slumps
iron formation precipitated
due to mixing of hydrothermal
fluids and "normal" sea water
sea level
rift
blocks
hydrothermal fluids

situation which would have inhibited lonestone incorporation in the overlying IF but could have led to deposition of diamictite above the striated diamictite/IF contact (Figure 2.8). A subarctic, tidewater or outlet glacier is a probable source of icebergs to zone 3 since the former is characterized by intervals of rapid advance and retreat (Anderson and Molnia, 1989, p. 106), and both types are potential sources of debris-laden icebergs (Figure 6.9a). Icebergs derived from tidewater glaciers in Alaska (subarctic) and Svalbard (subarctic-subpolar) carry debris to distances of approximately 100 km from the ice front (Dowdeswell and Murray, 1990). The previously proposed (p. 237) north-northwesterly ice source is considered to have supplied the macroscopic sedimentary clasts typical of zone 3 (and zone 1) diamictites (Table 6.2), whereas the rare plutonic clasts observed near the top of measured sections in zone 3 indicate a minor influence of northeasterly ice, peripheral to the Curnamona Cratonic Nucleus (Figure 1.8). There is a general segregation of coarse debris derived from the north-northwest (zones 1 & 3) from that originating in the northeast (zone 2), supporting the suggestion that the restricted conditions of a rift setting inhibit wide dispersal of icebergs (Young and Gostin, 1991; Young, 1992b).

The facies described within zones 1 and 2 (Figures 2.4 - 2.7) are also considered to represent deposition during a period of retreating ice. As in zone 3, the finer grained lithologies of zones 1 and 2 are lonestone-free, but in contrast to zone 3, there is no evidence of ice grounding. Low Fe_2O_3 (<20%) diamictites are common near the base of measured sections in zones 1 and 2 (Figures 2.4 - 2.7 & 3.3 - 3.5). They are dominated by plutonic or extra-basinal clasts (Table 6.2), formed by iceberg melt-out and settling of suspended fines (Eyles *et al.*, 1985; cf. Unit 3 of Young and Gostin, 1990, 1991 and Young, 1992b). The high Fe_2O_3 (>30%) diamictites, which occur intercalated with iron formation, contain an intraformational component in addition to plutonic or extra-basinal material (as do low Fe_2O_3 diamictites at sections 12 & 21, Table 6.2). These diamictites formed by a combination of iceberg melt-out and resedimentation in a distal glacimarine setting (Eyles *et al.*, 1985, figure 4b). Associated with (zone 1), or in lieu of (zone 2), the high Fe_2O_3 diamictites, are several lithologies typical of such a basinal setting. They include:

i) coars· tail graded subarkosic Fe wacke beds interpreted as products of rapid deposition from high-concentration turbidity currents;

ii) unstratified, ungraded and structureless subarkosic Fe wacke or arenite, regarded as deposits from density-modified grain flows;

iii) couplets of subarkosic Fe siltstone and hematite-quartz lutite deposited by low-concentration turbidity currents; and

iv) iron formation deposited in association with low-concentration turbidity currents which have been modified by tractional flow or bottom current influxes of fine clastic material during a period otherwise dominated by chemical precipitation.

Within the primarily clastic facies of diamictite, wacke and siltstone, iron oxides occur in sufficient quantities to justify the prefix 'Fe' (Figure 2.3), which suggests that iron precipitation was ongoing during clastic deposition (cf. Yeo, 1981, p. 39; Yeo, 1984, p. 237). The thinning- and fining-upward sequences described at section #12 (zone 1, p. 79) and the sequence observed at section #16 (zone 2, p. 95) are interpreted as transgressive onlap deposits formed in response to eustatic sea-level rise. Synsedimentary faulting accompanied deposition on a NE-dipping paleoslope at section #20/14 (Table A.3, Figure 2.11).

As in Figure 7.1, iron (iron oxides) and phosphorous (apatite) are the main elements supplied to iron formation of zones 1 and 2 via hydrothermal fluids which emmanated from rift-induced conduits. Two forms of apatite were observed in IF of zone 1; the first is disseminated and probably of hydrothermal origin (cf. apatite of zone 3, Figure 6.4), the second occurs as bedding-parallel apatite-chlorite lenses (Plate 4.2a). These lenses appear in IF which is phosphorous-enriched relative to IF elsewhere (Figures 3.17, 3.18 & 3.23), and are considered to represent at least some diagenetic addition of apatite. This additional apatite may represent a seawater source of phosphorous, which was enriched during diagenesis due to the extreme insolubility of apatite in alkaline solution.

Comparison with Generalized Model for Neoproterozoic IF

The depositional setting outlined in Figure 7.1 is similar to the generalized model for Neoproterozoic iron formations developed by Yeo (1984, p. 243) and modified by Young (1988). The most apparent difference is that hydrothermal fluids host Si, Fe and Mn in the generalized model, whereas in the Yudnamutana IF, Fe and P are the most evident elements from a hydrothermal source (Plate 4.1d & f, Figure 6.4). Trace amounts of Ca (8P, Figure 5.2) and Mn (ankerite of Figure 4.5) rarely occur. As discussed in Chapter 6 (p. 217), either the higher solubility of Mn relative to Fe allowed currents to carry Mn away in solution or the hydrothermal fluids never contained much Mn (Boström and Widenfalk, 1984). The Yudnamutana IF differs from both the Neoproterozoic Chuos and Rapitan IFs in its general lack of chemically precipitated quartz or jasper. Thin units of laminated hematite-jasper are restricted to Holowilena IF (e.g., $14a_3$). They occur intercalated with the dominant form of iron formation; hematite lutite. This juxtaposition of cherty (hematite-jasper) and noncherty (hematite) IFs is attributed to the pressure-temperature controls on silica solubility outlined by Holland and Malinen (1979). In order for silica-bearing fluids to be generated, P-T conditions must remain high (relative to the P-T required for iron exhalation), otherwise silica precipitation will occur prior to exhalation. Silica precipitation is more sensitive to cooling and pressure reduction than iron, and hence Kimberley (1989, p. 66) suggests that "fluids which have formed noncherty iron formations probably were exhaled at lower temperature and pressure than those which formed cherty deposits".

Cherty IFs of the Chuos Formation and Rapitan Group are considered to have formed by the hydration of new oceanic crust in a rift basin (cf. Breitkopf, 1988; Yeo, 1981). A similar source is proposed for the cherty (subordinate) and noncherty (dominant) IFs of the Yudnamutana Subgroup. As evident from Figure 1.3a, basic volcanics (early rift) occur together with evaporitic clastics and carbonates (pre- & syn-rift) in the Callana Group near the base of the Adelaide geosyncline. These Callana Group lithologies are also evident in the diapiric breccia bodies outlined in Figure 1.3a. Hydrothermal source fluids to the iron formation are considered to have been focused by similar (more deep-seated) but not the same fault-controlled conduits that hosted the diapirs (Lemon, 1985), since diapirs are only locally associated with IF (Figure 2.4) and in these instances, the iron formation is not remarkably iron-rich (Table 3.2).

With regard to cherty IFs (e.g., Chuos, Rapitan, Holowilena), Kimberley (1989) notes that fluids exhaled from hydrating crust are commonly Si-bearing since essentially all primary igneous minerals lose silica upon hydration. Yeo (1984, p. 191-194) emphasized the occurrence of Si and Fe precipitation in experiments involving dilution of seawater:basalt mixtures (≈hydrothermal fluid) by normal seawater. At dilutions of 1:1, 1:3 and 1:39, Fe was rapidly precipitated, whereas only at the two lower dilutions was Si precipitated. Dilution-controlled fluctuations of silica saturation provide a means of explaining the alternating Si-rich and Si-poor laminae typical of cherty IFs. In noncherty IFs (e.g., Holowilena, Braemar), cooler temperatures and lower pressures may have accompanied fluid exhalation from a succession containing basic volcanics and evaporitic sediments. These source lithologies are conducive to deep weathering of iron-bearing silicates and oxides (source of Fe) but should inhibit production of H_2S (Kimberley, 1989). Rapid ascent of fluids along the faulted margins of rifted blocks (cf. Gross, 1983) would impede fluid contamination by other sources.

As mentioned above, the occurrence of laminated jasper-hematite IF in the Rapitan Group (i.e., cherty IF) is attributed to fluctuating silica concentrations in seawater:hydrothermal fluid mixtures (Figure 7.2a). During intervals of silica

Figure 7.2A Schematic relationships among hydrothermally-derived oxides of Fe, Si and Mn. Diagram modified from Yeo (1984, 1986).

Figure 7.2B Stability fields of hematite and magnetite in aqueous solution at 25° C and 1 atm pressure (after Garrels and Christ, 1965) with Eh-pH range for normal seawater (after Tucker, 1981) superposed on diagram.

(A)

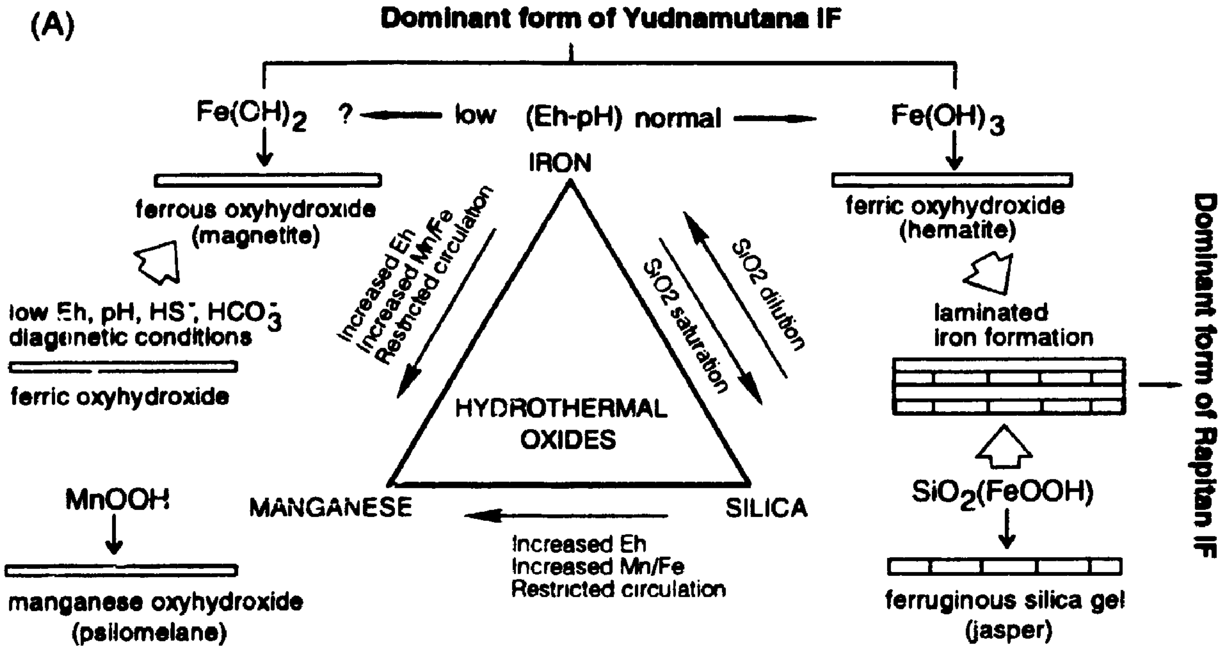

Dominant form of Yudnamutana IF
Fe(OH)2
? low (Eh-pH) normal
Fe(OH)3
IRON
ferrous oxyhydroxide (magnetite)
ferric oxyhydroxide (hematite)
low Eh, pH, HS⁻, HCO3⁻ diagenetic conditions
ferric oxyhydroxide
Increased Eh Increased Mn/Fe Restricted circulation
SiO2 saturation
SiO2 dilution
laminated iron formation
HYDROTHERMAL OXIDES
MnOOH
MANGANESE
SILICA
SiO2(FeOOH)
manganese oxyhydroxide (psilomelane)
Increased Eh Increased Mn/Fe Restricted circulation
ferruginous silica gel (jasper)
Dominant form of Rapitan IF

(B)

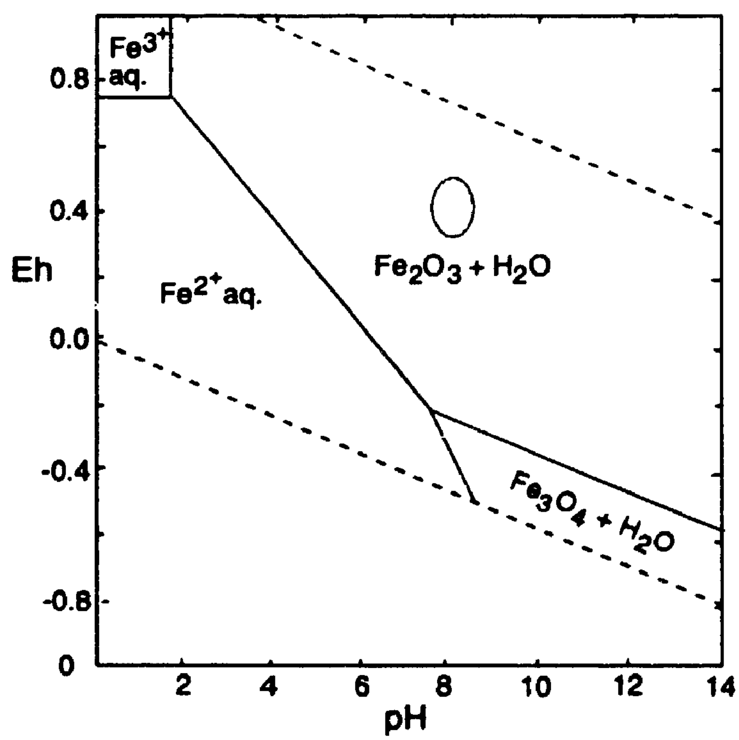

Fe3+ aq.
Fe2+ aq.
Fe2O3 + H2O
Fe3O4 + H2O
Eh
pH
0.8
0.4
0.0
-0.4
-0.8
0
2
4
6
8
10
12
14

oversaturation, silica will precipitate with iron to form an iron oxyhydroxide-silica gel lamina, which dehydrates to jasper. During intervals of silica undersaturation, only iron will precipitate as an oxyhydroxide lamina. This lamina would dehydrate to iron oxide (Yeo, 1984, p. 235). Within the Yudnamutana Subgroup, only at *Holowilena South* is there evidence of laminated jasper-hematite IF (e.g., $14a_3$). The majority of iron formation from zone 1 (Figure 2.1) probably formed from colloidal ferric oxyhydroxide [$Fe(OH)_3$, Figure 7.2a], which could precipitate under Eh-pH conditions of normal seawater (Figure 7.2b). Ferric oxyhydroxide would dehydrate to hematite, which is the dominant type of iron oxide in zone 1 (Holowilena IF). As previously mentioned (p. 240), there is localized evidence of magnetite precursors [$Fe(OH)_2$ + $Fe(OH)_3$] coexisting with those of hematite [$Fe(OH)_3$] in zones 1 ($21a_1$) and 2 (e.g., $9I_2$, $8A_L$, $8A_U$, Plate 4.1b & c). Precipitation of ferrous oxyhydroxide [$Fe(OH)_2$] requires Eh-pH levels below those of normal seawater, and very low sulphide and carbonate activity levels (Figure 7.2a & b). In samples $21a_1$, $9I_2$, $8A_L$ and $8A_U$, magnetite and hematite are considered to reflect the compositions of the primary minerals because: (1) magnetite and hematite form grain pairs with interpenetrating boundaries (Plate 4.1b & c), (2) sample mineralogy is mainly magnetite-quartz-hematite, and (3) quartz-magnetite, quartz-hematite and quartz-hematite-magnetite associations are generally preserved when metamorphism of higher rank is imposed (Klein, 1973, 1983). In contrast, hematite-free IF from zones 2 ($16d_1$, quartz-magnetite-biotite) and 3 (7J, magnetite-chlorite-quartz) contains significant amounts of Fe^{2+}-bearing silicate, which may have served as a reducing agent and forced the transformation of hematite to magnetite during prograde metamorphism (Mel'nik, 1982).

In a generalized model, Yeo (1984, p. 478) attributed phosphorous concentrations in Neoproterozoic iron formations to adsorption of seawater phosphorous onto the colloidal ferric hydroxide precursor to hematite. This suggestion was based partly on a lack of observed apatite in the Rapitan IF (Yeo, 1984, p. 229). However, in the Yudnamutana IF, apatite is evident in the IF proper, clastic laminae intimately enclosed by IF and high Fe_2O_3 diamictite matrices. Apatite forms grain pairs with, and inclusions within, iron oxides (Plate 4.1d-f), and the samples which host this apatite plot near the hydrothermal field on a Zr/Cr vs. Y/P_2O_5 diagram (Figure 6.4). These relationships suggest coprecipitation of iron oxide and apatite, and that P, like Fe, was derived from a hydrothermal source (Breitkopf, 1988; Gross, 1992).

Neoproterozoic Controls on the Yudnamutana IF

The mechanism proposed by Yeo (1981, 1984) and invoked in Figure 7.1 for transporting hydrothermally-derived elements to depositional sites of iron formation is supported by isotopic studies of carbonates and organic carbon from Neoproterozoic successions in Namibia (Kaufman *et al.*, 1991). One of these successions included the iron formation-bearing, glacigenic Chuos Formation (see Chapter 6). Sampling of pre-glacial carbonates revealed an enrichment of carbon-13 which was attributed to enhanced burial of organic carbon, whereas carbonates deposited during and directly after glacial intervals were depleted in ^{13}C. Carbonates which cap glacigenic, iron formation-bearing sequences in the Adelaide geosyncline are also ^{13}C-depleted (Williams, 1979; Donnelly, 1981; Williams, 1981). Kaufman *et al.* (1991) suggested that the pre-glacial oceanic conditions were conducive to high rates of organic burial and that marine waters were stratified, with deep waters anoxic. Ocean stratification for an extended time would permit hydrothermally-derived ferrous iron to accumulate. At the inception of glaciation, upwelling would bring iron-rich bottom waters onto shallow portions of rifted blocks where contact with cold, oxygenated surface waters lead to the precipitation of iron formation (Yeo, 1981, 1984, 1986; Young, 1988).

The initial cause of Neoproterozoic glaciation has been attributed to the occurrence of a low latitude, high standing supercontinent (e.g., Young, 1989, 1991; Worsley and Kidder, 1991). A substantial land mass (cf. Moores, 1991) would thermally insulate large portions of the mantle. Also, extensive exposure of low-latitude land to the atmosphere is conducive to drawdown of CO_2 via the weathering of silicate minerals. In this process, rainwater-dissolved CO_2 (carbonic acid) chemically weathers feldspars, which results in the release of Si, Ca, Na, K and HCO_3^- ions into groundwater. Transport of these ions ultimately leads to their incorporation in oceanic sediments, some of which are transferred to continental margins and subducted. Young (1991) suggested that continued drawdown of atmospheric CO_2 would diminish the greenhouse effect and favour the initiation of glacial conditions. Widespread glaciation would have inhibited weathering, which would permit an incremental build-up of atmospheric CO_2 and eventual disintegration of the ice.

The proposed Moores-Dalziel hypothesis (Moores, 1991; Dalziel, 1991) provides a plausible interpretation of how the continents were related at about 750 Ma. The inferred supercontinent suggests a triple junction of Precambrian rocks from southeastern Australia, northwestern North America and southeastern Antarctica. The most compelling evidence for this arrangement stems from the discovery of Grenville-age (≈ 1 Ga) rocks in northeastern Antarctica. These rocks are considered a possible extension of the Grenville belt which flanks eastern North America and extends westward through Texas and southern Arizona. The Moores-Dalziel reconstruction lends support to previously and subsequently proposed comparisons between the Neoproterozoic stratigraphy of southeastern Australia and that of northwestern Canada (e.g., Eisbacher, 1985; Bell and Jefferson, 1987; Young, 1992a). The relevance of these comparisons to the present study is that they correlate the iron formations of the Yudnamutana Subgroup (Australia) with those of the Rapitan Group (Canada). In the detailed comparison of Young (1992a), the Sayunei-Shezal IFs of the Rapitan Group occupy a slightly lower stratigraphic position than the Braemar-Holowilena IFs of the Yudnamutana Subgroup. The Rapitan IFs occur at a transition from interglacial to glacial conditions (unit 2/3 contact of Young, 1992a), whereas the Yudnamutana IFs occur at a transition from glacial to interglacial (unit 3/4 contact). The upwelling model for iron formation deposition concentrates iron $\pm$ silica prior to transport (Figure 7.1; Yeo, 1981; Kaufman *et al.*, 1991), which makes deposition simply an inverse function of clastic flux. The depositional intervals which intercede between the diamictite horizons of the lower Shezal Formation host the principal iron concentrations of the Rapitan Group (Crest deposit), whereas the most Fe-rich intervals occur both in diamictite and iron formation in the Yudnamutana Subgroup (Razorback Ridge, Table 1.1a). For both the Rapitan and the Yudnamutana, maximum iron abundances occur where glacigenic sediments are most apparent, which suggests that glacial conditions are important in the development of these iron formations.

Conclusions

(1) Five different facies are locally developed at the transitional contact between the Pualco "Tillite" (waning glacial stage) and the Benda "Siltstone" (interglacial stage) of the Yudnamutana Subgroup. These facies include: diamictite, iron formation, subarkosic Fe wacke, Fe siltstone and carbonate. The study area has been divided into three zones based on the type(s) of iron oxide which occurs in the three main facies of diamictite, iron formation and subarkosic Fe wacke (Figure 2.1). The dominant form(s) of iron oxide in zone 1 is hematite, magnetite in zone 2, and magnetite + hematite in zone 3. Holowilena IF occurs in zone 1 and Braemar IF occurs in zones 2 and 3.

(2) The diamictites are divisible into two main groups; low (<20%) and high (>30%) Fe_2O_3. The former commonly occur at the base of measured intervals, whereas the latter, if present, are intercalated with the iron formation. The low Fe_2O_3 diamictites are typified by plutonic or extrabasinal clasts, and are attributed to iceberg melt-out and settling of suspended fines in a glacimarine setting. The high Fe_2O_3 diamictites contain an additional intraformational component, and reflect deposition from both melt-out and sediment gravity processes. High Fe_2O_3 diamictites occur at a lower stratigraphic level

in the Braemar IF than they do in the Holowilena IF, which indicates a more intimate association of iron precipitation and glacigenic sedimentation in the Braemar diamictites.

(3) Iron formation is dominated by chemically precipitated iron oxides. The concentrations of these oxides is partly dependent on the amount of dilution by detrital silicates (Figures 3.2 - 3.5). Both the Holowilena and Braemar IFs contain clastic detritus, but clastic material is more intimately associated with Holowilena IF (zone 1) than Braemar IF (zones 2 & 3). This is demonstrated by the abundant macroscopic clastic laminae in, and the generally higher Al_2O_3 and K_2O contents of, zone 1 iron formation. This relationship between detritus and zone 1 IF is attributed to proximity of clastic source materials and deposition during a period of ice retreat, which would provide an abundant supply of fine material derived from proglacial meltwaters.

(4) In the primarily clastic facies of wacke and siltstone, iron oxides occur in sufficient quantities to justify the prefix 'Fe' (Figure 2.3). At least some of this iron oxide is redeposited (Plate 2.5a), but its profusion in clastic rocks closely associated with IF suggests that iron precipitation was ongoing during clastic deposition. Coarse-tail grading is widely developed in subarkosic Fe wacke beds, which are interpreted as products of rapid deposition from high-concentration turbidity currents.

(5) Hematite of zone 1 IF probably formed from the dehydration of colloidal ferric oxyhydroxide, but elsewhere in zone 1 (sample $21a_1$) and in zone 3 there is localized evidence of coexisting magnetite and hematite precursors. Hematite-magnetite pairs with mutually interpenetrating grain boundaries (Plate 4.1b & c) occur in samples whose mineralogy is mainly magnetite-quartz-hematite. These mineral pairs are considered to represent precursor phases (i.e., ferric and ferrous oxyhydroxide) which have crystallized during diagenesis and low-grade metamorphism.

(6) The Yudnamutana IF and high Fe_2O_3 diamictite matrices show major and trace element similarities to recent hydrothermal deposits (Figures 6.1 - 6.4, 6.7 & 6.8). Samples analyzed for REE also exhibit patterns which resemble those of hydrothermal

deposits (Figure 5.4) and contrast with patterns of hydrogenic concretions (Figure 5.3). The REE patterns of Yudnamutana IF ($14a_3$, $9I_3$), carbonate (8P) and magnetite separate ($8A_{1\text{-mag}}$) are light REE depleted, have negative Ce anomalies and slight positive Eu anomalies. The former two characteristics typify NASC-normalized patterns for seawater, whereas the latter (Eu anomaly) reflects input of Eu-bearing hydrothermal fluids into the water column.

(7) Iron-enriched hydrothermal fluids are considered to have emanated from the faulted margins of rifted blocks during evolution of a small marine basin (Figure 7.1). Mixing of these fluids with "normal" seawater was probably assisted by deep circulation of cold, oxygenated surface waters displacing warmer, relatively reduced, iron-rich bottom waters. Evidence of such fluid displacement includes the occurrence of iron-rich matrices ($>30\%$ Fe_2O_3) in diamictites which display features indicative of iceberg grounding.

Appendix A

Sample location maps, lithological descriptions and observed thicknesses of layers from each measured stratigraphic section in this study.

Numbers shown in **bold** within a description indicate specific samples and the following abbreviations indicate laboratory examinations of these samples:

t.s. = thin sectioned
p.t.s. = polished thin section
geo = lithogeochemistry.

Figure A.1 Map of a portion of South Australia showing the locations of station homesteads (H.S.), stratigraphic sections and samples sites. Zones 1, 2 and 3 are defined in Figure 2.1.

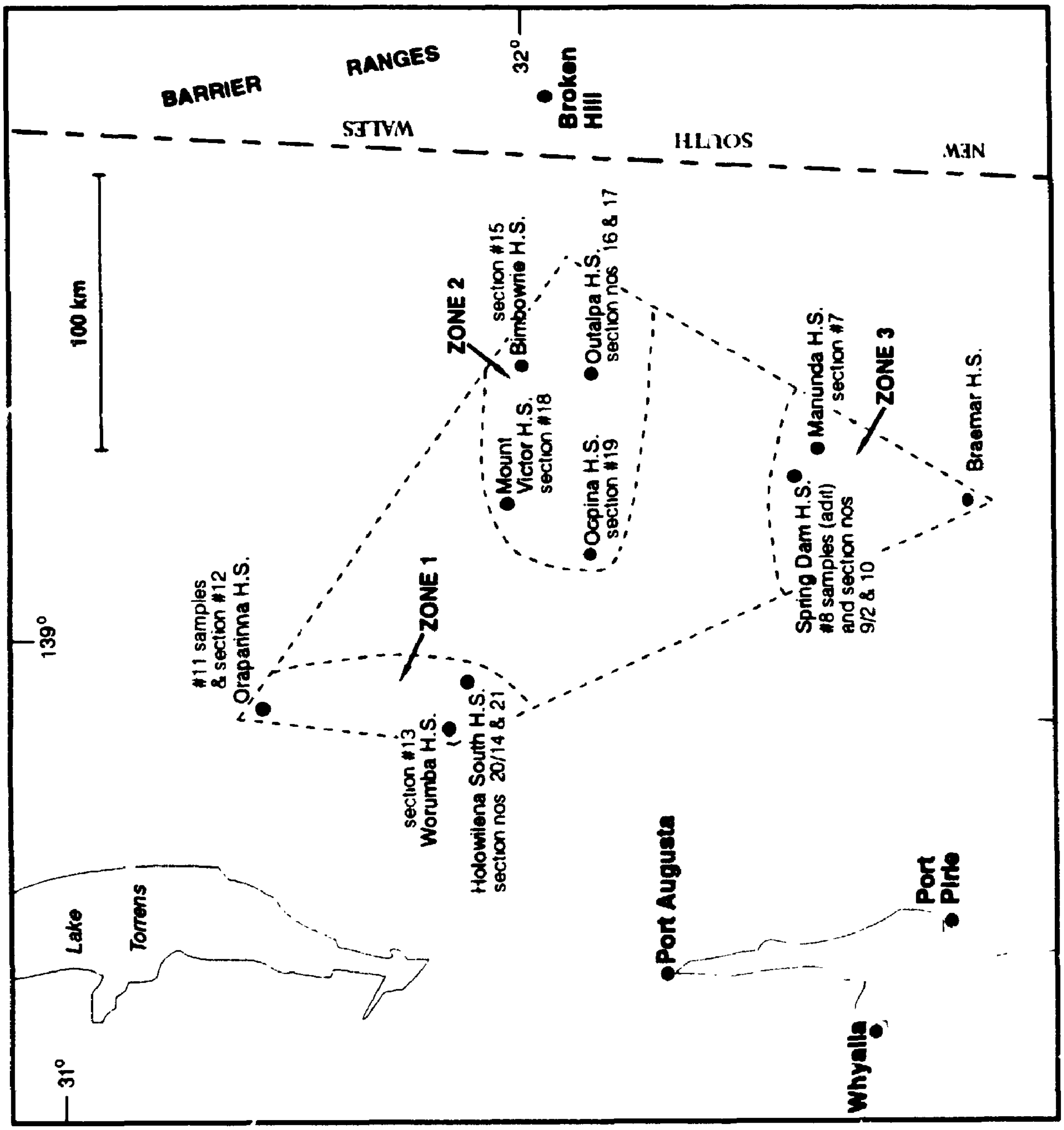
BARRIER RANGES
Broken Hill
32°
NEW SOUTH WALES
100 km
ZONE 1
ZONE 2
ZONE 3
section #15
Bimbowrie H.S.
Outalpa H.S.
section nos 16 & 17
Mount Victor H.S.
section #18
Oopina H.S.
section #19
Manunda H.S.
section #7
Braemar H.S.
Spring Dam H.S.
#8 samples (adit)
and section nos
9/2 & 10
#11 samples
& section #12
Oraparinna H.S.
section #13
Worumba H.S.
Holowilena South H.S.
section nos 20/14 & 21
139°
Lake
Torrens
Port Augusta
Port
Pirie
Whyalla
31°

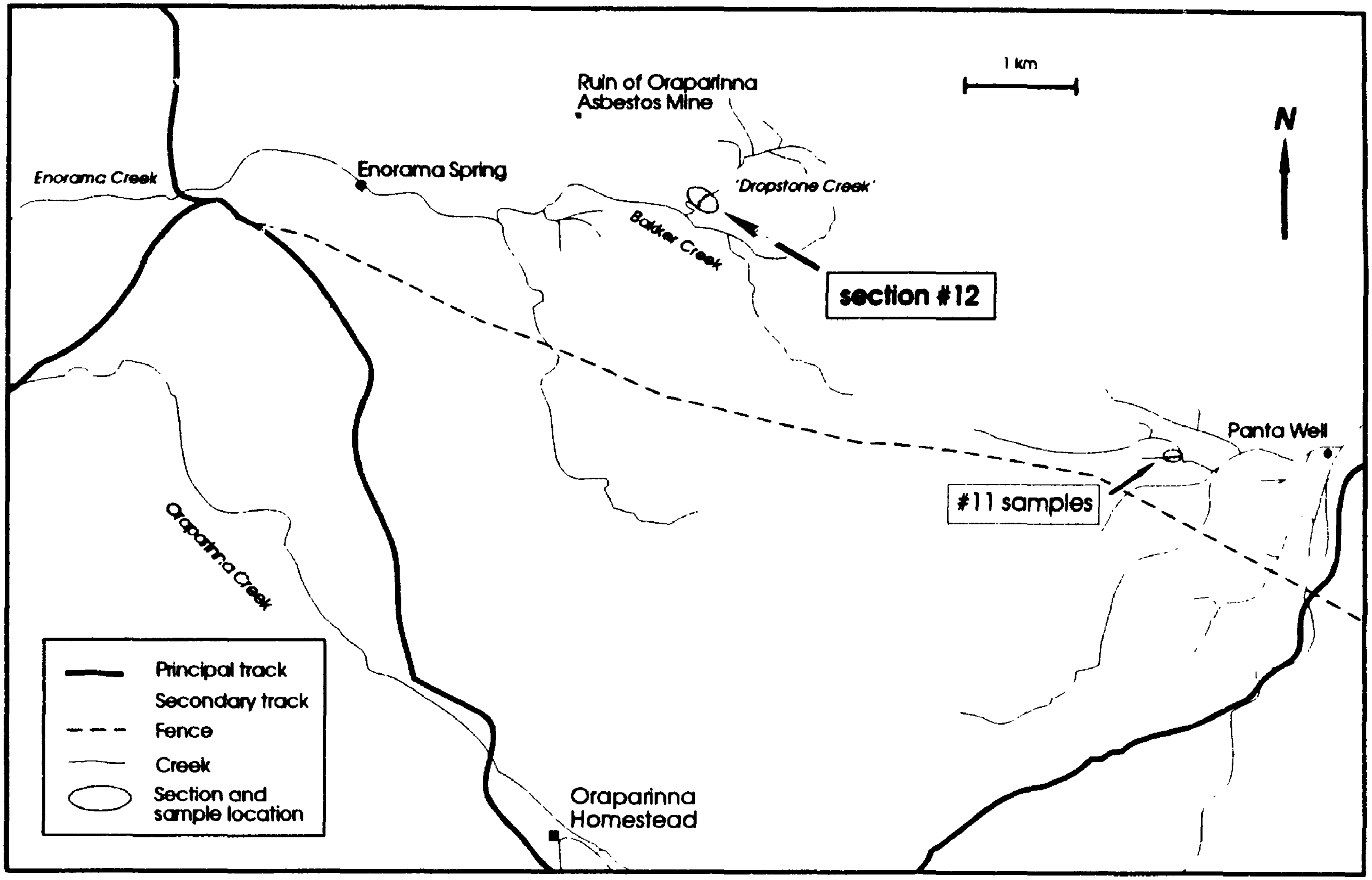

Figure A.2 Locations of sample site #1! and stratigraphic section #12 on Oraparinna station.

Table A.1: Description and thicknesses of stratigraphic section #12 at 'Dropstone Creek', Oraparinna station. Distances are measured from first exposure of Pualco "Tillite" below iron formation-bearing interval.

Description	From	To	Notes
Diamictite: sand-granule-(rare pebble) in reddish-brown quartz-hematite lutite (Fe_2O_3 = 5.68%, geo **12a$_2$**). Unstratified. Dominant micro-framework components (0.02 - 0.8 mm) in decreasing order of abundance are: solitary (monocrystalline) quartz, potassium feldspar and hematite-ferroan dolomite intraclasts. t.s. **12a$_1$**	0.00	3.35 m	
Laminated (3 - 13 mm) couplets of hematite-quartz lutite (red, Fe_2O_3 = 27.10%, geo **12b$_2$**) and hematite lutite (purple) in which the red:purple ratio varies from 5:1 to 1:2. Noted one 18 mm thick red layer which contained three subarkosic wacke lenses. Two lonestones/plausible dropstones (1.5 - 3 cm in size, adjacent laminae recessively weathered) within uppermost 27 cm.	29.49	31.23 m	t.s. 12b$_1$
Hematite ± quartz lutite stratified by thin laminae containing 0.5 - 1.5 cm clasts.	31.23	31.35 m	
Thinning- and fining-upward cycle #1. Base marked by a flat-based/undulate top cobble-bearing subarkosic Fe layer (Fe-poor, medium-grained) which pinches and swells from 3 - 9 cm. Upsection, hematite content of the Fe wacke increases (from 8.57% to 12.10% Fe_2O_3, compositional grading, geo **12d$_1$** & **12d$_2$**) and starved ripples are locally developed (Plate 2.3c). A 23 cm thick bed contains laminated couplets of subarkosic Fe arenite (Fe-poor, 0.1 - 0.3 mm framework) and hematite-quartz lutite at base, overlain by a lithic subarkosic Fe wacke (Fe-moderate, 0.1 -0.5 framework) in which framework size decreases (coarse-tail) as hematite matrix content increases (compositional).	31.39	32.15 m	t.s. 12D$_3$
Flat-based couplets (4 - 12 mm thick) of subarkosic wacke and hematite ± quartz lutite (typically flame-bearing). Laminated to very thin-bedded (1.6 cm max.) couplets of hematite-quartz (red) and hematite (purple) lutite. These couplets are rhythmic both with respect to red:purple layer ratios and thicknesses of successive beds.	32.89	34.37 m	
Cycle #2. Based by a 11.5 cm thick, compositionally graded bed of subarkosic Fe wacke (Fe-poor, 0.04 -0.6 mm framework) → hematite lutite with preserved Bouma divisions BC (B division has Fe_2O_3 = 13.85%, geo **12f$_2$**, Plate 2.3d). Directly overlain by basally loaded triplets (1 - 4 cm thick) of subarkosic wacke, hematite-quartz Fe lutite (Fe_2O_3 = 24.18%, geo **12g$_2$**) and hematite lutite. Evidence of minor slumping and synsedimentary faulting with dextral offset of 4 mm.	34.37	35.39 m	t.s 12f$_1$, 12f$_3$; p t.s 12f$_1$
Typified by layers/beds(?) of quartz-phyric hematite-quartz lutite (1 - 3 cm thick) alternating with laminated sections of hematite-quartz (red, Fe_2O_3 = 25.19%, geo **12h**) and hematite (purple) lutite couplets.	35.39	39.47 m	
Cycle #3. Basal layer (3 - 7 cm thick) of sand- to granule-size quartz and feldspar set in a hematite-quartz lutite matrix. Larger clasts are intraformational hematite-quartz lutite rip-ups (0.3 x 5.5 cm max., slab **12i$_1$**, Plate 2.4b). This coarse layer fines upward then at the 0.27 m mark have a 3.5 cm thick parallel laminated B division and a 2.5 cm thick locally cross-laminated C division. Soft-sediment slumping has precluded development of a more complete C division. The remainder of cycle #3 consists of laminated hematite-quartz (red) and hematite (purple) lutite couplets which have an approximate red:purple ratio of 1:1.	39.47	41.14 m	geo 12J$_1$
Cycle #4 commences with 20 cm of laminated to very thin-bedded couplets of starved subarkosic (Fe) wacke ripples and hematite-quartz lutite. This is overlain by quartz-phyric hematite-quartz lutite with thin discontinuous subarkosic Fe wacke laminae defining stratification. At the 60 cm from cycle base mark have a granule-bearing layer which has a planar top but an irregular base. There are two outsized pebbles within this layer.	41.14	43.07 m	
Cycle #5. Base marked by a 0.27 m plano-convex (flat top) lens of subarkosic Fe wacke (Fe_2O_3 = 9.83%, geo **12J$_2$**). Superceded by very thin-bedded to thickly laminated couplets of quartz-phyric hematite-quartz lutite and hematite ± quartz lutite (Fe_2O_3 = 27.14%, geo **12k$_2$**). Observed a boulder-size (30 x 45 cm) dropstone	43.07	47.69 m	t.s. 12K$_1$

enveloped by these couplets.

Cycle #6. Based by parallel laminated zone (6.5 cm thick) of subarkosic (Fe) wacke and hematite ± quartz lutite in which the hematite content increases upward. Overlain by laminated (2 - 5 mm thick) couplets in which the red:purple ratio is either 1:1 or red is slightly dominant. Basally concentrated a/phyric quartz grains occur in several of the hematite-quartz (red) lutite divisions. 47.69 50.07 m

Cycle #7. Basal layer (1.6 cm thick) is a thinner and finer-grained version of that at cycle #3. Coarse- to very coarse sand-size clasts set in a hematite-quartz lutite matrix and injected by flames from the underlying hematite ± quartz lutite layer. Superceded by a few thicker-than-normal (1.0 - 1.4 cm) hematite-quartz (red) lutite layers (± basal subarkosic (Fe) wacke division) which are capped by 1.0 mm thick hematite (purple) lutite layers. } p.t.s. $12n_1$ geo $12n_2$ Remainder of cycle #7 composed of laminated couplets (1 - 6 mm thick couplets have red:purple ratio of 1:1; 2 - 6 mm thick couplets have 3:2 ratio). 50.07 53.19 m

Cycle #8. Initiated by two flat-based quartz-phyric hematite-quartz lutite beds (3.7 and 2.7 cm thick) one of which contains starved ripples. Moderately to strongly foliated couplets (< 1 cm thick) occur upsection in which the hematite ± quartz (red, Fe_2O_3 = 22.84%, geo 12o) lutite layers are most apparent. The hematite (purple) lutite layers are obscured by their coincidence with foliation/flattening planes. Lonestone/plausible dropstone (7.0 x 4.5 cm) located 0.64 m above cycle base. At the 5.9 m mark have a 0.5 - 2.5 cm thick clast-bearing layer comparable to that noted in cycle #4. 53.19 60.04 m

Cycle #9. Base is marked by three closely spaced (5 & 8 cm) laterally continuous subarkosic (Fe) wacke layers (1.6 - 2.0 cm thick) separated by hematite-quartz lutite. Thin section across layer contacts reveals dilution of framework grains by matrix (i.e., hematite orthomatrix increases at expense of framework quartz and feldspar, Plate 2.3f). } t.s. 12p Upsection, subarkosic (Fe) wacke laminations sporadically occur throughout hematite-quartz lutite up to the 0.64 m mark. These laminae tend to pinch and swell from 2 - 5 mm, and in two instances, there are small pebble-size clasts perched in the upper part of a lamina. Laminated hematite-quartz (red) and hematite (purple) lutite couplets (8 - 10 mm thick) in which 'red' dominant over 'purple' (e.g., 5 mm:3 mm) constitute the remainder of cycle #9. 60.04 61.48 m

Cycle #10. Base is defined by two (4.0 & 4.5 cm thick) flat-based subarkosic (Fe) wacke beds. The remaining exposure of this cycle is moderately foliated and fractured (planes spaced 8 - 10 mm apart) red hematite-quartz lutite (Fe_2O_3 = 18.50%, geo 12q) which locally exhibits thin (<0.5 mm) subarkosic laminae. 61.48 66.59 m

Typically unstratified, ferroan dolomite subarkosic Fe arenite (Fe-poor, 0.1 - 0.5 framework, Fe_2O_3 = 2.89%, SiO_2 = 73.77%, geo $12r_2$). Framework-supported monocrystalline quartz and feldspar (both potassium and plagioclase) with some interstitial hematite mud. Much less abundant than either quartz or feldspar are subrounded intraformational clasts of hematite-quartz lutite (usually 0.3 - 0.5 mm). } t.s. $12r_1$ At mid interval, iron content of the wacke has decreased to 1.45% and SiO_2 increased to 81.85%. 66.59 73.73 m

Very weathered hematite-quartz lutite (Fe_2O_3 = 22.57%, geo 12s). 73.73 upward

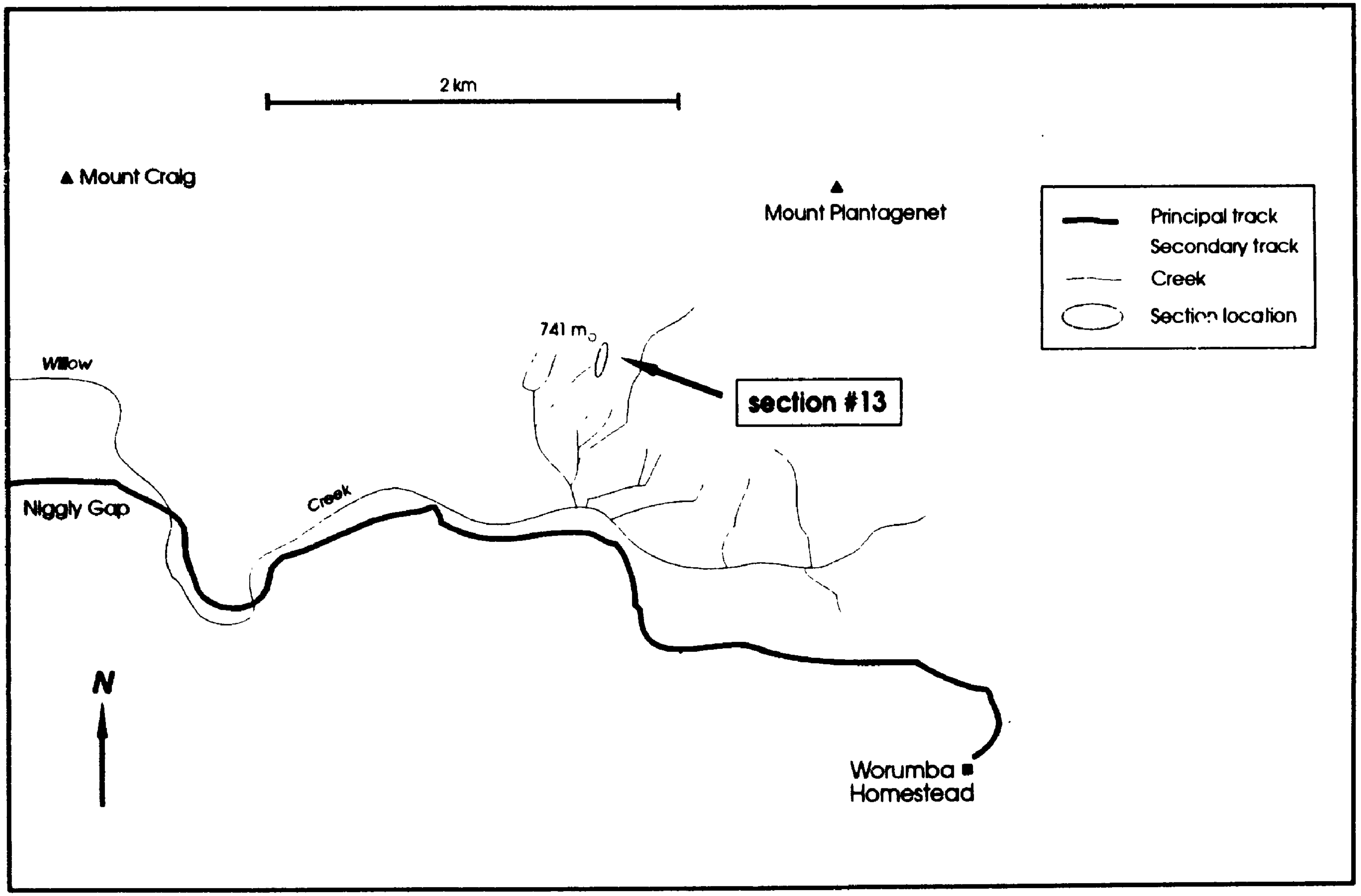

Figure A.3 Location of stratigraphic section #13 on Worumba station.

Table A.2: Description and thicknesses of stratigraphic section #13 on Worumba Station. Distances are measured from first exposure of Pualco "Tillite" below iron formation-bearing interval.

Diamictite: sand-granule-(sporadic 4 - 7 mm size pebbles) set in dark grey weathering matrix dominated by quartz and platy hematite lutite (Fe_2O_3 = 13.26%, geo $13a_2$). Coarser pebbles (0.7 - 5 cm) occur only in two framework-supported eye-shaped lenses which have maximum dimensions of 1.3 x 0.45 m. Most apparent macroscopic clast-type is a pink-tinged greyish-white subarkosic arenite, whereas microscopically the dominant framework components (0.02 - 0.4 mm, subangular) in decreasing order of abundance are: solitary (monocrystalline) quartz, potassium feldspar, chlorite-after-phlogopite and ferroan dolomite. t.s. $13a_1$	0.00	26.68 m
Diamictite: comparable to basal section (see above) except pebble lenses are not apparent and at 30.41 m have a 12 cm interval of thickly laminated couplets of hematite (dominant) and ferroan dolomite Fe siltstone. Diamictite matrix has Fe_2O_3 = 16.32%. t.s. $13b_1$, $13c_1$; p.t.s. $13c_1$; geo $13b_2$, $13c_2$	26.68	55.49 m
Iron formation: weathers blackish-grey. Thinly laminated hematite-potassium feldspar-quartz-phlogopite lutite (Fe_2O_3 = 20.40%, geo $13d_2$) with sporadic ferroan dolomite-phlogopite arkosic Fe wacke layers (Fe-poor, 0.6 -3 mm thick). Laminations within the lutite are defined by slight changes in hematite content. t.s. $13d_1$	55.49	57.57 m
Diamictite: comparable to 26.68 - 55.49 m except no stratified interval.	57.57	60.43 m
Iron formation: comparable to 55.49 - 57.57 m except arkosic Fe wacke layers are less evident. Fe_2O_3 = 27.93%. p.t.s. $13e_2$; geo $13e_1$	60.43	60.77 m
Fe siltstone (dominant): laminated to very thin-bedded couplets of ferroan dolomite arkosic arenite (weathers yellowish-white, subordinate, 0.02 - 0.3 mm framework) and hematite-ferroan dolomite-phlogopite subarkosic Fe siltstone (Fe-moderate, weathers olive green). Top of interval marked by a 12 cm thick light reddish-brown weathering subarkosic wacke (Fe_2O_3 = 5.71%, geo 13g). } t.s. $13F_1$	60.77	61.23 m
Fe wacke/Micro-diamictite: lithic subarkosic Fe wacke (Fe-moderate, Fe_2O_3 = 12.21%, geo $13h_2$). Lithic fragments (0.5 - 1.0 mm) comprise 35% of weathered surface. Unstratified and matrix has a dark green hue. Dominant micro-framework components (0.02 - 0.4 mm) in decreasing order of abundance are: solitary quartz, potassium feldspar and chlorite-after-phlogopite. t.s. $13h_1$	61.23	62.63 m
Iron formation: comparable to 60.43 - 60.77 m	62.63	62.88 m
Fe wacke/Micro-diamictite: comparable to 61.23 - 62.63 m	69.63	71.33 m
Iron formation: comparable to 55.49 - 57.57 m	71.33	71.53 m
Fe wacke/Micro-diamictite: comparable to 61.23 - 62.63 m	71.53	73.51 m
Arenite: discontinuous lens of subarkosic arenite which weathers a pink-tinged pale grey.	73.51	74.41 m
Fe siltstone: blackish-green weathering hematite-ferroan dolomite-phlogopite subarkosic Fe siltstone (Fe-moderate, dominant) with rhythmically spaced (8 - 10 mm) millimetre-thick subarkosic arenite laminae.	74.41	74.57 m
Fe wacke/Micro-diamictite: comparable to 61.23 - 62.63 m except locally see subarkosic wacke laminae which vascillate from 1 - 5 mm in thickness.	74.57	94.17 m
Iron formation: comparable to 55.49 - 57.57 m	94.17	94.47 m
Fe siltstone: comparable to 74.41 - 74.57 m	94.77	95.42 m
Fe wacke: dark green. Unstratified subarkosic Fe wacke (Fe-moderate, Fe_2O_3 = 13.62%, geo $13i_2$).	95.42	98.22 m

Fe siltstone: comparable to 74.41 - 74.57 m	98.22 100.45	99.00 m 102.42 m
Fe wacke: comparable to 95.42 - 98.22 m	105.02	106.36 m
Fe wacke (silt-size, dominant): thinly laminated couplets of ferroan dolomite sub/arkosic(?) Fe arenite (Fe-poor, weathers yellowish-white, subordinate, 0.02 - 0.2 mm framework) and hematite-ferroan dolomite-phlogopite subarkosic Fe wacke (Fe-moderate, weathers olive green, ≤ 0.004 - 0.14 mm grains). t.s. and p.t.s. **13k**	106.36	111.36 m
Fe wacke (silt-size, dominant): thickly laminated version of 106.36 - 111.36 m	111.36	111.66 m
Fe wacke/Micro-diamictite: lithic subarkosic Fe wacke (Fe-moderate, Fe_2O_3 averages 11.14%, geo **13l$_2$ & 13m$_2$**). Unstratified. Lithic fragments (0.5 - 1.0 mm) comprise 10 - 25% of the brownish-green weathered surface. Granules (2 - 4 mm) and small pebbles (15 mm max.) form 1.5% and 0.5% of the exterior rock face respectively. The three main micro-framework components (0.02 - 0.56 mm) in decreasing order of abundance are: solitary quartz, potassium feldspar and phlogopite. t.s. **13l$_1$** and **13m$_1$**	111.66	139.54 m
Iron formation: comparable to 55.49 - 57.57 m	139.54	139.79 m

Holowilena IF

Wilyerpa Fmtn.

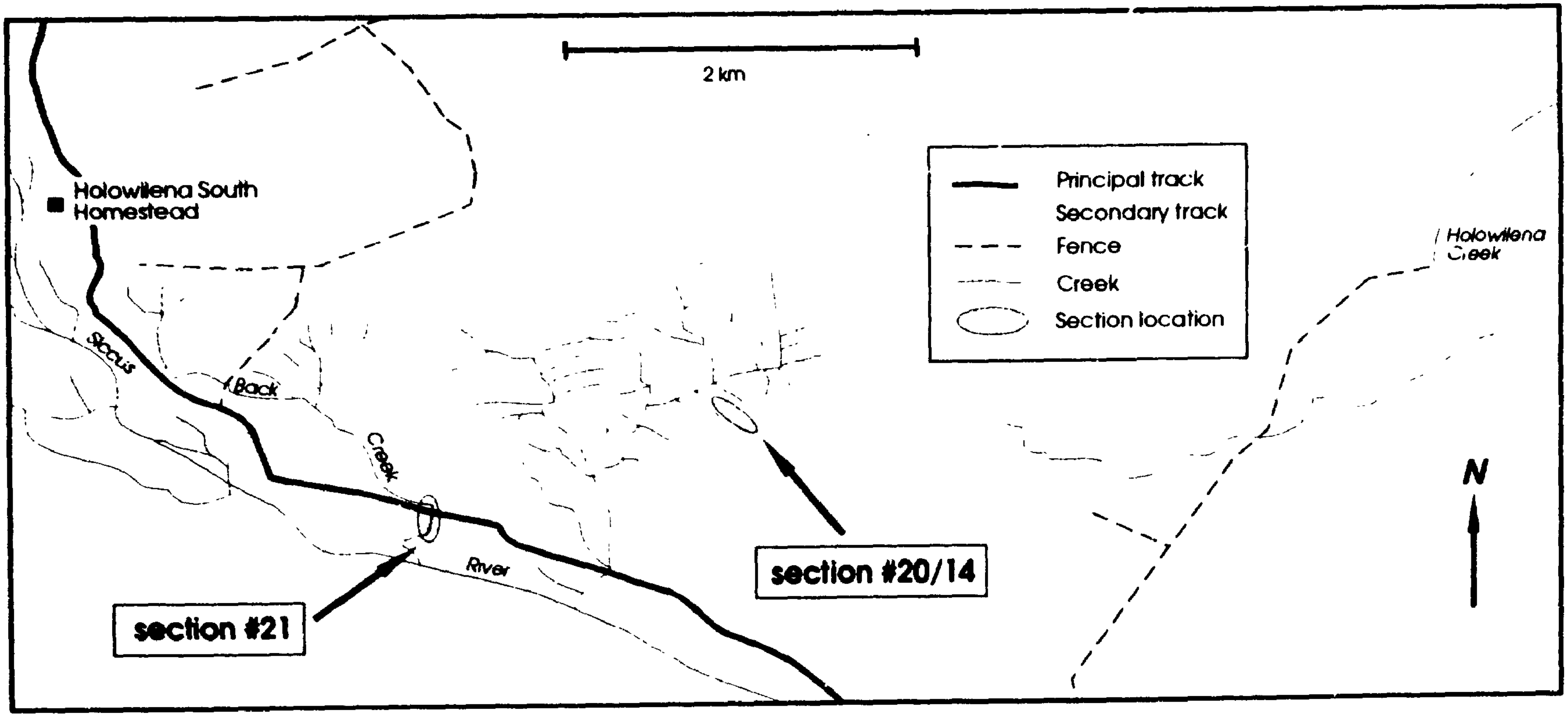

Figure A.4 Locations of stratigraphic section nos. 20/14 and 21 on Holowilena South station.

Table A.3: Description and thicknesses of stratigraphic section #20/14 on Holowilena South station. Distances are measured from first exposure of Pualco "Tillite" below iron formation-bearing interval.

Fe wacke (dominant): light reddish-brown weathering ferroan dolomite subarkosic Fe wacke (Fe-poor, 0.02 - 0.3 mm framework) which is stratified either by discontinuous (up to 1.2 m long x 0.3 m thick) framework-supported lenses/pods (e.g., 0.02 - 0.8 mm framework) or diffuse zones of light green weathering Fe siltstone (Fe-poor, Fe_2O_3 = 7.22%, geo **20b**, compositionally similar to 25.62 - 30.06 m). The irregular, commonly lobate, boundaries of the lenses or pods are locally offset by syndepositional faults.	0.00	3.20 m
Fe wacke & Fe siltstone: equal amounts of light reddish-brown fine-grained subarkosic Fe wacke (Fe-poor) and orange ferroan dolomite-enriched Fe siltstone (Fe-poor) occur as intercalated, undulate layers/zones.	3.20	10.90 m
Micro-diamictite: sand-size (commonly 0.3 - 2.0 mm) supported by greenish-grey weathering, fine-grained subarkosic Fe wacke (Fe-poor). Unstratified.	10.90	17.74 m
Diamictite: pebble-granule set in fine- to medium-grained subarkosic Fe wacke (Fe-poor). Unstratified. Clasts, ranging from 0.2 - 5 cm (commonly 0.2 - 2.5 cm) cover 20% of the exterior surface. Main clast types are in decreasing order of abundance: recessive-weathering ferroan dolomite, orange-stained fine- to medium-grained (1 - 3 mm) tonalite, translucent vein quartz and fine-grained subarkosic green wacke. t.s. **20c** From 23.58 - 25.24 m, have a diffusely laminated, clast-free lens of subarkosic arenite which is laterally continuous for 23 m.	17.74 25.24	23.58 m 25.62 m
Fe siltstone: thinly laminated, light reddish-brown weathering ferroan dolomite-quartz-(chlorite-after-phlogopite) Fe siltstone (Fe-poor, hematite < 5%). t.s. **20d**	25.62	30.06 m
Fe siltstone (dominant) & iron formation: laminated to very thin-bedded couplets of subarkosic Fe siltstone (Fe-poor, 0.1 - 3 cm thick) and hematite-quartz lutite (Fe-rich, 0.05 - 1.5 cm thick). At base of interval is a 32 cm thick wacke bed which consists of: clast-supported granules in coarse-grained matrix (7 cm) overlain by dispersed granules (6.5 cm), then a structureless medium-grained wacke interval (19 cm).	30.06	32.06 m
Micro-diamictite: crudely stratifed lenses of sand-silt-(rare granule) supported by a dark brown weathering matrix of quartz-ferroan dolomite-hematite lutite (Fe_2O_3 = 10.83%, L.O.I. = 9.20%, geo $\mathbf{20f_1}$). Localized development of ferroan dolomite subarkosic Fe wacke (Fe-poor) balls (e.g., 13 mm long x 2 mm thick) and sinistral faults; both soft-sediment features. p.t.s. $\mathbf{20f_2}$	32.06	34.18 m
Fe siltstone (dominant) & iron formation: laminated couplets of light rust-coloured subarkosic Fe siltstone (Fe-poor, 1 - 2.5 mm thick) and black weathering hematite-quartz lutite (Fe-rich, 0.5 - 0.9 mm thick).	34.18	36.04 m
Micro-diamictite: comparable to 32.06 - 34.18 m	36.04	54.48 m
Fe siltstone & iron formation: comparable to 34.18 - 36.04 m except siltstone layers are 0.02 - 1 cm thick and lutite layers are 1.5 - 5 mm thick. Also, at top of interval are 3 wacke beds (15, 9 & 45 cm thick) which are similar to 30.06 - 30.38 m.	54.48	56.90 m
Fe wacke: light reddish-brown weathering ferroan dolomite subarkosic Fe wacke (Fe-poor, Fe_2O_3 = 5.06%, geo $\mathbf{20g_1}$, 0.04 - 0.24 mm framework, p.t.s. $\mathbf{20g_1}$). Unstratifed and only a few granules.	56.90	59.94 m
Diamictite: sand-granule-(rare pebble) supported by a fine-grained subarkosic Fe wacke (Fe-poor/Fe-moderate) matrix. Clasts, which range from 0.5 - 9 mm, are dominated by recessive-weathering ferroan dolomite.	60.80	61.39 m
Micro-diamictite: comparable to 32.06 - 34.18 m	61.39	66.37 m

Diamictite: stratification in this fining-upward interval is defined by changes in clast size starting with a pebble-granule-sand-(rare cobble) layer at base (1.4 m thick), then a pebble-granule-sand layer (65 cm thick), superceded by a sand-granule layer and a sand-size micro-diamictite layer. The clasts of the first three layers are close-set, but still matrix-supported. Dominant clast type is considered to be an intraformational ferroan dolomite-quartz siltstone (slab **20h**, Plate 2.1a).	67.97	73.34 m
Fe wacke: comparable to 56.90 - 59.94 m, except Fe_2O_3 = 5.34% and ball & pillow structures developed along base. geo **20i$_2$**	73.34	78.44 m
Fe siltstone: comparable to 25.62 - 30.06 m except locally appears mustard-coloured and dolomite-enriched (Fe_2O_3 = 7.94%, L.O.I. = 23.30%). Unit is sinistrally offset (3 m along 327°) by a synsedimentary fault located 14 m northeast of section line. geo **20j**	78.44	79.54 m
Diamictite: comparable to 67.97 - 73.34 m except unstratified; simply fines-upward	79.54	84.22 m
Fe wacke: comparable to 56.90 - 59.94 m. Interval is dextrally offset (2.9 m along 100°/82°).	84.22	88.94 m
Fe siltstone: dark brown weathering, faintly laminated quartz-hematite-ferroan dolomite Fe siltstone (Fe-moderate, Fe_2O_3 = 15.83%, L.O.I. = 17.32%, geo **20k$_2$**).	89.64	94.00 m
Fe siltstone: comparable to 25.62 - 30.06 m except laminae not as well developed/preserved.	94.00 99.03	98.36 m 100.15 m
Fe siltstone: comparable to 89.64 - 94.00 m	100.15	100.43 m
Fe siltstone & iron formation (dominant): comparable to 34.18 - 36.04 m, except the Fe lutite/iron formation laminae are dominant and ripple cross-laminated lenses (e.g., 6 cm long x 1.2 cm thick) are locally developed within the Fe siltstone to fine-grained sandstone layers.	100.43	102.03 m
Conglomerate: clast-supported pebbles. The most prevalent clast types are intraformational light rust-coloured Fe siltstone and fine-grained subarkosic green wacke.	102.99	103.65 m
Fe siltstone: alternating laminae of light rust-coloured Fe siltstone (Fe-poor, dominant, 2 - 10 mm thick) and light green-coloured Fe siltstone (Fe-poor, 1 - 3 mm thick).	103.65	104.24 m
Fe siltstone (dominant) & iron formation: interval consists mainly of flat-based, laminated couplets of light rust-coloured subarkosic Fe siltstone (Fe-poor, 1 - 5 mm) and black weathering hematite-quartz Fe lutite (Fe-rich, 0.5 - 2 mm). Ripple cross-laminae, load, flame and slump structures are locally developed. Exceptions to the norm include: a sharp-based bi-layered bed (24 cm thick) of ferroan dolomite subarkosic Fe arenite (Fe-poor) and subarkosic Fe siltstone (Fe-poor) based at 106.32 m, plus a normally graded bed (5 cm thick) and a parallel laminated bed (5.5 cm thick) of subarkosic Fe arenite (Fe-poor), which are based at 107.73 m and 109.68 m respectively.	104.24	111.63 m
Fe arenite: two sharp-based beds (28 & 23 cm thick) of subarkosic Fe arenite (Fe-poor); the first of which is basally graded then structureless and the second is non graded and structureless except for the uppermost 5 cm which has diffuse parallel laminae.	111.63	112.33 m
Fe siltstone & iron formation: strongly foliated version of 34.18 - 36.04 m except for a jasper layer (2 cm thick).	112.33	116.83 m
Fe wacke & Fe siltstone (dominant): alternating laminae of greyish-white weathering ferroan dolomite subarkosic Fe wacke (Fe-poor, 0.1 - 3.3 mm thick) and greyish-green weathering ferroan dolomite-quartz-(chlorite-after-phlogopite) Fe siltstone (Fe-poor, dominant, commonly 8 - 10 mm thick). Cross-laminae and syndepositional faulting are present in the Fe wacke layers. p.t.s. **20L$_1$**	116.83	117.55 m

Diamictite: sand-granule-(rare pebble) supported by a light reddish-brown weathering fine-grained subarkosic Fe wacke (Fe-poor). Crudely stratified by clast-free layers.	117.55	119.71 m
Fe wacke: two sharp-based beds (8.5 & 14 cm thick); the first of which is structureless except for parallel laminae in the uppermost 1 cm and the second is basally graded then structureless with diffuse parallel laminae in the uppermost 3 cm. A third fine-grained subarkosic Fe wacke bed (Fe-poor, 28 cm thick), based at 120.8 m, is structureless except for parallel laminae at the 2/3 mark.	119.71 120.80	119.93 m 121.08 m
Fe wacke & Fe siltstone (dominant): comparable to 116.83 - 117.55 m except the Fe wacke layers are 5 -10 mm thick and the Fe siltstone are 1 - 5.5 cm thick.	119.93 121.95	120.80 m 123.0 m
Fe arenite: two sharp-based beds of subarkosic Fe arenite (Fe-poor, 45 & 15 cm thick); the first of which has normally graded granules and sand within the basal 10 cm and the second has wispy siltstone and lutite rip-ups within the basal 3 cm. Between the two arenite beds are thinly laminated couplets of light rust-coloured siltstone and black lutite; a plausible source of rip-ups in overlying bed.	123.48	124.10 m
Fe siltstone (dominant) & iron formation: comparable to 34.18 - 36.04 m except for an 8 cm thick interval of thinly laminated hematite lutite.	124.10	124.88 m
Fe siltstone: comparable to 103.65 - 104.24 m	124.88	125.44 m
Fe siltstone (dominant) & iron formation: thin, sharp-based beds of subarkosic Fe siltstone (e.g., 4.5 cm thick) in which coarse-tail grading 'may' be present. That is, framework size decreases as hematite lutite content increases. Thinly laminated couplets comparable to 34.18 - 36.04 cap the beds.	125.44	126.00 m
Diamictite: two fining-upward cycles of sand-granule (commonly 0.5 - 2.6 mm) in dark brown weathering quartz-hematite lutite changing to micro-diamictite: sand-size supported by quartz-ferroan dolomite-hematite lutite (Fe_2O_3 = 6.60%, L.O.I. = 9.00%, geo $20m_1$). The micro-framework of the sand-granule diamictite is close-set and consists mainly of: solitary quartz, potassium feldspar, ferroan dolomite-quartz siltstone (comparable to dominant layer of $20L_1$) and hematite intraclasts. p.t.s. $20M_1$	128.53	131.44 m
Micro-diamictite: comparable to that found within 128.53 - 131.44 m	132.85	134.76 m
Fe siltstone: comparable to 89.64 - 94.0 m	135.23	136.06 m
Iron formation (dominant): laminated burgundy-coloured hematite ± quartz lutite within which there are two jasper horizons (3.5 & 3 cm thick) and several light rust-coloured subarkosic Fe siltstone (Fe-poor) laminae.	138.46 140.24	139.43 m 142.49 m
Fe siltstone: comparable to 89.64 - 94.0 m except thinly laminated throughout.	142.49	145.73 m
The interval from 145.73 - 167.63 m is dextrally offset (3.5 m) by a synsedimentary fault which strikes at 330°, then 312° and 309°.		
Fe siltstone (dominant) & iron formation: comparable to the dominant lithology from 104.24 - 111.63 m	145.73	147.96 m
Iron formation (dominant): laminated couplets of hematite-quartz lutite (grey, < 1 mm thick) and hematite lutite (purple, dominant, 0.5 - 1.0 mm thick). Rare light rust-coloured subarkosic Fe siltstone (Fe-poor) laminae.	147.96	150.03 m
Fe siltstone: comparable to 142.49 - 145.73 m	150.03	151.61 m
Fe siltstone (dominant) & iron formation: comparable to the dominant lithology from 104.24 - 111.63 m, except for interval of burgundy-coloured, laminated hematite ± quartz lutite (60 cm thick).	151.61	154.01 m
Fe siltstone & iron formation (dominant): comparable to 34.18 - 36.04 m, except the Fe lutite/iron formation laminae are dominant and multiple load and flame structures can be developed along a single Fe lutite//Fe siltstone contact. Laminated jasper	154.01	156.46 m

horizon occurs at base (6 cm thick).

Iron formation (dominant): comparable to 147.96 - 150.03 m except the Fe siltstone layers are locally ripple cross-laminated. 156.46 157.8 m

Fe siltstone & iron formation (dominant): comparable to 154.01 - 156.46 m except the loaded Fe siltstone layers can be up to 3.5 cm thick (slab 20p, Plate 2.4e). 157.8 158.79 m

Fe arenite: three horizons of high weathering, medium-grained subarkosic Fe arenite (Fe-poor, Fe_2O_3 = 4.34%, geo $20q_b$). Typically unstratified. 158.79 159.36 m

Fe siltstone (dominant) & iron formation: comparable to the dominant lithology from 104.24 - 111.63 m. 159.36 160.67 m

Iron formation (dominant): comparable to 156.46 - 157.8 m. Laminated jasper horizon at top (5 cm thick). 160.67 161.32 m

Fe siltstone (dominant): two thinning- and fining-upward cycles; the first of which is based by 25 cm of laminated to very thin-bedded couplets of subarkosic Fe siltstone (Fe-poor) and hematite-quartz lutite (Fe-rich), then 55 cm of a thinly laminated version of same. The second cycle begins with a sharp, flat-based bed; the lowermost division of which is a coarse sand-size subarkosic Fe arenite (Fe-poor, 8 cm thick), then an abrupt change to medium sand-size coincides with a horizon of hematite lutite rip-ups (4 cm thick). The rip-ups are overlain by a structureless (29 cm) and a parallel laminated (15 cm) division. This second cycle is capped by laminated coupl 's like those atop cycle one. 161.32 163.42 m

Fe siltstone & iron formation (dominant): comparable to 34.18 - 36.04 m, except Fe lutite/iron formation laminae are dominant. Laminated jasper horizon at base (3.5 cm thick). 163.42 165.61 m

Jasper (dominant) & hematite: three main lamina types in decreasing order of abundance are: brick red weathering jasper (Fe-rich), steel grey weathering platy hematite (Fe-rich), and greyish-white weathering jasper (Fe-moderate). Combined Fe_2O_3 content of the brick red and steel grey laminae = 37.07% (geo $14a_3$). Localized development of jasper nodules (brick red, up to 3 mm long), specular hematite lenses and syndepositional faults. 165.61 166.02 m; 166.71 167.63 m

t.s. & p.t.s $14a_2$
slab $14a_4$

Fe siltstone, iron formation & Fe arenite: comparable to the dominant lithology from 104.24 - 111.63 m. Exceptions to the norm include atleast three bi-layered beds (2 - 10 cm thick) of ungraded, ferroan dolomite subarkosic Fe arenite (Fe-poor, 0.04 - 0.8 mm framework) abruptly overlain by subarkosic Fe 'siltstone' (Fe-poor, ≤ 0.004 - 0.12 mm framework). t.s. $14B_1$ 167.63 173.71 m

Diamictite: comparable to 128.53 - 131.44 m since here have sand-granule set in a dark brown weathering matrix dominated by quartz-hematite lutite. Some pockets of clast-free matrix. This is overlain by micro-diamictite: crudely stratified lenses (< 1 cm thick) of silt-sand supported by hematite-quartz lutite (Fe_2O_3 = 33.84%, geo $14d_2$). The main framework components (0.02 - 1.4 mm) are in decreasing order of abundance: solitary quartz, potassium feldspar, ferroan dolomite-quartz siltstone (comparable to dominant layer of $20L_1$), olive green biotite and hematite intraclasts. 173.71 176.97 m

t s $14d_1$

Diamictite: sand-(rare granule) set in a matrix dominated by quartz hematite lutite. Stratification is defined by a few subarkosic Fe arenite laminae (Fe-poor, 0.1 - 0.8 mm thick), one of which is isoclinally folded. t.s. and p.t.s. **14e** 176.97 177.49 m

Fe wacke (dominant): laminated through medium-bedded (commonly 9 - 25 cm thick) structureless, lithic subarkosic Fe wacke (Fe-moderate, Fe_2O_3 = 11.52%, geo $14g_2$, 0.04 - 0.8 mm framework, t.s. $14g_1$, up to 15 cm thick) overlain by a parallel laminated division (up to 10 cm thick) of subarkosic Fe arenite (Fe-poor, 0.04 - 0.44 mm framework, 0.2 - 3.2 mm thick) alternating either with framework diluted by hematite lutite (8 - 16 mm thick) or lithic subarkosic Fe wacke (Fe-moderate. 0.04 - 0.5 mm framework, 0.6 - 2.4 mm thick). A cross-laminated division (9 mm thick) caps the sequence in 14f. Loaded sole structures (i.e., flute casts) and coarse-tail 177.49 183.47 m

t s. 14f

grading (Plate 2.4d) are locally developed, and there is an isolated instance of a sand-granule diamictite (5 mm thick) at the structureless//parallel laminated interface.

Fe siltstone (dominant) & iron formation: comparable to the dominant phase from 104.24 - 111.63 m, except that within the second interval there are at least eight beds of dark reddish-brown, high weathering lithic subarkosic Fe wacke (Fe-moderate, 2.5 - 16 cm thick).	184.32 188.87 198.33	186.00 m 195.23 m 200.03 m
Iron formation: moderately foliated, laminated couplets (<8 mm thick) of hematite-quartz lutite (red) and hematite lutite (purple).	200.53 201.63 203.56	200.93 m 202.33 m 203.86 m
Fe siltstone, iron formation & Fe wacke: comparable to the dominant phase from 104.24 - 111.63 m, except there are two beds of lithic subarkosic Fe wacke (Fe-moderate, 15 & 17 cm thick). The second bed has a basal concentration of coarse - very coarse sand-size grains (2.5 cm thick) overlain by a division of hematite lutite rip-ups (6 cm thick, slab 14j, Plate 2.4c).	202.63 207.81	202.93 m 208.83 m
Micro-diamictite: comparable to that found within 173.71 - 176.97 m except here have layers, rather than lenses, of matrix-supported silt and sand.	209.83 210.98	210.38 m 211.33 m
Fe siltstone (dominant) & iron formation: comparable to the dominant phase from 104.24 - 111.63 m. The contact with the overlying unit has a stepped appearance (southwestward movement) due to soft-sediment thrust faulting.	212.63	213.03 m
Micro-diamictite: comparable to 209.83 - 211.33 m	213.03	214.03 m
Micro-diamictite: sand (0.1 - 2.0 mm) set in a blackish-grey weathering matrix dominated by hematite-quartz lutite (Fe_2O_3 = 33.10%, geo 14k). Unstratified. Locally developed pockets of clast-free matrix (e.g., 3 x 5 cm).	214.03	215.15 m
Iron formation: comparable to 200.53 - 203.86 m, except there is one bed of lithic subarkosic Fe wacke (Fe-moderate, 15 cm thick).	215.15	216.57 m
Fe siltstone (dominant) & iron formation: comparable to the dominant phase from 104.24 - 111.63 m.	216.57	217.99 m
Fe wacke (dominant): thin- to medium-bedded lithic subarkosic Fe wacke (Fe-poor) separated by laminated couplets similar to 216.57 - 217.99 m. The basal portion of the lithic subarkosic Fe wacke beds is locally flamed and coarse-tail graded, whereas the upper portion can have alternating parallel laminae of lithic subarkosic Fe wacke (Fe-poor, dominant, 0.04 - 1 mm framework) and subarkosic Fe wacke (Fe-poor, 0.04 - 0.4 mm framework, 1.6 - 5 mm thick). t.s. $14l_2$	217.99	219.41 m
Micro-diamictite: comparable to 209.83 - 211.33 m except there is one bed of lithic subarkosic Fe wacke (Fe-poor, 18 cm thick). This interval is scoured by the overlying diamictite.	219.41	221.23 m
Diamictite: sand-(rare granule) version of 214.03 - 215.15 m in which macro-matrix (<0.1 mm) Fe_2O_3 content = 32.40% (geo $14M_1$). The dominant micro-framework components (0.02 - 2.0 mm) are in decreasing order of abundance: solitary quartz, potassium feldspar, ferroan dolomite-quartz siltstone (comparable to dominant layer of $20L_1$) and hematite intraclasts. t.s. $14M_2$ At 224.8 m, there is a wavy and pervasively slumped layer (50 cm thick), within which there are faulted blocks of laminated Fe siltstone and Fe lutite.	221.23	228.42 m
Iron formation: clast-free macro-matrix which is dominated by hematite-quartz lutite.	228.42	233.02 m
Fe wacke: interval dominated by a sharp-based bed (40 cm thick) of subarkosic Fe wacke (Fe-poor), which contains numerous clasts (1 - 6 mm) of subarkosic siltstone and hematite lutite.	233.02	233.66 m
Iron formation: moderately foliated, laminated and burgundy-coloured, quartz poikilitic hematite lutite with trace apatite-chlorite micro-lenses (Fe_2O_3 = 53.36%, P_2O_5 = 1.71%). t.s. $14n_1$; geo $14n_2$	239.46	251.22 m

At 249.58 m, the Fe_2O_3 content has decreased to 32.27% and P_2O_5 content has increased to 6.61%. t.s. **14o$_1$**; geo **14o$_2$**	
Iron formation: comparable to 200.53 - 203.86 m, except there are 3 horizons of laminated jasper (3 - 11 cm thick) within the first interval and six jasper layers (1.5 - 10 cm thick) within the second interval.	252.79 253.16 m 254.59 255.89 m
Fe siltstone: comparable to 89.64 - 94.0 m, except one jasper horizon (3 & 1.5 cm thick) within the first and third intervals and five jasper layers (1.5 - 7 cm thick) within the second interval. Also, an orangy-brown recessive-weathering, ferroan dolomite-enriched layer (6 cm thick) occurs near top of third interval.	255.89 257.21 m 258.88 260.09 m 261.34 262.22 m
Fe siltstone (dominant): alternating layers of light brownish-green weathering quartz-chlorite-hematite Fe siltstone (Fe-poor, 0.4 - 0.9 mm thick) and blackish-grey weathering quartz-hematite lutite (Fe-moderate, 0.2 - 4 mm thick).	262.22 262.55 m Holowilena IF Wilyerpa Fmtn.
Fe siltstone: comparable to the dominant lithology from 262.22 - 262.55 m except clast-bearing. Clast size and percent increase from southwest (sand-granule, 3% of surface) to northeast (pebble-granule, 15% of surface), as does percent dolomite as fresh surface changes from medium green to mustard-coloured. The dominant clast types are light grey (smokey) tonalite-derived quartz and intact tonalite.	264.81 266.29 m
Wacke: fine-grained subarkosic green wacke which is basally stratified by framework-supported medium- to coarse sand (0.1 - 2 cm thick). The wacke is laterally equivalent to a framework-supported lens (6 x 0.9 m) of cobble-pebble-boulder conglomerate which occurs several metres along strike to the northeast.	269.41 270.31 m
Arenite: weathers beigy-white. Fine-grained subarkosic arenite is stratified by diffuse, light reddish-brown parallel laminae.	274.80 279.17 m

Table A.4: Description and thicknesses of stratigraphic section #21 in Back Creek, Holowilena South station. Distances are measured from the lowermost exposure of iron formation.

Iron formation: laminated, quartz poikilitic (0.2 mm maximum) magnetite-quartz-hematite lutite (Fe_2O_3 = 41.20%). p.t.s. **21a$_1$**; geo **21a$_2$**	0.00 7.13 m
Fe siltstone (dominant) & iron formation: weakly undulate couplets of light rust-coloured subarkosic Fe siltstone (Fe-poor, 2 - 7 mm) and black weathering hematite-quartz Fe lutite (Fe-rich, 1 - 3 mm). Ripple cross-laminae and flame structures are locally developed.	105.10 105.42 m
Diamictite: sand-granule-pebble set in a matrix dominated by hematite-quartz lutite. Clasts commonly range from 0.5 - 5 mm (2 x 1 cm max.) and the most prevalent type is recessive-weathered, ferroan dolomite. Stratified by irregular, clast-supported pods (range from 7 x 6 cm to 60 x 30 cm). The main micro-framework components (0.02 - 1.2 mm) are in decreasing order of abundance: solitary quartz, potassium feldspar, quartz-ferroan dolomite ± sericite siltstone and hematite intraclasts. p.t.s. **21b**	105.42 107.08 m
Fe siltstone (dominant) & iron formation: comparable to 105.1 - 105.42 m, except for four interlayers of sand-size diamictite (1 - 5 cm thick).	107.08 107.44 m
Diamictite: comparable to 105.42 - 107.08 m, except for a few clast-free layers (up to 10 cm thick) of laminated, subarkosic Fe siltstone (Fe-moderate).	107.44 110.44 m
Fe siltstone (dominant) & iron formation: comparable to 105.1 - 105.42 m, except for two interlayers of sand-size diamictite (1.5 - 3 cm thick).	110.44 110.74 m
Micro-diamictite: sand set in a blackish-grey weathering matrix dominated by hematite-quartz lutite in first interval, which changes to a clast-free version of the matrix at 112.29 m (Fe_2O_3 = 31.05%, geo **21d**).	110.74 112.39 m 112.29 114.19 m
Fe siltstone: laminated grey-green weathering Fe siltstone (Fe-moderate), the fresh surface of which is weakly magnetic. Sand-(rare pebble) diamictite layer (15 cm	114.19 115.16 m

thick) near top of interval.

	Holowilena IF	
	Wilyerpa Fmtn.	
Siltstone (dominant): light green weathering quartz-ferroan dolomite siltstone (Fe_2O_3 = 5.94%, L.O.I. = 13.71%, geo **$21f_3$**) stratified by undulate-based, flat-topped fine-grained subarkosic wacke laminae, which are commonly 1 - 3 mm thick but locally 1 - 6 cm thick (e.g., seven such layers within middle third of second interval). Synsedimentary dextral faults (4 mm offset) were observed within first interval and starved ripples occur near top of fourth interval.	115.16 170.33 184.19 190.18	116.49 m 184.19 m 190.18 m 196.89 m
Wacke: two basally loaded and flamed beds (13 & 10 cm thick) of green subarkosic wacke capped by light green siltstone (4 & 2 cm thick).	196.89	197.3 m
Diamictite: pebble-boulder-(minor cobble-granule) supported by a greyish-green subarkosic wacke. The close-set clasts include light reddish-brown ferroan dolomite, subarkosic arenite, and intraformational hematite-quartz lutite (iron formation) & light green siltstone (comparable to 170.33 - 184.19 m). Typically unstratified.	197.3	206.81 m
Siltstone (dominant): comparable to 184.19 - 196.89 m, except no starved ripples and the thickest wacke layer = 2 cm.	206.81	217.31 m
Diamictite: pebble-(minor cobble-boulder-granule) in which the matrix and clast types comparable to 197.3 - 206.81 m. Basally loaded contact with underlying siltstone.	217.31	224.36 m
Fe siltstone (dominant): diffusely laminated, quartz-hematite-ferroan dolomite Fe siltstone (Fe-moderate) within which there are two subarkosic Fe wacke layers (Fe-poor, 11 & 3 cm thick). Pebble-bearing horizons occur along the base and the top (12 & 73 cm thick) of interval.	224.36	226.11 m
Diamictite: granule-pebble-sand-(rare cobble) set in a dark grey matrix dominated by quartz-hematite-ferroan dolomite lutite (Fe_2O_3 = 11.96%, L.O.I. = 10.69%, geo **$21h_3$**). Unstratified. The dominant macro-framework is ferroan dolomite, and the main micro-framework components (0.02 - 0.7 mm) are in decreasing order of abundance: solitary quartz, potassium feldspar, hematite-quartz (iron formation) clasts, ferroan dolomite and chlorite. t.s. and p.t.s. **$21h_1$**	236.55	242.03 m
Diamictite: pebble-cobble-boulder-granule supported by a fine-grained subarkosic green wacke. Clast coverage of the weathered surface varies from 10 - 60%; it is highest beneath a rectangular slumpball (1.7 m long x 0.52 m thick) of subarkosic arenite. The slumpball is clast-free, faintly laminated and contains syndepositional faults. The main clast types are reddish-brown ferroan dolomite and medium green siltstone. Minor types include oomicrite, carbonate-bearing subarkosic arenite, translucent vein quartz, jasper and granodiorite.	242.03	248.96 m
Fe siltstone: comparable to 251.9 - 281.29 m except sporadic granule- and pebble-size lonestones occur throughout.	248.96	251.57 m
Micrite: orangy-brown weathering, laminated micrite within which there is an undulate-based, flat-topped, pebble-bearing lens. The basal pebbles have loaded into the underlying laminae.	251.57	251.90 m
Fe siltstone: light yellowish-brown weathering ferroan dolomite-quartz Fe siltstone (Fe-poor, dominant, Fe_2O_3 = 5.14%, L.O.I. = 26.60%, geo **$21i_3$**) which is laminated by ferroan dolomite subarkosic Fe wacke (Fe-poor, subordinate, 0.06 - 0.8 mm thick, not included in geochemical aliquot, t.s. **$21i_3$**). A cobble-size (22 x 3 cm) lonestone of subarkosic arenite occurs at 275.25 m.	251.90	281.29 m
Diamictite: pebble-granule-sand in which the green weathering matrix and main clast types (2) are comparable to 242.03 - 248.96 m. Clasts cover 10% of the exterior surface.	281.29	283.78 m
Diamictite: pebble-granule-sand-(rare cobble-boulder) comparable to 236.55 - 242.03 m. Recessive-weathered, reddish-brown ferroan dolomite and black hematite-quartz (iron formation) clasts prevail).	283.78	294.39 m

Arenite: buff-coloured, medium-grained subarkosic arenite, which has from base to top: a 24 cm thick layer of dispersed clasts (1 - 4 mm), a 3 cm thick lens/layer of granule-pebble-size clasts (5.. cm maximum), a 95 cm thick zone containing five lenticular, bedding parallel, light green siltstone rip-ups, and a 24 cm thickness of silt- to fine sand-size subarkosic arenite.	294.39	295.85 m
Siltstone: comparable to 170.33 - 184.19 m	296.73	297.97 m
Diamictite: pebble-granule-sand comparable to 281.29 - 283.78 m, except hematite-quartz (iron formation) clasts rank second in abundance.	297.97	300.05 m
Plausible sinistral fault offsets the diamictite at approximately 300.05 m. Non exposure within centre of creekbed precludes measurement of offset or delineation of fault trace.		
Diamictite: pebble-granule-sand-(sporadic cobble-boulder) set in a dark grey matrix dominated by quartz-hematite-ferroan dolomite lutite (Fe_2O_3 = 12.23%, L.O.I. = 11.70%, geo **$21j_2$**). The main macro-framework components are rusty-brown ferroan dolomite and black hematite-quartz (iron formation) which occur in a ratio of 5:1. Minor clast types include jasper, medium-grained tonalite, light green siltstone and fine-grained purple quartzite. The main micro-framework components (0.02 - 0.4 mm) are similar to 236.55 - 242.03 m, namely: monocrystalline quartz, potassium feldspar, hematite-quartz (iron formation) clasts, ferroan dolomite and chlorite-after-phlogopite. p.t.s. **$21j_1$**	300.05	314.11 m
Siltstone (dominant): alternating laminae of grey-green siltstone (dominant, 0.8 - 1.5 mm thick) and dark grey Fe siltstone (Fe-moderate, 0.2 - 0.6 mm thick). The uppermost laminae flame into the overlying diamictite.	314.11	314.82 m
Diamictite: pebble-granule-sand supported by a light green, fine-grained subarkosic wacke. Clasts cover 12% of the weathered surface and are mostly of ferroan dolomite and iron formation (1:1 ratio).	314.82	315.25 m
Siltstone (dominant): comparable to 314.11 - 314.82 m except the exposure here is lensoid as it passes laterally into diamictite.	315.25	315.41 m
Diamictite: comparable to 314.82 - 315.25 m	315.41	318.13 m
Conglomerate & wacke: interval has alternating layers of framework-supported pebble-granule conglomerate and medium-grained subarkosic wacke. Cobble- and boulder-size (48 cm maximum) clasts are most prevalent in the two thickest conglomerate layers (80 & 82 cm thick). Sand-size layers locally display diffuse cross-laminae (24° to horizontal) or parallel, discontinuous "layers" of one grain thick granules. Based at 322.59 m is a 20 cm thick interval of laminated green siltstone, within which is a cobble-size (11 x 10 cm) dropstone of tonalite(?). The succeeding bed is conglomeratic and inversely graded.	319.20	324.29 m
Arenite (dominant): medium-grained subarkosic arenite stratified by granule-bearing layers (4 - 7 cm thick).	324.29	326.11 m
Conglomerate & wacke: comparable to 319.2 - 324.29 m except atleast two conglomerate layers appear to be normally graded.	326.11	327.83 m

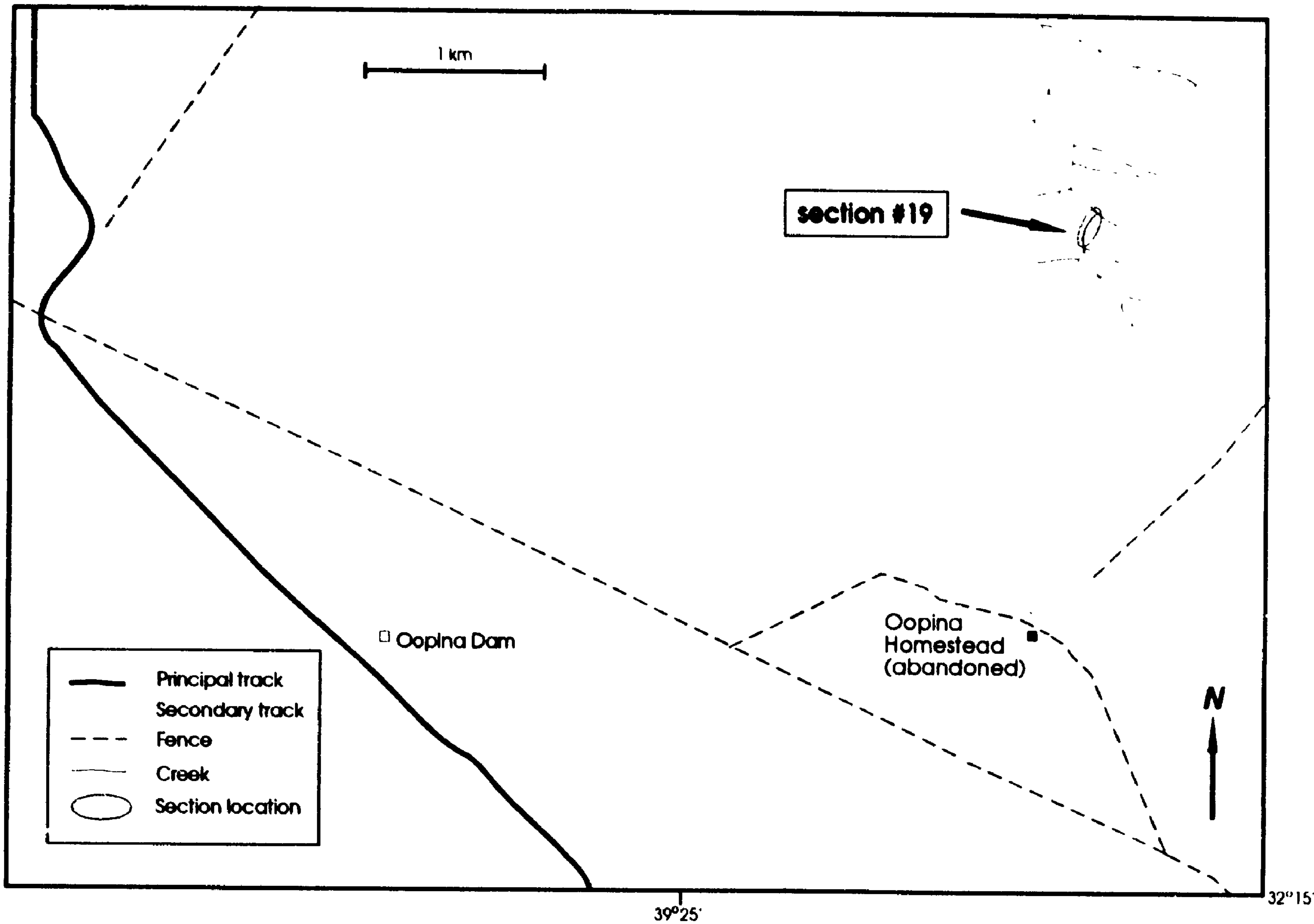

Figure A.5 Location of stratigraphic section #19 on Oopina station.

Table A.5: Description and thicknesses of stratigraphic section #19 on Oopina Station. Distances are measured from first exposure of Belair Subgroup below iron formation-bearing interval.

Siltstone: light green exterior surface consists of flat, very thin (0.1 - 3 mm) rhythmic laminae. Non magnetic fresh surface. The main components, in decreasing order of abundance are quartz, biotite, sericite and Ti hematite (Fe_2O_{3t} = 7.79%). Locally see cross-laminated starved ripples and parallel 8 - 20 mm thick layers, both of which are biotite-depleted.	0.00	40.81 m
Beginning at approximately 40.3 m is a 0.5 metre wide shear zone (094°/64°), which lies within the siltstone and is intruded by foliation-parallel quartz veins.		
	Kadlunga Slate / Pualco Tillite	
Diamictite: granule-pebble (commonly 2 - 10 mm) set in a subarkosic wacke matrix. Unstratified. Clast coverage of the greenish-grey weathered surface increases from less that 1% at base of interval to 5% at top. The predominant clast type is a light grey and white quartz arenite, two of which were observed to be significantly coarser than the norm (e.g., 4 x 9.5 cm, 5 x 6.5 cm). slab **19c**	40.81	42.70 m
Iron formation: comparable to 109.06 - 114.84 m	96.13	100.65 m
Iron formation: laminated, steel grey weathered and fresh surfaces, the latter of which varies from weakly to moderately magnetic.	104.48	105.22 m
Fe wacke & Fe siltstone: alternating laminae of buff-coloured subarkosic Fe wacke (Fe-poor, 1 - 6 mm thick) and dark grey weathering Fe siltstone (Fe-moderate, ≤ 3 mm thick).	105.22 108.54	106.24 m 109.06 m
Iron formation: macroscopic features comparable to 104.48 - 105.22 m. Microscopic examination reveals a laminated quartz-magnetite-hematite-(chlorite-after-biotite) Fe lutite. p.t.s. **$19E_2$**	109.06	114.84 m
Iron formation with Fe siltstone: comparable to 109.06 - 114.84 m except have flat-based, flat-topped, slightly recessive and weakly to moderately magnetic light grey Fe siltstone layers (Fe-moderate, 8 - 10 mm thick) which are spaced from 1.5 - 22 cm apart.	166.69	184.03 m
Iron formation: strongly foliated version of 109.06 - 114.84 m except have sporadic mauve-coloured hematite-quartz lutite layers (0.5 - 7 cm thick) from 187.42 - 188.44 m.	187.42	204.40 m
Iron formation: alternating diffuse brownish-grey and greyish-black laminae typify the weathered surface. Consists of quartz-magnetite-hematite-chlorite Fe lutute (dominant) with a few thin laminae which are quartz-enriched and iron oxide-depleted relative to the dominant phase (Fe_2O_3 = 43.06%). p.t.s. **$19G_1$**; geo **$19G_2$**	209.57	229.26 m
Diamictite: granule-pebble supported by light brown subarkosic wacke. Unstratified. The majority of clasts measure 2 - 9 mm, a size range occupied mainly by tonalite-derived quartz (covers 4% of exterior surface). The subordinate size range is 0.9 - 3.3 cm and consists of either fine- to medium-grained tonalite or translucent vein quartz, both of which are present in roughly equal amounts and together cover 2% of the weathered surface.	231.28	241.60 m
Diamictite: pebble-granule set in a ferroan dolomite-biotite subarkosic wacke (non Fe, Fe_2O_3 = 3.00%, geo **$19h_2$**). In contrast to the 231.28 - 241.6 m interval, clasts within the 12 - 30 mm range (i.e., tonalite, vein quartz and aphyric purple quartzite) cover 4% of the weathered surface, whereas the 2 - 11 mm range (i.e., tonalite-derived quartz, recessive carbonate) cover less that 2%. With respect to the micro-framework, the components (0.06 - 0.9 mm) in decreasing order of abundance are: solitary (monocrystalline) quartz, plagioclase feldspar, ferroan dolomite and olive green biotite. p.t.s. **$19h_1$**	242.38	252.21 m
Diamictite: granule-pebble comparable to 231.28 - 241.6 m	256.59	259.17 m

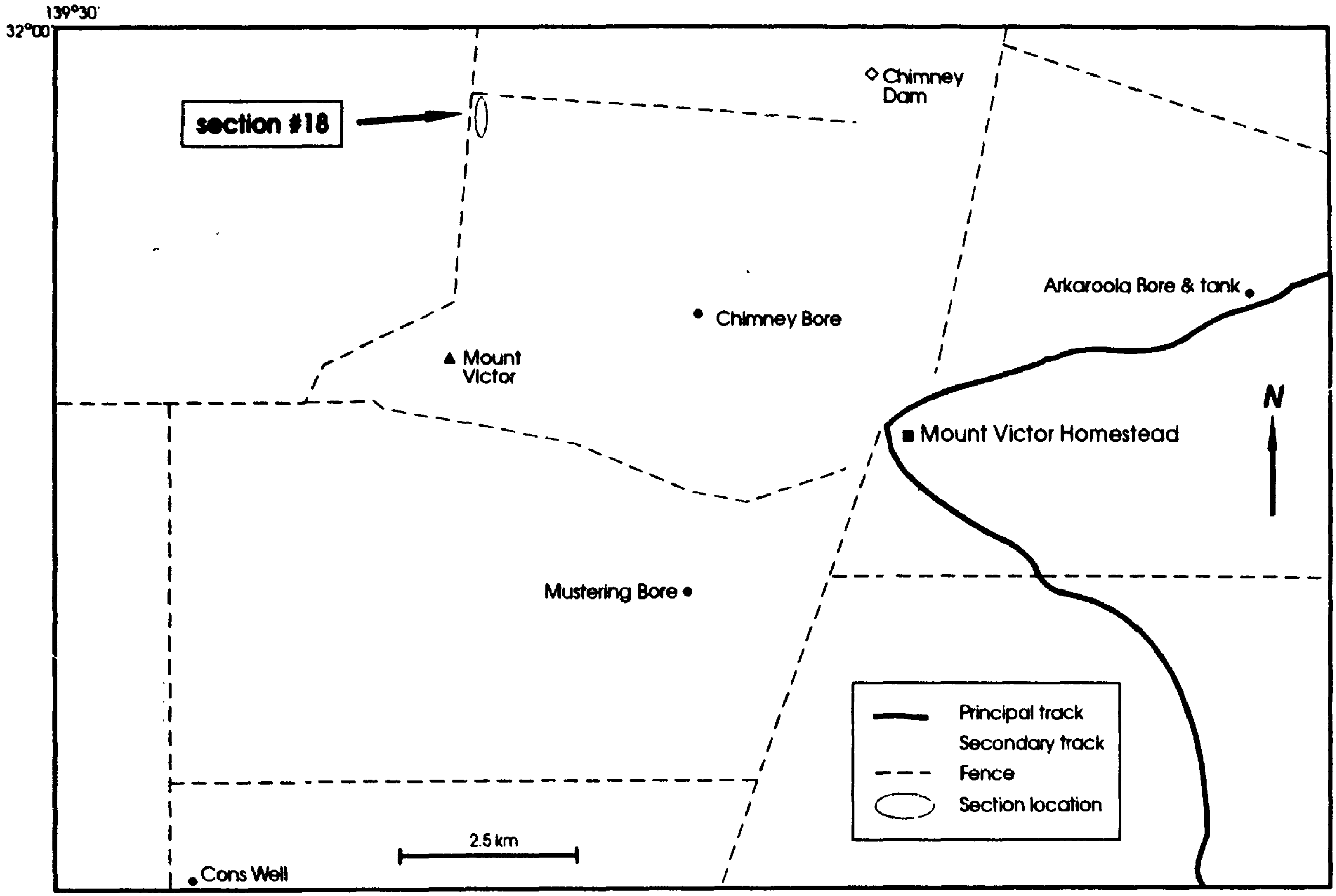

Figure A.6 Location of stratigraphic section #18 on Mount Victor station.

Table A.6: Description and thicknesses of stratigraphic section #18 at Razorback hill, Mount Victor Station. Distances are measured from first exposure of Pualco "Tillite" below iron formation-bearing interval.

Diamictite: granule-pebble-(± sand) supported by an orangy-buff-coloured subarkosic wacke matrix. Unstratified. Clasts, ranging from 1 - 20 mm (commonly 2 - 10 mm), cover 10% of the exterior surface. The dominant clast type is a semi-transparent grey-white quartz. Second in abundance are recessively-weathered/pitted out ferroan dolomite(?) clasts which are ovoid-shaped and foliation-parallel. Noted one 9.5 x 3 cm size clast resemblant of the quartz arenite exposed on the south slope of Mount Victor.	0.00	19.42 m
Wacke: unstratified subarkosic wacke with only a few sporadic granule-size clasts.	20.81	26.71 m
Diamictite: granule-pebble-sand comparable to 0.00 - 19.42 m. Maximum clast size of 3 cm, but typically ≤ 1 cm.	26.71	31.34 m
Wacke: unstratified, clast-free subarkosic lens is laterally continuous for 18 m.	36.14	36.80 m
Diamictite: pebble-granule-(rare cobble) set in a ferroan dolomite-biotite subarkosic wacke matrix (non Fe, Fe_2O_3 = 2.04%, geo **18a₂**). Unstratified. Clasts, ranging from 0.1 - 9 cm (commonly 2 - 30 mm), cover 10 - 15% of the weathered surface. Competent, non-foliation-parallel clasts are of two sizes and types: small (2 - 10 mm) light grey (smokey) tonalite-derived quartz and large (2 - 9 cm) intact tonalites. Non competent, foliation-parallel and recessively-weathered ferroan dolomite(?) clasts are subordinate. Microscopically, the dominant framework components (0.06 - 0.5 mm) in decreasing order of abundance are: solitary (monocrystalline) quartz, twinned plagioclase, ferroan dolomite and yellowish-brown biotite. p.t.s. **$18a_1$**	36.80	38.70 m
Wacke: plano-convex (flat top) subarkosic wacke lens extends laterally for 7.5 m	38.70	39.80 m
Diamictite: comparable to 36.8 - 38.7 m except near top of interval where the order of macroscopic clast dominance has changed to: (1) recessively-weathered ferroan dolomite, (2) light green-tinged quartz arenite, (3) tonalite and tonalite-derived quartz. Also, matrix composition at 84.01 m is a ferroan dolomite-biotite-sericite subarkosic Fe wacke (Fe-poor, Fe_2O_3 = 4.44%, geo **$18b_2$**, 0.06 - 0.5 mm micro-framework). Magnetite visible in thin section **$18b_1$** (Plate 2.1c), but not in $18a_1$.	39.80	100.26 m
Diamictite: pebble-granule-(rare cobble) comparable to 36.8 - 38.7 m except the matrix now weathers brownish-green and is a weakly magnetic ferroan dolomite-biotite subarkosic Fe wacke (Fe-poor/Fe-moderate). Clast abundances are somewhat similar to the upper third of the 39.8 - 100.26 m interval with: (1) approximately equal amounts of recessive ferroan dolomite and light green-tinged quartz arenite and (2) minor tonalite and tonalite-derived quartz present only in the 1 - 10 mm size fraction.	123.02	127.62 m
Diamictite: comparable to 123.02 - 127.62 except here the matrix is a weakly magnetic ferroan dolomite-biotite-magnetite subarkosic wacke Fe wacke (Fe-moderate, Fe_2O_3 = 6.41%, 0.06 - 0.5 mm micro-framework). p.t.s. **$18c_1$**; geo **$18c_2$**	173.16	177.30 m
Diamictite: comparable to 173.16 - 177.30 m except for a high weathering 6 m^2 zone wherein the matrix is light-coloured and non magnetic. However, thin section examination reveals magnetite is a component of this ferroan dolomite subarkosic Fe wacke (Fe-poor, 0.04 - 0.6 mm micro-framework). t.s. **18d**	.79.66	183.08 m
Diamictite: comparable to 123.02 - 127.62 m	189.10	191.52 m
Iron formation: blackish-green weathering, quartz-biotite-magnetite lutite is moderately magnetic and locally stratified by yellowish-white felsic siltstone laminae (1 - 2 mm thick).	198.40	200.70 m
Iron formation: exterior is dominantly greyish-black and strongly magnetic with thin brown recessive laminae (1 - 2 mm) typically spaced from 0.1 - 1 cm apart (6 cm apart where geochem sample taken. Namely, quartz-magnetite-(with chlorite-after-	224.74	226.61 m

biotite = ferroan dolomite)-hematite Fe lutite with thin laminations of quartz-magnetite-ferroan dolomite-hematite Fe lutite. The Fe_2O_3 content with thin laminae removed is 34.86%. p.t.s. **18E₁**; geo **18E₂**

Fe siltstone: weakly foliated, thinly laminated (1 - 3 mm) pale green:dark green couplets in which the laminae are flat and continuous. The weakly magnetic couplets appear to be of quartz-biotite (pale green) and quartz-biotite-magnetite (dark green).	245.05 245.95 m
Fe siltstone: very thin-bedded (1 - 3 cm) couplets of quartz-biotite (pale green, dominant) and quartz-magnetite-biotite (dark grey, strongly magnetic). A plausible transition zone from Fe siltstone (245.05 - 245.95 m) to iron formation (246.40 - 246.90 m).	245.95 246.40 m
Iron formation: comparable to 224.74 - 226.61 m except thin, brown (ferroan dolomite-bearing) laminae are absent.	241.22 242.30 m 246.40 246.90 m
Fe siltstone: comparable to 245.05 - 245.95 m (Fe_2O_3 = 13.40%, geo **$18f_2$**; p.t.s. **$18f_1$**)	246.90 251.17 m
Iron formation: comparable to 246.40 - 246.90 m	251.17 252.55 m 254.55 255.42 m 266.86 267.88 m
Fe wacke: comparable to 286.74 - 289.54 m except not visibly stratified	281.88 283.82 m
Fe wacke: light pinkish-brown weathered surface has locally developed thin black laminae spaced 4 - 5 mm apart. Laminae can be contorted due to soft-sediment folding. Fresh surface is weakly magnetic. Thin section examination reveals a ferroan dolomite-Ti hematite-(chlorite-after-biotite) subarkosic Fe wacke (Fe-poor, Fe_2O_3 = 4.73%, geo **$18g_2$**) in which framework components range from 0.04 - 0.3 mm. p.t.s. **$18g_1$**	286.74 289.54 m
Wacke: comparable to 286.74 - 289.54 m but is non magnetic.	295.22 295.97 m
Iron formation: comparable to 246.40 - 246.90 m (Fe_2O_3 = 54.29%, geo **18h**).	295.97 296.60 m
Wacke: comparable to 295.22 - 295.97 m	296.60 298.13 m
Iron formation: comparable to 295.97 - 296.60 m	305.93 306.34 m
Wacke: comparable to 295.22 - 295.97 m	319.20 320.76 m
Iron formation: comparable to 295.97 - 296.60 m	321.66 325.62 m
Fe siltstone: comparable to 245.05 - 245.95 m except ferroan dolomite now present (Fe_2O_3 = 17.03%, L.O.I. = 6.39%, geo **$18i_2$**).	337.95 338.95 m
Iron formation: comparable to 369.23 - 370.48 m	365.90 366.18 m 366.91 367.30 m
Iron formation: stratification is not apparent on either the dark greyish-black weathered surface nor the greyish-green fresh surface. Consists of quartz-magnetite-(with chlorite-after-biotite = ferroan dolomite)-hematite Fe lutite (Fe_2O_3 = 36.54%). p.t.s. **$18j_1$**; geo **$18j_2$**	369.23 370.48 m 373.00 373.86 m
Iron formation: comparable to 369.23 - 370.48 m except for a few thin (< 1 mm thick) yellowish-white felsic siltstone laminae.	377.58 378.76 m 381.21 381.87 m 382.53 383.06 m 388.50 389.14 m
Iron formation: comparable to 224.74 - 226.61 m	399.72 400.28 m

Iron formation & Fe siltstone: quartz-magnetite-(with chlorite-after-biotite = ferroan dolomite)-hematite Fe lutite (1 - 1.5 cm thick) alternating with quartz-biotite-magnetite Fe siltstone (Fe-moderate, 2 - 3 cm thick).	401.50	402.91 m
Iron formation: comparable to 369.23 - 370.48 m	418.34	419.20 m
	421.63	422.20 m
	422.52	424.60 m
Iron formation: macroscopically comparable to 369.23 - 370.48 m but Fe_2O_3 = 55.85%. geo **18k**	447.84	449.15 m
Fe arenite: weathers medium brown. Typically unstratified except for discontinuous (2 cm strike length) cross-laminae which are defined mainly by titaniferous hematite. Classify as a ferroan dolomite subarkosic Fe arenite (Fe-poor, Fe_2O_3 = 4.81%, 0.04 - 0.16 mm framework). p.t.s. **$18l_1$**; geo **$18l_2$**	449.88	450.57 m
Iron formation: comparable to 447.84 - 449.15 m	451.43	453.33 m
	454.74	455.99 m
	466.39	467.75 m
	472.80	474.01 m
	477.18	478.58 m
	483.14	483.79 m
	484.89	485.89 m
	487.09	487.78 m
	488.68	489.60 m

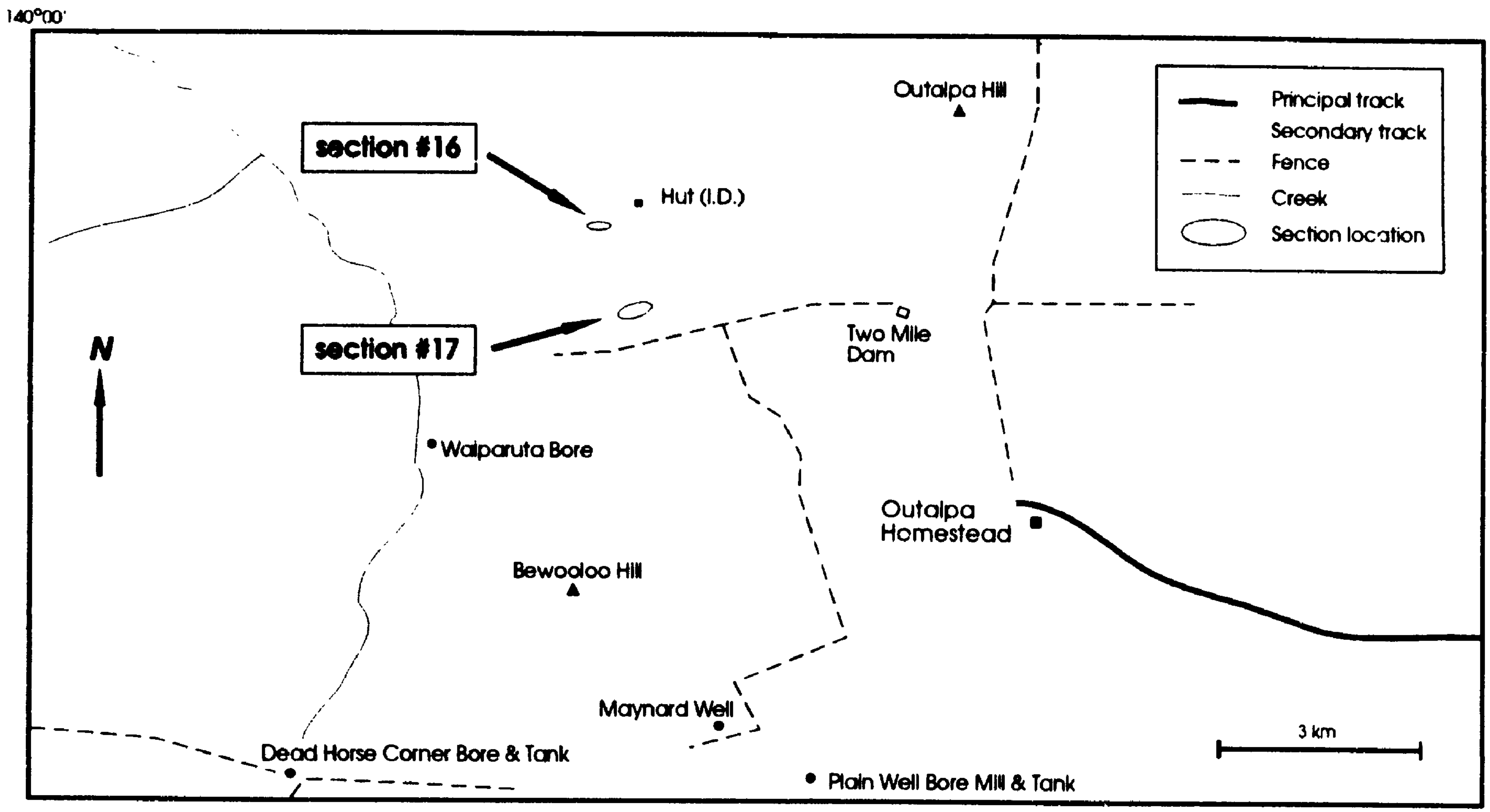

Figure A.7 Locations of stratigraphic section nos. 16 and 17 on Outalpa station.

Table A.7: Description and thicknesses of stratigraphic section #17 on Outalpa station. Distances are measured from first exposure of Pualco "Tillite" below iron formation-bearing interval.

Diamictite: pebble-granule-sand-(sporadic 8 - 75 cm size cobbles and boulders) supported by a dark brown weathering biotite-ferroan dolomite subarkosic wacke matrix (Fe_2O_3 = 6.62%, geo $17a_2$). Roughly 40% of the exterior surface is covered by clasts, most of which are tonalitic in composition. Far less prevalent are vein quartz (second) and recessively weathered, reddish-brown ferroan dolomite (third). Also, the five largest clasts (11 - 75 cm) observed at this locale were all tonalites. The dominant micro-framework components (0.06 - 0.5 mm) are in decreasing order: solitary (monocrystalline) quartz, potassium feldspar, biotite and ferroan dolomite. } p t s. $17a_1$	0.00	15.00 m
Biotite quartz wacke: unbroken contact between diamictite and an unstratified, clast-free quartz wacke lens in which framework grains vary from 0.04 - 0.5 mm. The light brown weathering lens is laterally continuous for 100 m before it fades into diamictite.	15.00	16.00 m
Iron formation: both the weathered and fresh surfaces of this unit are dark green and strongly magnetic. Faintly laminated (2 - 4 mm thick) quartz-biotite-magnetite lutite.	16.00	16.50 m
Calcite-biotite quartz wacke: stratified throughout the lower 3 m by discontinuous matrix-supported granule lenses (3 - 5 cm thick). Lower and upper contacts of these lenses are neither sharp nor flat; they are locally undulate but not erosive. The upper 2 m of the quartz wacke (SiO_2 = 82.75%, geo 17c) is devoid of clasts and strata.	16.50	21.50 m
Iron formation: comparable to 16 - 16.5 m except layer thicknesses have increased to 0.5 - 2.0 cm	21.50	25.50 m
Diamictite: matrix-supported throughout the lowermost 0.5 m, then changing to a framework-supported pebble conglomerate. Common size of tonalite (predominant) and vein quartz (subordinate) clasts is 1 - 7 cm.	25.50	39.00 m
Fe siltstone/Iron formation: typically unstratified and aphyric, dark brown weathering quartz-biotite-magnetite Fe siltstone (Fe-moderate/Fe-rich, Fe_2O_3 = 20.80%, geo 17d).	39.00	64.50 m

Table A.8: Description and thicknesses of stratigraphic section #16 near I.D. Hut, Outalpa station. Distances are measured from first exposure of Benda "Siltstone" below iron formation-bearing interval.

Fe wacke (dominant): stratification in this weakly magnetic, biotite subarkosic Fe wacke (Fe-poor, Fe_2O_3 = 3.17%, geo $16A_1$) is defined by brownish-yellow weathering, non magnetic subarkosic arenite layers (13 - 36 mm thick) generally spaced atleast 16 cm apart. These felsic layers locally exhibit basal loading, internal parallel or cross-lamination, and tight soft-sediment folding (h = 3 cm, λ = 6 cm). At 35.45 m noted several ovoid nodules (3 x 10 mm to 15 x 32 mm; calcite core) within a 0.6 m thick Fe wacke layer.	0.00	36.70 m
Fe wacke (dominant): comparable to 0 - 36.70 m except that the more felsic, non magnetic subarkosic arenite interlayers are less apparent. They are visible on fresh surface as diffuse laminae alternating with Fe wacke laminae (both types are 2 - 3 mm thick) over a 1 - 2 cm thick zone (zones spaced up to 20 cm apart).	56.30	65.20 m
Fe wacke (dominant): comparable to 56.30 - 65.20 m except that the non magnetic, subarkosic arenite interlayers are evident on weathered surface.	69.10	79.67 m
Fe wacke (dominant): comparable to 69.10 - 79.67 m except that a third layer-type is present here. Namely, high weathering, thin to thickly laminated quartz-biotite-magnetite Fe siltstone (alternating Fe-poor and Fe-moderate with combined Fe_2O_3 = 14.64%, Plate 2.5c). This third layer-type occurs in $\leq$ 10 cm thick intervals and } p + s $16b_1$ represents the culmination of an upward increase in iron content from < 1% Fe_2O_3 in the soft-sediment-folded subarkosic arenite laminae, to 5.74% Fe_2O_3 in the biotite subarkosic Fe wacke (geo $16b_4$), to 14.64% Fe_2O_3 in the quartz-biotite-magnetite Fe	79.67	88.18 m

siltstone laminae (geo **16b**$_2$).

Fe wacke (dominant): comparable to 56.30 - 65.20 m	88.18	105.78 m
Zone of wavy laminae, soft-sediment-folding, numerous load and flame structures. Composition: biotite subarkosic Fe wacke layers (Fe-poor, typically 1 - 3 cm thick, locally 20 - 40 cm thick) with diffuse internal felsic laminae alternate with one cm thick zones of thinly laminated biotite subarkosic Fe wacke (Fe-poor) and subarkosic (non Fe) arenite. It is the latter cm thick zones which are commonly loaded and flamed. At 125.38 m, have a greyish-black weathering, 25 cm thick section (Plate 2.2d) of strongly magnetic iron formation: thinly laminated quartz-magnetite-biotite Fe lutite (Fe_2O_3 = 41.67%) p.t.s. **16d**$_1$; geo **16d**$_2$).	108.38	140.13 m
Section comparable to 108.38 - 140.13 m except that here the biotite subarkosic Fe wacke (Fe-poor) layers with diffuse internal felsic laminae are commonly 30 - 40 cm thick, not 1 - 3 cm thick. The uppermost 0.6 m is akin to 79.67 - 88.18 m, except for collinear starved ripples (felsic) and randomly distributed nodules.	140.13	147.23 m
Fe wacke (dominant): comparable to 56.30 - 65.20 m except for a 20 cm thick, non magnetic ferroan dolomite-biotite subarkosic wacke layer (Fe_2O_3 = 3.00%, geo **15e**$_3$) at base of interval.	147.23	153.73 m
Three lithologies similar to 79.67 - 88.18 m with 3 - 20 cm thick triplets of: (1) soft-sediment-folded subarkosic (non Fe) arenite laminae, (2) biotite subarkosic Fe wacke (Fe-poor) and (3) quartz-biotite-magnetite Fe siltstone laminae. Locally see poorly developed cross-lamination within the subarkosic (non Fe) arenite layers and sporadic non layer specific nodules.	153.73	155.73 m
Wacke (dominant): comparable to 56.30 - 65.20 m except the fresh surface is non magnetic, hence no Fe prefix.	164.73	166.33 m
Comparable to 153.73 - 155.73 m except triplets vary from 6 - 11 cm thick rather than 3 - 20 cm.	166.33	167.93 m
Comparable to 108.38 - 140.13 m except that the biotite subarkosic wacke layers are non magnetic, hence no Fe prefix.	167.93	171.18 m
Comparable to 108.38 - 140.13 m	180.08	183.38 m
Fe wacke (dominant): comparable to 69.10 - 79.67 m. The biotite subarkosic Fe wacke (Fe-poor) here has Fe_2O_3 = 3.76% (geo **16h**$_2$). At approximately 193 m have a 30 cm thickness of iron formation: unstratified and moderately magnetic quartz-biotite-magnetite lutite. At 198.43 m have a 20 cm thick interval of quartz-biotite-ferroan dolomite-magnetite Fe siltstone (Fe-poor, dominant) with weakly undulate laminae of quartz-biotite-magnetite-ferroan dolomite Fe siltstone (Fe-moderate & Fe-rich). t.s. **16g**	183.38	202.83 m
Fe siltstone/Iron formation: weathers blackish-green. Quartz-biotite-magnetite Fe siltstone (Fe-moderate/Fe-rich) is unstratified. Sporadic occurrence of calcitic nodules and 0.3 - 1.2 mm clasts. t.s. **16i**	202.83	205.98 m
Fe wacke (dominant): comparable to 56.30 - 65.20 m	205.98 219.63	215.33 m 221.53 m

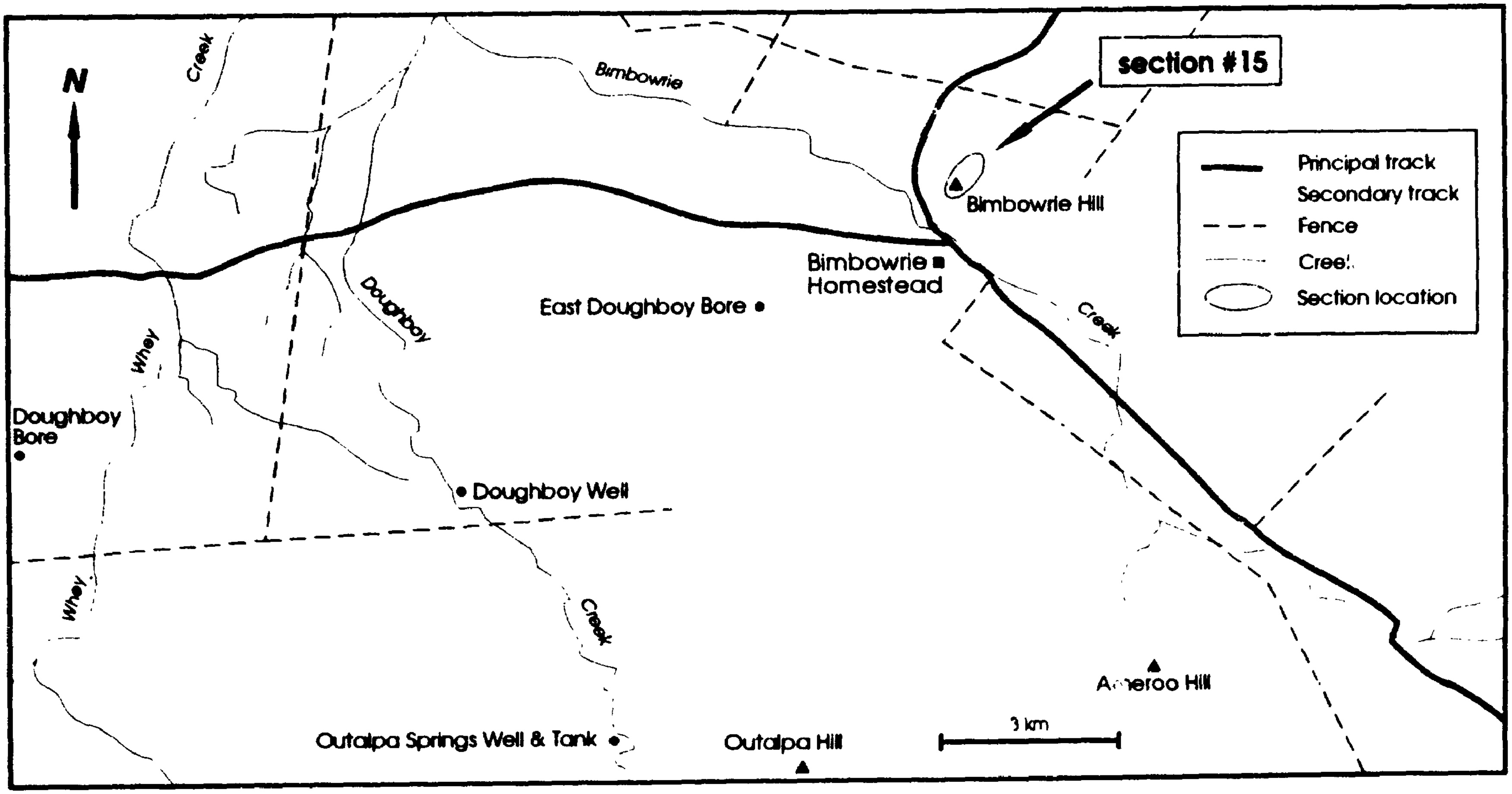

Figure A.8 Location of stratigraphic section #15 on Bimbowrie station.

Table A.9: Description and thicknesses of stratigraphic section #15 at Bimbowrie Hill, Bimbowrie station. Distances are measured from first exposure of Pualco "Tillite" below iron formation-bearing interval.

Arenite: light grey weathering and typically unstratified subarkosic arenite (non Fe, Fe_2O_3 = 0.39%, 0.06 - 0.24 mm framework, t.s. **15a₁**) with only rare development of thin discontinous greyish-green laminae. Noted two adjacent boulder-size (14.5 x 11 cm, 13 x 11 cm) subangular tonalite lonestones, the larger of which has several tonalite clasts (2 - 6 mm) rimming its upper edge.	0.00	12.57 m
Arenite: most prevalent feature within this subarkosic arenite is an irregularly-shaped, poorly sorted, matrix- bordering on framework-supported, pebble-cobble-boulder-granule lens. Internally, this lens is crudely stratified because granule- to small pebble-size clasts predominate in the uppermost 10 cm. Clast types include tonalite, mafic volcanic and a white mica-chlorite-feldspar schist. Upsection of the lens, scattered clasts (0.5 - 10 cm) of tonalite and vein quartz comprise 2% of the weathered surface.	12.57	18.39 m
Arenite: massive subarkosic arenite except for occurrence of two tonalite pebbles within a 9 m^2 area.	18.39	19.99 m
Arenite: small patches of finely disseminated magnetite ± biotite impart a darker hue to the fresh surface of this subarkosic arenite (Fe_2O_3 = 0.80%, 0.06 - 0.20 mm framework). Unstratified and clast-free.	26.59	32.38 m
Arenite(?): moderately to strongly foliated quartz-white mica schist	32.38	33.03 m
Siltstone: strongly foliated army green siltstone. Locally biotite-phyric but non magnetic.	34.18	34.78 m
Diamictite: pebble-cobble-boulder-granule-sand set in a matrix of biotite subarkosic Fe wacke (Fe-poor, Fe_2O_3 = 4.24%, geo **$15d_3$**). Poorly sorted with subangular to subrounded clasts, ranging from 0.5 - 55 cm, covering 10% of the blackish-green weathered surface. The most prevalent clast type, tonalite, is also the largest (i.e., 22 x 55 cm). The second and third most abundant clast types are diorite (0.3 x 0.5 m max.) and vein quartz (3 cm max.) respectively. At approximately 45 m, noted a subangular clast of subarkosic arenite which resembles the arenite sampled downsection (i.e., $15a_1$). At 51.89 m, the matrix is a magnetite-biotite-garnet subarkosic Fe wacke (Fe-moderate, Fe_2O_3 = 11.53%, geo $15f_2$, 0.06 - 0.4 mm micro-framework). Increased metamorphic grade suggested by presence of the euhedral Mn-Fe garnets. p.t.s. **$15f_1$** At 62.39 m, clast dimensions maintain variance from sand through to boulder, with a slight preponderance of sizes in the 0.5 - 3.0 cm range. Medium-grained tonalite and milky white vein quartz are dominant. The matrix Fe_2O_3 content has increased to 41.19% (geo **$15g_3$**).	35.99	84.02 m
Iron formation: black, clast-free and unstratified quartz-magnetite-biotite lutite	84.02	88.47 m

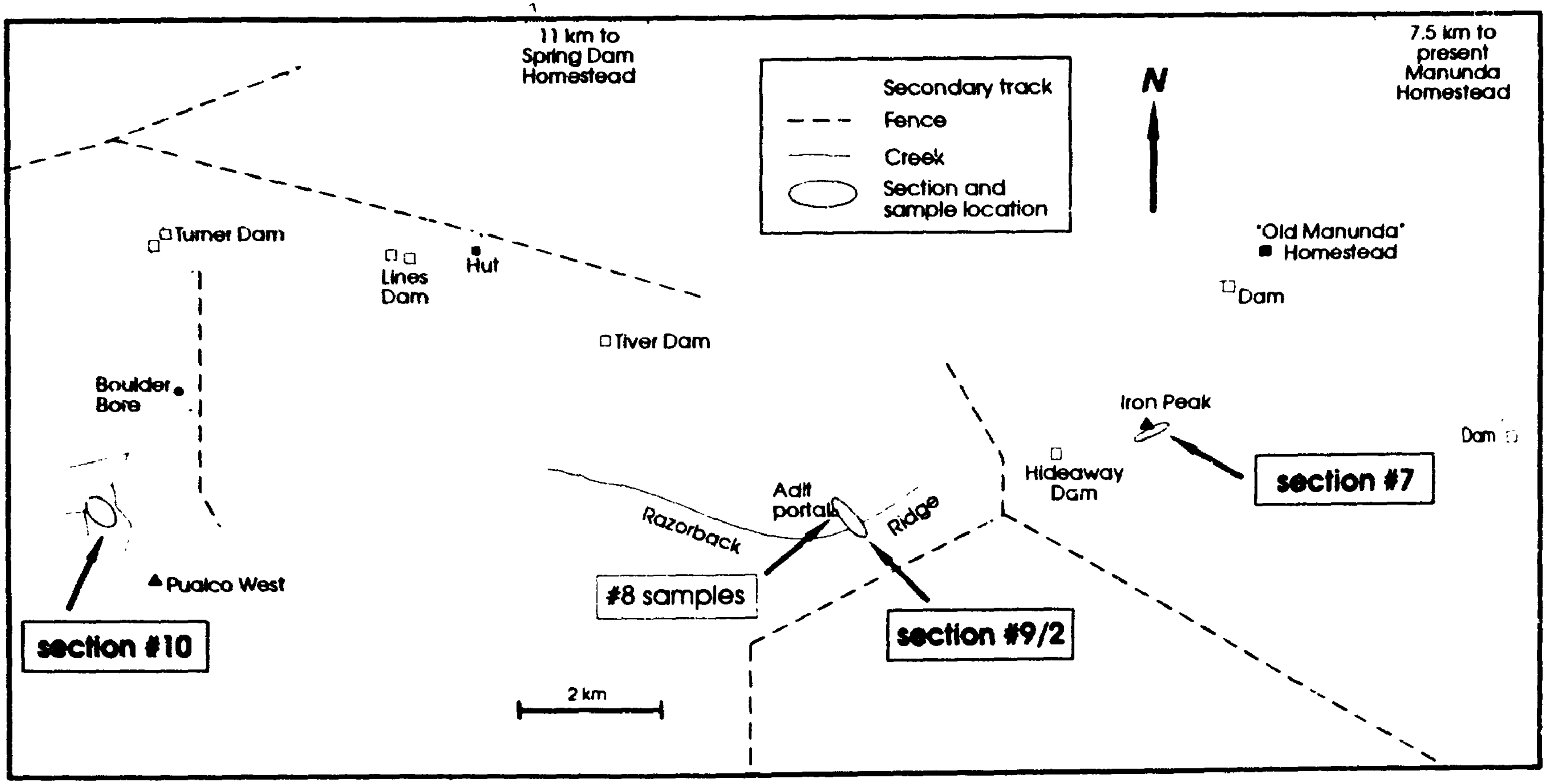

Figure A.9 Locations of stratigraphic section nos. 8 (adit), 9/2 and 10 on Spring Dam station, and section #7 on Manunda station.

Table A.10: Description and thicknesses of stratigraphic section #10 near Pualco West, Spring Dam station. Distances are measured from first exposure of Pualco "Tillite" below iron formation-bearing interval.

Diamictite: pebble-granule supported by orangy-brown weathering subarkosic wacke. Non magnetic fresh surface.	0.00	6.68 m
Argillite: laminated, weakly undulate couplets of siltstone (1 - 2 mm thick) and argillite (3 - 6 mm thick, dominant)	16.78	17.53 m
Iron formation: comparable to 27.82 - 28.10 m	20.05	21.49 m
Arenite: high weathering, pinkish-brown coloured subarkosic arenite. Non magnetic fresh surface hence no Fe prefix.	26.24	27.82 m
Iron formation: blackish-grey weathering, thinly laminated magnetite-quartz-chlorite-ferroan dolomite Fe lutite (dominant, Fe_2O_3 = 52.51%, geo **10d$_2$**) within which there are sporadic calcite subarkosic Fe arenite (Fe-poor) laminae. t.s. and p.t.s **10d$_1$**	27.82	28.10 m
Diamictite: granule-pebble(?) supported by blackish-green weathering subarkosic Fe wacke (Fe-poor/Fe-moderate)	29.27	30.62 m
Diamictite: comparable to 70.08 - 72.83 m except granules prevail over pebbles	34.12	35.91 m
Iron formation: comparable to 27.82 - 28.10 m	63.81	64.33 m
	67.53	68.08 m
Diamictite: pebble-granule-sand-(rare cobble) supported by a light grey weathering biotite-ferroan dolomite subarkosic Fe wacke (Fe-poor, Fe_2O_3 = 3.21%, geo **10g$_2$**). Clasts (0.1 - 2.1 cm) covering 10% of the exterior surface are mainly white weathering, fine-grained quartz arenite or recessive weathering, reddish-brown ferroan dolomite(?). The dominant micro-framework components (0.02 - 1.1 mm) in decreasing order of abundance are: solitary (monocrystalline) quartz, plagioclase, olive green biotite-replacing-plagioclase and ferroan dolomite. t.s. **10g$_1$**	70.08	72.83 m
Arenite: comparable to 26.24 - 27.82 m	90.63	91.23 m
	93.33	94.13 m
	94.77	95.65 m
Fe arenite & Fe wacke (dominant): rhythmic, weakly undulate couplets of greyish-white subarkosic Fe arenite (Fe-poor, 0.1 - 2 cm thick) and brown subarkosic Fe wacke (Fe-moderate, 0.7 - 2.1 cm thick). The Fe arenite layers can vary in thickness from 1 - 8 mm along a 6 cm strike length and it can be either the base or top boundary which undulates, but not usually both.	98.15	98.75 m
Iron formation: comparable to 159.12 - 159.67 m	98.75	99.61 m
Fe siltstone: laminated pale green:dark green weathering Fe siltstone (Fe-moderate) couplets which consist of quartz-white mica-magnetite (pale green) and quartz-chlorite-magnetite (dark green).	99.61	100.71 m
Fe arenite & Fe wacke (dominant): comparable to 98.15 - 98.75 m except the Fe arenite locally forms collinear starved ripples (± cross-laminae).	101.81	104.27 m
Iron formation: comparable to 27.82 - 28.10 m except felsic laminae absent.	104.27	104.69 m
Fe arenite & Fe wacke (dominant): comparable to 101.81 - 104.27 m, Fe_2O_3 = 7.69% (geo **10h**). Ripple marked bedding plane atop of interval.	104.69	108.14 m
Diamictite: granule-pebble supported by a blackish-brown weathering matrix of what is probably biotite-magnetite subarkosic Fe wacke (Fe-moderate, Fe_2O_3 = 7.37%, geo **10i$_2$**). Greyish-white quartz is the dominant clast type both in the diamictite and the locally developed light pinkish-brown weathering subarkosic (non Fe) wacke lenses (e.g., 1.4 x 0.4 m). These lenses may be internally stratified by thin dark laminae	108.14	133.60 m

and have diffuse contacts with the enclosing diamictite.

Fe arenite & Fe wacke (dominant): comparable to 101.81 - 104.27 m except laminae of high weathering, pale green coloured Fe siltstone may occur.	134.98	136.18 m
Arenite: pale grey weathering, ferroan dolomite subarkosic arenite (non Fe, Fe_2O_3 = 0.65%, geo **10J$_2$**) in which the main framework components (0.06 - 0.8 mm) are: solitary (monocrystalline) quartz, plagioclase, ferroan dolomite and chlorite + biotite-replacing-plagioclase. t.s. and p.t.s. **10J$_1$**	136.18	137.88 m
The flat-based arenite bed from 144.84 - 145.18 m is normally graded throughout the lower 24 cm (A division), then diffuse parallel lamination within the next 8 cm (B division) and ripple cross-laminae in the uppermost 1.5 cm (C division).	138.98	139.84 m
	140.52	140.92 m
	143.52	143.78 m
	144.84	145.18 m
	145.79	146.16 m
Fe arenite & Fe wacke (dominant): comparable to 98.15 - 98.75 m	146.16	147.31 m
Fe arenite & Fe siltstone: laminated triplets of greyish-white subarkosic Fe arenite (Fe-poor), pale green Fe siltstone (Fe-moderate) and dark green Fe siltstone (Fe-moderate) in which the layer ratios may be 2:4:1. Aproximately 50% of the triplets have Fe arenite base; the remainder are Fe siltstone couplets in which the pale green:dark green ratio varies from 1:1 to 4:1. From 151.5 - 152.5 m, there are several subarkosic Fe arenite layers (Fe-poor, 1 - 4 cm thick) separated by intervals (2 - 10 cm thick) of Fe siltstone couplets. The Fe arenite layers are basally loaded and flamed and locally cross-laminated.	150.46	153.80 m
Iron formation: comparable to 159.12 - 159.67 m	153.80	154.28 m
	154.92	155.50 m
	155.70	156.35 m
Fe arenite & Fe siltstone (dominant): comparable to 151.5 - 152.5 m	156.35	157.86 m
Iron formation: blackish-grey weathering, thinly laminated magnetite-quartz-chlorite-ferroan dolomite Fe lutite (dominant) with minor quartz-sericite-magnetite Fe siltstone (Fe-poor) lenses (Fe_2O_3 = 49.46%). t.s. and p.t.s. **10k$_1$**; geo **10k$_2$**	159.12	159.67 m
	160.78	161.09 m
	162.85	163.12 m
Fe siltstone: comparable to 150.46 - 151.50 m. A thin section across the laminated pale green:dark green weathering couplets reveals quartz-sericite-magnetite Fe siltstone (pale green, Fe-moderate) and quartz-chlorite-magnetite Fe siltstone (dark green, Fe-moderate). } pts. 10L Undulate, possibly lobed Fe siltstone//diamictite contact; there is an ovoid (3.1 x 2.4 m) slumpball of diamictite within the Fe siltstone (located 24 m northeast of section line).	160.15	160.78 m
	161.09	162.85 m
	163.12	167.82 m
Diamictite: granule-pebble-(± sand) supported by a light brown weathering matrix, which is at 172.52 m, a magnetite-ferroan dolomite-chlorite subarkosic Fe wacke (Fe-moderate, Fe_2O_3 = 18.11%, geo **10m$_2$**, 0.02 - 0.7 mm micro-framework). } ts 10m$_1$ However, the matrix is more commonly Fe-poor, like the biotite-chlorite subarkosic Fe wacke (0.02 - 1.2 mm micro-framework) sampled at 180.76 m. } ts 10M$_3$ The diamictite is unstratified and clasts, ranging from 0.1 - 10.5 cm (commonly 2 - 15 mm) are dominated by green-tinged subarkosic wacke.	167.82	183.05 m
Fe wacke: greyish-green weathering, unstratified subarkosic Fe wacke (Fe-poor).	185.00	185.74 m
Iron formation: black weathering exposure of what is probably magnetite-quartz-hematite lutite (Fe_2O_3 = 55.55%, geo **10N$_1$**). Strongly magnetic fresh surface.	186.22	189.09 m
	190.19	190.73 m
Arenite: comparable to 136.18 - 137.88 m	186.78	187.02 m
	194.81	194.99 m
Fe wacke: comparable to 185.00 - 185.74 m	194.99	195.73 m
Iron formation: comparable to 186.22 - 189.09 m except recessive-weathering, reddish-brown ferroan dolomite-enriched interlayers (up to 5.5 cm thick) occur from 196.43 - 196.88 m.	195.73	196.88 m

Arenite: comparable to 136.18 - 137.88 m	199.88	200.44 m
Iron formation: comparable to 136.22 - 189.09 m except that the Fe lutite is here locally stratified by weakly undulate subarkosic Fe siltstone layers (Fe-poor, 6 - 10 mm thick).	201.66 203.55 204.56 205.40	202.02 m 204.31 m 204.86 m 205.75 m
Fe arenite & Fe wacke (dominant): comparable to 98.15 - 98.75 m	205.96	206.48 m
Fe wacke: comparable to 185.00 - 185.74 m	208.76	209.00 m
Fe arenite: subarkosic Fe arenite (Fe-poor) has locally developed thin laminae which on fresh surface, are weakly magnetic.	210.50 211.80	210.68 m 212.04 m
Iron formation: comparable to 201.66 - 205.75 m except from 214.22 - 214.72 m which is comparable to 196.43 - 196.88 m.	212.04 213.72 217.14	212.90 m 214.72 m 218.06 m
Iron formation: comparable to 196.43 - 196.88 m	228.10	228.44 m
Micrite: orangy-brown weathering, laminated micrite (Fe-moderate, Fe_2O_3 = 10.91%, L.O.I. = 28.98%, geo $10q_b$). The dominant framework components of quartz, biotite and magnetite (0.02 - 0.3 mm) have a poikilitic distribution within the dolomitic micrite. t.s. and p.t.s. $10q_h$	228.44	229.04 m
Diamictite: granule-pebble-sand supported by a light brown weathering matrix of magnetite-chlorite subarkosic Fe wacke (Fe-moderate) in which the micro-framework components range from 0.02 - 0.7 mm. Unstratified. t.s. $10R_t$	231.04	238.26 m
Iron formation: comparable to 186.22 - 189.09 m	238.26	238.84 m
Iron formation: black weathering, thinly laminated magnetite-quartz-hematite-chlorite Fe lutite within which there are two (8 & 8.5 cm thick) recessive-weathering, reddish-brown ferroan dolomite-enriched interlayers. Localized development of ovoid nodules (0.5 mm long) within the Fe lutite.	240.04 243.81 t.s. & p.t.s. 10S$_3$ 244.73 245.84	242.93 m 244.21 m 245.47 m 246.29 m
Micrite: comparable to 228.44 - 229.04 m	246.79	247.31 m
Iron formation: greyish-black weathering, thinly laminated couplets of magnetite-quartz-hematite-chlorite Fe lutite (0.4 - 1 mm thick) and quartz-magnetite-hematite-chlorite Fe lutite (0.28 - 2 mm thick). Reddish-brown colouration on exterior surface corresponds to iron-stained quartz within the magnetite-dominated laminae, except for a non magnetic, ferroan dolomite-enriched layer from 259.15 - 259.37 m.	252.05 p t.s. 10T$_1$ 254.53 258.17	253.20 m 255.07 m 258.57 m
Fe siltstone: within the lower half of interval is laminated dark grey:black Fe siltstone (Fe-moderate) couplets (< 1 cm thick) in which the grey:black ratio is typically 1:1. Upper half of outcrop consists of laminated pale green:dark green Fe siltstone (Fe-moderate) couplets (< 1 cm thick) in which the pale green:dark green ratio is 5:1.	260.91	262.60 m
Iron formation: comparable to 252.05 - 253.20 m	263.32 264.96	264.12 m 265.58 m
Iron formation: comparable to 186.22 - 189.09 m except that a non magnetic, reddish-brown weathering ferroan dolomite-enriched layer occurs from 268.66 - 268.86 m. Also, from 273.79 - 274.24 m, there are quartz-white mica siltstone (4 - 5 mm thick) and micro-diamictite (1.5 - 2.5 cm thick) interlayers. The framework (0.02 - 0.6 mm) of the micro-diamictite is set in a quartz-magnetite-hematite lutite. t.s. 10u	266.86 272.15 273.79 274.59 276.21	268.96 m 273.19 m 274.24 m 275.21 m 277.43 m
Siltstone: comparable to ferroan dolomite-enriched layer from 268.66 - 268.86 m. High weathering magnetite laminae (3 - 4 mm thick) are restricted to the second interval.	281.33 290.08	281.60 m 290.38 m

Iron formation: comparable to 186.22 - 189.09 m	329.10	330.29 m
Fe arenite: comparable to 210.50 - 210.68 m	337.26	337.82 m

Table A.11: Description and thicknesses of stratigraphic section #9/2 at Razorback Ridge, Spring Dam station. Distances are measured from first exposure of Pualco "Tillite" below iron formation-bearing interval.

Diamictite: pebble-granule-(rare cobble) supported by a weakly foliated, green weathering matrix of biotite-ferroan dolomite subarkosic Fe wacke (Fe-poor). Unstratified and non magnetic. Clasts commonly range from 0.4 - 5 cm and are subrounded. Clast types include green-tinged subarkosic wacke, milky white vein quartz, recessively-weathered reddish-brown ferroar dolomite and white weathering quartz arenite, which are the largest clasts observed (e.g., 22.0 x 15.5 cm). The dominant micro-framework components (0.02 - 0.64 mm) in decreasing order of abundance are: solitary (monocrystalline) quartz, untwinned or relict albite-twinned plagioclase, olive green biotite and ferroan dolomite. t.s. **$9a_1$**	0.00	12.00 m
Diamictite: granule-(rare pebble) comparable to 0.0 - 12.0 m except the matrix here is a subarkosic Fe wacke (Fe-moderate).	43.54 56.69 62.39 64.34 67.74	53.89 m 58.59 m 63.24 m 65.54 m 68.44 m
Fe arenite: pinkish-buff weathering, clast-free subarkosic Fe arenite (Fe-poor, Fe_2O_3 = 3.19%, geo **$9B_2$**) is not visibly stratified. The fresh surface varies from non to weakly magnetic.	68.44	69.94 m
Wacke: clast-free version of the diamictite matrix from 0.0 - 12.0 m. The subarkosic wacke is here moderately foliated, green-coloured, unstratified and non to weakly magnetic (hence no Fe prefix).	73.29	74.34 m
Fe wacke & iron formation: very thin-bedded couplets of subarkosic Fe wacke (Fe-moderate, 1.6 - 2.3 cm thick) and Fe lutite (0.9 - 1.1 cm thick). The green weathering Fe wacke layers are moderately magnetic on fresh surface, whereas the black, higher weathering Fe lutite laminae are strongly magnetic.	79.64	80.24 m
Iron formation: dark grey weathering and thinly laminated Fe lutite is moderately magnetic (Fe_2O_3 = 39.18%, geo **$9c_2$**). It contains sporadic lenticles (e.g., 3 cm long x 0.5 mm thick) of ferroan dolomite-quartz-plagioclase Fe siltstone (Fe-poor).	80.24	81.09 m
Fe siltstone: soft-sediment slumping of a locally cross-laminated, ferroan dolomite-bearing Fe siltstone (Fe-moderate, chemically similar to 91.81 to 94.95 m)	91.01	91.29 m
Iron formation: high weathering and thinly laminated Fe lutite	91.29	91.81 m
Fe siltstone: comparable to 91.01 - 91.29 m (Fe_2O_3 = 10.79%, L.O.I. = 7.53%, geo **$9d_{2a}$**).	91.81	94.95 m
Diamictite: pebble-granule-sand supported by greyish-green matrix of magnetite-ferroan dolomite-biotite subarkosic Fe wacke (Fe-moderate, Fe_2O_3 = 14.55%, geo **$9e_2$**). Unstratified. Types of clasts include smokey grey polycrystalline quartz, buff-coloured subarkosic arenite and reddish-brown ferroan dolomite. Micro-framework components (0.02 - 0.5 mm) in decreasing order of abundance are: solitary (monocrystalline) quartz, magnetite, plagioclase feldspar, ferroan dolomite and biotite. t.s. **$9e_1$**	94.95	100.20 m
Iron formation: alternating laminae (0.6 - 1.8 mm thick) of quartz-magnetite-hematite(?)-chlorite Fe lutite and magnetite-quartz-hematite(?)-chlorite Fe lutite. } t.s $9F_1$ Strongly magnetic and average Fe_2O_3 content is 48.33% (geo **$9F_2$ & $9F_3$**). A synsedimentary fault was observed in $9F_1$. Within the iron formation are a few intervals (5 - 12 cm thick) of laminated Fe siltstone couplets which appear to consist of quartz-magnetite-white mica (dark grey, Fe-moderate) and quartz-chlorite-	106.50	112.54 m

magnetite (black, Fe-moderate). Couplet thicknesses together with the dark grey:black ratio thin and decrease upward from 10 mm thick and 3:1 at base of sequence to 3 mm thick and 1:1 at the top. Beginning at the 109.14 m mark are five subarkosic Fe siltstone layers (Fe-poor, 0.7 - 2 cm thick) which are commonly flat-based and flat-topped.

Iron formation: comparable to 106.50 - 112.54 m except poorly exposed	116.59	117.64 m
Fe siltstone: laminated Fe siltstone couplets (Fe-moderate, ≤ 1.2 cm thick) compositionally similar to those between 106.5 to 112.54 m. The dark grey:black ratio is commonly 1:1 and the fresh surface is moderately magnetic.	118.14	118.84 m
Fe arenite: comparable to 68.44 - 69.94 m (Fe-poor, < 5% Fe oxide)	118.84	119.44 m
Fe siltstone: laminated pale green:dark green weathering Fe siltstone (Fe-moderate) in which the couplets are 1 - 6 cm thick and consist of quartz-white mica-magnetite (pale green) and quartz-chlorite-magnetite (dark green). Both lamina types are laterally continuous and locally undulate. Fresh surface is moderately magnetic.	123.29	123.59 m
Fe wacke & Fe siltstone: comparable to 305.10 - 309.70 m (Fe_2O_3 = 7.70%, geo 9H).	127.34	133.94 m
Fe siltstone: comparable to the couplets within the iron formation from 106.5 - 112.54 m	142.54	143.28 m
Fe siltstone: laminated medium grey:white weathering Fe siltstone (Fe-moderate) with couplet thicknesses of 2 - 3 mm. The couplets are undulate and composed mainly of quartz-ferroan dolomite-white mica-magnetite (medium grey) and quartz-white mica-magnetite (white).	143.28	143.99 m
Iron formation: black weathering magnetite-hematite-quartz Fe lutite (dominant, 1.4 - 5 cm thick, Fe_2O_3 = 67.23%, geo $9I_1$) stratified by white weathering ferroan dolomite-quartz-plagioclase Fe siltstone (Fe-poor, 2 - 10 mm thick, Plate 2.2f). The laterally continuous Fe siltstone layers commonly contain ripple cross-lamination (e.g., 5 cm long by 0.7 cm thick). t.s. and p.t.s. $9I_2$ From 144.59 - 145.34 m, have intervals (8.5 - 36 cm thick) of undulate Fe siltstone couplets (comparable to 143.28 - 143.99 m) within the Fe lutite iron formation.	143.99	146.84 m
Fe siltstone: laminated medium grey (8 - 10 mm thick) and white (1 - 2 mm thick) weathering couplets of Fe siltstone (Fe-moderate, Fe_2O_3 = 12.12%, geo $9j_2$). The couplets are flat-based and consist mainly of quartz-ferroan dolomite-sericite-magnetite (medium grey) and quartz-sericite-magnetite (white). Within one basal layer, have crudely developed normal grading of quartz grains in lower 2/3 and increased sericite content in the upper 1/3. The sericite increase represents a transition into the thin upper layer (1 - 2 mm thick) of the couplet. These mica-enriched layers locally contain flame structures. t.s. $9j_1$	150.59	151.45 m
Iron formation: black weathering magnetite-hematite-quartz Fe lutite. Unstratified.	151.45	151.79 m
Fe siltstone: comparable to 150.59 - 151.45 m	151.79 153.75	153.33 m 154.51 m
Fe siltstone: comparable to 118.14 - 118.84 m	154.51	156.11 m
Fe siltstone & iron formation: strongly foliated (231°/56°), laminated pale green (Fe-moderate siltstone) and black (Fe-rich lutite) couplets in which the green:black layer ratio is typically 4:1. Moderately magnetic.	156.11	159.31 m
Fe siltstone: reddish-brown weathering ferroan dolomite-quartz-magnetite-chlorite-plagioclase Fe siltstone (Fe-moderate, Fe_2O_3 = 16.93%, L.O.I. = 20.50%, geo $9K_1$) within which there are compositionally similar ovoid concretions. t.s. & p.t.s. $9K_2$	159.31	161.11 m

Fe siltstone: two types of Fe siltstone (both Fe-moderate) equally alternate throughout this interval. The first type is laminated pale green:dark green Fe siltstone (Fe_2O_3 = 22.26%, geo $9L_2$) in which the couplets are < 1 cm thick and consist of quartz-white mica-magnetite (pale green) and quartz-chlorite-magnetite (dark green). The couplets are generally flat-based but where undulate, the wavelength = 20 cm and the amplitude = 5 cm. Pale green:dark green ratios range from 9:1 to 1:1. The second type is laminated dark grey:black Fe siltstone which has couplet thicknesses of 1 - 5 mm. They consist of quartz-magnetite-sericite (dark grey) and quartz-chlorite-magnetite (black). t.s. $9L_1$

161.11 165.61 m
161.11 161.56 m
161.71 162.07 m
162.71 163.91 m
165.21 165.61 m

Diamictite: granule-pebble-sand-(rare boulder) set in a matrix dominated by hematite-magnetite-quartz lutite (Fe_2O_3 = 35.09%, geo $2m_2$). Unstratified. Macroscopic clast types include recessive-weathering, reddish-brown ferroan dolomite and white weathering, rectangular rip-ups (0.8 - 4.5 cm in length) of ferroan dolomite-quartz-plagioclase Fe siltstone (Fe-poor) which are considered equivalent to the Fe siltstone layer within iron formation thin section $9I_2$. Rare boulder-size clasts include a greyish-white subarkosic arenite (52 x 40 cm) and a medium-grained quartz porphyry in an intermediate groundmass (31 x 16 cm). Dominant micro-framework components (0.02 - 1.4 mm) in decreasing order of abundance are: solitary (monocrystalline) quartz, magnetite, chlorite and ferroan dolomite. t.s. $2m_1$

184.19 205.35 m (crest of Razorback Ridge)

Diamictite: continuation of 184.19 - 205.35 m. The blackish-grey weathering, macroscopic matrix sampled at 208.45 m and 211.17 m has Fe_2O_3 content of 35.83% and 38.01%, respectively. t.s. $2j_1$; geo 2L and $2j_2$

205.35 211.17 m

Diamictite: comparable to 184.19 - 205.35 m except that the diamictite is here stratified. Glacial striae were observed on the upper surfaces of four successive bedding planes (25 - 30°N dip), the first of which occurs at 211.17 m (31 striae measured), second at 211.37 m (129 striae measured, Plate 2.1e), third at 212.57 m (13 striae measured) and fourth at 215.57 m (20 striae measured). The striae are commonly 2 - 4 mm wide, ≤ 5 mm deep and 5 - 40 cm long. A width maxima of 3 cm corresponded to maximum lengths of 1.0 and 1.5 m. Because topographic dip approximately parallels stratigraphic dip on the north side of Razorback Ridge, the nature of the diamictite stratification is obscured. It is best observed in the adit (see Table A.13).

211.17 216.37 m

Iron formation: black weathering, thinly laminated magnetite-quartz-hematite lutite is the dominant phase. The average Fe_2O_3 content of five Fe lutite samples taken throughout the interval is 59.87% (geo $2h_2$, 2G, 2F, $8A_U$ & 2A). Felsic Fe siltstone interlayers (0.5 - 3 cm) are widespread, whereas reddish-brown weathering ferroan dolomite-enriched beds (3 - 8 cm thick, L.O.I. = 20.28%, geo 4A) are most apparent from 241.95 - 247.12 m. The carbonate is locally cross-laminated or lensoid.

The iron formation/Fe lutite dominated interval from 216.37 - 248.32 m is more completely exposed in the adit and microscopically detailed by thin sections $8H_3$ → 8A (see Table A.13).

216.37 219.97 m
225.67 227.79 m
229.29 230.43 m
233.23 236.75 m
240.45 241.95 m
243.45 243.81 m
244.61 249.87 m
252.37 m, N. tip of adit portal

Fe siltstone: brown weathering, ferroan dolomite-bearing Fe siltstone (Fe-moderate). 257.41 257.81 m

Fe wacke: greyish-green weathering, magnetite subarkosic Fe wacke (Fe-moderate) is locally strongly foliated. The dominant micro-framework components (0.02 - 0.08 mm) in decreasing order of abundance are: quartz, plagioclase feldspar, magnetite and chlorite. t.s. 2p

267.01 269.21 m

Iron formation: comparable to the dominant phase from 216.37 - 249.87 m. Fresh surface is here strongly magnetic.

270.73 271.13 m

Fe arenite: pinkish-brown weathering, subarkosic Fe arenite (Fe-poor) has locally developed thin laminae which on fresh surface, are very weakly magnetic.

272.53 273.13 m

Fe arenite & Fe wacke (dominant): rhythmic couplets of Fe arenite (3 - 4 mm thick) and Fe wacke (8 - 10 mm thick) in which the arenite:wacke ratio is consistently 1:2. The individual layers are compositionally similar to 272.53 - 273.13 m (Fe arenite) and 267.01 - 269.21 m (Fe wacke).

276.35 276.91 m

Fe wacke: comparable to 267.01 - 269.21 m	276.91	278.01 m
Fe arenite: comparable to 272.53 - 273.13 m	279.71 280.81	279.86 m 281.61 m
Iron formation: comparable to the dominant phase from 216.37 - 249.87 m. Fe_2O_3 = 59.08% (geo $2S_2$).	283.01 284.96 286.86	283.31 m 285.96 m 287.70 m
Fe siltstone: brown weathering, ferroan dolomite-bearing Fe siltstone (Fe-moderate, Fe_2O_3 = 8.50%, L.O.I. = 11.90%, geo $2T_2$) which is locally stratified by laminated to very thin-bedded magnetite subarkosic Fe wacke (Fe-moderate, 0.02 - 0.07 mm size framework) grading into quartz-magnetite-sericite Fe siltstone (Fe-moderate). } t.s. $2T_1$	289.80	291.00 m
Fe wacke: comparable to 267.01 - 269.21 m	291.76	299.40 m
Possible stratigraphic break? East-west-trending ditch within which are small-scale (e.g., h = 15 cm, λ = 7 cm) plunging-normal folds with angular fold closures and axes which have a trend and plunge of 033°-25°.		
Fe arenite & Fe siltstone: greyish-green weathering interval is dominated by alternating laminae of biotite subarkosic Fe arenite (Fe-poor, 0.6 - 5 mm thick layers) and quartz poikilitic quartz-magnetite-sericite Fe siltstone (Fe-moderate, 0.4 - 2.4 mm thick). The two layer-combined Fe_2O_3 content is 7.61% (geo $2u_1$). } t.s. $2u_3$ The Fe arenite layers are locally cross-laminated, basally scoured or loaded, and may be flamed into by thin laminae of quartz-sericite-plagioclase-magnetite Fe siltstone (Fe-poor). This latter layer type locally alternates with laminae of the forementioned Fe-moderate siltstone.	305.10	309.70 m
Diamictite: granule-sand-pebble-(rare cobble) set in a blackish-grey weathering matrix which is dominated by hematite-magnetite-quartz lutite. Matrix sampled at 335.17 m and 344.17 m has Fe_2O_3 content of 35.16% and 31.69%, respectively (geo 2V & $2w_2$). The unit is strongly foliated locally and seemingly unstratified. Clasts, ranging from 0.1 - 3 cm include reddish-brown ferroan dolomite and greyish-white felsic siltstone. The sporadic cobble-size clasts are granitoids. The dominant micro-framework components (0.02 - 1.1 mm) in decreasing order of abundance are: monocrystalline quartz, magnetite, chlorite and plagioclase feldspar. t.s. $2w_1$	319.72 325.27 335.17	320.77 m 331.27 m 348.67 m
Iron formation: comparable to the dominant phase from 216.37 - 249.87 m. Fe_2O_3 = 48.99% (geo $2x_2$).	354.52	361.12 m
Arenite: high weathering, pale brownish-white coloured, subarkosic arenite (non Fe, Fe_2O_3 = 1.08%, geo $2y_2$) has locally developed diffuse, thin laminae. The fresh surface is non magnetic and consist almost entirely of quartz (0.3 - 0.7 mm) and plagioclase (0.1 - 0.34 mm). t.s. $2y_1$	365.82 368.97	366.57 m 371.57 m
Iron formation: comparable to the dominant phase from 216.37 - 249.87 m	377.57 380.97 398.22 401.02 425.72	378.07 m 381.57 m 398.92 m 401.72 m 426.62 m

Table A.12: Description and thicknesses of stratigraphic section #7 at Iron Peak, Manunda station. Distances are measured from first exposure of Pualco "Tillite" below iron formation-bearing interval.

Diamictite: pebble-granule-(rare cobble) supported by a reddish-brown weathering matrix of biotite-ferroan dolomite subarkosic Fe wacke (Fe-poor, Fe_2O_3 = 7.05%, geo 7A). Unstratified and non magnetic. The dominant clast type is greyish-white subarkosic arenite, one of which measured 22 x 11.5 cm.	0.00	109.80 m
Arenite: light reddish-brown weathering ferroan dolomite subarkosic arenite (Fe_2O_3 = 3.33%, geo 6A, 0.06 - 0.24 mm framework). The arenite is unstratified and the pink-coloured fresh surface is non magnetic.	109.80	116.80 m
Fe siltstone (dominant): dark green weathering quartz-chlorite-biotite Fe siltstone (Fe-poor) which is stratified by fine-grained quartz arenite layers (1 - 6 mm thick) spaced from 2 - 30 mm apart. The arenite laminae are commonly folded and locally cross-laminated.	116.80 ts & pts 7B	120.80 m
Arenite: comparable to 109.80 - 116.8 m except here the arenite forms a lens which is laterally continuous for 6 m and varies from 2.25 - 5.5 m thick. Liesegang rings present.	120.80	123.05 m
Fe siltstone (dominant): comparable to 116.8 - 120.8 m	123.05	125.55 m
Arenite: comparable to lens between 120.8 - 123.05 m except diffuse parallel laminae and limonite spotting visible here.	127.25	130.05 m
Fe siltstone (dominant): comparable to 116.8 - 120.8 m except locally see high weathering chlorite-magnetite-quartz lutite laminae (Fe-rich, 1 - 2 mm thick). This third layer-type marks the culmination of an upward increase in iron content throughout an arenite-siltstone-lutite triplet.	130.90	133.63 m
Iron formation: blackish-green weathering, thinly laminated quartz-magnetite-chlorite-biotite Fe lutite (dominant) and magnetite-chlorite-quartz Fe lutite. Combined Fe_2O_3 content = 55.71%. p.t.s. 7J; geo 7I	133.63	134.33 m
Fe siltstone: laminated greyish-black (Fe-moderate) and dark green (Fe-poor, dominant) couplets which are mainly quartz-biotite-magnetite (black, 0.2 - 1.2 mm thick) and quartz-chlorite-biotite-plagioclase (green, 0.8 - 5.4 mm thick). Combined Fe_2O_3 content = 16.51%. t.s. and p.t.s. 7L; geo 7K	134.33	135.43 m
Iron formation: comparable to 133.63 - 134.33 m except locally developed subarkosic Fe arenite (Fe-poor) layers (≈ 1 cm thick).	135.43	135.91 m
Fe siltstone: laminated couplets of orangy-white (Fe-poor) and dark green (Fe-moderate) Fe siltstone which are seemingly composed mainly of quartz-chlorite-biotite (Fe-poor) and quartz-chlorite-magnetite (Fe-moderate).	135.91	136.53 m
Iron formation: comparable to 135.43 - 135.91 m	136.53	137.70 m
Fe wacke: greenish-grey weathering subarkosic wacke which is transected by a 1 m wide fracture-filling, subarkosic Fe arenite (Fe-poor) dyke. This dyke is an apparent offshoot from 143.5 - 146.45 m interval.	137.70	139.70 m
Arenite & Fe wacke (dominant): typically thin-bedded triplets of basally loaded orangy-white arenite (0.8 - 2.5 cm thick), massive orangy-buff Fe wacke (Fe-poor, 1.6 - 8 cm thick) and parallel laminated dark reddish-brown Fe wacke (Fe-poor, 2 - 7.4 cm thick, Plate 2.5e). The arenite layers are locally ripple cross-laminated or isoclinally folded. Limonite spotting common.	139.70	141.20 m
Fe siltstone: comparable to 135.91 - 136.53 m	141.20	143.50 m
Fe arenite: reddish-coloured, limonite-bearing (secondary) fine-grained (0.02 - 0.14 mm) subarkosic Fe arenite (Fe-poor). Typically unstratified. Undulate	143.50 ts 7D	146.45 m

arenite//diamictite contact along which there are some fault-bounded(?) pockets of extensively folded siltstone laminae, or green subarkosic wacke containing whitish arenite laminae (< 1.5 cm thick) which have undergone flexure and slip (Plate 2.5f). The forementioned, fracture-filling dyke also crosses the arenite//diamictite contact.

Diamictite: granule-pebble-(rare cobble-boulder) supported by a green weathering matrix of biotite-magnetite-ferroan dolomite subarkosic Fe wacke (Fe-moderate), which at 153.23 m has Fe_2O_3 = 15.89% (geo 7S). Unstratified. Clast types include green-tinged subarkosic wacke (commonly 1.2 - 4 cm), greyish-white subarkosic arenite (18.5 - 43 cm) and recessive-weathered reddish-brown ferroan dolomite (< 1 cm). The dominant micro-framework components (0.02 - 0.7 mm) in decreasing order of abundance are: solitary quartz, olive green biotite, untwinned or relict albite-twinned plagioclase and ferroan dolomite. t.s. and p.ts. 7T	146.45 176.73	169.33 m 187.33 m
Iron formation (dominant): black weathering magnetite-quartz ± hematite lutite is the dominant phase (Fe_2O_3 = 63.45%, geo 1A). The lutite is stratified by orangy-white ferroan dolomite-bearing subarkosic Fe arenite (Fe-poor), which can form either laterally continuous, sharp-based layers (0.5 - 2.5 cm thick, Plate 2.2e) that are commonly folded , or collinear starved ripples (Plate 2.2e).	191.83	193.33 m
Fe siltstone (dominant) & iron formation: laminated to very thin-bedded, weakly undulate couplets of light green Fe siltstone (Fe-moderate) and dark green Fe siltstone (Fe-moderate/Fe-rich), in which the light green:dark green ratio varies from 1:1 to 5:1 and the combined Fe_2O_3 content can equal 27.07% (geo 7u).	193.33	197.23 m
Fe wacke: light green weathering subarkosic Fe wacke (Fe-poor). Unstratified and weakly magnetic.	197.23	198.13 m
Iron formation (dominant): comparable to 191.83 - 193.33 m. The Fe_2O_3 content of the dominant phase = 61.04% (geo 7V).	198.13 200.63	198.93 m 204.63 m
Fe siltstone (dominant) & iron formation: laminated version of 193.33 - 197.23 m	204.63 207.63	205.16 m 207.98 m
Micrite: orangy-brown weathering laminated micrite (Fe-moderate, Fe_2O_3 = 9.53%, L.O.I. = 22.80%, geo $7W_1$). The dominant framework components of quartz, magnetite and biotite (0.02 - 0.3 mm) have a poikilitic distribution within the dolomitic micrite. p.t.s. $7W_2$	212.58 217.08	213.78 m 218.03 m
Fe siltstone (dominant) & iron formation: laminated version of 193.33 - 197.23 m which here consists of quartz-magnetite-plagioclase Fe siltstone (Fe-moderate, weathers light green, 0.9 - 5 mm thick) alternating with magnetite-quartz-biotite Fe lutite (Fe-rich, weathers dark green, 0.3 - 5 mm thick). Also present are sporadic subarkosic Fe arenite (Fe-poor, 0.8 mm thick) and Fe wacke (Fe-moderate, 6.3 mm thick) laminae. Bedding plane surfaces (top) of the Fe lutite, Fe arenite and Fe wacke layers are locally fluted, (Plate 2.3b). Dimensions of the southwest-northeast-trending flutes (224 measured) range from 0.6 - 7 cm (length), 0.1 - 0.6 cm (width), and ≤ 0.5 cm deep. They tend to be deepest at their southwest end. } t.s. $7X_1$	220.63 227.71 230.16	221.11 m 228.71 m 230.96 m
Diamictite: very coarse sand-granule set in a brown weathering matrix which is dominated by quartz-magnetite ± hematite lutite (Fe_2O_3 = 45.25%, geo $7Y_1$). The diamictite is stratified by weakly magnetic subarkosic Fe arenite layers (Fe-poor, 0.2 - 1.3 cm thick) which can be either basally loaded or flute-infilling. Within a 40 cm thick interval, there are 3 fluted bedding planes from which 46 southwest-northeast-trending flutes were measured.	230.96	231.76 m
Fe siltstone (dominant) & iron formation: laminated version of 193.33 - 197.23 m	231.76	232.24 m
Fe siltstone & iron formation (dominant): laminated couplets(?) of quartz-magnetite-potassium feldspar Fe siltstone (Fe-moderate, subordinate, 0.4 - 1.6 mm thick) and magnetite-quartz-biotite Fe lutite (Fe-rich, dominant, 0.2 - 3.5 mm thick). Fe_2O_3 content of the Fe lutite only = 54.44% (geo $7Z_1$). The Fe lutite//Fe siltstone contacts are locally flamed/loaded. } t.s. $7Z_2$	232.24	234.39 m

Diamictite: granule-pebble-sand set in a blackish-grey weathering matrix which is dominated by hematite-magnetite-quartz lutite (Fe_2O_3 = 31.01%, geo **7aa$_2$**). The unit is strongly foliated locally and seemingly unstratified. The most apparent clasts are orangy-white weathering, rectangular rip-ups of subarkosic Fe arenite (Fe-poor, 1.1 - 14.5 cm in length, Plate 2.1f). Other clasts types include recessive-weathering, reddish-brown ferroan dolomite, tonalite and vein quartz. The dominant micro-framework components (0.02 - 0.7 mm) in decreasing order of abundance are: solitary (monocrystalline) quartz, magnetite, plagioclase and chlorite. t.s. **7aa$_1$**	242.39 254.53 m 265.93 274.33 m

Table A.13: Description and positions of samples collected within the adit through Razorback Ridge, Spring Dam station. Stratigraphic distances are measured from entrance of adit and samples are listed from base of section upward.

Iron formation (dominant) & Fe siltstone: laminated couplets of quartz-sericite-ferroan dolomite-hematite (Fe-moderate) and hematite-quartz-magnetite-sericite lutite (Fe-rich). p.t.s. **8r$_1$**; geo **8r$_2$** (Fe_2O_3 = 21.30%).	54.02 m
Iron formation (dominant): hematite-magnetite-quartz lutite (Fe-rich) stratified by a quartz-ferroan dolomite-plagioclase Fe siltstone layer (arenaceous, Fe-poor, trace apatite). p.t.s. **8q$_b$**; geo **8q$_b$** (Fe_2O_3 = 66.82%).	52.47 m
Carbonate layer (7.5 cm thick) in iron formation: REE **8P**	48.66 m
Iron formation: geo **8o** (Fe_2O_3 = 46.20%).	45.86 m
Fe siltstone layer (35 cm thick) in iron formation: geo **8M** (Fe_2O_3 = 8.34%; L.O.I. = 11.78%).	44.40 m
Contact between iron formation and diamictite at 42.80 m.	
Diamictite: granule-pebble-sand set in a blackish-grey weathering matrix which is dominated by hematite-magnetite-quartz lutite (Fe-rich). Dominant micro-framework components in decreasing order of abundance are: monocrystalline quartz, magnetite and ferroan dolomite. p.t.s. and t.s. **8l$_1$**; geo **8l$_2$** (Fe_2O_3 = 37.65%).	41.73 m
Diamictite: continuation of unit sampled at 41.73 m. t.s. **8k$_1$**; geo **8k$_2$** (Fe_2O_3 = 37.47%).	29.13 m
Diamictite: continuation of unit sampled at 41.73 m. geo **8J** (Fe_2O_3 = 33.90%).	22.36 m
Contact between diamictite and iron formation at 21.10 m.	
Iron formation: geo **8i** (Fe_2O_3 = 64.06%).	20.03 m
Fe siltstone (dominant) and iron formation: alternating laminae of quartz-plagioclase-ferroan dolomite-magnetite-sericite Fe siltstone (Fe-moderate) and quartz-hematite-magnetite-sericite lutite (Fe-rich). Iron formation rip-ups are locally apparent in the Fe siltstone laminations. t.s. and p.t.s. **8H$_1$**	18.70 m
Iron formation: geo **8G$_3$** (Fe_2O_3 = 58.61%).	16.01 m
Iron formation (dominant) & Fe siltstone: alternating laminae of hematite-magnetite-quartz lutite (Fe-rich) and quartz-ferroan dolomite-hematite-magnetite Fe siltstone (Fe-moderate). t.s. **8G$_2$**; geo **8G$_1$** (Fe_2O_3 = 39.18%).	15.58 m
Iron formation (dominant) & Fe siltstone: alternating laminae of hematite-quartz-magnetite-sericite (Fe-rich) and quartz-sericite-ferroan dolomite-magnetite Fe siltstone (Fe-moderate, trace apatite). p.t.s. **8F**	12.05 m
Carbonate layer (15.2 cm thick) in iron formation: geo **8E$_1$** (Fe_2O_3 = 12.26%, L.O.I. = 19.05%).	9.32 m

Iron formation (dominant): hematite-magnetite-quartz lutite (Fe-rich) stratified by a quartz-ferroan dolomite-magnetite Fe siltstone layer (Fe-moderate, trace apatite). p.t.s. $8E_1$; geo $8E_1$ (Fe_2O_3 = 54.90%).	9.17 m
Fe siltstone (dominant) & iron formation: alternating laminae of quartz-magnetite-ferroan dolomite-sericite Fe siltstone (Fe-moderate) and hematite-quartz-magnetite lutite (Fe-rich). p.t.s. 8D	6.60 m
Iron formation: hematite-magnetite-quartz lutite in which fluctuations in iron oxide content define the laminations. t.s. $8C_3$	2.85 m
Iron formation (dominant): continuation of unit sampled at 2.85 m, except that there are laminae and lenses of quartz-ferroan dolomite-magnetite Fe siltstone (arenaceous, Fe-moderate, trace apatite). Soft-sediment folding and cross-lamination are apparent in this latter layer type (Plate 2.3a). p.t.s. 8C-1 and 8C-2	2.63 m
Iron formation (dominant): alternating laminae of hematite-magnetite-quartz lutite (Fe-rich) and quartz-magnetite-chlorite-hematite lutite (Fe-rich). Single layer of ferroan dolomite-quartz-plagioclase Fe siltstone (Fe-poor, trace apatite). t.s. and p.t.s. $8B_2$	2.04 m
Fe siltstone & iron formation: a 12.5 cm thick, coarse-tail graded bed of quartz-hematite-magnetite-ferroan dolomite-apatite Fe siltstone (Fe-moderate, Fe_2O_3 = 24.30%, p.t.s. $8A_L$, geo $8A_L$) is overlain by iron formation. The IF consists of alternating laminae of magnetite-quartz-hematite-chlorite lutite (Fe-rich) and hematite-quartz-magnetite lutite (Fe-rich). p.t.s. $8A_U$; geo $8A_U$ (Fe_2O_3 = 65.19%).	0.39 m

Appendix B

Geochemical Methodology

Sample Preparation

Approximately 150 samples were collected for geochemical analysis during mapping and measurement of stratigraphic sections. As mentioned in Chapter 3, individual geochemical aliquots are considered to be representative and homogeneous by virtue of: collecting only the matrices of the diamictite facies; excluding macroscopic, clastic-dominated laminae of the iron formation facies; avoiding laminated portions of the subarkosic Fe wacke facies and excluding sand-dominated laminae of the Fe siltstone facies. An attempt was made in the field to break the samples into pieces suitable for milling (≤ 5 mm), so that the samples did not have to be fed into a Sturtevant jawcrusher (possible contamination) during laboratory preparations at the University of Adelaide. At least some of the field pieces were not small enough for milling, and were broken down in the laboratory using a hand driven rotary rock splitter. The samples were ground in a tungsten carbide mill vessel. Between successive samples, cleaned quartz chips (99% pure) were milled in the vessel, then the vessel was blown with compressed air and rinsed with acetone. The first milled run of each sample was discarded as a means of 'contaminating' the system with its own kind.

University of Adelaide Analytical Procedure

Introduction. As mentioned in Chapter 3, the geochemical samples were split into two groups; the first of which includes all samples from zone 3 (Figure A.1) which were analyzed for major and trace elements at the University of Adelaide. The elements of Si, Al, total Fe as Fe_2O_3, Mn, Mg, Ca, K, Ti, P, Rb, Sr, Ba, Y, Zr, Nb, V, Cr, Ni, Cu, Zn and Pb were determined by x-ray fluorescence spectrometry. Sodium was determined on a VARIAN AA-6 atomic absorption spectrometer. The second group of samples is from zones 1 and 2 (Figure A.1), for which the x-ray fluorescence spectrometer at the University of Western Ontario was used to analyze all major elements, including Na (multi-layer synthetic crystal PX-1 in machine).

Loss on ignition. Approximately 3-4 gms of finely crushed rock powder was measured into a clean glass vial. Duplicate aliquots were taken from the diamictite matrices since they were the most inhomogeneous samples. The vial was placed in a 110°C oven to dry for 3-4 hours, then removed from oven and placed in a dessicator where it was allowed to cool to room temperature. The sample was placed into a preweighed alumina crucible (crucible wgt.) and the new weight was recorded (crucible + sample wgt.). The weighed crucible was placed onto a silica tray and put into a muffle furnace at 400°C. Temperature was set to 960°C and the sample was left in the furnace overnight. The sample was removed from furnace, allowed to cool for 15 minutes, then placed in dessicator to cool to room temperature. The crucible was then reweighed (ignited wgt.). Loss on ignition was calculated for the sample, using the formula: LOI (%) = Total weight loss / sample weight * 100

Fused disc for major elements. The following components were weighed out (to the nearest 0.0020 gm) using a 4 decimal place SARTORIUS electronic balance, and placed in a clean glass vial:

0.02 gm sodium nitrate
0.28 gm ignited sample
1.50 gm sigma x-ray flux (Norrish formula)

The flux was dried at 500°C and kept in a dessicator when not in use. Contents of the vial were completely transferred to a Pt/Au crucible for fusion by heating above an oxy-propane flame (T = 1100°C). The crucible was heated for five minutes until fusion completed, then the melt was poured onto a graphite disc and pressed into a glass disc using an aluminum plunger (both disc and plunger kept at T = 230°C). The fused disc was annealed at 230°C for 30 minutes, then cooled down to room temperature. After labelling of sample disc it was then ready for whole rock analysis by XRF.

Major element analysis. The major elements were analyzed by x-ray fluorescence spectrometry following the method outlined by Norrish and Hutton (1969). The materials used for machine calibration included internal reference materials (100% SiO_2, 100% CaO, 25% Fe_2O_3/75% SiO_2, 50% Fe_2O_3/50% SiO_2, 50% Mn-2/50% SiO_2 and 50% Mn-3/50% SiO_2), internal standards (BHN-1, VHG-1), and international standards (DTS-1, MRG-1, AGV-1). The counting standard used was C9; a synthetic fused mixture of all the major oxides and some minor and trace elements. The criteria for acceptance of an analysis are:

i) admissable results obtained on a suite of standard rock samples;
ii) a total in the range 99.3 to 100.3% (i.e., 99.8 ± 0.5%)

With respect to (i), triplicate analyses of international standards Mica-Fe and MRG-1 were procured as a means of determining precision and accuracy. Relative precision, calculated from the replicate analyses of the standards, ranges from a maximum ±3.15% (MgO of MRG-1) to a minimum ±0.08% (Fe_2O_3 of Mica-Fe). Accuracy, which is the relative error (from reference values of Govindaraju, 1989) converted to percent, is a maximum -0.51 and +0.27 (SiO_2 of MRG-1; MgO of MRG-1) and a minimum -0.01 and +0.01 (TiO_2 of Mica-Fe; MnO of MRG-1).

Trace element analysis. Approximately 4-5 gms of finely crushed, unignited rock powder was incorporated into a pressed pellet (encased by boric acid powder) for trace element analysis by x-ray fluorescence spectrometry. The counting standards used for analysis of each element are listed below:

Rb	MBM + BLC + Y	1841 ppm Rb (local standard)
Sr	" " "	1345 ppm Sr
Y	" " "	588 ppm Y
Ba	VHG + Ba + Sc	2330 ppm Ba (local standard)
Zr	331/371 Zr, Nb spike #3	1896 ppm Zr (local standard)
Nb	331/371 Zr, Nb spike #3	1800 ppm Nb
V	MDP + V	568 ppm V (local standard)
Cr	DTS-1	3990 ppm Cr (USGS standard)
Ni	PCC-1	2380 ppm Ni (USGS standard)
Cu	MRG-1	134 ppm Cu (CCRMP standard)
Zn	"	191 ppm Zn
Pb	SY-3	133 ppm Pb (CCRMP standard)

When choosing a suitable counting standard, the concentration of interfering elements needs to be at a low level. Sr interferes with Zr, so a standard low in Sr was used. Also, Ti interferes with Ba and V. Correction factors were applied for interferences. Trace element results of international geostandards are compared with the recommended values of Govindaraju (1989) in Appendix Table B.1.

Table B.1 Trace element XRF analyses of reference standards. Recommended values of Govindaraju (1989) are shown in **bold**.

	Rb	Sr	Ba	Zr	Nb	Y	V	Cr	Ni	Cu	Pb	Zn
AGV-1	66	658	1209	234	13.3	21	125	8	17	62	35	
	66	657	1202			21						
	67	659				20						
	67.3	**662**	**1226**	**227**	**15**	**20**	**121**	**10.1**	**16**	**60**	**36**	
GSP-1	252	234				23	53		10			
	254	**234**				**26**	**53**		**8.8**			
SCO-1	116	173				25						
	112	**174**				**26**						
MRG-1	8.1	271	45	101	20	14.8			191		9	
	8.5	**266**	**61**	**108**	**19.2**	**14**			**193**		**10**	
G-2	168	479				10.4	37,37	8	3,3			
	170	**478**				**11**	**36**	**8.7**	**5**			
BCR-1	48	335	726	186	11.8	39			11	20		
	47.2	**330**	**681**	**190**	**14**	**38**			**13**	**19**		
BHVO-1			128	176	18.7							
			139	**179**	**19**							
GH			16									
			20									
BR											6	138
											8	**160**
JG-1								61			26	41
								64.6			**26.8**	**41.5**
W-1												89
												84
DTS-1							9			8		
							11			**7.1**		
SDC-1								71				
								64				

Appendix C

ELECTRON MICROPROBE ANALYSES

Oxide minerals

HEMATITE & RUTILE: analyses from samples collected on Oraparinna near Panta Well and at section #12 in 'Dropstone Creek'

	1	2	3	4	5	6	7	8	9	10
TIO2	.13	.08	.09	.08	.08	.10	.12	.07	.18	90.72
AL2O3	.02	.03	.00	.05	.18	.01	.11	.06	.17	.04
CR2O3	.04	.03	.04	.01	.01	.03	.01	.03	.04	.58
FEO	90.08	89.06	89.03	90.38	90.67	88.94	88.94	89.87	89.84	.41
MNO	.05	.02	.10	.07	.00	.07	.06	.07	.07	.00
MGO	.00	.00	.00	.00	.00	.00	.00	.00	.00	.03
SUM	90.32	89.22	89.26	90.59	90.94	89.15	89.24	90.10	90.30	91.78
* RECALCULATED ANALYSIS - MAGNETITE-ULVOSPINEL BASIS *										
FE2O3	66.50	65.79	65.82	66.80	66.89	65.72	65.64	66.42	66.19	-120.61
FEO	30.17	29.79	29.73	30.20	30.41	29.73	29.81	30.03	30.21	109.07
TOTAL	96.91	95.74	95.78	97.21	97.57	95.66	95.74	96.68	96.86	79.83
USP	.39	.24	.27	.24	.24	.30	.36	.21	.54	296.12
* RECALCULATED ANALYSIS - ILMENITE-HEMATITE BASIS *										
FE2O3	99.88	98.76	98.82	100.28	100.42	98.68	98.58	99.70	99.47	-90.37
FEO	.10	.09	.00	.04	.20	.04	.13	.05	.23	81.83
TOTAL	100.22	99.01	99.05	100.53	100.89	98.93	99.01	99.98	100.16	82.82
ROMB	.26	.16	.18	.16	.16	.20	.24	.14	.36	198.14

MOL PROPS	RO2	RO	R_2O_3	DESCRIPTION
1	.19	50.00	49.81	I.F. SAMPLE 11e1: Base of circle 3, specular hematite composite
2	.12	50.00	49.88	11e1: adjacent spot
3	.14	50.00	49.86	11e1: another specular hematite composite
4	.12	50.00	49.88	11e1: same composite as previous
5	.12	50.00	49.88	11e1: Mid-point of thin section, specular hematite
6	.15	50.00	49.85	11e1: same grain as previous
7	.18	50.00	49.82	11e1: Top of thin section, specular hematite
8	.10	50.00	49.90	11e1: adjacent specular hematite euhed
9	.27	50.00	49.73	11e1: same euhed as previous
10	.00	.00	.00	Subarkosic Fe wacke SAMPLE 12f1: rutile from clast within circle 6

Ti-bearing OXIDE: analyses from samples collected at section #12 on Oraparinna and section #13 on Worumba

	11	12	13	14	15	16	17	18	19	20
TIO2	91.36	2.53	2.72	1.26	2.76	11.89	53.07	.55	.46	1.85
AL2O3	.04	.09	.05	.06	.07	.45	.37	.09	.00	.00
CR2O3	.67	.09	.10	.08	.04	.06	.01	.14	.11	.00
FEO	.42	89.06	87.53	87.88	85.80	76.51	38.67	90.78	88.91	87.96
MNO	.00	.00	.00	.00	.00	.00	.00	.00	.00	.00
MGO	.08	.07	.01	.12	.07	.31	.45	.12	.00	.00
SUM	92.57	91.84	90.41	89.40	88.74	89.22	92.57	91.68	89.48	89.81
* RECALCULATED ANALYSIS - MAGNETITE-ULVOSPINEL BASIS *										
FE2O3	-121.42	62.55	61.10	63.45	59.86	40.95	-41.61	66.51	65.14	62.63
FEO	109.81	32.71	32.48	30.72	31.87	39.62	76.16	30.86	30.22	31.54
TOTAL	80.54	98.04	96.47	95.69	94.67	93.28	88.45	98.27	95.94	96.02
USP	295.49	7.45	8.14	3.80	8.41	36.27	163.20	1.62	1.39	5.57
* RECALCULATED ANALYSIS - ILMENITE-HEMATITE BASIS *										
FE2O3	-90.95	96.35	94.37	96.44	92.55	73.29	-9.45	100.31	98.17	95.79
FEO	82.36	2.26	2.51	1.00	2.43	10.48	47.19	.41	.47	1.66
TOTAL	83.56	101.39	99.76	98.96	97.91	96.48	91.63	101.62	99.21	99.30
RONB	197.81	4.97	5.43	2.54	5.61	24.27	109.13	1.08	.93	3.71

MOL PROPS	RO2	RO	R_2O_3	DESCRIPTION
11	.00	.00	.00	12f1: rutile from same clast as previous
12	3.72	50.00	46.28	Diamictite matrix SAMPLE 13c1: hematite, Area #1, spot 1
13	4.07	50.00	45.93	13c1: repeat of previous spot
14	1.90	50.00	48.10	13c1: adjacent hematite platy, Area #1-3
15	4.20	50.00	45.80	13c1: hematite rim (overgrowth) on zoned serrate, Area #2-1
16	18.13	50.00	31.87	13c1: detrital core of same serrate, Area #2-2
17	.00	.00	.00	13c1: core/rim boundary of same serrate, Area #2-3
18	.81	50.00	49.19	13c1: bright half of another hematite serrate, Area #3-1
19	.69	50.00	49.31	13c1: dark half of same serrate, Area #3-2
20	2.78	50.00	47.22	13c1: clast-rimming hematite within circle 2

Ti-bearing OXIDE: analyses from diamictite matrix sample $13c_1$ collected at stratigraphic section #13 on Worumba

	21	22	23	24	25	26	27	28	29	30
TIO2	1.66	.26	94.48	1.69	.97	6.51	.61	34.15	15.17	.62
AL2O3	.00	.05	.00	.30	.00	.13	.00	.28	.08	.00
CR2O3	.01	.18	.23	.00	.11	.05	.02	.00	.00	.05
FEO	86.94	88.85	1.36	86.50	90.57	84.04	90.94	56.54	77.60	91.24
MNO	.00	.00	.00	.00	.00	.00	.00	.00	.00	.00
MGO	.00	.02	.00	.29	.03	.04	.00	.35	.06	.00
SUM	88.61	89.36	96.07	88.78	91.68	90.77	91.57	91.32	92.91	91.91
* RECALCULATED ANALYSIS - MAGNETITE-ULVOSPINEL BASIS *										
FE2O3	62.12	65.34	-124.81	61.99	65.73	53.49	66.48	-3.29	37.27	66.67
FEO	30.97	29.99	113.80	30.66	31.35	35.85	31.05	59.51	44.02	31.17
TOTAL	94.77	95.84	83.70	94.92	98.19	96.07	98.16	90.99	96.60	98.52
USP	5.06	.78	294.53	5.12	2.86	19.47	1.80	104.37	44.74	1.82
* RECALCULATED ANALYSIS - ILMENITE-HEMATITE BASIS *										
FE2O3	94.84	98.27	-92.91	94.67	99.57	86.74	100.32	29.15	71.05	100.63
FEO	1.50	.32	85.07	1.21	.87	5.90	.56	30.28	13.59	.58
TOTAL	98.01	99.10	86.86	98.16	101.55	99.37	101.51	94.21	99.95	101.88
ROMB	3.38	.52	196.60	3.42	1.91	13.00	1.20	69.74	29.85	1.21

MOL PROPS	RO2	RO	R_2O_3	DESCRIPTION
21	2.53	50.00	47.47	13c1: clast-rimming hematite euhed, circle 2
22	.39	50.00	49.61	13c1: hematite subhed, Area #15
23	.00	.00	.00	13c1: rutile core of hematite serrate within circle 4, Plate 4.1e, spot 2
24	2.56	50.00	47.44	13c1: rim of same serrate, Plate 4.1e, spot 3
25	1.43	50.00	48.57	13c1: adjacent hematite serrate, Plate 4.1e, spot 4
26	9.74	50.00	40.26	13c1: detrital core of adjoining hematite serrate, Plate 4.1e, spot 5
27	.90	50.00	49.10	13c1: rim of same serrate, Plate 4.1e, spot 6
28	69.74	.00	30.26	13c1: detrital core of same serrate, Plate 4.1e, spot 7
29	22.37	50.00	27.63	13c1: another spot in detrital core of same serrate, Plate 4.1e, spot 8
30	.91	50.00	49.09	13c1: rim of same serrate, Plate 4.1e, spot 9

Ti-bearing OXIDE: analyses from samples collected at stratigraphic section #13 on Worumba

	31	32	33	34	35	36	37	38	39	40
TIO2	.46	.91	93.60	1.00	1.20	1.07	6.13	1.14	1.50	1.17
AL2O3	.00	.00	.00	.46	.46	.08	.07	.14	.04	.01
CR2O3	.02	.00	.08	.01	.00	.03	.18	.07	.03	.04
FEO	88.94	88.30	1.83	88.71	87.85	87.60	84.31	86.49	88.99	87.35
MNO	.00	.00	.00	.03	.08	.10	.00	.00	.11	.02
MGO	.00	.00	.00	.04	.65	.00	.02	.09	.00	.04
SUM	89.42	89.21	95.51	90.25	90.24	88.88	90.71	87.93	90.67	88.63
* RECALCULATED ANALYSIS - MAGNETITE-ULVOSPINEL BASIS *										
FE2O3	65.20	64.13	-123.24	64.15	64.09	63.42	54.16	62.51	63.91	63.13
FEO	30.21	30.52	112.86	30.92	30.11	30.46	35.52	30.18	31.42	30.48
TOTAL	95.88	95.57	83.30	96.61	96.59	95.17	96.08	94.12	97.00	94.89
USP	1.39	2.75	293.35	2.99	3.56	3.25	18.35	3.50	4.47	3.56
* RECALCULATED ANALYSIS - ILMENITE-HEMATITE BASIS *										
FE2O3	98.25	97.10	-91.44	97.22	97.33	96.20	87.36	94.90	97.36	95.86
FEO	.42	.82	84.20	1.13	.16	.93	5.61	1.00	1.28	.99
TOTAL	99.16	98.83	86.45	99.88	99.89	98.41	99.37	97.33	100.32	98.13
RONB	.93	1.84	195.66	2.00	2.38	2.17	12.25	2.33	2.98	2.38

MOL PROPS	RO2	RO	R2O3	DESCRIPTION
31	.69	50.00	49.31	13c1: another spot in rim of previous serrate, Plate 4.1e, spot 10
32	1.38	50.00	48.62	13c1: yet another spot in rim of same serrate, Plate 4.1e, spot 12
33	.00	.00	.00	13c1: rutile anhed within circle 4, Area #18
34	1.49	50.00	48.51	Diamictite matrix SAMPLE 13c1: probe day 2, hematite replacing phlogopite
35	1.78	50.00	48.22	13c1: hematite replacing same phlogopite, Area #1-6
36	1.63	50.00	48.37	13c1: adjacent hematite subhed, Area #1-7
37	9.17	50.00	40.83	13c1: detrital core of twinned hematite, Area #5-2
38	1.75	50.00	48.25	13c1: hematite serrate rim (overgrowth) on twinned hematite, Area #5-3
39	2.23	50.00	47.77	I.F. SAMPLE 13e2: hematite subhed, Area #2-1
40	1.78	50.00	48.22	13e2: repeat of previous subhed

IRON OXIDE: analyses from samples collected at section #13 on Worumba and section #21 in Back Creek, Holowilena South

	41	42	43	44	45	46	47	48	49	50
TIO2	1.24	.36	.01	.01	.18	.09	1.32	4.92	18.41	15.43
AL2O3	.30	.26	.05	.02	.06	.04	.36	.23	.03	.13
CR2O3	.04	.00	.01	.00	.00	.03	.02	.01	.01	.01
FEO	87.19	88.07	89.46	91.01	88.34	91.32	87.17	84.95	69.75	73.18
MNO	.04	.00	.00	.00	.00	.00	.00	.00	.00	.00
MGO	.22	.03	.00	.01	.00	.00	.00	.00	.00	.05
SUM	89.03	88.72	89.53	91.05	88.58	91.48	88.87	90.11	88.20	88.80
* RECALCULATED ANALYSIS - MAGNETITE-ULVOSPINEL BASIS *										
FE2O3	63.02	64.60	66.16	67.34	65.10	67.43	62.55	56.19	27.09	33.61
FEO	30.42	29.88	29.86	30.35	29.69	30.58	30.82	34.33	45.34	42.90
TOTAL	95.28	95.12	96.09	97.72	95.03	98.16	95.07	95.68	90.89	92.13
USP	3.75	1.09	.03	.03	.55	.27	4.01	14.80	57.51	47.66
* RECALCULATED ANALYSIS - ILMENITE-HEMATITE BASIS *										
FE2O3	95.77	97.25	99.25	101.02	97.83	101.23	95.15	89.20	59.02	65.82
FEO	.91	.45	.05	.01	.20	.12	1.45	4.59	16.58	13.88
TOTAL	98.52	98.36	99.37	101.06	98.27	101.51	98.30	98.95	94.05	95.32
RONB	2.51	.73	.02	.02	.37	.18	2.68	9.88	38.35	31.81

MOL PROPS	RO2	RO	R_2O_3	DESCRIPTION
41	1.88	50.00	48.12	13e2: adjacent hematite subhed, Area #2-15
42	.55	50.00	49.45	13e2: hematite parallel to phlogopite cleavage, Plate 4.2c, spot 2
43	.02	50.00	49.98	I.F. SAMPLE 21a1: hematite-after-magnetite rhomb, Area #1-1
44	.01	50.00	49.99	21a1: hematite-after-magnetite rhomb, Area #1, stop 2
45	.27	50.00	49.73	21a1: hematite-after-magnetite rhomb, Area #2
46	.13	50.00	49.87	21a1: hematite-after-magnetite rhomb, Area #3
47	2.00	50.00	48.00	Diamictite matrix SAMPLE 21j1: hematite in I.F. clast, Area #1-1
48	7.40	50.00	42.60	21j1: hematite serrate, Area #4
49	28.76	50.00	21.24	21j1: hematite serrate, Area #5, spot 1
50	23.83	50.00	26.17	21j1: another spot in same hematite serrate, Area #5, spot 2

OXIDE: analyses from samples collected at stratigraphic sections 21 (Holowilena South), 19 (Oopina) and 18 (Mount Victor)

	51	52	53	54	55	56	57	58	59	60
TIO2	17.85	58.63	.01	.01	.00	1.92	.13	1.97	96.45	7.33
AL2O3	.29	.04	.00	.03	.02	.09	.00	.14	.00	.01
CR2O3	.01	.01	.00	.00	.03	.03	.04	.03	.00	.04
FEO	68.69	35.61	94.03	88.98	89.57	89.59	92.03	90.64	1.05	85.50
MNO	.02	.00	.00	.02	.00	.03	.10	.11	.06	.09
MGO	.05	.00	.00	.01	.00	.02	.04	.04	.00	.00
SUM	86.91	94.29	94.04	89.05	89.62	91.68	92.34	92.93	97.56	92.97
* RECALCULATED ANALYSIS - MAGNETITE ULVOSPINEL BASIS *										
FE2O3	27.00	-51.70	69.57	65.84	66.26	63.73	68.04	64.50	-127.54	53.56
FEO	44.36	82.19	31.36	29.66	29.88	32.17	30.73	32.53	115.95	37.25
TOTAL	89.59	89.17	100.93	95.58	96.19	98.00	99.08	99.32	84.92	98.28
USP	56.47	178.92	.03	.03	.00	5.66	.38	5.73	296.20	21.44
* RECALCULATED ANALYSIS - ILMENITE-HEMATITE BASIS *										
FE2O3	58.37	-19.03	104.36	98.78	99.39	97.52	102.19	98.72	-95.04	87.66
FEO	16.15	52.75	.01	-.01	.03	1.74	-.04	1.70	86.67	6.53
TOTAL	92.69	92.40	104.38	98.84	99.47	101.34	102.47	102.71	88.14	101.66
ROMB	37.74	119.33	.02	.02	.00	3.78	.25	3.82	197.47	14.30

MOL PROPS	RO2	RO	R_2O_3	DESCRIPTION
51	28.24	50.00	21.76	21j1: hematite subhed-serrate, Area #7
52	.00	.00	.00	21j1: triangular clast, Area #8
53	.01	50.00	49.99	I.F. SAMPLE 19E2: magnetite rhomb, Area #1
54	.02	50.00	49.98	19E2: hematite-after-magnetite rhomb, Area #2, spot 1
55	.00	50.00	50.00	19E2: another spot in same rhomb, Area #2, spot 2
56	2.83	50.00	47.17	19E2: different probe day, hematite subhed, Area #1, spot 4
57	.19	50.00	49.81	19E2: magnetite euhed, Area #1, spot 7
58	2.86	50.00	47.14	19E2: adjacent hematite anhed, Area #1, spot 8
59	.00	.00	.00	Subarkosic Fe arenite (Fe-poor) SAMPLE 18l1: rutile in hematite serrate, Area #2-1
60	10.72	50.00	39.28	18l1: another spot in same hematite serrate

MAGNETITE & HEMATITE: analyses from samples collected at stratigraphic sections 16 (<u>Outalpa</u>), 15 (<u>Bimbowrie</u>) and 10 (<u>Spring Dam</u>)

	61	62	63	64	65	66	67	68	69	70
TIO2	.03	.04	.16	.11	.02	.01	.15	.15	.11	.13
AL2O3	.05	.05	.00	.05	.01	.00	.01	.01	.01	.01
CR2O3	.06	.03	.02	.06	.03	.08	.14	.10	.11	.05
FEO	91.96	92.06	93.29	93.12	92.22	92.54	92.15	92.68	91.20	91.66
MNO	.01	.04	.14	.09	.12	.09	.11	.07	.11	.13
MGO	.03	.03	.01	.02	.02	.00	.00	.00	.00	.00
SUM	92.14	92.25	93.62	93.45	92.42	92.72	92.56	93.01	91.54	91.98
* RECALCULATED ANALYSIS - MAGNETITE-ULVOSPINEL BASIS *										
FE2O3	68.01	68.10	68.93	68.81	68.32	68.51	68.02	68.40	67.38	67.73
FEO	30.69	30.71	31.19	31.13	30.67	30.82	30.87	31.06	30.50	30.64
TOTAL	98.88	99.00	100.45	100.27	99.19	99.51	99.30	99.79	98.22	98.69
USP	.09	.12	.46	.32	.06	.03	.44	.44	.32	.38
* RECALCULATED ANALYSIS - ILMENITE-HEMATITE BASIS *										
FE2O3	102.05	102.20	103.56	103.32	102.50	102.77	102.18	102.74	101.18	101.72
FEO	.03	-.01	-.01	.04	-.12	-.04	.10	.12	.05	.02
TOTAL	102.25	102.38	103.88	103.69	102.58	102.90	102.69	103.19	101.57	102.06
RONB	.06	.08	.31	.21	.04	.02	.29	.29	.22	.25

MOL PROPS	RO2	RO	R_2O_3	DESCRIPTION
61	.04	50.00	49.96	I.F. SAMPLE 16d1: magnetite rhomb, Area #2
62	.06	50.00	49.94	16d1: magnetite rhomb, Area #3
63	.23	50.00	49.77	16d1: magnetite, Area #4, spot 2
64	.16	50.00	49.84	16d1: magnetite euhed, Area #5
65	.03	50.00	49.97	Diamictite matrix SAMPLE 15f1: magnetite euhed, Area #1, spot 3
66	.01	50.00	49.99	15f1: magnetite euhed within a clast, Area #2-1
67	.22	50.00	49.78	Calcite subarkosic Fe arenite (Fe-poor) layer in I.F. SAMPLE 10d1: magnetite
68	.22	50.00	49.78	10d1: same rhomb as previous
69	.16	50.00	49.84	10d1: adjacent rhomb composite, hematite-after-magnetite
70	.19	50.00	49.81	10d1: same composite as previous, partially hematized

MAGNETITE & HEMATITE: analyses from samples collected at stratigraphic section #10 near Pualco West, <u>Spring Dam</u>

	71	72	73	74	75	76	77	78	79	80
TIO2	.11	.02	.02	3.93	.04	.05	.02	.05	.00	.05
AL2O3	.00	.00	.00	.03	.00	.00	.00	.01	.00	.00
CR2O3	.05	.08	.09	.10	.00	.00	.10	.08	.06	.08
FEO	91.20	92.86	93.06	84.57	94.29	90.00	90.20	91.81	93.41	92.42
MNO	.07	.00	.00	.00	.00	.00	.00	.00	.00	.00
MGO	.00	.00	.01	.84	.02	.00	.02	.01	.00	.02
SUM	91.43	92.96	93.18	89.47	94.35	90.05	90.34	91.96	93.47	92.57
* RECALCULATED ANALYSIS - MAGNETITE-ULVOSPINEL BASIS *										
FE2O3	67.38	68.66	68.82	58.41	69.75	66.53	66.71	67.85	69.10	68.32
FEO	30.50	31.00	31.06	31.95	31.45	30.06	30.10	30.68	31.16	30.87
TOTAL	98.11	99.76	100.00	95.26	101.26	96.64	96.95	98.68	100.32	99.34
USP	.32	.06	.06	11.81	.11	.15	.06	.15	.00	.15
* RECALCULATED ANALYSIS - ILMENITE-HEMATITE BASIS *										
FE2O3	101.17	103.01	103.25	91.54	104.66	99.85	100.09	101.83	103.65	102.53
FEO	.05	.06	.04	2.11	.00	.04	.03	.07	.03	.05
TOTAL	101.46	103.17	103.41	98.54	104.72	99.95	100.26	102.05	103.74	102.73
ROMB	.22	.04	.04	7.88	.08	.10	.04	.10	.00	.10

MOL PROPS	RO2	RO	R_2O_3	DESCRIPTION
71	.16	50.00	49.84	10d1: equant subhed, hematite-after-magnetite
72	.03	50.00	49.97	Carbonate SAMPLE 10q1: magnetite within circle 2, Area #2
73	.03	50.00	49.97	10q1: magnetite within circle 2, Area #3
74	5.91	50.00	44.09	10q1: hematite subhed within circle 2, Area #4
75	.06	50.00	49.94	10q1: magnetite euhed, Area #6, spot 1
76	.07	50.00	49.93	10q1: hematite-after-magnetite portion of previous euhed, Area #6-2
77	.03	50.00	49.97	10q1: repeat of previous spot
78	.07	50.00	49.93	10q1: adjacent magnetite subhed, Area #6, spot 3
79	.00	50.00	50.00	10q1: magnetite subhed, Area #8
80	.07	50.00	49.93	10q1: magnetite, Area #9, stop 2

OXIDE: analyses from samples collected at stratigraphic section #10 near Pualco West, Spring Dam

	81	82	83	84	85	86	87	88	89	90
TIO2	.07	4.93	.00	93.50	.01	4.18	4.43	.11	4.84	4.22
AL203	.00	.01	.00	.00	.00	.05	.06	.04	.04	.05
CR203	.00	.09	.08	.04	.10	.02	.05	.05	.04	.08
FEO	91.04	83.64	91.48	.73	92.83	86.58	86.82	90.19	85.49	87.02
MNO	.46	.02	.00	.00	.00	.01	.08	.05	.05	.08
MGO	.00	.51	.04	.00	.02	.00	.00	.00	.00	.00
SUM	91.57	89.20	91.60	94.27	92.96	90.84	91.44	90.44	90.46	91.45
* RECALCULATED ANALYSIS - MAGNETITE-ULVOSPINEL BASIS *										
FE203	67.62	55.98	67.72	-123.91	68.67	58.48	58.36	66.59	56.82	58.78
FEO	30.12	33.20	30.47	112.36	30.96	33.90	34.24	30.20	34.30	34.06
TOTAL	98.27	94.75	98.31	81.99	99.77	96.64	97.22	97.04	96.09	97.28
USP	.21	14.93	.00	297.28	.03	12.47	13.13	.33	14.51	12.50
* RECALCULATED ANALYSIS - ILMENITE-HEMATITE BASIS *										
FE203	101.50	88.90	101.58	-92.54	103.02	91.89	91.97	100.00	90.07	92.39
FEO	-.40	3.55	-.03	84.10	.02	3.79	3.97	.10	4.35	3.79
TOTAL	101.63	98.01	101.67	85.10	103.17	99.95	100.55	100.35	99.39	100.61
ROMB	.14	9.96	.00	198.23	.02	8.32	8.76	.22	9.68	8.34

MOL PROPS	RO2	RO	R_2O_3	DESCRIPTION
81	.10	50.00	49.90	10q1: another adjoining magnetite, partially hematized, Area #9, stop 3
82	7.46	50.00	42.54	10q1: adjacent hematite anhed, Area #9, stop 4
83	.00	50.00	50.00	10q1: adjacent magnetite euhed, partially hematized, Area #9, stop 5
84	.00	.00	.00	10q1: rutile within circle 1, Area #10
85	.01	50.00	49.99	10q1: magnetite from iron oxide string which parallels bedding
86	6.23	50.00	43.77	I.F. SAMPLE 10T1: hematite subhed
87	6.57	50.00	43.43	10T1: adjacent hematite subhed
88	.16	50.00	49.84	10T1: hematite-after-magnetite rhomb
89	7.25	50.00	42.75	10T1: hematite-replacing-biotite?
90	6.25	50.00	43.75	10T1: adjacent hematite subhed

HEMATITE & MAGNETITE: analyses from samples collected on Spring Dam near Pualco West (#10) and within adit at Razorback Ridge (#8)

	91	92	93	94	95	96	97	98	99	100
TIO2	.10	.12	.00	.85	.84	.85	.91	.99	.00	.86
AL2O3	.07	.03	.00	.01	.05	.09	.04	.06	.01	.03
CR2O3	.04	.02	.00	.00	.03	.00	.00	.01	.00	.00
FEO	90.92	91.48	94.28	87.97	87.61	88.95	87.83	89.34	94.62	90.33
MNO	.10	.15	.05	.00	.04	.00	.05	.00	.04	.03
MGO	.00	.00	.00	.00	.00	.02	.00	.01	.02	.01
SUM	91.23	91.80	94.33	88.83	88.57	89.91	88.83	90.41	94.69	91.26
* RECALCULATED ANALYSIS - MAGNETITE-ULVOSPINEL BASIS *										
FE2O3	67.17	67.62	69.80	63.96	63.71	64.67	63.80	64.77	70.07	65.72
FEO	30.41	30.56	31.39	30.33	30.22	30.69	30.35	30.99	31.49	31.12
TOTAL	97.89	98.50	101.25	95.17	94.88	96.32	95.15	96.83	101.63	97.77
USP	.30	.35	.00	2.58	2.56	2.55	2.77	2.96	.00	2.54
* RECALCULATED ANALYSIS - ILMENITE-HEMATITE BASIS *										
FE2O3	100.86	101.56	104.71	96.79	96.40	97.86	96.61	98.15	105.10	99.44
FEO	.06	-.01	-.05	.77	.76	.79	.80	.92	-.07	.75
TOTAL	101.22	101.86	104.71	98.42	98.12	99.61	98.40	100.14	105.11	101.11
ROMB	.20	.24	.00	1.72	1.71	1.70	1.84	1.97	.00	1.70

MOL PROPS	RO2	RO	R_2O_3	DESCRIPTION
91	.15	50.00	49.85	10T1: rim of adjoining hematite-after-magnetite rhomb
92	.18	50.00	49.82	10T1: core of same rhomb, partially hematized
93	.00	50.00	50.00	I.F. SAMPLE 8q1: magnetite euhed within iron-rich layer
94	1.29	50.00	48.71	8q1: adjoining hematite platy, Area #1, spot 2
95	1.28	50.00	48.72	8q1: hematite serrate, Area #1, spot 4
96	1.28	50.00	48.72	8q1: hematite platy within iron-rich layer
97	1.38	50.00	48.62	8q1: adjoining hematite subhed, Area #2, spot 2
98	1.48	50.00	48.52	8q1: hematite subhed within iron-rich layer, Plate 4.1a, spot 1
99	.00	50.00	50.00	8q1: rim of magnetite subhed, Plate 4.1a, spot 2
100	1.27	50.00	48.73	8q1: adjoining hematite platy, Plate 4.1a, spot 3

HEMATITE & MAGNETITE: analyses from iron formation sample $8q_1$ collected within the adit through Razorback Ridge, <u>Spring Dam</u>

	101	102	103	104	105	106	107	108	109	110
TIO2	.00	.00	.00	.79	.79	.79	.02	.77	.00	.89
AL2O3	.05	.02	.02	.02	.03	.03	.00	.02	.03	.02
CR2O3	.13	.00	.00	.00	.00	.00	.00	.03	.00	.00
FEO	91.09	89.52	94.34	89.21	88.73	89.81	92.96	89.66	93.32	89.11
MNO	.03	.00	.00	.00	.03	.07	.00	.07	.08	.00
MGO	.01	.00	.00	.01	.01	.00	.02	.00	.13	.01
SUM	91.31	89.54	94.36	90.03	89.59	90.70	93.00	90.55	93.56	90.03
* RECALCULATED ANALYSIS - MAGNETITE-ULVOSPINEL BASIS *										
FE2O3	67.37	66.23	69.80	64.97	64.63	65.44	68.79	65.35	69.27	64.76
FEO	30.40	29.85	31.46	30.68	30.51	30.85	30.99	30.78	30.91	30.77
TOTAL	97.99	96.10	101.28	96.47	95.99	97.19	99.82	97.03	100.42	96.45
USP	.00	.00	.00	2.37	2.38	2.35	.06	2.30	.00	2.67
* RECALCULATED ANALYSIS - ILMENITE-HEMATITE BASIS *										
FE2O3	101.06	99.35	104.70	98.24	97.73	98.96	103.21	98.80	103.91	98.03
FEO	.05	.01	.01	.71	.68	.66	-.02	.65	-.29	.80
TOTAL	101.32	99.39	104.74	99.77	99.28	100.51	103.23	100.34	103.86	99.74
ROMB	.00	.00	.00	1.58	1.59	1.57	.04	1.53	.00	1.78

MOL PROPS	RO2	RO	R_2O_3	DESCRIPTION
101	.00	50.00	50.00	8q1: circular hematite-after-magnetite, Area #4, spot 1
102	.00	50.00	50.00	8q1: hematized-half of magnetite euhed, Plate 4.2d, spot 1
103	.00	50.00	50.00	8q1: magnetite-half of same euhed, Plate 4.2d, spot 2
104	1.18	50.00	48.82	8q1: adjoining hematite platy, Plate 4.2d, spot 3
105	1.19	50.00	48.81	8q1: adjacent hematite just 'south' of Plate 4.2d
106	1.18	50.00	48.82	8q1: hematite subhed, Area #7, spot 1
107	.03	50.00	49.97	8q1: adjacent magnetite euhed, Area #7, spot 2
108	1.15	50.00	48.85	8q1: hematite, Area #8, spot 1
109	.00	50.00	50.00	8q1: adjacent magnetite, Area #8, spot 2
110	1.33	50.00	48.67	8q1: hematite, Area #9-1

IRON OXIDE: analyses from the adit ($8q_1$) and a drill hole (RD#3) through Razorback Ridge, <u>Spring Dam</u>

	111	112	113	114	115	116	117	118	119	120
TIO2	.00	2.71	12.18	2.59	2.77	.00	.00	2.26	2.17	.00
AL2O3	.01	.00	.07	.04	.05	.00	.00	.04	.03	.00
CR2O3	.00	.02	.00	.00	.00	.00	.01	.00	.00	.00
FEO	94.40	88.10	79.83	89.47	86.52	90.74	92.47	89.18	88.19	93.31
MNO	.07	.00	.07	.06	.05	.06	.09	.00	.03	.07
MGO	.00	.00	.02	.00	.00	.01	.00	.01	.00	.00
SUM	94.48	90.83	92.17	92.16	89.39	90.81	92.57	91.49	90.42	93.38
* RECALCULATED ANALYSIS - MAGNETITE-ULVOSPINEL BASIS *										
FE2O3	69.90	61.58	42.91	62.78	60.35	67.21	68.49	62.98	62.38	69.10
FEO	31.42	32.62	41.18	32.91	32.15	30.19	30.77	32.44	31.99	31.06
TOTAL	101.41	96.93	96.42	98.38	95.37	97.47	99.36	97.73	96.60	100.23
USP	.00	8.07	36.11	7.60	8.38	.00	.00	6.68	6.49	.00
* RECALCULATED ANALYSIS - ILMENITE-HEMATITE BASIS *										
FE2O3	104.85	95.08	76.52	96.76	93.29	100.81	102.74	96.72	95.74	103.65
FEO	-.06	2.45	10.90	2.30	2.48	-.08	-.09	2.04	1.94	-.07
TOTAL	104.87	100.25	99.75	101.75	98.63	100.80	102.75	101.08	99.91	103.65
RONB	.00	5.38	24.09	5.07	5.59	.00	.00	4.45	4.33	.00

MOL PROPS	RO2	RO	R_2O_3	DESCRIPTION
111	.00	50.00	50.00	8q1: adjacent magnetite, Area #9, spot 2
112	4.04	50.00	45.96	Diamictite SAMPLE RD#3-11': Area #1 within carbonate clast
113	18.06	50.00	31.94	RD#3-11': Area #2 within same carbonate clast
114	3.80	50.00	46.20	RD#3-11': Area #3 within same carbonate clast
115	4.19	50.00	45.81	RD#3-11': Area #4 within same carbonate clast
116	.00	50.00	50.00	RD#3-11': core of hematite-after-magnetite subhed in diamictite matrix, #5-1
117	.00	50.00	50.00	RD#3-11': relict magnetite rim of same subhed, Area #5-2
118	3.34	50.00	46.66	RD#3-11': adjacent hematite subhed, Area #5-3
119	3.24	50.00	46.76	RD#3-11': another spot in previous subhed
120	.00	50.00	50.00	RD#3-11': relict magnetite portion of another subhed, Area #6, spot 1

HEMATITE & MAGNETITE: analyses from a drill hole (RD#3) and the adit ($8E_1$) through Razorback Ridge, Spring Dam

	121	122	123	124	125	126	127	128	129	130
TIO2	.01	2.36	2.26	2.27	2.36	2.16	.04	.04	.00	.00
AL2O3	.01	.04	.05	.03	.00	.03	.00	.00	.00	.00
CR2O3	.00	.00	.04	.02	.00	.00	.00	.00	.10	.00
FEO	89.27	88.03	87.87	89.76	86.93	87.05	92.05	90.22	93.95	93.70
MNO	.07	.08	.07	.01	.00	.04	.04	.00	.00	.00
MGO	.00	.00	.00	.00	.00	.00	.02	.00	.00	.00
SUM	89.36	90.51	90.29	92.09	89.29	89.28	92.15	90.26	94.05	93.70
* RECALCULATED ANALYSIS - MAGNETITE-ULVOSPINEL BASIS *										
FE2O3	66.09	62.04	62.03	63.39	61.19	61.56	68.12	66.71	69.49	69.34
FEO	29.73	32.14	31.99	32.66	31.81	31.59	30.68	30.12	31.35	31.23
TOTAL	95.91	96.66	96.44	98.37	95.35	95.38	98.90	96.87	100.94	100.57
USP	.03	7.05	6.77	6.67	7.15	6.54	.12	.12	.00	.00
* RECALCULATED ANALYSIS - ILMENITE-HEMATITE BASIS *										
FE2O3	99.15	95.42	95.30	97.35	94.14	94.49	102.22	100.10	104.23	104.01
FEO	-.05	2.07	2.02	2.06	2.12	1.92	-.04	.04	.05	.00
TOTAL	99.19	99.97	99.73	101.74	98.62	98.64	102.28	100.18	104.38	104.01
ROMB	.02	4.70	4.51	4.45	4.77	4.36	.08	.08	.00	.00

MOL PROPS	RO2	RO	R_2O_3	DESCRIPTION
121	.02	50.00	49.98	RD#3-11': same hematite-after-magnetite subhed as previous, Area #6, spot 2
122	3.53	50.00	46.47	RD#3-11': hematite serrate, Area #7, spot 1
123	3.38	50.00	46.62	RD#3-11': adjacent hematite subhed, Area #7, spot 2
124	3.33	50.00	46.67	RD#3-11': hematite within a clast, Area #8-1
125	3.57	50.00	46.43	RD#3-11': another hematite within same clast, Area #8-3
126	3.27	50.00	46.73	RD#3-11': yet another hematite within same clast, Area #8-4
127	.06	50.00	49.94	RD#3-11': relict magnetite portion of euhed in same clast, Area #8-5
128	.06	50.00	49.94	RD#3-11': same hematite-after-magnetite euhed, Area #8-6
129	.00	50.00	50.00	Carbonate-enriched layer within I.F. SAMPLE 8E1: magnetite subhed, Area #1-1
130	.00	50.00	50.00	8E1: adjoining magnetite subhed, Area #1, stop 3

MAGNETITE & HEMATITE: analyses from sample $8E_1$ collected within the adit through Razorback Ridge, Spring Dam

	131	132	133	134	135	136	137	138	139	140
TIO2	1.22	.05	.04	.05	.00	1.34	.03	.00	.07	.03
AL2O3	.00	.03	.00	.00	.00	.01	.00	.00	.00	.00
CR2O3	.04	.00	.03	.04	.00	.10	.00	.00	.04	.07
FEO	90.22	94.36	92.43	94.85	94.75	87.80	91.97	92.06	92.98	93.34
MNO	.00	.00	.00	.00	.00	.00	.00	.00	.00	.00
MGO	.00	.00	.00	.00	.00	.00	.00	.00	.00	.00
SUM	91.48	94.44	92.50	94.94	94.75	89.25	92.00	92.06	93.09	93.44
* RECALCULATED ANALYSIS - MAGNETITE-ULVOSPINEL BASIS *										
FE2O3	65.12	69.74	68.33	70.11	70.11	63.15	68.02	68.12	68.70	69.01
FEO	31.55	31.53	30.87	31.69	31.58	30.91	30.69	30.69	31.09	31.17
TOTAL	97.93	101.35	99.27	101.89	101.70	95.51	98.74	98.81	99.90	100.28
USP	3.60	.14	.12	.14	.00	4.06	.09	.00	.20	.09
* RECALCULATED ANALYSIS - ILMENITE-HEMATITE BASIS *										
FE2O3	98.91	104.67	102.54	105.21	105.17	96.06	102.06	102.19	103.12	103.54
FEO	1 12	.07	.05	.06	.00	1.26	.03	.00	.08	.06
TOTAL	101.28	104.81	102.66	105.37	105.17	98.77	102.11	102.19	103.31	103.70
RQMB	2.40	.10	.08	.09	.00	2.71	.06	.00	.14	.06

MOL PROPS	RO2	RO	R_2O_3	DESCRIPTION
131	1.80	50.00	48.20	8E1: hematite subhed in carb.-enriched layer, Area #3, stop 2
132	.07	50.00	49.93	8E1: adjacent magnetite subhed, Area #3, stop 3
133	.06	50.00	49.94	8E1: adjacent magnetite subhed, Area #3, stop 4
134	.07	50.00	49.93	8E1: magnetite subhed from E-W mid slide in carb.-enriched layer
135	.00	50.00	50.00	8E1: same subhed as previous, Area #4, stop 2
136	2.03	50.00	47.97	8E1: adjacent hematite euhed, Area #4, stop 3
137	.04	50.00	49.96	8E1: adjacent magnetite subhed, Area #4, stop 4
138	.00	50.00	50.00	8E1: same subhed as previous, Area #4, stop 5
139	.10	50.00	49.90	8E1: magnetite subhed in iron-rich layer, Area #5, stop 4
140	.04	50.00	49.96	8E1: adjacent magnetite subhed, Area #5, stop 5

MAGNETITE & HEMATITE: analyses from samples collected within the adit through Razorback Ridge, Spring Dam

	141	142	143	144	145	146	147	148	149	150
TIO2	1.62	1.20	1.34	.03	.00	.00	.00	.00	.04	3.67
AL2O3	.04	.05	.00	.01	.00	.00	.03	.00	.00	.03
CR2O3	.00	.03	.00	.00	.00	.03	.07	.00	.00	.06
FEO	88.11	89.34	89.59	94.42	94.54	93.13	93.22	92.39	93.82	85.33
MNO	.00	.00	.00	.00	.01	.00	.06	.06	.05	.05
MGO	.00	.00	.00	.00	.03	.03	.04	.00	.00	.01
SUM	89.77	90.62	90.93	94.46	94.58	93.19	93.42	92.45	93.91	89.15
* RECALCULATED ANALYSIS - MAGNETITE-ULVOSPINEL BASIS *										
FE2O3	63.02	64.48	64.51	69.82	70.01	68.94	69.04	68.41	69.41	58.27
FEO	31.33	31.25	31.47	31.51	31.47	31.02	31.02	30.76	31.29	32.83
TOTAL	96.02	97.01	97.32	101.38	101.52	100.02	100.26	99.23	100.79	94.92
USP	4.88	3.58	3.98	.09	.00	.00	.00	.00	.11	11.15
* RECALCULATED ANALYSIS - ILMENITE-HEMATITE BASIS *										
FE2O3	96.15	97.91	98.11	104.77	105.01	103.42	103.56	102.62	104.16	91.07
FEO	1.48	1.13	1.20	.03	-.06	-.04	-.08	-.06	-.01	3.28
TOTAL	99.30	100.32	100.65	104.84	104.99	103.44	103.68	102.62	104.23	98.18
RONB	3.25	2.39	2.65	.06	.00	.00	.00	.00	.08	7.44

MOL PROPS	RO2	RO	R_2O_3	DESCRIPTION
141	2.44	50.00	47.56	BE1: hematite subhed, Area #6, stop 2
142	1.79	50.00	48.21	BE1: hematite serrate from carb.-enriched layer, Area #7, stop 2
143	1.99	50.00	48.01	BE1: same hematite serrate, Area #7, stop 3
144	.04	50.00	49.96	BE1: magnetite subhed still in carb.-enriched layer, Area #9-2
145	.00	50.00	50.00	Fe siltstone SAMPLE BAL (L = Lower): magnetite subhed, #5
146	.00	50.00	50.00	BAL: core of magnetite subhed, Area #6, spot 1
147	.00	50.00	50.00	BAL: core of same subhed, Area #6, spot 2
148	.00	50.00	50.00	BAL: rim of magnetite subhed, Plate 4.1b, spot 1
149	.06	50.00	49.94	BAL: another spot in rim of same magnetite subhed, Plate 4.1b, spot 3
150	5.57	50.00	44.43	BAL: core of adjoining hematite serrate, Plate 4.1b, spot 2

OXIDE: analyses from Fe siltstone sample $8A_L$ collected within the adit through Razorback Ridge, <u>Spring Dam</u>

	151	152	153	154	155	156	157	158	159	160
TIO2	1.60	.01	.00	.00	.06	1.55	2.07	90.79	6.23	6.20
AL2O3	.03	.00	.01	.01	.01	.06	.03	.00	.05	.02
CR2O3	.00	.01	.07	.00	.07	.01	.03	.00	.03	.07
FEO	88.15	93.71	91.83	93.29	93.80	87.40	88.06	5.32	86.97	87.10
MNO	.03	.14	.00	.00	.00	.00	.00	.00	.00	.00
MGO	.00	.00	.00	.00	.04	.00	.00	.14	.00	.00
SUM	89.81	93.87	91.91	93.30	93.98	89.02	90.19	96.25	93.28	93.39
* RECALCULATED ANALYSIS - MAGNETITE-ULVOSPINEL BASIS *										
FE2O3	63.11	69.43	67.92	69.03	69.35	62.58	62.38	-116.71	56.03	56.17
FEO	31.30	31.16	30.64	31.10	31.32	31.02	31.86	110.46	36.49	36.50
TOTAL	96.06	100.75	98.64	100.14	100.85	95.22	96.37	84.68	98.83	98.96
USP	4.81	.03	.00	.00	.17	4.70	6.21	280.84	18.14	18.03
* RECALCULATED ANALYSIS - ILMENITE-HEMATITE BASIS *										
FE2O3	96.26	104.16	101.89	103.54	104.09	95.41	95.64	-84.44	90.26	90.44
FEO	1.43	-.13	.04	.01	.02	1.44	1.90	81.39	5.65	5.62
TOTAL	99.35	104.19	102.01	103.56	104.30	98.48	99.67	87.88	102.23	102.35
ROMB	3.21	.02	.00	.00	.11	3.14	4.14	187.23	12.10	12.03

MOL PROPS	RO2	RO	R_2O_3	DESCRIPTION
151	2.41	50.00	47.59	8AL: rim of previous hematite serrate, Plate 4.1b, spot 4
152	.01	50.00	49.99	8AL: magnetite subhed, Area #9-2
153	.00	50.00	50.00	8AL: magnetite subhed, Area #10, spot 1
154	.00	50.00	50.00	SAMPLE 8AL (L = Lower): probe day 2, magnetite
155	.09	50.00	49.91	8AL: magnetite, Area #1
156	2.35	50.00	47.65	8AL: hematite, Area #2
157	3.10	50.00	46.90	8AL: rim of hematite serrate, Plate 4.1f, spot 1
158	.00	.00	.00	8AL: detrital core of same serrate, Plate 4.1f, spot 2
159	9.07	50.00	40.93	8AL: another spot in detrital core of same serrate, Plate 4.1f, spot 3
160	9.01	50.00	40.99	8AL: yet another spot in detrital core of same serrate, Plate 4.1f, spot 4

HEMATITE & MAGNETITE: analyses from Fe siltstone sample $8A_L$ collected within the adit through Razorback Ridge, Spring Dam

	161	162	163	164	165	166	167	168	169	170
TIO2	1.86	.03	5.20	7.92	5.01	5.56	1.65	1.78	2.23	1.69
AL2O3	.03	.07	.02	.01	.02	.04	.05	.00	.05	.00
CR2O3	.03	.09	.14	.18	.00	.10	.00	.00	.02	.05
FEO	89.36	92.46	85.38	83.94	85.91	86.38	88.92	88.60	88.73	88.99
MNO	.00	.00	.00	.00	.00	.00	.00	.00	.00	.00
MGO	.00	.01	.00	.00	.00	.00	.00	.00	.00	.02
SUM	91.28	92.66	90.74	92.05	90.94	92.08	90.62	90.38	91.03	90.75
* RECALCULATED ANALYSIS - MAGNETITE-ULVOSPINEL BASIS *										
FE2O3	63.62	68.32	56.20	51.51	56.89	56.47	63.58	63.19	62.66	63.61
FEO	32.04	30.91	34.75	37.54	34.65	35.51	31.64	31.67	32.28	31.68
TOTAL	97.59	99.43	96.31	97.15	96.58	97.68	96.92	96.64	97.24	97.05
USP	5.51	.09	15.55	23.42	14.94	16.39	4.92	5.32	6.62	5.03
* RECALCULATED ANALYSIS - ILMENITE-HEMATITE BASIS *										
FE2O3	97.29	102.52	89.49	85.17	90.34	90.25	97.02	96.57	96.21	97.11
FEO	1.71	.10	4.76	7.21	4.52	5.08	1.52	1.60	2.05	1.51
TOTAL	100.92	102.82	99.61	100.49	99.89	101.02	100.23	99.95	100.56	100.37
ROMB	3.67	.06	10.38	15.63	9.96	10.93	3.28	3.55	4.42	3.36

MOL PROPS	RO2	RO	R_2O_3	DESCRIPTION
161	2.75	50.00	47.25	8AL: rim of same serrate, Plate 4.1f, spot 5
162	.04	50.00	49.96	8AL: magnetite subhed, Area #5, spot 2
163	7.77	50.00	42.23	8AL: detrital core of hematite serrate, Area #4-1
164	11.71	50.00	38.29	8AL: another spot in detrital core of same serrate, Area #4-2
165	7.47	50.00	42.53	8AL: another spot in detrital core of same serrate, Area #4-3
166	8.19	50.00	41.81	8AL: yet another spot in core of same serrate, Area #4-4
167	2.46	50.00	47.54	8AL: rim of same serrate, Area #4-5
168	2.66	50.00	47.34	8AL: another spot in rim of same serrate, Area #4-6
169	3.31	50.00	46.69	8AL: adjacent hematite subhed, Area #4-7
170	2.52	50.00	47.48	8AL: another spot in previous subhed, Area #4-8

HEMATITE & MAGNETITE: analyses from Fe siltstone sample $8A_L$ collected within the adit through Razorback Ridge, Spring Dam

	171	172	173	174	175	176	177	178	179	180
TIO2	1.61	1.65	1.64	1.63	1.57	.02	.05	.28	1.16	1.65
AL2O3	.03	.04	.01	.05	.00	.01	.02	.24	.00	.07
CR2O3	.00	.06	.05	.03	.07	.00	.00	.00	.08	.04
FEO	89.78	88.14	88.56	89.40	89.99	94.09	92.81	90.87	90.46	86.97
MNO	.00	.00	.00	.00	.00	.00	.00	.00	.00	.00
MGO	.00	.02	.00	.01	.00	.00	.00	.00	.00	.00
SUM	91.42	89.91	90.26	91.12	91.63	94.12	92.88	91.39	91.70	88.73
* RECALCULATED ANALYSIS - MAGNETITE-ULVOSPINEL BASIS *										
FE2O3	64.28	63.01	63.33	63.96	64.48	69.59	68.60	66.75	65.37	62.11
FEO	31.87	31.37	31.51	31.78	31.90	31.39	31.01	30.74	31.57	31.01
TOTAL	97.79	96.15	96.54	97.46	98.02	101.02	99.68	98.00	98.18	94.89
USP	4.76	4.96	4.91	4.83	4.63	.06	.15	.83	3.42	5.02
* RECALCULATED ANALYSIS - ILMENITE-HEMATITE BASIS *										
FE2O3	98.03	96.17	96.63	97.57	98.29	104.41	102.95	100.40	99.21	94.81
FEO	1.47	1.50	1.51	1.50	1.44	.03	.06	.42	1.08	1.55
TOTAL	101.13	99.44	99.86	100.79	101.37	104.47	103.08	101.34	101.53	98.13
ROMB	3.17	3.31	3.27	3.22	3.09	.04	.10	.55	2.28	3.35

MOL PROPS	RO2	RO	R_2O_3	DESCRIPTION
171	2.38	50.00	47.62	8AL: another spot in rim of hematite serrate, Area #4-9
172	2.48	50.00	47.52	8AL: another spot in rim of same serrate, Area #4-10
173	2.46	50.00	47.54	8AL: another spot in rim of same serrate, Area #4-11
174	2.42	50.00	47.58	8AL: yet another spot in rim of same serrate, Area #4-12
175	2.32	50.00	47.68	8AL: last spot in rim of same serrate, Area #4-13
176	.03	50.00	49.97	8AL: magnetite subhed within circle 9, Area #6-1
177	.07	50.00	49.93	8AL: same subhed as previous, Area #6, stop 2
178	.41	50.00	49.59	8AL: core of hematite serrate, circle 1, Area #7-1
179	1.71	50.00	48.29	8AL: rim of same serrate, Area #7-2
180	2.51	50.00	47.49	8AL: another spot in rim of same serrate, Area #7-3

MAGNETITE & HEMATITE: analyses from iron formation sample $8A_U$ collected within the adit through Razorback Ridge, Spring Dam

	181	182	183	184	185	186	187	188	189	190
TIO2	1.44	.00	.00	.00	.00	.00	.00	.00	.00	1.26
AL2O3	.04	.01	.00	.00	.00	.00	.20	.03	.03	.05
CR2O3	.00	.00	.00	.00	.00	.02	.00	.00	.00	.00
FEO	88.64	91.73	94.19	93.82	94.24	90.51	88.27	90.27	90.27	89.22
MNO	.05	.07	.09	.00	.09	.00	.08	.04	.04	.16
MGO	.00	.05	.00	.00	.00	.00	.01	.00	.01	.01
SUM	90.17	91.86	94.28	93.82	94.33	90.53	88.56	90.34	90.35	90.70
* RECALCULATED ANALYSIS - MAGNETITE-ULVOSPINEL BASIS *										
FE2O3	63.69	67.99	69.77	69.43	69.80	66.97	65.29	66.81	66.83	64.45
FEO	31.26	30.48	31.34	31.27	31.35	30.18	29.45	30.08	30.07	31.15
TOTAL	96.48	98.60	101.19	100.70	101.25	97.17	95.03	96.96	96.97	97.09
USP	4.31	.00	.00	.00	.00	.00	.00	.00	.00	3.75
* RECALCULATED ANALYSIS - ILMENITE-HEMATITE BASIS *										
FE2O3	96.98	101.99	104.65	104.14	104.71	100.46	97.93	100.22	100.24	97.94
FEO	1.27	-.15	-.09	.00	-.09	.01	.04	-.02	-.04	.99
TOTAL	99.78	101.97	104.65	104.14	104.71	100.49	98.27	100.27	100.28	100.41
RONB	2.88	.00	.00	.00	.00	.00	.00	.00	.00	2.50

MOL PROPS	RO2	RO	R_2O_3	DESCRIPTION
181	2.16	50.00	47.84	I.F. SAMPLE 8AU (U = Upper): hematite subhed, Plate 4.1c, spot 2
182	.00	50.00	50.00	8AU: adjoining magnetite euhed, partially hematized, Plate 4.1c, spot 3
183	.00	50.00	50.00	8AU: core of same euhed, Plate 4.1c, spot 4
184	.00	50.00	50.00	8AU: another spot in core of same euhed, Plate 4.1c, spot 5
185	.00	50.00	50.00	8AU: core of adjoining magnetite subhed, Plate 4.1c, spot 8
186	.00	50.00	50.00	8AU: rim of adjoining hematite-after-magnetite euhed, Plate 4.1c, spot 9
187	.00	50.00	50.00	8AU: another spot in rim of same hematite-after-magnetite euhed, Plate 4.1c, spot 10
188	.00	50.00	50.00	8AU: another spot in rim of same hematite-after-magnetite euhed, Plate 4.1c, spot 12
189	.00	50.00	50.00	8AU: opposite rim of same hematite-after-magnetite euhed, Plate 4.1c, spot 14
190	1.88	50.00	48.12	8AU: adjoining hematite subhed, Plate 4.1c, spot 16

HEMATITE & MAGNETITE: analyses from iron formation sample $8A_U$ collected within the adit through Razorback Ridge, Spring Dam

	191	192	193	194	195	196	197	198	199	200
TIO2	1.52	1.48	1.57	1.10	.00	1.89	.00	1.46	1.45	1.55
AL2O3	.02	.00	.05	.03	.00	.01	.02	.03	.03	.05
CR2O3	.00	.00	.02	.00	.00	.00	.00	.00	.00	.00
FEO	87.46	87.23	86.99	87.83	92.09	86.78	88.88	87.54	88.14	86.92
MNO	.07	.00	.00	.00	.04	.06	.05	.07	.00	.12
MGO	.00	.00	.02	.01	.00	.00	.00	.00	.02	.03
SUM	89.07	88.71	88.65	88.97	92.13	88.74	88.95	89.10	89.64	88.67
* RECALCULATED ANALYSIS - MAGNETITE-ULVOSPINEL BASIS *										
FE2O3	62.74	62.58	62.28	63.53	68.18	61.74	65.80	62.87	63.30	62.36
FEO	30.94	30.85	30.89	30.60	30.67	31.16	29.60	30.90	31.11	30.74
TOTAL	95.29	94.91	94.82	95.27	98.89	94.86	95.47	95.33	95.91	94.85
USP	4.61	4.51	4.78	3.34	.00	5.76	.00	4.43	4.37	4.72
* RECALCULATED ANALYSIS - ILMENITE-HEMATITE BASIS *										
FE2O3	95.63	95.35	94.98	96.39	102.26	94.50	98.70	95.77	96.40	95.09
FEO	1.31	1.33	1.42	.99	-.04	1.65	-.04	1.26	1.29	1.25
TOTAL	98.55	98.16	98.06	98.52	102.26	98.10	98.73	98.59	99.19	98.09
ROMB	3.07	3.01	3.19	2.23	.00	3.84	.00	2.95	2.91	3.15

MOL PROPS	RO2	RO	R_2O_3	DESCRIPTION
191	2.31	50.00	47.69	8AU: adjacent hematite subhed, Plate 4.1c, spot 17
192	2.25	50.00	47.75	8AU: repeat of previous subhed, Plate 4.1c, spot 17
193	2.39	50.00	47.61	8AU: repeat of adjacent hematite subhed, Plate 4.1c, spot 2
194	1.67	50.00	48.33	8AU: hematite anhed, Area #2, spot 1
195	.00	50.00	50.00	8AU: adjoining subhed, Area #2, spot 2
196	2.88	50.00	47.12	8AU: hematite subhed, Area #3-1
197	.00	50.00	50.00	8AU: adjacent hematite-after-magnetite subhed, Area #3-2
198	2.21	50.00	47.79	8AU: hematite subhed, Area #3-3
199	2.18	50.00	47.82	8AU: another hematite subhed, Area #3-4
200	2.36	50.00	47.64	8AU: hematite serrate, Area #4, spot 1

Appendix D

ELECTRON MICROPROBE ANALYSES

Apatite

Fluor-APATITE: analyses from samples collected within the adit through Razorback Ridge on Spring Dam

	1	2	3	4	5	6	7	8
SIO2	.00	.00	.09	.00	.00	.00	.05	.02
AL2O3	.04	.04	.07	.02	.05	.04	.07	.06
FEO	.53	.21	.50	.42	.85	1.09	3.04	.93
MGO	.00	.00	.01	.01	.00	.00	.11	.02
CAO	56.33	57.53	56.84	56.22	55.18	56.18	55.81	57.72
NA2O	.03	.05	.03	.06	.02	.24	.15	.22
K2O	.05	.06	.14	.04	.09	.14	.16	.08
P2O5	40.89	40.73	40.87	41.56	40.28	39.34	39.20	40.32
SRO	.23	.35	.29	.24	.25	.32	.24	.36
BAO	.14	.04	.11	.00	.08	.08	.09	.05
F	3.49	4.54	4.85	3.65	4.18	4.26	4.55	3.46
CL	.07	.07	.03	.09	.04	.08	.04	.07
SUM	101.80	103.62	103.83	102.31	101.02	101.77	103.51	103.31
-O = F+CL	1.49	1.93	2.05	1.56	1.77	1.81	1.92	1.47
SUM	100.31	101.69	101.78	100.75	99.25	99.96	101.59	101.84

	1		2		3		4		5		6		7		8	
SI	.000	*	.000	*	.014	*	.000	*	.000	*	.000	*	.008	*	.003	*
AL	.008	*	.008	*	.013	*	.004	*	.010	*	.008	*	.013	*	.011	*
P	5.640	5.655	5.539	5.546	5.539	5.567	5.687	5.691	5.606	5.616	5.486	5.493	5.410	5.432	5.536	5.550
CA	9.846	*	9.901	*	9.749	*	9.736	*	9.719	*	9.914	*	9.749	*	10.029	*
FE	.072	*	.028	*	.067	*	.057	*	.117	*	.150	*	.414	*	.126	*
MG	.000	*	.000	*	.002	*	.002	*	.000	*	.000	*	.027	*	.005	*
NA	.009	*	.016	*	.009	*	.019	*	.006	*	.077	*	.047	*	.069	*
K	.010	*	.012	*	.029	*	.008	*	.019	*	.029	*	.033	*	.017	*
SR	.022	*	.033	*	.027	*	.022	*	.024	*	.031	*	.023	*	.034	*
BA	.009	9.969	.003	9.992	.007	9.890	.000	9.845	.005	9.890	.005	10.206	.006	10.299	.003	10.283
F	1.801	*	2.306	*	2.456	*	1.866	*	2.173	*	2.219	*	2.346	*	1.775	*
CL	.019	*	.019	*	.008	*	.025	*	.011	*	.022	*	.011	*	.019	*
O	25.000	*	25.000	*	25.000	*	25.000	*	25.000	*	25.000	*	25.000	*	25.000	*
F/M	.000		.000		33.500		28.500		.000		.000		15.333		25.200	
F/FM	1.000		1.000		.971		.966		1.000		1.000		.939		.962	

1 I.F. SAMPLE 8r1: Table 3, crystal 45
2 8r1: Table 3, crystal 46
3 8r1: " ", " 47
4 8r1: " ", " 49, Plate 4.1d
5 8r1: Table 3, crystal 50
6 8r1: " ", " 51
7 8r1: " ", " 53
8 8r1: " ", " 54

Fluor-APATITE: analyses from samples collected within the adit through Razorback Ridge on Spring Dam

	9	10	11	12	13	14	15	16
SIO2	.16	.00	.72	.00	.00	.17	.00	.31
AL2O3	.04	.04	.16	.05	.06	.15	.05	.04
FEO	1.06	.93	.67	.69	.96	1.64	.82	.85
MGO	.07	.01	.00	.00	.00	.01	.00	.02
CAO	56.45	57.22	55.40	57.54	56.87	56.27	56.85	54.91
NA2O	.14	.00	.16	.01	.00	.00	.07	.12
K2O	.12	.10	.12	.16	.14	.23	.15	.14
P2O5	39.80	40.17	38.73	39.99	40.82	39.60	40.01	39.35
SRO	.00	.24	.20	.26	.16	.21	.16	.09
BAO	.10	.04	.02	.09	.05	.03	.00	.14
F	3.74	4.22	3.94	5.05	5.02	4.66	3.90	3.62
CL	.11	.03	.07	.06	.05	.03	.04	.08
SUM	101.79	103.00	100.19	103.90	104.13	103.00	102.05	99.67
-O = F+CL	1.60	1.78	1.67	2.14	2.13	1.97	1.65	1.54
SUM	100.19	101.22	98.52	101.76	102.00	101.03	100.40	98.13

	9		10		11		12		13		14		15		16	
SI	.026	*	.000	*	.120	*	.000	*	.000	*	.028	*	.000	*	.052	*
AL	.008	*	.008	*	.031	*	.009	*	.011	*	.029	*	.010	*	.008	*
P	5.529	5.563	5.517	5.525	5.455	5.607	5.450	5.460	5.523	5.535	5.451	5.507	5.541	5.551	5.565	5.625
CA	9.924	*	9.945	*	9.876	*	9.925	*	9.739	*	9.802	*	9.964	*	9.828	*
FE	.145	*	.126	*	.093	*	.093	*	.128	*	.223	*	.112	*	.119	*
MG	.017	*	.002	*	.000	*	.000	*	.000	*	.002	*	.000	*	.005	*
NA	.045	*	.000	*	.052	*	.003	*	.000	*	.006	*	.022	*	.039	*
K	.025	*	.021	*	.025	*	.033	*	.029	*	.048	*	.031	*	.030	*
SR	.000	*	.023	*	.019	*	.024	*	.015	*	.020	*	.015	*	.009	*
BA	.006	10.163	.003	10.120	.001	10.067	.006	10.084	.003	9.913	.002	10.097	.000	10.145	.009	10.038
F	1.941	*	2.165	*	2.073	*	2.571	*	2.538	*	2.396	*	2.018	*	1.913	*
CL	.031	*	.008	*	.020	*	.016	*	.014	*	.008	*	.011	*	.023	*
O	25.000	*	25.000	*	25.000	*	25.000	*	25.000	*	25.000	*	25.000	*	25.000	*
F/M	8.529		63.000		.000		.000		.000		111.500		.000		23.800	
F/FM	.895		.984		1.000		1.000		1.000		.991		1.000		.960	

9 8r1: Table 3, crystal 55
10 8r1: " ", " 57
11 8r1: " ", " 58
12 8r1: " ", " 59

13 8r1: Table 3, crystal 60
14 8r1: " ", " 61
15 8r1: " ", " 62
16 8r1: " ", " 63

Fluor-APATITE: analyses from the adit (Br_1) and a drill hole (RD#3) through Razorback Ridge, <u>Spring Dam</u>

	17	18	19	20	21	22	23	24
SIO2	.34	.00	.00	.00	.00	.00	.00	.08
AL2O3	.12	.04	.04	.05	.04	.00	.04	.03
FEO	1.08	.81	.77	.85	.92	.90	.85	1.61
MGO	.04	.00	.00	.00	.00	.00	.00	.19
CAO	55.27	56.29	56.40	56.33	56.31	56.09	56.89	55.02
NA2O	.19	.04	.17	.03	.02	.20	.03	.04
K2O	.20	.05	.07	.10	.09	.06	.06	.06
P2O5	38.96	42.03	40.78	42.28	40.50	40.66	40.77	41.33
SRO	.10	.42	.21	.22	.20	.22	.17	.14
BAO	.07	.08	.13	.00	.00	.02	.10	.12
F	3.75	4.12	4.01	3.82	4.15	4.46	3.83	3.26
CL	.07	.07	.07	.06	.03	.05	.05	.16
SUM	100.19	103.95	102.65	103.74	102.26	102.66	102.79	102.04
-O = F+CL	1.59	1.75	1.70	1.62	1.75	1.89	1.62	1.41
SUM	98.60	102.20	100.95	102.12	100.51	100.77	101.17	100.63

	17		18		19		20		21		22		23		24	
SI	.057	*	.000	*	.000	*	.000	*	.000	*	.000	*	.000	*	.013	*
AL	.024	*	.008	*	.008	*	.009	*	.008	*	.000	*	.008	*	.006	*
P	5.500	5.580	5.668	5.676	5.596	5.604	5.701	5.711	5.578	5.586	5.575	5.575	5.591	5.599	5.689	5.708
CA	9.875	*	9.608	*	9.795	*	9.613	*	9.815	*	9.733	*	9.874	*	9.584	*
FE	.151	*	.108	*	.104	*	.113	*	.125	*	.122	*	.115	*	.219	*
MG	.010	*	.000	*	.000	*	.000	*	.000	*	.000	*	.000	*	.046	*
NA	.061	*	.012	*	.053	*	.009	*	.006	*	.063	*	.009	*	.013	*
K	.043	*	.010	*	.014	*	.020	*	.019	*	.012	*	.012	*	.012	*
SR	.010	*	.039	*	.020	*	.020	*	.019	*	.021	*	.016	*	.013	*
BA	.005	10.154	.005	9.782	.008	9.995	.000	9.777	.000	9.984	.001	9.952	.006	10.033	.008	9.895
F	1.978	*	2.076	*	2.056	*	1.924	*	2.135	*	2.284	*	1.962	*	1.676	*
CL	.020	*	.019	*	.019	*	.016	*	.008	*	.014	*	.014	*	.044	*
O	25.000	*	25.000	*	25.000	*	25.000	*	25.000	*	25.000	*	25.000	*	25.000	*
F/M		15.100		52.000		.000		.000		.000		.000		.000		4.761
F/FM		.938		1.000		1.000		1.000		1.000		1.000		1.000		.826

17 Br1: Table 3, crystal 64 (euhedral)
18 Diamictite matrix SAMPLE RD#3-11': Table 3-24
19 RD#3 - 11': Table 3, crystal 25
20 RD#3 - 11': " ", " 27
21 RD#3 - 11': Table 3, crystal 29
22 RD#3 - 11': " ", " 30
23 RD#3 - 11': " ", " 31
24 RD#3 - 11': " ", " 32

Fluor-APATITE: analyses from a drill hole (RD#3) through Razorback Ridge on <u>Spring Dam</u>

	25		26		27		28		29		30		31		32	
SIO2	.00		.10		.18		.05		.00		.09		.00		.00	
AL2O3	.05		.04		.04		.05		.05		.06		.05		.02	
FEO	.57		.71		1.34		.84		.99		1.26		1.15		.76	
MGO	.01		.02		.00		.03		.00		.04		.00		.00	
CAO	56.41		56.22		54.85		57.07		55.80		56.50		56.67		57.89	
NA2O	.01		.01		.08		.12		.16		.08		.03		.03	
K2O	.06		.04		.12		.04		.07		.12		.07		.03	
P2O5	40.81		41.05		40.81		41.73		40.98		41.76		41.12		41.37	
SRO	.62		.00		.10		.10		.00		.07		.95		.25	
BAO	.07		.00		.03		.08		.00		.00		.07		.07	
F	3.89		3.66		3.95		3.07		3.91		3.93		3.08		3.98	
CL	.06		.05		.05		.08		.07		.09		.06		.05	
SUM	102.56		101.90		101.55		103.26		102.12		104.00		103.25		104.45	
-O = F+CL	1.65		1.55		1.67		1.31		1.66		1.68		1.31		1.69	
SUM	100.91		100.35		99.88		101.95		100.46		102.32		101.94		102.76	
SI	.000	*	.016	*	.029	*	.008	*	.000	*	.014	*	.000	*	.000	*
AL	.010	*	.008	*	.008	*	.009	*	.010	*	.011	*	.010	*	.004	*
P	5.608	5.617	5.646	5.670	5.638	5.675	5.678	5.695	5.635	5.644	5.637	5.662	5.638	5.647	5.584	5.587
CA	9.810	*	9.786	*	9.590	*	9.827	*	9.710	*	9.651	*	9.833	*	9.888	*
FE	.077	*	.096	*	.183	*	.113	*	.134	*	.168	*	.156	*	.101	*
MG	.002	*	.005	*	.000	*	.007	*	.000	*	.010	*	.000	*	.000	*
NA	.003	*	.003	*	.025	*	.037	*	.050	*	.025	*	.009	*	.009	*
K	.012	*	.008	*	.025	*	.008	*	.015	*	.024	*	.014	*	.006	*
SR	.058	*	.000	*	.009	*	.009	*	.008	*	.006	*	.089	*	.023	*
BA	.004	9.968	.000	9.899	.002	9.834	.005	10.007	.000	9.918	.000	9.884	.004	10.106	.004	10.033
F	1.997	*	1.881	*	2.039	*	1.560	*	2.008	*	1.982	*	1.578	*	2.007	*
CL	.017	*	.014	*	.014	*	.022	*	.019	*	.024	*	.016	*	.014	*
O	25.000	*	25.000	*	25.000	*	25.000	*	25.000	*	25.000	*	25.000	*	25.000	*
F/M	38.500		19.200		.000		16.143		.000		16.800		.000		.000	
F/FM	.975		.950		1.000		.942		1.000		.944		1.000		1.000	

25 RD#3 - 11': Table 3, crystal 33
26 RD#3 - 11': " ", " 34
27 RD#3 - 11': " ", " 36
28 RD#3 - 11': " ", " 37

29 RD#3 - 11': Table 3, crystal 38
30 RD#3 - 11': " ", " 39
31 RD#3 - 11': " ", " 40
32 RD#3 - 11': " ", " 41

Fluor-APATITE: analyses from a drill hole (RD#3) and the adit (8C-1) through Razorback Ridge on <u>Spring Dam</u>

	33	34	35	36	37	38	39	40
SIO2	.00	.00	.00	.00	.00	.00	.00	.00
AL2O3	.04	.05	.05	.02	.02	.04	.04	.06
FEO	.47	.81	.41	.30	.37	.43	.95	.19
MGO	.00	.00	.00	.00	.12	.00	.00	.00
CAO	58.17	56.10	56.35	56.90	58.06	56.98	56.31	56.11
NA2O	.04	.03	.04	.04	.03	.16	.02	.06
K2O	.04	.15	.00	.02	.03	.05	.03	.02
P2O5	41.62	40.49	40.35	39.95	38.94	39.20	38.90	40.65
SRO	.26	.21	.30	.28	.24	.15	.29	.24
BAO	.00	.03	.05	.07	.04	.08	.00	.12
F	3.69	4.23	3.64	3.76	4.32	3.03	3.77	3.78
CL	.05	.04	.08	.07	.07	.05	.05	.05
SUM	104.38	102.14	101.27	101.41	102.24	100.17	100.36	101.28
-O = F+CL	1.57	1.79	1.55	1.60	1.83	1.29	1.60	1.60
SUM	102.81	100.35	99.72	99.81	100.41	98.88	98.76	99.68

	33		34		35		36		37		38		39		40	
SI	.000	*	.000	*	.000	*	.000	*	.000	*	.000	*	.000	*	.000	*
AL	.008	*	.010	*	.010	*	.004	*	.004	*	.008	*	.008	*	.012	*
P	5.612	5.619	5.581	5.591	5.609	5.618	5.561	5.565	5.414	5.417	5.546	5.554	5.498	5.506	5.634	5.646
CA	9.926	*	9.786	*	9.913	*	10.024	*	10.215	*	10.203	*	10.073	*	9.843	*
FE	.063	*	.110	*	.056	*	.041	*	.051	*	.060	*	.133	*	.026	*
MG	.000	*	.000	*	.000	*	.000	*	.029	*	.000	*	.000	*	.000	*
NA	.012	*	.009	*	.013	*	.013	*	.010	*	.052	*	.006	*	.019	*
K	.008	*	.031	*	.000	*	.004	*	.006	*	.011	*	.006	*	.004	*
SR	.024	*	.020	*	.029	*	.027	*	.023	*	.015	*	.028	*	.023	*
BA	.000	10.033	.002	9.959	.003	10.014	.005	10.113	.003	10.337	.005	10.345	.000	10.246	.008	9.922
F	1.859	*	2.178	*	1.890	*	1.955	*	2.244	*	1.602	*	1.991	*	1.957	*
CL	.013	*	.011	*	.022	*	.020	*	.019	*	.014	*	.014	*	.014	*
O	25.000	*	25.000	*	25.000	*	25.000	*	25.000	*	25.000	*	25.000	*	25.000	*
F/M	.000		.000		.000		.000		1.759		.000		.000		.000	
F/FM	1.000		1.000		1.000		1.000		.638		1.000		1.000		1.000	

33 RD#3 - 11': Table 3, crystal 43
34 RD#3 - 11': " ", " 44
35 Carbonate-rich arenite layer in SAMPLE 8C-1: Table 3, crystal 65
36 8C-1: Table 3, crystal 66

37 8C-1: Table 3, crystal 67
38 8C-1: " ", " 68
39 8C-1: " ", " 69
40 8C-1: " ", " 70

Fluor-APATITE: analyses from sample 8C-1 collected within the adit through Razorback Ridge on <u>Spring Dam</u>

	41	42	43	44	45	46	47	48
SIO2	.04	.00	.00	.00	.00	.00	.02	.00
AL2O3	.07	.03	.03	.04	.01	.04	.05	.04
FEO	.65	.46	.24	1.59	1.49	1.22	1.31	1.44
MGO	.10	.00	.00	.04	.00	.01	.02	.00
CAO	57.14	56.96	57.66	56.86	56.24	56.54	57.18	56.66
NA2O	.14	.03	.00	.09	.25	.02	.43	.06
K2O	.03	.03	.04	.01	.02	.02	.06	.04
P2O5	38.62	39.85	40.01	40.48	39.19	38.50	37.91	39.21
SRO	.17	.25	.27	.04	.26	.23	.22	.05
BAO	.04	.04	.00	.06	.07	.08	.00	.10
F	3.12	3.13	3.38	3.73	3.87	3.69	3.32	3.08
CL	.07	.08	.05	.12	.06	.05	.07	.04
SUM	100.19	100.86	101.68	103.06	101.46	100.40	100.59	100.72
-O = F+CL	1.33	1.34	1.43	1.60	1.64	1.57	1.41	1.31
SUM	98.86	99.52	100.25	101.46	99.82	98.83	99.18	99.41

	41		42		43		44		45		46		47		48	
SI	.007	*	.000	*	.000	*	.000	*	.000	*	.000	*	.003	*	.000	*
AL	.014	*	.006	*	.006	*	.008	*	.002	*	.008	*	.010	*	.008	*
P	5.481	5.502	5.584	5.590	5.561	5.567	5.556	5.564	5.490	5.492	5.460	5.468	5.398	5.411	5.532	5.539
CA	10.264	*	10.102	*	10.142	*	9.877	*	9.972	*	10.148	*	10.304	*	10.116	*
FE	.091	*	.064	*	.033	*	.216	*	.206	*	.171	*	.184	*	.201	*
MG	.025	*	.000	*	.000	*	.010	*	.000	*	.002	*	.005	*	.000	*
NA	.046	*	.010	*	.000	*	.028	*	.080	*	.006	*	.140	*	.019	*
K	.006	*	.006	*	.008	*	.002	*	.004	*	.004	*	.013	*	.009	*
SR	.017	*	.024	*	.026	*	.004	*	.025	*	.022	*	.021	*	.005	*
BA	.003	10.451	.003	10.208	.000	10.209	.004	10.140	.005	10.292	.005	10.359	.000	10.667	.007	10.356
F	1.654	*	1.639	*	1.755	*	1.913	*	2.025	*	1.955	*	1.766	*	1.623	*
CL	.020	*	.022	*	.014	*	.033	*	.017	*	.014	*	.020	*	.011	*
O	25.000	*	25.000	*	25.000	*	25.000	*	25.000	*	25.000	*	25.000	*	25.000	*
F/M		3.640		.000		.000		21.600		.000		85.500		36.800		.000
F/FM		.784		1.000		1.000		.956		1.000		.988		.974		1.000

41 8C-1: Table 3, crystal 71
42 8C-1: " ", " 73
43 8C-1: " ", " 74
44 I.F. portion of 8C-1: Table 3, crystal 75
45 8C-1: Table 3, crystal 76
46 8C-1: " ", " 77
47 8C-1: " ", " 78
48 8C-1: " ", " 79

Fluor-APATITE: analyses from samples collected within the adit through Razorback Ridge on <u>Spring Dam</u>

	49	50	51	52	53	54	55	56
SIO2	.00	.00	.00	.00	.00	.00	.00	.00
AL2O3	.04	.04	.05	.04	.02	.04	.05	.03
FEO	.31	.30	1.32	.99	1.01	1.11	1.23	.16
MGO	.00	.00	.01	.00	.06	.00	.00	.00
CAO	57.95	57.10	57.06	57.62	55.29	56.54	56.91	55.69
NA2O	.03	.00	.02	.00	.04	.02	.02	.03
K2O	.01	.03	.06	.02	.04	.04	.02	.02
P2O5	39.07	39.53	39.65	39.13	39.01	38.41	37.68	41.98
SRO	.30	.33	.23	.27	.09	.25	.27	.07
BAO	.07	.06	.05	.05	.09	.00	.10	.14
F	3.82	3.66	4.12	3.36	4.84	3.55	3.83	2.31
CL	.07	.05	.06	.06	.11	.08	.05	.09
SUM	101.67	101.10	102.63	101.54	100.60	100.04	100.16	100.52
-O = F+CL	1.62	1.55	1.75	1.43	2.06	1.51	1.62	.99
SUM	100.05	99.55	100.88	100.11	98.54	98.53	98.54	99.53

	49		50		51		52		53		54		55		56	
SI	.000	*	.000	*	.000	*	.000	*	.000	*	.000	*	.000	*	.000	*
AL	.008	*	.008	*	.010	*	.008	*	.004	*	.008	*	.010	*	.006	*
P	5.460	5.468	5.532	5.540	5.483	5.493	5.484	5.492	5.480	5.484	5.465	5.473	5.382	5.392	5.823	5.829
CA	10.249	*	10.113	*	9.987	*	10.221	*	9.829	*	10.182	*	10.288	*	9.777	*
FE	.043	*	.041	*	.180	*	.137	*	.140	*	.156	*	.174	*	.022	*
MG	.000	*	.000	*	.002	*	.000	*	.015	*	.000	*	.000	*	.000	*
NA	.010	*	.000	*	.006	*	.000	*	.013	*	.007	*	.007	*	.010	*
K	.002	*	.006	*	.013	*	.004	*	.008	*	.009	*	.004	*	.004	*
SR	.029	*	.032	*	.022	*	.026	*	.009	*	.024	*	.026	*	.007	*
BA	.005	10.337	.004	10.197	.003	10.214	.003	10.391	.006	10.020	.000	10.377	.007	10.506	.009	9.828
F	1.994	*	1.914	*	2.129	*	1.759	*	2.540	*	1.887	*	2.044	*	1.197	*
CL	.020	*	.014	*	.017	*	.017	*	.031	*	.023	*	.014	*	.025	*
O	25.000	*	25.000	*	25.000	*	25.000	*	25.000	*	25.000	*	25.000	*	25.000	*
F/M	.000		.000		90.000		.000		9.333		.000		.000		.000	
F/FM	1.000		1.000		.989		1.000		.903		1.000		1.000		1.000	

49 8C-1: Table 3, crystal 80
50 8C-1: " ", " 81
51 8C-1: " ", " 82
52 8C-1: " ", " 83

53 8C-1: Table 3, crystal 84
54 8C-1: " ", " 85
55 8C-1: " ", " 86
56 Fe siltstone SAMPLE 8AL (L = Lower):

Fluor-APATITE: analyses from sample $8A_L$ collected within the adit through Razorback Ridge on Spring Dam

	57	58	59	60	61	62	63	64
SIO2	.00	.00	.00	.00	.00	.00	.00	.00
AL2O3	.03	.04	.03	.02	.03	.04	.04	.04
FEO	.26	.16	.53	.29	.31	.31	.19	.23
MGO	.00	.01	.00	.00	.00	.00	.00	.00
CAO	56.65	55.84	56.95	57.63	56.65	56.25	56.82	56.34
NA2O	.04	.02	.02	.02	.04	.01	.01	.06
K2O	.03	.05	.04	.04	.05	.02	.03	.04
P2O5	41.69	42.06	41.52	42.93	41.31	42.55	41.79	41.43
SRO	.08	.06	.09	.00	.05	.08	.00	.17
BAO	.00	.04	.05	.05	.09	.09	.05	.04
F	2.42	2.54	2.50	2.70	3.18	3.38	2.68	2.85
CL	.10	.10	.09	.06	.07	.08	.05	.06
SUM	101.30	100.92	101.82	103.74	101.78	102.81	101.66	101.26
-O = F+CL	1.04	1.09	1.07	1.15	1.35	1.44	1.14	1.21
SUM	100.26	99.83	100.75	102.59	100.43	101.37	100.52	100.05

	57		58		59		60		61		62		63		64	
SI	.000	*	.000	*	.000	*	.000	*	.000	*	.000	*	.000	*	.000	*
AL	.006	*	.008	*	.006	*	.004	*	.006	*	.008	*	.008	*	.008	*
P	5.759	5.765	5.808	5.816	5.723	5.729	5.777	5.781	5.690	5.696	5.766	5.774	5.748	5.755	5.728	5.736
CA	9.903	*	9.759	*	9.935	*	9.815	*	9.875	*	9.648	*	9.890	*	9.859	*
FE	.035	*	.022	*	.072	*	.039	*	.042	*	.042	*	.026	*	.031	*
MG	.000	*	.002	*	.000	*	.000	*	.000	*	.000	*	.000	*	.000	*
NA	.013	*	.006	*	.006	*	.006	*	.013	*	.003	*	.003	*	.019	*
K	.006	*	.010	*	.008	*	.008	*	.010	*	.004	*	.006	*	.008	*
SR	.008	*	.006	*	.008	*	.000	*	.005	*	.007	*	.000	*	.016	*
BA	.000	9.965	.003	9.808	.003	10.034	.003	9.871	.006	9.950	.006	9.709	.003	9.929	.003	9.936
F	1.249	*	1.310	*	1.287	*	1.357	*	1.636	*	1.711	*	1.377	*	1.472	*
CL	.028	*	.028	*	.025	*	.016	*	.019	*	.022	*	.014	*	.017	*
O	25.000	*	25.000	*	25.000	*	25.000	*	25.000	*	25.000	*	25.000	*	25.000	*
F/M		.000		11.000		.000		.000		.000		.000		.000		.000
F/FM		1.000		.917		1.000		1.000		1.000		1.000		1.000		1.000

57 8AL: another spot in previous crystal
58 8AL: New Area
59 8AL: New Area
60 8AL: Table 1, crystal 3
61 8AL: Table 1, crystal 4
62 8AL: " ", " 5
63 8AL: " ", " 6
64 8AL: " ", " 7

Fluor-APATITE: analyses from sample $8A_L$ collected within the adit through Razorback Ridge on <u>Spring Dam</u>

	65	66	67	68	69	70	71	72
SIO2	.00	.00	.00	.00	.00	.00	.00	1.05
AL2O3	.03	.02	.02	.03	.02	.03	.02	.79
FEO	.28	.35	.29	.32	.13	.24	.13	.38
MGO	.01	.00	.00	.00	.00	.01	.01	.07
CAO	55.25	57.86	56.47	55.56	55.25	55.72	56.15	54.72
NA2O	.05	.05	.03	.04	.01	.05	.04	.01
K2O	.03	.03	.04	.08	.03	.02	.04	.03
P2O5	41.22	42.28	42.41	40.59	41.31	41.48	42.02	40.46
SRO	.03	.13	.07	.11	.12	.16	.07	.13
BAO	.04	.05	.00	.06	.12	.06	.00	.00
F	2.72	2.25	2.39	2.60	2.79	2.76	2.58	2.91
CL	.10	.05	.07	.07	.07	.11	.08	.03
SUM	99.76	103.07	101.79	99.46	99.85	100.64	101.14	100.58
-O = F+CL	1.17	.96	1.02	1.11	1.19	1.19	1.10	1.23
SUM	98.59	102.11	100.77	98.35	98.66	99.45	100.04	99.35

	65		66		67		68		69		70		71		72	
SI	.000	*	.000	*	.000	*	.000	*	.000	*	.000	*	.000	*	.172	*
AL	.006	*	.004	*	.004	*	.006	*	.004	*	.006	*	.004	*	.152	*
P	5.769	5.775	5.752	5.756	5.811	5.814	5.723	5.729	5.775	5.779	5.761	5.767	5.793	5.797	5.600	5.924
CA	9.786	*	9.962	*	9.792	*	9.914	*	9.775	*	9.793	*	9.798	*	9.585	*
FE	.039	*	.047	*	.039	*	.045	*	.018	*	.033	*	.018	*	.052	*
MG	.002	*	.000	*	.000	*	.000	*	.000	*	.002	*	.002	*	.017	*
NA	.016	*	.016	*	.009	*	.013	*	.003	*	.016	*	.013	*	.003	*
K	.006	*	.006	*	.008	*	.017	*	.006	*	.004	*	.008	*	.006	*
SR	.003	*	.012	*	.007	*	.011	*	.011	*	.015	*	.007	*	.012	*
BA	.003	9.855	.003	10.046	.000	9.855	.004	10.003	.008	9.822	.004	9.868	.000	9.845	.000	9.676
F	1.422	*	1.144	*	1.223	*	1.370	*	1.457	*	1.432	*	1.329	*	1.505	*
CL	.028	*	.014	*	.019	*	.020	*	.020	*	.031	*	.022	*	.008	*
O	25.000	*	25.000	*	25.000	*	25.000	*	25.000	*	25.000	*	25.000	*	25.000	*
F/M	19.500		.000		.000		.000		.000		16.500		9.000		3.059	
F/FM	.951		1.000		1.000		1.000		1.000		.943		.900		.754	

65 8AL: Table 1, crystal 8
66 8AL: " ", " 9
67 8AL: " ", " 10
68 8AL: " ", " 11

69 8AL: Table 1, crystal 13
70 8AL: " ", " 14
71 8AL: " ", " 15
72 8AL: " ", " 16

Fluor-APATITE: analyses from sample 8A$_L$ collected within the adit through Razorback Ridge on <u>Spring Dam</u>

	73	74	75	76	77	78	79	80
SIO2	.00	.00	.00	.00	.00	.00	.00	.00
AL2O3	.02	.03	.03	.01	.02	.03	.03	.04
FEO	.71	.37	.32	.31	.25	.30	.31	.24
MGO	.00	.01	.00	.00	.00	.00	.00	.01
CAO	55.07	56.85	54.88	55.39	55.79	56.12	54.00	56.84
NA2O	.04	.03	.00	.02	.02	.01	.04	.10
K2O	.07	.08	.03	.04	.05	.02	.03	.02
P2O5	41.50	41.70	41.57	42.75	41.28	41.62	41.92	42.25
SRO	.13	.09	.12	.00	.10	.11	.04	.55
BAO	.00	.07	.01	.10	.06	.07	.07	.00
F	2.39	2.04	2.41	1.96	2.66	2.85	2.78	3.61
CL	.06	.06	.08	.06	.09	.07	.07	.08
SUM	99.99	101.33	99.45	100.64	100.32	101.20	99.29	103.74
-O = F+CL	1.02	.87	1.03	.84	1.14	1.22	1.19	1.54
SUM	98.97	100.46	98.42	99.80	99.18	99.98	98.10	102.20

	73		74		75		76		77		78		79		80	
SI	.000	*	.000	*	.000	*	.000	*	.090	*	.000	*	.000	*	.000	*
AL	.004	*	.006	*	.006	*	.002	*	.004	*	.006	*	.006	*	.008	*
P	5.799	5.803	5.769	5.775	5.824	5.830	5.901	5.903	5.755	5.759	5.750	5.756	5.858	5.864	5.702	5.710
CA	9.739	*	9.954	*	9.730	*	9.676	*	9.844	*	9.812	*	9.550	*	9.709	*
FE	.098	*	.051	*	.044	*	.042	*	.034	*	.041	*	.043	*	.032	*
MG	.000	*	.002	*	.000	*	.000	*	.000	*	.000	*	.000	*	.002	*
NA	.013	*	.010	*	.000	*	.006	*	.006	*	.003	*	.013	*	.031	*
K	.015	*	.017	*	.006	*	.008	*	.011	*	.004	*	.006	*	.004	*
SR	.012	*	.009	*	.012	*	.000	*	.010	*	.010	*	.004	*	.051	*
BA	.000	9.877	.004	10.046	.001	9.793	.006	9.739	.004	9.909	.004	9.875	.005	9.620	.000	9.829
F	1.248	*	1.054	*	1.261	*	1.011	*	1.385	*	1.471	*	1.451	*	1.820	*
CL	.017	*	.017	*	.022	*	.017	*	.025	*	.019	*	.020	*	.022	*
O	25.000	*	25.000	*	25.000	*	25.000	*	25.000	*	25.000	*	25.000	*	25.000	*
F/M		.000		25.500		.000		.000		.000		.000		.000		16.000
F/FM		1.000		.962		1.000		1.000		1.000		1.000		1.000		.941

73 8AL: Table 1, crystal 17
74 8AL: " ", " 18
75 8AL: " ", " 19
76 8AL: " ", " 20

77 8AL: Table 1, crystal 21
78 8AL: " ", " 22
79 8AL: " ", " 23
80 8AL: repeat of Table 1, crystal 21

Fluor-APATITE: analyses from samples collected within the adit through Razorback Ridge on <u>Spring Dam</u>

	81	82	83	84	85	86	87	88
SIO2	.00	.00	.00	.00	.00	.00	.00	.00
AL2O3	.02	.01	.03	.02	.02	.03	.02	.02
FEO	.20	.38	.71	.76	.71	1.40	1.09	1.08
MGO	.00	.00	.01	.00	.00	.00	.00	.00
CAO	57.07	56.78	56.20	55.11	55.14	55.18	55.28	54.78
NA2O	.05	.03	.03	.02	.02	.05	.03	.06
K2O	.03	.02	.02	.02	.03	.03	.02	.02
P2O5	42.62	42.07	41.80	40.91	41.18	41.64	42.07	41.56
SRO	.24	.25	.08	.07	.11	.12	.12	.12
BAO	.13	.00	.05	.09	.00	.00	.08	.00
F	2.92	3.44	2.48	2.51	4.12	4.26	3.95	3.64
CL	.09	.07	.07	.13	.09	.05	.04	.06
SUM	103.37	103.05	101.48	99.64	101.42	102.76	102.70	101.34
-O = F+CL	1.25	1.46	1.06	1.09	1.76	1.81	1.67	1.55
SUM	102.12	101.59	100.42	98.55	99.66	100.95	101.03	99.79

	81		82		83		84		85		86		87		88	
SI	.000	*	.000	*	.000	*	.000	*	.000	*	.000	*	.000	*	.000	*
AL	.004	*	.002	*	.006	*	.004	*	.004	*	.006	*	.004	*	.004	*
P	5.764	5.767	5.711	5.713	5.766	5.772	5.754	5.757	5.676	5.680	5.671	5.677	5.721	5.725	5.729	5.733
CA	9.767	*	9.756	*	9.811	*	9.809	*	9.618	*	9.512	*	9.514	*	9.557	*
FE	.027	*	.051	*	.097	*	.106	*	.097	*	.188	*	.146	*	.147	*
MG	.000	*	.000	*	.002	*	.000	*	.000	*	.000	*	.000	*	.000	*
NA	.015	*	.009	*	.009	*	.006	*	.006	*	.016	*	.009	*	.019	*
K	.006	*	.004	*	.004	*	.004	*	.006	*	.006	*	.004	*	.004	*
SR	.022	*	.023	*	.008	*	.007	*	.010	*	.011	*	.011	*	.011	*
BA	.008	9.846	.000	9.843	.003	9.935	.006	9.938	.000	9.738	.000	9.733	.005	9.690	.000	9.738
F	1.475	*	1.745	*	1.278	*	1.319	*	2.121	*	2.168	*	2.007	*	1.874	*
CL	.024	*	.019	*	.019	*	.037	*	.025	*	.014	*	.011	*	.017	*
O	25.000	*	25.000	*	25.000	*	25.000	*	25.000	*	25.000	*	25.000	*	25.000	*
F/M	.000		.000		48.500		.000		.000		.000		.000		.000	
F/FM	1.000		1.000		.980		1.000		1.000		1.000		1.000		1.000	

81 8AL: repeat of Table 1, crystal 22
82 8AL: repeat of Table 1, " 23
83 I.F. SAMPLE 8AU (U = Upper): Table 10, crystal 1
84 8AU: Table 1, crystal 2
85 8AU: Table 2, crystal 1
86 8AU: " ", " 2
87 8AU: " ", " 3
88 8AU: " ", " 4

Fluor-APATITE: analyses from sample $8A_U$ collected within the adit through Razorback Ridge on <u>Spring Dam</u>

	89	90	91	92	93	94	95	96
SIO2	.00	.02	.00	.00	.00	.00	.00	.00
AL2O3	.00	.04	.04	.04	.04	.03	.04	.02
FEO	1.24	.82	1.34	.68	1.38	1.30	1.20	1.14
MGO	.00	.00	.00	.00	.00	.00	.00	.00
CAO	53.43	55.29	54.81	54.06	54.80	55.07	55.80	55.04
NA2O	.04	.03	.00	.00	.04	.01	.01	.00
K2O	.00	.01	.03	.03	.04	.03	.03	.02
P2O5	40.86	41.47	40.12	41.71	42.04	42.41	41.85	40.96
SRO	.08	.12	.05	.08	.10	.13	.11	.08
BAO	.08	.13	.00	.00	.04	.10	.06	.03
F	3.78	3.00	4.25	3.79	4.28	2.94	2.93	3.92
CL	.05	.05	.06	.06	.06	.04	.07	.07
SUM	99.56	100.98	100.70	100.45	102.82	102.06	102.10	101.28
-O = F+CL	1.60	1.27	1.80	1.61	1.82	1.25	1.25	1.67
SUM	97.96	99.71	98.90	98.84	101.00	100.81	100.85	99.61

	89		90		91		92		93		94		95		96	
SI	.000	*	.003	*	.000	*	.000	*	.000	*	.000	*	.000	*	.000	*
AL	.000	*	.008	*	.008	*	.008	*	.008	*	.006	*	.008	*	.004	*
P	5.731	5.731	5.746	5.757	5.599	5.607	5.772	5.779	5.708	5.716	5.801	5.807	5.742	5.750	5.667	5.671
CA	9.484	*	9.695	*	9.681	*	9.467	*	9.417	*	9.533	*	9.690	*	9.637	*
FE	.172	*	.112	*	.185	*	.093	*	.185	*	.176	*	.163	*	.156	*
MG	.000	*	.000	*	.000	*	.000	*	.000	*	.000	*	.000	*	.000	*
NA	.013	*	.010	*	.000	*	.000	*	.012	*	.003	*	.003	*	.000	*
K	.000	*	.002	*	.006	*	.006	*	.008	*	.006	*	.006	*	.004	*
SR	.008	*	.011	*	.005	*	.008	*	.009	*	.012	*	.010	*	.008	*
BA	.005	9.682	.008	9.839	.000	9.877	.000	9.574	.003	9.634	.006	9.737	.004	9.876	.002	9.806
F	1.981	*	1.553	*	2.216	*	1.959	*	2.171	*	1.502	*	1.502	*	2.026	*
CL	.014	*	.014	*	.017	*	.017	*	.016	*	.011	*	.019	*	.019	*
O	25.000	*	25.000	*	25.000	*	25.000	*	25.000	*	25.000	*	25.000	*	25.000	*
F/M		.000		.000		.000		.000		.000		.000		.000		.000
F/FM		1.000		1.000		1.000		1.000		1.000		1.000		1.000		1.000

89 8AU: Table 2, crystal 5
90 8AU: " ", " 6
91 8AU: " ", " 7
92 8AU: " ", " 8

93 8AU: Table 2, crystal 9
94 8AU: " ", " 10
95 8AU: " ", " 11
96 8AU: " ", " 12

Fluor-APATITE: analyses from sample $8A_U$ collected within the adit through Razorback Ridge on Spring Dam

	97	98	99	100	101	102
SIO2	.00	.00	.00	.00	.00	.00
AL2O3	.04	.04	.03	.02	.04	.03
FEO	1.17	1.33	1.76	.56	.87	.81
MGO	.00	.00	.00	.00	.01	.00
CAO	54.55	54.35	54.22	55.25	55.83	55.18
NA2O	.00	.01	.04	.03	.00	.01
K2O	.01	.02	.00	.02	.02	.03
P2O5	40.67	40.73	40.81	41.59	41.19	41.14
SRO	.04	.09	.09	.12	.06	.11
BAO	.03	.11	.09	.00	.03	.03
F	3.78	4.19	3.85	4.17	3.82	3.68
CL	.07	.06	.06	.08	.05	.06
SUM	100.38	100.93	100.95	101.84	101.92	101.08
-O = F+CL	1.61	1.78	1.63	1.77	1.62	1.56
SUM	98.77	99.15	99.32	100.07	100.30	99.52

	97		98		99		100		101		102	
SI	.000	*	.000	*	.000	*	.000	*	.000	*	.000	*
AL	.007	*	.008	*	.006	*	.004	*	.008	*	.006	*
P	5.674	5.683	5.656	5.664	5.673	5.679	5.697	5.701	5.663	5.670	5.695	5.701
CA	9.634	*	9.552	*	9.539	*	9.579	*	9.714	*	9.667	*
FE	.161	*	.182	*	.242	*	.076	*	.118	*	.111	*
MG	.000	*	.000	*	.000	*	.000	*	.002	*	.000	*
NA	.000	*	.003	*	.013	*	.009	*	.000	*	.003	*
K	.002	*	.004	*	.000	*	.004	*	.004	*	.006	*
SR	.006	*	.009	*	.009	*	.011	*	.006	*	.010	*
BA	.002	9.805	.007	9.757	.006	9.807	.000	9.679	.002	9.846	.002	9.799
F	1.971	*	2.174	*	1.999	*	2.134	*	1.962	*	1.903	*
CL	.020	*	.017	*	.017	*	.022	*	.014	*	.017	*
O	25.000	*	25.000	*	25.000	*	25.000	*	25.000	*	25.000	*
F/M		.000		.000		.000		.000		59.000		.000
F/FM		1.000		1.000		1.000		1.000		.983		1.000

97 8AU: Table 2, crystal 13
98 8AU: " ", " 14
99 8AU: " ", " 15

100 8AU: Table 2, crystal 16
101 8AU: " ", " 17
102 8AU: " ", " 18

Appendix E

ELECTRON MICROPROBE ANALYSES

Phyllosilicate minerals

PHLOGOPITE: analyses from samples collected at stratigraphic section #13 on <u>Worumbe</u>

	1	2	3	4	5	6	7	8
SIO2	42.30	39.61	39.81	38.20	40.27	39.26	39.80	39.32
TIO2	1.13	1.06	.77	.88	.95	.86	.90	.91
AL2O3	14.21	13.82	14.06	14.01	13.45	13.38	13.60	13.12
CR2O3	.00	.00	.00	.00	.00	.00	.00	.00
FEO	9.43	8.92	10.79	10.37	9.13	9.94	9.60	9.52
MNO	.00	.00	.00	.00	.00	.00	.00	.00
MGO	19.43	19.62	20.68	21.04	20.55	19.95	19.78	19.58
CAO	.04	.03	.02	.11	.06	.07	.02	.04
NA2O	.03	.04	.04	.07	.03	.05	.01	.00
K2O	8.93	8.93	8.21	7.62	7.67	7.93	8.69	8.54
BAO	.00	.00	.00	.00	.00	.00	.00	.00
F	1.00	.90	.83	.76	.91	.91	.91	.91
CL	.00	.02	.00	.00	.00	.02	.02	.01
SUM	96.50	92.95	95.21	93.06	93.02	92.37	93.33	91.95
-O = F+CL	.42	.38	.35	.32	.38	.39	.39	.39
SUM	96.08	92.57	94.86	92.74	92.64	91.98	92.94	91.56

	1		2		3		4		5		6		7		8	
SI	5.980	*	5.842	*	5.758	*	5.649	*	5.889	*	5.830	*	5.855	*	5.873	*
AL	2.020	8.000	2.158	8.000	2.242	8.000	2.351	8.000	2.111	8.000	2.170	8.000	2.145	8.000	2.127	8.000
AL	.347	*	.244	*	.155	*	.090	*	.207	*	.171	*	.213	*	.182	*
TI	.120	*	.118	*	.084	*	.098	*	.104	*	.096	*	.100	*	.102	*
CR	.000	*	.000	*	.000	*	.000	*	.000	*	.000	*	.000	*	.000	*
FE	1.115	*	1.100	*	1.305	*	1.282	*	1.117	*	1.234	*	1.181	*	1.189	*
MN	.000	*	.000	*	.000	*	.000	*	.000	*	.000	*	.000	*	.000	*
MG	4.094	5.676	4.313	5.775	4.458	6.002	4.637	6.107	4.479	5.907	4.415	5.917	4.337	5.831	4.359	5.332
CA	.006	*	.005	*	.003	*	.017	*	.009	*	.011	*	.003	*	.006	*
NA	.008	*	.011	*	.011	*	.020	*	.009	*	.014	*	.003	*	[illegible]	*
BA	.000	*	.000	*	.000	*	.000	*	.000	*	.000	*	.000	*	.000	*
K	1.610	1.624	1.680	1.696	1.515	1.529	1.437	1.475	1.431	1.449	1.502	1.527	1.631	1.637	1.627	1.633
F	.447	*	.420	*	.380	*	.355	*	.421	*	.427	*	.423	*	.430	*
CL	.000	*	.005	*	.000	*	.000	*	.000	*	.005	*	.005	*	.003	*
O	22.000	*	22.000	*	22.000	*	22.000	*	22.000	*	22.000	*	22.000	*	22.000	*
FE	21.40		20.32		22.65		21.66		19.95		21.85		21.40		21.43	
MG	78.60		79.68		77.35		78.34		80.05		78.15		78.60		78.57	
F/M	.272		.255		.293		.277		.249		.280		.272		.273	
F/FM	.214		.203		.226		.217		.200		.218		.214		.214	

1 Diamictite matrix SAMPLE 13c1: phlogopite, Area #3-1
2 I.F. SAMPLE 13e2: phlogopite, Area #0-1
3 13e2: another spot in previous grain
4 13e2: phlogopite, Area #1-2
5 13e2: relict phlogopite, Area #2-6
6 13e2: phlogopite, Area #3-4
7 13e2: another spot in previous grain
8 13e2: repeat of previous spot

MICA: analyses from samples collected at section #13 on Worumba and section #18 on Mount Victor

	9	10	11	12	13	14	15	16
SIO2	38.47	40.97	42.45	37.54	38.44	38.42	36.59	37.75
TIO2	.92	.88	.67	2.52	2.21	2.16	2.14	1.24
AL2O3	14.10	13.54	13.53	18.12	17.84	18.12	16.79	15.29
CR2O3	.00	.00	.00	.00	.00	.00	.00	.00
FEO	9.74	9.40	7.85	15.84	15.50	15.40	16.07	12.40
MNO	.00	.00	.03	.09	.06	.06	.06	.08
MGO	18.85	20.57	21.55	12.71	13.19	13.02	12.88	15.56
CAO	.02	.04	.01	.02	.00	.00	.03	2.40
NA2O	.01	.01	.03	.08	.03	.05	.07	.07
K2O	9.03	8.69	9.15	8.94	8.58	9.74	9.48	9.34
BAO	.00	.00	.00	.09	.10	.09	.07	.01
F	.86	.94	1.35	.35	.54	.48	.44	.70
CL	.00	.00	.00	.05	.04	.02	.03	.00
SUM	92.00	95.04	96.62	96.35	96.53	97.56	94.65	94.84
-O = F+CL	.36	.40	.57	.16	.24	.21	.19	.29
SUM	91.64	94.64	96.05	96.19	96.29	97.35	94.46	94.55

	9		10		11		12		13		14		15		16	
SI	5.771	*	5.898	*	5.965	*	5.520	*	5.606	*	5.578	*	5.526	*	5.621	*
AL	2.229	8.000	2.102	8.000	2.035	8.000	2.480	8.000	2.394	8.000	2.422	8.000	2.474	8.000	2.379	8.000
AL	.264	*	.195	*	.206	*	.660	*	.672	*	.677	*	.514	*	.304	*
TI	.104	*	.095	*	.071	*	.279	*	.242	*	.236	*	.243	*	.139	*
CR	.000	*	.000	*	.000	*	.000	*	.000	*	.000	*	.000	*	.000	*
FE	1.222	*	1.132	*	.923	*	1.948	*	1.890	*	1.870	*	2.030	*	1.544	*
MN	.000	*	.000	*	.004	*	.011	*	.007	*	.007	*	.008	*	.010	*
MG	4.215	5.804	4.414	5.837	4.514	5.716	2.786	5.683	2.867	5.679	2.817	5.608	2.899	5.694	3.454	5.451
CA	.003	*	.006	*	.002	*	.003	*	.000	*	.000	*	.005	*	.383	*
NA	.003	*	.003	*	.008	*	.023	*	.008	*	.014	*	.020	*	.020	*
BA	.000	*	.000	*	.000	*	.005	*	.006	*	.005	*	.004	*	.001	*
K	1.728	1.734	1.596	1.605	1.640	1.650	1.677	1.708	1.596	1.610	1.804	1.823	1.826	1.856	1.774	2.178
F	.408	*	.428	*	.600	*	.163	*	.249	*	.220	*	.210	*	.330	*
CL	.000	*	.000	*	.000	*	.012	*	.010	*	.005	*	.008	*	.000	*
O	22.000	*	22.000	*	22.000	*	22.000	*	22.000	*	22.000	*	22.000	*	22.000	*
FE	22.48		20.41		16.97		41.15		39.73		39.89		41.18		30.90	
MG	77.52		79.59		83.03		58.85		60.27		60.11		58.82		69.10	
F/M	.290		.256		.205		.703		.662		.666		.703		.450	
F/FM	.225		.204		.170		.413		.398		.400		.413		.310	

9 13e2: another spot in previous grain
10 13e2: phlogopite, Plate 4.2c, spot 7
11 Subarkosic Fe arenite SAMPLE 13k: phlogopite
12 Diamictite matrix SAMPLE 18a1: biotite, Area #1
13 18a1: another biotite, Area #2
14 18a1: biotite, Area #3
15 18a1: biotite, Area #5
16 I.F. SAMPLE 18E1: phlogopite, Area #2

MICA: analyses from samples collected at section #18 on <u>Mount Victor</u> and section #17 on <u>Outalpe</u>

	17	18	19	20	21	22	23	24
SIO2	37.73	37.48	39.21	39.47	37.77	37.60	38.59	37.98
TIO2	1.20	1.19	1.96	2.08	2.15	2.05	2.06	2.07
AL2O3	16.39	15.94	18.66	18.20	17.98	17.17	17.72	16.98
CR2O3	.00	.00	.00	.00	.00	.00	.00	.00
FEO	13.41	13.31	15.57	15.91	15.77	15.09	15.82	15.36
MNO	.14	.15	.00	.11	.13	.14	.10	.14
MGO	15.68	15.50	13.46	13.08	13.11	13.09	13.20	13.06
CAO	.06	.12	.00	.00	.01	.02	.00	.02
NA2O	.07	.09	.13	.09	.14	.15	.10	.05
K2O	9.25	9.15	8.86	8.93	8.94	9.44	9.43	8.78
BAO	.09	.09	.12	.16	.07	.09	.10	.09
F	.67	.69	.36	.33	.38	.40	.46	.31
CL	.01	.02	.01	.00	.00	.00	.00	.02
SUM	94.70	93.73	98.34	98.36	96.45	95.24	97.58	94.86
-O = F+CL	.28	.30	.15	.14	.16	.17	.19	.14
SUM	94.42	93.43	98.19	98.22	96.29	95.07	97.39	94.73

	17		18		19		20		21		22		23		24	
SI	5.605	*	5.629	*	5.607	*	5.656	*	5.544	*	5.599	*	5.605	*	5.656	*
AL	2.395	8.000	2.371	8.000	2.393	8.000	2.344	8.000	2.456	8.000	2.401	8.000	2.395	8.000	2.344	8.000
AL	.474	*	.449	*	.751	*	.730	*	.654	*	.611	*	.637	*	.635	*
TI	.134	*	.134	*	.211	*	.224	*	.237	*	.230	*	.225	*	.232	*
CR	.000	*	.000	*	.000	*	.000	*	.000	*	.000	*	.000	*	.000	*
FE	1.666	*	1.672	*	1.862	*	1.907	*	1.936	*	1.879	*	1.921	*	1.913	*
MN	.018	*	.019	*	.000	*	.013	*	.016	*	.018	*	.012	*	.018	*
MG	3.472	5.764	3.470	5.744	2.869	5.693	2.794	5.668	2.868	5.711	2.905	5.643	2.857	5.653	2.899	5.696
CA	.010	*	.019	*	.000	*	.000	*	.002	*	.003	*	.000	*	.003	*
NA	.020	*	.026	*	.036	*	.025	*	.040	*	.043	*	.028	*	.014	*
BA	.005	*	.005	*	.007	*	.009	*	.004	*	.005	*	.006	*	.005	*
K	1.753	1.788	1.753	1.803	1.616	1.659	1.632	1.666	1.674	1.719	1.793	1.845	1.747	1.781	1.668	1.690
F	.315	*	.328	*	.163	*	.150	*	.176	*	.188	*	.211	*	.146	*
CL	.003	*	.005	*	.002	*	.000	*	.000	*	.000	*	.000	*	.005	*
O	22.000	*	22.000	*	22.000	*	22.000	*	22.000	*	22.000	*	22.000	*	22.000	*
FE	32.43		32.51		39.36		40.56		40.30		39.28		40.21		39.75	
MG	67.57		67.49		60.64		59.44		59.70		60.72		59.79		60.25	
F/M	.485		.487		.649		.687		.681		.653		.677		.666	
F/FM	.327		.328		.394		.407		.405		.395		.404		.400	

17 18E1: core of phlogopite, Area #4-1
18 18E1: another spot in previous phlogopite
19 Diamictite matrix SAMPLE 17a1: biotite, Area #1
20 17a1: biotite with visible cleavage
21 17a1: biotite with visible cleavage, Area #1-3
22 17a1: biotite, non cleav., Area #2
23 17a1: biotite, non cleav., Area #4-1
24 17a1: adjacent biotite to previous

BIOTITE: analyses from samples collected at section #16 on Outalpa and section #15 on Bimbowrie

	25	26	27	28	29	30	31	32
SIO2	36.94	36.24	36.66	35.64	36.25	35.24	38.29	37.47
TIO2	1.86	1.90	1.84	1.82	1.69	1.69	1.73	1.56
AL2O3	18.26	18.73	18.75	17.71	17.16	17.91	17.25	16.86
CR2O3	.00	.00	.00	.00	.00	.02	.00	.04
FEO	14.99	15.57	15.55	15.27	15.46	15.40	14.25	14.46
MNO	.15	.12	.08	.00	.00	.00	.49	.41
MGO	12.71	12.74	12.64	12.68	13.07	12.62	13.68	13.15
CAO	.00	.01	.00	.01	.00	.01	.00	.01
NA2O	.12	.11	.08	.09	.09	.10	.10	.11
K2O	9.47	9.69	8.82	9.00	9.36	9.53	9.33	8.86
BAO	.09	.12	.07	.00	.00	.00	.09	.10
F	.26	.29	.29	.28	.33	.35	.72	.76
CL	.00	.02	.00	.00	.01	.02	.01	.01
SUM	94.85	95.54	94.78	92.50	93.42	92.89	95.94	93.80
-O = F+CL	.11	.13	.12	.12	.14	.15	.31	.32
SUM	94.74	95.41	94.66	92.38	93.28	92.74	95.63	93.48

	25		26		27		28		29		30		31		32	
SI	5.522	*	5.409	*	5.474	*	5.472	*	5.523	*	5.415	*	5.629	*	5.638	*
AL	2.478	8.000	2.591	8.000	2.526	8.000	2.528	8.000	2.477	8.000	2.585	8.000	2.371	8.000	2.362	8.000
AL	.738	*	.704	*	.773	*	.676	*	.605	*	.659	*	.618	*	.628	*
TI	.209	*	.213	*	.207	*	.210	*	.194	*	.195	*	.191	*	.177	*
CR	.000	*	.000	*	.000	*	.000	*	.000	*	.002	*	.000	*	.005	*
FE	1.874	*	1.944	*	1.942	*	1.961	*	1.970	*	1.979	*	1.752	*	1.820	*
MN	.019	*	.015	*	.010	*	.000	*	.000	*	.000	*	.061	*	.052	*
MG	2.832	5.672	2.834	5.710	2.813	5.744	2.902	5.749	2.968	5.736	2.891	5.726	2.998	5.620	2.949	5.630
CA	.000	*	.002	*	.000	*	.002	*	.000	*	.002	*	.000	*	.002	*
NA	.035	*	.032	*	.023	*	.027	*	.027	*	.030	*	.029	*	.032	*
BA	.005	*	.007	*	.004	*	.000	*	.000	*	.000	*	.005	*	.006	*
K	1.806	1.846	1.845	1.885	1.680	1.707	1.763	1.791	1.819	1.846	1.868	1.899	1.750	1.783	1.700	1.740
F	.123	*	.137	*	.137	*	.136	*	.159	*	.170	*	.335	*	.362	*
CL	.000	*	.005	*	.000	*	.000	*	.003	*	.005	*	.002	*	.003	*
O	22.000	*	22.000	*	22.000	*	22.000	*	22.000	*	22.000	*	22.000	*	22.000	*

	25	26	27	28	29	30	31	32
FE	39.82	40.68	40.84	40.32	39.89	40.64	36.89	38.16
MG	60.18	59.32	59.16	59.68	60.11	59.36	63.11	61.84
F/M	.668	.691	.694	.676	.664	.685	.605	.635
F/FM	.401	.409	.410	.403	.399	.406	.377	.388

25 I.F. SAMPLE 16d1: biotite with visible cleavage
26 16d1: biotite with visible cleavage, Area #2
27 16d1: biotite with visible cleavage, Area #3-1
28 16d1: different probe day, biotite
29 16d1: another spot in previous grain
30 16d1: biotite, Area #4
31 Diamictite matrix SAMPLE 15f1: biotite, Area #1-4
32 15f1: biotite, Area #2-2

MICA: analyses from samples collected at section #15 on <u>Bimbowrie</u> and section #7 on <u>Manunda</u>

	33	34	35	36	37	38	39	40
SIO2	37.38	36.38	37.22	37.56	36.95	36.41	37.76	47.14
TIO2	1.51	1.93	1.88	1.94	1.90	1.89	1.68	.79
AL2O3	17.49	15.28	15.28	14.98	14.77	14.48	15.79	26.88
CR2O3	.00	.00	.00	.00	.00	.00	.00	.00
FEO	15.82	18.95	19.33	19.03	18.30	18.52	17.13	7.35
MNO	.38	.00	.16	.05	.02	.06	.14	.02
MGO	13.73	11.94	11.80	12.05	11.79	12.01	11.39	4.01
CAO	.00	.01	.02	.04	.01	.00	.09	.06
NA2O	.07	.05	.01	.00	.01	.00	.33	.10
K2O	9.27	9.63	9.24	9.26	9.58	9.29	9.01	9.50
BAO	.04	.08	.10	.11	.07	.11	.10	.25
F	.71	.45	.43	.37	.42	.50	.38	.00
CL	.01	.03	.04	.06	.00	.03	.04	.00
SUM	96.41	94.73	95.51	95.45	93.82	93.30	93.84	96.10
-O= F+CL	.30	.20	.19	.17	.18	.22	.17	.00
SUM	96.11	94.53	95.32	95.28	93.64	93.08	93.67	96.10

	33		34		35		36	
SI	5.515	*	5.585	*	5.653	*	5.696	*
AL	2.485	8.000	2.415	8.000	2.347	8.000	2.304	8.000
AL	.556	*	.350	*	.387	*	.373	*
TI	.168	*	.223	*	.215	*	.221	*
CR	.000	*	.000	*	.000	*	.000	*
FE	1.952	*	2.433	*	2.455	*	2.413	*
MN	.047	*	.000	*	.021	*	.006	*
MG	3.020	5.743	2.732	5.738	2.671	5.749	2.724	5.737
CA	.000	*	.002	*	.003	*	.006	*
NA	.020	*	.015	*	.003	*	.000	*
BA	.002	*	.005	*	.006	*	.007	*
K	1.745	1.767	1.886	1.907	1.790	1.802	1.791	1.804
F	.331	*	.218	*	.207	*	.177	*
CL	.003	*	.008	*	.010	*	.015	*
O	22.000	*	22.000	*	22.000	*	22.000	*
FE	39.26		47.10		47.89		46.98	
MG	60.74		52.90		52.11		53.02	
F/M	.662		.890		.927		.888	
F/FM	.398		.471		.481		.470	

	37		38		39		40	
SI	5.701	*	5.661	*	5.760	*	6.423	*
AL	2.299	8.000	2.339	8.000	2.240	8.000	1.577	8.000
AL	.386	*	.314	*	.598	*	2.739	*
TI	.220	*	.221	*	.193	*	.081	*
CR	.000	*	.000	*	.000	*	.000	*
FE	2.361	*	2.408	*	2.185	*	.838	*
MN	.003	*	.008	*	.018	*	.002	*
MG	2.711	5.682	2.783	5.735	2.590	5.584	.814	4.474
CA	.002	*	.000	*	.015	*	.009	*
NA	.003	*	.000	*	.098	*	.026	*
BA	.004	*	.007	*	.006	*	.013	*
K	1.885	1.894	1.842	1.849	1.753	1.871	1.651	1.700
F	.205	*	.246	*	.183	*	.000	*
CL	.000	*	.008	*	.010	*	.000	*
O	22.000	*	22.000	*	22.000	*	22.000	*
FE	46.55		46.39		45.77		50.70	
MG	53.45		53.61		54.23		49.30	
F/M	.872		.868		.851		1.031	
F/FM	.466		.465		.460		.508	

33 15f1: another spot in previous grain
34 Diamictite matrix SAMPLE 7T: biotite, Area #1
35 7T: biotite, Area #2
36 7T: biotite, Area #3
37 7T: biotite, Area #4
38 7T: biotite, Area #5
39 7T: biotite, Area #6
40 7T: phengite portion of previous grain

MICA: analyses from diamictite sample 7T collected at stratigraphic section #7 at Iron Peak, Manunda

	41	42	43	44	45	46	47	48
SIO2	37.63	37.41	37.07	37.04	36.89	38.18	36.29	36.75
TIO2	1.85	1.80	1.91	1.93	2.01	1.98	1.96	1.97
AL2O3	14.44	14.56	15.22	14.60	14.81	14.52	14.72	15.28
CR2O3	.00	.00	.04	.00	.00	.03	.07	.13
FEO	18.73	18.55	19.34	19.26	18.66	18.72	19.10	19.18
MNO	.00	.00	.02	.02	.00	.00	.03	.04
MGO	11.96	12.06	12.27	12.63	12.17	12.44	12.05	12.38
CAO	.00	.05	.02	.16	.01	.00	.05	.00
NA2O	.03	.02	.03	.06	.02	.00	.02	.00
K2O	8.96	9.52	9.90	9.45	9.59	9.76	9.09	9.96
BAO	.12	.18	.14	.05	.09	.06	.04	.11
F	.44	.47	.35	.30	.36	.34	.41	.41
CL	.05	.05	.03	.11	.05	.02	.04	.04
SUM	94.21	94.67	96.34	95.61	94.66	96.05	93.87	96.25
-O = F+CL	.20	.21	.15	.15	.16	.15	.18	.18
SUM	94.01	94.46	96.19	95.46	94.50	95.90	93.69	96.07

	41		42		43		44		45		46		47		48	
SI	5.765	*	5.725	*	5.607	*	5.636	*	5.654	*	5.751	*	5.616	*	5.567	*
AL	2.235	8.000	2.275	8.000	2.393	8.000	2.36'	8.000	2.346	8.000	2.249	8.000	2.384	8.000	2.433	8.000
AL	.372	*	.350	*	.320	*	.253	*	.329	*	.328	*	.300	*	.294	*
TI	.213	*	.207	*	.217	*	.221	*	.232	*	.224	*	.228	*	.224	*
CR	.000	*	.000	*	.005	*	.000	*	.000	*	.004	*	.009	*	.016	*
FE	2.400	*	2.374	*	2.446	*	2.451	*	2.392	*	2.358	*	2.472	*	2.430	*
MN	.000	*	.000	*	.003	*	.003	*	.000	*	.000	*	.004	*	.005	*
MG	2.731	5.716	2.751	5.682	2.766	5.757	2.864	5.792	2.780	5.733	2.793	5.707	2.779	5.791	2.795	5.764
CA	.000	*	.008	*	.003	*	.026	*	.002	*	.000	*	.008	*	.000	*
NA	.009	*	.006	*	.009	*	.018	*	.006	*	.000	*	.006	*	.000	*
BA	.007	*	.011	*	.008	*	.003	*	.005	*	.004	*	.002	*	.007	*
K	1.751	1.767	1.858	1.883	1.910	1.930	1.834	1.881	1.875	1.888	1.875	1.879	1.794	1.811	1.924	1.931
F	.213	*	.227	*	.167	*	.144	*	.175	*	.162	*	.201	*	.196	*
CL	.013	*	.013	*	.008	*	.028	*	.013	*	.005	*	.010	*	.010	*
O	22.000	*	22.000	*	22.000	*	22.000	*	22.000	*	22.000	*	22.000	*	22.000	*
FE	46.77		46.32		46.93		46.11		46.24		45.78		47.07		46.50	
MG	53.23		53.68		53.07		53.89		53.76		54.22		52.93		53.50	
F/M	.879		.863		.885		.857		.860		.844		.891		.871	
F/FM	.468		.463		.470		.461		.462		.458		.471		.466	

41 7T: phengite portion of same grain
42 7T: biotite, Area #6-4
43 7T: biotite, Area #7-1
44 7T: another spot in previous biotite
45 7T: another spot in same biotite
46 7T: biotite, Area #8
47 7T: biotite, Area #9
48 7T: bioti*e, Area #10-3 within a CLAST

MICA: analyses from diamictite sample 7T collected at stratigraphic section #7 at Iron Peak, Manunda

	49	50	51	52	53	54	55	56
SIO2	37.52	37.84	38.30	53.04	51.49	37.14	37.02	49.95
TIO2	1.82	2.00	2.08	.24	.55	1.97	2.07	.71
AL2O3	14.46	14.44	13.91	25.87	27.80	15.35	14.47	28.50
CR2O3	.02	.11	.00	.00	.00	.05	.07	.05
FEO	18.61	18.83	18.70	5.84	5.23	19.32	18.70	6.18
MNO	.08	.00	.06	.00	.04	.00	.03	.00
MGO	13.03	12.74	12.80	3.38	2.98	12.24	12.56	2.62
CAO	.00	.00	.00	.00	.00	.05	.00	.00
NA2O	.00	.00	.00	.12	.11	.01	.00	.10
K2O	9.93	10.01	8.92	8.64	9.12	9.68	9.82	7.62
BAO	.02	.07	.03	.00	.10	.07	.05	.18
F	.40	.44	.41	.00	.00	.46	.43	.00
CL	.04	.08	.05	.00	.01	.04	.02	.01
SUM	95.93	96.56	95.20	97.13	97.43	96.38	95.24	95.92
-O = F+CL	.18	.20	.18	.00	.00	.20	.19	.00
SUM	95.75	96.36	95.02	97.13	97.43	96.18	95.05	95.92

	49		50		51		52		53		54		55		56	
SI	5.676	*	5.692	*	5.794	*	6.957	*	6.751	*	5.601	*	5.648	*	6.639	*
AL	2.324	8.000	2.308	8.000	2.206	8.000	1.043	8.000	1.249	8.000	2.399	8.000	2.352	8.000	1.361	8.000
AL	.253	*	.251	*	.273	*	2.955	*	3.047	*	.329	*	.250	*	3.102	*
TI	.207	*	.226	*	.237	*	.024	*	.054	*	.223	*	.238	*	.071	*
CR	.002	*	.013	*	.000	*	.000	*	.000	*	.006	*	.008	*	.005	*
FE	2.354	*	2.369	*	2.366	*	.641	*	.573	*	2.437	*	2.386	*	.687	*
MN	.010	*	.000	*	.006	*	.000	*	.004	*	.000	*	.004	*	.000	*
MG	2.938	5.765	2.856	5.715	2.886	5.761	.661	4.280	.582	4.261	2.751	5.747	2.856	5.742	.519	4.384
CA	.000	*	.000	*	.000	*	.000	*	.000	*	.008	*	.000	*	.000	*
NA	.000	*	.000	*	.000	*	.031	*	.028	*	.003	*	.000	*	.026	*
BA	.001	*	.304	*	.002	*	.000	*	.005	*	.004	*	.003	*	.009	*
K	1.916	1.917	1.920	1.924	1.721	1.723	1.445	1.476	1.525	1.558	1.862	1.877	1.911	1.914	1.292	1.327
F	.191	*	.209	*	.196	*	.000	*	.000	*	.219	*	.207	*	.000	*
CL	.010	*	.020	*	.013	*	.000	*	.002	*	.010	*	.005	*	.002	*
O	22.000	*	22.000	*	22.000	*	22.000	*	22.000	*	22.000	*	22.000	*	22.000	*
FE		44.49		45.33		45.05		49.22		49.61		46.97		45.51		56.96
MG		55.51		54.67		54.95		50.78		50.39		53.03		54.49		43.04
F/M		.805		.829		.820		.969		.992		.886		.837		1.323
F/FM		.446		.453		.450		.492		.498		.470		.456		.570

49 7T: another spot in previous grain, Area #10-4
50 7T: biotite, Area #11 within same clast
51 7T: biotite, Area #12-1 within same clast
52 7T: phengite portion of previous grain, Area #12-2
53 7T: phengite portion of same grain, Area #12-3
54 7T: biotite portion of same grain, Area #12-4
55 7T: adjacent biotite, Area #12-7
56 7T: adjoining phengite, Area #12-8

MICA: analyses from diamictite sample 7T collected at stratigraphic section #7 at Iron Peak, <u>Manunda</u>

	57	58	59	60	61	62	63	64
SIO2	50.08	37.41	37.25	37.87	37.86	37.58	37.70	36.26
TIO2	.72	1.77	2.01	1.80	2.01	1.90	1.92	1.93
AL2O3	29.53	14.89	14.68	14.96	14.68	15.28	15.27	13.75
CR2O3	.00	.05	.00	.05	.00	.07	.03	.00
FEO	5.70	18.68	18.82	18.73	19.04	18.80	19.05	18.29
MNO	.00	.01	.05	.00	.04	.02	.00	.11
MGO	2.52	12.32	12.59	12.57	12.26	12.30	12.29	12.01
CAO	.00	.00	.00	.16	.00	.00	.02	.21
NA2O	.13	.00	.00	.00	.01	.03	.02	.00
K2O	7.64	9.96	9.76	9.67	8.73	9.81	9.86	9.40
BAO	.14	.00	.09	.00	.03	.07	.08	.08
F	.00	.34	.41	.35	.32	.35	.32	.39
CL	.00	.01	.07	.03	.03	.04	.00	.03
SUM	96.46	95.44	95.73	96.19	95.01	96.25	96.56	92.46
-O = F+CL	.00	.15	.19	.15	.14	.16	.13	.17
SUM	96.46	95.29	95.54	96.04	94.87	96.09	96.43	92.29

SI	6.596	*	5.685	*	5.652	*	5.696	*	5.742	*	5.659	*	5.664	*	5.701	*
AL	1.404	8.000	2.315	8.000	2.348	8.000	2.304	8.000	2.258	8.000	2.341	8.000	2.336	8.000	2.299	8.000
AL	3.179	*	.352	*	.276	*	.347	*	.366	*	.370	*	.367	*	.249	*
TI	.071	*	.202	*	.229	*	.204	*	.229	*	.215	*	.217	*	.228	*
CR	.000	*	.006	*	.000	*	.006	*	.000	*	.008	*	.004	*	.000	*
FE	.628	*	2.374	*	2.388	*	2.356	*	2.415	*	2.368	*	2.393	*	2.405	*
MN	.000	*	.001	*	.006	*	.000	*	.005	*	.003	*	.000	*	.015	*
MG	.495	4.373	2.791	5.726	2.847	5.747	2.818	5.730	2.772	5.787	2.761	5.725	2.752	5.733	2.815	5.711
CA	.000	*	.000	*	.000	*	.026	*	.000	*	.000	*	.003	*	.035	*
NA	.033	*	.000	*	.000	*	.000	*	.003	*	.009	*	.006	*	.000	*
BA	.007	*	.000	*	.005	*	.000	*	.002	*	.004	*	.005	*	.005	*
K	1.283	1.324	1.931	1.931	1.889	1.894	1.855	1.881	1.689	1.694	1.884	1.897	1.889	1.903	1.885	1.925
F	.000	*	.163	*	.197	*	.166	*	.153	*	.167	*	.152	*	.194	*
CL	.000	*	.003	*	.018	*	.008	*	.008	*	.010	*	.000	*	.008	*
O	22.000	*	22.000	*	22.000	*	22.000	*	22.000	*	22.000	*	22.000	*	22.000	*
FE	55.93		45.97		45.61		45.53		46.56		46.17		46.52		46.08	
MG	44.07		54.03		54.39		54.47		53.44		53.83		53.48		53.92	
F/M	1.269		.851		.841		.836		.873		.859		.870		.860	
F/FM	.559		.460		.457		.455		.466		.462		.465		.462	

57 7T: another phengite, Area #12-9
58 7T: adjacent biotite, Area #12-10
59 7T: another biotite, Area #12-13
60 7T: biotite, Area #13 within same clast
61 7T: biotite, Area #14-1 within same clast
62 7T: biotite, Area #14-3
63 7T: biotite, Area #17 within MATRIX
64 7T: biotite, Area #18-1 within matrix

CHLORITE: analyses from samples collected at stratigraphic section #13 on <u>Worumba</u>

	1	2	3	4	5	6	7	8
SIO2	22.98	29.07	30.68	29.02	31.79	28.92	28.93	28.13
TIO2	.31	.00	.00	.09	.21	.02	.00	.02
AL2O3	14.23	19.88	17.96	19.57	20.81	18.69	19.15	19.50
CR2O3	.01	.00	.00	.00	.00	.00	.01	.00
FEO	23.68	10.46	11.02	9.76	10.39	12.66	12.67	12.13
MNO	.01	.00	.00	.00	.02	.02	.00	.02
MGO	21.95	27.41	27.17	24.32	22.95	26.51	26.22	26.42
CAO	.08	.00	.00	.01	.01	.00	.00	.00
NA2O	.00	.00	.01	.06	.06	.00	.00	.00
K2O	.11	.01	.07	1.12	2.00	.04	.02	.02
BAO	.03	.00	.00	.00	.00	.00	.00	.00
F	.23	.04	.08	.23	.13	.17	.18	.13
CL	.03	.00	.00	.01	.01	.00	.00	.00
SUM	83.65	86.87	86.99	84.19	88.38	87.03	87.18	86.37
-O = F+CL	.10	.02	.03	.10	.06	.07	.08	.05
SUM	83.55	86.85	86.96	84.09	88.32	86.96	87.10	86.32

	1		2		3		4		5		6		7		8	
SI	5.161	*	5.693	*	6.007	*	5.873	*	6.132	*	5.730	*	5.716	*	5.605	*
AL	2.839	8.000	2.307	8.000	1.993	8.000	2.127	8.000	1.868	8.000	2.270	8.000	2.284	8.000	2.395	8.000
AL	.926	*	2.282	*	2.150	*	2.541	*	2.862	*	2.093	*	2.175	*	2.183	*
TI	.052	*	.000	*	.000	*	.014	*	.030	*	.003	*	.000	*	.003	*
CR	.002	*	.000	*	.000	*	.000	*	.000	*	.000	*	.002	*	.000	*
FE	4.447	*	1.713	*	1.804	*	1.652	*	1.676	*	2.098	*	2.094	*	2.021	*
MN	.002	*	.000	*	.000	*	.000	*	.003	*	.003	*	.000	*	.003	*
MG	7.347	*	8.002	*	7.929	*	7.337	*	6.598	*	7.828	*	7.722	*	7.846	*
CA	.019	*	.000	*	.000	*	.002	*	.002	*	.000	*	.000	*	.000	*
NA	.000	*	.000	*	.004	*	.024	*	.022	*	.000	*	.000	*	.000	*
BA	.003	*	.000	*	.000	*	.000	*	.000	*	.000	*	.000	*	.000	*
K	.032	12.830	.002	11.999	.017	11.905	.289	11.858	.492	11.686	.010	12.035	.005	11.997	.005	12.062
F	.163	*	.025	*	.050	*	.147	*	.079	*	.107	*	.112	*	.082	*
CL	.011	*	.000	*	.000	*	.003	*	.003	*	.000	*	.000	*	.000	*
O	28.000	*	28.000	*	28.000	*	28.000	*	28.000	*	28.000	*	28.000	*	28.000	*
FE		37.71		17.64		18.54		18.38		20.26		21.13		21.33		20.48
MG		62.29		82.36		81.46		81.62		79.74		78.87		78.67		79.52
F/M		.606		.214		.228		.225		.255		.268		.271		.258
F/FM		.377		.176		.185		.184		.203		.212		.213		.205

1 Diamictite matrix SAMPLE 13c1: chl-hem replacing phlogopite
2 13c1: chlorite, Area #2
3 13c1: chlorite-after-phlogopite, Area #3-2
4 I.F. SAMPLE 13e2: chlorite-after-phlogopite
5 13e2: chlorite-after-phlogopite, Area #1-1
6 13e2: chlorite-after-phlogopite, Area #1-3
7 13e2: another spot in previous grain
8 13e2: chlorite-after-phlogopite, Area #2-3

CHLORITE: analyses from samples collected at section #13 on Yorumba and section #19 on Oopina

	9	10	11	12	13	14	15	16
SIO2	28.13	29.80	28.97	28.58	28.84	31.71	30.92	27.10
TIO2	.00	.03	.00	.00	.00	.05	.02	.00
AL2O3	19.84	19.13	20.28	17.95	20.41	18.59	19.27	22.77
CR2O3	.00	.00	.00	.00	.00	.00	.00	.00
FEO	11.81	11.45	12.35	12.50	10.98	18.30	16.53	14.10
MNO	.00	.00	.00	.00	.02	.15	.12	.07
MGO	26.88	25.44	23.67	26.86	26.61	17.03	18.40	24.14
CAO	.00	.00	.00	.04	.01	.18	.19	.00
NA2O	.00	.00	.02	.00	.00	.06	.07	.00
K2O	.00	.50	.79	.07	.06	1.54	.49	.00
BAO	.00	.00	.00	.00	.00	.00	.00	.00
F	.13	.14	.11	.23	.12	.24	.19	.09
CL	.00	.00	.00	.00	.00	.00	.01	.00
SUM	86.79	86.49	86.19	86.23	87.05	87.85	86.21	88.27
-O = F+CL	.05	.06	.05	.10	.05	.10	.08	.04
SUM	86.74	86.43	86.14	86.13	87.00	87.75	86.13	88.23

	9		10		11		12		13		14		15		16	
SI	5.567	*	5.897	*	5.790	*	5.723	*	5.652	*	6.397	*	6.265	*	5.327	*
AL	2.433	8.000	2.103	8.000	2.210	8.000	2.277	8.000	2.348	8.000	1.603	8.000	1.735	8.000	2.673	8.000
AL	2.193	*	2.357	*	2.566	*	1.958	*	2.366	*	2.816	*	2.866	*	2.602	*
TI	.000	*	.004	*	.000	*	.000	*	.000	*	.008	*	.003	*	.000	*
CR	.000	*	.000	*	.000	*	.000	*	.000	*	.000	*	.000	*	.000	*
FE	1.955	*	1.895	*	2.064	*	2.093	*	1.800	*	3.087	*	2.801	*	2.318	*
MN	.000	*	.000	*	.000	*	.000	*	.003	*	.026	*	.021	*	.012	*
MG	7.929	*	7.503	*	7.051	*	8.016	*	7.773	*	5.121	*	5.557	*	7.073	*
CA	.000	*	.000	*	.000	*	.009	*	.002	*	.039	*	.041	*	.000	*
NA	.000	*	.000	*	.008	*	.000	*	.000	*	.023	*	.027	*	.000	*
BA	.000	*	.000	*	.000	*	.000	*	.000	*	.000	*	.000	*	.000	*
K	.000	12.077	.126	11.886	.201	11.890	.018	12.094	.015	11.959	.396	11.516	.127	11.443	.000	12.005
F	.081	*	.088	*	.070	*	.146	*	.074	*	.153	*	.122	*	.056	*
CL	.000	*	.000	*	.000	*	.000	*	.000	*	.000	*	.003	*	.000	*
O	28.000	*	28.000	*	28.000	*	28.000	*	28.000	*	28.000	*	28.000	*	28.000	*
FE	19.78		20.16		22.65		20.70		18.80		37.61		33.51		24.68	
MG	80.22		79.84		77.35		79.30		81.20		62.39		66.49		75.32	
F/M	.247		.253		.293		.261		.232		.608		.508		.329	
F/FM	.198		.202		.226		.207		.188		.378		.337		.248	

9 13e2: another spot in previous grain
10 13e2: yet another spot in previous grain
11 13e2: chlorite-after-phlogopite, Area #3-3
12 13e2: chlorite-after-phlogopite, Plate 4.2c, spot 3
13 Subarkosic Fe arenite (Fe-poor) SAMPLE 13k:
14 I.F. SAMPLE 19E2: chlorite-after-biotite
15 19E2: another spot in previous grain
16 19E2: adjacent individual grain

CHLORITE: analyses from samples collected at stratigraphic section #7 at Iron Peak, Manunda

	17	18	19	20	21	22	23	24
SIO2	23.69	23.90	24.50	23.95	22.89	23.81	25.82	28.90
TIO2	.13	.12	.04	.13	.16	.18	.05	.17
AL2O3	20.10	20.53	20.03	20.77	20.45	20.24	21.07	20.48
CR2O3	.02	.02	.00	.00	.00	.00	.00	.00
FEO	34.16	34.31	34.60	34.95	34.87	35.72	22.40	19.86
MNO	.05	.10	.09	.14	.05	.10	.06	.00
MGO	8.87	8.44	9.20	8.78	8.17	8.76	18.12	16.23
CAO	.02	.01	.03	.16	.02	.00	.00	.00
NA2O	.00	.00	.00	.00	.00	.00	.00	.00
K2O	.00	.00	.00	.01	.00	.00	.00	1.35
BAO	.08	.06	.07	.10	.02	.13	.00	.00
F	.26	.34	.34	.28	.36	.36	.04	.00
CL	.03	.01	.03	.02	.03	.02	.01	.01
SUM	87.41	87.84	88.93	89.27	87.02	89.32	87.57	87.00
-O = F+CL	.12	.15	.15	.12	.16	.16	.02	.00
SUM	87.29	87.69	88.78	89.15	86.86	89.16	87.55	87.00

	17		18		19		20		21		22		23		24	
SI	5.287	*	5.301	*	5.367	*	5.243	*	5.161	*	5.236	*	5.362	*	5.953	*
AL	2.713	8.000	2.699	8.000	2.633	8.000	2.757	8.000	2.839	8.000	2.764	8.000	2.638	8.000	2.047	8.000
AL	2.573	*	2.667	*	2.537	*	2.600	*	2.594	*	2.481	*	2.518	*	2.924	*
TI	.022	*	.020	*	.007	*	.021	*	.027	*	.030	*	.008	*	.026	*
CR	.004	*	.004	*	.000	*	.000	*	.000	*	.000	*	.000	*	.000	*
FE	6.376	*	6.364	*	6.338	*	6.394	*	6.575	*	6.569	*	3.890	*	3.421	*
MN	.009	*	.019	*	.017	*	.026	*	.010	*	.019	*	.011	*	.000	*
MG	2.951	*	2.790	*	3.004	*	2.865	*	2.746	*	2.871	*	5.609	*	4.983	*
CA	.005	*	.002	*	.007	*	.038	*	.005	*	.000	*	.000	*	.000	*
NA	.000	*	.000	*	.000	*	.000	*	.000	*	.000	*	.000	*	.000	*
BA	.007	*	.005	*	.006	*	.009	*	.002	*	.011	*	.000	*	.000	*
K	.000	11.946	.000	11.871	.000	11.915	.003	11.955	.000	11.958	.000	11.980	.000	12.035	.355	11.708
F	.184	*	.238	*	.236	*	.194	*	.257	*	.250	*	.026	*	.000	*
CL	.011	*	.004	*	.011	*	.007	*	.011	*	.007	*	.004	*	.003	*
O	28.000	*	28.000	*	28.000	*	28.000	*	28.000	*	28.000	*	28.000	*	28.000	*
FE		68.36		69.52		67.85		69.06		70.54		69.59		40.95		40.71
MG		31.64		30.48		32.15		30.94		29.46		30.41		59.05		59.29
F/M		2.164		2.288		2.116		2.241		2.398		2.294		.695		.687
F/FM		.684		.696		.679		.691		.706		.696		.410		.407

17 Fe siltstone SAMPLE 7B: network texture, Area #1
18 7B: network texture, Area #2
19 7B: network texture, Area #3
20 7B: network texture, Area #4
21 7B: network texture, Area #5
22 7B: network texture, Area #6
23 Diamictite SAMPLE 7T: within a CLAST
24 7T: another spot in previous grain

CHLORITE: analyses from sample 7T of section #7 at Iron Peak, Manunda

	25	26	27	28
SIO2	25.39	25.60	25.60	25.66
TIO2	.13	.07	.07	.04
AL2O3	21.01	20.46	20.55	20.58
CR2O3	.02	.03	.00	.00
FEO	22.37	23.30	23.18	22.77
MNO	.06	.09	.00	.06
MGO	17.85	17.49	17.44	18.12
CAO	.00	.00	.02	.01
NA2O	.00	.00	.00	.00
K2O	.00	.00	.00	.00
BAO	.06	.01	.00	.00
F	.00	.00	.00	.00
CL	.01	.02	.02	.01
SUM	86.90	87.07	86.88	87.25
-O = F+CL	.00	.00	.00	.00
SUM	86.90	87.07	86.88	87.25

	25		26		27		28	
SI	5.323	*	5.383	*	5.387	*	5.366	*
AL	2.677	8.000	2.617	8.000	2.613	8.000	2.634	8.000
AL	2.514	*	2.452	*	2.483	*	2.438	*
TI	.020	*	011	*	.011	*	.006	*
CR	.003	*	.005	*	.000	*	.000	*
FE	3.922	*	4.097	*	4.079	*	3.982	*
MN	.011	*	.016	*	.000	*	.011	*
MG	5.578	*	5.481	*	5.470	*	5.648	*
CA	.000	*	.000	*	.005	*	.002	*
NA	.000	*	.000	*	.000	*	.000	*
BA	.005	*	.001	*	.000	*	.000	*
K	.000	12.054	.000	12.063	.000	12.048	.000	12.087
F	.000	*	.000	*	.000	*	.000	*
CL	.004	*	.007	*	.007	*	.004	*
O	28.000	*	28.000	*	28.000	*	28.000	*
FE		41.29		42.77		42.72		41.35
MG		58.71		57.23		57.28		58.65
F/M		.705		.750		.746		.707
F/FM		.414		.429		.427		.414

25 7T: subhedral flake within same clast
26 7T: equant monocryst in MATRIX, Area #15-1
27 7T: repeat of previous spot
28 7T: another spot in same grain

Appendix F

ELECTRON MICROPROBE ANALYSES

Carbonate minerals

Ferroan DOLOMITE: analyses from sample $20L_1$ collected at stratigraphic section #20/14 on Holowilena South

	1		2		3		4		5		6		7		8	
FEO	7.14		7.13		3.43		6.97		6.62		2.59		3.04		2.85	
MNO	.33		.42		.15		.39		.41		1.57		1.31		1.80	
MGO	16.91		17.12		19.13		16.89		17.21		19.79		19.57		19.36	
CAO	28.56		28.60		29.58		28.74		28.81		27.94		28.53		27.82	
CO2	47.77		47.77		47.77		47.77		47.77		47.77		47.77		47.77	
SUM	100.71		101.04		100.06		100.76		100.82		99.66		100.22		99.60	
FE	.186	*	.185	*	.089	*	.182	*	.172	*	.067	*	.079	*	.074	*
MN	.009	*	.011	*	.004	*	.010	*	.011	*	.041	*	.034	*	.047	*
MG	.786	*	.794	*	.884	*	.784	*	.798	*	.915	*	.903	*	.897	*
CA	.954	1.934	.953	1.943	.982	1.958	.959	1.936	.960	1.942	.929	1.953	.946	1.962	.927	1.945
C	2.033	2.033	2.028	2.028	2.021	2.021	2.032	2.032	2.029	2.029	2.024	2.024	2.019	2.019	2.027	2.027
O	6.000	*	6.000	*	6.000	*	6.000	*	6.000	*	6.000	*	6.000	*	6.000	*
CAL	49.53		49.33		50.25		49.83		49.74		48.60		49.08		48.83	
DOL	40.80		41.08		45.21		40.74		41.34		47.89		46.84		47.27	
SID	9.67		9.60		4.55		9.43		8.92		3.52		4.08		3.90	
F/M	.237		.233		.101		.232		.216		.073		.087		.082	
F/FM	.191		.189		.091		.188		.177		.068		.080		.076	

1 Lower subarkosic Fe wacke (Fe-poor) layer of SAMPLE $20L_1$:
2 20L1: ferroan dolomite subhed
3 20L1: ferroan dolomite anhed
4 20L1: another ferroan dolomite anhed
5 20L1: lighter rim of zoned ferroan dolomite euhed, spot 1
6 20L1: dark core of previous euhed, spot 2
7 20L1: another spot in dark core of same euhed
8 Upper subarkosic Fe wacke layer of 20L1: euhed core

Ferroan DOLOMITE: analyses from samples collected at section #20/14 on <u>Holowilena South</u> and section #18 on <u>Mount Victor</u>

	9		10		11		12		13		14		15		16	
FEO	6.75		6.88		3.25		6.54		6.82		5.41		5.25		5.56	
MNO	.30		.37		.28		.32		.38		1.41		1.42		1.50	
MGO	17.39		16.72		19.74		17.21		16.30		16.95		17.20		16.80	
CAO	28.47		28.35		29.11		28.53		27.62		28.68		28.63		28.46	
CO2	47.77		47.77		47.77		47.77		47.77		47.77		47.77		47.77	
SUM	100.68		100.09		100.15		100.37		98.89		100.22		100.27		100.09	
FE	.176	*	.18[illegible]	*	.084	*	.171	*	.180	*	.141	*	.137	*	.145	*
MN	.008	*	.0[illegible]	*	.007	*	.008	*	.010	*	.037	*	.038	*	.040	*
MG	.807	*	.7[illegible]	*	.910	*	.800	*	.766	*	.789	*	.800	*	.783	*
CA	.949	1.940	.950	1.920	.965	1.966	.553	1.932	.933	1.889	.960	1.927	.957	1.931	.953	1.922
C	2.030	2.030	2.040	2.040	2.017	2.017	2.034	2.034	2.056	2.056	2.037	2.037	2.034	2.034	2.039	2.039
O	6.000	*	6.000	*	6.000	*	6.000	*	6.000	*	6.000	*	6.000	*	6.000	*
CAL	49.14		49.75		49.25		49.55		49.66		50.78		50.53		50.67	
DOL	41.76		40.82		46.46		41.58		40.77		41.75		42.23		41.61	
SID	9.09		9.42		4.29		8.87		9.57		7.48		7.23		7.73	
F/M	.218		.231		.092		.214		.235		.179		.171		.185	
F/FM	.179		.188		.085		.176		.210		.152		.146		.156	

9 20L1: lighter rim of same zoned ferroan dolomite euhed
10 20L1: another spot in lighter rim of same euhed
11 Fe siltstone layer of 20L1: ferroan dolomite anhed
12 20L1: ferroan dolomite anhed
13 20L1: another ferroan dolomite anhed
14 Carbonate-enriched layer of I.F. SAMPLE $18E_1$: subhed
15 18E1: ferroan dolomite composite
16 18E1: ferroan dolomite subhed

CARBONATE: analyses from iron formation sample $18E_1$ collected at stratigraphic section #18 on <u>Mount Victor</u>

	17	18	19	20	21	22	23	24
FEO	5.78	5.66	5.61	5.54	5.96	5.96	5.78	6.13
MNO	1.58	1.53	1.46	1.39	1.50	1.54	1.28	1.16
MGO	17.01	16.84	17.12	17.29	16.59	16.97	16.96	17.05
CAO	28.80	28.67	28.66	28.77	28.73	28.70	28.96	28.26
CO2	47.77	47.77	47.77	47.77	47.77	47.77	47.77	47.77
SUM	100.94	100.47	100.62	100.76	100.55	100.64	100.75	100.37

	17		18		19		20		21		22		23		24	
FE	.150	*	.148	*	.146	*	.144	*	.156	*	.155	*	.151	*	.160	*
MN	.042	*	.040	*	.039	*	.037	*	.040	*	.041	*	.034	*	.031	*
MG	.789	*	.783	*	.795	*	.802	*	.772	*	.789	*	.787	*	.793	*
CA	.960	1.941	.959	1.930	.957	1.936	.959	1.942	.961	1.928	.949	1.933	.966	1.938	.945	1.929
C	2.029	2.029	2.035	2.035	2.032	2.032	2.029	2.029	2.036	2.036	2.033	2.033	2.031	2.031	2.036	2.036
O	6.000	*	6.000	*	6.000	*	6.000	*	6.000	*	6.000	*	6.000	*	6.000	*

	17	18	19	20	21	22	23	24
CAL	50.55	50.73	50.41	50.34	50.88	50.12	50.75	49.79
DOL	41.53	41.45	41.89	42.09	40.88	41.67	41.35	41.79
SID	7.92	7.82	7.70	7.57	8.24	8.21	7.91	8.43
F/M	.190	.189	.184	.180	.202	.196	.192	.202
F/FM	.160	.159	.155	.180	.168	.164	.161	.168

17 18E1: ferroan dolomite composite
18 18E1: same composite as previous
19 18E1: core of ferroan dolomite subhed
20 18E1: rim of same subhed
21 18E1: ankerite parallelogram
22 18E1: core of ankerite subhed
23 18E1: ferroan dolomite spot in core of previous subhed
24 18E1: ferroan dolomite subhed

CARBONATE: analyses from samples collected at stratigraphic section #10 near Pualco West, <u>Spring Dam</u>

	25		26		27		28		29		30		31		32	
FEO	1.45		1.55		1.67		1.78		1.36		1.46		1.42		1.63	
MNO	1.64		1.76		1.70		1.98		1.81		1.75		.66		.73	
MGO	1.04		1.13		.93		.98		.96		1.03		20.80		20.35	
CAO	50.72		51.63		52.36		51.90		52.03		51.92		29.02		28.74	
CO2	44.00		44.00		44.00		44.00		44.00		44.00		47.77		47.77	
SUM	98.85		100.07		100.66		100.64		100.16		100.16		99.67		99.22	
FE	.041	*	.043	*	.046	*	.050	*	.038	*	.041	*	.037	*	.042	*
MN	.047	*	.050	*	.048	*	.056	*	.051	*	.049	*	.017	*	.019	*
MG	.052	*	.056	*	.046	*	.049	*	.048	*	.051	*	.957	*	.940	*
CA	1.825	1.965	1.845	1.994	1.865	2.006	1.850	2.004	1.858	1.995	1.854	1.995	.960	1.972	.955	1.956
C	2.018	2.018	2.003	2.003	1.997	1.997	1.998	1.998	2.002	2.002	2.002	2.002	2.014	2.014	2.022	2.022
O	6.000	*	6.000	*	6.000	*	6.000	*	6.000	*	6.000	*	6.000	*	6.000	*
CAL	95.16		94.89		95.27		94.96		95.60		95.28		49.13		49.28	
DOL	2.71		2.89		2.35		2.49		2.45		2.63		48.99		48.54	
SID	2.12		2.22		2.37		2.54		1.95		2.09		1.88		2.18	
F/M	.788		.768		1.000		1.020		.792		.804		.039		.045	
F/FM	.441		.434		.500		.505		.442		.446		.037		.043	

25 Carbonate-enriched subarkosic Fe arenite (Fe-poor) layer in I.F. SAMPLE $10d_1$:
26 10d1: calcite anhed
27 10d1: another calcite anhed
28 10d1: same anhed as previous
29 10d1: another calcite anhed
30 10d1: calcite subhed
31 Carbonate SAMPLE 10q1: ferroan dolomite
32 10q1: adjacent ferroan dolomite

DOLOMITE: analyses from samples collected at ($10q_1$) and near ($5A_U$) stratigraphic section #10 on <u>Spring Dam</u>

	33		34		35		36		37		38		39		40	
FEO	1.05		2.37		.61		.92		2.22		.64		6.87		6.44	
MNO	.59		.71		.38		.49		.34		.21		.49		.59	
MGO	20.69		20.32		20.90		20.94		20.74		20.24		17.02		16.78	
CAO	29.60		27.72		29.40		29.98		29.28		27.83		28.45		28.49	
CO2	47.77		47.77		47.77		47.77		47.77		47.77		47.77		47.77	
SUM	99.70		98.89		99.06		100.10		100.35		96.69		100.60		100.07	
FE	.027	*	.062	*	.016	*	.024	*	.057	*	.017	*	.179	*	.168	*
MN	.015	*	.019	*	.010	*	.013	*	.009	*	.006	*	.013	*	.016	*
MG	.952	*	.942	*	.964	*	.961	*	.952	*	.947	*	.791	*	.782	*
CA	.979	1.973	.923	1.945	.975	1.964	.989	1.986	.966	1.984	.936	1.905	.950	1.933	.955	1.921
C	2.013	2.013	2.027	2.027	2.018	2.018	2.007	2.007	2.008	2.008	2.047	2.047	2.033	2.033	2.040	2.040
O	6.000	*	6.000	*	6.000	*	6.000	*	6.000	*	6.000	*	6.000	*	6.000	*
CAL	50.00		47.93		49.87		50.11		48.91		49.27		49.49		50.11	
	48.62		48.87		49.32		48.69		48.20		49.85		41.19		41.05	
SID	1.38		3.20		.81		1.20		2.89		.88		9.33		8.84	
F/M	.028		.066		.017		.025		.060		.018		.226		.215	
F/FM	.028		.062		.016		.024		.056		.018		.185		.177	

33 10q1: dolomite
34 10q1: ferroan dolomite
35 10q1: dolomite, outside circle #2
36 10q1: ferroan dolomite
37 10q1: ferroan dolomite
38 10q1: dolomite
39 Carbonate SAMPLE 5AU (U = upper): ferroan dolomite
40 5Au: ferroan dolomite composite

CARBONATE: analyses from samples collected near section #10 ($5A_U$) and within the adit (BC-1) on <u>Spring Dam</u>

	41	42	43	44	45	46	47	48
FEO	7.17	7.14	6.97	6.28	5.35	6.32	6.78	5.89
MNO	.58	.60	.57	1.23	1.85	1.39	1.27	1.44
MGO	16.41	16.59	16.41	16.72	16.98	16.31	16.09	16.97
CAO	28.15	28.56	28.39	28.98	28.42	28.60	28.88	29.10
CO2	47.77	47.77	47.77	47.77	47.77	47.77	47.77	47.77
SUM	100.08	100.66	100.11	100.98	100.37	100.39	100.79	101.17
FE	.188 *	.186 *	.183 *	.164 *	.140 *	.165 *	.177 *	.153 *
MN	.015 *	.016 *	.015 *	.032 *	.049 *	.037 *	.034 *	.038 *
MG	.766 *	.772 *	.766 *	.776 *	.790 *	.760 *	.749 *	.786 *
CA	.945 1.914	.955 1.929	.952 1.916	.967 1.939	.950 1.929	.958 1.921	.966 1.926	.969 1.946
C	2.043 2.043	2.035 2.035	2.042 2.042	2.031 2.031	2.036 2.036	2.040 2.040	2.037 2.037	2.027 2.027
O	6.000 *	6.000 *	6.000 *	6.000 *	6.000 *	6.000 *	6.000 *	6.000 *
CAL	49.76	49.92	5[illegible]	50.72	50.55	50.87	51.06	50.78
DOL	40.35	40.34	40.29	40.71	42.02	40.36	39.58	41.20
SID	9.89	9.74	9.60	8.58	7.43	8.77	9.36	8.02
F/M	.245	.241	.239	.211	.177	.217	.236	.195
F/FM	.197	.194	.193	.174	.151	.178	.191	.163

41 5Au: ankerite suhed
42 5Au: ankerite anhed
43 5Au: ankerite composite
44 Carbonate-rich Fe arenite lens in I.F. SAMPLE BC-1: ankerite

45 BC-1: ankerite euhed
46 BC-1: ankerite euhed
47 BC-1: ankerite euhed
48 BC-1: ferroan dolomite with apatite?

CARBONATE: analyses from sample 8C-1 collected within the adit through Razorback Ridge, <u>Spring Dam</u>

	49		50		51		52		53		54		55	
FEO	5.93		5.96		8.07		6.28		6.15		6.11		6.40	
MNO	1.34		1.23		1.39		1.28		1.45		1.34		1.37	
MGO	16.40		16.55		15.06		16.46		16.64		16.28		16.66	
CAO	28.43		28.74		28.76		27.78		28.89		28.33		28.60	
CO2	47.77		47.77		47.77		47.77		47.77		47.77		47.77	
SUM	99.87		100.25		101.05		99.57		100.90		99.83		100.80	
FE	.155	*	.156	*	.211	*	.165	*	.160	*	.160	*	.167	*
MN	.036	*	.033	*	.037	*	.034	*	.038	*	.036	*	.036	*
MG	.766	*	.771	*	.703	*	.770	*	.773	*	.761	*	.774	*
CA	.955	1.912	.963	1.922	.965	1.916	.935	1.904	.964	1.936	.952	1.909	.955	1.933
C	2.044	2.044	2.039	2.039	2.042	2.042	2.048	2.048	2.032	2.032	2.046	2.046	2.034	2.034
O	6.000	*	6.000	*	6.000	*	6.000	*	6.000	*	6.000	*	6.000	*
CAL	50.88		50.94		51.35		49.98		50.83		50.82		50.38	
DOL	40.83		40.81		37.41		41.20		40.73		40.63		40.82	
SID	8.28		8.25		11.25		8.82		8.45		8.55		8.80	
F/M	.202		.202		.300		.214		.207		.210		.216	
F/FM	.168		.168		.231		.176		.171		.174		.177	

49 Carbonate-rich Fe arenite layer in 8C-1: ferroan dolomite subhed
50 8C-1: same subhed as previous
51 8C-1: ankerite
52 8C-1: ankerite euhed
53 8C-1: another ankerite euhed
54 8C-1: ankerite subhed
55 8C-1: another ankerite subhed

REFERENCES

ANDERSON, J. B., BRAKE, C., DOMACK, E., MYERS, N. and WRIGHT, R. 1983. Development of a polar glacial-marine sedimentation model from Antarctic quaternary deposits and glaciological information. *In* B. F. Molnia (ed.), Glacial-marine sedimentation. Plenum Press, New York, p. 233-264.

ANDERSON, J. B. and MOLNIA, B. F. 1989. Glacial-marine sedimentation. Short course in Geology, v. 9, 28th International Geological Congress, Washington, D.C., American Geophysical Union, 127 pp.

ANNERSTEN, H. 1968. A mineral chemical study of a metamorphosed iron formation in Northern Sweden. Lithos, v. 1, p. 374-397.

ANNERSTEN, H. and EKSTRÖM, T. 1971. Distribution of major and minor elements in coexisting minerals from a metamorphosed iron formation. Lithos, v. 4, p. 185-204.

BAILEY, S. W. 1984. Classification and structures of the micas. *In* S. W. Bailey (ed.), Micas. Mineral. Soc. of Amer., Reviews in Mineralogy, v. 13, p. 1-12.

BAILEY, S. W. 1988. Chlorites: structures and crystal chemistry. *In* S. W. Bailey (ed.), Hydrous phyllosilicates (exclusive of micas). Mineral. Soc. of Amer., Reviews in Mineralogy, v. 19, p. 347-403.

BARNES, P. W. 1987. Morphologic studies of the Wilkes Land continental shelf, Antarctica - glacial and iceberg effects. *In* S. L. Eittreim and M. A. Hampton (eds.), The Antarctic continental margin: geology and geophysics of offshore Wilkes Land. Circum-Pacific Council for Energy and Mineral Resources, Earth Science Series, v. 5A, p. 175-194.

BARRETT, T. J. 1981. Chemistry and mineralogy of Jurassic bedded chert overlying ophiolites in the north Appenines, Italy. Chem. Geol., v. 34, p. 289-317.

BARRETT, T. J. and FRALICK, P. W. 1984. Sediment redeposition in Archean iron formation: examples from the Beardmore-Geraldton Greenstone Belt, Ontario. Jour. Sed. Petrol., v. 55, p. 205-212.

BARRETT, T. J., FRALICK, P. W. and JARVIS, I. 1988a. Rare-earth-element geochemistry of some Archean iron formations north of Lake Superior, Ontario. Can. Jour. Earth Sci., v. 25, p. 570-580.

BARRETT, T. J. and JARVIS, I. 1988. Rare-earth element geochemistry of metalliferous sediments from DSDP Leg 92: the East Pacific Rise transect. Chem. Geol., v. 67, p. 243-259.

BARRETT, T. J., JARVIS, I., LONGSTAFFE, F. J. and FARQUHAR, R. 1988b. Geochemical aspects of hydrothermal sediments in the eastern Pacific Ocean: an update. Can. Mineral., v. 26, p. 841-858.

BATES, R. L. and JACKSON, J. A. (eds.) 1980. Glossary of geology, second edition. Amer Geol. Inst., Virginia, U.S.A., 751 pp.

BELL, R. T. and JEFFERSON, C. W. 1987. An hypothesis for an Australian-Canadian connection in the Late Proterozoic and the birth of the Pacific Ocean. *In* Proceedings, Pacific Rim Congress '87, Parkville, Victoria. Australas. Inst. Min. Metall., p. 39-50.

BERRY, R. F., FLINT, R. B. and GRADY, A. E. 1978. Deformation history of the Outalpa area and its application to the Olary Province, South Australia. Trans. Roy. Soc. S. Aust., v. 102, p. 43-53.

BINKS, P. J. 1968. ORROROO map sheet, Geological Atlas of South Australia, 1:250,000 series. Sheet SI/54-1. Geol. Surv. S. Aust.

BINKS, P. J. 1971. The geology of the ORROROO 1:250,000 map area. Geol. Surv. S. Aust., Rep. of Invest. 36, 114 pp.

BISCHOFF, J. L. 1969. Red Sea geothermal brine deposits: their mineralogy, chemistry, and genesis. *In* E. T. Degens and D. A. Ross (eds.), Hot brines and recent heavy metal deposits in the Red Sea. Springer-Verlag, New York, p. 368-401.

BONATTI, E. 1975. Metallogenesis at oceanic spreading centers. Ann. Rev. Earth Planet. Sci., v. 3., p. 401-431.

BONATTI, E., FISHER, D. E., JOENSUU, O., RYDELL, H. S. and BEYTH, M. 1972a. Iron-manganese-barium deposit from the northern Afar Rift (Ethiopia). Econ. Geol., v. 67, p. 717-730.

BONATTI, E., KRAEMER, T. and RYDELL, H. 1972b. Classification and genesis of submarine iron-manganese deposits. *In* D. R. Horn (ed.), Ferromanganese deposits on the ocean floor. National Science Foundation, IDOE, Washington, D. C., p. 149-166.

BOSTRÖM, K. 1973. The origin and fate of ferromanganoan active ridge sediments. Stockholm Contr. Geol., v. 27, p. 149-243.

BOSTRÖM, K. 1983. Genesis of ferromanganese deposits - diagnostic criteria for recent and old deposits. *In* P. A. Rona, K. Boström, L. Laubier and K. L. Smith, Jr. (eds.), Hydrothermal processes at seafloor spreading centers. NATO Conference Series, IV, Marine Sciences, v. 12, p. 473-489.

BOSTRÖM, K. and PETERSON, M. N. A. 1969. The origin of aluminum-poor ferromanganoan sediments in areas of high heat flow on the East Pacific Rise. Marine Geol., v. 7, p. 427-447.

BOSTRÖM, K., RYDELL, H. and JOENSUU, O. 1979. Långban--an exhalative sedimentary deposit? Econ. Geol., v. 74, p. 1002-1011.

BOSTRÖM, K. and WIDENFALK, L. 1984. The origin of iron-rich muds at the Kameni Islands, Santorini, Greece. Chem. Geol., v. 42, p. 203-218.

BOULTON, G. S. and DEYNOUX, M. 1981. Sedimentation in glacial environments and the identification of tills and tillites in ancient sedimentary sequencs. Precambrian Res., v. 15, p. 397-422.

BREITKOPF, J. H. 1988. Iron formations related to mafic volcanism and ensialic rifting in the southern margin of the Damara Orogen, Namibia. Precambrian Res., v. 38, p. 111-130.

BUDDINGTON, A. F., FAHEY, J. and VLISIDIS, A. 1955. Thermometric and petrogenetic significance of titaniferous magnetite. Amer. Jour. Sci., v. 253, p. 497-532.

BÜHN, B., STANISTREET, I. G. and OKRUSCH, M. 1992. Late Proterozoic outer shelf manganese and iron deposits at Otjosondu (Namibia) related to the Damara oceanic opening. Econ. Geol., v. 87, p. 1393-1411.

BYRNE, R. H., KUMP, L. R., and CANTRELL, K. J. 1988. The influence of temperature and pH on trace metal speciation in seawater. Marine Chem., v. 25, p. 163-181.

CALVERT, S. E. and PRICE, N. B. 1977. Shallow water, continental margin and lacustrine nodules: distribution and geochemistry. *In* G. P. Glasby (ed.), Marine manganese deposits. Elsevier, Amsterdam, p. 45-86.

CAMPANA, B. 1958. The Mount Lofty-Olary region and Kangaroo Island. *In* M. F. Glaessner and L. W. Parkin (eds.), The Geology of South Australia. Geol. Soc. Aust., Melbourne University Press, p. 3-27.

CAMPANA, B. and KING, D. 1958. Regional geology and mineral resources of the Olary Province. Geol. Surv. S. Aust., Bulletin 34, 133 pp.

CANN, J. H. 1985. Geology of the Bakker Creek Walking Trail, Oraparinna. Flinders Ranges National Park, South Australia. Unpublished guide, Salisbury Campus of the South Australian College of Advanced Education.

CANN, J. H., CLARK, I. F. and FANNING, C. M. 1981. Geology of the Bakker Creek Walking Trail, Oraparinna. Unpublished map, Salisbury Campus of the South Australian College of Advanced Education.

CANN, J. H., CLARK, I. F., COOK, B. J. and SHACKLETON, W. G. 1983. Enorama Diapir contact relationships. *In* Adelaide Geosyncline sedimentary environments and tectonic settings symposium, Adelaide, 1983. Geol. Soc. Aust., Abstracts No. 10, p. 36-38.

CARMICHAEL, D. M. 1969. On the mechanism of prograde metamorphic reactions in quartz-bearing pelitic rocks. Contr. Mineral. and Petrol., v. 20, p. 244-267.

CARMICHAEL, I. S. E. 1967. The iron-titanium oxides of salic volcanic rocks and their associated ferromagnesian silicates. Contr. Mineral. and Petrol., v. 14, p. 36-64.

CIRCOSTA, G. 1978. The stratigraphy of the Sturtian glacigene and ferruginous sediments, southwest of Mattawarrangala Station, Central Flinders Ranges, South Australia. Unpublished B.Sc. thesis, University of Adelaide, Adelaide, South Australia, 29 pp. plus appendices.

CIRCOSTA, G., NEW, D. and GOSTIN, V. A. 1983. Sturtian glaciation, ironstone deposition, penecontemporaneous faulting, northern Yednalue Anticline, central Flinders Ranges, South Australia. *In* Adelaide Geosyncline sedimentary environments and tectonic settings symposium, Adelaide, 1983. Geol. Soc. Aust., Abstracts No. 10, p. 21.

CLARKE, G. L. and POWELL, R. 1989. Basement-cover interaction in the Adelaide Foldbelt, South Australia: the development of an arcuate foldbelt. Tectonophysics, v. 158, p. 209-226.

COATS, R. P. 1962. The control of sedimentation by faulting in the Adelaide System. Geol. Surv. S. Aust., Q. Geol. Notes, no. 4, p. 7-8.

COATS, R. P. 1965. Diapirism in the Adelaide Geosyncline. Aust. Petrol. Explor. Assoc. Jour., v. 5, p. 98-102.

COATS, R. P. 1967. The "Lower Glacial Sequence"--Sturtian type area. Geol. Surv. S. Aust., Q. Geol. Notes, no. 23, p. 1-3.

COATS, R. P. 1973. COPLEY, South Australia. Explanatory Notes, 1:250,000 geological series. Sheet SH/54-9. Geol. Surv. S. Aust., 38 pp.

COATS, R. P. 1981. Late Proterozoic (Adelaidean) tillites of the Adelaide Geosyncline. *In* M. J. Hambrey and W. B. Harland (eds.), Earth's Pre-Pleistocene glacial record. Cambridge University Press, Cambridge, p. 537-548.

COATS, R. P. and FORBES, B. G. 1977. Evidence for two Sturtian glaciations in South Australia -- a reply. Geol. Surv. S. Aust., Q. Geol. Notes, no. 64, p. 19-20.

COATS, R. P. and PREISS W. V. 1987. Stratigraphy of the Umberatana Group. *In* W. V. Preiss (compiler). The Adelaide Geosyncline-- late Proterozoic stratigraphy, sedimentation, palaeontology and tectonics. Geol. Surv. S. Aust., Bulletin 53, p. 125-209.

CONDIE, K. C. 1967. Geochemistry of early Precambrian greywackes from Wyoming. Geochim. Cosmochim. Acta, v. 31, p. 2135-2149.

CONDIE, K. C., MACKE, J. E. and REIMER, T. O. 1970. Petrology and geochemistry of early Precambrian greywackes from the Fig Tree Group, South Africa. Geol. Soc. Amer. Bull., v. 81, p. 2759-2775.

CORLISS, J. B., LYLE, M., DYMOND, J. and CRANE, K. 1978. The chemistry of hydrothermal mounds near the Galapagos Rift. Earth Planet. Sci. Lett., v. 40, p. 12-24.

CROCKET, J. H. and BOWINS, R. J. 1985. Rare earth element properties of Archean iron formations and their host rocks--some results from the Temagami and Boston iron formations. Ontario Geol. Surv., Miscellaneous Paper 127, p. 10-14.

DAILY, B. and FORBES, B. G. 1969. Notes on the Proterozoic and Cambrian, southern and central Flinders Ranges, South Australia. *In* B. Daily (ed.), Geological Excursions Handbook, 41st Aust. N.Z. Assoc. Advmt. Sci. Congr., Adelaide 1969, sect. 3, p. 23-30.

DALGARNO, C. R. 1983a. Marinoan mud islands, Mount Frome, South Australia. *In* Adelaide Geosyncline sedimentary environments and tectonics settings symposium, Adelaide, 1983. Geol. Soc. Aust., Abstracts No. 10, p. 34-35.

DALGARNO, C. R. 1983b. Sturtian and Cambrian growth faults, Oraparinna Diapir. *In* Adelaide Geosyncline sedimentary environments and tectonics settings symposium, Adelaide, 1983. Geol. Soc. Aust., Abstracts No. 10, p. 71-72.

DALGARNO, C. R. and JOHNSON, J. E. 1965. The Holowilena Ironstone, a Sturtian glacigene unit. Geol. Surv. S. Aust., Q. Geol. Notes, no. 13, p. 2-4.

DALGARNO, C. R. and JOHNSON, J. E. 1966. PARACHILNA map sheet, Geological Atlas of South Australia, 1:250,000 series. Sheet SH/54-13. Geol. Surv. S. Aust.

DALGARNO, C. R. and JOHNSON, J. E. 1968. Diapiric structures and Late Precambrian-Early Cambrian sedimentation in Flinders Ranges, South Australia. *In* J. Braunstein and G. D. O'Brien (eds.), Diapirism and Diapirs, a symposium. Amer. Assoc. Petrol. Geol., Memoir 8, p. 301-314.

DALZIEL, I. W. D. 1991. Pacific margins of Laurentia and East Antarctica-Australia as a conjugate rift pair: evidence and implications for an Eocambrian supercontinent. Geology, v. 19, p. 598-601.

DAVIS, J. C. 1973. Statistics and data analysis in geology. John Wiley & Sons, New York, 550 pp.

DEER, W. A., HOWIE, R. A. and ZUSSMAN, J. 1962. Rock-forming minerals, Volume 3, Sheet silicates. Longmans, Green and Co. Ltd., London, 270 pp.

DEER, W. A., HOWIE, R. A. and ZUSSMAN, J. 1966. An introduction to the rock-forming minerals. Longman Group Ltd., London, 528 pp.

DERRY, L. A. and JACOBSEN, S. B. 1990. The chemical evolution of Precambrian seawater: evidence from REEs in banded iron formations. Geochim. Cosmochim. Acta, v. 54, p. 2965-2977.

DICKINSON, W. R. 1970. Interpreting detrital modes of graywacke and arkose. Jour. Sed. Petrol., v. 40, p. 695-707.

DICKINSON, S. B. and SPRIGG, R. C. 1953. Geological structure of South Australia in relation to mineralization. *In* A. B. Edwards (ed.), Geology of Australian ore deposits. 5th Empire Mining and Metallurgical Congress, Australia and New Zealand, Melbourne, 1953. Australas. Inst. Min. Metall., v. 1, p. 426-448.

DIBONA, P. A. 1991. A previously unrecognised Late Proterozoic succession: Upper Wilpena Group, northern Flinders Ranges, South Australia. Geol. Surv. S. Aust., Q. Geol. Notes, no. 117, p. 2-9.

DONNELLY, T. H. 1981. Discussion: Sedimentology, stable-isotope geochemistry and palaeoenvironment of dolostones capping late Precambrian glacial sequences in Australia. Jour. Geol. Soc. Aust., v. 28, p. 99-101.

DOWDESWELL, J. A. and MURRAY, T. 1990. Modelling rates of sedimentation from icebergs. *In* J. A. Dowdeswell and J. D. Scourse (eds.), Glacimarine environments: processes and sediments. Geol. Soc. London, Special Publication No. 53, p. 121-137.

DYMEK, R. F. and KLEIN, C. 1988. Chemistry, petrology and origin of banded iron-formation lithologies f m the 3800 Ma Isua Supracrustal Belt, West Greenland. Precambrian Res., v. 39, p. 247-302.

EISBACHER, G. H. 1985. Late Proterozoic rifting, glacial sedimentation, and sedimentary cycles in the light of Windermere deposition, western Canada. Palaeogeogr., Palaeoclimatol., Palaeoecol., v. 51, p. 231-254.

ELDERFIELD, H. 1988. The oceanic chemistry of the rare-earth elements. Phil. Trans. Roy. Soc. London, Series A, v. 325, p. 105-126.

ELDERFIELD, H. and GREAVES, M. J. 1982. The rare earth elements in seawater. Nature, v. 296, p. 214-219.

ELDERFIELD, H., UPSTILL-GODDARD, R. and SHOLKOVITZ, E. R. 1990. The rare earth elements in rivers, estuaries, and coastal seas and their significance to the composition of ocean waters. Geochim. Cosmochim. Acta, v. 54, p. 971-991.

EYLES, C. H., EYLES, N. and MIALL, A. D. 1985. Models of glaciomarine sedimentation and their application to the interpretation of ancient glacial sequences. Palaeogeogr., Palaeoclimatol., Palaeoecol., v. 51, p. 15-84.

FAIRCHILD, I. J. and SPIRO, B. 1990. Carbonate minerals in glacial sediments: geochemical clues to palaeoenvironment. *In* J. A. Dowdeswell and J. D. Scourse (eds.), Glacimarine environments: processes and sediments. Geol. Soc. London, Special Publication No. 53, p. 201-216.

FANNING, C. M., LUDWIG, K. R., FORBES, B. G. and PREISS, W. V. 1986. Single and multiple grain U-Pb zircon analyses for the early Adelaidean Rook Tuff, Willouran Ranges, South Australia. *In* 8th Australian Geological Convention, Adelaide, 1986. Geol. Soc. Aust., Abstracts No. 15, p. 71-72.

FLEET, A. J. 1983. Hydrothermal and hydrogenous ferro-manganese deposits: do they form a continuum? The rare earth element evidence. *In* P. A. Rona, K. Boström, L. Laubier and K. L. Smith, Jr. (eds.), Hydrothermal processes at seafloor spreading centers. NATO Conference Series, IV, Marine Sciences, v. 12, p. 535-55. .

FLORAN, R. J. and PAPIKE, J. J. 1978. Mineralogy and petrology of the Gunflint Iron Formation, Minnesota-Ontario: correlation of compositional and assemblage variations at low to moderate grade. Jour. Petrol., v. 19, p. 215-288.

FORBES, B. G. 1970. Benda Siltstones. Geol. Surv. S. Aust., Q. Geol. Notes, no. 33, p. 1-2.

FORBES, B. G. 1972. PARACHILNA, South Australia. Explanatory Notes, 1:250,000 geological series. Sheet SH/54-13. Geol. Surv. S. Aust., 24 pp.

FORBES, B. G. (compiler) 1989. OLARY map sheet. Geological Atlas of South Australia, 1:250,000 series. Sheet SI/54-2. Geol. Surv. S. Aust.

FORBES, B. G. and COOPER, R. S. 1976. The Pualco Tillite of the Olary region, South Australia. Geol. Surv. S. Aust., Q. Geol. Notes, no. 60, p. 2-5.

FREY, M. 1969. Die metamorphose des Keupers vom Tafeljura bis zum Lukmanier-Gebiet (Veränderungen tonig-mergeliger Gesteine vom Bereich der Diagenese bis zur Staurolith-Zone). Beitr. Geol. Karte Schweiz NF 137.

FROST, B. R. 1979. Metamorphism of iron-formation: parageneses in the system Fe-Si-C-O-H. Econ. Geol., v. 74, p. 775-785.

FRYER, B. J. 1977a. Rare earth evidence in iron-formations for changing Precambrian oxidation states. Geochim. Cosmochim. Acta, v. 41, p. 361-367.

FRYER, B. J. 1977b. Trace element geochemistry of the Sokoman Iron Formation. Can. Jour. Earth Sci., v. 14., p. 1598-1610.

GARRELS, R. M. and CHRIST, C. L. 1965. Solutions, minerals and equilibria. Harper and Row, New York, 450 pp.

GARRELS, R. M. and MACKENZIE, F. T. 1971. Evolution of sedimentary rocks. W. Norton and Co., 397 pp.

GLAESSNER, M. F. and PARKIN, L. W. (eds.), 1958. The geology of South Australia. Geol. Soc. Aust., Melbourne University Press, 163 pp.

GOLDSTEIN, S. J. and JACOBSEN, S. J. 1988. Rare earth elements in river waters. Earth Planet. Sci. Lett., v. 89, p. 35-47.

GOVINDARAJU, K. (ed.) 1989. Compilation of working values and sample descriptions for 272 geostandards. Geostandards Newsletter, Special Issue, v. 13, 113 pp.

GRAF, J. L., Jr. 1978. Rare earth elements, iron formation and sea water. Geochim. Cosmochim. Acta, v. 42, p. 1845-1850.

GRAFF, D. A. 1985. Paragenesis of iron formation within the Kingston Peak Formation, southern Death Valley region, California. Unpublished M.Sc. thesis, University of California, Davis, California, 170 pp.

GROSS, G. A. 1983. Tectonic systems and the deposition of iron-formation. Precambrian Res., v. 20, p. 171-187.

GROSS, G. A. 1992. Element distribution patterns as metallogenetic indicators in siliceous metalliferous sediments. International Geological Congress, Kyoto, Japan. Abstracts, p. 754.

GUIDOTTI, C. V. 1984. Micas in metamorphic rocks. *In* S. W. Bailey (ed.), Micas. Mineral. Soc. of Amer., Reviews in Mineralogy, v. 13, p. 357-467.

HAGGERTY, S. E. 1991. Oxide textures - a mini-atlas. *In* D. H. Lindsley (ed.), Oxide minerals: petrologic and magnetic significance. Mineral. Soc. of Amer., Reviews in Mineralogy, v. 25, p. 129-219.

HASKIN, L. A., HASKIN, M. A., FREY, F. A. and WILDEMAN, T. R. 1968. Relative and absolute terrestrial abundances of the rare earths. *In* L. H. Ahrens (ed.), Origin and distribution of the elements. Pergamon Press Ltd., London, p. 889-912.

HASLETT, P.G. 1983. Lower Cambrian syndepositional tectonics at Wirrealpa, South Australia. *In* Adelaide Geosyncline sedimentary environments and tectonic settings symposium, Adelaide, 1983. Geol. Soc. Aust., Abstracts No. 10, p. 55-56.

HEIN, F. J. 1979. Deep-sea valley-fill sediments: Cap Enragé Formation, Québec. Unpublished Ph.D. thesis, McMaster University, Hamilton, Ontario, 514 pp.

HEIN, F. J. 1982. Depositional mechanisms of deep-sea coarse clastic sediments, Cap Enragé Formation, Quebec. Can. Jour. Earth Sci., v. 19, p. 267-287.

HEIN, F. J. and WALKER, R. G. 1982. The Cambro-Ordovician Cap Enragé Formation, Québec, Canada: conglomeratic deposits of a braided submarine channel with terraces. Sedimentology, v. 29, p. 309-329.

HEINRICH, E. W. 1965. Microscopic identification of minerals. McGraw-Hill Inc., U.S.A., 414 pp.

HENRY, G., STANISTREET, I. G. and MAIDEN, K. J. 1986. Preliminary results of a sedimentological study of the Chuos Formation in the Central Zone of the Damara Orogen: evidence for mass flow processes and glacial activity. Communs Geol. Surv. S. W. Africa/Namibia, v. 2, p. 75-92.

HOLLAND, H. D. and MALININ, S. D. 1979. The solubility and occurrence of non-ore minerals. *In* H. L. Barnes (ed.), Geochemistry of hydrothermal ore deposits, second edition. John Wiley & Sons, New York, p. 461-508.

HONNOREZ, J., von HERZEN, R. P., BARRETT, T. J., BECKER, K., BENDER, M. L., BORELLA, P. E., HUBBERTEN, H.-W., JONES, S. C., KARATO, S., LAVERNE, C., LEVI, S., MIGDISOV, A. A., MOORBY, S. A. and SCHRADER, E. L. 1981. Hydrothermal mounds and young ocean crust of the Galapagos: preliminary deep sea drilling results, Leg 70. Geol. Soc. Amer. Bull., v. 92, p. 457-472.

HOPPE, A., SCHOBBENHAUS, C. and WALDE, D. 1987. Precambrian iron formation in Brazil. *In* P. W. U. Appel and G. L. LaBerge (eds.), Precambrian iron-formations. Theophrastus Publications, Athens, Greece, p. 347-390.

HOUNSLOW, A. W. and J. M. MOORE, JR. 1967. Chemical petrology of Grenville schists near Fernleigh, Ontario. Jour. Petrol., v. 8, p. 1-28.

INESON, P. R. 1989. Introduction to practical ore microscopy. Longman Group Ltd., Harlow, England, 181 pp.

INGRAM, R. L. 1954. Terminology for the thickness of stratification and parting units in sedimentary rocks. Geol. Soc. Amer. Bull., v. 65, p. 937-938.

INGRI, J. and PONTÉR, C. 1987. Rare earth abundance patterns in ferromanganese concretions from the Gulf of Bothnia and the Barents Sea. Geochim. Cosmochim. Acta, v. 51, p. 155-161.

IXER, R. A., TURNER, P. and WAUGH, B. 1979. Authigenic iron and titanium oxides in Triassic red beds: St. Bees Sandstone, Cumbria, northern England. Geol. Jour., v. 14, p. 179-192.

JACK, R. L. 1922. The iron ore resources of South Australia. Geol. Surv. S. Aust., Bulletin 9, 71 pp.

JAMES, H. L. 1954. Sedimentary facies of iron formation. Econ. Geol., v. 49, p. 235-291.

JAMES, H. L. 1969. Comparison between Red Sea deposits and older ironstone and iron-formation. *In* E. T. Degens and D. A. Ross (eds.), Hot brines and recent heavy metal deposits in the Red Sea. Springer-Verlag, New York, p. 525-532.

JENKINS, R. J. F. 1989. The Adelaide Fold Belt: tectonic reappraisal. *In* J. B. Jago and P. S. Moore (eds.), The evolution of a Late Precambrian--Early Palaeozoic rift complex: The Adelaide Geosyncline. Geol. Soc. Aust., Special Publication No. 16, p. 396-420.

JIAFU, T., HEQIN, F. and ZHIQING, Y. 1987. Stratigraphy, type and formation conditions of the late Precambrian banded iron ores in south China. Chinese Jour. Geochem., v. 6, p. 331-341.

JOLLY, W. T., DICKIN, A. P. and WU, C. T. 1992. Geochemical stratigraphy of the Huronian continental volcanics at Thessalon, Ontario: contributions of two-stage crustal fusion. Contr. Mineral. and Petrol., v. 110, p. 411-428.

KAUFMAN, A. J., HAYES, J. M., KNOLL, A. H. and GERMS, G. J. B. 1991. Isotopic compositions of carbonates and organic carbon from upper Proterozoic successions in Namibia: stratigraphic variation and the effects of diagenesis and metamorphism. Precambrian Res., v. 49, p. 301-327.

KELLOGG, T. B. and KELLOGG, D. E. 1988. Antarctic cryogenic sediments: biotic and inorganic facies of ice shelf and marine-based ice sheet environments. Palaeogeogr., Palaeoclimatol., Palaeoecol., v. 60, p. 51-74.

KIMBERLEY, M. M. 1978. Paleoenvironmental classifications of iron formations. Econ. Geol., v. 73, p. 215-229.

KIMBERLEY, M. M. 1989. Exhalative origins of iron formations. Ore Geol. Rev., v. 5, p. 13-145.

KLEIN, C., JR. 1966. Mineralogy and petrology of the metamorphosed Wabush Iron Formation, southwestern Labrador. Jour. Petrol., v. 7, p. 246-305.

KLEIN, C., JR. 1973. Changes in mineral assemblages with metamorphism of some banded Precambrian iron-formations. Econ. Geol., v. 68, p. 1075-1088.

KLEIN, C. 1983. Diagenesis and metamorphism of Precambrian banded iron-formations. *In* A. F. Trendall and R. C. Morris (eds.), Iron-formation: facts and problems. Elsevier, Amsterdam, p. 417-490.

KLEIN, C. and BEUKES, N. J. 1989. Geochemistry and sedimentology of a facies transition from limestone to iron-formation deposition in the Early Proterozoic Transvaal Supergroup, South Africa. Econ. Geol., v. 84, p. 1733-1774.

KRAMM, U. 1973. Chloritoid stability in manganese rich low-grade metamorphic rocks, Venn-Stavelot Massif, Ardennes. Contr. Mineral. and Petrol., v. 41, p. 179-196.

KRAUSKOPF, K. B. 1957. Separation of manganese from iron in sedimentary processes. Geochim. Cosmochim. Acta, v. 12, p. 61-84.

LAAJOKI, K. V. and GEHÖR, S. A. 1986. Phosphogenic Precambrian banded iron formations in Finland. 12th International Sedimentological Congress, Canberra, Australia. Abstracts, p. 171.

LALOU, C. 1983. Genesis of ferromanganese deposits: hydrothermal origin. *In* P. A. Rona, K. Boström, L. Laubier and K. L. Smith, Jr. (eds.), Hydrothermal processes at seafloor spreading centers. NATO Conference Series, IV, Marine Sciences, v. 12, p. 503-534.

LEMON, N. M. 1985. Physical modelling of sedimentation adjacent to diapirs and comparison with late Precambrian Oratunga breccia body in central Flinders Ranges, South Australia. Amer. Assoc. Petrol. Geol. Bull., v. 69, p. 1327-1338.

LIEN, R. 1981. Sea bed features in the Blacenga area, Weddell Sea, Antarctica. POAC 81 Proceedings, v. 2, p. 706-716.

LINDSLEY, D. H. 1962. Investigation in the system Fe_2O_3--FeO--TiO_2. Carnegie Inst. Wash. Yearbook 61, p. 100-106.

LINK, P. K. and GOSTIN, V. A. 1981. Facies and palaeogeography of Sturtian glacial strata (late Precambrian), South Australia. Amer. Jour. Sci., v. 281, p. 353-374.

LOBERG, B. E. H. and HORNDAHL, A.-K. 1983. Ferride geochemistry of Swedish Precambrian iron ores. Mineral. Deposita, v. 18, p. 487-504.

LOVELL, J. P. B. and STOW, D. A. V. 1981. Identification of ancient sandy contourites. Geology, v. 9, p. 347-349.

LOWE, D. R. 1976. Grain flow and grain flow deposits. Jour. Sed. Petrol., v. 46, p. 188-199.

LOWE, D. R. 1982. Sediment gravity flows: II. Depostional models with special reference to the deposits of high-density turbidity currents. Jour. Sed. Petrol., v. 52, p. 279-297.

MARCHIG, V., GUNDLACH, H., MÖLLER, P. and SCHLEY, F. 1982. Some geochemical indicators for discrimination between diagenetic and hydrothermal metalliferous sediments. Marine Geol., v. 50, p. 241-256.

MAWSON, D. 1912. Pre-Cambrian areas in the north-eastern portion of South Australia and the Barrier, New South Wales. Rep. Australas. Assoc. Advmt. Sci., v. 13, p. 188-191.

MAWSON, D. 1949. The Late Precambrian Ice-Age and glacial record of the Bibliando Dome. Jour. Proc. Roy. Soc. N.S.W., v.82, no. 2, p. 150-174.

MAWSON, D. and SPRIGG, R. C. 1950. Subdivision of the Adelaide System. Aust. Jour. Sci., v. 13, p. 69-72.

MAYNARD, J. B. 1991. Iron: syngenetic deposition controlled by the evolving ocean-atmosphere system. *In* E. R. Force, J. J. Eidel and J. B. Maynard (eds.), Sedimentary and diagenetic mineral deposits: a basin analysis approach to exploration. Reviews in Economic Geology, v. 5, p. 141-145.

McLENNAN, S. M., FRYER, B. J. and YOUNG, G. M. 1979. Rare earth elements in Huronian (Lower Proterozoic) sedimentary rocks: composition and evolution of the post-Kenoran upper crust. Geochim. Cosmochim. Acta, v. 43, p. 375-388.

McLEOD, R. L. and STANTON, R. L. 1984. Phyllosilicates and associated minerals in some Paleozoic stratiform sulfide deposits of southeastern Australia. Econ. Geol., v. 79, p. 1-22.

MEL'NIK, Yu. P. 1982. Precambrian banded iron-formations: physiochemical conditions of formation. Elsevier, Amsterdam, 310 pp.

MIDDLETON, G. V. 1967. Experiments on density and turbidity currents. III. Deposition of sediment. Can. Jour. Earth Sci., v. 4, p. 475-505.

MILES, K. R. 1951. Inspection of iron ores near Radium Hill. S. Aust. Dept. Mines, Unpublished Report Book 30/53, 3 pp.

MILLER, J. M. G. 1985. Glacial and syntectonic sedimentation: the upper Proterozoic Kingston Peak Formation, southern Panamint Range, eastern California. Geol. Soc. Amer. Bull., v. 96, p. 1537-1553.

MILODOWSKI, A. E. and ZALASIEWICZ, J. A. 1991. Redistribution of rare earth elements during diagenesis of turbidite/hemipelagite mudrock sequences of Llandovery age from central Wales. *In* A. C. Morton, S. P. Todd and P. D. W. Haughton (eds.), Developments in sedimentary provenance studies. Geol. Soc. London, Special Publication No. 57, p. 101-124.

MIRAMS, R. C. 1962. The geology of the Manunda military sheet. Geol. Surv. S. Aust., Rep. of Invest. 19, 40 pp.

MOORES, E. M. 1991. Southwest U.S.-East Antarctic (SWEAT) connection: a hypothesis. Geology, v. 19, p. 425-428.

MOUNT, T. J. 1975. Diapirs and diapirism in the Adelaide "Geosyncline", South Australia. Unpublished Ph.D. thesis, University of Adelaide, Adelaide, South Australia.

MURRELL, B., LINK, P. K. and GOSTIN, V. A. 1977. Evidence of only one Sturtian glacial period in the Copley map area. Geol. Surv. S. Aust., Q. Geol. Notes, no. 64, p. 16-19.

NESBITT, H. W., MacRAE, N. D. and KRONBERG, B. I. 1990. Amazon deep-sea fan muds: light REE enriched products of extreme chemical weathering. Earth Planet. Sci. Lett., v. 100, p. 118-123.

NORRISH, K. and HUTTON, J. T. 1969. An accurate spectrographic method for the analysis of a wide range of geological samples. Geochim. Cosmochim. Acta, v. 33, p. 431-453.

PARKER, A. J. 1983. Tectonic development of the Adelaide fold belt. *In* Adelaide Geosyncline sedimentary environments and tectonic settings symposium, Adelaide, 1983, Geol. Soc. Aust., Abstracts No. 10, p.23-28.

PETTIJOHN, F. J., POTTER, P. E. and SIEVER, R. 1972. Sand and sandstone. Springer-Verlag, New York, 619 pp.

PICKERING, K. T., HISCOTT, R. N. and HEIN, F. J. 1989. Deep-marine environments. Unwin Hyman Ltd., London, 416 pp.

PICKERING, K. T., STOW, D. A. V., WATSON, M. P. and HISCOTT, R. N. 1986. Deep-water facies, processes and models: a review and classification scheme for modern and ancient sediments. Earth-Sci. Rev., v. 23, p. 75-174.

PIPER, D. J. W. 1978. Turbidite muds and silts on deep-sea fans and abyssal plains. *In* D. J. Stanley and G. Kelling (eds.), Sedimentation in submarine canyons, fans, and trenches. Dowden, Hutchinson and Ross, Inc., Stroudsburg, Penn., p. 163-176.

PIPER, D. Z. 1974. Rare earth elements in the sedimentary cycle: a summary. Chem. Geol., v. 14, p. 285-304.

PIPER, D. Z., VEEH, H. H., BERTRAND, W. G. and CHASE, R. L. 1975. An iron-rich deposit from the northeast Pacific. Earth Planet. Sci. Lett., v. 26, p. 114-120.

PITT, G. M. 1971. Progress report of geology: Plumbago 1:63,360 map area. S. Aust. Dept. Mines, Unpublished Report Book 71/63, 41 pp.

PLIMER, I. R. 1983. The association of B- and F-rich rocks with stratiform mineralization. Unpublished Course Notes, Department of Geology, University of Witwatersrand.

PREISS, W. V. 1979. Adelaidean sedimentation: the Adelaide Geosyncline and Stuart Shelf. S. Aust. Dept. Mines, Unpublished Report Book 79-24, 37 pp.

PREISS, W. V. 1983a. Depositional and tectonic contrasts between Burra Group and Umberatana Group sedimentation. *In* Adelaide Geosyncline sedimentary environments and tectonic settings symposium, Adelaide, 1983. Geol. Soc. Aust., Abstracts No. 10, p. 13-16.

PREISS, W. V. (compiler) 1983b. Adelaide Geosyncline and Stuart Shelf: Precambrian and Palaeozoic geology, Geological Atlas Special Series, 1:600,000. Geol. Surv. S. Aust.

PREISS, W. V. 1983c. Geology of the Worumba Anticline. Geological Atlas Special Series, 1:25,000. Geol. Surv. S. Aust.

PREISS, W. V. 1985. Stratigraphy and tectonics of the Worumba Anticline and associated intrusive breccias. Geol. Surv. S. Aust., Bulletin 52, 85 pp.

PREISS, W. V. 1987a. Tectonics of the Adelaide Geosyncline. *In* W. V. Preiss (compiler), The Adelaide Geosyncline--late Proterozoic stratigraphy, sedimentation, palaeontology and tectonics. Geol. Surv. S. Aust., Bulletin 53, p. 255-281.

PREISS, W. V. 1987b. A synthesis of palaeogeographic evolution of the Adelaide Geosyncline. *In* W. V. Preiss (compiler), The Adelaide Geosyncline--late Proterozoic stratigraphy, sedimentation, palaeontology and tectonics. Geol. Surv. S. Aust., Bulletin 53, p. 315-409.

PREISS, W. V. 1987c. Basement to the Adelaide Geosyncline. *In* W. V. Preiss (compiler), The Adelaide Geosyncline--late Proterozoic stratigraphy, sedimentation, palaeontology and tectonics. Geol. Surv. S. Aust., Bulletin 53, p. 35-42.

PREISS, W. V. 1987d. A review of available geochronology for the Adelaidean. *In* W. V. Preiss (compiler), The Adelaide Geosyncline--late Proterozoic stratigraphy, sedimentation, palaeontology and tectonics. Geol. Surv. S. Aust., Bulletin 53, p. 249-254.

PREISS, W. V. 1989. A stratigraphic and tectonic overview of the Adelaide Geosyncline, South Australia. *In* J. B. Jago and P. S. Moore (eds.), The evolution of a Late Precambrian--Early Palaeozoic rift complex: The Adelaide Geosyncline. Geol. Soc. Aust., Special Publication No. 16, p. 1-33.

PREISS, W. V. and FORBES, B. G. 1987. Introductory remarks. *In* W. V. Preiss (compiler), The Adelaide Geosyncline--late Proterozoic stratigraphy, sedimentation, palaeontology and tectonics. Geol. Surv. S. Aust., Bulletin 53, p. 11-20.

RICHERT, J. P. 1976. Thrust faulting in the northern Flinders Ranges, South Australia. Jour. Geol. Soc. Aust., v. 23, p. 361-366.

ROBERTSON, A. H. F. and HUDSON, J. D. 1973. Cyprus umbers: chemical precipitates on a Tethyan ocean ridge. Earth Planet. Sci. Lett., v. 18, p. 93-101.

ROBERTSON, A. H. F. and BOYLE, J. F. 1983. Tectonic setting and origin of metalliferous sediments in the Mesozoic Tethys Ocean. *In* P. A. Rona, K. Boström, L. Laubier and K. L. Smith, Jr. (eds.), Hydrothermal processes at seafloor spreading centers. NATO Conference Series, IV, Marine Sciences, v. 12, p. 595-663.

RUHLIN, D. E. and OWEN, R. M. 1986. The rare earth element geochemistry of hydrothermal sediments from the East Pacific Rise: examination of a seawater scavenging mechanism. Geochim. Cosmochim. Acta, v. 50, p. 393-400.

RUTLAND, R. W. R. 1973. Tectonic evolution of the continental crust of Australia. *In* D. H. Tarling and S. K. Runcorn (eds.), Continental drift, sea floor spreading and plate tectonics: implications to the earth sciences. Academic Press, London, p. 1003-1025.

RUTLAND, R. W. R., PARKER, A. J., PITT, G. M., PREISS, W. V. and MURRELL, B. 1981. The Precambrian of South Australia. *In* D. R. Hunter (ed.), Precambrian of the Southern Hemisphere. Developments in Precambrian geology series, 2. Elsevier, Amsterdam, p. 309-360.

SAYLES, F. L. and BISCHOFF, J. L. 1973. Ferromanganoan sediments in the equatorial East Pacific. Earth Planet. Sci. Lett., v. 19, p. 330-336.

SCHNEIBNER, E. 1973. A plate tectonic model of the Palaeozoic tectonic history of New South Wales. Jour. Geol. Soc. Aust., v. 20, p. 405-426.

SLACK, J. F. 1982. Tourmaline in Appalachian-Caledonian massive sulphide deposits and its exploration significance. Trans. Inst. Min. Metall., Section B, v. 91, p. B81-B89.

SPRIGG, R. C. 1952. Sedimentation in the Adelaide Geosyncline and the formation of the continental terrace. *In* M. F. Glaessner and E. A. Rudd (eds.), Sir Douglas Mawson Anniversary Volume. University of Adelaide, Adelaide, p. 153-159.

SPRIGG, R. C. 1954. Geology of the Radium Hill Mining Field. Geol. Surv. S. Aust., Bulletin 30, p. 7-69.

STANTON, R. L. 1976. Petrochemical studies of the ore environment at Broken Hill, New South Wales: 2--regional metamorphism of banded iron formations and their immediate associates. Trans. Inst. Min. Metall., Section B, v. 85, p. B118-B131.

STANTON, R. L. 1989. The precursor principle and the possible significance of stratiform ores and related chemical sediments in the elucidation of processes of regional metamorphic mineral formation. Phil. Trans. Roy. Soc. London, Series A, v. 328, p. 529-646.

STOW, D. A. V. and BOWEN, A. J. 1980. A physical model for the transport and sorting of fine-grained sediment by turbidity currents. Sedimentology, v. 27, p. 31-46.

STOW, D. A. V. and LOVELL, J. P. B. 1979. Contourites: their recognition in modern and ancient sediments. Earth-Sci. Rev., v. 14, p. 251-291.

TAYLOR, S. R. and McLENNAN, S. M. 1985. The continental crust: its composition and evolution. Blackwell Scientific Publications Ltd., 312 pp.

THOMAS, W. N. 1950. Investigation of the Braemar Ironstone Deposits. S. Aust. Dept. Mines, Unpublished Report Book 27/99, 7 pp.

THOMSON, B. P. 1969a. Precambrian basement cover: the Adelaide System. *In* L. W. Parkin (ed.), Handbook of South Australian geology. Geol. Surv. S. Aust., p. 49-83.

THOMSON, B. P. 1969b. Precambrian crystalline basement. *In* L. W. Parkin (ed.), Handbook of South Australian geology. Geol. Surv. S. Aust., p. 21-48.

THOMSON, B. P. 1969c. Palaeozoic Era. *In* L. W. Parkin (ed.), Handbook of South Australian geology. Geol. Surv. S. Aust., p. 97-108.

THOMSON, B. P. 1970. A review of the Precambrian and lower Palaeozoic tectonics of South Australia. Trans. Roy. Soc. S. Aust., v. 94, p. 193-221.

THOMSON, B. P., COATS, R. P., MIRAMS, R. C., FORBES, B. G., DALGARNO, C. R. and JOHNSON, J. E. 1964. Precambrian rock groups in the Adelaide Geosyncline: a new subdivision. Geol. Surv. S. Aust., Q. Geol. Notes, no. 9, p. 1-19.

THOMSON, B. P., DAILY, B., COATS, R. P. and FORBES, B. G. 1976. Late Precambrian and Cambrian geology of the Adelaide "geosyncline" and Stuart Shelf, South Australia. 25th Int. geol. Congr., Sydney, 1976, Excursion Guide No. 33A, 53 pp.

TILL, R. 1974. Statistical methods for the earth scientist: An introduction. John Wiley & Sons, New York, 154 pp.

TOTH, J. R. 1980. Deposition of submarine crusts rich in manganese and iron. Geol. Soc. Amer. Bull., v. 91, p. 44-54.

TRENDALL, A. F. 1973. Precambrian iron formtions of Australia. Econ. Geol., v. 68, p. 1023-1034.

TRENDALL, A. F. 1983. Introduction. *In* A. F. Trendall and R. C. Morris (eds.), Iron-formation: facts and problems. Elsevier, Amsterdam, p. 1-12.

TUCKER, M. E. 1981. Sedimentary petrology: an introduction. Wiley, 252 pp.

URBAN, H., STRIBRNY, B. and LIPPOLT, H. J. 1992. Iron and manganese deposits of the Urucum district, Mato Grosso do Sul, Brazil. Econ. Geol., v. 87, p. 1375-1392.

VISSER, J. N. J. 1991. The paleoclimatic setting of the late Paleozoic marine ice sheet in the Karoo Basin of southern Africa. *In* J. B. Anderson and G. M. Ashley (eds.), Glacial marine sedimentation; paleoclimatic significance. Geol. Soc. Amer., Special Paper 261, p. 181-189.

von der BORCH, C. C. 1980. Evolution of late Proterozoic to early Palaeozoic Adelaide Foldbelt, Australia: comparisons with post-Permian rifts and passive margins. Tectonophysics, v. 70, p. 115-134.

WALKER, R. G. 1985. Mudstones and thin-bedded turbidites associated with the Upper Cretaceous Wheeler Gorge conglomerates, California: a possible channel-levee complex. Jour. Sed. Petrol., v. 55, p. 279-290.

WALKER, R. G. and MUTTI, E. 1973. Turbidite facies and facies associations. *In* G. V. Middleton and A. H. Bouma (eds.), Turbidites and deep-water sedimentation. Soc. Econ. Paleontol. Mineral., Short Course Notes, Anaheim, p. 119-157.

WEBB, A. W., COATS, R. P., FANNING, C. M. and FLINT, R. B. 1983. Geochronological framework of the Adelaide Geosyncline. *In* Adelaide Geosyncline sedimentary environments and tectonic settings symposium, Adelaide, 1983. Geol. Soc. Aust., Abstracts No. 10, p. 7-9.

WEDEPOHL, K. H. (ed.), 1978. Handbook of geochemistry, v. 2, parts 1-5, Springer-Verlag, Berlin, Germany.

WHITE, A. H. 1983. Speculations on the Adelaide Rift and the origin of diapirs. *In* Adelaide Geosyncline sedimentary environments and tectonic settings symposium, Adelaide, 1983. Geol. Soc. Aust., Abstracts No. 10, p. 3-6.

WHITTEN, G. F. 1965. Iron ore deposits in South Australia outside the Middleback Ranges. *In* J. McAndrew (ed.), Geology of Australian ore deposits, second edition. 8th Commonwealth Mining and Metallurgical Congress, Australia and New Zealand, Melbourne, 1965, p. 309-311.

WHITTEN, G. F. 1966a. The geology of some South Australian iron deposits. Unpublished M.Sc. thesis, University of Adelaide, Adelaide, South Australia, 154 pp.

WHITTEN, G. F. 1966b. Suggested correlation of iron ore deposits within South Australia. Geol. Surv. S. Aust., Q. Geol. Notes, no. 18,p. 7-11.

WHITTEN, G. F. 1970. The investigation and exploitation of the Razorback Ridge iron deposit. Geol. Surv. S. Aust., Rep. of Invest. 33, 165 pp.

WILLIAMS, G. E. 1979. Sedimentology, stable-isotope geochemistry and palaeoenvironment of dolostones capping late Precambrian glacial sequences in Australia. Jour. Geol. Soc. Aust., v. 26, p. 377-386.

WILLIAMS, G. E. 1981. Reply: Sedimentology, stable-isotope geochemistry and palaeoenvironment of dolostones capping late Precambrian glacial sequences in Australia. Jour. Geol. Soc. Aust., v. 28, p. 102-105.

WONDER, J. D., SPRY, P. G. and WINDOM, K. E. 1988. Geochemistry and origin of manganese-rich rocks related to iron-formation and sulfide deposits, western Georgia. Econ. Geol., v. 83, p. 1070-1081.

WORSLEY, T. R. and KIDDER, D. L. 1991. First-order coupling of paleogeography and CO_2 with global surface temperature and its latitudinal contrast. Geology, v. 19, p. 1161-1164.

WRIGHT, R. and ANDERSON, J. B. 1982. The importance of sediment gravity flow to sediment transport and sorting in a glacial marine environment: eastern Weddell Sea, Antarctica. Geol. Soc. Amer. Bull., v. 93, p. 951-963.

WRIGHT, R., ANDERSON, J. B. and FISCO, P. P. 1983. Distribution and association of sediment gravity flow deposits and glacial/glacial-marine sediments around the continental margin of Antarctica. *In* B. F. Molnia (ed.), Glacial-marine sedimentation. Plenum Press, New York, p. 265-300.

YEO, G. M. 1981. The Late Proterozoic Rapitan glaciation in the northern Cordillera. *In* F. H. A. Campbell (ed.), Proterozoic basins of Canada. Geol. Surv. Can., Paper 81-10, p. 25-46.

YEO, G. M. 1984. The Rapitan Group: relevance to the global association of Late Proterozoic glaciation and iron-formation. Unpublished Ph.D. thesis, University of Western Ontario, London, Ontario, 603 pp.

YEO, G. M. 1986. Iron-formation in the late Proterozoic Rapitan Group, Yukon and Northwest Territories. *In* J. A. Morin (ed.), Mineral deposits of the northern Cordillera. Can. Inst. Min. Metall., Special Volume 37, p. 142-153.

YOUNG, G. M. 1976. Iron-formation and glaciogenic rocks of the Rapitan Group, Northwest Territories, Canada. Precambrian Res., v. 3, p. 137-158.

YOUNG, G. M. 1988. Proterozoic plate tectonics, glaciation and iron-formations. Sediment. Geol., v. 58, p. 127-144.

YOUNG, G. M. 1989. Glaciation and tectonics. Episodes, v. 12, p. 117.

YOUNG, G. M. 1991. The geologic record of glaciation: relevance to the climatic history of Earth. Geoscience Canada, v. 18, p. 100-108.

YOUNG, G. M. 1992a. Late Proterozoic stratigraphy and the Canada-Australia connection. Geology, v. 20, p. 215-218.

YOUNG, G. M. 1992b. Neoproterozoic glaciation in the Broken Hill area, New South Wales, Australia. Geol. Soc. Amer. Bull., v. 104, p. 840-850.

YOUNG, G. M. and GOSTIN, V. A. 1988. Stratigraphy and sedimentology of Sturtian glacigenic deposits in the western part of the north Flinders basin, South Australia. Precambrian Res., v. 39, p. 151-170.

YOUNG, G. M. and GOSTIN, V. A. 1989a. An exceptionally thick upper Proterozoic (Sturtian) glacial succession in the Mount Painter area, South Australia. Geol. Soc. Amer. Bull., v. 101, p. 834-845.

YOUNG, G. M. and GOSTIN, V. A. 1989b. Depositional environment and regional stratigraphic significance of the Serle Conglomerate: a Late Proterozoic submarine fan complex, South Australia. Palaeogeogr., Palaeoclimatol., Palaeoecol., v. 71, p. 237-252.

YOUNG, G. M. and GOSTIN, V. A. 1990. Sturtian glacial deposition in the vicinity of the Yankaninna Anticline, North Flinders Basin, South Australia. Aust. Jour. Earth Sci., v. 37, p. 447-458.

YOUNG, G. M. and GOSTIN, V. A. 1991. Late Proterozoic (Sturtian) succession of the North Flinders Basin, South Australia; an example of temperate glaciation in an active rift setting. *In* J. B. Anderson and G. M. Ashley (eds.), Glacial marine sedimentation; paleoclimatic significance. Geol. Soc. Amer., Special Paper 261, p. 207-222.